



SAPIENZA
UNIVERSITÀ DI ROMA

Sapienza University of Rome

Department of Structural and Geotechnical Engineering

XXXIV PhD cycle

THESIS FOR THE DEGREE OF DOCTOR OF PHILOSOPHY

**Movable Façades for vibration reduction of
buildings**

Thesis Advisor

Prof. Davide Bernardini

Candidate

Giulia Di Giovanni

1580925

Academic Year 2021-2022

This work is licensed under a Creative Commons “Attribution-NonCommercial-NoDerivatives 4.0 International” license.



This thesis has been typeset by \LaTeX and the Sapthesis class.
Author's email: giulia.digiovanni@uniroma1.it

To my family

Abstract

The growing international demand for energy efficiency has paved the way for new attempts in the architectural field, moving towards significant improvements in sustainable building design. The desire to reduce the energy consumption is closely related to the spread of Nearly Zero-Energy Buildings (NZEB) capable of coupling the aesthetic and functional features with energetic aspects to minimize building consumptions. Among the latest generation strategies that have made it possible to achieve this appealing target, façade systems play a fundamental role for the entire building system, not only from an aesthetic point of view but above all in terms of energy saving. Since the nineteenth century, the façade industry has evolved rapidly, leading to the transition from the load-bearing masonry wall to the external self-supporting envelope (the so-called *curtain wall*) and, subsequently, to the shift of climate-energy functions from inside to outside, from which the Double Skin Façade (DSF) system was born. Recently, the concept to let DSF be movable with respect to the structure in order to improve the dynamical response of buildings has been proposed by Moon. While, in the past, the idea to let the cladding surfaces to undergo potentially large displacements, was hindered by the difficulty to realize suitable connections, due to the renewed interaction between technology and architecture, the possibility to realize movable and adaptive façades could nowadays be considered technically feasible. All the above mentioned facts provide the main motivation for the work described in this thesis, which aims to investigate advantages and disadvantages of the use of Movable Façade (MF) for vibration reduction of buildings.

After a critical analysis of the state of the art, in the first part of the work, the performances of buildings equipped with MF are compared to those of analogous structures equipped with standard Tuned Mass Damper (TMD). As compared to classic TMD, MF offer an important advantage stemming from the fact that they use mass already available in the building, without wasting useful indoor space. The analyses show that, despite the strong similarities in the resulting equation of motions, the two systems may exhibit quite different responses and a critical analysis of the differences between the two systems is provided. The comparison shows that, depending on the mass and stiffness ratios, MF can be potentially very efficient in reducing vibrations of the main structure, reaching levels of efficiency even larger than those obtainable by TMD. However, the same study also shows that high efficiency of the MF can be obtained only at the price of displacements of the façade so large to significantly exceed functionally admissible levels. The main outcome of the first part of the work is that the limitation of the façade displacements is the paramount issue to be solved to let any application of MF feasible. Accordingly, the rest of the thesis is devoted to propose solutions aimed to solve this problem.

In the second part of the thesis, a new connection device for MF is proposed. The device combines two main functional principles: a friction slider, inspired by the Variable Friction Cladding Connection (VFCC) device proposed by Laflamme and coworkers, and a system of dissipative bumper dampers, inspired by solutions adopted in the field of seismic pounding. The conception of the device and its nonlinear modeling are addressed in order to identify the main design parameters that influence the performances of the connection.

In the third part of the thesis, the performances of MF connected to the building by simple friction sliders without bumpers are subject to a preliminary evaluation, based on a simplified Two-Degrees-of-Freedom (2DOF) model of a mid-rise RC frame building under harmonic excitation. This study shows that, although the presence of large friction dissipation can be, in some conditions, beneficial, large displacements of the façade remain an issue, hence strongly confirming the need of a complete device equipped with bumpers. The performances of the complete device are then studied by means of parametric nonlinear dynamic analyses aimed to investigate the influence of the main design parameters. The main outcome of this part is that bumpers may be very efficient in reducing the façade displacements while keeping dynamical efficiency. However, it also turns out that the balance between the vibration reduction efficiency and façade displacement control may be delicate, as quite different results can be obtained depending on the frequency of the excitation. This result pointed out the need to re-evaluate the performances of MF under the more realistic situation of a building subject to wind actions, as the combination of several frequencies may give different results with respect to single-harmonic forcing.

In the fourth part of the thesis, a Multi-Degrees-of-Freedom (MDOF) model of the same building considered in the third one, under the action of wind excitation is developed and used to investigate the performances of the MF connected to the structure by the complete device proposed in the second part. The analyses show that the use of connection devices with larger gaps with respect to bumpers provide better performances in terms of structure displacement although in some conditions acceleration performances may be reduced by impacts with bumpers. In the last part of the thesis, the case of the Isozaki tower, a 51-floors, 220-meters tall building recently realized in Milan (Italy) is studied. To mitigate wind-induced vibrations, Isozaki tower has been equipped with four pairs of Viscous Damper (VD) installed on the top of inclined trusses anchored to the façade and to the ground, externally to the building. Since such trusses have a strong impact in the visual appearance of the building, this case is a prominent example of interaction between structural and architectural aspects. The idea has been to redesign the façade of the tower in such a way to let eight cladding blocks to rigidly move, relatively to the structure. A MDOF nonlinear model of the Isozaki tower with a multi-block MF has been realized and the performances of the building under the action of wind has been evaluated. The analyses show that, after a proper calibration of the various design parameters, the MF could achieve the desired serviceability performance levels both in terms of accelerations and displacements, without impacting in a significant way the architecture of the building. In conclusion, although real applications of MF are still to come, this thesis addressed some of the main conceptual issues to be solved. Of course, several other problems remain to be solved, especially at the technological level, but the preliminary results obtained here, seem to confirm that the idea initially advanced by Moon could become applicable.

Keywords: Nearly Zero-Energy Buildings; Double Skin Façade; Movable Façade; Tuned Mass Damper; Friction Slider; Bumper Damper; Tall Building; Wind-induced Vibration.

Sommario

La crescente domanda internazionale di efficienza energetica ha aperto la strada a nuovi tentativi in campo architettonico, orientandosi verso significativi miglioramenti nella progettazione dell'edilizia sostenibile. La volontà di ridurre i consumi energetici è strettamente correlata alla diffusione di Edifici a Energia Quasi Zero (EEQZ) in grado di coniugare le caratteristiche estetiche e funzionali con gli aspetti energetici per ridurre al minimo i consumi degli edifici. Tra le strategie di ultima generazione che hanno permesso di raggiungere questo traguardo, i sistemi di facciata giocano un ruolo fondamentale per l'intero sistema edilizio, non solo dal punto di vista estetico ma soprattutto in termini di risparmio energetico. A partire dal XIX secolo l'industria delle facciate si è evoluta rapidamente, portando al passaggio dalla parete portante in muratura all'involucro esterno autoportante (la cosiddetta "facciata continua") e, successivamente, allo spostamento delle funzioni climatico-energetiche dall'interno verso l'esterno degli edifici, da cui è nata la facciata a doppia pelle. Recentemente, Moon ha proposto l'idea di rendere mobile la facciata a doppia pelle rispetto alla struttura per migliorare la risposta dinamica degli edifici. Se in passato l'idea di far subire alle superfici di rivestimento spostamenti potenzialmente importanti rispetto alla struttura era ostacolata dalla difficoltà di realizzare opportuni collegamenti, grazie alla rinnovata interazione tra tecnologia e architettura, la possibilità di realizzare Facciate Mobili (FM) e adattabili potrebbe oggi essere considerata tecnicamente fattibile. Tutti i fatti sopra citati forniscono la motivazione principale per lo sviluppo del lavoro descritto in questa Tesi, che mira ad indagare vantaggi e svantaggi dell'uso delle FM per la riduzione delle vibrazioni degli edifici.

Dopo un'analisi critica dello stato dell'arte, nella prima parte del lavoro, le prestazioni di edifici dotati di FM vengono confrontate con quelle di analoghe strutture dotate di smorzatori a massa accordata tradizionali, meglio noti come TMD. Rispetto ai classici TMD, le FM offrono un importante vantaggio derivante dal fatto che utilizzano massa già disponibile all'esterno dell'edificio, senza sprecare spazio utile interno. Le analisi mostrano che, nonostante le somiglianze nell'equazione del moto risultante, i due sistemi possono mostrare risposte abbastanza diverse, pertanto, viene fornita un'analisi critica delle differenze tra i due sistemi. Il confronto mostra che, a seconda dei rapporti di massa e rigidità, le FM possono essere potenzialmente molto efficienti nel ridurre le vibrazioni della struttura principale, raggiungendo livelli di efficienza anche maggiori di quelli ottenibili dai TMD; tuttavia l'elevata efficienza delle FM può essere ottenuta solo al prezzo di spostamenti di facciata così grandi da superare i livelli funzionalmente ammissibili. Il principale risultato della prima parte del lavoro è che la limitazione degli spostamenti di facciata è la questione fondamentale da risolvere per rendere fattibile qualsiasi applicazione delle FM.

Nella seconda parte della Tesi viene proposto un nuovo dispositivo di connessione per FM. Il dispositivo combina due principi funzionali principali: un cursore ad attrito ispirato ad un dispositivo di connessione ad attrito variabile proposto da Laflamme e suoi collaboratori, e un sistema di ammortizzatori dissipativi in gomma, ispirato alle soluzioni adottate nel campo del martellamento sismico. La concezione del dispositivo e la sua modellazione non lineare sono affrontate al fine di identificare i principali parametri progettuali che influenzano le prestazioni

della connessione. Nella terza parte della Tesi, le prestazioni delle FM collegate all'edificio da semplici cursori ad attrito senza paraurti sono oggetto di una valutazione preliminare, basata su un modello semplificato a 2 gradi di libertà (GDL) di un edificio medio-alto in c.a. sotto eccitazione armonica. Questo studio mostra che, sebbene la presenza di una grande dissipazione per attrito possa essere, in alcune condizioni, benefica, i grandi spostamenti di facciata rimangono un problema, confermando quindi con forza la necessità di ricorrere a dispositivi completi dotati di paraurti. Le prestazioni del dispositivo completo vengono quindi studiate mediante analisi dinamiche parametriche non lineari volte ad indagare l'influenza dei principali parametri di progetto. Il risultato principale di questa parte è che i paraurti possono essere molto efficienti nel ridurre gli spostamenti di facciata mantenendo l'efficienza dinamica. Tuttavia, risulta anche che l'equilibrio tra l'efficienza di riduzione delle vibrazioni e il controllo degli spostamenti di FM può essere delicato, poiché si possono ottenere risultati molto diversi al variare della frequenza di eccitazione. Questo risultato ha messo in evidenza la necessità di rivalutare le prestazioni delle FM in uno scenario più realistico di edifici soggetti all'azione del vento, poiché la combinazione di più frequenze può fornire risultati diversi rispetto al forza prodotta da una singola armonica.

Nella quarta parte della Tesi viene sviluppato un modello a più-GDL dello stesso edificio considerato nella terza fase, sotto l'azione dell'eccitazione del vento, utilizzato per indagare le prestazioni di FM collegata alla struttura con il dispositivo completo. Le analisi mostrano che l'uso di dispositivi di connessione con gap maggiori rispetto ai paraurti fornisce prestazioni migliori in termini di spostamento strutturale anche se, in alcune condizioni, le prestazioni di accelerazione possono essere ridotte dai contatti con i paraurti. Nell'ultima parte della Tesi viene studiato il caso della torre Isozaki, un edificio di 51 piani alto 220 metri recentemente realizzato a Milano (Italia). Per mitigare le vibrazioni indotte dal vento, la torre Isozaki è stata dotata di quattro coppie di dissipatori viscosi installati alla base di puntoni inclinati ancorati alla facciata, esternamente all'edificio. Poiché tali puntoni hanno un forte impatto sull'aspetto visivo dell'edificio, questo caso è un esempio lampante di interazione tra aspetti strutturali e architettonici. L'idea è stata quella di ridisegnare la facciata della torre in modo tale che gli otto blocchi di rivestimento si muovano rigidamente rispetto alla struttura. È stato realizzato un modello non lineare a più-GDL della torre Isozaki con una FM multiblocco e sono state valutate le prestazioni dell'edificio sotto l'azione del vento. Le analisi mostrano che, dopo un'opportuna calibrazione dei vari parametri progettuali, la FM potrebbe raggiungere i livelli prestazionali desiderati sia in termini di accelerazione che di spostamento, senza incidere in modo significativo sull'architettura dell'edificio. In conclusione, sebbene debbano ancora arrivare applicazioni reali di FM, questa Tesi ha affrontato alcuni dei principali problemi concettuali da risolvere. Naturalmente restano da risolvere altri problemi soprattutto a livello tecnologico, ma i risultati preliminari qui ottenuti sembrano confermare che l'idea inizialmente avanzata da Moon potrebbe diventare applicabile.

Parole chiave: Edifici a Energia Quasi Zero; Facciata a Doppia Pelle; Facciata Mobile; Smorzatore a Massa Accordata; Cursore ad Attrito; Ammortizzatore Dissipativo; Edificio Alto; Azione del Vento.

Acknowledgements

It was a long and tiring journey, marked by continuous, frantic climbs and descents that often disoriented me, making me lose my way. However, the presence of a few people was of great help for me to get up from moments of despair, keeping on the race. For this reason, I would like to say a few words to thank all those who, in one way or another, have been close to me during the entire doctoral course, which lasted longer than expected due to the Covid-19 pandemic.

A dutiful thanks goes to my supervisor, prof. Davide Bernardini, whose indications and wise guidance have accompanied me during these years of study and research. My deepest respect and gratitude go to him, not only for the trust placed in me by accepting the role of supervisor of my Ph.D. Thesis, but above all, for having transmitted to me his unparalleled passion for this subject.

I have to thank my mother, my father, my grandmother, my sister and my partner for the closeness and support, for the love and pride I know they feel for me right now. I do not want to dwell on specific dedications, it is enough for me to say that I am sincerely grateful to each of you because, in your own way, you have contributed to making real a goal that was unbelievable for me until a few years ago.

Humbly, I would also like to dedicate this target to myself, to my resolve, will and determination that have made me overcome countless obstacles to achieve, today, the greatest professional satisfaction of my life.

Giulia Di Giovanni

May 23, 2022

Rome

Ringraziamenti

E' stato un percorso lungo e faticoso, segnato da continue, affannose salite e discese che spesso mi hanno disorientata e fatta smarrire. Tuttavia, la presenza di poche, fondamentali persone è stata per me di grande aiuto per risollevarmi dai momenti di sconforto e proseguire lungo il tragitto. Per questo vorrei spendere due parole per ringraziare tutti coloro che, in un modo o nell'altro, mi sono stati vicino durante l'intero corso di dottorato, durato più del previsto a causa della pandemia da Covid-19.

Un doveroso ringraziamento lo rivolgo al mio supervisore, il prof. Davide Bernardini, le cui indicazioni e la cui guida sapiente mi hanno accompagnata durante questi anni di studio e ricerca. A lui va la mia più profonda stima e gratitudine, non solo per la fiducia riposta in me accettando il ruolo di relatore della mia Tesi di dottorato, ma soprattutto per avermi trasmesso la sua impareggiabile passione verso questa materia.

Ringrazio mia madre, mio padre, mia nonna, mia sorella e il mio fidanzato per la vicinanza e il sostegno, per l'amore e l'orgoglio che so che provano per me in questo momento. Non voglio dilungarmi con dediche specifiche, mi basta dirvi che sono sinceramente grata a ciascuno di voi perché, a modo vostro, avete contribuito a concretizzare un obiettivo per me inimmaginabile fino a pochi anni fa.

Con grande umiltà, vorrei dedicare questo traguardo anche a me stessa, alla mia risolutezza, volontà e determinazione che mi hanno permesso di superare innumerevoli ostacoli fino a raggiungere, oggi, la più grande soddisfazione professionale della mia vita.

Giulia Di Giovanni

23 Maggio 2022

Roma

Contents

1	Introduction	1
1.1	Background	1
1.2	Research objectives and methodology	2
1.2.1	Objectives	2
1.2.2	Methodology	3
1.3	Thesis overview	4
2	State of the art	8
2.1	Introduction	8
2.2	Façade systems	8
2.2.1	Typical façade connections	11
2.2.2	Curtain Wall (CW)	14
2.2.3	Double Skin Façade (DSF)	18
2.2.4	Adaptive Façade	26
2.3	Wind design and performance of tall buildings	29
2.3.1	Wind velocity characterization	31
2.3.2	Simulation domain	35
2.3.3	Digital processing of wind turbulence	37
2.3.4	Equivalent modeling of structures	38
2.3.5	Wind performance criteria	44
2.4	Structural control strategies	48
2.4.1	Aerodynamic Façade	50
2.4.2	Manipulation of structural properties	54
2.4.3	Auxiliary energy-absorbing devices	56
2.4.4	Movable Façade (MF)	59
3	Comparative study between Movable Façades and Tuned Mass Dampers	68
3.1	Introduction	68
3.2	Basic Modeling of MF and TMD	69
3.3	Performance indexes and tuning levels	72
3.3.1	Tuned systems	73
3.3.2	Undertuned systems	74
3.3.3	Overtuned systems	76
3.4	Effect of connection damping	78
3.5	Closing remarks	79
4	Proposal of dissipative sliders for Movable Façades	82
4.1	Introduction	82
4.2	Reference models for the bumper	84

4.2.1	Momentum-based stereomechanical approach	86
4.2.2	Contact force-based models	87
4.2.3	Bilinear truss contact model	91
4.3	Reference model for the slider	95
4.4	Technological development of the connection system	98
4.5	Mechanical characterization of the constitutive behavior	103
4.6	Dynamic characterization of the basic operating modes	109
4.6.1	<i>Sliding</i> mode	110
4.6.2	<i>Sliding-bumping</i> mode	111
4.6.3	<i>Colliding</i> mode	112
4.7	Closing remarks	114
5	Preliminary evaluation of MF under harmonic load	116
5.1	Introduction	116
5.2	Equivalent 2DOF modeling	117
5.2.1	Movable Façade modeling	119
5.3	Description of the case study	126
5.3.1	Sinusoidal modeling	128
5.4	Efficiency measures	130
5.5	Performance of the friction device without bumpers	132
5.6	Performance of the friction device with bumpers	142
5.6.1	Influence of the initial gap	142
5.6.2	Influence of the impact stiffness	148
5.7	Results and discussion	153
5.8	Closing remarks	155
6	Generic building with MF under wind load	158
6.1	Introduction	158
6.2	Generality on the case study	159
6.3	Equivalent MDOF modeling	162
6.4	Wind load simulation	167
6.5	Design of monolithic MF	183
6.5.1	Connector sizing and layout	184
6.5.2	Modeling of the MF connection system	186
6.6	Evaluation of MF dynamic performances	190
6.6.1	Building response with fixed façade	191
6.6.2	Building response with monolithic MF	192
6.6.3	Parametric investigation	196
6.7	Closing remarks	206
7	Isozaki tower with MF under wind load	209
7.1	Introduction	209
7.2	Generality on Isozaki tower	210
7.2.1	Study of the structural system	214
7.2.2	Study of the glazed envelope	217
7.3	Equivalent MDOF modeling	221
7.4	Wind load simulation	226
7.4.1	Preliminary assessment of aeroelastic instability	237
7.5	Design of multiblock MF	240
7.5.1	Connector sizing and layout	242

7.5.2	Modeling of the MF connection system	244
7.6	Evaluation of MF dynamic performances	247
7.6.1	Building response with fixed façade	247
7.6.2	Building response with multiblock MF	249
7.6.3	Parametric investigation	253
7.7	Results and discussion	264
7.8	Closing remarks	266
8	Conclusions	268
	References	273

List of Figures

2.1	Examples of origami-inspired geometric patterns for high-tech building envelopes	10
2.2	Different type of loads affecting the façade structure, including the self-weight of the cladding components, wind load (push and pull forces) and live loads. Source: Knaack, U. et al. (2014). <i>Façades. Principles of Construction</i>	12
2.3	Façade bearing systems: a suspended structure on the left, a single-storey supported structure in the centre and a two-storey supported structure on the right. Source: Knaack, U. et al. (2014). <i>Façades. Principles of Construction</i>	13
2.4	Schematic representation of the three construction areas identified in a typical façade. Source: Knaack, U. et al. (2014). <i>Façades. Principles of Construction</i>	14
2.5	Curtain wall application on Lever House by Skidmore, Owings & Merrill (right) and on the Seagram Building by Ludwig Mies van der Roe (left)	15
2.6	Basic components of a typical curtain wall system	16
2.7	Assembly diagram and application examples of a stick curtain wall system . .	17
2.8	Assembly diagram and application examples of a unitized curtain wall system	17
2.9	Intesa San Paolo skyscraper in Turin (Italy) awarded the LEED Platinum certification in 2015 by the U.S. Green Building Council (USGBC), making it the most ecological European skyscraper	18
2.10	Basic types of DSF: a) box-window façade, b) shaft-box façade, c) corridor façade and d) multi-storey (or second skin) façade	20
2.11	Storey-high box-window façade with ventilation flaps at the top and bottom .	20
2.12	Shaft-box façade with lateral air inlets alternating with continuous ventilation paths	21
2.13	Corridor-type façade with separate air circulation per floor and diagonal flow to avoid recontamination	21
2.14	Multi-storey façade with continuous air cavity that supplies air in the lower part and extracts it in the upper part of the outer skin without the need for openings on each floor	22
2.15	Diagrams of natural ventilation in a) summer: the heat is extracted from the cavity by the stack effect, and b) winter: the outside air is preheated before the immission	23
2.16	Diagrams of mechanical ventilation in a) summer: the cavity is cooled with exhaust air, and b) winter: the exhaust air is re-heated and recirculated . . .	23
2.17	DSF airflow patterns: a) buffer system, b) extract air system, and c) twin face system	24
2.18	Typical annual energy consumption in cooling (left) and heating (right) of a traditional glazed CW and two different types of DSF. Source: Oesterle, E. (2001). <i>Double-Skin Façades: Integrated Planning</i>	25

2.19	Investment costs of a DSF compared with the costs of a conventional glass CW. Source: Streicher, W. (2006). <i>State of the Art of Double Skin Façades in Europe: The results of WP1 of the BESTFAÇADE Project</i>	26
2.20	Conceptual sketches of adaptive façade glass panels. Source: Ribeiro Silveira, R. (2018). <i>Adaptive and composite thin glass concepts for architectural applications</i>	27
2.21	Arab World Institute by Jean Nouvel (Paris, 1987)	27
2.22	Intelligent adaptive envelope of Aedas Architecture's Al Bahar Towers (Abu Dhabi, 2012) that opens and closes following sunrays	28
2.23	Adaptive thin glass facade model. Source: Ribeiro Silveira, R. (2016). <i>Flexible transparency: a study on thin glass adaptive façade panels</i>	28
2.24	Adaptive thin glass façade model with SMA. Source: Miri, B. (2018). <i>Flexible transparency with smart materials: a study on adaptive thin glass façade developed with shape memory alloy</i>	29
2.25	Effect of wind and seismic load on structures with variable fundamental frequency of vibration	30
2.26	Wind speed diagram consisting of a mean and a turbulent component	32
2.27	Typical wind gust	34
2.28	Decomposition of wind load in the along-, across- and torsional direction of a high-rise building. Source: Sinhamahapatra (2019). <i>Along and Across Wind Parameters Acting on Tall Structures</i>	34
2.29	Vibration data analysis in the time- a) and frequency- b) domain	35
2.30	Typical repeated "cell" in reticular structures a) and continuous displacement field b)	39
2.31	Typical equivalent beam models: a) flexural cantilever beam and b) pure shear-type cantilever beam	40
2.32	Rectangular cross-section cantilever beam undergoing free vibrations	41
2.33	First three natural undamped frequencies and modes of vibrations of an elementary cantilever beam	42
2.34	Force-displacement diagram with elastic strain energy highlighted a) and hysteretic cycle with parameters for EVDR computation b)	44
2.35	Performance targets related to wind hazard average return period. Source: Griffis, L.G, et al. (2013). <i>A framework for performance-based wind engineering</i>	45
2.36	Peak acceleration perception thresholds [CNR Figure N.1]	46
2.37	Limit values of peak acceleration with $T_R = 1$ yr [CNR Figure N.2]	47
2.38	Possible strategies for wind-induced vibration control	49
2.39	Summary of typical passive mitigation strategies used to reduce wind-induced dynamic response of tall buildings	50
2.40	On the left, the 829.8-metre-tall Burj Khalifa (Dubai) that is the tallest structure and building in the world; on the center, the 306-metre-tall Cayan Tower, known as Infinity Tower (Dubai), that was the world's tallest high-rise building with a twist of 90° up to 2015; on the right, the 492-metre-tall Shanghai World Financial Center (Shanghai), which is the tenth tallest building in the world	52
2.41	Cross-sectional modifications to improve the aerodynamic performance of high-rise square-based section buildings	52
2.42	Typical shape modifications applied to tall buildings to interrupt the vortex-shedding	53

2.43	Internal structural systems. Source: Moon, K.S. (2018). <i>Advances in Structural Systems for Tall Buildings: Emerging Developments for Contemporary Urban Giants</i>	54
2.44	External structural systems. Source: Moon, K.S. (2018). <i>Advances in Structural Systems for Tall Buildings: Emerging Developments for Contemporary Urban Giants</i>	55
2.45	Force-displacement relation for a) friction device, b) viscoelastic damper, and c) fluid viscous damper	56
2.46	Schematic view of a basic TMD system attached to the primary building structure	58
2.47	Schematic view of a basic TLD system attached to the primary building structure	59
2.48	Schematic view of an Impact Damper (ID) attached to the primary building structure	59
2.49	Blast-induced vibration control with sacrificial metal foam panels and ideal model of blast pressure	60
2.50	Double-layer aluminum façade panels for the absorption of blast loads. Source: Ma, G.W., and Ye, Z.Q. (2007). <i>Energy absorption of double-layer foam cladding for blast alleviation</i>	61
2.51	Connection methods between the façade and the primary building structure obtained through a) a passive control with dampers and springs, and b) an active control with dampers, springs and actuators. Source: T.S., Fu, and Zhang, R. (2016). <i>Integrating Double-Skin Façades and Mass Dampers for Structural Safety and Energy Efficiency</i>	61
2.52	Three-dimensional and cross-sectional view of a four-arm rigid connector (RSC) and a possible four-arm viscoelastic device (VESC). Source: Amadio, C., and Bedon, C. (2012). <i>Viscoelastic spider connectors for the mitigation of cable-supported façades subjected to air blast loading</i>	62
2.53	Integrated DSF-mass damper system. Source: Moon, K.S. (2009). <i>Tall Building Motion Control Using Double Skin Façades</i>	63
2.54	Simplified model of a primary building structure equipped with a) a TMD and b) a MF system connected by an energy dissipation mechanism. Source: Moon, K.S. (2009). <i>Tall Building Motion Control Using Double Skin Façades</i>	65
2.55	Conceptual diagrams on the operation of DSF connectors with low axial stiffness. Source: Moon, K.S. (2009). <i>Tall Building Motion Control Using Double Skin Façades</i>	65
2.56	Variable friction connection device (VFCC) in the double locked (a) and semi-locked (b) configuration. Source: Gong, Y. et al. (2020). <i>Numerical verification of variable friction cladding connection for multihazard mitigation</i>	66
3.1	Schematic representation of a) monolithic MF and b) multiple block MF . . .	69
3.2	2DOF modeling of a building equipped with monolithic MF (a) and standard TMD (b)	70
3.3	On the first line: H_1 transfer functions for TMD (a) and MF (b) with $f = 1.00$, $\xi_1 = 0.03$, $\xi_2 = 0.10$ and $\mu \in [0.05, 0.10]$. The isolated red curves show the amplification of the main structure without any additional mass. On the second line: positive vibration damping efficiency values η for TMD (c) and MF (d). Blue curves correspond to lower μ values, dark red curves to higher μ values	74

3.4	Transfer functions H_2 for the displacement of the secondary masses corresponding to figure 3.3. Blue curves correspond to lower values of μ , dark red curves to higher values of μ	74
3.5	Transfer functions H_1 for TMD (a) and MF (b) and vibration damping efficiencies η for TMD (c) and MF (d) for tuning ratios $f \in [0.2, 1.0]$ and fixed mass ratio ($\mu = 0.05, \xi_1 = 0.03, \xi_2 = 0.10$); blue curves correspond to lower values of f	75
3.6	Transfer functions H_1 for TMD (a) and MF (b) and vibration damping efficiencies η for TMD (c) and MF (d) for $f = 0.4$ and various mass ratios $\mu \in [0.05, 0.10]$ with a zoom on the range $\rho \in [0.8, 1.2]$ in the case of MF (b). The other parameters are the same as in figure 3.5	76
3.7	Transfer functions H_2 for the displacement of the secondary masses corresponding to figure 3.6 for $f = 0.4$ with a zoom on the interval $\rho \in [0.8, 1.2]$ in the case of MF (b). The other parameters are the same as in figure 3.6. Blue curves correspond to lower mass ratios	76
3.8	Transfer functions H_1 for TMD (a) and MF (b) and vibration damping efficiencies η for TMD (c) and MF (d) for tuning ratios $f \in [1.0, 3.0]$ with $\mu = 0.05, \xi_1 = 0.03, \xi_2 = 0.10$. Blue curves correspond to lower values of f	77
3.9	Transfer functions H_1 for TMD (a) and MF (b) and vibration damping efficiencies η for TMD (c) and MF (d) for $f = 1.6$ and $\mu \in [0.05, 0.10]$ with a zoom on the $\rho \in [0.8, 1.2]$ region for the case of MF. The other parameters are the same as in figure 3.8. Blue curves correspond to lower values of μ	77
3.10	Transfer functions H_2 for the displacement of the secondary masses corresponding to figure 3.9 for $f = 1.6$. The other parameters are the same as in figure 3.9. Blue curves correspond to lower values of μ	78
3.11	Effect of the connection damping ratio $\xi_2 \in [0.05, 0.60]$ on the performance of undertuned MF systems for $f = 0.4$ (the other parameters are the same as in figure 3.6). On the left, the vibration damping efficiency, on the right, the transfer functions H_2 . Blue curves correspond to lower damping	79
3.12	Effect of the connection damping ratio $\xi_2 \in [0.05, 0.60]$ on the performance of overtuned MF systems for $f = 1.6$ (the other parameters are the same as in figure 3.9). On the left, the vibration damping efficiency, on the right, the transfer functions H_2 . Blue curves correspond to lower damping	79
4.1	Phases characterizing the impact based on Poisson's hypothesis. Source: Muthukumar, S. (2003). <i>A contact element approach with hysteresis damping for the analysis and design of pounding in bridges</i>	85
4.2	The one degree-of-freedom impact mechanical oscillator with a single rigid constraint	85
4.3	Impact models available in literature: a) linear spring element, b) Kelvin-voigt element, c) Hertz nonlinear spring element and d) Hertz damp model	88
4.4	Hysteresis loop from a) the Kelving-voigt model and b) the application and removal of a compressive force. Source: Muthukumar, S. (2003). <i>A contact element approach with hysteresis damping for the analysis and design of pounding in bridges</i>	89
4.5	Inelastic truss contact element in series with a gap vs. Hertz damp model for impact simulation. Source: Muthukumar, S. (2003). <i>A contact element approach with hysteresis damping for the analysis and design of pounding in bridges</i>	91

4.6	Parameters of the inelastic truss model. Source: Muthukumar, S. (2003). <i>A contact element approach with hysteresis damping for the analysis and design of pounding in bridges</i>	92
4.7	Response of an impact material a) during a pounding event and b) for displacement cycles of increasing amplitude. Source: https://opensees.berkeley.edu/wiki/index.php/Impact_Material	95
4.8	Schematic diagram of the VFCC. Source: Gong et al. (2019). <i>Motion-based design approach for a novel variable friction cladding connection used in wind hazard mitigation</i>	95
4.9	Example of configuration with diagram of forces (a) and picture of the full-scale experimental prototype (b) of the VFCC. Source: Gong et al. (2019). <i>Variable friction cladding connection for seismic mitigation</i>	96
4.10	Force-displacement (a) and force-velocity (b) loops experienced by the VFCC prototype. Source: Gong et al. (2020). <i>Numerical verification of variable friction cladding connection for multihazard mitigation</i>	97
4.11	Layout proposal for the connection system consisting of a dissipative sliding device and two-sided rubber bumpers incorporated into the MF design	99
4.12	Examples of rubber bumper shapes with foldable bulb design for shock- and impact-absorption	99
4.13	Pre-sizing sketches of the sliding connector in the three main design layouts: 1) closed façade, 2) partially open/closed façade and 3) open façade	101
4.14	Force-velocity diagram of friction models: a) Coulomb friction, b) viscous friction combined with Coulomb friction, c) viscous friction combined with Coulomb and static friction and d) Stribeck friction	103
4.15	Frictional behavior of the slider (a) and pure Coulomb friction curve (b)	104
4.16	Force-displacement diagrams of Coulomb friction device for different friction threshold	104
4.17	Bilinear truss contact model in series with a gap for impact simulation (S. Muthukumar, 2003)	105
4.18	Initial stiffness, K_{t_1} , expressed as a function of the yield parameter, a	107
4.19	Secondary stiffness, K_{t_2} , expressed as a function of the yield parameter, a	107
4.20	Strain hardening ratio, γ , expressed as a function of the yield parameter, a	108
4.21	Force-displacement cycle of the friction device with bumpers (c) obtained from a perfect rigid-plastic model (a) and a bilinear contact model in series with a gap (b) combined in parallel	109
4.22	Sample dynamic trajectory related to the <i>sliding</i> mode	110
4.23	Sample dynamic trajectory related to the <i>sliding-bumping</i> mode	112
4.24	Sample dynamic trajectory related to negative <i>colliding</i> mode	113
4.25	Sample dynamic trajectory related to positive <i>colliding</i> mode	113
5.1	Structural frame of the 25-storey mid-rise building subjected to wind pressures (on the left) and 2DOF modeling of the building equipped with a monolithic MF system subjected to harmonic load (on the right)	127
5.2	Frequency-response curves for the maximum displacements of the main structure (a) and façade (b) with $\alpha \in [0.2, 1.0]$. Displacements are normalized with respect to the static displacement P/k_s . It should be noted that the purple curve in (a) related to $\alpha = 1.0$ tends to the response of the structure with fixed façade (red curve)	133
5.3	Force-displacement diagrams of the friction slider for $\alpha \in [0.2, 1.0]$ recorded at low excitation frequency $\rho = 0.5$ (a) and at resonant frequency $\rho = 1.0$ (b)	134

5.4	Absolute displacement of the primary mass (a), relative displacement of the secondary mass (b), relative force-displacement loop of the slider (c), absolute phase portrait of the primary mass (d), absolute phase portrait of the secondary mass (e) and relative phase portrait of the secondary mass (f) for $\alpha \in [0.2, 1.0]$ in correspondence of the superharmonic resonance at $\rho = 0.11$ (1/9)	134
5.5	Absolute displacement of the primary mass (a), relative displacement of the secondary mass (b), relative force-displacement loop of the slider (c), absolute phase portrait of the primary mass (d), absolute phase portrait of the secondary mass (e) and relative phase portrait of the secondary mass (f) for $\alpha \in [0.2, 1.0]$ in correspondence of the superharmonic resonance at $\rho = 0.14$ (1/7)	135
5.6	Absolute displacement of the primary mass (a), relative displacement of the secondary mass (b), relative force-displacement loop of the slider (c), absolute phase portrait of the primary mass (d), absolute phase portrait of the secondary mass (e) and relative phase portrait of the secondary mass (f) for $\alpha \in [0.2, 1.0]$ in correspondence of the superharmonic resonance at $\rho = 0.20$ (1/5)	136
5.7	Absolute displacement of the primary mass (a), relative displacement of the secondary mass (b), relative force-displacement loop of the slider (c), absolute phase portrait of the primary mass (d), absolute phase portrait of the secondary mass (e) and relative phase portrait of the secondary mass (f) for $\alpha \in [0.2, 1.0]$ in correspondence of the superharmonic resonance at $\rho = 0.33$ (1/3)	137
5.8	Absolute displacement of the primary mass (a), relative displacement of the secondary mass (b), relative force-displacement loop of the slider (c), absolute phase portrait of the primary mass (d), absolute phase portrait of the secondary mass (e) and relative phase portrait of the secondary mass (f) for $\alpha \in [0.2, 1.0]$ in correspondence of the primary resonance at $\rho = 1.0$ (1/1)	138
5.9	Phase portraits (absolute velocity-displacement diagrams) of the main structure (a) and façade (b) for $\alpha = 0.2$ in correspondence with the superharmonic resonances recorded at $\rho = 0.14$ (1/7), $\rho = 0.20$ (1/5) and $\rho = 0.33$ (1/3)	138
5.10	Time histories of (a) absolute velocity of the primary mass, v_1 (b) absolute velocity of the secondary mass, v_2 , and (c) relative velocity between the primary and secondary mass, $v_2 - v_1$, for $\alpha = 0.2$ in $\rho \in [0.2, 1.2]$	139
5.11	Time histories of (a) absolute velocity of the primary mass, v_1 (b) absolute velocity of the secondary mass, v_2 , and (c) relative velocity between the primary and secondary mass, $v_2 - v_1$, for $\alpha = 0.5$ in $\rho \in [0.2, 1.2]$	139
5.12	Time histories of (a) absolute velocity of the primary mass, v_1 (b) absolute velocity of the secondary mass, v_2 , and (c) relative velocity between the primary and secondary mass, $v_2 - v_1$, for $\alpha = 0.8$ in $\rho \in [0.2, 1.2]$	140
5.13	Displacement efficiency η (a), acceleration efficiency κ (b) and façade efficiency ζ (c) for $\alpha \in [0.2, 1.0]$	141
5.14	Frequency-response curves for the maximum displacements of the main structure (a) and façade (b) with $g \in [0.1, 0.7]$ m, $\alpha = 0.2$ and $k_h = 300$ MN/m. Displacements are normalized with respect to the static displacement P/k_s . The red curve represents the maximum displacement of the structure without MF	143
5.15	Displacement efficiency η (a), acceleration efficiency κ (b) and façade efficiency ζ (c) with $g \in [0.1, 0.7]$ m, $\alpha = 0.2$ and $k_h = 300$ MN/m	143

5.16	Absolute displacement of the primary mass (a), relative displacement of the secondary mass (b), relative force-displacement loop of the slider (c), absolute phase portrait of the primary mass (d), absolute phase portrait of the secondary mass (e) and relative phase portrait of the secondary mass (f) for $g \in [0.1, 0.7]$ m in correspondence of the superharmonic resonance at $\rho = 0.14$ (1/7)	144
5.17	Absolute displacement of the primary mass (a), relative displacement of the secondary mass (b), relative force-displacement loop of the slider (c), absolute phase portrait of the primary mass (d), absolute phase portrait of the secondary mass (e) and relative phase portrait of the secondary mass (f) for $g \in [0.1, 0.7]$ m in correspondence of the superharmonic resonance at $\rho = 0.33$ (1/3)	144
5.18	Absolute displacement of the primary mass (a), relative displacement of the secondary mass (b), relative force-displacement loop of the slider (c), absolute phase portrait of the primary mass (d), absolute phase portrait of the secondary mass (e) and relative phase portrait of the secondary mass (f) for $g \in [0.1, 0.7]$ m in correspondence of the primary resonance at $\rho = 1.0$	145
5.19	Absolute displacement of the primary mass (a), relative displacement of the secondary mass (b), relative force-displacement loop of the slider (c), absolute phase portrait of the primary mass (d), absolute phase portrait of the secondary mass (e) and relative phase portrait of the secondary mass (f) for $g \in [0.1, 0.7]$ m in correspondence of high-frequency excitation at $\rho = 1.2$. . .	146
5.20	Time histories of (a) absolute velocity of the primary mass, v_1 (b) absolute velocity of the secondary mass, v_2 , and (c) relative velocity between the primary and secondary mass, $v_2 - v_1$, for $g = 0.1$ m in $\rho \in [0.2, 1.2]$	146
5.21	Time histories of (a) absolute velocity of the primary mass, v_1 (b) absolute velocity of the secondary mass, v_2 , and (c) relative velocity between the primary and secondary mass, $v_2 - v_1$, for $g = 0.4$ m in $\rho \in [0.2, 1.2]$	147
5.22	Time histories of (a) absolute velocity of the primary mass, v_1 (b) absolute velocity of the secondary mass, v_2 , and (c) relative velocity between the primary and secondary mass, $v_2 - v_1$, for $g = 0.7$ m in $\rho \in [0.2, 1.2]$	147
5.23	Frequency-response curves for the maximum displacements of the main structure (a) and façade (b) with $k_h \in [100, 500]$ MN/m, $\alpha = 0.2$ and $g = 0.10$ m . Displacements are normalized with respect to the static displacement f/k . The red curve represents the maximum displacement of the structure without MF	149
5.24	Displacement efficiency η (a), acceleration efficiency κ (b) and façade efficiency ζ (c) for $k_h \in [100, 500]$ MN/m	150
5.25	Absolute displacement of the primary mass (a), relative displacement of the secondary mass (b), relative force-displacement loop of the slider (c), absolute phase portrait of the primary mass (d), absolute phase portrait of the secondary mass (e) and relative phase portrait of the secondary mass (f) for $k_h \in [100, 500]$ MN/m at $\rho = 0.14$ (1/7)	151
5.26	Absolute displacement of the primary mass (a), relative displacement of the secondary mass (b), relative force-displacement loop of the slider (c), absolute phase portrait of the primary mass (d), absolute phase portrait of the secondary mass (e) and relative phase portrait of the secondary mass (f) for $k_h \in [100, 500]$ MN/m at $\rho = 0.33$ (1/3)	151

5.27	Absolute displacement of the primary mass (a), relative displacement of the secondary mass (b), relative force-displacement loop of the slider (c), absolute phase portrait of the primary mass (d), absolute phase portrait of the secondary mass (e) and relative phase portrait of the secondary mass (f) for $k_h \in [100, 500]$ MN/m at $\rho = 1.0$	152
5.28	Absolute displacement of the primary mass (a), relative displacement of the secondary mass (b), relative force-displacement loop of the slider (c), absolute phase portrait of the primary mass (d), absolute phase portrait of the secondary mass (e) and relative phase portrait of the secondary mass (f) for $k_h \in [100, 500]$ MN/m at $\rho = 1.2$	152
5.29	Positive efficiency areas for variable friction threshold, α : (a) superposition of the structure efficiency E_η (blue curve) and the façade efficiency E_ζ (orange curve) and (b) acceleration efficiency E_κ	154
5.30	Positive efficiency areas for variable initial gap, g : (a) superposition of the structure efficiency E_η (blue curve) and the façade efficiency E_ζ (orange curve) and (b) acceleration efficiency E_κ	154
5.31	Positive efficiency areas for variable impact stiffness, k_h : (a) superposition of the structure efficiency E_η (blue curve) and the façade efficiency E_ζ (orange curve) and (b) acceleration efficiency E_κ	155
6.1	Diagram of the mid-rise building frame in the YZ plane with a typical floor plan	159
6.2	First three vibrating modes of the 25-storey building FEM implemented in SAP 2000: on the left, 1° flexural mode around y -axis, in the center, 2° flexural mode around x -axis; on the right, 3° torsional mode	161
6.3	Transition from the 25-storey structural frame (a) to an equivalent cantilever beam model (b) subject to a linear distribution of wind pressures, $p(z, t)$. . .	162
6.4	Computation of the core's inertia with respect to the barycentric x -axis, J_x .	164
6.5	Calibration of the equivalent inertia, J_z , as a function of the vibration frequency, f_{target}	166
6.6	Equivalent MDOF model of the mid-rise building with highlighting of the main elements assigned	167
6.7	Different reference speed values for the Italian zones [CNR Figure 3.1]	169
6.8	Diagram of the return coefficient c_r as a function of the return period T_R [CNR Figure 3.2]	170
6.9	Profiles of $c_m(z)$ associated with IV exposure category (a) and $v_m(z)$ associated with $T_R = 1$ yr (b)	171
6.10	NatHaz wind simulator user interface	174
6.11	Turbulent wind velocities, $v_t(t)$, applied on the 2nd ($z = 6.20$ m), 12th ($z = 37.20$ m) and 24th ($z = 74.40$ m) floor of the mid-rise building	175
6.12	Profiles of $c_e(z)$ associated with IV exposure category (a) and $q_p(z)$ associated with $T_R = 1$ yr (b)	177
6.13	Wind pressures, $q(t)$, applied on the 2nd ($z = 6.20$ m), 12th ($z = 37.20$ m) and 24th ($z = 74.40$ m) floor of the mid-rise building	177
6.14	Drag coefficients for rectangular sections [CNR Figure G.49]	178
6.15	Fluctuating wind forces, $F(t)$, applied on the 2nd ($z = 6.20$ m), 12th ($z = 37.20$ m) and 24th ($z = 74.40$ m) floor of the mid-rise building	179
6.16	Profiles of turbulence intensity I_v (a) and length scale L_v (b) for the 77.5 m high generic building used to generate the wind inflow in the longitudinal direction	180

6.17	Cross-sectional detail of the connection device integrated into the monolithic MF portrayed in its partially open/closed layout	185
6.18	Representative diagram of the dissipative slider with bumpers that makes the connection at the i -th floor between the structural mass, $m_{s,i}$, and the façade mass, $m_{MF,i}$ subjected to wind force, $F(t)_i$	187
6.19	Equivalent MDOF model of the monolithic MF-equipped mid-rise building with highlighting of the main elements assigned	189
6.20	Maximum absolute displacement (a) and acceleration (b) of the multi-storey building with conventional fixed façade under wind load	191
6.21	Top floor absolute displacement of the multi-storey building with conventional fixed façade under wind load	192
6.22	Force-displacement diagram of the connection device	193
6.23	Absolute displacement of MF-equipped building superimposed on that with conventional façade (a) and relative displacement of monolithic MF (b) . . .	194
6.24	Habitability check of the mid-rise building top floor with conventional façade (red dot) and with monolithic MF (blue dot) based on CNR-DT 207/2008 guidelines	196
6.25	Force-displacement diagrams of the connection device for variable friction threshold, F_F	197
6.26	Absolute displacement of MF-equipped building superimposed on the structure response with conventional façade (a) and relative displacement of monolithic MF (b) for variable friction threshold, F_F	198
6.27	Habitability check of the mid-rise building top floor with conventional façade (red dot) and with monolithic MF (blue dot) for variable friction threshold, F_F , based on CNR-DT 207/2008 guidelines. Gray curve defines the acceleration limit value, a_p , for different fundamental frequencies	199
6.28	Force-displacement diagrams of the connection device for variable initial gap, g	201
6.29	Absolute displacement of MF-equipped building superimposed on the structure response with conventional façade (a) and relative displacement of monolithic MF (b) for variable initial gap, g	201
6.30	Habitability check of the mid-rise building top floor with conventional façade (red dot) and with monolithic MF (blue dot) for variable initial gap, g , based on CNR-DT 207/2008 guidelines. Gray curve defines the acceleration limit value, a_p , for different fundamental frequencies	202
6.31	Force-displacement diagrams of the connection device for variable impact stiffness parameter, k_h	203
6.32	Absolute displacement of MF-equipped building superimposed on the structure response with conventional façade (a) and relative displacement of monolithic MF (b) for variable impact stiffness, k_h	204
6.33	Habitability check of the mid-rise building top floor with conventional façade (red dot) and with monolithic MF (blue dot) for variable impact stiffness, k_h , based on CNR-DT 207/2008 guidelines. Gray curve defines the acceleration limit value, a_p , for different fundamental frequencies	205
7.1	Isozaki tower located in the CityLife district of Milan, Italy	211
7.2	Arata Isozaki study sketches for the CityLife tower in Milan (2003). Source: Biagi, M. <i>Non è solo bella: la torre Allianz a Milano di IsozakiMaffei. Casabella 855</i>	211
7.3	Worksite pictures of Isozaki tower under construction (2012-2015)	212
7.4	Typical floor plan	213

7.5	Detail of the strut connected at the top to the curved glazed façade and constrained at the base to a pair of viscous dampers	213
7.6	First three vibrating modes of Isozaki tower FEM implemented in Straus7: on the left, 1st flexural mode around y -axis, in the center, 2nd flexural mode around x -axis; on the right, 3rd torsional mode. Source: Crespi, P., and Longarini, N. (2010). <i>Analisi al vento dei nuovi alti edifici di Milano</i>	216
7.7	Worksite picture of on-site installation of the glazed modules. Source: https://www.focchi.it/it/	217
7.8	Perspective from below of the south-west corner with the alternately opaque and transparent façades of the elevators and the overhang of the curved glass panels (on the left) and lateral view of the rhomboidal volumes of the glazed façade (on the right). Source: https://www.focchi.it/it/	218
7.9	Detail of the curved glass cantilevered at the extremity of the façade. Source: https://www.focchi.it/it/	218
7.10	Interior views of the double-height lobby illuminated by the surrounding glass façades at the level of the entrance from the raised plaza	219
7.11	Cross-sectional detail of the curved glazed façade with assignment of the main components	220
7.12	Main elevation and cross-section of Isozaki tower (on the left) and three-dimensional views of the top shell FEM made in SAP 2000 (on the right)	221
7.13	Characteristic section and dimensions of a) mullions and b) transoms	221
7.14	Transition from the 51-storey structural frame (a) to an equivalent cantilever beam model (b)	222
7.15	Computation of the core's inertia with respect to the barycentric y -axis, J_y	223
7.16	Calibration of the equivalent inertia, J_z , as a function of the vibration frequency, f_{target}	224
7.17	Equivalent MDOF model of Isozaki tower with highlighting of the main elements assigned	225
7.18	Design wind direction in the building reference system	226
7.19	Profiles of $c_m(z)$ associated with IV exposure category (a) and $v_m(z)$ associated with $T_R = 1$ yr (b)	228
7.20	Profiles of turbulence intensity I_v (a) and length scale L_v (b) for the 202.20 m high Isozaki tower used to generate the wind inflow in the longitudinal direction	230
7.21	Turbulent wind velocities, $v_t(t)$, applied on the 5th ($z = 22.80$ m), 25th ($z = 100.80$ m) and 50th ($z = 198.30$ m) floor of Isozaki tower	232
7.22	Wind pressures, $q(t)$, applied on the 5th ($z = 22.80$ m), 25th ($z = 100.80$ m) and 50th ($z = 198.30$ m) floor of Isozaki tower	233
7.23	Profiles of c_e associated with IV exposure category (a) and $q_p(z)$ associated with $T_R = 1$ yr (b)	233
7.24	Diagram of longitudinal wind pressures, $q(t)$, applied on each inter-storey height, h , of Isozaki tower	235
7.25	Fluctuating wind forces, $F(t)$, applied on the 5th ($z = 22.80$ m), 25th ($z = 100.80$ m) and 50th ($z = 198.30$ m) floor of Isozaki tower	236
7.26	Values of the Strouhal number for rectangular cross-sections with sharp corners [CNR Figure O.5]	238
7.27	3D render of Isozaki tower (a) with struts, (b) without struts and (c) with a multiblock Movable Façade	241
7.28	Cross-sectional detail of the connection device integrated into the multiblock MF portrayed in its open (upper part), partially open/closed (in the center) and closed (lower part) layout	243

7.29	Equivalent MDOF model of the multiblock MF-equipped Isozaki tower with highlighting of the main elements assigned	246
7.30	Maximum absolute displacement (a) and acceleration (b) of Isozaki tower with conventional fixed façade under wind load	248
7.31	Top floor absolute displacement of Isozaki tower with conventional fixed façade under wind load	248
7.32	Force-displacement diagram of the connection device	249
7.33	Absolute displacement of MF-equipped building superimposed on that with conventional façade (a) and relative displacement of multiblock MF (b) . . .	250
7.34	Top floor absolute displacement of the MF-equipped building (blue curve) superimposed on the structure response with conventional façade (red curve) under wind load (a) and relative displacement of the multiblock MF under wind load (b)	251
7.35	Habitability check of Isozaki tower top floor with the current façade (red dot) and with multiblock MF (blue dot) based on CNR-DT 207/2008 guidelines. The gray curve defines the acceleration limit value, a_p , for different fundamental frequencies of the buildings	252
7.36	Force-displacement diagrams of the connection device for variable friction threshold, F_F	254
7.37	Absolute displacement of MF-equipped building superimposed on that with conventional façade (a) and relative displacement of multiblock MF (b) for variable friction threshold, F_F	255
7.38	Top floor absolute displacement of MF-equipped building (a) and top floor relative displacement of multiblock MF (b) for variable friction threshold, F_F	255
7.39	Habitability check of Isozaki tower top floor with conventional façade (red dot) and with multiblock MF for variable friction threshold, F_F , based on CNR-DT 207/2008 guidelines. Gray curve defines the acceleration limit value, a_p , for different fundamental frequencies	256
7.40	Force-displacement diagrams of the connection device for variable initial gap, g	257
7.41	Absolute displacement of MF-equipped building superimposed on that with conventional façade (a) and relative displacement of multiblock MF (b) for variable initial gap, g	258
7.42	Top floor absolute displacement of MF-equipped building (a) and top floor relative displacement of multiblock MF (b) for variable initial gap, g	259
7.43	Habitability check of Isozaki tower top floor with conventional façade (red dot) and with multiblock MF for variable initial gap, g , based on CNR-DT 207/2008 guidelines. Gray curve defines the acceleration limit value, a_p , for different fundamental frequencies	260
7.44	Force-displacement diagrams of the connection device for variable impact stiffness, k_h	261
7.45	Absolute displacement of MF-equipped building superimposed on that with conventional façade (a) and relative displacement of multiblock MF (b) for variable impact stiffness, k_h	262
7.46	Top floor absolute displacement of MF-equipped building (a) and top floor relative displacement of multiblock MF (b) for variable impact stiffness, k_h	262
7.47	Habitability check of Isozaki tower top floor with conventional façade (red dot) and with multiblock MF for variable impact stiffness, k_h , based on CNR-DT 207/2008 guidelines. Gray curve defines the acceleration limit value, a_p , for different fundamental frequencies	263

7.48	Maximum structural absolute displacements for variable a) friction threshold F_F , b) impact stiffness k_h and c) initial gap g . The red line represents the maximum displacement of the building with fixed façade (= 0.838 m)	264
7.49	Maximum façade relative displacements for variable a) friction threshold F_F , b) impact stiffness k_h and c) initial gap g . The red line represents the allowable façade opening (= 0.75 m)	265
7.50	Maximum structural absolute accelerations for variable a) friction threshold F_F , b) impact stiffness k_h and c) initial gap g . The red line represents the standard acceleration limit value (= 17 cm/s ²)	265

List of Tables

2.1	Typical values of properties describing the wind speed profile	32
2.2	Peak acceleration limit for each comfort level	46
2.3	Performance levels and corresponding damage states associated with inter-storey drift limits	47
4.1	Coefficients of restitution, e , related to different damping ratios, ξ . Source: Anagnostopoulos, S. (1988). <i>Pounding of buildings in series during earthquakes</i>	87
4.2	Properties of DRAIN-2DX model used to test the truss impact element. Source: Muthukumar, S (2003). <i>A contact element approach with hysteresis damping for the analysis and design of pounding in bridges</i>	94
4.3	Examples of inner connector sizing as a function of the initial gap imposed	102
4.4	Impact parameters for the rubber bumper model adopted	109
5.1	Parameters of the equivalent 2DOF model	128
5.2	Equivalent viscous damping (EVD) ratios for variable friction ratios, α	141
5.3	Equivalent viscous damping (EVD) ratios for variable initial gaps, g	148
5.4	Equivalent viscous damping (EVD) ratios for variable impact stiffnesses, k_h	153
6.1	Mechanical properties of C 40/50 reinforced concrete	160
6.2	Mechanical properties of A615-60 grade steel reinforcing bars	160
6.3	General characteristics of the mid-rise building	160
6.4	Modal periods and frequencies	161
6.5	Estimate of structural mass of the mid-rise building	161
6.6	Estimate of conventional façade mass of the mid-rise building	162
6.7	Mechanical properties of the cores	164
6.8	Mechanical properties of the columns	165
6.9	Modal period and frequencies of the equivalent beam model	166
6.10	Mechanical parameters of the equivalent beam model	166
6.11	Beaufort Scale	172
6.12	3-sec wind gust speed as a function of the mean wind speed based on Beaufort scale and building height	172
6.13	Mean wind speeds, $v_m(z)$, and gust speeds, $v_g(z)$, applied on heights z of the multi-storey building	173
6.14	Maximum longitudinal wind pressures (in kPa) and forces (in kN) per floor	178
6.15	Turbulence intensities, $I_v(z)$, and length scales, $L_v(z)$, for heights z of the mid-rise building	181
6.16	Parameters for evaluating the structural factor, c_{dD}	182
6.17	Geometric and mechanical properties of steel mullions	184
6.18	Geometric and mechanical properties of steel transoms	184
6.19	Estimate of the mass ratio with steel and glass Movable Façade	184

6.20	Sizing of the façade connectors	185
6.21	Geometric and mechanical properties of the connection devices for various sizing calculations performed	186
6.22	Mechanical parameters of the façade beam-column elements	187
6.23	Wind-induced reactions in the beam-column elements	188
6.24	Displacement values of multi-storey building top floor with conventional fixed façade	192
6.25	Properties of the connection device	193
6.26	Top floor displacement efficiency of the MF-equipped building	194
6.27	Compliance with wind performance criteria of the MF-equipped mid-rise building	196
6.28	Fixed properties of the connection device for the parametric investigation on the friction threshold	198
6.29	Top floor displacement efficiency for variable friction threshold, F_F	199
6.30	Top floor acceleration efficiency for variable friction threshold, F_F	199
6.31	Fixed properties of the connection device for the parametric investigation on the initial gap	200
6.32	Top floor displacement efficiency for variable initial gap, g	202
6.33	Top floor acceleration efficiency for variable initial gap, g	202
6.34	Fixed properties of the connection device for the parametric investigation on the impact stiffness	204
6.35	Top floor displacement efficiency for variable impact stiffness, k_h	205
6.36	Top floor acceleration efficiency for variable impact stiffness, k_h	205
7.1	General characteristics of Isozaki tower	212
7.2	Structural materials used during construction	214
7.3	Materials and sections of the structural system	215
7.4	Modal periods and frequencies	216
7.5	Mechanical properties	216
7.6	General characteristics of Isozaki tower façade	219
7.7	Material properties and section of mullions	219
7.8	Material properties and section of transoms	222
7.9	Estimate of conventional façade mass of Isozaki tower	222
7.10	Modal period and frequencies of the equivalent beam model	224
7.11	Mechanical parameters of the equivalent beam model	224
7.12	Turbulence intensities, $I_v(z)$, and length scales, $L_v(z)$, for heights z of Isozaki tower	229
7.13	Mean wind speeds, $v_m(z)$, and gust speeds, $v_g(z)$, applied on heights z of Isozaki tower	231
7.14	Maximum longitudinal wind pressures (in kPa) and forces (in kN) per floor .	234
7.15	Parameters for evaluating the structural factor, c_{dD}	237
7.16	Estimate of the mass ratio with steel and glass Movable Façade	240
7.17	Geometric characteristics of the Movable Façade	241
7.18	Sizing of the façade connectors	242
7.19	Geometric and mechanical properties of the connection devices for various sizing calculations performed	244
7.20	Mechanical parameters of the façade beam-column elements	245
7.21	Wind-induced reactions in the beam-column elements (levels 44-51)	245
7.22	Displacement values of Isozaki tower top floor with conventional fixed façade	249
7.23	Properties of the connection device	249
7.24	Top floor displacement efficiency of the MF-equipped building	251

7.25	Compliance with wind performance criteria of MF-equipped Isozaki tower . . .	253
7.26	Fixed properties of the MF connection device for the parametric investigation on the friction threshold	254
7.27	Top floor displacement efficiency for variable friction threshold, F_F	256
7.28	Fixed properties of the connection device for the parametric investigation on the initial gap	258
7.29	Top floor displacement efficiency for variable initial gap, g	259
7.30	Fixed properties of the connection device for the parametric investigation on the impact stiffness	261
7.31	Top floor displacement efficiency for variable impact stiffness, k_h	263

List of Symbols

A list of all the dimensional and non-dimensional symbols occurring during the dissertation is provided below, including their meaning. It should be noted that the same symbol can take on different meanings throughout the text. The context in which it is placed clarifies its interpretation.

$\bar{u}(\rho)$	Absolute displacement of uncontrolled SDOF structure
$x_j(t)$	Absolute displacement with respect to ground ($j = 1, \dots, n$)
$\kappa(\rho)$	Acceleration efficiency
a_g	Acceleration gravity
a_p	Acceleration limit value for habitability check
R_h, R_b	Aerodynamic admittance functions
ρ	Air density
Δ_p	Allowable inter-storey drift ratio
a_s	Altitude above sea level of the building site
c_a	Altitude coefficient
$H_j(\rho)$	Amplification factor ($j = 1, \dots, n$)
B^2	Background factor
v_b	Basic reference wind velocity at 10 m above ground ($T = 10 \text{ min}$)
$v_{b,0}$	Basic reference wind velocity at sea level
K_{eff}	Bumper effective stiffness
$K_{t,1}$	Bumper initial stiffness
$K_{t,2}$	Bumper strain-hardening stiffness
f_{ck}	Characteristics of compressive strength
ω_j	Circular frequency ($j = 1, \dots, n$)
μ_F	Coefficient of friction
e	Coefficient of restitution
A_t	Coefficient of thermal expansion
τ	Computation time of wind gust velocity
F_c	Contact force during impact
ξ_j	Critical damping ratio ($j = 1, \dots, n$)
$v_{crit,i}$	Critical vortex-shedding velocity for the i -th mode ($i = 1, \dots, n$)

v_{CG}	Critical wind velocity of galloping
A	Cross-sectional area
f_c	Cut-off frequency
L_d	Dead load
v_r	Design reference wind velocity
D	Diameter of the equivalent beam model
E_D	Dissipated energy
C_D	Drag coefficient in the longitudinal wind direction
T_p	Duration of the sampled signal
ω_j^2	Eigenvalue ($j = 1, \dots, n$)
ξ_{el}	Elastic damping ratio
E_S	Elastic strain energy
d/b	Elongation ratio for sharp-edge rectangular section
ξ_{eq}	Equivalent damping ratio
ν_D	Expected up-crossing frequency
$c_e(z)$	Exposure coefficient
\mathcal{L}_{ext}	External virtual work
$\zeta(\rho)$	Façade efficiency
a_g	Factor of galloping instability
Ω	Forcing frequency
ρ	Forcing frequency ratio
F_F	Friction force
α	Friction threshold
\tilde{f}_j	Generalized force coefficient ($j = 1, \dots, n$)
\tilde{m}_j	Generalized mass coefficient ($j = 1, \dots, n$)
\tilde{k}_j	Generalized stiffness coefficient ($j = 1, \dots, n$)
\tilde{c}_j	Generalized viscous damping coefficient ($j = 1, \dots, n$)
E_κ	Global acceleration efficiency
E_η	Global displacement efficiency
E_ζ	Global façade efficiency
k_r	Ground factor
z_0	Ground roughness length
$G_v(z)$	Gust factor
H	Height
n	Hertz coefficient
A_{hys}	Hysteresis area
ξ_{hys}	Hysteretic damping ratio
k_h	Impact stiffness parameter
$I(x, t)$	Inertia forces on the structure
g	Initial gap
\mathcal{L}_{int}	Internal virtual work

h_j	Inter-storey height ($j = 1, \dots, n$)
L	Length
L_l	Live load
M	Mass
m	Mass per unit length
ρ	Mass per unit volume
μ	Mass ratio
$\bar{v}(\rho)$	Maximum allowable relative displacement of façade
δ_m	Maximum penetration during impact
$c_m(z)$	Mean wind profile coefficient
$v_m(z)$	Mean wind velocity
z_{min}	Minimum height
E	Modulus of elasticity
W_i	Modulus of resistance relative to the i -th axis ($i = x, y$)
J_i	Moment of inertia relative to the i -th axis ($i = x, y$)
f_j	Natural vibration frequency ($j = 1, \dots, n$)
F_N	Normal force
$g_v(z)$	Peak factor
$q_p(z, t)$	Peak wind pressure
Ψ_j	Phase shift angle ($j = 1, \dots, n$)
U	Poisson coefficient
$S_v(\Omega)$	Power spectrum of wind turbulence
$u_j(t)$	Relative displacement with respect to ground ($j = 1, \dots, n$)
δ	Relative penetration during impact
v'_j	Relative velocity after impact ($j = 1, \dots, n$)
v_j	Relative velocity before impact ($j = 1, \dots, n$)
$M_{rd,i}$	Resisting moment relative to the i -th axis ($i = x, y$)
R_D^2	Resonance response factor
c_r	Return coefficient
Δ_t	Sampling step
Sc_i	Scruton number for the i -th vibrating mode
$\psi_j(x)$	Shape function ($j = 1, \dots, n$)
A^*	Shear area
u^*	Shear velocity
a_0, k_a	Specific-site wind coefficients
u	Static displacement of the SDOF structure
$\sigma_v(z)$	Standard deviation of the fluctuation rate
St	Strouhal number
c_{dD}	Structural factor
G	Tangential modulus of elasticity
f	Tuning frequency ratio

$v_t(z, t)$	Turbulent wind velocity
$c_t(z)$	Topography coefficient
$\eta(\rho)$	Vibration damping efficiency
T_j	Vibration period ($j = 1, \dots, n$)
$\tilde{v}_j(x)$	Virtual displacement ($j = 1, \dots, n$)
V	Volume of the equivalent beam model
P	Weight per unit length
W_s	Weight per unit volume
B	Width
T_R	Wind average return period
$F(z, t)$	Wind force in the longitudinal direction
$v_g(z)$	Wind gust velocity
T	Wind observation time interval
\bar{A}	Wind pressure area
$q(z, t)$	Wind pressure in the longitudinal direction
$I_v(z)$	Wind turbulence intensity in the longitudinal direction
$L_v(z)$	Wind turbulence length scale in the longitudinal direction
$v(z, t)$	Wind velocity
δ_y	Yield deformation
a	Yield parameter
F_y	Yield strength

List of Abbreviations

2DOF	Two Degrees-of-Freedom
COR	Coefficient of Restitution
CW	Curtain Wall
DED	Direct Energy Dissipation
DSF	Double Skin Façade
EBB	Euler-Bernoulli Beam
EPDB	Ethylene Propylene Diene Monomer
EVD	Equivalent Viscous Damping
FD	Friction Damper
FEM	Finite Element Method
FFT	Fast Fourier Transform
FRC	Frequency-Response Curve
ID	Impact Damper
IED	Indirect Energy Dissipation
MD	Metallic Damper
MDOF	Multi-Degrees-of-Freedom
MF	Movable Façade
NBR	Nitrile Butadiene Rubber
NOWS	NatHaz Online Wind Simulator
NR	Natural Rubber
NZEB	Nearly Zero-Energy Buildings
PSD	Power Spectral Density
RC	Rigid Connector
RMS	Root Mean Square

SAP	Structural Analysis Program
SB	Shear Beam
SBR	Styrene-Butadiene Rubber
SDOF	Single-Degree-of-Freedom
SGF	Structural Glass Façade
SMA	Shape Memory Alloy
SRC	Steel Reinforced Concrete
TB	Timoshenko Beam
TLD	Tuned Liquid Damper
TMD	Tuned Mass Damper
VD	Viscous Damper
VED	Viscoelastic Damper
VESC	Viscoelastic Spider Connector
VFCC	Variable Friction Cladding Connection

Chapter 1

Introduction

1.1 Background

The unstoppable race to skyscrapers and the increasing use of lightweight materials in the high-rise building construction have the advantage of making the structures more flexible and less massive but, at the same time, they help to increase their vulnerability to wind actions. High-intensity wind events can induce tall buildings to undergo non-negligible oscillations and accelerations on the upper floors with important consequences in terms of both user discomfort and serious damage to structural members. In this scenario, the worst hazard condition for a tall and slender building, which has not been designed to withstand lateral loads, is represented by the wind blowing at the same vibration frequency as that of the structure, causing resonance phenomena and amplifying its dynamic response. The wind-induced resonant vibrations can be mitigated due to installation of additional masses of considerable size and weight in strategic points of the structure, capable of modifying the building dynamic properties and moving it away from the resonance condition. Among the available devices, the *tuned mass damper* (TMD) has proved to be the most common and reliable technique for this purpose; however, the loss of useful space coupled with a high initial cost of installing large size damper systems has led the experts to looking for any viable alternative solution.

To date, the possibility of using the building skin as a potential wind-induced vibration absorber for multi-storey structures has been investigated only marginally: this is due to the fact that the engineering community has always seen façade systems as simple barriers between external and internal environment, with high aesthetic value but with little structural contribution, thus excluding them from computer modeling as an analysis tool. With the technological advancement, it is now possible to realize smart enclosures that are no longer fixed to the load-bearing structure of buildings; instead, they are designed as independent self-supporting elements in which conventional rigid brackets are replaced by sacrificial supports which can have back and forth movements under dynamic excitations, filtering the input energy and breaking down the dynamic response of the building to be protected. In this context, this type of envelope will be renamed *Movable Façade* (MF). From a constructive point of view, the MF can be made in various ways depending on whether the cladding surface

is conceived as a single vertical element, thus defining a monolithic MF, or is divided into several independent parts, giving rise to a multiblock MF.

The advantages that MF systems can bring to the analysis of building dynamic behavior convinced researchers to in-depth the topic, coming to consider envelopes as structural components participating in the dynamic response of wind-excited buildings. Based on this, a method using MF in the form of *double skin façades* (DSF) integrated with energy-absorbing devices has been proposed by Moon in 2005 in order to damp the amount of energy transferred to the main supporting structure during wind activities. The goal of changing the conventional concept and using MF systems is to reduce and come up with a better response in terms of structural displacement and acceleration; however, it has been shown by the author that the applicability of this solution cannot ignore the problem of the excessive façade relative displacement which is not acceptable to the engineering community. This issue, which will be referred to as *Moon's problem*, constitutes the starting point of the current dissertation.

1.2 Research objectives and methodology

The primary purpose of this Ph.D. Thesis is to offer a contribution to the resolution of Moon's problem through the application of MF incorporated with suitable sliding connections on civil structures. The investigation on the potential use of MF for the purposes of wind-induced vibration control leads to a proper design of dissipative sliding devices integrated with shock-absorber layers, which make the MF able to undergo controlled movements under wind loading, proposing itself as a possible solution to the starting issue of the excessive façade movements. Developing a façade system that can work in a wide range of applications (on common mid- and high-rise buildings, with different cladding surface layouts, under several wind intensities, and so on) capable of solving Moon's problem, while exerting a remarkable vibration control on the structure, is the ultimate target of this research.

1.2.1 Objectives

Specifically, the following key objectives want to be achieved, which can be distinguished into three main phases.

1. The aim of the first phase is to introduce the MF system for structural purposes, defining the two main types (namely, the monolithic and the multiblock version) and showing the familiarity existing between the functioning of monolithic MF and classic TMD. Both systems are conceived to undergo wind vibrations due to a flexible connection which reduces the transmissibility of dynamic loading to the structure, with the advantage for the MF of using mass already available outside the building and without occupying additional space inside. A preliminary comparison between the vibration damping efficiency of a classic TMD and a monolithic MF is performed in the simple set of 2DOF modeling under harmonic excitation. By means of a parametric study conducted in a context of linear dynamics, the influence of mass, tuning frequency, forcing frequency

and damping ratios on the dynamic performance of both systems is evaluated. Finally, the potential for use of the MF in the field of dynamic motion control is validated despite the highlighting of Moon's problem;

2. the second phase aims to conceive and develop a suitable connection device incorporated in the MF design which is able to contain the façade motion within acceptable limits and also reduce the top response of the structural model compared to the case in the absence of the façade system. A preliminary investigation on the effectiveness of the proposed friction device additionally equipped with rubber bumpers is carried out on a harmonically excited 2DOF model of a typical multi-storey building equipped with a monolithic MF. The influence of the key parameters that characterize the behavior of the connection system, that is, the friction threshold of the sliding device (or simply *slider*), the impact stiffness of the bumpers and the initial gap between the structure and the façade, is assessed through parametric analysis performed in the field of nonlinear dynamics;
3. validating the dynamic performance of the dissipative slider with bumpers on mid- and high-rise buildings equipped with either a monolithic or a mutiblock façade experiencing turbulent wind load is the final aim of the research. Numerical simulations are performed on more refined wind-excited MDOF distributed-mass models of a 25-storey building and the 51-storey Isozaki tower in Milan (Italy). Parametric investigations are carried out in order to evaluate the influence of the key variables of the proposed MF connection device on the system's dynamic response when subject to random excitation.

1.2.2 Methodology

The method used to investigate the feasibility and performance of the proposed MF connection system is mainly based on analytical observations. A great part of the research is conducted using computer simulations involving nonlinear analyses of equivalent 2DOF and MDOF models and Finite Element Method (FEM) analysis for a preliminary check and modeling. Specifically, Python codes and Structural Analysis Program (SAP) 2000 are used for this purpose. Two building test cases, specifically, a 25-storey 77 m-high building directly simulated in SAP 2000 and the 51-storey 220 m-high Milan's Isozaki tower, are chosen to be modeled and implemented in the simulation domain. A series of linear and nonlinear, static and dynamic, transient analyses are carried out both in the time- and frequency- domain resorting to force-displacement diagrams, phase portraits (that is, relative displacement versus relative velocity diagrams), Frequency-Response Curve (FRC), time-histories in steady-state conditions and vertical floor profiles built in terms of absolute and relative response of the structure and the façade. Extensive and detailed numerical analyses fully explore the MF dynamic performances under harmonic excitation and fluctuating wind force. A sinusoidal load having an amplitude consistent with the design peak wind pressure defined according to standard codes is assumed for the analysis of the harmonically excited 2DOF model, while a stationary random wind field for the analysis of the wind-excited MDOF models is processed

within the NatHaz Online Wind Simulator (NOWS). The mean wind velocity and turbulence profiles are estimated following the instructions contained in the Italian CNR-DT 207/2008 guidelines, whereas fluctuating wind velocity and force time histories are derived after setting a specific peak gust speed and cut-off frequency of the signal processed in accordance with Monte Carlo methodology. The key variables which characterize the system's response concern both the topology of the MF system and the mechanical configuration of the connection device. In this context, the MF design is conceived either as a single joined vertical element (monolithic façade) or divided into several detached parts (multiblock façade). On the other hand, three main parameters defining the behavior of the connector can be identified: the friction threshold of the slider (F_F), the impact stiffness of the bumpers (k_h) and the width of the at-rest gap between the structure and façade (g). As for the 2DOF harmonic analyses, the friction threshold is conveniently expressed in terms of the dimensionless ratio, α , between the friction force, F_F , and the applied load, P . By conducting a parametric study, the influence that these variables exert on the dynamic performance of the connection system is investigated and the beneficial trend obtained from the incorporation of both types of MF integrated with dissipative connection devices within civil buildings is pointed out.

1.3 Thesis overview

This dissertation is organized into eight Chapters and an initial summary, with the first two Chapters containing the theoretical background and a state-of-the-art review on the topic addressed, respectively, and the next six presenting and discussing the main findings of the research.

Chapter 1. An introduction to the topic of MF, underlining the advantages linked to a potential use in the field of dynamic motion control, is provided in the first Chapter. Reference is made to the research methodologies, objectives, gap and issues, finally, formulating the proposals and defining the main points. The methodology section allows the reader to critically assess the overall validity and reliability of the study; therefore, an overview of the research strategies, procedures and techniques which have been taken in order to identify, select, process and analyze informations on the topic, ensuring understanding of how findings were gathered and the research was approached, is also supplied.

Chapter 2. A literature review on the main arguments covered by the research theme, establishing familiarity with and understanding of the current research in the field of interest before carrying out the proposed investigation is described here. First of all, providing an overview of the façade technological advancement, followed by a foundation of knowledge on the basics of wind velocity characterization and the digital simulation methods of wind-related processes, allows readers to frame the research theme in a multidisciplinary context. Conducting a detailed state-of-the-art review of the previous relevant research in the context of wind-induced vibration control aims to find out what research has already been done, iden-

tify what is unknown within the topic, highlighting any gaps, conflicts in previous studies, open questions left by other research and, ultimately, justify the research and the need for further investigation.

Chapter 3. A comparative study on the vibration damping efficiency of monolithic MF and standard TMD in the simple 2DOF modeling under harmonic excitation is presented and the main differences between the well-known dynamic response of TMD and the less known dynamic response of MF are argued. The basic modeling and related mathematical formulation of the two systems is followed by the definition of specific efficiency indexes and by the introduction of three performance levels related to the connection stiffness between the two masses. A parametric study aimed at investigating the effect of the dimensionless mass, tuning frequency, forcing frequency and damping ratios on both the MF and TMD dynamic response is performed. The outcomes of the study are discussed by highlighting the first theoretical and practical contributions which form the basis for the next research step.

Chapter 4. A proposal and related steps for design and modeling of a dissipative connection system consisting in a friction slider integrated with two-sided bumper dampers to be inserted in the gap between the structural building and the MF is suggested, in order to control the large relative displacement of façade panels and also achieve a similar reduction in the response of the main structure. A literature review on the available impact models and the reference friction device (namely, the VFCC conceived and tested by Laflamme and coworkers) provides a useful background to ensure a proper design and modeling of the proposed connection system.

Chapter 5. A preliminary investigation on the vibration damping performances of the proposed connection devices is conducted on a harmonically excited 2DOF model of a MF-equipped multi-storey building. A Rayleigh-like discretization procedure is applied to derive the equivalent parameters related to the 2DOF numerical model. Parametric analyses focus on the effect of the key variables that characterize the behavior of the connection device (namely, the friction threshold of the slider, the impact stiffness of the bumper and the initial gap between the primary and secondary masses) on the system's response. The results of the preliminary study constitute the starting point for a more in-depth and refined investigation reported in the following Chapters.

Chapter 6. Provides a concrete and reliable context for the interpretation of results of the preliminary analyses is the main purpose of both the sixth and seventh Chapters. The evaluation of the dynamic performance of the smart façade connection system moves to the study of a monolithic MF-equipped mid-rise building experiencing turbulent wind load. From the FEM of the building, useful mechanical and dynamic properties for managing the equivalent MDOF modeling are obtained, enabling to approximate the structural behavior with a Timoshenko cantilever beam, which is implemented in Python simulation platform and

subject to transient analyses. Based on the random signal built in the NOWS and on the resultant wind forces computed according to the Italian CNR-DT 207/2008, the response of the structure with conventional fixed façade is obtained and comparative simulations with the monolithic MF-equipped building incorporated with dissipative connection devices are undertaken. Parametric studies are conducted as the key variables of the device are made to vary and the main results are discussed in terms of lateral displacement and acceleration control of the building, also extending this logic to the façade relative displacement response as well.

Chapter 7. Numerical modeling and related steps of simulation and parametric investigation that the mid-rise building is submitted to in Chapter 6, are now executed on the wind-excited MDOF model of Isozaki tower with a multiblock MF.

Chapter 8. Conclude the dissertation and restate the main topic, reminding the readers of the strengths of the main arguments and reiterating the most important evidence supporting them, ultimately, consider the limitations and future research avenues to be taken, are the key points of the last Chapter.

Chapter 2

State of the art

2.1 Introduction

A literary overview of the main arguments constituting the theoretical background related to the topic of this Ph.D. Thesis is provided in this Chapter. First of all, the main types of façade currently available in the technological panorama (*curtain walls, double skin façades, adaptive façades*) are described in their intrinsic energy-saving functions, construction methods and typical ways of connection to structural buildings. After that, the inherent characteristics of the wind excitation are underlined, in terms of the statistical description of wind velocity, the computation of fluctuating forces and the analysis of digital simulation processes for a proper modeling of the turbulent wind load applied to structural design; then, the basis for the definition of wind performance criteria to which high-rise buildings must respond are supplied. Based on this, the most common and well-known strategies for mitigating wind-related issues on tall and slender structures are reviewed, focusing mainly on passive approaches including Movable Façades. A meticulous state-of-the-art review involving the current knowledge on the structural use of MF is the key to make the research offering an original contribution to the field of investigation.

2.2 Façade systems

The historical evolution of building skins as autonomous constructive elements with respect to gravitational and lateral load-bearing systems has led to new aesthetic considerations released from the previous structural limits. With the progress in the technology and material fields, new advanced solutions for tall building design and construction are now available. In order for a high-rise building to emerge in the city skyline, the aesthetic configuration of its façade plays a primary role, not only from a functional point of view but also from a qualitative aspect. Due to their ability to shape an iconic image of the building, the cladding systems determine the appearance of the constructions, defining both their geometry and volume; hence, they constitute a major element in their architecture. Due to the development and optimization of advanced structural systems for tall buildings (such as DiaGrid, tube or framed structures), which have encouraged a return to collaboration between building

envelopes and structural systems, modern façades (particularly origami-inspired as in Figure 2.1) have the potential to act as a critical link for structural and architectural interaction [1]. Several strategies like origami, topology optimization and architecture combined in parametric design studies, are examples of how the architectural expression can help the efficiency of high-tech building envelopes from both structural and architectural point of view. The benefits linked to an integrated functional design can include desired aesthetic, structural (bending increases stiffness) and energy (solar-shading) performances, efficient transport of components and dynamic performance optimization [2]. At the same time, the envelopes have important functions to fulfil, such as lighting, weatherproofing, thermal insulation, load transfer and sound insulation. Generally, the choice of a cladding varies according to the internal functions of the building, being linked to the needs of flexibility, comfort, safety and energy saving. The preference for an innovative solution rather than another depends on its effectiveness in improving the overall behavior of the building and the long-term effects, against a higher initial construction cost.

Typically, the conventional façades are designed as fixed systems rigidly connected to the primary structures and their main task is to offer protection and shelter from the environmental actions, providing both thermal and acoustic insulation. These systems are therefore conceived to have purely static properties, no ability to behave in response to external changes and, by now, they are largely energetically depleted [3]. Not being able to adapt to the changing environmental conditions linked to daily and annual cycles or to the changing needs of users, a general reconsideration of the role of the envelope in the overall performance of a building is required [4]. Starting from the 60s-70s of the nineteenth century, the façade industry evolved rapidly: the widespread use of steel and reinforced concrete in response to the increased loads and the use of glass for the natural lighting maximization lead to a separation of functions between the building components, resulting in the transition from the load-bearing masonry wall to the non-load-bearing external façade, lighter and completely independent of the building structure. This first stage gives rise to the birth of the *curtain wall* (Curtain Wall (CW)) system [5]. In the 30s of the twentieth century, the emerging objectives linked to the energy saving and the growing needs of occupants' well-being have led to the demand for ever more efficient façade systems, conceived as highly technological construction components capable of significantly influencing the energy quality and comfort of the buildings. The growing international demand for energy efficiency stimulated the search for approaches and strategies capable of reducing the building consumption, including new solutions and types of envelopes [6]. In addition to determining the architectural value of a building organism, modern envelopes are demanded to meet various requirements in terms of energy efficiency, indoor quality, structural performance and simple construction. Therefore, they perform a multitude of interdependent functions aimed at balancing the variable climatic conditions of the external environment with respect to the internal condition [7]. The optimization of the construction properties and the performances of enclosures allows significant savings related to the functioning of the buildings, which are becoming more and more energy-intensive, and due to the rapid advances in the architectural and engineering

field, today's practitioners have various means and options to meet this challenge.

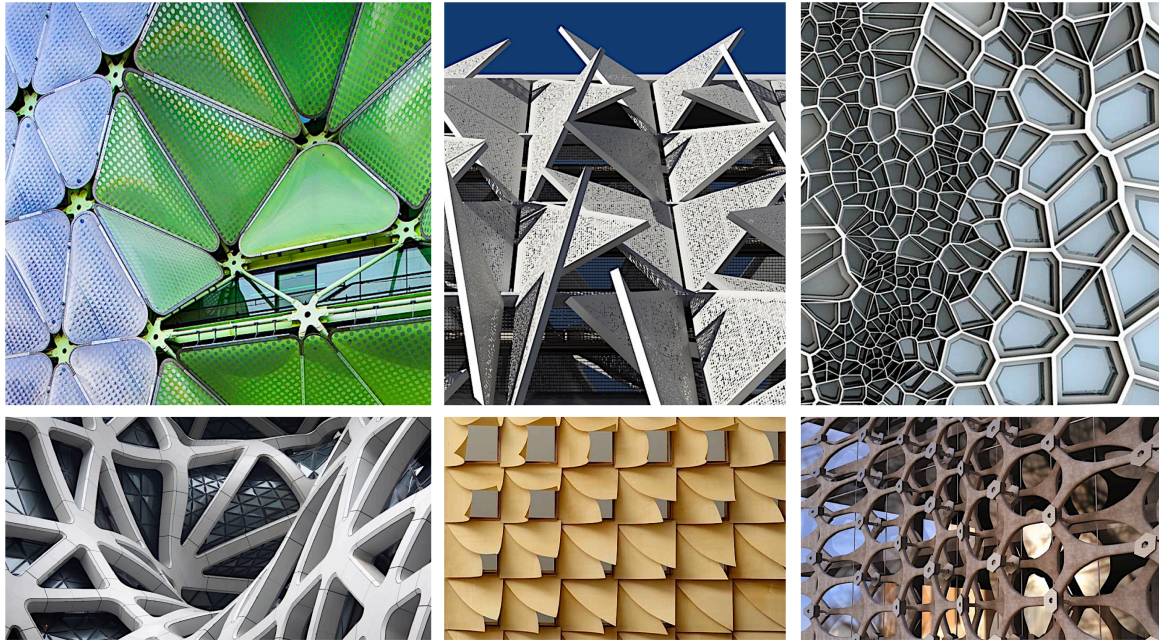


Figure 2.1: Examples of origami-inspired geometric patterns for high-tech building envelopes

The new needs mark the shift of the climate-energy functions from inside the building towards the façade, giving rise to an emerging type of cladding, which aims at improving the thermal performance of the glazed envelopes. This is the *double skin façade* (DSF) which consists of three distinct layers: an interior glazed wall system, an exterior glazed wall system and, between them, a ventilated air cavity which acts as a thermal buffer. The different typologies in which this system is available allow it to be combined in several ways for a wide variety of design possibilities [8]. As a further development, DSF are combined with single skin envelopes to create the so-called *alternating façades*. By arranging these two well-known constructive and functional technologies, it is possible to achieve high performances as compared to conventional single glazed configurations. Alternating façades are also called *hybrid façades* [9]. In the 80s of the twentieth century, due to the integration between the bioclimatic architecture and the digital technology, the concept of a *dynamic* enclosure, intended as a *moving* solution for the optimal management of energy flows and for the reduction of environmental impact, takes place in the construction world, becoming in clear contrast with the idea of immobility that was at the basis of traditional buildings [10]. Added to this, the use of sensors, actuators and smart materials, such as the Shape Memory Alloy (SMA) [11]-[12], for both the manual and automatic control of the movable cladding elements (such as, solar shading, openings, air intakes, photovoltaic panels) promotes a greater adaptation of the building to the external environment and the changing needs of users. In the evolutionary field of façade engineering, the researchers have attributed great potential to the emerging adaptive systems, considered a milestone in the contemporary architectural and technological community. Over the past 15 years, the façades have become increasingly complex *smart* skins capable, for instance, of adapting to the changing climate and the lighting conditions.

Newly developed materials and technologies have extended the scope of façade functions: this is partly due to the new stringent rules in terms of the energy efficiency that have forced both the adoption of high-performance façades in the new high-rise buildings and the replacement of low-performance envelopes in the old tall buildings [13]. In the following sections, the façade solutions commonly adopted in the contemporary constructions are investigated.

2.2.1 Typical façade connections

In general, an envelope is defined as the membrane separating indoor from outdoor, qualifying the architectural character of a building and, at the same time, performing specific protection and insulation functions, such as allowing sunlight to penetrate the building or providing shelter from overheating and unwanted lighting. Besides improving the energy efficiency by avoiding heat losses and reducing the building consumptions, the façade systems are also able to perform structural tasks related to the civil building safety. From a structural point of view, the enclosures are generally conceived as fixed elements designed to withstand their self-weight and the weight of other building components and may be capable of absorbing push and pull forces induced by wind, earthquake and thermal expansion [14]. In some cases, they could even resist blast events. With modern flexible connectors and smart brackets for anchoring to the supporting structure, façades can become dynamic components if designed to move with the building structural components, such as pillars, beams and floor slabs, under the applied loads, including dead load physically attached to the structure (that is, the self-weight of the building elements), live load (for example, people hitting the cladding), snow weight, stress load (due to the thermal variations) and wind load (causing push and pull forces). Each structural component of the building tend to react both to vertical and horizontal load imposed. The former induce the bending of beams and floor slabs and the shortening of pillars; the latter can cause the entire frame to move or tilt, inducing high floor displacements and accelerations [15]. Since these can occur simultaneously, they represent a key element to be taken into account in the façade technological layout, in order to suitably design the connections and the anchoring component dimension of the cladding frame. The structural behavior of the envelope, in fact, is strongly affected by the anchoring method to the building skeleton and the amount of movement and rotation allowed at the joints, which must be ductile and stiff enough to ensure adequate strength to the entire structural system. Taking into account the possible local failure in the anchoring area, the latter should be designed to prevent the façade panels from falling out [16].

Depending on the structural type and constructive scheme, the load transfer path from the façade to the building structure can vary. Typically, envelopes rely on anchoring elements to support their self-weight and accomodate the building movements; the glass panels act downwards parallel to the cladding, they receive the push and pull forces by the wind or other horizontal loads and transfer them from the functional layer (cladding) to the secondary structure (frame) in order to ensure the façade structural integrity. In turn, the secondary structure supports the glass weight, transferring the lateral loads to the anchorage system; finally, the anchoring elements move them to the load-bearing structure of the building, as

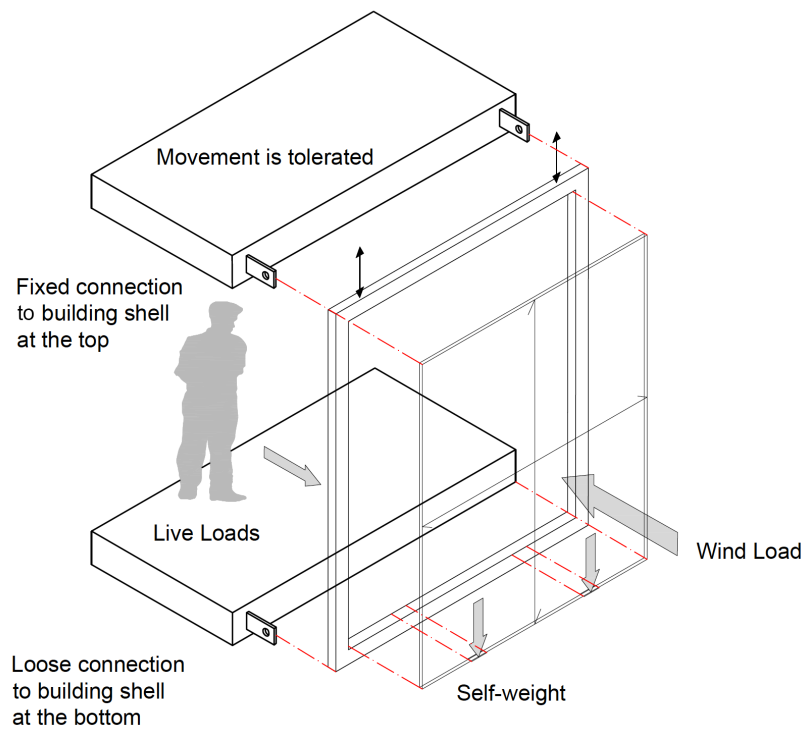


Figure 2.2: Different type of loads affecting the façade structure, including the self-weight of the cladding components, wind load (push and pull forces) and live loads. Source: Knaack, U. et al. (2014). *Façades. Principles of Construction*

illustrated in Figure 2.2. In most cases, it makes sense to transfer the façade loads floor by floor and to add expansion joints so that the size variations do not add up across multiple floors [17]. As regards the construction method, claddings can be conceived as load-bearing or non load-bearing systems. A non-load-bearing envelope has only a protective task and it can be suspended, single-storey supported or two-storey supported by the main structural system of the building, as shown in Figure 2.3. This is designed to have sufficient strength to accommodate its self-weight, which is assumed to be taken as a vertical reaction force by the bottom anchors and, therefore, transferred through the fasteners to the load-bearing structure of the building; in addition, the anchoring elements must withstand the horizontal reaction forces induced by the wind pressure [18]. A load-bearing envelope, in addition to providing shelter from the outside, represents the main or secondary structural system of the building. As a self-supporting system, it must be resistant enough to meet the building structural needs and transfer the vertical forces directly to the foundation.

Modern façade systems are characterized by a metal and glass structure, within which three main construction areas can be distinguished (Fig. 2.4):

- level 1 (the primary structure, i.e. the building envelope): it assumes the load-bearing function of the entire building and transfers loads from the façade to the foundation;
- level 2 (the secondary structure, i.e. the façade load-bearing support): it constitutes the connecting element between levels 1 and 3 and transfers cladding loads to the primary

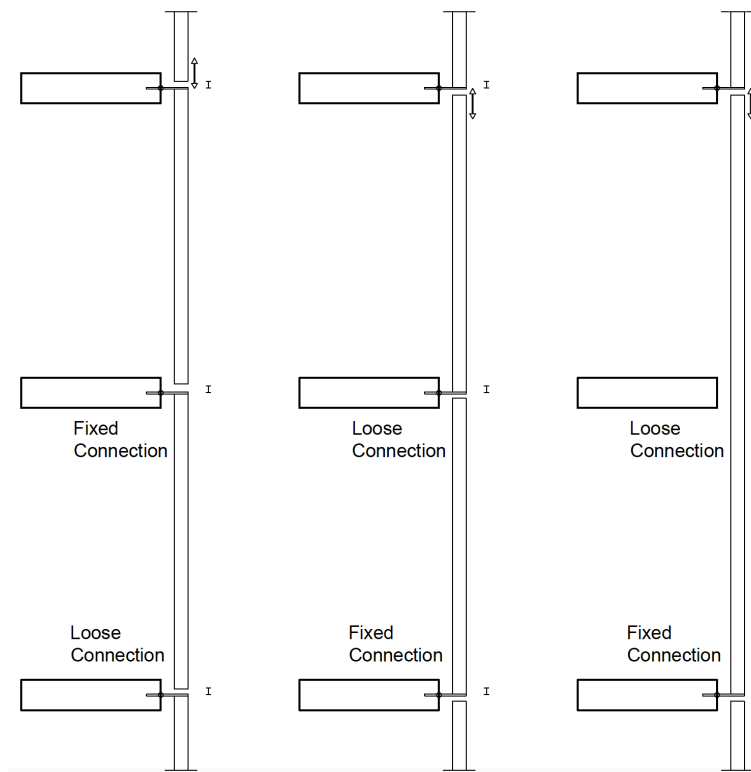


Figure 2.3: Façade bearing systems: a suspended structure on the left, a single-storey supported structure in the centre and a two-storey supported structure on the right. Source: Knaack, U. et al. (2014). *Façades. Principles of Construction*

structure;

- level 3 (the infill elements, i.e. the glass panels): it is mounted on the secondary structure and must perform specific functions (such as, air and water penetration resistance, tolerance of movements between levels 2 and 3, elimination of thermal bridges, etc).

It is possible to identify two main classes within this category: the CW, consisting of a metal frame and a glass envelope supported by the building structure and placed outside it, and the Structural Glass Façade (SGF) which encompasses the building from floor to ceiling and is placed inside the frame.

CW typically consist of an aluminum (or stainless steel) frame and a filling made of transparent (insulating, laminated or monolithic glass) or opaque (aluminum, fiber-reinforced panels) materials which can be supported or inserted inside the frame. They are non-load-bearing systems, so the infill material and the frame are designed to accommodate the lateral loads, such as wind and earthquake, and transfer them to the building structure [19]. All-glass enclosures, such as the SGF, the point-supported and the suspended glass façades, use glass as the primary cladding material, attached to unidirectional steel cables or cable networks, trusses and other support systems, with visually minimal connections [20]. Their objective is to ensure the maximum transparency by maximizing the glass dimensions, with a consequent reduction of joints, or by reducing the framework dimensions. These are also

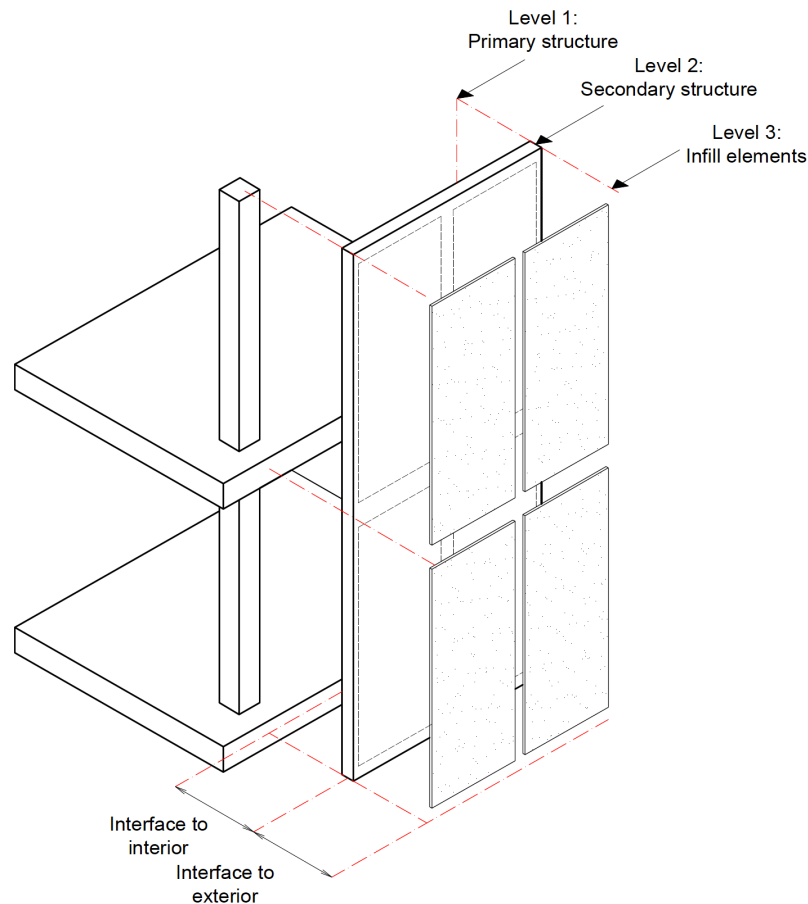


Figure 2.4: Schematic representation of the three construction areas identified in a typical façade. Source: Knaack, U. et al. (2014). *Façades. Principles of Construction*

generally non-load-bearing systems: glass, anchors and the supporting skeleton are designed to accommodate and transfer their self-weights and the lateral loads at the top or at the foot of the structure. From the cladding corners, loads are transferred to the secondary supporting frame or the building structure. Unlike CW, fully glazed envelopes are more flexible as they are designed to withstand the bending moments. In turn, the bending of the support system affects the dimensions of the cladding panels, the joints and the method of glass fixing (which can be clamped or adherent [21]). As the cladding systems are the first line of defense against external actions, not only wind but also blast and impact events, an appropriate selection of the materials and connection is required. According to [22], heavy façades with stiff connections are not suitable since they can cause premature failure of the system, while lighter and ductile envelopes with flexible connections are preferable.

2.2.2 Curtain Wall (CW)

The curtain wall (CW) is a particular type of building envelope ensuring high performances, with the advantage of a dry and prefabricated construction system. Its aluminum grid confers lightness and allows the transfer of building loads to the primary structural elements. The origin of the name *curtain wall* derives from the geometric continuity effect that this

technology gives to the outer surface of the building: the cladding panels are positioned to the exterior of the structure, which allow the combined window and spandrel framing to span multiple levels, ultimately forming a continuous façade. The modern CW is born following the spread of frame structures in the second half of the 19th century and then developed in the early 1900s [23]. Due to the use of materials such as steel and reinforced concrete, it has become a technology that features the most famous contemporary buildings. The success of CW is mainly linked to the prefabrication technique, developed in the first two decades of the 1900s and used by famous architects like Walter Gropius in Germany and Le Corbusier in France. In the United States, this cladding system has been perfected, studied and in-depth, giving rise to important projects, including the Lever House by Skidmore, Owings & Merrill and the Seagram Building by Ludwig Mies van der Roe (Fig. 2.5).



Figure 2.5: Curtain wall application on Lever House by Skidmore, Owings & Merrill (right) and on the Seagram Building by Ludwig Mies van der Roe (left)

Basically, a CW is defined as a thin, usually aluminum-framed wall, containing in-fills of glass, metal panels or thin stone, in addition to glazed-in window and door openings [24]. The infill material is hooked to a metal frame and, in turn, fixed to the underlying structure, creating a self-supporting envelope that does not carry the floor or roof building loads. The CW transfer their self-weight and accidental loads, mainly consisting of local wind pressure and aerodynamic force acting on the building surface [25], to the floor level of the structure, therefore the anchoring system is designed to allow differential movements while resisting the applied loads. The ability of CW to withstand wind loads depends on their shape and how they are fixed to the structure at floor level by means of brackets that transfer wind pressure to the building's load-bearing system [26]. During the load transfer, CW are also subject to bending, therefore, their shape and size are critical to ensure that the maximum bending is not exceeded [27].

The main components include the load-bearing framework made up of vertical (mullion) and horizontal (transom) elements, generally made of extruded aluminum, which support the infill panel, the glass (or opaque) paneling, the gasket and joints and the shielding elements. An example of CW framing system is shown in Figure 2.6. The mullions and transoms can be self-supporting or anchored to the main structure; they are sized to withstand strong wind

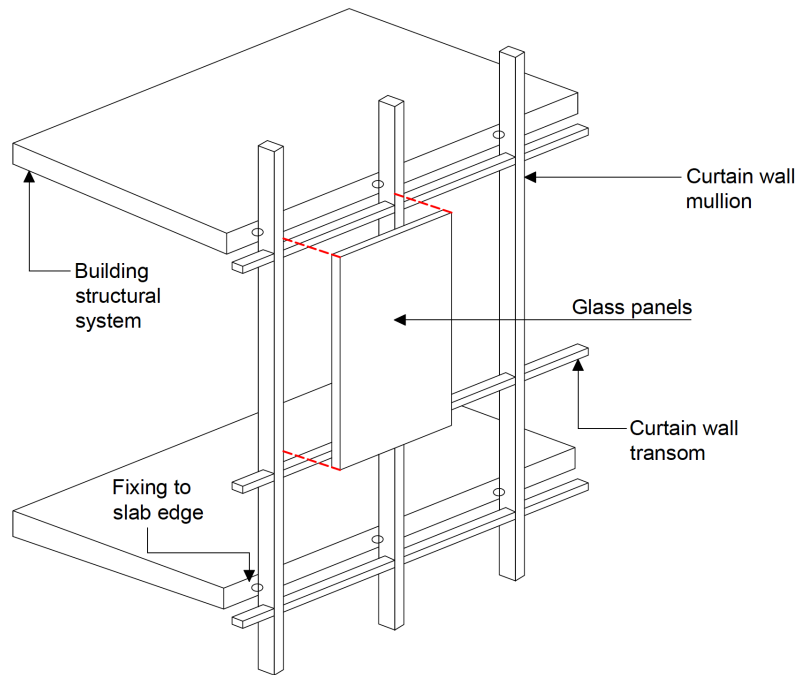


Figure 2.6: Basic components of a typical curtain wall system

gusts and are characterized by well-defined aesthetic peculiarities [28]. The glazed paneling is composed of a single, low-emissivity, double or triple chamber glass, which can be combined with protective or reflective films or photovoltaic cells. Large-format glass sheets are possible due to the use of structural silicone which allows the windows to be joined with minimal visual impact. The fixed or movable shielding elements, consisting of photovoltaic, solar thermal or even vertical green panels, can be mounted outside the panels or integrated into them. These systems manage the supply of sunlight and flow of natural ventilation indoor, leading to the creation of CW with bioclimatic, biomimetic and interactive functions.

The curtain walling constructions can be classified according to their manufacturing and installation method into two main types: *stick* and *unitized* systems. A stick system is based on a structure of components assembled directly on site, with mullions and transoms supporting glass, spandrel panels, metal panels and brise-soleils, connected piece by piece and installed on the building structure. The mullions extend along the full cladding height and are connected to the transoms by means of angle cleats, sleeves, spigots or brackets (Fig. 2.7). In the façade grid, all the elements are made from standard or bespoke extruded aluminum profiles, cut and manufactured in the factory. The weatherproofing is ensured by the gasket, placed between the grid and the cladding, or by the glass panel, which can be fixed or openable and is inserted after the grid is finished. A unitized system is composed of large prefabricated units, having a grid in extruded aluminum profiles, which are pre-assembled and pre-glazed in the factory and then delivered to the construction site for the distribution to floor slabs and the subsequent installation on the building. Depending on the type of construction, some wall elements can be prefabricated and assembled on site, or the entire system wall can be prefabricated off site and then installed as a whole [29]. Mullions



Figure 2.7: Assembly diagram and application examples of a stick curtain wall system

and transoms of each module are coupled with adjacent modules, which generally have floor height. Unit systems (Fig. 2.8) allow for quick installation, making it particularly suitable for tall buildings [30]. The weatherproofing is ensured by watertight gaskets that are positioned in the vertical and horizontal joints.



Figure 2.8: Assembly diagram and application examples of a unitized curtain wall system

Due to their wide design flexibility, the CW systems have gained structural importance

equivalent to that of other structural elements. In the current era, the need for quick solutions to combat climate change and improve energy performance of the buildings have made CW evolve into double skin structure that allow the creation of natural ventilation chambers (*ventilated façades*) which regulate both the summer heating and the winter cooling as well as the indoor lighting with the use of sunshades.

2.2.3 Double Skin Façade (DSF)

Double skin façade (DSF) is a European architectural trend mostly driven by the aesthetic desire for an all-glass façade which leads to an increased transparency, the practical need for an improved indoor environment and the wish of energy use reduction during the occupation stage of a building. Although the concept of DSF is not new, there is a growing tendency by architects and engineers to use them as they are acclaimed as an example of *green* building strategy (Fig. 2.9) and the introduction of adaptive systems and passive energy design with DSF may represent an important starting point for the development of a more sustainable architecture that also involves the construction engineering [31]. In modern era, the first architects to explore this new technology were Le Corbusier, with his *mur-neutralisant*, and Alvar Aalto, in the window design of the Paimio Sanitorium. Subsequently, the idea has evolved with the first passive solar design of the *trombe wall*, which is also seen as a precursor of modern double skin systems, to become, in recent years, a responsible measure for environmental protection [32].

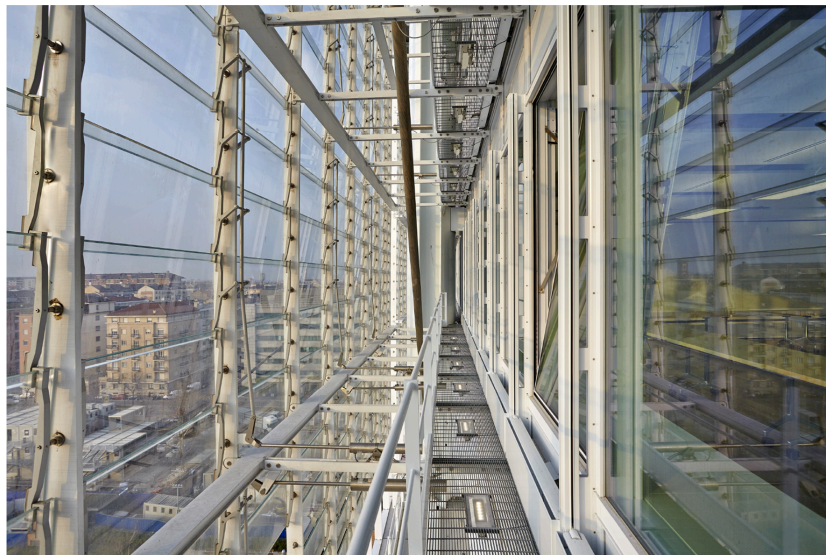


Figure 2.9: Intesa San Paolo skyscraper in Turin (Italy) awarded the LEED Platinum certification in 2015 by the U.S. Green Building Council (USGBC), making it the most ecological European skyscraper

DSF are based on the concept of external walls which dynamically interact with the changing environmental conditions and which can incorporate passive design solutions such as natural ventilation, daylighting and solar heat gain into the fabric of the building itself. These key components, in terms of energy efficiency and microclimatic comfort, are directly controllable and manageable by users, thus, representing a great potential especially for

tall glazed office buildings which, currently, are not designed for energy saving purposes [33]. In this way, however, many advantages would be obtained, including the occupants' better control of the local environment for natural ventilation needs, due to the internal opening windows, and the possibility of managing the incoming solar radiation for heating or lighting needs, due to the solar shading devices interposed between the two skins. These design tools make it possible to reduce the overall energy consumption of a tall building, compatibly with the microclimatic condition in which it is located, offering solutions for the daylight maximization with the integrated control of solar heat gain, natural ventilation and moderation of the temperature range. All this inevitably leads to a greater energy efficiency: the potential greenhouse effect created in the air cavity can be used for the heat production and exchange, while the natural ventilation may reduce air conditioning loads, and so on. It is worth noting that there is no need for double façades on all sides of a high-rise building; under certain circumstances, however (e.g. high levels of street noise, high wind loads or increase in building height) such façades may be the most appropriate and economical solution.

Basic types of DSF

From a structural point of view, a DSF consists of three functional layers: a double glass closure layer with an interposed cavity in which the air can circulate naturally, mechanically or be fan supported. The external skin can be completely glazed; the internal one, on the other hand, is typically composed of double insulating, transparent or low-emission glazing with a variable distance (from 200 – 300 mm up to 1.5 – 2.0 m [34]-[35], with a typical value being 1 m [36]), depending on the specific design of the system. Apart from the ventilation mode inside the cavity, the air origin and destination may vary according to the climatic conditions, the use, the working hours of the building and the heating, ventilation and air conditioning (HVAC) strategy employed. Often, for reasons of protection and heat extraction during the cooling period, the solar shading devices can be placed inside the cavity [37]. There are multiple ways on how to build DSF, which can be classified according to three different criteria, independent of each other and based not only on the geometric features of the envelope, but also on its functioning, from which the physical behavior of the whole system depends: the air cavity partitioning (i.e. the façade type), the ventilation mode and the airflow pattern [38]. Obviously, the optimal combination of the various typologies is dictated by the climate, the orientation of the building and the overall design energy requirements.

The façade *partitioning* refers to how the cavity located between the two glazed skins is physically divided. In general, four basic types of DSF are recognized (Fig. 2.10):

- *box-window* type

which has both horizontal and vertical partitions at each floor level that subdivide the façade in smaller and independent boxes; in each box, the air cavity is typically naturally ventilated (Fig. 2.11). The advantage of this model is the freedom it gives to the users in controlling

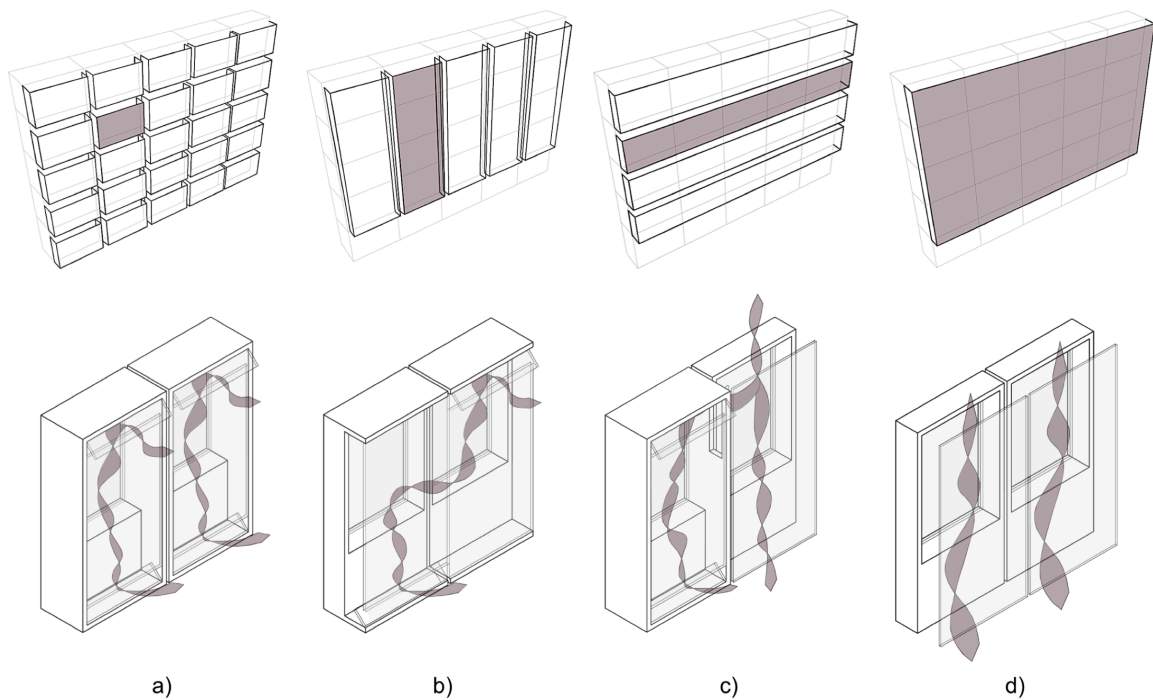


Figure 2.10: Basic types of DSF: a) box-window façade, b) shaft-box façade, c) corridor façade and d) multi-storey (or second skin) façade

their own internal environment. A serious limitation is that the same freedom granted to one user may not be appreciated by another;

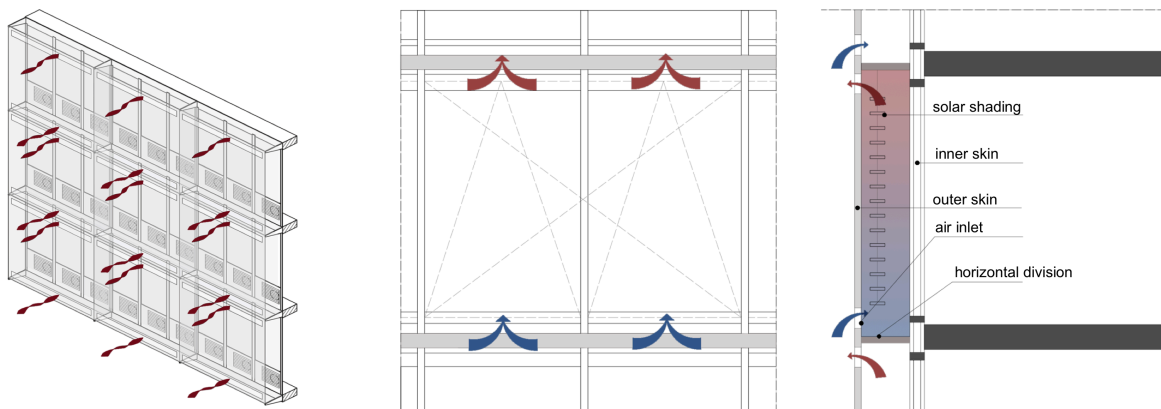


Figure 2.11: Storey-high box-window façade with ventilation flaps at the top and bottom

- *shaft-box* type

which is composed of a set of box-window elements connected via vertical shafts placed inside the façade, which ensure a natural stack-effect ventilation; the hybrid mode ventilation is often used for this DSF type (Fig. 2.12). This model represents the most effective version of the double façade, but at the same time it involves the maximum constructive and engineering effort, thus, becoming suitable for low-rise buildings;

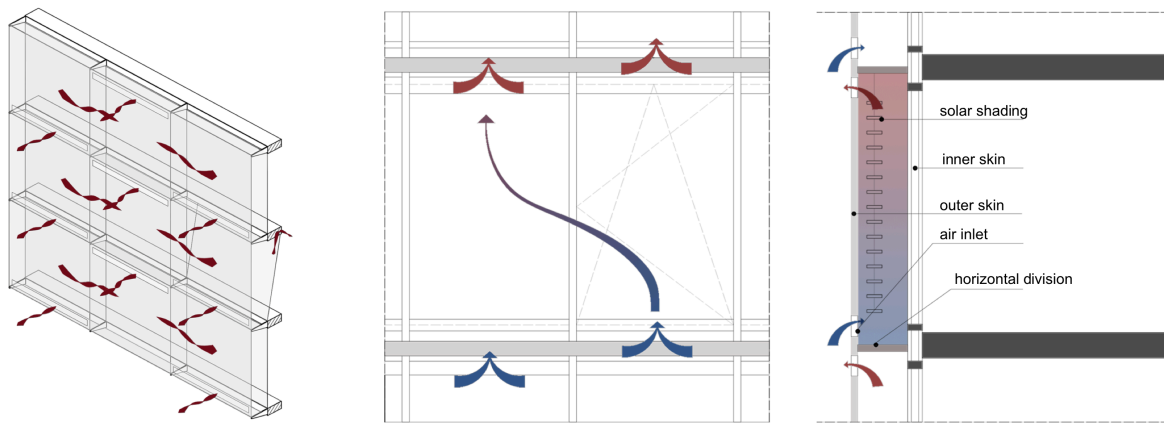


Figure 2.12: Shaft-box façade with lateral air inlets alternating with continuous ventilation paths

- *corridor type*

which has uninterrupted horizontal air cavities at floor level (for acoustical, fire security or ventilation reasons), but it is physically partitioned for each of them; in this case, all three ventilation modes are possible (Fig. 2.13). The advantage of this system is that, due to the uninterrupted space between the two skins, the building can be naturally ventilated from all directions. On the other hand, the uninterrupted horizontal airflow may give rise to acoustic interference between adjacent rooms;

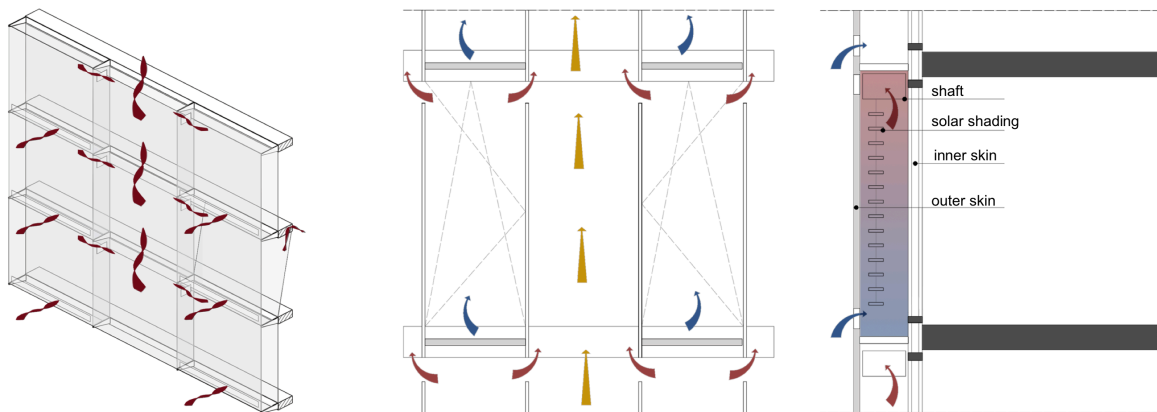


Figure 2.13: Corridor-type façade with separate air circulation per floor and diagonal flow to avoid recontamination

- *multi-storey (or second skin) type*

which has uninterrupted air cavities spanning the full height and width of the façade; the air cavity ventilation is realized via large openings placed near the floor and roof of the building and all the three ventilation modes can be used (Fig. 2.14). This has the advantage of technical and structural simplicity since it does not involve a large number of moving parts and the outer glass skin is simply mounted on the inner façade structure. Critical issues can be the low possibility of controlling the internal building environment, the lack of fire protection

and the risk of overheating.

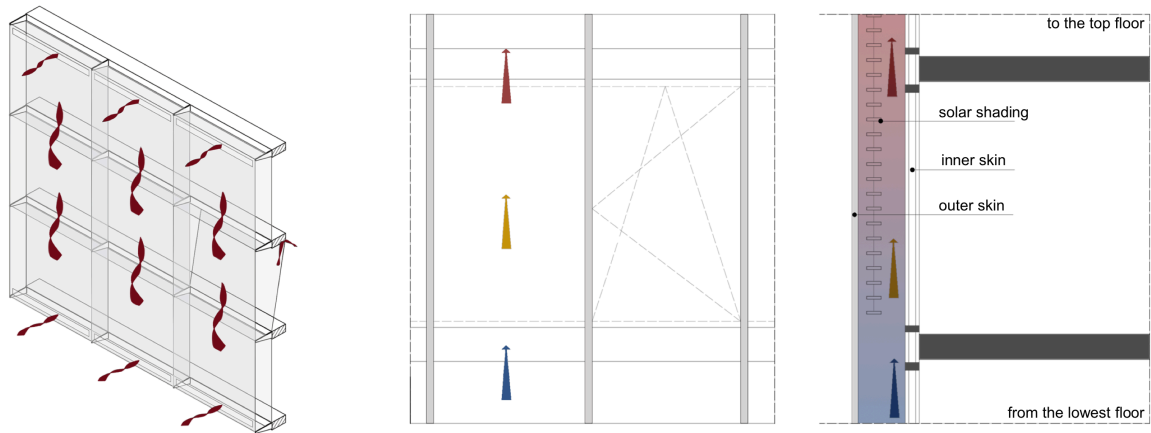


Figure 2.14: Multi-storey façade with continuous air cavity that supplies air in the lower part and extracts it in the upper part of the outer skin without the need for openings on each floor

The *ventilation* mode refers to the driving forces at the origin of the cavity ventilation between the two glazed skins. Depending on the behavior of the enclosure system, there are three different functional models:

- *natural* ventilation

it is possible due to the difference in the air current pressure and temperature. The warm air, also known as *stack* or *chimney effect*, raises towards the top of the building as it is much lighter than cold air. Heating up in the closed cavity, the air tends to rise upwards; at the same time, the cooler fresh air enters the cavity from below, thus providing a constant air circulation within the cavity [39]. In this process, the cavity can be in contact only with the outside (the air enters and exits from external environment) or with both the inside and outside; depending on the needs and climatic conditions, the air enters from outside and exits inwards or enters from inside and exits outwards (Fig. 2.15);

- *mechanical* ventilation

it is also widely implemented in DSF as it is more reliable than the natural type, being independent of the environmental conditions, temperature differences, wind speed and direction. In this process, the air is introduced from inside and, once treated, returns back to the building: the façade system is connected to the shafts of mechanical ventilation system through the openings in the cavity. The building requires the continuous working of an air conditioning system (Fig. 2.16);

- *hybrid* ventilation

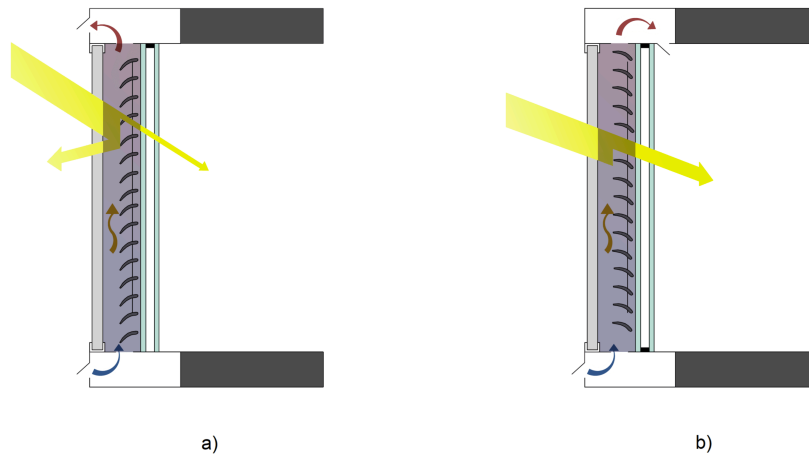


Figure 2.15: Diagrams of natural ventilation in a) summer: the heat is extracted from the cavity by the stack effect, and b) winter: the outside air is preheated before the immission

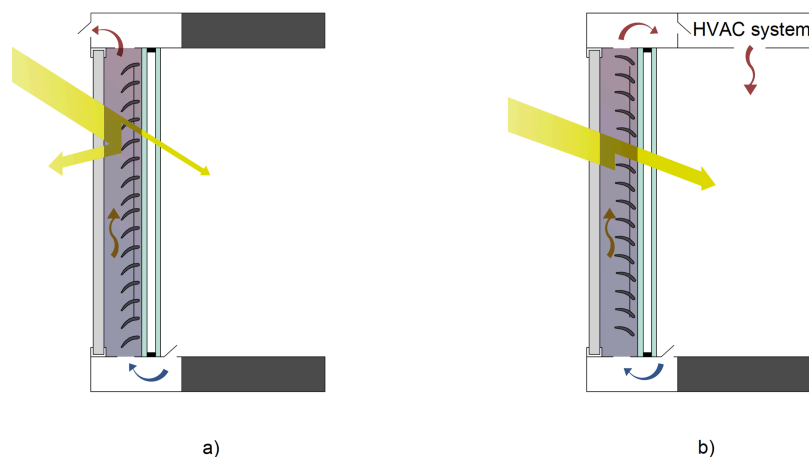


Figure 2.16: Diagrams of mechanical ventilation in a) summer: the cavity is cooled with exhaust air, and b) winter: the exhaust air is re-heated and recirculated

as the term suggests, this arises from the mixture of both types mentioned above. It is based on the natural ventilation with the possibility of switching to the mechanical type when the former cannot be provided due to the external circumstances. However, this type is not often applied due to the high installation complexity.

The *airflow pattern* refers to the origin and destination of the air circulating in the ventilated cavity and it is independent of the ventilation mode applied (natural or mechanical). Three main pattern can be distinguished:

- *buffer system*

it is composed of two sealed single glass layers that allow the air to enter the building through a separate HVAC system or box-type windows which cross the entire double skin; the shading devices can be included in the cavity, which has a variable width from 250 mm to 900 mm (Fig. 2.17 a);

- *extract air* system

it consists of a second glass layer placed inside the main double-glazed façade. The air gap between the two skins ranges from approximately 150 mm to 900 mm and is part of the HVAC system. The heated air between the glass layers is extracted through the cavity with the use of fans, while the fresh air is supplied by the HVAC system and precludes natural ventilation (Fig. 2.17 b);

- *twin face* system

it is based on a conventional curtain wall placed inside a single glazed skin and it differs from the buffer and extract air systems for the inclusion of openings in the outer skin, allowing for natural ventilation. The inner skin is insulated to minimize heat losses while the outer glass layer slows down the wind in high-rise buildings and allows the fresh air to enter inside without associated noise and turbulence; the air cavity placed between them is at least $500 - 600\text{ mm}$ wide (Fig. 2.17 c).

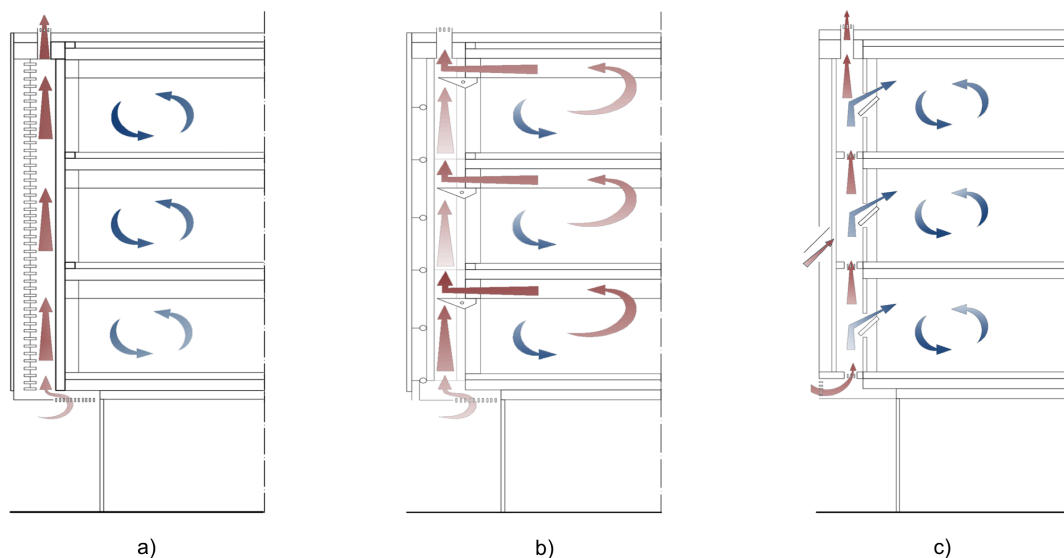


Figure 2.17: DSF airflow patterns: a) buffer system, b) extract air system, and c) twin face system

DSF vs CW

As a main component of the building envelopes, the façade plays a fundamental role in protecting indoor environments and managing the interactions between external and internal spaces. The glass enclosures find wide application in modern architectural projects, especially in office buildings, due to their aesthetics, lightness and daylight potential. Despite their widespread use, conventional glass CW show some critical issues, such as poor natural ventilation and noise reduction index, low daylight levels, thermal discomfort and increased energy consumption, which could worsen the overall energy performance of the building they enclose [40]. These weaknesses can be further increased in modern all-glass envelopes which

may cause a non-negligible energy consumption due to the risk of overheating and unwanted lighting during hot summer days and significant thermal losses during the night or in colder climates [41].

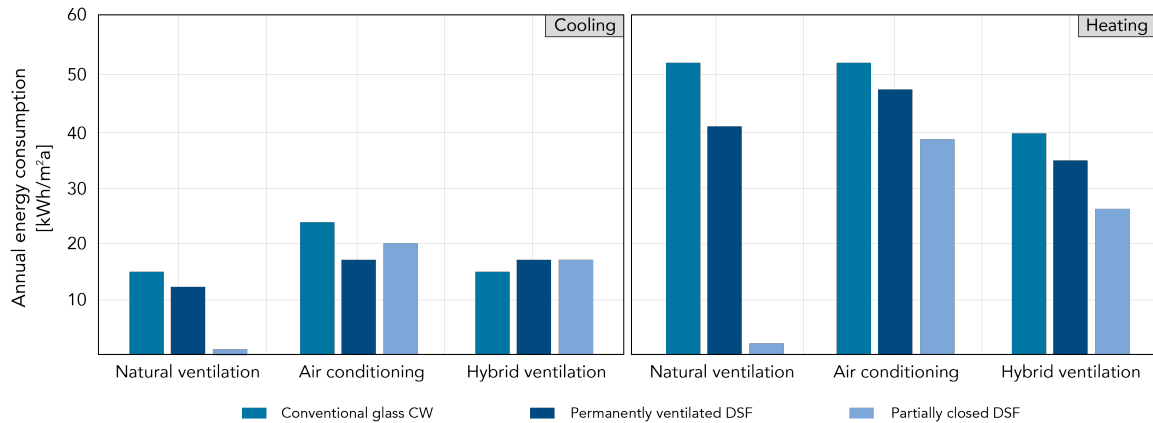


Figure 2.18: Typical annual energy consumption in cooling (left) and heating (right) of a traditional glazed CW and two different types of DSF. Source: Oesterle, E. (2001). *Double-Skin Façades: Integrated Planning*

With the possibility of obtaining a totally transparent envelope without sacrificing energy benefit and thermo-hygrometric well-being, as well as the aesthetic taste, DSF represent an optimal solution, increasingly globally accepted. Both technically and architecturally advantageous arguments exist for investing in a double envelope: the acoustic and thermal insulation, the night ventilation, the energy saving and reduced environmental impact are just some of the main qualities offered by this system as compared to a traditional glazed curtain wall, as shown in Figure 2.18. According to some authors [42]-[43], the sound insulation can be one of the main reasons for using a DSF, with which it is possible to reduce both internal and external noise pollution levels. Clearly, the façade type, the cavity width (minimum 200 mm [44]) and the number and positioning of the air inlets on the exterior skin can significantly influence this property. Moreover, with a DSF it is possible to provide a greater thermal insulation to the building both in the winter and summer season, reducing the heating and cooling costs. Due to the gap between the two glass skins, the internal air is exploited to increase the well-being of indoor environment. In accordance with [45], the energy efficiency of a DSF is highly dependent on the climatic conditions, performing better than a traditional glass CW in a warm habitat. During the winter, the openings on the outer skin are typically closed, thus, the air stays inside the cavity, minimizing the heat loss; during the summer, the heated air inside the cavity is extracted with natural or mechanical ventilation, thus, the system works by subtracting heat from the building. During the hot summer season, the natural night ventilation is used to pre-cool room offices, thus, preventing internal spaces from daytime overheating and providing thermal comfort and better air quality for occupants.

Unfortunately, there are also several disadvantages associated with DSF [46]. The main obstacles to the installation of such a cladding system on a building include the loss of useful space due to the width of intermediate cavity, the uncertainty in the choice of the type

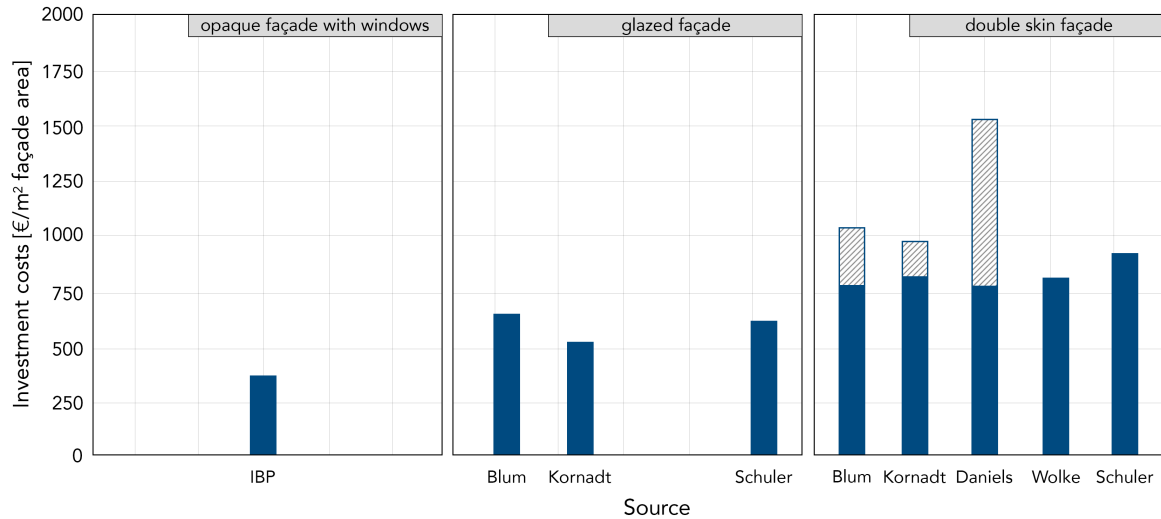


Figure 2.19: Investment costs of a DSF compared with the costs of a conventional glass CW. Source: Streicher, W. (2006). *State of the Art of Double Skin Façades in Europe: The results of WP1 of the BESTFAÇADE Project*

of glass and the ventilation mode, the high additional maintenance and operational costs. Likewise, the difficulty in fire protection design, the overheating problem and reduction of indoor daylight levels, due to the addition of double glazing, are other inevitable challenges that require extensive research to propose reliable solutions. Above all, the higher investment costs of a DSF, which exceed by 60 – 80% those of a traditional CW, and by 100 – 150% those of an opaque cladding with windows, represent the main critical aspect [47], as shown in Figure 2.19. Typical European construction costs per square meter of façade are in the order of 300 – 500 € for a glass CW and 600 – 800 € for a standard DSF (for instance, a mechanically ventilated shaft-box type with solar shading included), which can go up to 1000 – 1300 € if the opening vents are included on the outer skin [48].

2.2.4 Adaptive Façade

As the name suggests, *adaptive* means *changing* according to the needs of the surrounding environment [49]. Buildings can be adapted following several multi-disciplinary approaches such as mobility, reusability and standardisation, automation or building independence. In this context of continuous transformation, a strategic role is played by the building enclosures. An adaptive (or dynamic) façade is a framework which changes its structure, behaviour or resources according to the request (Fig. 2.20).

The modern façade generation consists of highly flexible multifunctional systems, thanks to which a building is able to change its functions over the time in response to the required performance and the transitory external conditions, with the aim of improving its overall behavior [50]. Generally, the constructions that can adapt to changing climatic conditions are called *smart* buildings. In this case, the term *adaptation* means the possibility that buildings and façades adapt themselves to the current weather conditions: instead of excluding the environment, they involve it as this will have a positive impact on both the thermohygro-metric

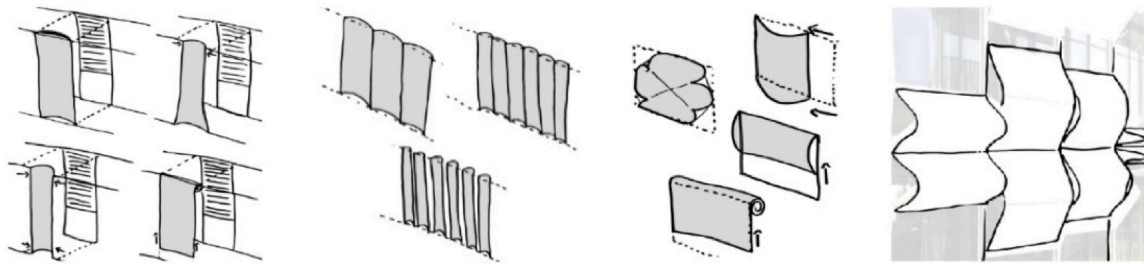


Figure 2.20: Conceptual sketches of adaptive façade glass panels. Source: Ribeiro Silveira, R. (2018). *Adaptive and composite thin glass concepts for architectural applications*

well-being of users and the energy well-being of the building. Recently, in Central Europe this technology has evolved from traditional construction methods due to particularly favorable climatic conditions and, today, the implementation of adaptive envelopes often includes the automation technology. As a matter of fact, with the help of sensors, actuators and intelligent materials like SMA [51]-[52], these dynamic cladding models allow to manage the energy flows [53], alter the properties of fixed devices and manually or automatically control the movable elements (such as solar shading, openings and vents) related to the type of users and building complexity [54].



Figure 2.21: Arab World Institute by Jean Nouvel (Paris, 1987)

In the past, architects and engineers have investigated the possibility that future buildings possess adaptive responsiveness to changing environmental scenarios. Already in 1929, Le Corbusier had formulated the *mur neutralisant* concept for a building envelope that had a positive impact on the indoor climate. In the 1940s, Buckminster Fuller had developed the idea of a dome-shaped structure to be used as a secondary envelope to generate an independent microclimate with only passive means. Furthermore, at the end of the 1960s, the possibility of applying cybernetics to architecture was explored with Negroponte's definition of *sensitive architecture* and, above all, with the concept of variability of the building's skin introduced by Michael Davies in 1981 [55]. Davies was responsible for the idea of a *multi-purpose wall*; that is, a set of functional layers within a glass element capable of providing sun and heat protection and automatically adjusting functions according to the current conditions.



Figure 2.22: Intelligent adaptive envelope of Aedas Architecture’s Al Bahar Towers (Abu Dhabi, 2012) that opens and closes following sunrays

Over the time, the concept of a *wall for all seasons* was defined in the image of an envelope capable of changing conformation with respect to the external thermo-physical stresses (*intelligent skin*), then merged into the design of kinetic elements, such as the shielding system of Jean Nouvel’s Arab World Institute (1987), the manifesto work that started this transformation (Fig. 2.21). However, only in the last few decades, the technological research has evaluated new experimentation boundaries in the field of intelligent envelopes with dynamic and interactive behavior [56] which have guided the choices and design of the Al Bahar Towers computerized façade (2012) made by Aedas Architects (Fig. 2.22).



Figure 2.23: Adaptive thin glass facade model. Source: Ribeiro Silveira, R. (2016). *Flexible transparency: a study on thin glass adaptive façade panels*

Despite several projects already carried out, the development of adaptive building envelopes is still in a preliminary phase of research and prototyping. The trend of the recent years is to explore the potential of thin glass, commonly used for electronic device displays

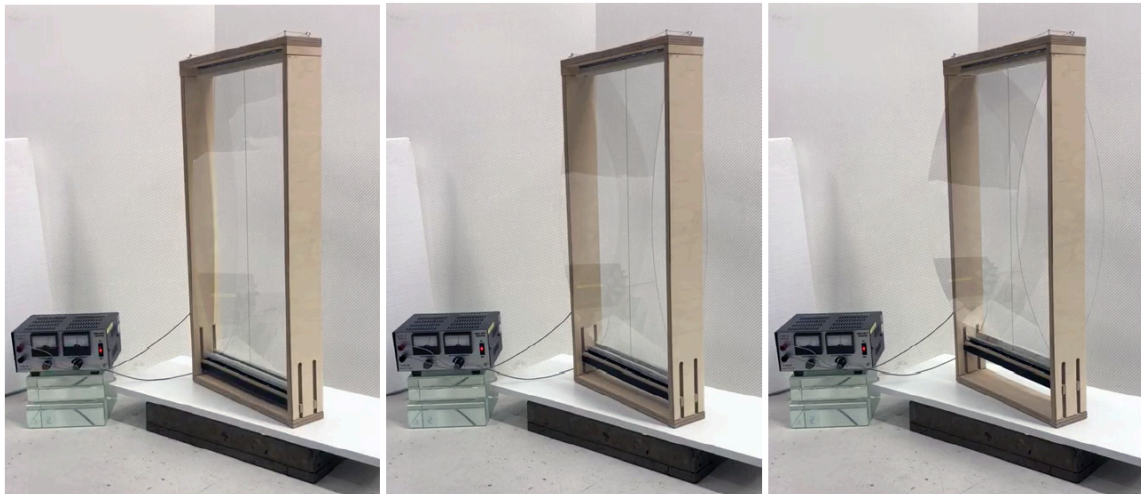


Figure 2.24: Adaptive thin glass façade model with SMA. Source: Miri, B. (2018). *Flexible transparency with smart materials: a study on adaptive thin glass façade developed with shape memory alloy*

and touch screens such as smartphones and tablets, for architectural applications on adaptive panels. Due to its high strength and small thickness, the glass can be easily bent into architecturally appealing curves, which can be adjusted to withstand wind loads. Furthermore, the extremely low weight, as compared to traditional glass, can be used to create lightweight façades that can change their shape in response to the external parameters [57]. A first step in the development of adaptive thin glass envelopes was taken by Silveira [58] who in 2016 created a prototype of a double skin adaptive façade in which thin glass is framed on the long edges of the panel and connected to guides up and down (Fig. 2.23). In 2017 Topcu [59] explored different design solutions to make façade water- and air-proof in its closed configuration, for example, by adding a magnetic strip along the glass perimeter or an elastic stretch fabric along the curved sides. Latest advances concern the possibility of driving glass through SMA: in 2018 Miri [60] had the idea to integrate the panels with SMA cables that shorten when heated by solar radiation or electricity, pulling and bending the façade panels (Fig. 2.24).

2.3 Wind design and performance of tall buildings

Wind velocity is typically modeled as the sum of a mean component plus a fluctuating component resulting from the assumption of a zero-mean *stationary*¹ random process following the *Gaussian*² distribution [61]. Existing fluctuating wind speed analysis methods can basically follow two different approaches depending on whether the mean wind speed is intended

¹In mathematics and statistics, a stationary process is a stochastic process whose probability distribution is time-independent; consequently, the mean and variance of a stationary process do not change over time. White noise is the simplest example of a stationary process.

²In the probability theory and statistics, a Gaussian process is a stochastic process composed by an ensemble of random variables indexed by time or space, each of them with a multivariate normal distribution. The distribution of a Gaussian process is the joint distribution of all the random variables.

as a time-independent component (*constant mean approach*) or a time-dependent component (*time-varying trend approach* [62]). Regardless of the analysis method adopted, wind-excited buildings generally tend to experience low-frequency accelerations and vibrations, mostly between 0.08 and 1 Hz [63], which can be extremely annoying if the buildings in question are particularly tall and slender. As the fundamental frequency of high-rise structures is usually less than 1 Hz, it can fall into the same frequency range as the wind *gusts*, which are defined as peak wind speeds lasting less than 20 seconds. For design purposes, 3-second duration wind gust velocity is typically used [64]. On particularly thin structures not designed to withstand wind load, large resonant vibrations can occur [65]; in this case, wind effects become considerable enough to get predominant with respect to dead and live loads, and in some cases, even with respect to earthquakes [66], as shown in Figure 2.25.

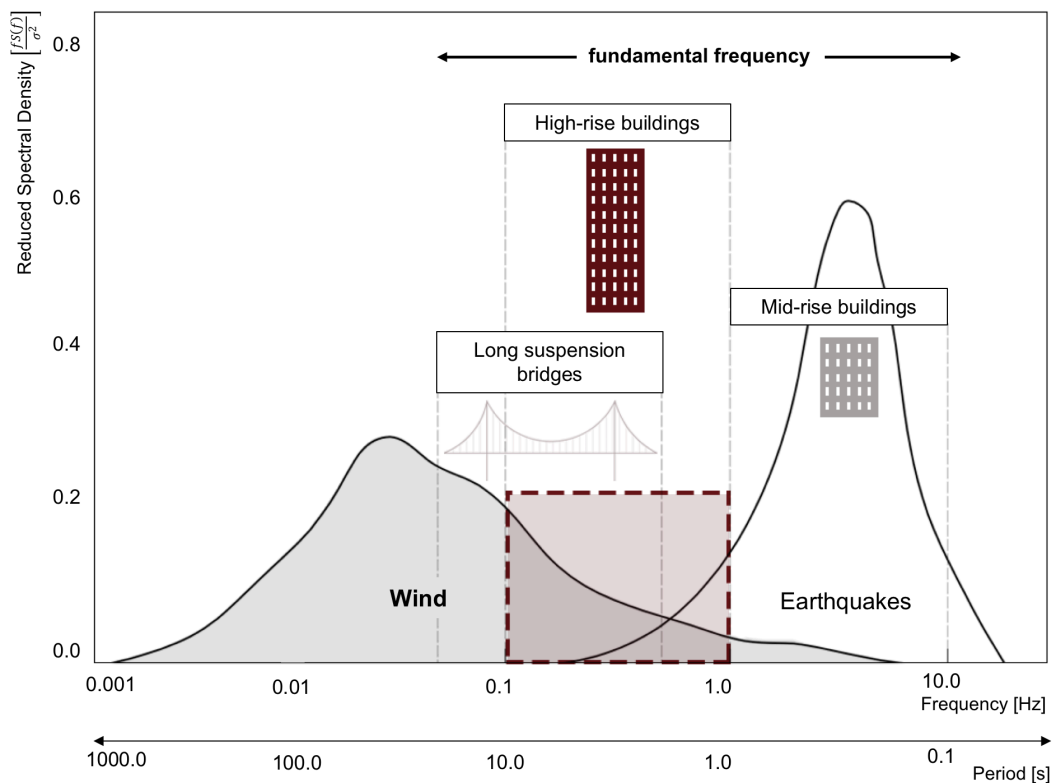


Figure 2.25: Effect of wind and seismic load on structures with variable fundamental frequency of vibration

For a well-designed construction, the wind-induced wave motion, also known as *wind drift*, should be kept within acceptable limits (specifically, it should not exceed $H/500$, where H is the height of the building [67]) so as not to affect the building users who are able to perceive it and experience feelings of fear, discomfort and, more generally, symptoms of motion sickness [68]. However, the effect of this movement on the occupant comfort is still unclear and this is why no international guidelines have yet been agreed that can quantify the acceptable level of the building drift. Modern tall buildings, unlike mid-rise conventional structures, are increasingly flexible, lightweight and low-damped and interact dynamically with the wind, compromising their structural safety and stability. The wind flow interaction with a typical

low-rise or mid-rise building only occurs with its external shape: since it is characterized by high vibration frequency that makes it stiffer, its deflection under dynamic load is not significant and the design wind speed can be estimated reliably enough through analytical or numerical procedure, not taking into account the dynamic properties of the building, with the exception of its height. In the analysis of high-rise structures, however, the identification of a specific digital simulation technique for generating possible realizations of Gaussian stationary random processes consistent with turbulent wind fields is required. For the digital simulation of wind turbulence, many computational techniques are now available and the choice of one rather than the other is essentially linked to the size of the problem. One of the most used methods is the Monte Carlo procedure [69]. Clearly, a faithful reproduction of the building dynamic behavior under wind field is rather complicated and burdensome if computations are carried out on a three-dimensional FEM which faithfully reproduces all degrees-of-freedom of the complete structure. To reduce the high computing time caused by the large number of nodes distributed in the 3D space, in which all the three components of wind turbulence occur, simplified equivalent models able to approach the building dynamic properties with sufficient accuracy may be utilized.

2.3.1 Wind velocity characterization

The wind velocity, $v(z, t)$, varies randomly over time and space and, according to the *constant mean approach*, it can be statistically defined as the sum of a time-independent mean component, $v_m(z)$, acting in the longitudinal x direction, and three turbulent components, (u, v, w) , acting in three orthogonal directions, (x, y, z) , as can be seen from Figure 2.26. The mean wind speed, $v_m(z)$, is given by the mean of the fluctuating velocity, $v_t(t)$, over time T ; the turbulent wind speed, on the other hand, can be described by different types of statistics, such as the turbulence intensity, $I_v(z)$, the turbulence scale, $L_v(z)$, the gust factor, G_v (or peak factor, g_v), the power spectrum, $S_v(z)$, space-time correlations, and so on. The magnitude of the wind fluctuating component is called *gust* and it depends on the average computation time, τ : the smaller τ , the greater the magnitude of the gust [70]. The estimate of the mean wind velocity should be based on the longest time interval considered to be stationary; generally, this requirement can be met by accounted for a standard range of $T = 10$ minutes, although not all international building codes use the same values.

The obstructions near the ground surface delay the air movement, leading to a reduction of the wind velocity: for a flat terrain with uniform roughness features, the mean wind speed varies with height, z , according to the Ekman spiral profile [71], which is related to velocity, ground roughness, geographic latitude and atmosphere stratification. At a certain height from the ground, however, the air movement is no longer affected by the presence of obstacles. This height is called *gradient height*, z_g , and is a function of the ground roughness. The unobstructed wind speed is called *gradient wind speed*, v_g , and is constant above the gradient height. In the reference standard codes, the mathematical models used to describe the wind speed profile are the logarithmic and power laws. Based on the physics of the atmospheric boundary layer, the logarithmic law is mainly used in the meteorological field.

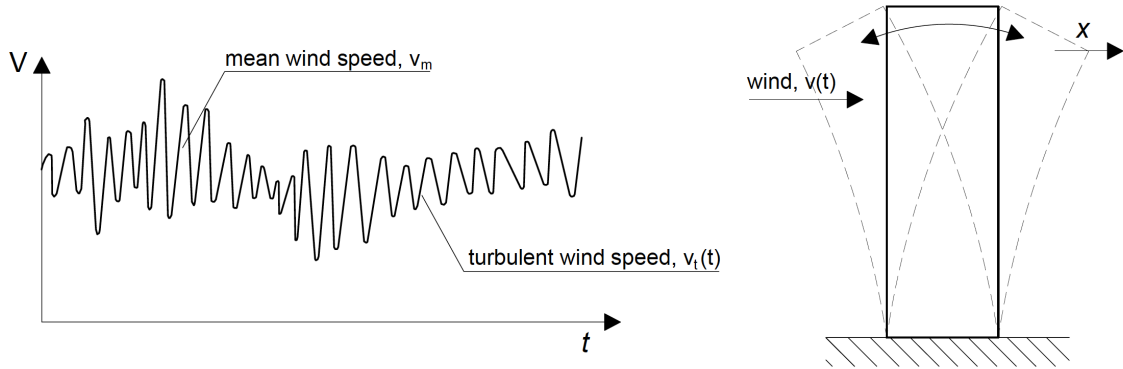


Figure 2.26: Wind speed diagram consisting of a mean and a turbulent component

Table 2.1: Typical values of properties describing the wind speed profile

Category	Description	z_g [m]	z_0 [m]	α [-]	Gust speed exponent
1	calm open sea, flat desert	250	0.001	0.11	0.07
2	open country, scattered trees	300	0.03	0.15	0.09
3	suburban areas, forest	400	0.3	0.25	0.14
4	city center, industrial areas	500	3	0.36	0.20

In this case, the mean wind speed profile is defined as

$$v_z = 2.5u^* \ln\left(\frac{z}{z_0}\right) \quad (2.1)$$

where u^* is the shear velocity and z_0 is the ground roughness length, affecting the increasing wind speed rate with height.

On the other hand, the estimate of wind load for structural design purposes requires the wind velocity variation with height to be represented in accordance with the power law, which is an empirical equation defined as

$$\frac{v_z}{v_g} = \left(\frac{z}{z_g}\right)^\alpha \quad (2.2)$$

where z_g and z are functions of the ground roughness and α is the power law index. Typical values of z_g and α are shown in Table 2.1.

The instantaneous wind speed varies randomly over time and space, inducing dynamic effects on structures. The assessment of the wind action for a suitable high-rising building design must be related to the determination of the micro-meteorological fluctuations [72], that is, the turbulent actions due to topographical effects, such as ground roughness, obstructions around the site, and so on. The simplest indicator of the atmospheric turbulence is the intensity, $I_v(z)$, which can be defined for each component of the turbulence as the ratio between the standard deviation of the fluctuation rate, $\sigma_v(z)$, and the mean wind velocity,

$v_m(z)$. By focusing on the longitudinal component only, one has

$$I_v(z) = \frac{\sigma_v(z)}{v_m(z)} \quad (2.3)$$

where

$$\sigma_v^2 = \sum_{-\infty}^{\infty} S_v(\Omega) d\Omega \quad (2.4)$$

being Ω the forcing frequency and $S(\Omega)$ the turbulence power spectrum provided by the relation [CNR-DT 207/2008 Eq.E.1a]

$$S_v(z, \Omega) = \frac{6.868 \frac{L_v(z)}{v_m(z)}}{\left[1 + 10.302\Omega \frac{L_v(z)}{v_m(z)}\right]^{5/3}} \sigma_v^2(z) \quad (2.5)$$

where $L_v(z)$ is the turbulence length scale which expresses the average size of the vortices making up the atmospheric turbulence.

Given the mean wind velocity, $v_m(z)$, in a fixed observation period, T , and the maximum mean velocity (or wind *gust*), $v_g(z)$, for a fixed interval, τ (with $\tau \ll T$), it is possible to define a conversion factor between the two quantities, known as the *gust factor* (Davenport, 1967)

$$G_v(z) = \frac{v_g(z)}{v_m(z)} = \frac{(v_m(z) + v_g(z))}{v_m(z)} \quad (2.6)$$

or the peak factor, g_v , that is the ratio between the gust speed and its standard deviation, $\sigma_v(z)$

$$g_v(z) = \frac{v_g(z)}{\sigma_v(z)} \quad (2.7)$$

from which one has

$$G_v(z) = 1 + \frac{v_g(z)}{v_m(z)} = 1 + g_v(z) \frac{\sigma_v(z)}{v_m(z)} \quad (2.8)$$

The peak factor depends on the time interval; typically, $g_v \in [3.00, 4.00]$ and with good approximation, $g_v = 3.5 - 3.7$ can be set (Eurocode-ENV 1994). Wind gusts directly induce fluctuating forces on the structures that fall within the wind flow (Fig. 2.27). Given the randomly nature of the turbulent wind speed, the resulting forces and structural response will also be. The magnitude of the turbulent wind load is a function of the turbulence intensity, I_v , which determines the local entity of the fluctuation forces, and of its length scale, L_v , which defines how the turbulent component is related to the structure, according to the building size.

The rapidly and even abruptly changing wind forces can cause structures to undergo aerodynamic forces in the longitudinal direction (*along-wind* forces), normal to wind direction

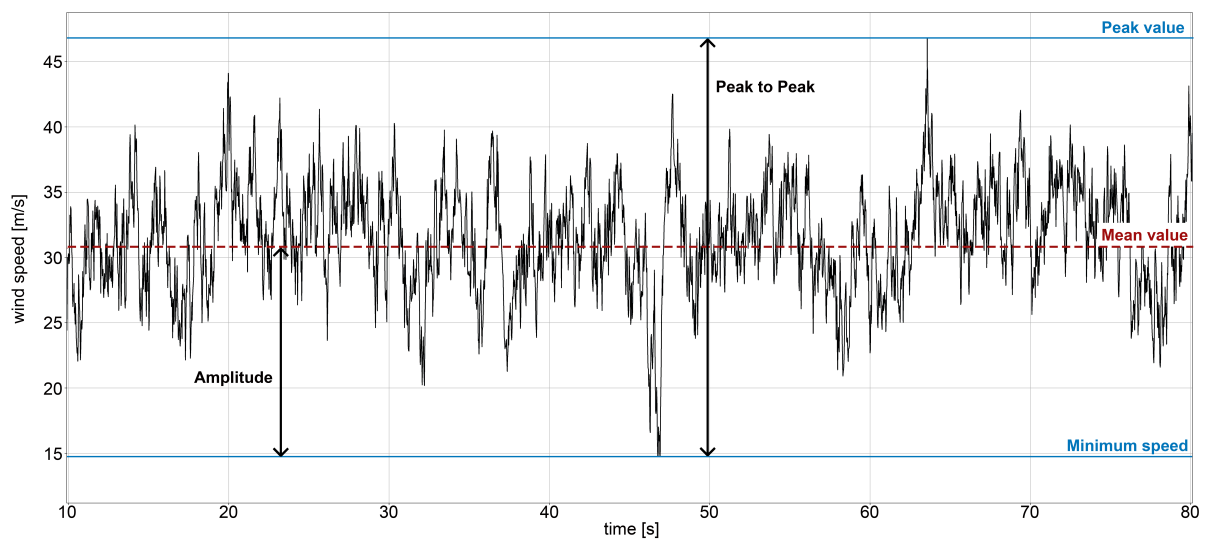


Figure 2.27: Typical wind gust

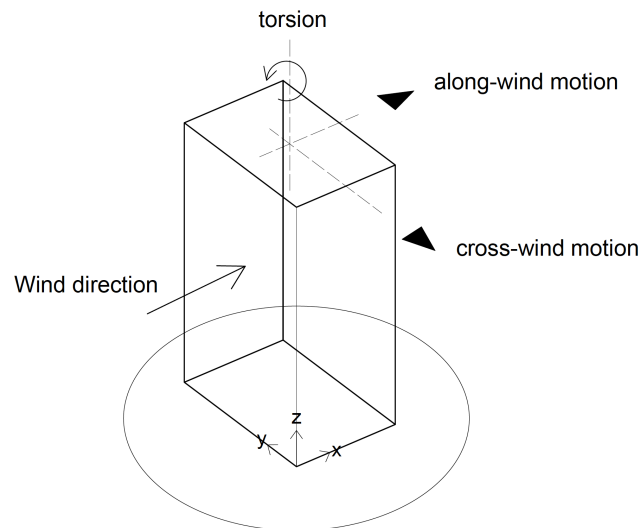


Figure 2.28: Decomposition of wind load in the along-, across- and torsional direction of a high-rise building. Source: Sinhamahapatra (2019). *Along and Across Wind Parameters Acting on Tall Structures*

(*across-wind* forces) and torsional forces [73], as schematically illustrated in Figure 2.28. For structural engineering purposes, it can be very useful to decompose the wind excitation, and the consequent structural vibration, into a longitudinal and a transversal direction. The *along-wind* excitation mainly arises from *drag pressures* and is strongly dependent on the incoming turbulence. The *across-wind* excitation, on the other hand, is affected by the incoming turbulence as well as the building shape and movement. On particularly tall and slender structures, the vibrations induced by the cross-wind gusts or by vortices dispersion (the so-called *vortex-shedding*), can become particularly dangerous if the ratio $l/b > 2$, being l and b the two main dimensions of the building. This context deals with a *constant mean approach* to estimate the effect of longitudinal wind velocity on the dynamic behavior of

structures; therefore, the *along-wind* velocity within the atmospheric boundary layer flow can be expressed as

$$v(z, t) = v_m(z) + v_t(z, t) \quad (2.9)$$

where $v_m(z)$ is the constant mean wind velocity and $v_t(z, t)$ is the turbulent wind velocity in the longitudinal direction.

For a well-defined structure of area, A (in m^2), placed inside the flow, the longitudinal wind force experienced is given by [CNR Eq.3.13a]

$$F(t) = C_D \frac{1}{2} \rho A v(t)^2 = C_D \frac{1}{2} \rho A [v_m^2 + 2v_m v_t(t) + v_t(t)^2] \quad (2.10)$$

where C_D is the drag coefficient and ρ is the air density.

By neglecting the second order term, one has

$$F(t) = \underbrace{\frac{1}{2} \rho C_D A v_m^2}_{F_m} + \underbrace{\rho C_D A v_m v_t(t)}_{F_t(t)}$$

where F_m is the constant mean wind force and $F_t(t)$ is the time-dependent turbulent wind force.

2.3.2 Simulation domain

As is known, a wind-induced vibration is a wave motion around a balance position and the number of times a complete motion cycle occurs during a period of 1 s determines the vibration frequency, f , which is measured in Hertz (Hz). For simple sine waves, the vibration frequency could be determined from looking at the waveform in the time-domain (Fig. 2.29 a); but as we add different frequency components and noise, a spectrum analysis is required to obtain a clearer picture of the vibration frequency (Fig. 2.29 b).

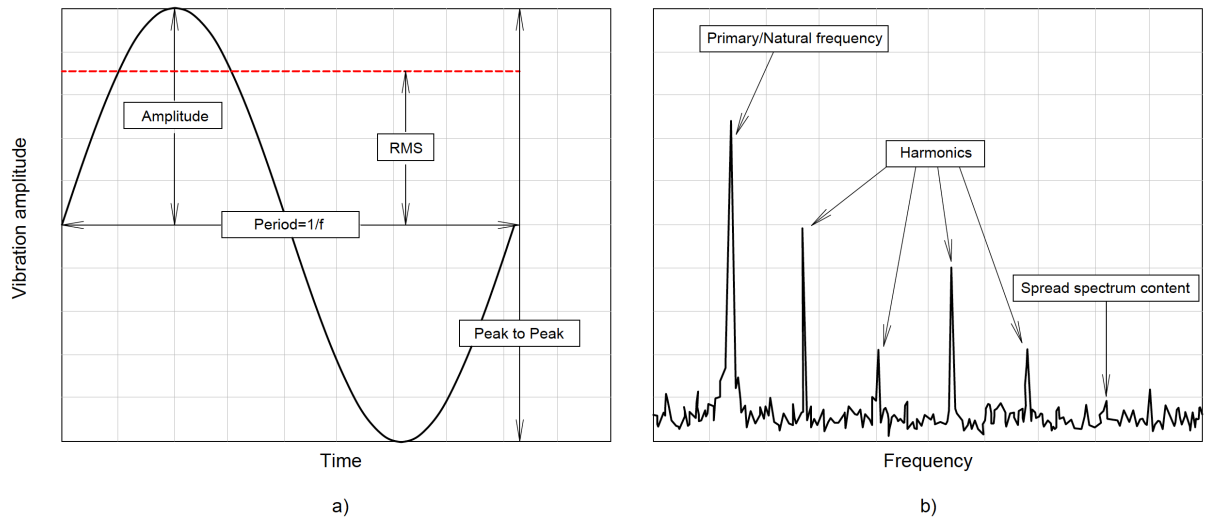


Figure 2.29: Vibration data analysis in the time- a) and frequency- b) domain

When analyzing vibration data in the time-domain, only few parameters are available in quantifying the strength of the vibration profile:

- the peak (or amplitude), which is valuable for shock events but it does not take into account the time duration and, thus, the energy in the event;
- the peak-to-peak value, which provides the maximum excursion of the wave, useful when looking at the displacement response;
- the Root Mean Square (RMS) value, which is generally the most useful indicator as it is directly related to the energy content of the vibration profile and, thus, its destructive capability; the RMS also takes into account the time-history of the waveform.

In the real world, a lot of vibration can be referred to as *random* vibrations, since they include many frequencies at the same time. In many applications, the vibration frequencies change fastly over time and this phenomenon can only be observed with a Fast Fourier Transform (FFT) algorithm that allows to perform the analysis in the frequency-domain in order to clearly identify the main existing frequencies and help the analyzer to determine the cause of any vibration signal. The FFT is a tool that breaks a periodic function, $x(t)$, with period, $T = 2\pi/\omega$ (if Dirichlet conditions ³ are met) in an infinite sum of harmonic functions (sines and cosines) of frequency $f_k = kf$, where $f = 1/T$ represents the fundamental frequency

$$x(t) = \frac{a_0}{2} + \sum_{k=1}^{\infty} a_k \cos(2\pi kft) + b_k \sin(2\pi kft) \quad (2.11)$$

by introducing Euler's relations ⁴

$$\cos(2\pi kft) = \frac{e^{j2\pi kft} + e^{-j2\pi kft}}{2}; \quad \sin(2\pi kft) = \frac{e^{j2\pi kft} - e^{-j2\pi kft}}{2j} \quad (2.12)$$

and substituting Eq. 2.12 into Eq. 2.11, the Fourier Series with complex coefficients is obtained

$$x(t) = \sum_{k=-\infty}^{\infty} X(k)e^{j2\pi kft} \quad (2.13)$$

³In mathematics, the Dirichlet conditions are sufficient conditions for a real-valued periodic function f to be equal to the sum of its Fourier series at each point where f is continuous. The conditions are:

1. f must be absolutely integrable over a period;
2. f must be of bounded variation in any given bounded interval;
3. f must have a finite number of discontinuities in any given bounded interval and the discontinuities cannot be infinite.

⁴In complex analysis, Euler's formula is a mathematical expression that establishes the fundamental relationship between the trigonometric function and the complex exponential function. It states that for any real number, x : $e^{ix} = \cos x + i \sin x$, where e is the base of the natural logarithm, i is the imaginary unit, and \cos and \sin are the trigonometric functions cosine and sine, respectively.

The series in which the starting signal is decomposed must have the same size as the signal; thus, the function $x(t)$ has EU (*Engineering Units*) as dimension, which depends on the type of quantity considered. The number of discrete frequencies that are tested as part of a Fourier transform is directly proportional to the number of samples in the original waveform. Being N the signal length, the number of frequency lines is equal to $N/2$. By multiplying each frequency bin in a FFT by its complex conjugate, a Power Spectral Density (PSD) function is computed, which is a more useful tool than the FFT for random vibration analysis since the amplitude value is then normalized to the frequency bin width to get units of EU^2/Hz .

2.3.3 Digital processing of wind turbulence

The complexity of modern structural systems requires an increasingly accurate numerical simulation of what buildings can expect to experience over their useful life. For an optimal structural design, or for the evaluation of the functionality and safety associated with external loads, Monte Carlo analysis approaches are often used, which require the definition of a set of random signals as input, to generate compatible structural responses as output. For simplicity, the random processes simulated for analysis purposes are often considered to be Gaussian and stationary. According to Shinozuka [74], methods for digitally generating sample functions of a wind-related process, such as the fluctuating part of atmospheric wind velocities, are a prerequisite to successful implementation of the time- and space- domain analysis of wind-induced structural response, especially for tall and slender structures. The simulation schemes can be classified into two categories:

1. methods based on the sum of trigonometric functions (wave superposition);
2. methods based on the convolution of the *white noise*⁵ with a kernel function or the integration of a differential equation driven by the white noise (digital filtering)

The traditional approach for the simulation of multivariate and multidimensional processes consists in using a superposition of trigonometric functions with random frequencies and random phase angles [75], in which the Gaussianity of the simulated data is based on the Central Limit Theorem (CLT). This process is applicable to multivariate and multidimensional fields, but becomes computationally inefficient as the number of variables increases. In an attempt to improve the computational efficiency, the sum of trigonometric functions can be performed using a FFT-based algorithm [76]. However, due to the limitations imposed by the FFT-based implementation, Li and Kareem [77] introduced a numerical simulation scheme that combines the advantages of the wave superposition techniques with those of the digital filtering to simulate continuous long duration multivariate random processes. This approach involves simulating a large number of time-series segments using the FFT algorithm; subsequently, these segments are synthesized through a digital filter that provides the desired

⁵In signal processing, a white noise is a random signal having equal intensity at different frequencies, resulting in a constant PSD.

duration of the simulated processes. To reduce the computational effort in case of several simulated positions, the authors developed the decomposition in frequency-limited positions and larger time passages (Schur decomposition or Cholesky decomposition). In order to facilitate the construction of stochastic simulations in the design phase, the *NatHaz Modeling Laboratory* has developed a web portal that allows the simulation of multivariate Gaussian random processes with predetermined spectral characteristics, offering the possibility to select one of the four different simulation schemes:

1. conventional spectral representation method (Shinozuka and Deodatis, 1991 [78]);
2. discrete frequency function with Cholesky decomposition and FFT (Wittig and Sinha, 1975);
3. ergodic spectral representation with Cholesky decomposition and FFT (Deodatis, 1996; Ding et al., 2006);
4. Schur decomposition from autoregressive models (AR) with polynomial approximation (Di Paola, 1998; Di Paola and Gullo, 2001)

The schemes based on digital filtering offer efficient methods for random process simulation by using:

1. autoregressive models (AR)
2. moving average models (MA)
3. autoregressive moving average models (ARMA)

Unlike the FFT approaches, the ARMA representation does not require an excessive computational charge as only a limited amount of information is stored and long time series can be simulated with successive time increments. The approaches based on digital filtering can be implemented directly for multivariate and multidimensional fields or they can be simulated as univariate processes in combination with Cholesky or Schur decomposition measures.

2.3.4 Equivalent modeling of structures

In the last decade, the growing worldwide spread of complex-shaped tall buildings has led to an increasing complexity and computational effort of the structural modeling needed to estimate the building dynamic response to lateral loads. The greater number of degrees-of-freedom required of numerical models for carrying out structural investigations and transient analyzes and the need to reduce the construction and energy costs of such buildings constitute the motivations for the development of low-order models. While maintaining the ability to capture the dominant frequency, these models can lead to significant savings in the computational effort and costs typically associated with the dynamic analyzes of large structures, proving to be a useful tool for the preliminary design of high-rise structures [79].

The use of continuous models in the structural analysis has received considerable attention in recent years (Rahgozar et al., 2012; Giofrè et al., 2013; Piccardo et al., 2014, 2016; Ferretti, 2018), but the idea to reduce complex structural systems to equivalent beam models has been proposed by some authors as early as the last century [80]. One of the pioneers in this area was Engesser (1907) who developed an equivalent continuous beam model to estimate buckling loads in truss structures, followed by Timoshenko (1943) who demonstrated how the simple continuous models could be used to describe the behavior of complex structures. Since the second half of the 1990s, many researchers (Noor et al., 1978; Sun et al., 1981; Basu and Dar, 1982; Necib and Sun, 1989; Chajes et al., 1993; Miranda and Tagahvi, 2005) have used continuous models to study both the static and dynamic response of the structures. Noor et al. (1978) focused on the instability characteristics of lattice structures by proposing a model that takes into account the shear and torsion contribution. Sun et al. (1981), using a beam element developed by Yang (1973), performed vibrational analyzes of flat lattice systems. Basu and Dar (1982) analyzed the dynamic characteristics of flat wall-frame systems, by modeling the coupled wall as a uniform continuum and the frame as a uniform Shear Beam (SB) model. Necib and Sun (1989) used a higher-order Timoshenko beam element to solve the dynamic problems of lattice structures.

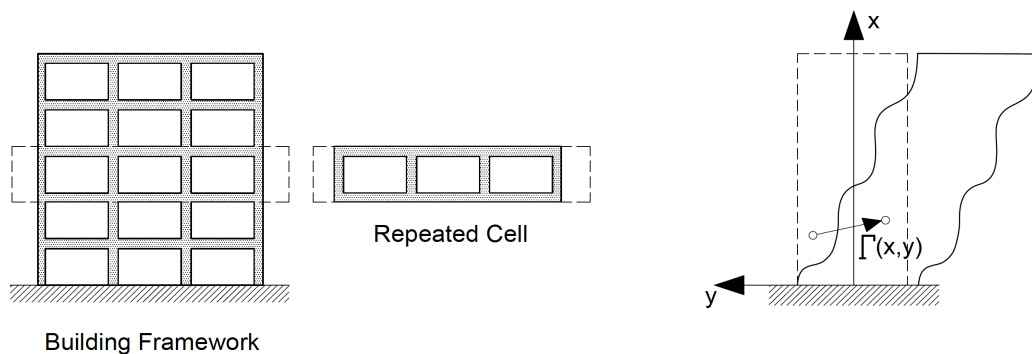


Figure 2.30: Typical repeated "cell" in reticular structures a) and continuous displacement field b)

Chajes et al. [81] adopted an energetic approach to obtain the characteristics of an equivalent continuous model for buildings supported by multi-span frame structures. The model they proposed (developed by McCallen and Romstad in 1986) replaces the discrete elements of the lattice structure connected together to create repeating geometric patterns (the so-called *cells*, each containing many beams and columns) with an equivalent continuous model, greatly reducing the number of elements used to model the frame and the number of global degrees-of-freedom needed to describe the structure (Fig. 2.30). The fundamental kinematic assumptions on which the reduced model is based are derived from Timoshenko beam theory [82] and are based on the double hypothesis of conservation of plane sections -not necessarily orthogonal to the longitudinal axis of the lattice- and negligence of deformations orthogonal to the axis. The equivalence of the continuum is established by equating its strain energy to an approximate expression for the lattice strain energy. This approach has been successfully applied to estimate the vibrational characteristics and the seismic response of

two lattice structures subjected to the 1989 Loma Prieta earthquake. Miranda and Tagahvi [83] proposed an equivalent model for estimating the maximum lateral displacement in multi-storey buildings, made of a combination of a flexural cantilever beam (Fig. 2.31 a) and a pure shear-type cantilever beam (Fig. 2.31 b). However, the equivalent beam formulation is limited to flat models and the values of the dimensionless parameters that manage the participation level of the bending and the shear behavior in the equivalent model are provided only empirically. Almost all methods presented so far essentially assume a series arrangement of the bending and shear stiffness. In 2007, Dym and Williams [84] proposed two equivalent beam models to estimate the fundamental frequencies of the buildings: a two-beam model called *coupled two-beam*, obtained by coupling in parallel of a pure flexural beam (Euler-Bernoulli Beam (EBB)) with a SB model, and a Timoshenko Beam (TB) model, obtained by adding to the EBB model the shear stiffness connected in series to the beam mass (Dym and Shames, 1973; Rahgozar et al., 2004).

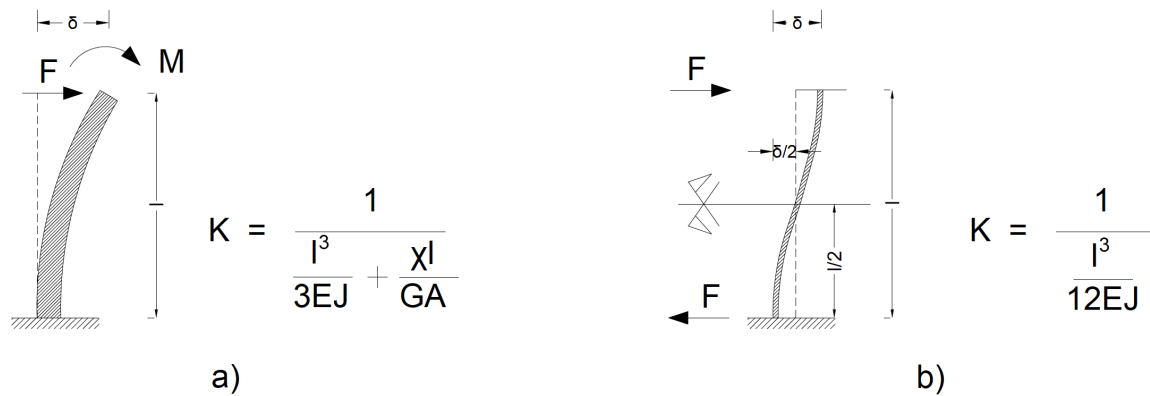


Figure 2.31: Typical equivalent beam models: a) flexural cantilever beam and b) pure shear-type cantilever beam

The simplified one-dimensional beam models can prove to be useful both in the preliminary structural design phase, to determine the best solutions that can be accounted for, and for a quick performance assessment of the existing buildings. In both cases, the procedure to be followed is divided into three main phases:

- choice of the appropriate equivalent beam model, i.e. the mechanical system that best describes the structural response to horizontal loads, and the optimal arrangement of bending and/or shear stiffness (*in series* or *in parallel* arrangement);
- calibration of the equivalent mechanical model parameters based on the building input data (such as structural damping and vibration frequency);
- development of a low-order model which approximates the overall response of the building regardless of its physical properties; for this reason, the resulting mechanical parameters of the equivalent beam model (mass, inertia, bending and shear stiffness) could significantly differ from reality.

Nevertheless, the formulation of a general equivalent beam is not always explicit and simple, especially for non-linear three-dimensional problems [85], hence, the reduction of complex structural systems to equivalent beam models still remains an open challenge, of great interest especially in the dynamic field of wind loads [86].

Estimation of building dynamic properties

In the evaluation of tall building wind response, the knowledge of dynamic characteristics such as natural vibration periods and frequencies, modal shapes and damping ratios plays a primary role. As a first approximation, the fundamental frequency of vibration, which is mainly a function of the mass and stiffness of the structural system, can be estimated by considering that the structure, excited by wind or seismic forces, behaves like an elementary cantilever beam (Taranath, 1988) as depicted in Figure 2.32.

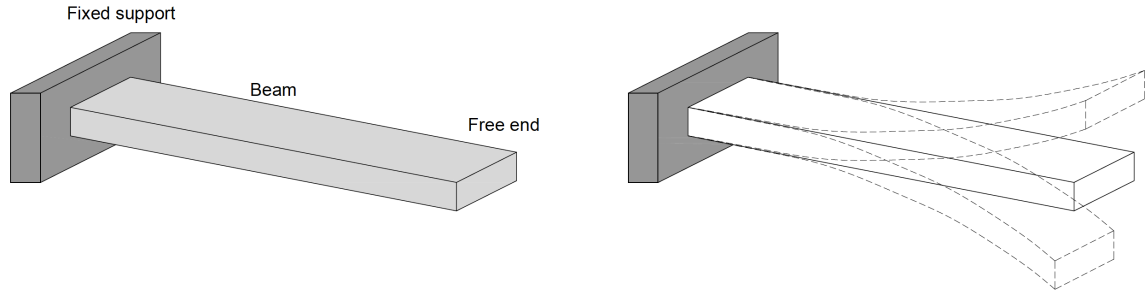


Figure 2.32: Rectangular cross-section cantilever beam undergoing free vibrations

By modeling the building as a vertically oriented uniform cross-section flexural cantilever beam (according to the EBB model), the resulting behavior is that of a continuum structure possessing mass and elasticity uniformly distributed along the span. Note from Meirovitch (1967) the equation of motion and imposing the boundary conditions, it is possible to derive the closed-form circular natural frequency, ω_{EBB}

$$\omega_{EBB} = \alpha_n^2 \sqrt{\frac{EI}{mL^4}} \quad (2.14)$$

where α_n^2 with $n = 1, 2, \dots, N$ is a dimensionless parameter related to the vibrating mode considered and $m = \rho \cdot A$ [kg/m] is the mass per unit length, with ρ (in kg/m^3) being the volume density of the material used.

By varying the parameter α_n^2 in the general formula, the circular frequencies related to the first three modes of vibrations are obtained, which are depicted in Figure 2.33

$$\omega_1 = 1,875^2 \sqrt{\frac{EI}{\rho AL^4}} \quad (2.15)$$

$$\omega_2 = 4,694^2 \sqrt{\frac{EI}{\rho AL^4}} \quad (2.16)$$

$$\omega_3 = 7,885^2 \sqrt{\frac{EI}{\rho AL^4}} \quad (2.17)$$

From the circular frequencies thus obtained (expressed in *rad/s*), it is easy to deduce the related natural vibration frequencies (expressed in *Hz*)

$$f_n = \frac{\omega_n}{2\pi} \quad (2.18)$$

where $n = 1, 2, \dots, N$.

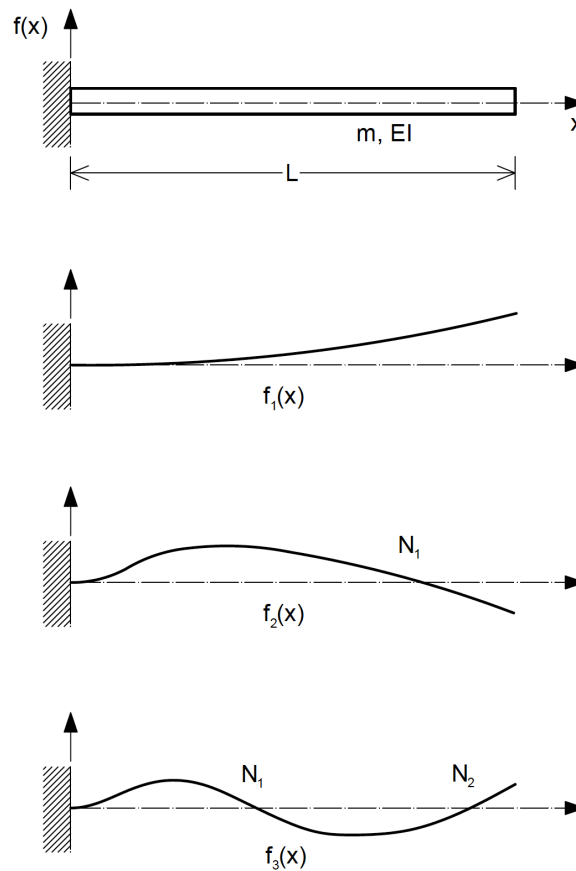


Figure 2.33: First three natural undamped frequencies and modes of vibrations of an elementary cantilever beam

In the structural dynamics, a key parameter for dissipating energy and reducing the amplitude of wind-induced vibrations is represented by the damping ratio, whose in-depth knowledge is required in order to optimize the building wind design. The current trend in numerical analysis is to use low damping values, often leading to an oversizing of the structure; on the contrary, if too high damping values are considered, the current stresses developed in the buildings subject to wind load can be underestimated. Despite the extensive literature available on the topic [87], damping remains one of the most complex aspects of structural problems. The impossibility of defining a universal mathematical model, similar to those for

determining the structural mass and stiffness, is the reason why the estimate of the dissipative forces can only be based on empirical considerations. It is well known that a structure can be dynamically damped by a series of energy dissipation mechanisms with different origins and characteristics, such as: material damping originating from complex molecular interactions, friction damping between structural and non-structural elements and connections, energy dissipation mechanisms occurring in the foundation system, aerodynamic damping, and so on [88]. Since damping originating from the aforementioned sources, also called intrinsic damping, is extremely difficult and unpractical to estimate, it can be conveniently studied using the concept of a viscous velocity-dependent damping, ξ , which is generally used in the structural engineering field to represent the combined effect of all the dissipation mechanisms cited.

The Equivalent Viscous Damping (EVD) may be interpreted as the superposition of an elastic and hysteretic damping, where the first term allows to take into account further dissipative contributions (such as, the non-linearity in the elastic range, the foundation damping and non-structural damping)

$$\xi_{eq} = \xi_{el} + \xi_{hys} \quad (2.19)$$

where the symbol "+" stands for a superposition rather than a common summation.

The elastic damping ratio, ξ_{el} , is generally taken as 5% of the critical damping and computed proportionally to the tangent stiffness, whereas the hysteretic damping ratio, ξ_{hys} , is normally taken proportionally to the secant stiffness, which is directly related to the structural response in its inelastic phase.

A first attempt to make use of EVD in order to take into account the hysteretic dissipation was made by Jacobsen (1930), who first introduced the areas' method [89]. In Jacobsen's areas' method, the author proposed an approximated solution of the steady-state response of a nonlinear Single-Degree-of-Freedom (SDOF) system, obtained by equating the energy dissipated by that system to the energy dissipated by one cycle of sinusoidal response of a linear system with equivalent viscous damping [90]. Considering a perfectly symmetric hysteretic response and a closed loop, as in the case of pure harmonic loading, the hysteretic equivalent damping, ξ_{hys} , can be given by the well-known expression [91]

$$\xi_{hys} = \frac{E_D}{4\pi E_S} = \frac{A_{loop}}{2\pi F_{max} u_{max}} \quad (2.20)$$

where E_D is the energy dissipated for each individual loading cycle, A_{loop} is the area of the corresponding closed loop in the total force-displacement diagram and E_S is the elastic strain energy (or the stored potential energy), associated with the maximum generalised force, F_{max} , and the maximum generalised displacement, u_{max} , reached in each cycle.

Up to the elastic limit, all the work done in stretching the spring is stored potential energy or elastic strain energy. This value can be determined by computing the area under the force-displacement diagram, as shown in Figure 2.34 a. For a purely linear spring which

obeys Hooke's Law⁶, the maximum stored elastic energy is given by

$$E_S = \frac{1}{2}Fu = \frac{1}{2}ku^2 \quad (2.21)$$

where k is the spring's constant stiffness.

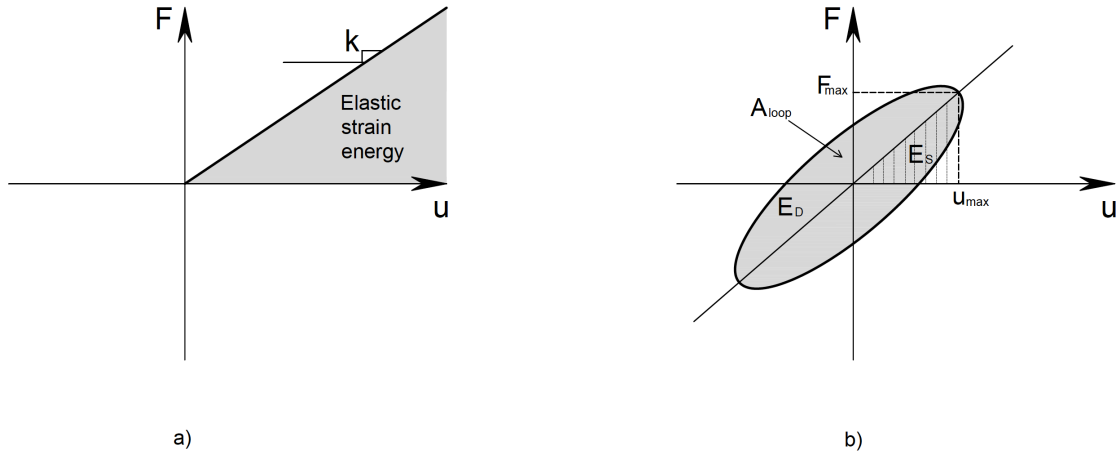


Figure 2.34: Force-displacement diagram with elastic strain energy highlighted a) and hysteretic cycle with parameters for EVDR computation b)

In summary, based on Jacobsen's approach, the EVD ratio can be evaluated for each cycle of a force-displacement curve by means of an energy equivalence approach (Fig. 2.34 b). The first step consists in identifying each cycle, delimited by a pair of zero-force points; next, for each force-displacement diagram, the maximum generalised force (F_{max}) and the maximum generalised displacement (u_{max}) are evaluated, which allow to calculate the elastic strain energy (E_S) according to Eq. 2.21. The computation of the dissipated energy (E_D) follows by performing the integral of the force-displacement curve, leading to the determination of A_{loop} value. Finally, from the hysteretic damping ratio (ξ_{hys}) given by Eq. 2.20, the equivalent damping ratio (ξ_{eq}) is obtained with Eq. 2.19.

2.3.5 Wind performance criteria

Structures designed to accommodate people must inspire confidence and ensure the well-being of the occupants with regard to wind actions and effects. Generally, the human body has no difficulty in tolerating high movements and velocities; instead, it is quite sensitive to the acceleration it is subject to, giving rise to a range of reactions involving non-perception, annoyance and, in some cases, intolerability. Such reactions depend on the frequency of occurrence of the oscillation and on other individual psychological factors. It is a designer's task to ensure that buildings host their inhabitants or users in physiologically favorable conditions. In the structural design of tall buildings, the wind-related serviceability issues

⁶Hooke's law is a law of physics that states that the force (F_s) needed to extend or compress a spring by some distance (x) scales linearly with respect to that distance; that is, $F_s = kx$, where k is a constant factor characteristic of the spring (i.e., its stiffness), and x is small compared to the total possible deformation of the spring.

which may influence the human comfort level are often a limiting design criterion [92]. The acceptance criteria defined by national and international building codes and regulations aim at vibration control in order to avoid human discomfort evaluated with respect to a moderate wind event (i.e. defined by a short return period, $1 < T_R < 10$ years), which occurs more frequently than an extreme one [93], as shown in Figure 2.35.

Wind Hazard (MRI)	Performance Objectives			
	Motion comfort	Continued Occupancy	Operational	Limited Interruption
1 year	●			
10 years	●	●		
50 years		●	●	
100 years		●	●	
300 years			●	●
700 years			●	●
1700 years				●

Figure 2.35: Performance targets related to wind hazard average return period. Source: Griffis, L.G, et al. (2013). *A framework for performance-based wind engineering*

It has been recognized that human perception of wind-induced vibrations can be simply based on the acceleration amplitude and the fundamental frequency of the building [94]. In particular, for the assessment of comfort levels and habitability in tall buildings, several guidelines suggest using the acceleration peak (or the RMS), which is considered as the best indicator for establishing a checking procedure for occupancy comfort criteria under wind action [95]. The acceleration threshold, a_p , for ensuring a suitable well-being of the occupants during wind events can be defined for both office and apartment use, according to the comfort criterion referred to in [96]

$$a_p = \sqrt{2 \ln(fT)} \left(0.68 + \frac{\ln T_R}{5} \right) e^{(-3.65 - 0.41 \ln f)} \quad (2.22)$$

where T_R (in *yr*) is the wind average return period, f (in *Hz*) is the first natural frequency of the structure and T (in *s*) is the observation time interval over which the maximum response is evaluated, with a typical value of $T = 3600$ *s* [97].

The tolerance criteria currently used in the wind design codes define a peak acceleration limit for each comfort level, as shown in Table 2.2. In accordance with the Italian CNR-DT 207/2008 [98] and also reported in [99], for the purposes of daily comfort compliance, the peak value of acceleration in the torsion center of the building upper floors, computed with respect to a return period, $T_R = 1$ *yr*, is recommended. This choice is more appropriate than a longer return period ($10 < T_R < 1700$ *yr*), which is consistent with an extreme and less fre-

Table 2.2: Peak acceleration limit for each comfort level

Peak acceleration, a_p	Comfort limit
$< 0.5\% g$	Not Perceptible
0.5% to 1.5% g	Threshold of Perceptibility
1.5% to 5.0% g	Annoying
5% to 15.0% g	Very Annoying
$> 15\% g$	Intolerable

quent wind event inducing damage to structural members. Specifically, the peak acceleration perception threshold, a_p , should be estimated as a function of the fundamental frequency in the longitudinal direction. In order to ensure a proper habitability of the building, it is suggested to check that the peak value of the longitudinal acceleration in the center of torsion, a_p , does not exceed the acceleration limit value provided by the relation [CNR Eq.N.1]

$$a_p = \frac{a_0}{f^{0.56}}; \quad \text{for } f < 1 \text{ Hz} \quad (2.23)$$

where a_0 is the acceleration reference limit value depending on whether the building floors are used for offices ($a_0 = 0.006 g$) or for housing ($a_0 = 0.004 g$) and f is the fundamental frequency expressed in Hz.

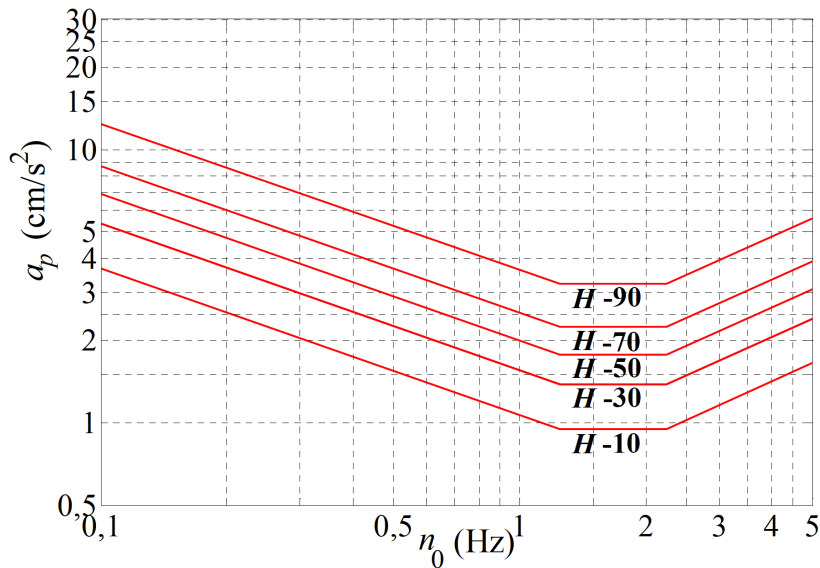
**Figure 2.36:** Peak acceleration perception thresholds [CNR Figure N.1]

Figure 2.36 taken from [CNR Figure N.1] reports some estimates of the peak acceleration perception threshold, a_p (in cm/s^2), as a function of the fundamental frequency of the building, n_0 (in Hz). Diagrams marked with the abbreviations H-10, H-30, H-50, H-70 and H-90 correspond to the peak acceleration values perceived, statistically, by 10%, 30%, 50%, 70% and 90% of the building inhabitants, respectively. Limit values of peak acceleration with $T_R = 1$ yr are shown in Figure 2.37 taken from [CNR Figure N.2], both for office buildings (curve a) and for residential buildings (curve b).

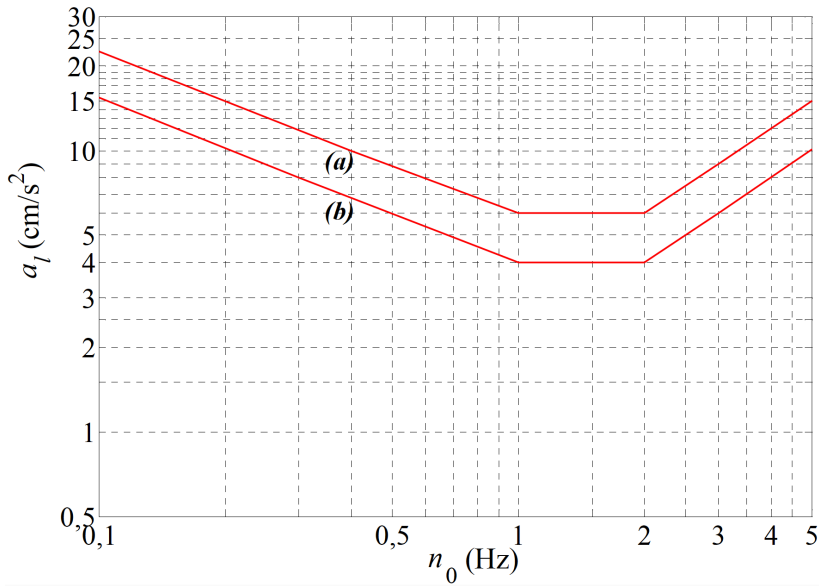


Figure 2.37: Limit values of peak acceleration with $T_R = 1$ yr [CNR Figure N.2]

The same wind load with a mean return period of 1-10 yr is even recommended for checking the associated maximum deformation level and/or local damage to building components. This wind serviceability limit state should be evaluated by analyzing the *inter-storey drift ratio*, that is, the distribution of the lateral displacement along the building height [100]. According to Griffis (1993), more specifically, this parameter can be defined as the lateral deflection of a floor relative to the one immediately below it, divided by the distance between them ($(\delta_n - \delta_{n-1})/h$). The identification of the appropriate inter-storey drift ratio, Δ_p , associated with different levels of damage is significant in terms of the building economy and stability [101]-[102], as listed in Table 2.3. Reducing excessive inter-storey drift responses means limiting damage to structural (e.g., beam and columns) and nonstructural (e.g., façades and partitions) members. Recurring values for the inter-storey drift parameter (or simply *drift index*) depend on the building type and the construction material used. In general, the allowable drift ratio, Δ_p , for a steel frame building appears to be within the range

$$\frac{1}{750} \leq \Delta_p \leq \frac{1}{250} \quad (2.24)$$

with 1/400 or 1/500 being typical values [103].

The façade peak relative displacement with respect to its attachment point to the structure seems to be another key design parameter to ensure an optimal behavior of the building under wind load. Due to their low weight and mass, modern glass façades can experience excessive movements with respect to the building skeleton, thus, resulting in relatively large displacement demands on the moving components (i.e., the cladding's connection devices and brackets) and preventing the effective functioning of the cladding system [104]. Large displacements require large gaps and special bearings, which generate significant architectural and construction challenges. However, the gap between the structure and façade can

Table 2.3: Performance levels and corresponding damage states associated with inter-storey drift limits

Performance level	Damage state	Drift limit, Δ_p
Fully operational	No damage	< 0.2%
Operational	Repairable damage	< 0.5%
Damage state	Irrepairable damage	< 1.5%
Near collapse	Severe damage	< 2.5%
Collapse	-	> 2.5%

be adjusted to reduce the energy consumption during the cooling and heating seasons and to allow the installation and maintenance of the cladding connection devices. According to T.S. Fu (2016), a minimum structure-cladding distance is required and its value can reach up to 100 *mm*, while the optimal depth values to obtain the highest airflow rates and reduce the cooling loads are 400-600 *mm*. Finally, large cavity depths, up to 1000 *mm*, are preferred to decrease building heating loads. According to [105], a high dissipative capacity of the connectors interposed in the cavity between the structure and façade may improve the overall system behavior: the structure-cladding spacing is reduced considerably, whereas the efficiency of the main structure remains almost unaffected.

2.4 Structural control strategies

The high demand for residential and commercial spaces and advances in construction techniques have led to the massive construction of high-rise buildings around the world. As buildings become slender, lighter and more flexible, they become susceptible to large-amplitude vibrations and accelerations deriving from lateral loads such as wind, blast and earthquakes [106]. In particular, the adoption of lightweight and low-damping materials has made tall buildings more vulnerable to wind loads that could lead to structural damage or compromise the occupant comfort [107]: large amplitude vibrations can easily occur in buildings whose slenderness (that is, the ratio of the buildings height to the smallest plan dimension) is greater than 5 or with a fundamental frequency less than 0.2 *Hz* [108]. This worldwide exponential growth of tall buildings poses new demands in terms of the performances required for minimizing the wind-induced lateral top displacements and accelerations, making it essential to develop measures that can contain them within functionally acceptable limits. In the engineering field, the use of structural control systems to alleviate the response of civil structures during wind activities has become a standard strategy [109] and, among the well-established passive approaches, aerodynamic and structural modifications and the use of passive, active or semi-active auxiliary energy absorbers can be included.

As is known, the dynamic behavior of tall buildings experiencing wind forces can be affected by both morphological (shape and height) and dynamic properties (vibration periods, modal shapes, mass and stiffness distribution, structural damping). A proper choice of building shape and structural topology can help minimize wind forces and efficiently transfer

them to the structural system [110]. The aerodynamic optimization is particularly important to interrupt the birth of vortices around the buildings and the methods conventionally used for this purpose consist in modifying the building geometry by rounding or cutting the corners, tapering or twisting it along the height, providing openings or set-backs, thus, giving rise to complex-shaped tall buildings which are a still recent architectural phenomenon [111]. According to [112], an interesting alternative could be designing a dynamic façade that allows the building to smartly adapt its profile to the changing and complex external environment, in order to minimize the source of the excitation, through the implementation of artificial smart devices and the use of modern computational technologies. A structural design transformation reduces wind-induced vibrations by modifying the building properties, such as mass and stiffness distribution, resulting both in a dimensional increase of the structural frame elements and a consequent increase in construction costs. Another reliable and widely used solution for structural control under wind or seismic load can be the implementation of additional damping devices with active, semi-active or passive mechanism. An attractive option in reducing excessive floor vibrations is offered by the passive auxiliary energy absorbers, such as the TMD, which increase the level of damping within the structure by means of indirect energy dissipation systems, that is, by incorporating a secondary mass directly connected to the main structure through a series of springs and dashpots [113]-[114]. In the context of damping strategies that face the challenge of mitigating hazards induced by dynamic excitations, the research community has recently investigated the potential offered by energy-absorbing devices installed at façade level and used as engineering flexible connectors attached to the load-bearing structure of buildings. This have resulted in a technological solution otherwise known as *Movable Façade* (MF), which is based on the cladding participation to the structural motion, occurring through a marked change in the design philosophy of the connection system placed between the envelope and the building skeleton.

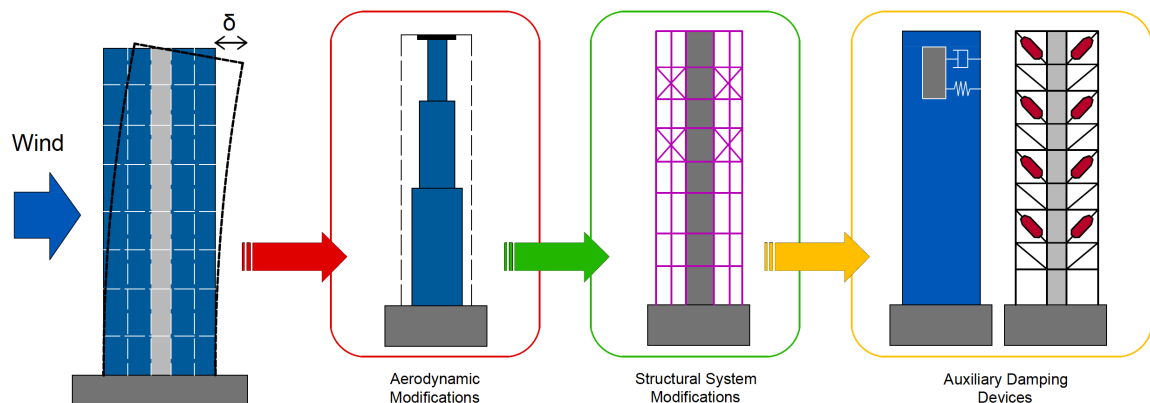


Figure 2.38: Possible strategies for wind-induced vibration control

The purpose of this Chapter is to provide a state-of-the-art review of the current control strategies needed to improve the performance of civil structures by exploring, in particular, the current state of knowledge on the use of the emerging solution of Movable Façades for a proper dynamic motion control of buildings. Figure 2.38 shows a schematic representation

Type	Means	Methods	Applications	Notes
Passive Mitigation Approaches	Structural Design	<input type="checkbox"/> Increasing stiffness (or natural frequency) to reduce lateral displacement and vortex shedding-induced lock-in condition <input type="checkbox"/> Increasing building mass to reduce acceleration	<input type="checkbox"/> Braced Frames Tubular Structures Core-Supported Outrigger Structures Diagrid Structures <input type="checkbox"/> Increase Building Materials	<input type="checkbox"/> Not practical to increase mass Amplifies seismic load
	Aerodynamic Design	<input type="checkbox"/> Improve aerodynamic properties to reduce wind forces by means of cross-section modifications or shape modifications	<input type="checkbox"/> Cross-section Modifications: Chamfered corners Rounded corners Triangle corners Recessed corners <input type="checkbox"/> Shape Modifications: Tapering Twisting Setbacks Openings	<input type="checkbox"/> Reduces occupiable building areas
	Auxiliary Damping Device	<input type="checkbox"/> Adding materials with energy-dissipating properties to increase damping ratio <input type="checkbox"/> Adding auxiliary mass system to generate counteracting inertia forces	<input type="checkbox"/> Viscous Damper Viscoelastic Damper Friction Damper Metallic Damper <input type="checkbox"/> Tuned Mass Damper Tuned Liquid Damper Impact Damper	<input type="checkbox"/> Occupies valuable building space near the top of a building

Figure 2.39: Summary of typical passive mitigation strategies used to reduce wind-induced dynamic response of tall buildings

of the aforementioned passive mitigation approaches, whose related operating modes and applications are summarized in Figure 2.39.

2.4.1 Aerodynamic Façade

In the complex wind-structure interaction, the external shape of a building plays an important role in determining the level of resulting loading. At the basis of the adoption of a particular aerodynamic façade configuration, there is, of course, an aesthetic reason associated with a deeper structural motivation that aims at a net reduction of the wind gust: the process of dynamic transformation of the envelope helps to substantially reduce loads produced by wind kinetic action on a tall building, due to the dynamic aeroelastic phenomena capable of confusing the flow [115]. The aerodynamic behavior of a high-rise structure can be characterized by some dimensionless numbers describing the aerodynamic forces/moments and pressure distribution around the building. In the design phase, the primary objective should be minimizing the mean and/or the fluctuating component of these numbers in order to reduce the wind response [116]. All the variables including loads, moments, the Strouhal

number ⁷, the Reynolds number ⁸ and the Scruton number ⁹, depend on the mean wind velocity, v_m , and as the wind velocity profile varies with height, they also change along the height of the building, affecting the vortex-induced response and making the aerodynamic behavior more complicated to predict [117]. Based on literature [118], another well-accepted approach to control the wind-induced vibration of a tall building is to change the cross-section and/or the overall shape along the height in order to interrupt the vortex-shedding and the boundary layer around the façade. As is known, the variation of the cross-section along the height generates a building with a longitudinal profile aerodynamically less favorable to wind load. This geometric variation along the height can be achieved through sudden shape changes (as in the case of the Burj Khalifa) or with more gradual changes and twisting movements (as in the case of the Infinity Tower, which is twisted by 90°). Furthermore, the introduction of large openings through the building, particularly near the top, can greatly improve its aerodynamic response, reducing the forces induced by vortex-shedding [119]. This design strategy has been used in several buildings, such as the Shanghai World Financial Center, which features a diagonal face shaved back with a 51 m wide hole at the top of the building (Fig. 2.40).

The aerodynamic shape modifications, typically used in the fields of aerospace and automotive engineering, may be applied to civil structures in several conventional ways, which can be classified as cross-section (or minor) changes and longitudinal profile (or major) changes. The first type modifies the buildings basic plan shape and the corner geometry, which turn out to be the most influential parts to improve the aerodynamic performance of a tall building (Fig. 2.41). The self-induced vortex shedding loads can be alleviated through rounded, chamfered and recessed corners, ameliorating the building response as compared to the performance of a square-based section. The second type adjusts the overall external shape of the building through openings, tapering, twisting and set-backs along the height mainly to interrupt the synchronization between the vortices and, thus, disorganize the formation of vortex-shedding, as depicted in Figure 2.42.

Both types are beneficial in containing the wind-induced responses in either *along-* or *across-wind* direction. Clearly, every geometric choice relating to aerodynamically efficient shapes is closely linked to the architectural concept behind the aesthetics and the functionality of the structure and can be integrated into the building design without sacrificing its

⁷Strouhal number is a dimensionless parameter dependent of the section shape and the Reynolds number, used in fluid dynamics for stationary flows and defined as: $St = f_s L / v_m$, where f_s is the dominant frequency of the vortex shedding in Hz, v_m is the mean wind speed and L is a characteristic dimension of the body section. The most critical conditions occur when the vortex-shedding frequency is equal to the natural frequency of a vibration mode of the structure, which will thus undergo a resonance phenomenon.

⁸Reynolds number is a dimensionless parameter that describes the relationship between the inertial ($\rho v^2 L^2$) and viscous ($\mu v L^2 / L$) forces affecting a fluid motion and is defined as: $Re = v L / \nu$, where $\nu = \mu / \rho$ is the kinematic viscosity, v is the flow velocity of the fluid, L is a characteristic dimension of the fluid volume and ρ is the air density.

⁹The relationship between the vortex shedding frequency, f_s and the mean wind speed, v_m , is linear until the critical speed, v_{cr} , is reached; starting from this value, a wind interval, called *synchronization* or *lock-in* domain, begins. Scruton number, S_{cr} , is a dimensionless parameter which describes the relationship between the width of the lock-in domain and the structural characteristics of the body, such as the mass per unit length, m , volume and structural damping, ξ_s , and is defined as: $S_{cr} = 4\pi\xi_s m / \rho D^2$, where ρ is the fluid density and D is the characteristic length of the body.



Figure 2.40: On the left, the 829.8-metre-tall Burj Khalifa (Dubai) that is the tallest structure and building in the world; on the center, the 306-metre-tall Cayan Tower, known as Infinity Tower (Dubai), that was the world's tallest high-rise building with a twist of 90° up to 2015; on the right, the 492-metre-tall Shanghai World Financial Center (Shanghai), which is the tenth tallest building in the world

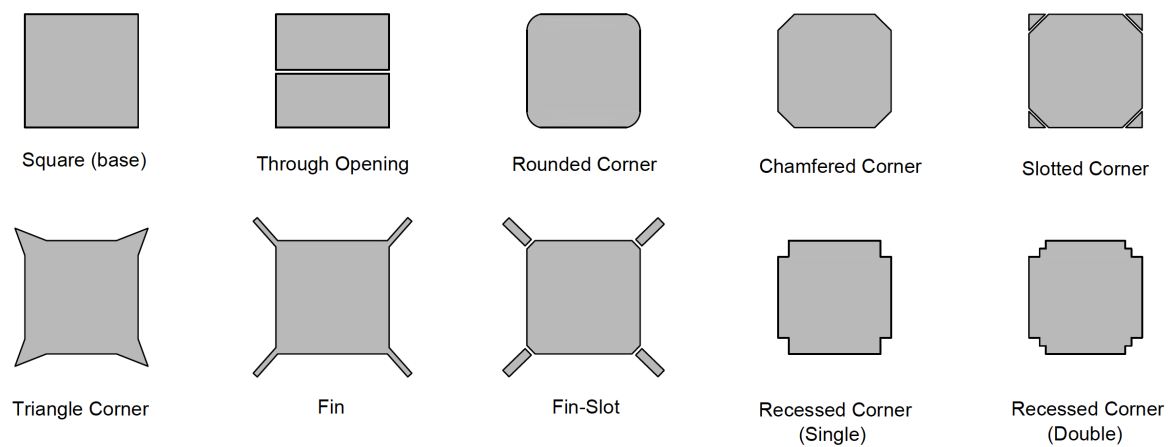


Figure 2.41: Cross-sectional modifications to improve the aerodynamic performance of high-rise square-based section buildings

appearance. Despite the advantages that can be obtained from an intelligent choice of the building morphology, the structural design limitation, the material costs and the construction difficulties do not always make the aerodynamic strategy sufficient to achieve the desired level of wind-induced structural response. When this approach cannot be applied, the desired dynamic performance may be achieved by following other ways, for example with an optimal structural design or with the incorporation of vibration damping devices. However, the problem of eddies formation still exists even by connecting external dampers to the structure.

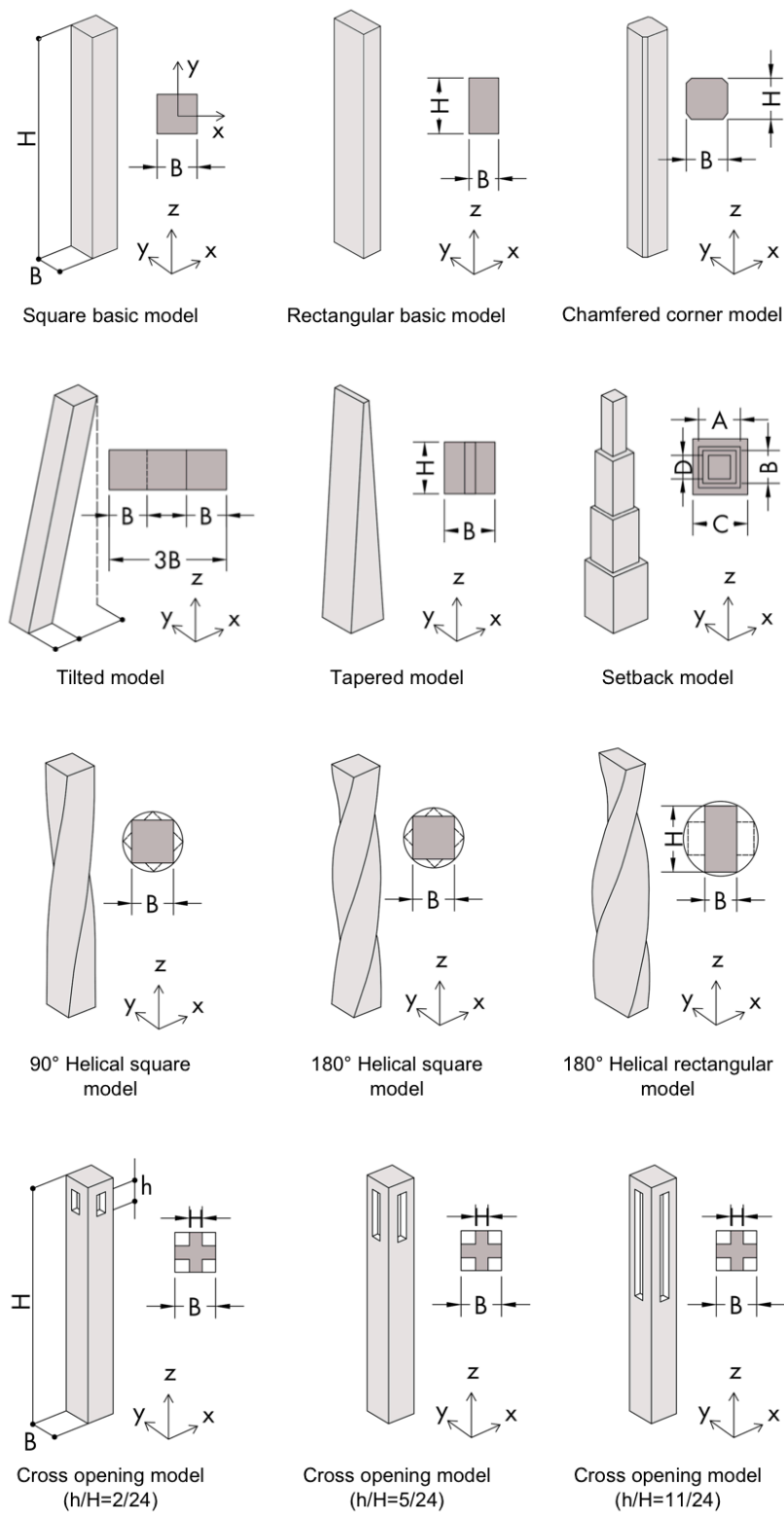


Figure 2.42: Typical shape modifications applied to tall buildings to interrupt the vortex-shedding

2.4.2 Manipulation of structural properties

The dynamic response of a building is mainly affected by its mass and stiffness distribution and its damping capacity; the appropriate manipulation of any of these properties in the structural design phase can be beneficial in minimizing the building's response to horizontal loads. The mass distribution that characterizes a building, while being fairly easy to estimate, is quite difficult to modify in order to obtain significant benefits in terms of reducing the structural response. Adding mass to the system lowers the vibration frequency of the building ($\omega = \sqrt{K/M}$), while increasing the Scruton number, Sc , for a given reduced velocity, RV : since the vortex-induced response is inversely proportional to Sc , this is attenuated by the addition of mass to the building. Despite the benefits of reducing the wind-induced response, however, the increasing mass raises the construction costs and can amplify the sensitivity to earthquake in seismic areas, making this solution impractical.

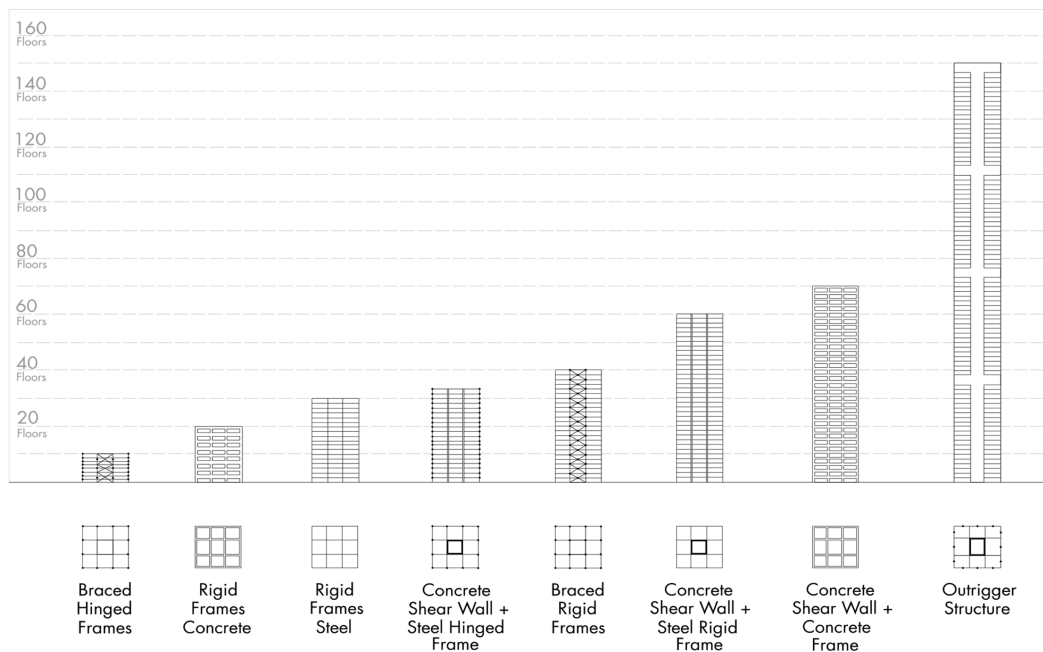


Figure 2.43: Internal structural systems. Source: Moon, K.S. (2018). *Advances in Structural Systems for Tall Buildings: Emerging Developments for Contemporary Urban Giants*

Another passive approach related to structural design modification consists in maximizing the lateral stiffness of the building, which can be evaluated and adapted relatively easily by means of suitable variations of the structural system. The choice of a structural system is closely related to the building height and, depending on whether the lateral-load-resisting elements are located mostly internally or along the perimeter of the building plan, it is possible to distinguish between internal or external systems [120]. Among the internal structures (Fig. 2.43), the core-outrigger systems with megacolumns have gained popularity in *super-tall* (over 300 m) and *mega-tall* (over 600 m) buildings, due to their ability to provide a greater flexibility in the façade design and configuration adaptability [121]. In mega-tall buildings, in particular, a new trend is represented by the buttressed core which can gain higher altitude with respect

to the core-outrigger system. As for the external systems (Fig. 2.44), tubular structures have been updated and modernized to increase lateral stiffness: from the traditional braced frame generally constrained to the internal core, DiaGrid structures and braced mega-tubes have originated, which identify the lateral load-resistant system along the building envelope, offering a greater aesthetic potential and structural efficiency. Furthermore, framed tubes have been repropose due to their integrated applicability to the increasingly tall, supertall and slender residential architecture of recent years. The stiffening approach leads to a higher fundamental frequency and to a decreased wind response, however, it has no influence on the reduction of the building acceleration response [122], which is a fundamental factor in assessing human comfort in high-rise structure design. Furthermore, the additional stiffness also increases the construction costs and reduces the availability of the internal space due to the use of larger pillars.

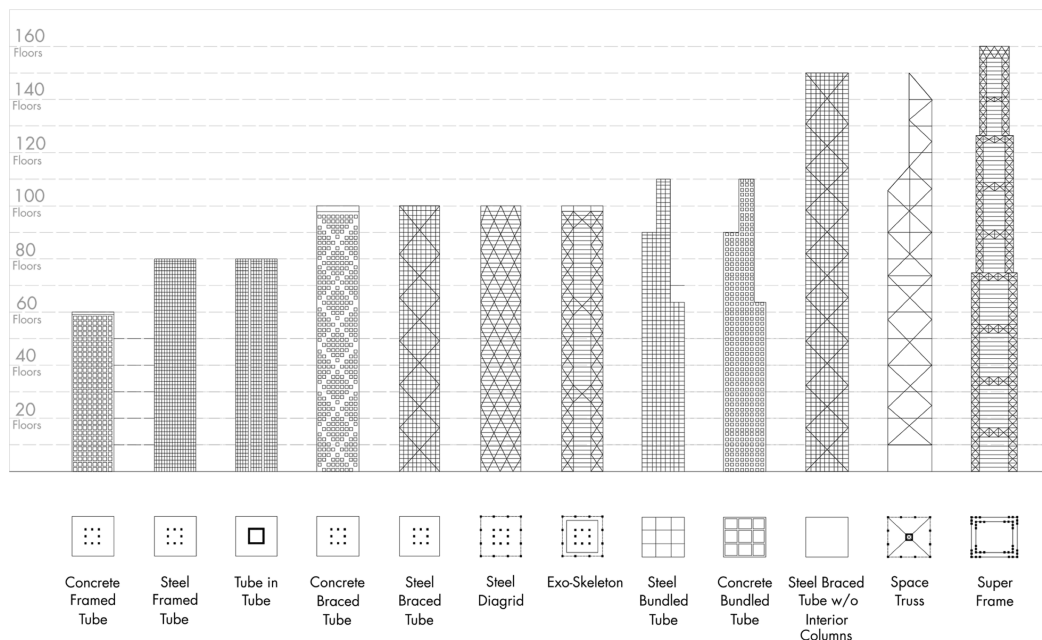


Figure 2.44: External structural systems. Source: Moon, K.S. (2018). *Advances in Structural Systems for Tall Buildings: Emerging Developments for Contemporary Urban Giants*

Finally, damping plays a key role in the structural response of tall buildings and, by increasing it, enormous benefits can be achieved [123]. Unlike the mass and stiffness properties, however, the estimation of damping which characterizes a civil structure is generally difficult due to the complex nature of the mechanisms underlying this phenomenon (see section 2.3.4). Nevertheless, this is not true for the damping provided by the auxiliary devices. The adoption of these devices, suitably designed to improve the dynamic behavior of particularly flexible and slender structures with insufficient intrinsic damping, has become widespread over time as it is undoubtedly a reliable method of providing further damping to the system, which is thus able to achieve the desired response level. Although additional damping devices with active, passive or semi-active energy dissipation mechanisms exist, in this context reference will be made only to the main passive energy dissipation devices.

2.4.3 Auxiliary energy-absorbing devices

The passive control techniques usually refer to those damping systems able to dissipate the unwanted energy inducing vibrations without requiring any sensors or actuators with external power source to work. With the auxiliary energy-absorbing devices, the overall damping of the structure can be increased by means of a Direct Energy Dissipation (DED) or Indirect Energy Dissipation (IED) mechanism (in this case, requiring a secondary system to allow for the energy dissipation). Some of the devices belonging to both the systems are mentioned below together with their major features.

Direct Energy Dissipation (DED) dampers

The main devices in this category are: Friction Damper (FD), Viscoelastic Damper (VED), fluid VD and Metallic Damper (MD); the latter becoming increasingly popular as it occupies less space and can be easily attached to the structure.

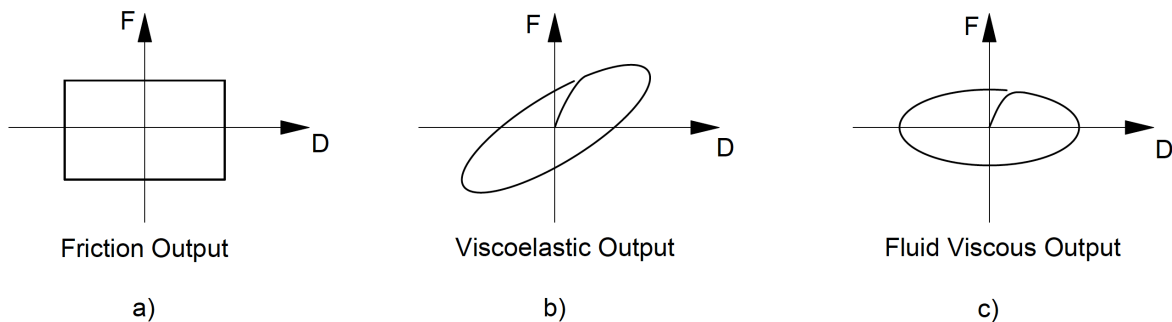


Figure 2.45: Force-displacement relation for a) friction device, b) viscoelastic damper, and c) fluid viscous damper

- Friction Damper FD

The FD uses the principle of friction induced by the sliding surfaces to provide the desired energy dissipation: when the parts slide over each other, they create friction which uses some of the excitation energy entering the building to dampen the structural response. The FD generally exhibits a rigid-plastic behavior, thus the force-displacement diagram is a rectangular loop, as shown in Figure 2.45 a. The friction force in the damper can be adjusted through a suitable pair of bolts that controls the pressure acting on the sliding surfaces. These devices have wide applications in civil structures and can be used to mitigate the wind-induced response of high-rise buildings.

- Viscoelastic Damper VED

The VED is a conventional damping system composed of steel plates alternating with layers of viscoelastic material (such as polymers or rubber) that dissipate energy if subject to shear deformation. When mounted on a structure, the shear deformation (hence, the energy dissipation) occurs when the structural vibration induces relative motion between the

outer steel plates and the center plate. The VED provides extra-damping and alleviates the mechanical vibrations, improving the overall dynamic response of the system. A typical force-displacement loop of VED is shown in Figure 2.45 b.

- Viscous Damper VD

The VD, also known as fluid viscous damper (FVD), bases its performances on the high flow resistance of the viscous fluid and the forces developed inside the damper are proportional to its deformation velocity, according to the typical force vs velocity constitutive law, $F = Cv^\alpha$. Depending on the different values assumed by the velocity exponent α in different ranges of velocity, the VD are available in both linear and nonlinear forms: the exponent α usually ranges from $0.01 \div 0.15$ (highly nonlinear devices) to 1.0 (linear devices). The main advantages of FVD include low maintenance and no need for external power. A typical force-displacement curve is shown in Figure 2.45 c.

- Metallic Damper MD

The MD is a displacement-activated device that dampens the energy of structures, exhibiting a hysteretic force-displacement behavior under cyclic load. These dampers depend on the yield and inelastic deformation of the components, which can be bending, shear or axial deformation. They can withstand a limited number of work cycles and must be replaced after repeated excitation. The existing MD can be of different types: torsional beam, flexural beam, U-shaped flexural plates, SMA, and so on.

Indirect Energy Dissipation (IED) dampers

These auxiliary dampers are also called indirect energy dissipation devices since they require a secondary system to allow for the energy dissipation (for example, a spring and dashpot attached to the supporting structure to prevent motion). A few important IED auxiliary dampers are:

- Tuned Mass Damper (TMD)

The TMD is the most widely used damping system to be implemented in tall buildings since the 1950s, in order to reduce demand for energy dissipation and mitigate large amplitude vibrations induced by external loads. Its basic principle of operation can be simply explained by schematizing the main structure as a linear SDOF system. In its simplest form, a TMD consists of an additional mass attached to the main system via springs and dashpots [124], so the overall system can be easily schematized as a 2DOF system, as shown in Figure 2.46. The vibration frequency associated with the secondary mass is tuned to a particular structural frequency: when that frequency is excited, the TMD resonates out of phase with the structural movement. However, a passive TMD is limited by the fact that it can only be tuned to a single structural frequency, thus the effectiveness of the system decreases if the dominant frequency of excitation moves away from the TMD tuning frequency. Typically,

a solid concrete or metal block acts as the secondary mass, whose weight is approximately 0.25–0.75% of the building weight, corresponding to approximately 1–2% of the first modal mass [125].

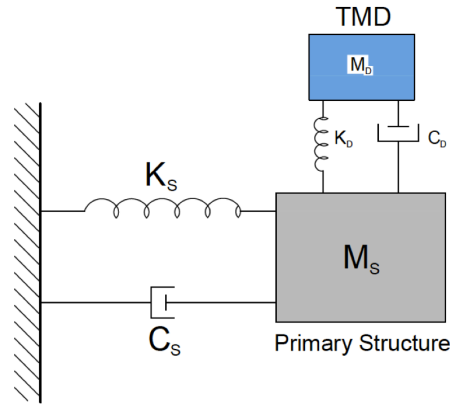


Figure 2.46: Schematic view of a basic TMD system attached to the primary building structure

Generally, the external loads can excite higher vibration modes in a building. To overcome the inherent limitation of classic TMDs, multiple TMD have been studied and implemented with the aim of distributing the natural frequencies of a number of TMD around the fundamental frequency of the building in order to have a wider control of the structural response.

- Tuned Liquid Damper (TLD)

Although not as common as classic TMD, the TLD has also proved to be effective in mitigating the wind-induced vibrations, particularly for absorbing low-frequency vibrations [126]–[127]. A rigid tank partially filled with water replaces the secondary mass and the sloshing of the liquid creates the mass-spring dashpot system: the liquid can slosh from one side to another inside the tank, therefore working according to the same principle as the mass in a TMD-like system, as shown in Figure 2.47. This damping system is mainly used in Japan to reduce the dynamic response of skyscrapers under wind or seismic load. In contrast to TMD, the damping of TLD is amplitude-dependent: this makes this device governed by nonlinear dynamics and, in general, more difficult to model, despite the lower initial cost and nearly maintenance-free operation. The TLD encompasses tuned sloshing dampers and tuned liquid column dampers.

- Impact Damper (ID)

The ID finds its main field of application in the mechanical engineering, but it is also used to damp building motion that occurs mainly on a single plane. A basic type of ID consists of a rigid mass sliding along the vibration axis of the building and whose movement, triggered by the structural vibration, is confined within a container (Fig. 2.48). When the mass reaches the container walls, alternatively from one side or another, it impacts in an inelastic way on the walls, dissipating energy. The lumped mass, the impact stiffness, the suspension length and the gap size are the major design parameters of this device.

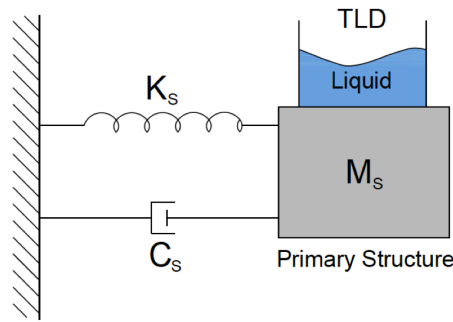


Figure 2.47: Schematic view of a basic TLD system attached to the primary building structure

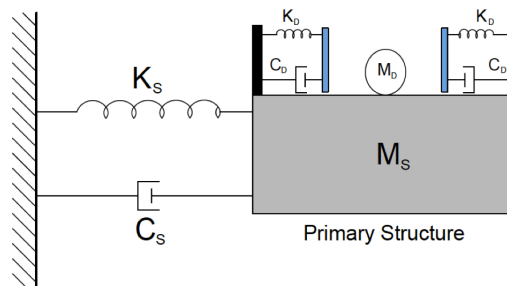


Figure 2.48: Schematic view of an Impact Damper (ID) attached to the primary building structure

2.4.4 Movable Façade (MF)

In addition to the common passive control strategies, a recently developed engineering solution for the mitigation of wind-induced vibrations of tall buildings is represented by the so-called *Movable Façades* (MF), defined as smart envelopes attached to the building structure by means of flexible or sliding connectors that enable them to undergo relative displacements with respect to the building supporting system, acting as a structural control mechanism against possible external dynamic loads. Both traditional single-skin and double-skin façades (DSFs) can be designed to function as MF.

The first studies on the potential use of the MF as a vibration damping system investigated the mitigation and energy absorption capacities mainly connected to blast loads [128]-[129], proposing two different strategies for this purpose: firstly, the design of sacrificial envelopes and, subsequently, the conception of dissipative connection devices.

Since the 1990s, the façade systems have been used to avoid the risk that shock waves generated during a blast event could enter the building (Fig. 2.49). In case of explosion, the façade components inevitably represent the weakest part of the building for their external location and, due to the flying debris, the blast-induced shock wave can pass through the cladding and harm the building users [130]. In the first cladding generation, the improvement of structural response to explosions is obtained by reinforcing the envelopes and providing them with a rigid behavior. The second generation design approach, on the other hand, makes it possible to take advantage from the dissipative capacity of the façade panels, transforming them into sacrificial elements: in case of explosion, they dissipate energy by means of perma-

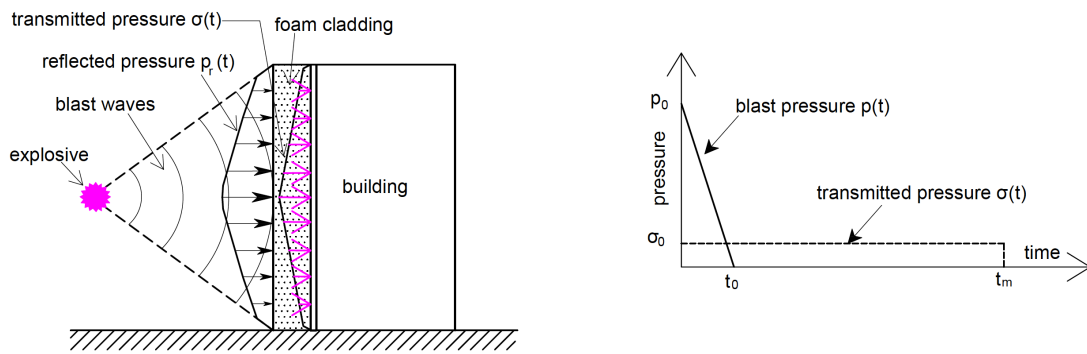


Figure 2.49: Blast-induced vibration control with sacrificial metal foam panels and ideal model of blast pressure

ment deformations, avoiding the overload of the primary structure. Typically, the sacrificial metal foam envelopes, consisting of a foam panel and a cover plate, are used to protect the structures from shocks and explosions. Due to the foams' own energy absorption capacity, when subjected to a nearby explosion, the sacrificial panels undergo high deformations and absorb energy, attenuating the impact loading. The main structure behind the sacrificial elements is then protected. Ma and Ye [131] in 2007 proposed a double-layer foam cladding system for the protection of civil structures under blast events (Fig. 2.50). Wu and Sheikh [132] in 2013 investigated the energy absorbing capacities of cellular metal foam coatings in order to protect the reinforced concrete floors of the structures. The foam cladding was modeled with a lumped mass-spring system that allowed describing the progressive densification of the foam layer in the direction of the applied load. The latter was obtained from a series of explosive tests carried out by the DSTO (*Defense Science and Technology Organization*, Australia).

The growing threat of terrorist attacks has led to a renewed interest in sacrificial sandwich panel structures which, due to the high strength-to-weight and stiffness-to-weight ratios, offer a greater resistance to explosions. An example of this type is given by the sandwich panels with different core configurations proposed by Yang et al. [133] in 2011. The authors studied the dynamic response of four configurations of circular sandwich panels with different core models under global and local explosive load conditions. The effect of additional intermediate layers on enhancing the blast resistance of the sandwich panels is investigated to ensure the sacrificial damage to the additional inner layers, preventing the main part of the core from being damaged by excessive shear deformation. A typical class of sandwich panels consists of metal reticular cores inserted between the solid plates. For these metal lattice core panels, the ability to withstand explosions is affected by the core topology. Alberdi et al [134] in 2013 analyzed the sandwich panels with different metal lattice topologies, comparing their performance under established explosive loads. Other examples of sacrificial façades are the composite tube façades proposed by Theobald and Nurick [135] and Van Paepegem et al. [136] in 2010 and 2014, respectively. The former investigated the blast response of sandwich panels with thin-walled square metal tube cores. Three panel layouts were identified, consisting of 4, 5 and 9 steel and aluminum alloy tubes, respectively. From the experimental tests,

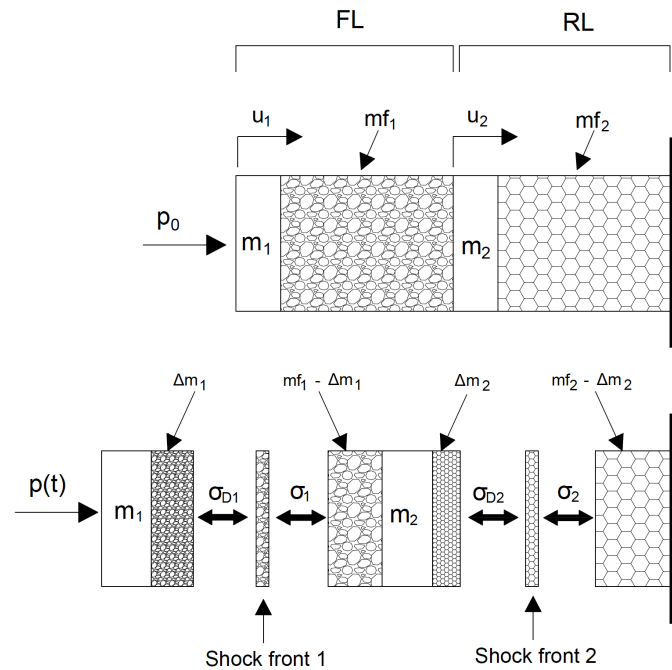


Figure 2.50: Double-layer aluminum façade panels for the absorption of blast loads. Source: Ma, G.W., and Ye, Z.Q. (2007). *Energy absorption of double-layer foam cladding for blast alleviation*

it emerged that, with the same explosive charge mass, the aluminum tube cores have a significantly greater crushing distance than the steel tube cores. From numerical parametric studies, it was found that the energy absorption efficiency of the panels is correlated to the uniformity of load, especially for the panels with fewer central tubes and thinner upper plates. Van Paepegem et al. conducted an experimental test on a sacrificial façade structure made of composite glass and polyester tubes. The peak force transferred to the non-sacrificial structure was compared for different composite pipe configurations.

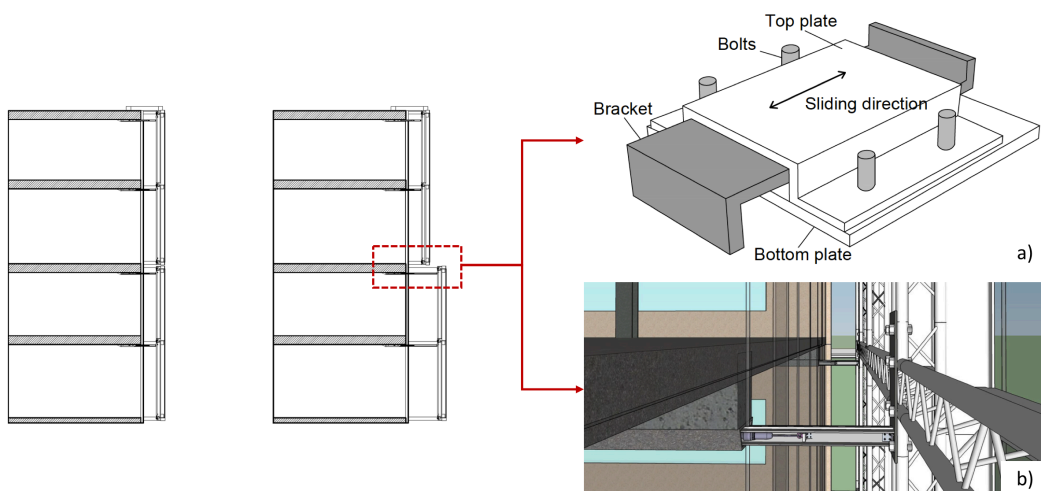


Figure 2.51: Connection methods between the façade and the primary building structure obtained through a) a passive control with dampers and springs, and b) an active control with dampers, springs and actuators. Source: T.S., Fu, and Zhang, R. (2016). *Integrating Double-Skin Façades and Mass Dampers for Structural Safety and Energy Efficiency*

The technological progress has led to the development of a third generation of façades which exploits the advantages of the dissipative connections to create a blast protection mechanism [137]. In a traditional conception, the cladding panels have a purely architectural function, so much so that they are classified as nonstructural components and considered as an additional permanent weight that does not contribute to any structural function of the building. However, there is a close relationship between the façade and the supporting structure of the building that comes out during an external dynamic load event. From literature researches [138], it emerged that façade systems can significantly contribute to the increase in lateral stiffness of the building, and this substantially depends on the connection system adopted. The conventional rigid brackets isolate the panels from the main structure, eliminating the shear forces that develop in the connectors due to the inter-storey drift resisted by the panels. However, slotted or flexible connections are preferable as they allow movement in the plane of the panel and, consequently, the interaction between the panel and the supporting frame. For this reason, the conventional rigid connection devices are now neglected in favor of advanced or engineering connectors capable of transferring the movement stresses, taking advantage of the interaction between the panels and the primary building structure to dissipate energy through hysteretic behaviors [139]. These flexible or sliding connectors can exhibit high ductility and damping properties, resulting in a greater energy dissipation under external load and in a substantial reduction of the building overall response [140]. The connection systems can exercise a passive control over the building by means of dampers and springs, whereas in the active control, the façades are connected to the building structures with dampers, springs and actuators, as shown in Figure 2.51.

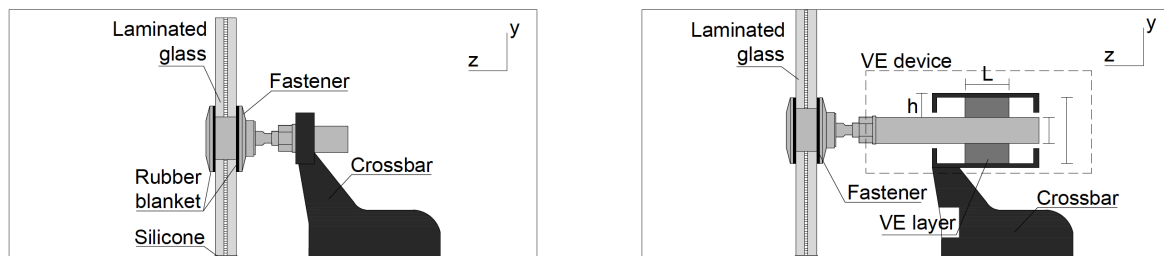


Figure 2.52: Three-dimensional and cross-sectional view of a four-arm rigid connector (RSC) and a possible four-arm viscoelastic device (VESC). Source: Amadio, C., and Bedon, C. (2012). *Viscoelastic spider connectors for the mitigation of cable-supported façades subjected to air blast loading*

Due to the combination of both energy dissipation and movement towards the floor, the connectors attract the shock wave energy instead of the cladding panels. The amount of energy transferred to the primary structure can be mitigated if the dissipative deformation available inside the connectors, which is limited by the distance between the façade and floor, is not exceeded. Within this space, the entire cladding can move towards the structure during a shock wave event. The idea of shock absorbing components is well-known in the engineering field and the possible application in the façade design is first illustrated by Amadio and Bedon [141] in 2012, through the proposal of viscoelastic connectors for the study of cable-supported curtain walls subject to blast loads (Fig. 2.52). In their study, Viscoelastic Spider Connector

(VESC) were introduced and compared with Rigid Connector (RC) in order to improve the overall blast response of the glass and steel cable-supported façade. As compared to RC, the maximum forces developed in glasses and cables were strongly reduced with VESC and, at the same time, the dissipative spiders proposed did not compromise the aesthetics of the transparent system. In subsequent works by the authors [142]-[143], it was shown that, with special mechanical connectors interposed between the primary building structure and the enclosing glass façade, the latter could act as a passive control system for the building, in the form of a distributed TMD under multi-hazard scenarios. Chen and Hao [144] in 2013 explored the use of friction dampers to absorb the high velocity impacts and energy of the explosions. Their study introduced a new sandwich panel consisting of a rotational friction hinge device and a spring inserted into a core between the outer and the inner plate. The rotational friction hinge was used to absorb the blast energy while the spring helped restore the panel original shape. The results showed that the proposed sandwich panel could partially recover its original configuration, thus maintaining its operational and load-bearing capacity after a blast event. Finally, a new prototype of curved plate and aluminum foam connector for the absorption and reduction of the blast energy transferred to the building was tested by Wang et al. in 2017 [145]. The performances of the proposed connectors were experimentally studied by subjecting the samples to compression load tests, from which it emerged that the energy absorption capacity could be improved by filling the connector with aluminum foam and increasing the thickness and radius of the curved plate. The integrated façade systems with passive dissipative connections have also been proposed in literature for the mitigation of wind vibrations and for the control of seismic response. Among the hypotheses advanced in this area, which originated from the 1993 studies of Goodno et al [146], the U-shaped flexural plate connectors by Baird et al. [147] in 2013 and the steel W-shaped bent sheet connectors for precast concrete cladding panels tested by Dal Lago et al. [148] in 2018 are cited.

Baird et al. examined the potential of the energy dissipation devices to make innovative passive connections in multi-storey buildings. The cladding panels were fixed to the frame by means of U-shaped plates that used the relative displacement between the structure and façade to dissipate energy during a seismic event. The outcomes showed that the proposed connectors were effective in halving the hysteretic energy of the structure and reducing the inter-storey *drift ratio*. Dal Lago et al. provided guidelines for the design of a dissipative connector consisting of a right angle bent steel plate with a W-shaped profile. Through experimental tests, the authors intended to study the hysteretic behavior of the device to ensure a safe fixing of prefabricated structure cladding panels under seismic action.

Recently, on an idea initially presented by K.S. Moon in 2005 [149] to reduce the effects of wind-induced vibrations on tall buildings, advanced structural control strategies based on the combination of DSF and *mass dampers*, capable of improving both the safety and energy efficiency of buildings, have been proposed [150]-[151]. Moon investigation focused on the use of DSF systems integrated by energy-absorbing devices inserted in an intermediate cavity, placed between the inner and the outer skin, for tall building dynamic motion control

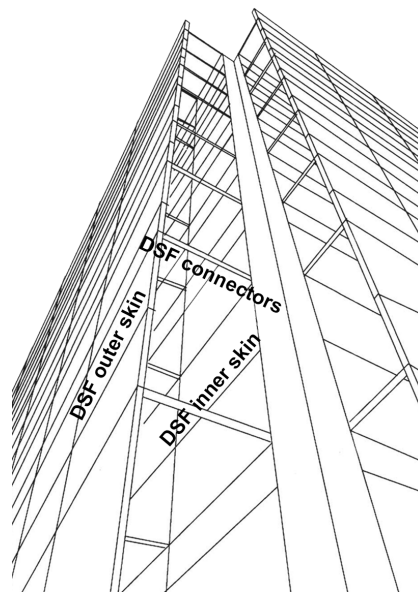


Figure 2.53: Integrated DSF-mass damper system. Source: Moon, K.S. (2009). *Tall Building Motion Control Using Double Skin Façades*

(Fig. 2.53). The conceptual idea consists in making the DSF work like a traditional TMD with the only difference -from a structural dynamics point of view- concerning the external location of the vibration control mechanism, as shown in Figure 2.54. Following Moon's approach of using suitable perpendicular connectors interposed between the DSF and the primary structure, the outer skin of the façade system is allowed to be moved in order to reduce the transmissibility of wind load between the cladding and the building. First hit by the wind action, it begins to vibrate, dampening the oscillation transferred to the primary structure behind it. Through an appropriate design of the damping and stiffness properties of the brackets, it is possible to significantly reduce the structural vibrations at the expense, however, of an excessive relative movement of the external skin, which still represents a serious design limitation of the system [152], as depicted in Figure 2.55.

Among the researchers who studied the structural performance of DSF, Fu and Zhang in 2016 [153] and Pipitone et al. in 2018 [154] focused on evaluating the optimal connection design of the DSF system for reducing the structural response under seismic excitation, while Zobec et al. in 2015 [155] conducted an experimental program on the potential use of DSF under blast pressures. By allowing the movement of the outer skin, Fu and Zhang proposed to use it as a distributed-TMD to reduce vibrations and structural damages during earthquakes and windstorms, while adjusting the size of the air cavity between the outer and inner skin to control the ventilation flow and improve the energy efficiency. By means of a parametric study, the authors optimized the damper parameters (such as, the stiffness and damping coefficient) for the passive control of the structural response under seismic excitation. In particular, among the five DSF configurations studied (1, 2, 4, 5 or 10 dampers, respectively), the one with 1 damper showed the best performances in terms of reduction of the structural vibrations. Various DSF layouts used as mass dampers under seismic events were also studied

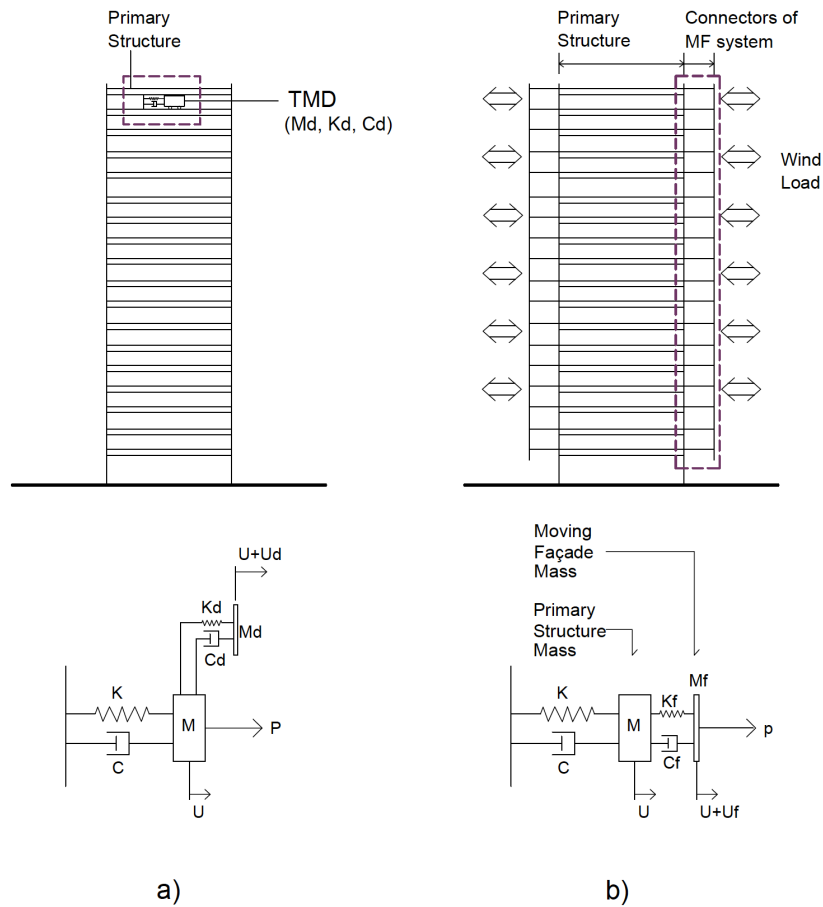


Figure 2.54: Simplified model of a primary building structure equipped with a) a TMD and b) a MF system connected by an energy dissipation mechanism. Source: Moon, K.S. (2009). *Tall Building Motion Control Using Double Skin Façades*

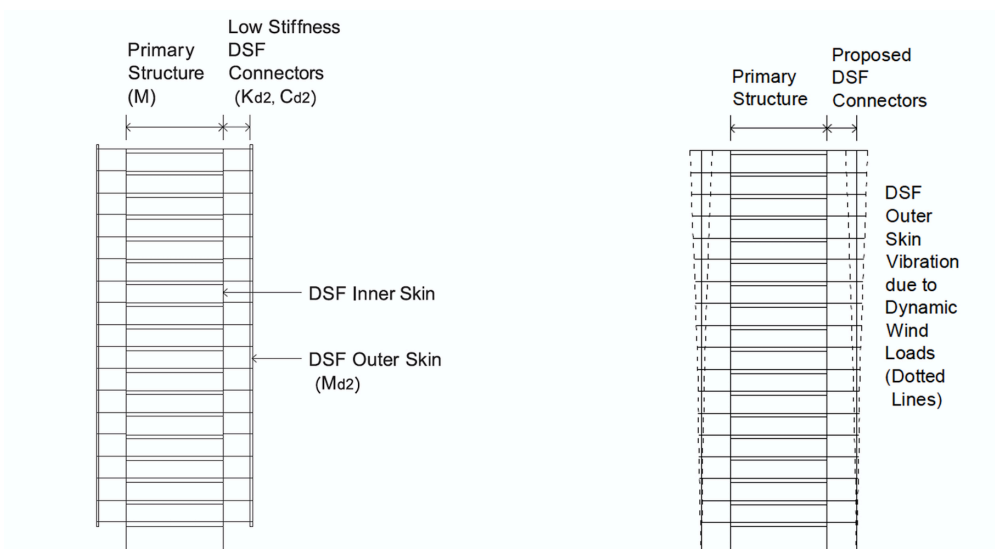


Figure 2.55: Conceptual diagrams on the operation of DSF connectors with low axial stiffness. Source: Moon, K.S. (2009). *Tall Building Motion Control Using Double Skin Façades*

by Pipitone et al. The researchers aimed to determine the optimal stiffness and damping values of the DSF connectors. By means of a parametric investigation carried out for four DSF configurations (with 1, 2, 3 and 6 independent panels, respectively) connected to the structure via elastic springs and viscous dashpots, it was observed that the spring stiffness uniformity is a prerogative for an effective design. With an experimental comparative analysis conducted on three DSF layouts with steel panels subject to an equivalent TNT charge weight of 250 kg at a safety distance of 52 m, Zobec et al. have argued that a DSF could increase the building blast resilience; however, due to the complex structural interactions between DSF and blast pressure waves, the authors signaled the lack of design codes that take into account the performance of DSF under explosions. Other authors proposed and developed moveable façade systems with an innovative parallel connection for reducing the wind-induced oscillation in tall buildings [156], which differs from a perpendicular connection as in this case the façade is fixed in the direction orthogonal to the primary building structure and movable in the parallel direction.

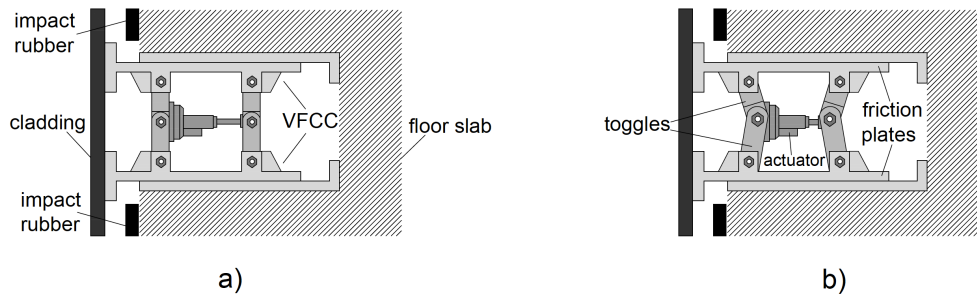


Figure 2.56: Variable friction connection device (VFCC) in the double locked (a) and semi-locked (b) configuration. Source: Gong, Y. et al. (2020). *Numerical verification of variable friction cladding connection for multihazard mitigation*

Most of the façade solutions for structural control investigated so far are conceived as passive protection systems, therefore applicable for the mitigation of a single type of load [157]. A significant step forward in the field of semi-active energy dissipation systems was made in 2018 by Gong et al. [158] who began experimenting with a VFCC device placed at façade level (Fig. 2.56), which takes advantage of the cladding inertia to minimize vibrations under blast [159], wind [160] and seismic [161] loads. The device prototype consists of two series of sliding friction plates on which a variable normal force could be applied. Due to its semi-active functioning, this could be used to mitigate different hazards considered individually or in combination with each other. Other mitigation systems based on the inertia of the building components were proposed by Xiang and Nishitani [162] in 2014, by showing a vibration control strategy that integrates the floor insulation system with the TMD robustness, and by Anajafi and Medina [163] in 2018, who considered a partial isolation technique based on the TMD principle to mitigate the building seismic response.

Chapter 3

Comparative study between Movable Façades and Tuned Mass Dampers

3.1 Introduction

Modern buildings are conceived as systems capable of performing complex functions that imply compliance with complex and stringent requirements. With the renewed interest in reducing the energy consumption at a national level, the search for innovative approaches and strategies to improve the building efficiency is today a topic of primary importance. As a part of the energy saving methods, a careful design of the façade system could significantly contribute to the overall sustainability of the building. The technological evolution of the cladding systems is also linked to the greater demand for structural resistance that the numerous tall buildings in continuous construction are called upon to satisfy, especially with regard to horizontal loads. Also in this context, the envelope design plays a crucial role for the general improvement of the building performance and, to date, can be considered sufficiently mature to lead to the development of adaptive facades capable of interacting with the environment, adapting their behavior to the external climate, user needs and environmental actions. It is therefore possible to consider technically feasible the possibility of making the envelopes undergo relative displacements with respect to the main load-bearing structure, through suitable flexible connections capable of improving the overall dynamic behavior of the buildings subject to external excitations. This is the concept behind the technology and feasibility of the MF system introduced in section 2.4.4. In this dual context, MF systems offer great potential both in the architectural field, managing the interaction between external and internal spaces, and in engineering. Indeed, in a MF-equipped structure, the façade mass can be used to reduce the structural vibrations in a way conceptually similar to that of a conventional TMD without the need to provide the building with additional mass and with the advantage of saving useful space indoors. Movable Façades can be made in various ways depending on the geometry of the building, by appropriately dividing the cladding

surface; façades characterized by several independent parts that allow for relative movement between each other in the direction of the applied load will be called *multiblock* MF; on the contrary, façades made up of a single vertical element extending over the entire height of the building will be called *monolithic* MF. Monolithic façades could be applied on common mid-rise buildings, while a multiblock façade would find a more suitable location on towers or high-rise structures, mainly for practical construction reasons. A schematic representation of the two types of system considered is shown in Figure 3.1. From a structural dynamics point of view, a building equipped with a monolithic façade is similar to one equipped with a standard TMD. Conceptually, when the structure undergoes a base excitation there is no difference; however, in the presence of wind or any other action that can be modeled with forces acting on the external surface of the building, the excitation is applied to the secondary mass instead of the primary one. Despite the substantial equality of the equations of motion, the resulting behavior of the two systems can be qualitatively very different. While the dynamic response of TMD has been well known since the 1960s and is explained in any textbook on the dynamics of structures [164]-[165], on the contrary, the MF behavior has not received the same attention, probably due to the lack of potential applications on concrete case studies. In light of the recent advances in façade engineering, a parametric study on the vibration damping performance of buildings equipped with a monolithic MF and a standard TMD in the simple 2DOF modeling under harmonic excitation is proposed in this Chapter.

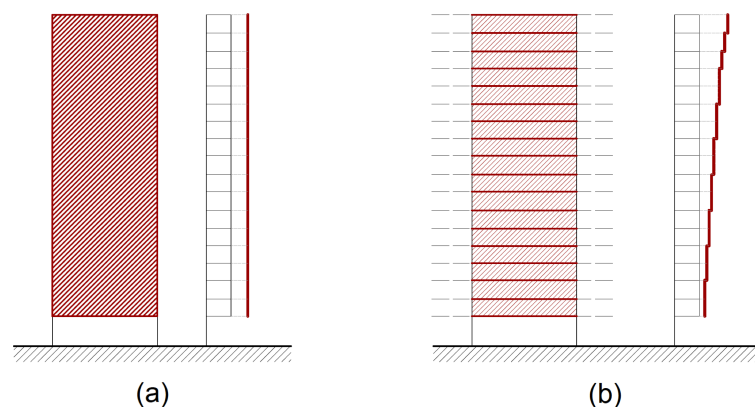


Figure 3.1: Schematic representation of a) monolithic MF and b) multiple block MF

The contents of this Chapter were published in: "Di Giovanni, G., Bernardini, D. Vibration Damping Performances of Moving Façades Under Harmonic Excitation. *Journal of Vibration Engineering & Technologies* (2020), [Springer]", [166].

3.2 Basic Modeling of MF and TMD

A building equipped with MF system can be described by a MDOF oscillator, considering a degree-of-freedom for each block. As a first approximation, the deformability of the façade blocks can be neglected, referring to a monolithic MF-equipped building with a TMD-like dynamic behavior. In the simplest numerical modeling, a building with monolithic MF (or

with a standard TMD) is simulated by a system with two masses, m_1 and m_2 , which represent, respectively, the main structure and the secondary mass, connected from springs with stiffnesses k_1 and k_2 and viscous dashpots c_1 and c_2 , as shown in Figure 3.2.

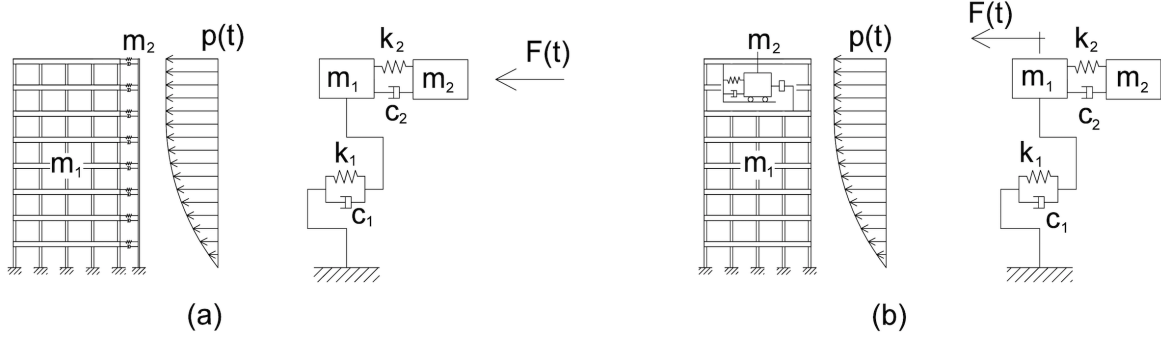


Figure 3.2: 2DOF modeling of a building equipped with monolithic MF (a) and standard TMD (b)

The equations of motion can be written in the form

$$\begin{cases} m_1 \ddot{x}_1 + (c_1 + c_2) \dot{x}_1 - c_2 \dot{x}_2 + (k_1 + k_2)x_1 - k_2 x_2 = f_1 \\ m_2 \ddot{x}_2 - c_2 \dot{x}_1 + c_2 \dot{x}_2 - k_2 x_1 + k_2 x_2 = f_2 \end{cases} \quad (3.1)$$

where x_1 and x_2 are the displacements of the two masses with respect to the ground and f_1 and f_2 are the excitations acting on each d.o.f.

Clearly, when $f_2 = 0$, the system reduces to a building model with standard TMD, while if $f_1 = 0$ it reduces to a building model with monolithic MF. By focusing on the response to harmonic excitation, it is useful to express the latter in a complex form using a **sans-serif** font to distinguish the complex numbers from the real ones.

$$\begin{cases} f_1 = F_1 e^{i\Omega t} & \text{with} & F_1 := F_1 e^{i\Psi_1} \\ f_2 = F_2 e^{i\Omega t} & & F_2 := F_2 e^{i\Psi_2} \end{cases} \quad (3.2)$$

where $\Psi_{1,2}$ are the angles describing the phase shifts between the excitation and the response.

By introducing the well-known standard notations

$$\omega_1^2 := \frac{k_1}{m_1} \quad \omega_2^2 := \frac{k_2}{m_2} \quad \xi_1 := \frac{c_1}{2m_1\omega_1} \quad \xi_2 := \frac{c_2}{2m_2\omega_2} \quad (3.3)$$

the mass, natural frequency and forcing frequency ratios can be defined as follows [167]

$$\mu := \frac{m_2}{m_1} \quad f := \frac{\omega_2}{\omega_1} \quad \rho := \frac{\Omega}{\omega_1} \quad (3.4)$$

The natural frequency and the mass ratio together determine the stiffness ratio

$$\sigma := \frac{k_2}{k_1} = \mu f^2 \quad (3.5)$$

To evaluate the performance of the two systems, it is useful to express the motion of the secondary mass with respect to the primary mass by introducing the variables

$$u_2 := x_2 - x_1 \quad u_1 := x_1$$

So that the system of Eq. 3.1 can be rewritten in the form

$$\begin{cases} \ddot{u}_1 + 2\omega_1(\xi_1\dot{u}_1 - \mu f\xi_2\dot{u}_2) + (\omega_1^2)(u_1 - \mu f^2u_2) = \omega_1^2\frac{f_1}{k_1} \\ \ddot{u}_2 + \ddot{u}_1 + (2\omega_1 f\xi_2)\dot{u}_2 + (\omega_1^2 f^2)u_2 = \omega_1^2\frac{f_2}{\mu k_1} \end{cases} \quad (3.6)$$

By assuming harmonic response

$$\begin{cases} u_1 = U_1 e^{i\Omega t} \\ u_2 = U_2 e^{i\Omega t} \end{cases} \quad (3.7)$$

the substitution of Eqs. (3.2) and (3.7) into Eq. (3.6) yields the following equations in the complex amplitudes of the response

$$\begin{cases} Z_{1,1}U_1 + Z_{1,2}U_2 = \frac{1}{k_1}F_1 \\ Z_{2,1}U_1 + Z_{2,2}U_2 = \frac{1}{\mu k_1}F_2 \end{cases} \quad (3.8)$$

where

$$\begin{aligned} Z_{1,1} &:= [1 - \rho^2] + i[2\rho\xi_1] \\ Z_{1,2} &:= [-\mu f^2] + i[-2\mu f\rho\xi_2] \\ Z_{2,1} &:= [-\rho^2] \\ Z_{2,2} &:= [f^2 - \rho^2] + i[2\rho f\xi_2] \end{aligned}$$

Solving the system of Eq. 3.8, the complex amplitudes can be written in the following form which emphasizes the contributions of the parts relevant to TMD and MF in terms of the corresponding transfer functions

$$\begin{cases} U_1 = H_1^{TMD}F_1 + H_1^{MF}F_2 \\ U_2 = H_2^{TMD}F_1 + H_2^{MF}F_2 \end{cases} \quad (3.9)$$

Each one of the four functions H can be seen as a special case of the formula

$$H := \frac{[-B_2\rho^2 + B_0] + i[B_1\rho]}{C_0 + iC_1}\alpha \quad (3.10)$$

where the coefficients of the denominator are common to all cases

$$\begin{aligned} C_0 &:= A_4\rho^4 - A_2\rho^2 + A_0 \\ C_1 &:= -A_3\rho^3 + A_1\rho \end{aligned} \quad (3.11)$$

with

$$\begin{aligned}
A_0 &:= f^2 \\
A_1 &:= 2(f\xi_1 + \xi_2)f \\
A_2 &:= 1 + (1 + \mu)f^2 + 4f\xi_1\xi_2 \\
A_3 &:= 2(\xi_1 + (1 + \mu)f\xi_2) \\
A_4 &:= 1
\end{aligned} \tag{3.12}$$

whereas the coefficients of the numerator take different expressions in the four cases

$$\begin{array}{cccc}
H_1^{TMD} & H_2^{TMD} & H_1^{MF} & H_2^{MF} \\
B_0 & f^2 & 0 & \mu f^2 & 1 \\
B_1 & 2f\xi_2 & 0 & \mu 2\mu f\xi_2 & 2\xi_1 \\
B_2 & 1 & 1 & 0 & 1 \\
\alpha & \frac{1}{k_1} & \frac{1}{k_1} & \frac{1}{\mu k_1} & \frac{1}{\mu k_1}
\end{array} \tag{3.13}$$

Substituting Eq. (3.9) into Eq. (3.7), the response to harmonic excitation can be written in the form

$$\begin{aligned}
u_1 &= H_1^{TMD} \frac{F_1}{k_1} e^{i(\Omega t + \psi_1 + \delta_1^{TMD})} + H_1^{MF} \frac{F_2}{k_1} e^{i(\Omega t + \psi_2 + \delta_1^{MF})} \\
u_2 &= H_2^{TMD} \frac{F_1}{k_1} e^{i(\Omega t + \psi_1 + \delta_2^{TMD})} + H_2^{MF} \frac{F_2}{k_1} e^{i(\Omega t + \psi_2 + \delta_2^{MF})}
\end{aligned}$$

where δ_i is the phase angle which describes the phase shift between excitation and response.

In terms of the respective amplification factors one has

$$H_1^{TMD} := \sqrt{\frac{\rho^4 + 2f^2(2\xi_2^2 - 1)\rho^2 + f^4}{C_0^2 + C_1^2}}, \quad H_2^{TMD} := \sqrt{\frac{\rho^4}{C_0^2 + C_1^2}}$$

and

$$H_1^{MF} := \sqrt{\frac{(f^2\mu)^2 + (2f\mu\rho\xi_2)^2}{\mu^2(C_0^2 + C_1^2)}}, \quad H_2^{MF} := \sqrt{\frac{\rho^4 + 2(2\xi_1^2 - 1)\rho^2 + 1}{\mu^2(C_0^2 + C_1^2)}}$$

3.3 Performance indexes and tuning levels

In general, the vibration amplitude of the controlled primary mass (that is, with secondary mass) can be greater or less than the corresponding response of the uncontrolled primary mass (therefore, in the absence of m_2), which is given by

$$H(\rho) := \frac{1}{\sqrt{(1 - \rho^2)^2 + (2\xi_1\rho)^2}}$$

It is therefore useful to define a numerical indicator of the vibration damping efficiency

of the additional mass by means of the quantities

$$\eta^{TMD}(\rho) := \frac{H(\rho) - H_1^{TMD}(\rho)}{H(\rho)} \quad \eta^{MF}(\rho) := \frac{H(\rho) - H_1^{MF}(\rho)}{H(\rho)} \quad (3.14)$$

Obviously, if $\eta(\rho) > 0$, the secondary mass dampens the vibrations of the primary mass, while negative values of $\eta(\rho)$ indicate that m_2 acts as an amplifier of the structural vibrations. Therefore, the efficiency is not a constant but varies according to the excitation frequency. Furthermore, the system response can be qualitatively different depending on the frequency ratio, f , defined in Eq. 3.4, which determines the tuning between the independent natural vibration frequencies of the two masses. To discuss these differences, three tuning intervals have been distinguished:

- *tuned* systems for $f \approx 1$: the peaks in the transfer functions are close to each other. In this situation, the stiffness ratio is numerically close to the mass ratio;
- *undertuned* systems for $f < 1$: the resonance of the secondary mass occurs at lower frequencies than the main one. Fixed μ , this is achieved with more flexible connections;
- *overtuned* systems for $f > 1$: the resonance of the secondary mass occurs at higher frequencies than the main one. Fixed μ , this is achieved with stiffer connections.

Clearly, the same tuning level can be achieved with different combinations of the mass and stiffness ratios, correlated according to Eq. 3.5. Fixed f , the response of the system is also affected by the damping ratios ξ of both masses.

3.3.1 Tuned systems

As is known, in a TMD-equipped building with values of f close to 1 it is possible to activate a transfer of kinetic energy from the main structure to the secondary mass. Thanks to this energy exchange, the TMD acts effectively in damping the vibrations of the structure in a frequency range centered around $\rho \approx 1$. Figure 3.3 shows the transfer function H_1 for $f = 1$ (with $\xi_1 = 0.03$ and $\xi_2 = 0.10$) for different values of the mass ratio, superimposed on the corresponding response of the uncontrolled main structure, i.e. without additional masses (red curve). When the H_1 curve is lower than the red curve, a positive efficiency is obtained and the secondary mass acts as a vibration damper (yellow region in the figure). The TMD efficiency depends on the mass ratio μ and on the damping ratios $\xi_{1,2}$. For the chosen parameter values, the positive efficiency range extends approximately between 0.9 and 1.1 with an efficiency peak of approximately 0.9 increasing with the mass ratio.

Under the same conditions, a tuned MF shows lower efficiency around $\rho = 1$ but tends to systematically reduce oscillations on higher frequencies ($\rho > 1.5$). Figure 3.4 shows the amplification of the two secondary masses under the same conditions as Figure 3.3. As can be seen, the façade displacement tends to be significantly greater than that of the TMD, except in a narrow range of frequencies around $\rho = 1$ and this effect increases for lower mass ratios (blue curves).

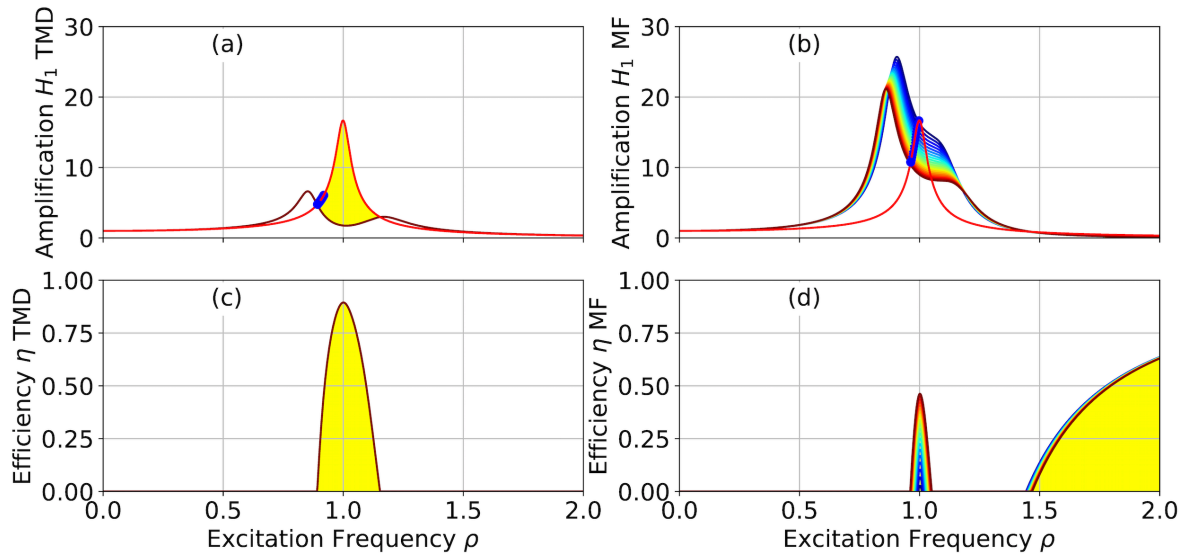


Figure 3.3: On the first line: H_1 transfer functions for TMD (a) and MF (b) with $f = 1.00$, $\xi_1 = 0.03$, $\xi_2 = 0.10$ and $\mu \in [0.05, 0.10]$. The isolated red curves show the amplification of the main structure without any additional mass. On the second line: positive vibration damping efficiency values η for TMD (c) and MF (d). Blue curves correspond to lower μ values, dark red curves to higher μ values

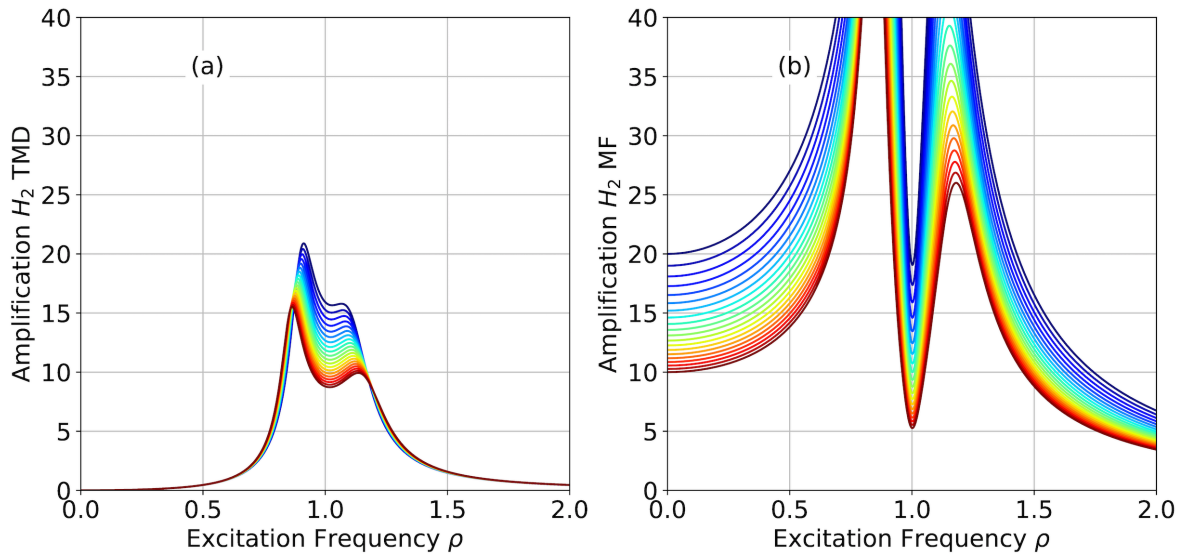


Figure 3.4: Transfer functions H_2 for the displacement of the secondary masses corresponding to figure 3.3. Blue curves correspond to lower values of μ , dark red curves to higher values of μ

3.3.2 Undertuned systems

Reducing the tuning ratio f , for a given mass ratio μ , means designing a more flexible connection between the two masses. Under such conditions, the response of the TMD and MF systems becomes significantly different. As shown in Figure 3.5, as the elastic coupling between the masses decreases (blue curves), the TMD progressively loses almost all its vibration damping efficiency (Fig. 3.5 c); on the contrary, MF gains very high efficiency over a wide range of excitation frequencies (Fig. 3.5 d). In Figure 3.5 a-b, blue points indicate

the points where the amplification function H_1 intersects the red curve (which represents the main structure without masses), thus defining the boundary of the positive efficiency interval. This phenomenon is easily understood if we consider that, for weaker couplings, the kinetic energy tends to remain on the same mass on which the excitation is applied. Therefore, the oscillations tend to localize on the main mass for the TMD and on the façade for the MF system.

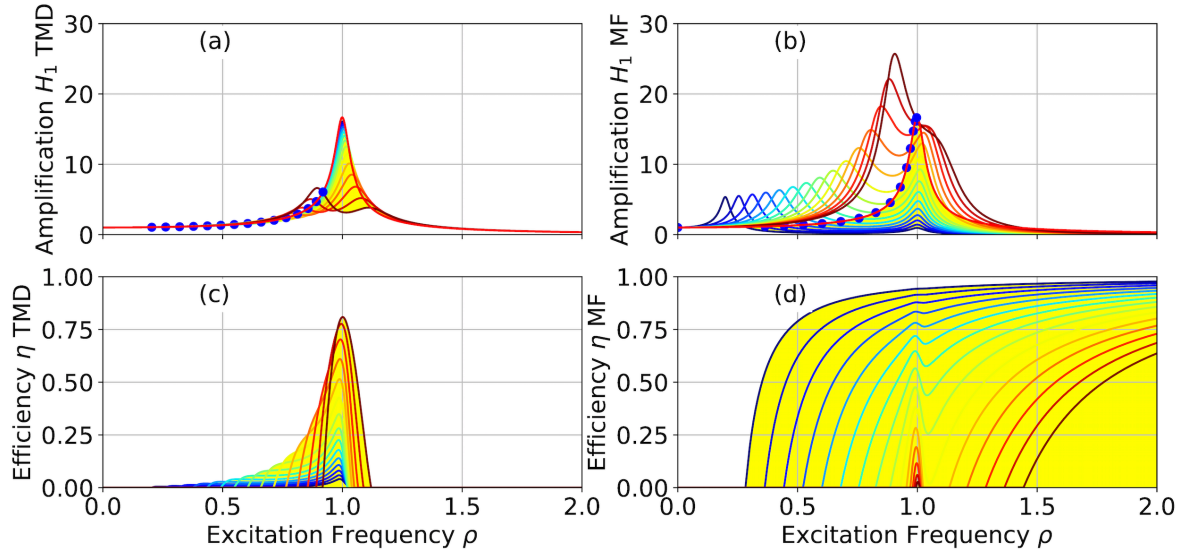


Figure 3.5: Transfer functions H_1 for TMD (a) and MF (b) and vibration damping efficiencies η for TMD (c) and MF (d) for tuning ratios $f \in [0.2, 1.0]$ and fixed mass ratio ($\mu = 0.05, \xi_1 = 0.03, \xi_2 = 0.10$); blue curves correspond to lower values of f

Figure 3.6 describes in more detail the undertuned case with $f = 0.4$ and various mass ratios μ confirming that, with not very stiff connections, the MF system is able to provide excellent performance vibration damping for excitation frequencies close to $\rho \approx 1$ (Fig. 3.6 d), even better than the corresponding performance provided by the TMD in the same case with $f = 1$. This effect is essentially independent of the mass ratio and is even more pronounced for further decreases of f . Locating oscillations on the secondary mass of a MF system with softer connections has a strong effect on the vibration damping efficiency, however it comes at the cost of high secondary mass displacements.

Figure 3.7 shows the transfer functions H_2 for $f = 0.4$ in both TMD (a) and MF (b) systems as μ varies. It is evident that the displacements of the secondary mass become extremely large at lower excitation frequencies. However, if the focus is on the $\rho \in [0.8, 1.2]$ region (Fig. 3.7 b) where the efficiency is still good, the secondary mass amplification values are still large, but are of the same order of magnitude as the corresponding values made by the TMD for $f = 1$ (this can be seen by comparing the zoom in the plot of Fig. 3.7 b with the plot of Fig. 3.4 a).

The analyzes just discussed show that, in general, the displacements of the secondary mass in a MF system increase strongly for lower mass ratios and vice versa. A similar effect is produced by a change in the connection damping, i.e. an increase in damping reduces the displacements of the secondary mass.

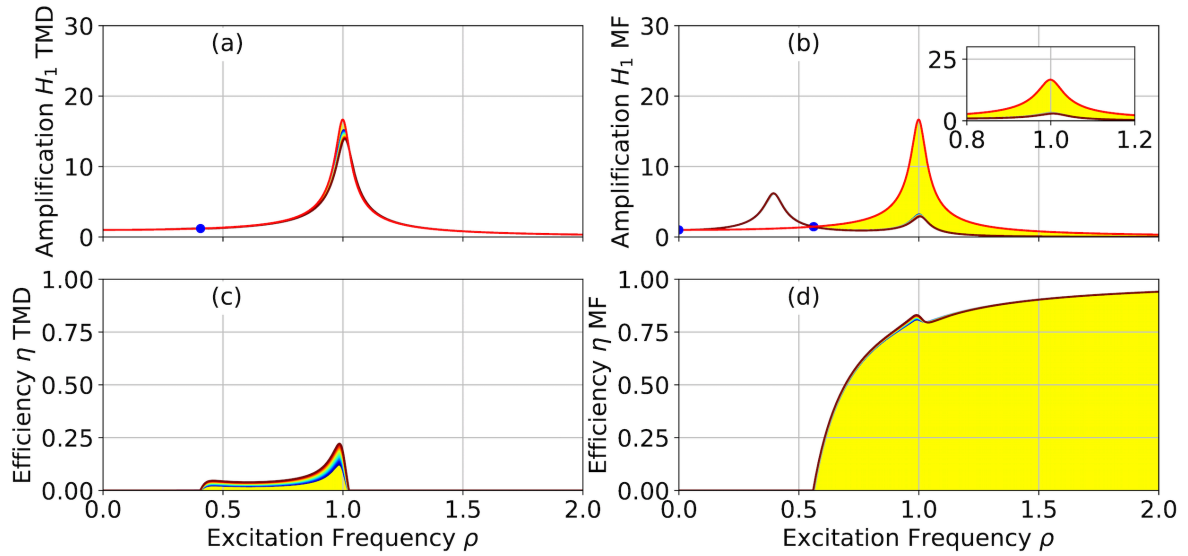


Figure 3.6: Transfer functions H_1 for TMD (a) and MF (b) and vibration damping efficiencies η for TMD (c) and MF (d) for $f = 0.4$ and various mass ratios $\mu \in [0.05, 0.10]$ with a zoom on the range $\rho \in [0.8, 1.2]$ in the case of MF (b). The other parameters are the same as in figure 3.5

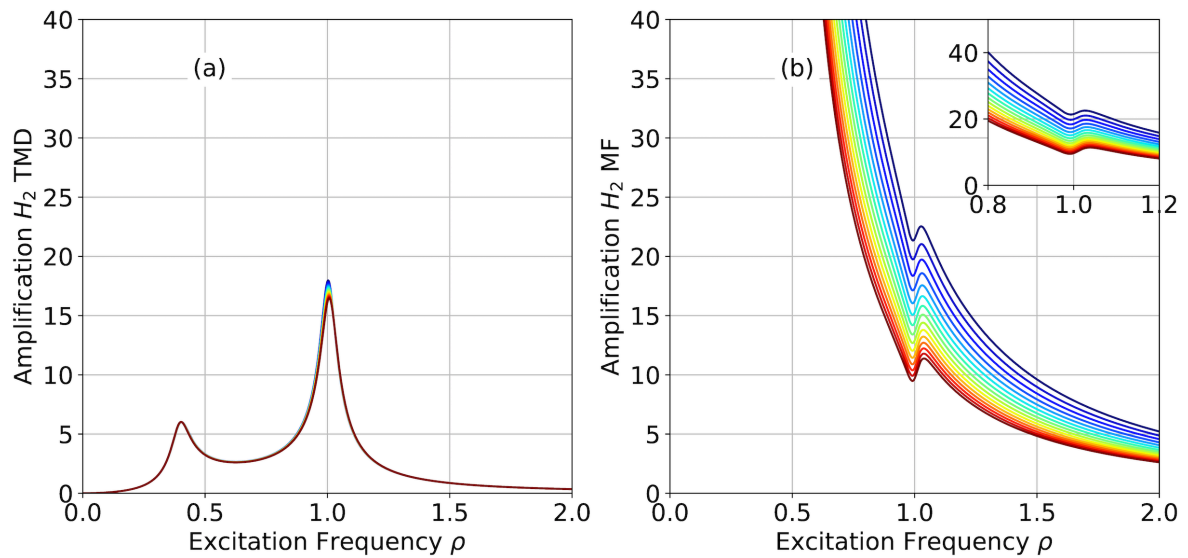


Figure 3.7: Transfer functions H_2 for the displacement of the secondary masses corresponding to figure 3.6 for $f = 0.4$ with a zoom on the interval $\rho \in [0.8, 1.2]$ in the case of MF (b). The other parameters are the same as in figure 3.6. Blue curves correspond to lower mass ratios

3.3.3 Overtuned systems

Increasing the tuning ratio f , for a specific μ , means making more stiffer connections between the two masses. This has the effect of shifting the second peak in the resonance curve towards higher and higher frequencies. In this case, for both TMD and MF systems, the vibration damping efficiency in the proximity of $\rho = 1$ decreases, replaced by a filtering effect of high frequency excitations. Figure 3.8 shows the performance variation of both systems for increasing values of f , specifically for $f \in [1.0, 3.0]$ and fixed mass ratio. In particular, for the TMD, the damping of the higher frequencies is less than 0.20 and ends at values of $\rho = 3$

(Fig. 3.8 c). On the other hand, MF systems show almost complete damping of the higher frequencies, with no upper limit (Fig. 3.8 d).

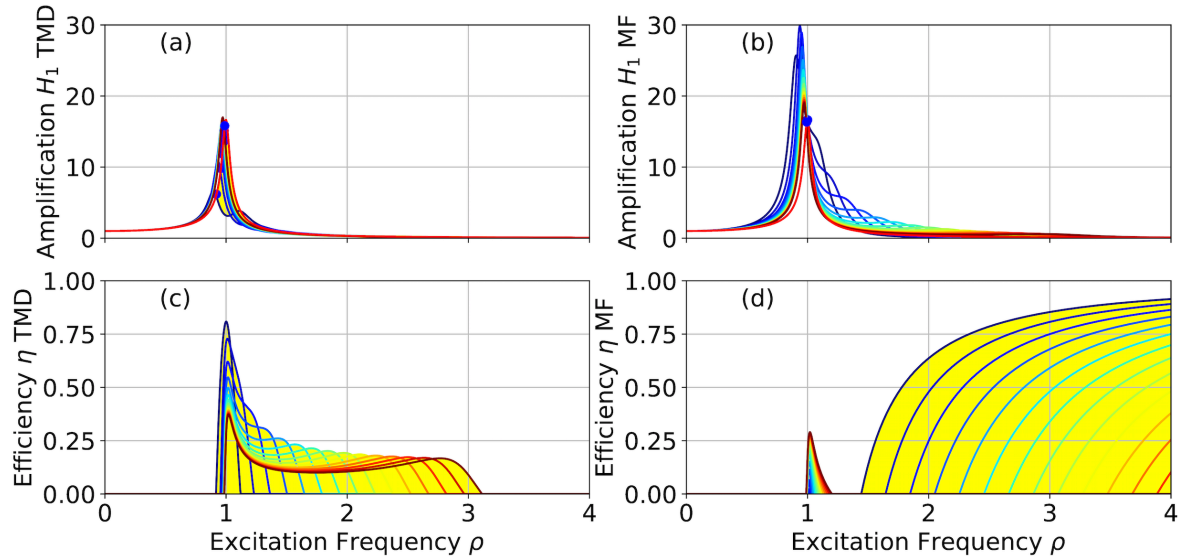


Figure 3.8: Transfer functions H_1 for TMD (a) and MF (b) and vibration damping efficiencies η for TMD (c) and MF (d) for tuning ratios $f \in [1.0, 3.0]$ with $\mu = 0.05, \xi_1 = 0.03, \xi_2 = 0.10$. Blue curves correspond to lower values of f

Figure 3.9 focuses on the case $f = 1.6$ for various mass ratios. Under these conditions, the TMD still maintains a vibration damping efficiency around $\rho = 1$ (Fig. 3.9 c) which, however, is lost at higher frequencies. On the contrary, the MF with more rigid connections has a very low efficiency around $\rho = 1$ but has a significant filtering effect of high frequency excitations (Fig. 3.9 d) and this trend is essentially independent of the mass ratio.

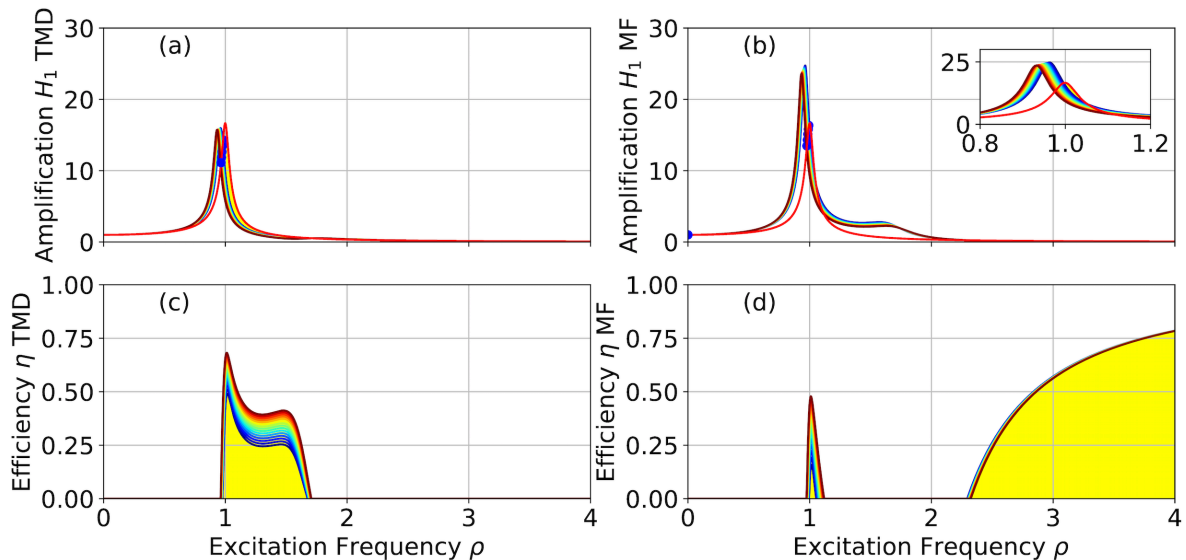


Figure 3.9: Transfer functions H_1 for TMD (a) and MF (b) and vibration damping efficiencies η for TMD (c) and MF (d) for $f = 1.6$ and $\mu \in [0.05, 0.10]$ with a zoom on the $\rho \in [0.8, 1.2]$ region for the case of MF. The other parameters are the same as in figure 3.8. Blue curves correspond to lower values of μ

The increased stiffness of the connectors tends to reduce the oscillations of the secondary mass for both TMD and MF systems as a greater elastic coupling forces the mass to stay closer and closer. This effect is described in Figure 3.10 which shows the transfer functions H_2 for $f = 1.6$ highlighting how the reduction of the oscillations of the secondary mass induced by the increase of f is further amplified with ratios of higher mass (red curves).

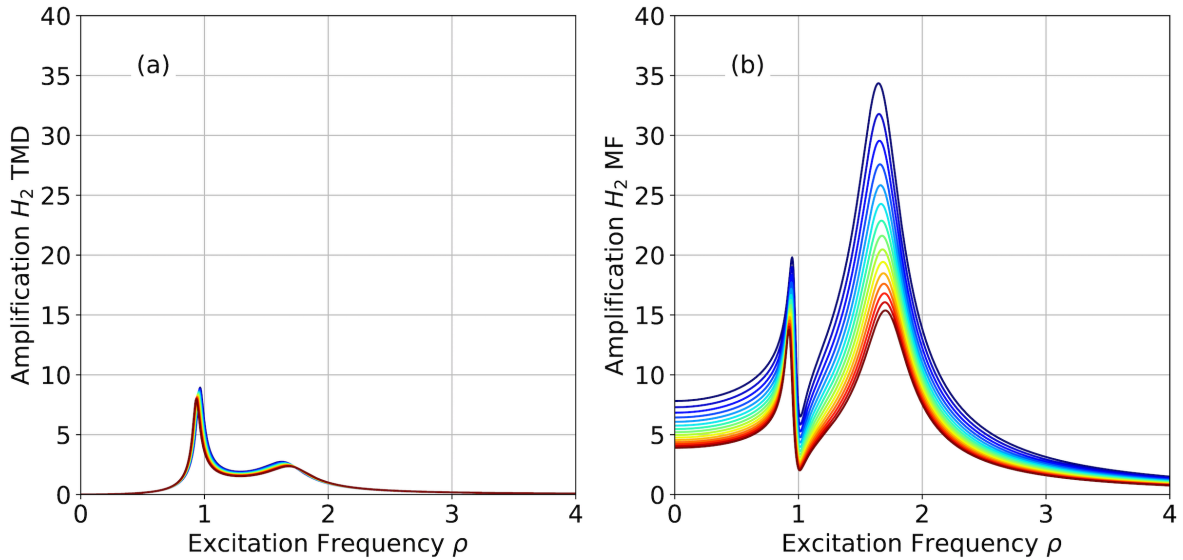


Figure 3.10: Transfer functions H_2 for the displacement of the secondary masses corresponding to figure 3.9 for $f = 1.6$. The other parameters are the same as in figure 3.9. Blue curves correspond to lower values of μ

3.4 Effect of connection damping

In the previous sections the effects of the tuning and mass ratios on the response of both systems were discussed, keeping the damping value of both the connection and the primary mass constant. While the damping of the structure is an inherent property of the building under consideration, the damping of the link can be considered a design variable. The effect of damping in TMD systems is well known; on the other hand, with regard to MF systems, it would be advisable to provide the connection with enhanced dissipative characteristics.

Various types of devices can be designed for this purpose and the use of high damping materials or intelligent materials (friction based alloys, shape memory alloys, etc.) could help improve the performance of these systems [168]. By focusing on MF, the increase in damping always involves a significant reduction in the displacements of the secondary mass, typically accompanied by a slight reduction in the vibratory efficiency. Figures 3.11 and 3.12 illustrate the effect of damping in the two cases of softer and stiffer connections for a given mass ratio. Figure 3.11 shows the case of $f = 0.4$ which was considered as a representative example of undertuned systems. In this case, an increase in the connection damping reduces the displacements of the secondary mass in the interval $\rho = 1$; but it has almost no effect in the other excitation frequency ranges. Figure 3.12 shows the case of $f = 1.6$ which was considered as a representative example of overtuned systems. In this case, the increase in

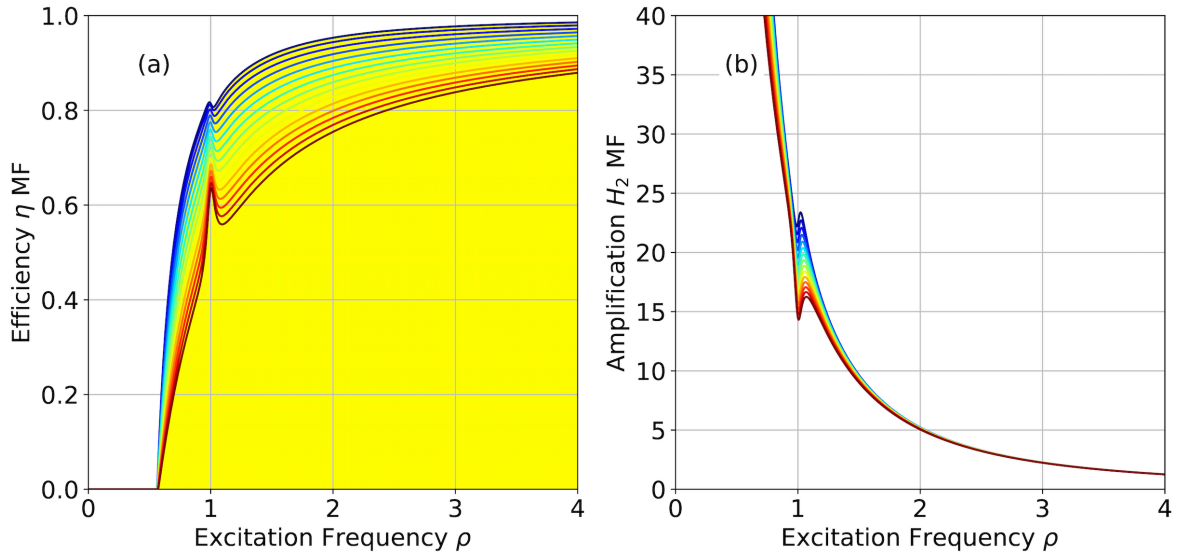


Figure 3.11: Effect of the connection damping ratio $\xi_2 \in [0.05, 0.60]$ on the performance of undertuned MF systems for $f = 0.4$ (the other parameters are the same as in figure 3.6). On the left, the vibration damping efficiency, on the right, the transfer functions H_2 . Blue curves correspond to lower damping

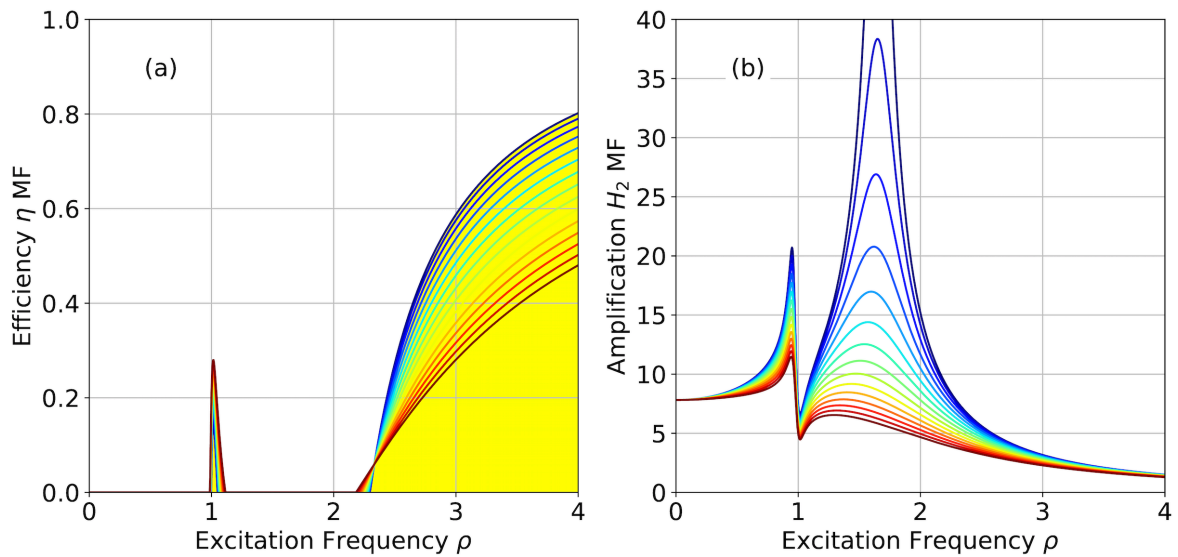


Figure 3.12: Effect of the connection damping ratio $\xi_2 \in [0.05, 0.60]$ on the performance of overtuned MF systems for $f = 1.6$ (the other parameters are the same as in figure 3.9). On the left, the vibration damping efficiency, on the right, the transfer functions H_2 . Blue curves correspond to lower damping

damping has a much greater effect in reducing the displacements of the secondary mass. In both cases, the reduction of the displacements of the additional mass is accompanied by a reduction of the vibration damping efficiency.

3.5 Closing remarks

With the advances made in the façade technological field, nowadays the possibility of designing buildings with cladding systems capable to undergo non-negligible displacements rel-

atively to the main structure is concretely conceivable. The idea of taking advantage from the façade vibrations to improve the dynamic performance of a building, first proposed by Moon and currently being studied by several authors, is truly fascinating. Movable Façades are seen as an emerging solution in the field of structural control and two main types can be distinguished according to the design layout that makes it possible to realize the flexible cladding surface: monolithic and multiblock MF. By focusing on the first type, a similarity of dynamic behavior can be found between the monolithic MF and the well-known TMD. From a structural dynamics viewpoint, a building with a monolithic MF is essentially the same thing as a building with a TMD. However, in presence of excitations directly acting on the external surface of the building there may be significant differences of behavior. In this Chapter, a first step towards a systematic comparison between the performances of buildings with MF and TMD is carried out in the simplest setting of 2DOF modeling and harmonic excitation. Despite the deceptive simplicity of the setting some of the aspects related to the potential applicability of MF to vibration damping and the correlated limitations are discussed and critically analyzed. The comparison between the performances of the two systems has been carried out in terms of the parameter η defined in eq. 3.14 which turns out to be a useful numerical indicator of the vibration damping efficiency. In the context of linear dynamics, it has been found that the efficiency of both MF and TMD can vary according to the connection stiffness between the structure and the secondary mass, making it possible to identify three performance levels (undertuning, tuning and overtuning) related to a progressively stiffer connection, respectively. The results of the comparison show that, although in the case of tuned systems ($f = 1.0$) the TMD certainly exhibits better vibration damping performances, the MF could potentially be very efficient for undertuned systems ($f < 0.5$). However, the good performance of these systems could be only achieved at the price of large façade relative displacements, confirming the issue already introduced by K.S. Moon in 2005. The possibility of pursuing potential applications of this type of structure, therefore, seems to be subordinated to the search for solutions that limit such displacements within functionally acceptable ranges. The results obtained from the comparison also showed that overtuned MF systems ($f > 2.0$) perform very well in isolating the building from high frequency excitations. This preliminary investigation was carried out in the simplest setting of 2DOF modeling under harmonic load, focusing on the response in terms of the displacement amplitude. More in-depth investigations will be carried out in the following Chapters, considering MDOF models capable of describing different topological layouts of the cladding, more realistic excitations and evaluating the vibration efficiency in terms of other structural response parameters, including floor accelerations.

Chapter 4

Proposal of dissipative sliders for Movable Façades

4.1 Introduction

Modern structures can experience excessive levels of vibration under the action of external forces due to their high flexibility and low inherent damping, causing both damage to structural members and discomfort to building users. The currently available vibration control techniques referred to in Chapter 2 can be applied in order to mitigate such an excitation, improving the performance of civil structures. Most of them consist in energy dissipation methods capable of absorbing or consuming a portion of the input energy, thereby reducing the energy dissipation demand on the primary building and minimizing possible structural damages. In the field of structural control, some authors have recently found an interesting solution [169] in the emerging movable façades, since they offer an important advantage linked to the mass availability in the existing building without taking up useful space indoor [170] compared to other conventional systems, like the classic TMD. Actually, their installation does not require additional space since the free gap available between the envelope and the structure behind is used for positioning the vibration control devices, typically showing a viscoelastic [171], tuned-mass [172] or frictional [173] behavior.

As anticipated in section 2.4.4, the first studies about MF concerned the possibility of mitigating sudden movements induced by blast [174] and seismic [175]-[176] events, initially by sacrificing cladding panels and, subsequently, the connections between the envelope and the primary building structure, designed to absorb the shock wave while safeguarding panels. As part of the application of façade systems for wind-induced vibration damping, the first proposal for the integration of MF and structural control dates back to 2005 when K.S. Moon investigated the potential of the system in mitigating continuous structural movements induced by dynamic wind load [177]. Advanced anti-vibration strategies based on the application of MF have later been investigated by several authors as well [178]-[179]. Literature outcomes show that the potential for use of these systems may be promising, however, their effectiveness is compromised by their large displacements which could preclude the overall

functionality of the building if not contained within acceptable limits, leading to the issue renamed as Moon's problem. From a construction point of view, movable façades can be made in various ways depending on the different design layouts that make it possible to create the cladding surface. Among them, two main types can be distinguished according to whether the cladding surface is conceived as a single vertical element, thus defining a monolithic MF, or it is divided into several independent parts, giving rise to multiblock MF. The main difference between the two solutions concerns the possibility of relative motion between the independent blocks, which is not feasible in the monolithic version.

In Chapter 3, the vibration damping performances of monolithic movable façades are studied. From the point of view of structural dynamics, they have a similar functioning to TMD: under a seismic event, the dynamic behavior of the two systems is substantially the same; on the contrary, under wind load quite different responses can occur although the equations of motion show only a small difference. A preliminary comparison between the vibration damping efficiency of monolithic MF and classical TMD is proposed on harmonically excited 2DOF models. Results of the analysis performed in the field of linear dynamics highlight that the relative efficiency of both MF and TMD can vary according to the connection stiffness between the primary building structure and the secondary mass. Depending on a more stiff or flexible connection, they can be classified into overtuned, tuned or undertuned systems, respectively, with associated different performance levels. Among the three categories, undertuned MF prove to be considerably more effective than TMD in dampening structural vibrations, but at the expense of a large relative displacement. This preliminary investigation clearly establishes the existence of Moon's problem, showing the need to identify solutions that allow the functionality of façade systems and their potential application in the context of structural vibration control.

Based on these premises, this Chapter proposes the conception, design and modeling of dissipative connection devices to be inserted in the gap between the façade and the building behind, capable of preserving the dynamic performances while solving Moon's problem and containing façade relative displacements within reasonable values. To ensure a suitable vibration control and limit of façade movement, the connection device takes advantage from two main mechanisms. As for the former, a friction damper (FD), inspired by the variable friction cladding connection (VFCC) device developed by Laflamme and coworkers [180], is incorporated as part of the connection between the supporting structure and the cladding panels, providing the desired level of dissipation needed for ensuring a suitable vibration control [181]. Advantageous properties, such as the ability to adapt to a wide excitation bandwidth [182], and the powerful dissipation capability of FD compared to other passive mechanisms [183], provide many researchers with a practical, economical and effective approach for the design of civil buildings to withstand excessive vibrations [184]-[185]. The VFCC is based on Coulomb's friction law¹⁰ and is able to reach high damping values (up to 60%) in order

¹⁰Coulomb's Law of Friction states that kinetic friction is independent of the sliding velocity. This approximation is fundamentally an empirical construct which follows from three main assumptions: a) surfaces are in close contact only over a small fraction of their overall area; b) the contact area is proportional to the normal force; and c) the frictional force is proportional to the applied normal force, regardless of the contact area.

to dissipate and reduce the amount of energy transferred to the structure behind. Despite being a simplified model, based on the assumption that kinetic friction is independent of the sliding velocity, Coulomb's law is a helpful rule used in many numerical applications to describe, in a simple and versatile way, the approximate result of the extremely complicated physical interaction of contacting surfaces. The second mechanism involved concerns the use of a system of dissipative bumper dampers, taken from the seismic pounding field for a typical shock-absorption use, which are functional to the brake of MF displacements and resolution of Moon's problem. Typically, bumpers can be made with various types of natural or synthetic rubbers, although more sophisticated or advanced materials, such as metal foams [186] and metal rubbers [187], could be advantageous due to their high dissipative power. In this context, reference will be made to the commonly adopted rubber bumpers. A brief review of the theoretical and experimental background that served as a reference for the development of the MF connection system, involved, on the one hand, the typical contact models adopted in literature for simulating the bumper response during impact and, on the other hand, the VFCC conceived and tested by Laflamme and coworkers for multihazard mitigation. Then, the connection system proposed in this context is carefully described in its mechanical configuration and a detailed explanation on how the numerical modeling of its constitutive behavior is addressed is provided, followed by a comprehensive overview of the basic operating modes of the connection device.

4.2 Reference models for the bumper

Out of phase vibrations between two adjacent structures having different dynamic characteristics can lead to an impact, commonly referred to as *pounding*, which generates high magnitude and short duration acceleration pulses. If the at-rest separation (that is, the initial gap) between two adjacent structures is insufficient to accommodate the relative displacements, these acceleration pulses can cause significant structural damage. In general, an impact can be considered to occur in two phases: a compression (or *approaching*) phase and a separation (or *restitution*) phase, as shown in Figure 4.1. During the compression phase, the colliding bodies undergo local deformations normal to the impact surface and, at the end, the relative velocity of the centers of mass reduces to zero. The restitution phase begins after the approaching one and lasts until the separation of the colliding masses [188].

Several strategies are available in literature to avoid pounding-induced collapse of buildings. These may be classified according to their approach to the problem into three main categories: strategies to avoid pounding, strategies to withstand pounding and strategies to reduce pounding structural effects [189]. The use of bumper elements with impact absorbing materials has been explored in several studies as a measure for limiting the pounding action [190]-[191]. When pounding occurs between two adjacent bodies, these can undergo high acceleration spikes as a consequence of the collision. To prevent acceleration peaks and forces

Although the relationship between normal force and frictional force is not exactly linear (hence, the frictional force is not completely independent of the contact area of the surfaces), the Coulomb model can be useful in many numerical simulation applications. Source: <https://en.wikipedia.org/wiki/Friction>

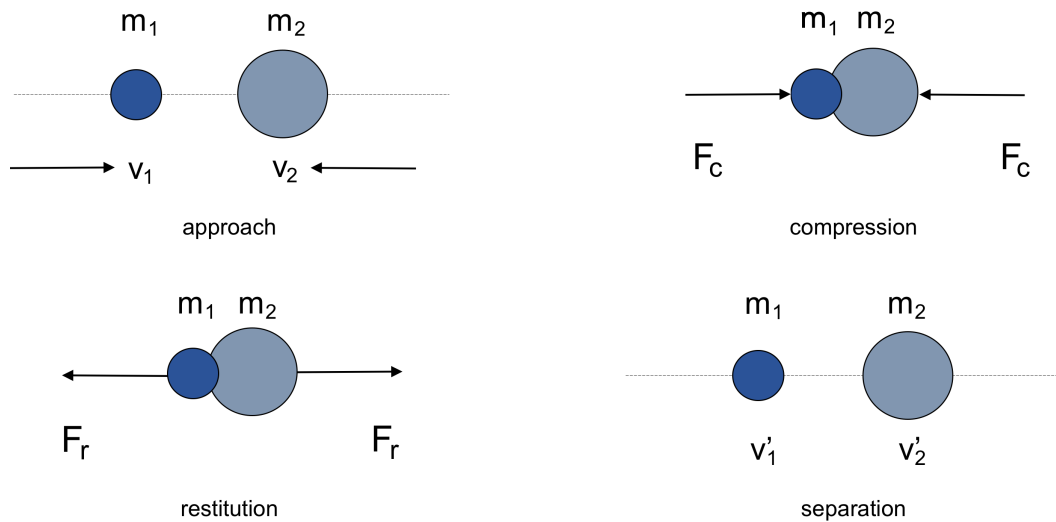


Figure 4.1: Phases characterizing the impact based on Poisson's hypothesis. Source: Muthukumar, S. (2003). *A contact element approach with hysteresis damping for the analysis and design of pounding in bridges*

during contact, pieces of flexible material [192] with soft behaviors are generally incorporated at the expected points where the impact is likely to occur. According to Anagnostopoulos (1988), with the application of flexible materials of soft viscoelastic behavior, the acceleration peaks and the high impact forces can be significantly reduced; however, the large relative displacements of structures are not prevented by deformable and not very rigid bumpers; thus, a higher stiffness of the obstacle is required for this purpose. Since pounding is a highly nonlinear phenomenon [193], which leads to several uncertainties in its mathematical formulation, a critical aspect when simulating an impact is the choice of the model employed and the values of its associated parameters, which may affect the computed results [194]-[195]. Researchers have identified two phenomenologically different techniques to simulate and model the dynamic impact: *contact force*-based (or *penalty*) approaches and *momentum*-based (or *stereo mechanical*) approaches. The former method introduces a combination of gap and link elements between two adjacent masses to simulate pounding [196], as shown in Figure 4.2.

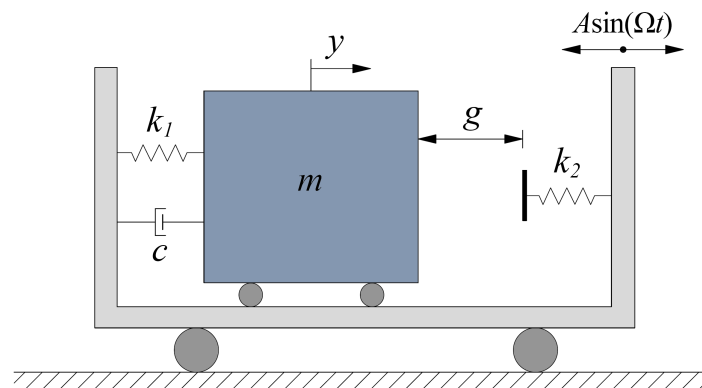


Figure 4.2: The one degree-of-freedom impact mechanical oscillator with a single rigid constraint

Typically, a high-stiffness spring is used to escape the overlapping between the colliding

masses, sometimes in conjunction with a damper. However, this method is limited as using a very high stiffness spring can result in unrealistically high impact forces and, to date, the exact value of the spring stiffness to be used remains unclear [197]. Many studies have been conducted on the topic using this approach (Anagnostopoulos, 1988; 1992; 2004; Muthukumar, 2003; Muthukumar & DesRoches, 2004; 2006). The stereomechanical approach is based on the conservation of the momentum principle and assumes that the impact is instantaneous and rigid, therefore, its duration is neglected [198]. Because of the unknown duration of the contact, the stereomechanical approach is limited in its application and it is no longer valid if the impact duration is large enough so that significant changes can occur in the configuration of the system. This technique has been used by authors such as Papadrakakis (1991), Athanassiadou (1994), DesRoches & Fenves (1997) and Malhotra (1998).

4.2.1 Momentum-based stereomechanical approach

The stereomechanical approach, also known as the Coefficient of Restitution (COR) approach, is a macroscopic method of modeling dynamic impact based on the assumption of instantaneous and rigid impact, therefore with neglected duration. Being the impact force equal to zero ($F_c = 0$), this approach applies the momentum conservation principle and the coefficient of restitution, e , to adjust the velocities of the colliding bodies after impact. In a one-dimensional impact between two rigid masses in pure translation, the COR is classically defined as the ratio of the separation velocities of the masses after impact to their approaching velocities before impact [199], so that

$$e = \frac{v'_2 - v'_1}{v_1 - v_2} \quad (4.1)$$

where v'_2, v'_1 are the velocities after impact (in m/s) and v_1, v_2 are the velocities before impact.

Typically, the COR depends on the material properties and geometry of the colliding structures and can assume values between 0 and 1. In the two boundary cases, $e = 1.0$ corresponds to a completely reversible elastic impact, therefore, with no energy loss; $e = 0$ corresponds to a permanent perfectly-plastic deformation of the two colliding bodies; finally, intermediate values of e correspond to some energy loss. In Anagnostopoulos (1988; 2004), the exponential law linking e to the impact damping ratio, ξ , is provided, allowing to express the damping coefficient of the impact element, c , in terms of energy losses

$$\xi = -\frac{\ln e}{\sqrt{\pi^2 + (\ln e)^2}} \quad (4.2)$$

$$c = 2\xi \sqrt{k \frac{m_1 m_2}{m_1 + m_2}} \quad (4.3)$$

where ξ is the impact damping ratio ($0.0 < \xi < 1.0$), m_1, m_2 are the masses of the colliding bodies and k is the spring stiffness of the impact element simulating the collision.

Hence, for any value of e , there exists a corresponding value of ξ and c which can be computed with Eqs. 4.2 and 4.3, respectively, in order to make the two simulations equivalent

Table 4.1: Coefficients of restitution, e , related to different damping ratios, ξ . Source: Anagnostopoulos, S. (1988). *Pounding of buildings in series during earthquakes*

e	ξ
1.00	0.00
0.94	0.02
0.85	0.05
0.73	0.10
0.53	0.20
0.16	0.50
0.00	1.00

in terms of energy losses. The values of e for a range of damping ratios, ξ , are listed in Table 4.1.

Based on the experimental results reported in Goldsmith (1960) and cited, among the others, in [200] and [201], it has been assessed that values of e ranging from 0.5 to 0.75, can provide realistic and reasonable approximations for practical purposes [202]. A number of researchers (Jankowski, 1988; Anagnostopoulos, 1988; Papadrakakis, Mouzakis et al, 1991; Azevedo & Bento, 1996) used $e = 0.65$ in the analysis of pounding between different types of structures; other studies (Zhu et al. 2002) have suggested that, with $e = 0.4$, the collision between structural elements may be more plastic; Maison and Kasai (1992) developed their impact models with spring damping ratios of 5% and 20%, corresponding to a COR of 0.85 and 0.53, respectively; finally, Komodromos & Polycarpou (2007; 2013) utilized $e = 0.5 - 0.7$ for their investigations. Nevertheless, according to [203], the study of structural response under impact does not require an accurate estimate of the COR since the differences between intermediate values of e are smaller and negligible. Due to the unknown duration of the contact and the assumption of instantaneous, central and direct impact with no deformations in the colliding bodies, the application of stereomechanical approaches is limited and cannot be implemented in the available structural analysis software.

4.2.2 Contact force-based models

In most research studies on structural pounding, the force-based impact method (also known as *penalty* method) is a widely used formulation due to its easy adaptability to impact modeling. Here, the forces generated during the collision of two adjacent structures are provided by a contact element which is activated only when the structures come into contact and it is assumed to act continuously. The contact element is usually a very high-stiffness spring which can be used in conjunction with a dashpot. The high stiffness of the spring serves to provide a realistic estimation of the impact force, ensuring a short impact duration and limiting the penetration or overlapping of the colliding bodies. This approach allows to take into account the deformability of the structures near the impact and their interpenetration during the contact. The interpenetration depth and the spring stiffness are used to estimate the contact forces to be applied to the structures. Anagnostopoulos [204], Jankowski [205],

Muthukumar & DesRoches [206], and others have proposed various methodologies using either a linear or nonlinear impact spring together with an energy dissipation mechanism for structural pounding modeling and simulation. In general, four basic modeling techniques are identified in this category (Fig. 4.3): linear spring model, energy-dissipating Kelvin-Voigt model, nonlinear Hertz contact model and nonlinear Hertzdamp model [207].

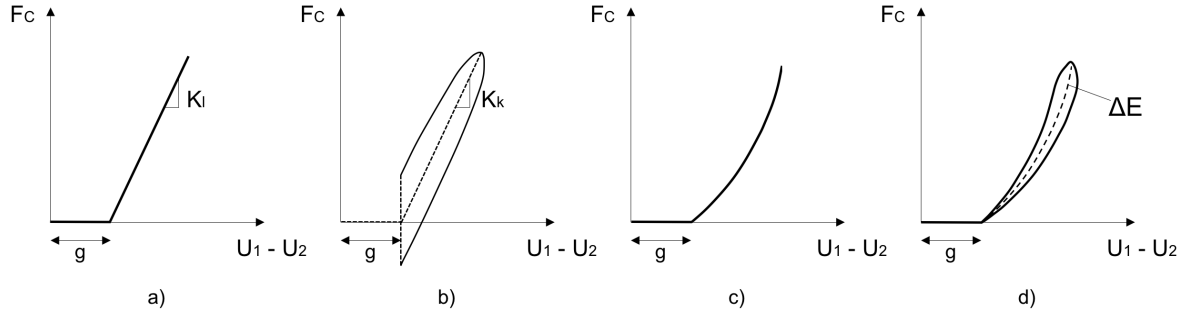


Figure 4.3: Impact models available in literature: a) linear spring element, b) Kelvin-voigt element, c) Hertz nonlinear spring element and d) Hertzdamp model

Linear spring model

The simplest method to implement the impact is represented by a linear spring model. The spring comes into action when the gap between the adjacent bodies closes, simulating the force developed during the contact. Some authors have used this model to study pounding between adjacent buildings, including Maison & Kasai (1990; 1992), due to its easily implementation in analysis software packages. However, this is limited by the fact that it cannot take into account the energy loss during impact, as observed by the absence of a hysteretic loop in Figure 4.3 a. The contact force during the impact, F_c , is taken as

$$F_c = \begin{cases} k_l(u_1 - u_2 - g) & \text{if } u_1 - u_2 - g \geq 0 \\ 0 & \text{if } u_1 - u_2 - g < 0 \end{cases}$$

where k_l is the linear stiffness of the spring and $u_1 - u_2 - g$ is the interpenetration depth of the colliding bodies.

Several studies have shown the system's response to be insensitive to changes in the impact spring stiffness, k , by one order of magnitude (Anagnostopoulos, 1988; Maison and Kasai, 1992). Hence, many authors select a value of 4.4E+06 kN/m as the impact spring stiffness (Muthukumar, 2003; Muthukumar & DesRoches, 2004; Muthukumar & DesRoches, 2006).

Linear viscoelastic model (Kelvin-Voigt model)

The linear viscoelastic impact model, also known as KelvinVoigt model, is one of the most commonly used in structural pounding as it consists of a linear impact spring (k_k), representative of the force developed during the impact, coupled in parallel with a viscous impact

dashpot, which models the energy loss in the collision (Fig. 4.3 b). When the impact occurs, the contact force is provided by the expression

$$F_c = \begin{cases} k_k(u_1 - u_2 - g) + c_k(\dot{u}_1 - \dot{u}_2) & \text{if } u_1 - u_2 - g \geq 0 \\ 0 & \text{if } u_1 - u_2 - g < 0 \end{cases}$$

where k_k is the stiffness of the linear spring, $u_1 - u_2 - g_p$ is the interpenetration depth of the colliding bodies that deform, $\dot{u}_1 - \dot{u}_2$ is the relative velocity between the colliding structures and c_k is the impact damping coefficient as defined in Eq. 4.3.

During the loading phase, the Kelvin-Voigt model exhibits an initial jump of the impact force due to the damping term; during the unloading phase, on the other hand, the damping term causes negative impact forces that bring the bodies in collision together rather than move them away. This approach has been used in several studies (Wolf and Skrikerud, 1980; Anagnostopoulos, 1988; Anagnostopoulos & Spiliopoulos, 1992; Jankowski et al., 1998). According to other authors (Hunt and Crossley, 1975), the Kelvin-Voigt model is unrepresentative of the physical nature of the energy transfer as it disagrees with the expected shape of the hysteresis loop (Fig. 4.4).

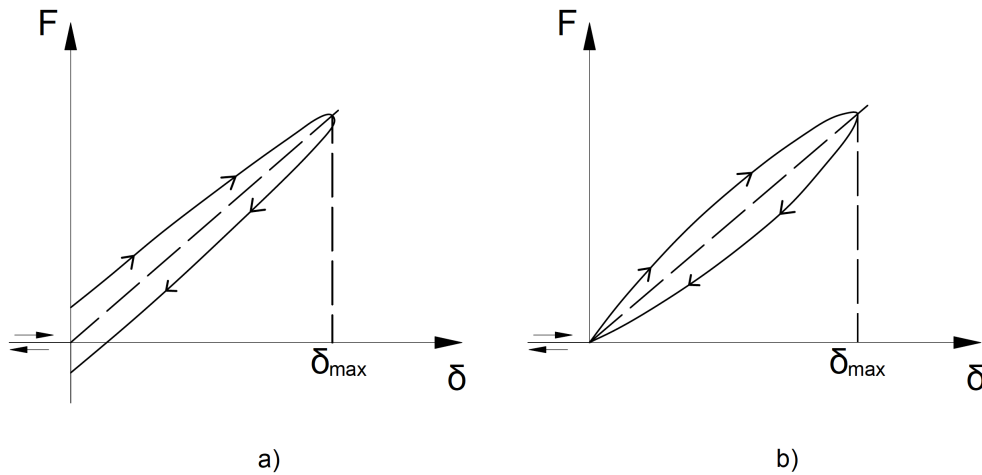


Figure 4.4: Hysteresis loop from a) the Kelving-voigt model and b) the application and removal of a compressive force. Source: Muthukumar, S. (2003). *A contact element approach with hysteresis damping for the analysis and design of pounding in bridges*

Modified linear viscoelastic model

In order to avoid the tensile impact forces that arise between the colliding structures at the end of the restitution period, a minor adjustment is proposed for the linear viscoelastic model [208]. When the impact force is about to change sign, the impact spring and dashpot are removed, assuming some remaining plastic deformations which increase the width of the available gap. Therefore, the equation that provides the contact force can be written as follows

$$F_c = \begin{cases} k_k(u_1 - u_2 - g_p) + c_k(\dot{u}_1 - \dot{u}_2) & \text{if } F_c > 0 \\ 0 & \text{if } F_c \leq 0 \end{cases}$$

where the parameters already defined in the Kelvin-Voigt impact model apply.

Nonlinear viscoelastic model (Hertz contact model)

The use of linear impact models for simulating the response of rubber bumpers during the impact loading is not the most appropriate, considering the stress-strain curves obtained from the static compressive test of rubber. The exponential trend in the load-displacement diagram of the material may be best represented using a nonlinear impact model. A commonly used structural impact model for this purposes is the Hertz contact model which employs a nonlinear spring, k_h . According to this, it is assumed that the contact force increases exponentially with the interpenetration depth

$$F_c = \begin{cases} k_h(u_1 - u_2 - g)^n & \text{if } u_1 - u_2 - g \geq 0 \\ 0 & \text{if } u_1 - u_2 - g < 0 \end{cases}$$

where k_h is the impact stiffness parameter related to the material properties of the colliding structures and the contact surface geometry, g is the at-rest gap and n is the Hertz coefficient usually taken as 3/2.

According to Polycarpou & Komodromos 2013, the impact stiffness is provided by the following relation

$$k_h = \alpha k_{st} = \alpha \frac{AK_r}{d^n} \quad (4.4)$$

where k_{st} is the bumper's static stiffness, $\alpha > 1$ is a multiplier ranging between values of 2 to 2.5 based on experimental tests [209], A is the contact area of the bumper, d is the bumper's thickness and K_r is the material stiffness.

Despite several authors have adopted this approach (Davis, 1992; Pantelides & Ma, 1998; Chau et al., 2003), it is only representative of the static contact between elastic bodies and does not include the energy dissipation during the impact (Fig. 4.3 c).

Nonlinear model with hysteretic damping (Hertz damp model)

In order to include an energy dissipation mechanism, some researchers (Mutukumar, 2003; Muthukumar & DesRoches, 2006) have added a nonlinear hysteresis damper (c_h) in parallel with a nonlinear spring element based on the Hertz's contact Law (k_h) during the approaching phase, leading to the improved version of the Hertz damp model, shown in Figure 4.3 d. The impact force during the compressive phase equals [210]

$$F_c = \begin{cases} k_h(u_1 - u_2 - g)^n + c_h(\dot{u}_1 - \dot{u}_2) & \text{if } u_1 - u_2 - g \geq 0 \\ 0 & \text{if } u_1 - u_2 - g < 0 \end{cases}$$

where k_h is the impact stiffness parameter of the Hertz model, $u_1 - u_2 - g$ is the relative penetration, $\dot{u}_1 - \dot{u}_2$ is the penetration velocity and c_h is the hysteretic damping coefficient.

The nonlinearities associated with impact and energy losses are both accounted for in the Hertzdamp model, which is based on the elastic Hertz law¹¹. Typically, the impact models are simulated by means of a linear spring element with a gap. In this case, the nonlinear Hertz spring can be approximated using a multilinear spring with a gap.

4.2.3 Bilinear truss contact model

By comparing the various impact models, researchers revealed that non-energy dissipating models (i.e., linear spring and Hertz model) overestimate the system response due to impact; on the other hand, implementing Kelvin-Voigt model with energy dissipation in structural analysis software may be complicated as it requires a damping element with a gap which may not be available in several packages. The stereomechanical approach is also not advantageous as it involves changing the velocity of colliding bodies at the instant of impact. The current limitations in the existing models can be overcome resorting to a Hertz contact model with hysteretic damping (Hertzdamp model), which has been identified as the most effective contact-based model. Unlike the previous ones, this model allows to take into account the loss of impact energy in a rational way even if it is not easily implemented in commercial software packages.

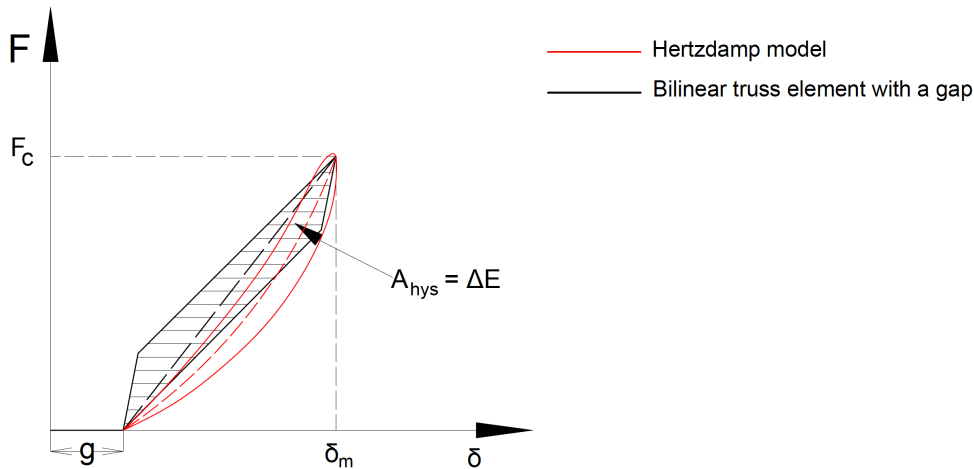


Figure 4.5: Inelastic truss contact element in series with a gap vs. Hertzdamp model for impact simulation. Source: Muthukumar, S. (2003). *A contact element approach with hysteresis damping for the analysis and design of pounding in bridges*

For these reasons, a simplified contact element approach with hysteretic damping developed by S. Muthukumar (2003), for the analysis and design of pounding in bridges, is adopted in this study to simulate the impact occurring between the structure and the MF system when the façade, set in motion by wind load, reaches its maximum allowable displacement. This

¹¹The Hertz theory assumes that surfaces are continuous and nonconforming, strains are small, each solid can be considered as an elastic half-space and surfaces are frictionless. Under these assumptions, due to the Hertz contact only normal pressure acts between two bodies producing normal displacements of the surfaces.

simplified contact model, based on the idealization of a bilinear truss element in series with a gap, derives from an approximation of the Hertz-damp model; hence, its parameters are to be determined so that the response of the masses involved in the contact, obtained using the inelastic truss element, is in line with the response related to the Hertz-damp model. By equating the hysteresis area of the truss element, A_{hys} , to the energy dissipated during impact, ΔE , as shown in Figure 4.5, the main parameters of the bilinear contact model are derived, which consist in the initial stiffness, K_{t1} , the strain hardening stiffness, K_{t2} , the yield deformation, δ_y , and the initial gap, g , as shown in Figure 4.6.

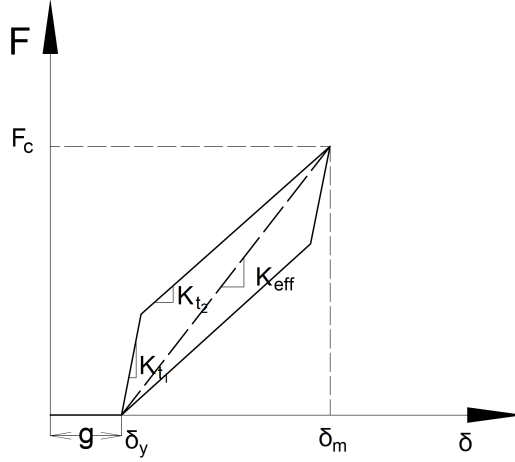


Figure 4.6: Parameters of the inelastic truss model. Source: Muthukumar, S. (2003). *A contact element approach with hysteresis damping for the analysis and design of pounding in bridges*

According to Muthukumar & DesRoches, the contact force during the loading phase, F_c , can be expressed in terms of the stiffness parameters as given below

$$F_c = K_{t1} \delta_y + K_{t2} (\delta_m - \delta_y) \quad (4.5)$$

where K_{t1} is the initial stiffness, K_{t2} is the strain hardening stiffness, δ_y is the yield displacement and δ_m is the maximum penetration observed during impact.

Using the stereomechanical approach, the energy loss as a result of impact, ΔE , can be expressed in terms of the coefficient of restitution, e , and the approaching velocities of the colliding masses as follows

$$\Delta E = \frac{1}{2} \frac{m_1 m_2}{m_1 + m_2} (1 - e^2) (v_1 - v_2)^2 \quad (4.6)$$

where m_1, m_2 are the masses of the colliding bodies, e is the coefficient of restitution and $v_1 - v_2$ is the relative velocity at the start of the impact.

Assuming the energy dissipated during impact to be small compared to the maximum absorbed elastic energy, an energy balance between the start and end of the compression phase gives

$$\frac{1}{2} m_1 v_1^2 + \frac{1}{2} m_2 v_2^2 = \frac{1}{2} (m_1 + m_2) V_{12}^2 + U_m \quad (4.7)$$

where V_{12} is the common velocity of the two masses at the end of the compression phase and U_m is the maximum strain energy stored.

Following the same approach, a momentum balance can be obtained between the start and end of the compression phase, giving

$$m_1 v_1 + m_2 v_2 = (m_1 + m_2) V_{12} \quad (4.8)$$

Equating Eqs. 4.7 and 4.8 provides an expression for the maximum strain energy stored, U_m

$$U_m = \frac{1}{2} \frac{m_1 m_2}{(m_1 + m_2)} (v_1 - v_2)^2 \quad (4.9)$$

By equating the work done by the Hertz contact force from the start of the contact ($\delta = 0$) up to the state of maximum penetration ($\delta = \delta_m$), the elastic strain energy stored can be expressed as

$$U_m = \int_0^{\delta_m} f d\delta = \frac{k_h \delta_m^{n+1}}{n+1} \quad (4.10)$$

where δ is the local relative penetration between the center of masses of the two bodies, k_h is the impact stiffness parameter taken from the Hertz model and depending on the material properties, δ_m is the maximum penetration during the impact and n is the Hertz coefficient taken as 3/2.

Equating Eqs. 4.9 and 4.10 yields an expression for the relative velocity at the start of contact, $v_1 - v_2$, which can be related to the maximum penetration observed during impact, δ_m , according to

$$(v_1 - v_2)^2 = \left[\frac{2(m_1 + m_2)}{m_1 m_2} \right] \left[\frac{k_h \delta_m^{n+1}}{n+1} \right] \quad (4.11)$$

Substituting Eq. 4.11 into Eq. 4.6, the amount of dissipated energy, ΔE , can be simplified as follows

$$\Delta E = \frac{k_h \delta_m^{n+1} (1 - e^2)}{n+1} \quad (4.12)$$

By equating the maximum impact force, F_m , related to the truss and Herzdamp models (from Eqs. 4.5 and 4.2.2, respectively), the effective stiffness of the truss element, K_{eff} , is derived

$$K_{eff} = k_h \sqrt{\delta_m} \quad (4.13)$$

which can be related to K_{t_1} and K_{t_2} , as shown below

$$K_{eff} \delta_m = K_{t_1} \delta_y + K_{t_2} (\delta_m - \delta_y) \quad (4.14)$$

Based on the hysteretic response introduced in Muthukumar & DesRoches (2006) [211],

Table 4.2: Properties of DRAIN-2DX model used to test the truss impact element. Source: Muthukumar, S (2003). *A contact element approach with hysteresis damping for the analysis and design of pounding in bridges*

k_h	K_{t_1}	K_{t_2}	a	e	δ_m	g
[kN/m]	[kN/m]	[kN/m]	[-]	[-]	[m]	[m]
$4378170^{3/2}$	8411340	2895721	0.1	0.8	0.016	0.0127

the dissipation of kinetic energy during impact is taken into account by following a different unloading path in the force-displacement curve, forming a hysteresis loop.

An expression for the hysteresis area, A_{hys} , in terms of the truss parameters is derived from Eq. 4.5

$$A_{hys} = (K_{t_1} - K_{t_2})\delta_y(\delta_m - \delta_y) \quad (4.15)$$

assuming that the area under the force-displacement curve of the truss contact model, A_{hys} , equals the energy dissipated during impact, ΔE .

Finally, the yield deformation, δ_y , is related to the maximum penetration, δ_m by means of the yield parameter a

$$\delta_y = a\delta_m \quad (4.16)$$

that must satisfy the following relation, in order to ensure that the strain hardening stiffness, K_{t_2} , is greater than zero

$$a < 1 - \frac{2}{5}(1 - e^2) \quad (4.17)$$

Based on this, the initial and secondary stiffness parameters of the inelastic truss element are derived

$$K_{t_1} = K_{eff} + \frac{\Delta E}{a\delta_m^2} \quad (4.18)$$

$$K_{t_2} = K_{eff} - \frac{\Delta E}{(1-a)\delta_m^2} \quad (4.19)$$

In the study carried out by Muthukumar (2003), the inelastic truss contact model was implemented in DRAIN-2DX using a rigid link in series with a zero-length inelastic truss having a near zero yield strength in tension. The assumed properties of the impact element used in the DRAIN-2DX model are summarized in Table 4.2.

A sample hysteretic response of the impact element implemented in OpenSees framework is illustrated in Figure 4.7.

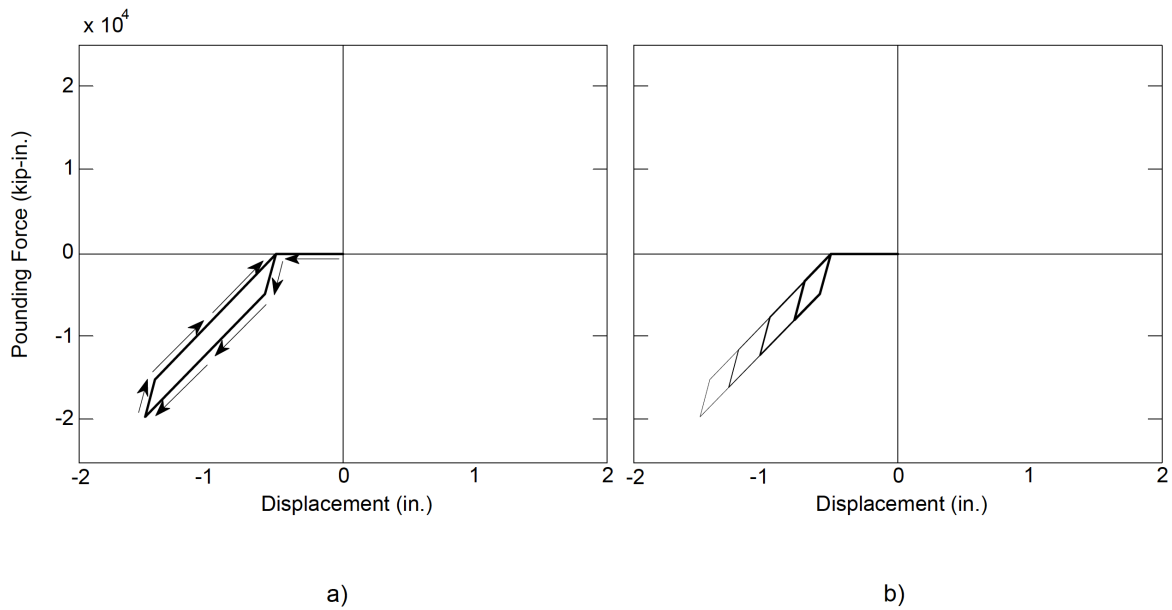


Figure 4.7: Response of an impact material a) during a pounding event and b) for displacement cycles of increasing amplitude. Source: https://opensees.berkeley.edu/wiki/index.php/Impact_Material

4.3 Reference model for the slider

As an integral part of the MF connection system, the sliding device equipped with two-sided rubber bumpers developed to be incorporated in the gap between the building structural floor and the MF system, is inspired by the variable friction cladding connection (VFCC) device conceived and tested by Laflamme and coworkers for multihazard mitigation (Fig. 4.8).

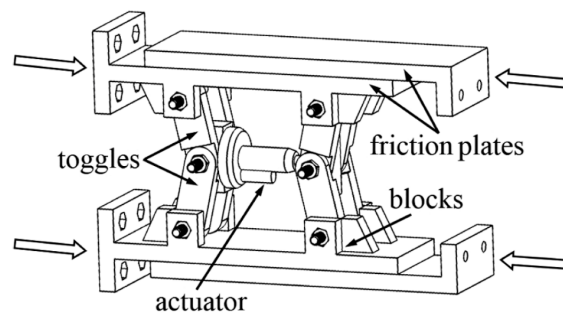


Figure 4.8: Schematic diagram of the VFCC. Source: Gong et al. (2019). *Motion-based design approach for a novel variable friction cladding connection used in wind hazard mitigation*

The semi-active connection device proposed by the researchers from Iowa State University, referred to in Chapter 2, is designed to laterally connect the cladding elements to the structural building behind, taking advantage from the façade inertia to dampen vibrations induced by different types of dynamic loads, including blast (Gong et al. 2018), wind (Gong et al. 2019) and earthquake (Gong et al. 2019). From a mechanical point of view, the main elements constituting the VFCC are two sets of friction plates whose sliding generates the friction force (F_f) and an actuator applying on them a normal force (F_N), according to the

following

$$p_c = \frac{F_N}{A_{c,max}} \quad (4.20)$$

being p_c the uniformly distributed compressive pressure on toggles and $A_{c,max}$ the maximum contact area of the friction plates subjected to normal pressure.

A Coulomb's law of friction is adopted to characterize the frictional behavior of the device, in accordance with

$$F_f = \mu_c F \frac{A_c}{A_{c,max}} \quad (4.21)$$

where μ_c is the friction coefficient and A_c is the effective contact area.

The possibility of exerting a variable pressure on the device, by means of a system of adjustable levers, makes it able to work differently depending on the applied load and the operational stage to be reached. The behavior of the VFCC can be basically divided into two stages: a passive or active mode. The first one is characterized by a high frictional force ensured by a vertical alignment of the levers, which do not allow any sliding under low or moderate loads; in this daily condition, hence, the VFCC essentially acts as a rigid connector between the façade and the structure for the mitigation of blast events. Due to a suitable adjustment of the levers, however, the device can take the role of variable friction damper determining the transition to the active mode. The latter comes into operation under high loads associated with wind activities and seismic events, during which the façade motion is exploited to limit the transfer of lateral accelerations to the structural building or to reduce the inter-storey drift.

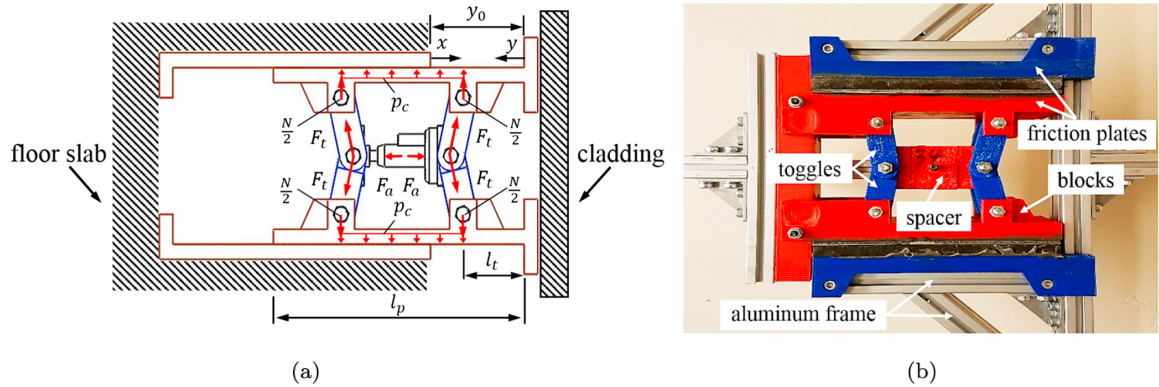


Figure 4.9: Example of configuration with diagram of forces (a) and picture of the full-scale experimental prototype (b) of the VFCC. Source: Gong et al. (2019). *Variable friction cladding connection for seismic mitigation*

From an experimental campaign conducted in a laboratory environment, the researchers have derived a full-scale prototype of the VFCC depicted in Figure 4.9. A modified LuGre friction model¹² was selected for the dynamic characterization of the VFCC prototype sub-

¹²The LuGre model is an integrated complex dynamic friction model based on the elasticity in the contact, whose name comes from the abbreviation of the Lund Institute of Technology and INPG Grenoble, the two

jected to various harmonic excitations under different actuation capacities. According to this model, the friction force, F_f , can be written as

$$F_f(x) = \sigma_0 z + \sigma_1 \dot{z} + \sigma_2 \dot{x} \quad (4.22)$$

where $\sigma_0, \sigma_1, \sigma_2$ are constants representing the bristle stiffness, the micro-damping and the viscous friction, respectively, while x and \dot{x} identify the sliding displacement and velocity of the device, respectively.

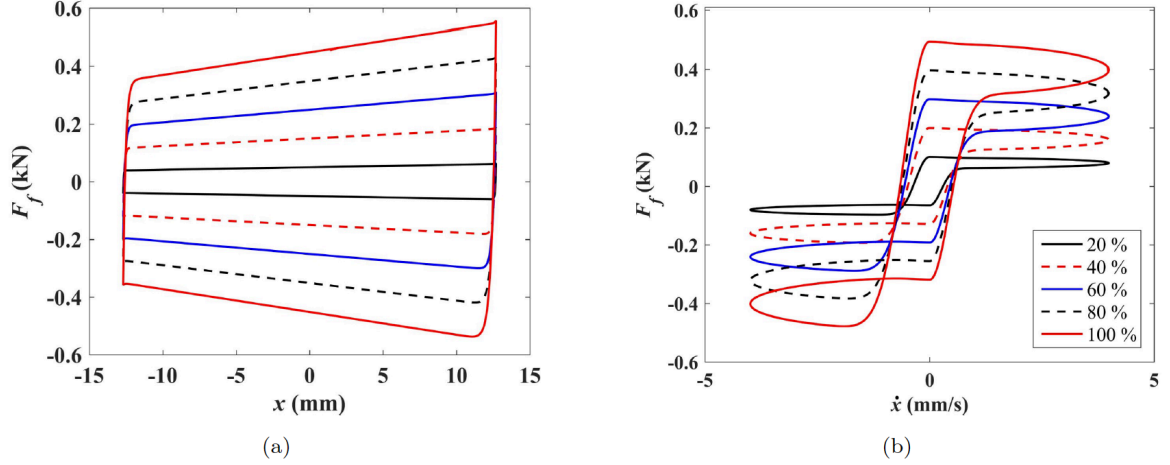


Figure 4.10: Force-displacement (a) and force-velocity (b) loops experienced by the VFCC prototype. Source: Gong et al. (2020). *Numerical verification of variable friction cladding connection for multihazard mitigation*

The dynamic response of the device prototype with 0.5 kN actuation capacity is portrayed in Figure 4.10, showing representative diagrams of the parametrized friction force, F_f , versus the sliding displacement, x (Fig. 4.10 a) and the sliding velocity, \dot{x} (Fig. 4.10 b). For the purpose of blast mitigation (Gong et al. 2018), the authors proposed the integration of the VFCC with rubber shock-absorbers simulated resorting to a nonlinear contact model developed by Polycarpou et al. (Polycarpou et al., 2013). Using a symbology consistent with notations adopted in section 4.2, for the impact model assumed the contact force, F_c , can be written as

$$F_c = \begin{cases} k_h \delta^n & \text{if } \delta < \delta_u, \dot{\delta} > 0 \\ k_h \delta^n + k_{h,y}(\delta - \delta_u) & \text{if } \delta > \delta_u, \dot{\delta} > 0 \\ k_h \delta^n (1 + c_h \dot{\delta}) & \text{if } \dot{\delta} > 0 \end{cases}$$

where δ and δ_u stand for the indentation and the ultimate compressive capacity of the rubber bumper, respectively, n is the impact exponent ($n > 1$), \dot{u} is the relative velocity of the colliding surfaces, k_h and $k_{h,y}$ indicate the impact stiffness constant and the linear post-yield stiffness, respectively, and c_h is the impact damping coefficient.

universities hosting the cooperating scientists. This model has the advantage of describing friction phenomena for both flat surfaces and rolling bearing elements.

The unknown values of k_h and c_h are derived from mathematical relations taken from the referenced [Polycarpou et al. 2013, par. 5-6].

4.4 Technological development of the connection system

A connection system composed of a friction device (also called *slider*) inspired by the VFCC experimented by Laflamme and coworkers as described in section 4.3 integrated by a system of dissipative rubber bumpers, taken from the context of seismic pounding for their typical shock-absorption use, is assumed to be incorporated in the Movable Façade design. Acting as a horizontal energy dissipation link between the structure and the façade, the device is configured to meet two main requirements:

- using the solid friction mechanism, realized through the relative sliding of the friction device, to provide the desired energy dissipation level which is functional to manage the amount of energy transferred from the wind-exposed façade to the building behind and to reduce the structural response in terms of wind-induced lateral vibrations and accelerations;
- creating a locking mechanism, through the insertion of two-sided bumper damper elements made with special shock-absorbing materials filling the gap between the structural building and the MF, which is capable of limiting wind-induced relative displacements of the façade system and keeping Moon's problem under control.

Based on the objectives to be pursued, a technological proposal for the mechanical design of the connector is advanced, although it should be noted that different solutions including various technical layouts can be attempted to conceive the device, getting similar functionality. The assumed configuration for the MF mechanical connection system is portrayed in Figure 4.11.

In the general configuration assumed in this context, the connection system is to be incorporated into the structural floor slab (1), on each level of the building under investigation. To allow the connector to be housed inside, the floor slab must respond to new specific structural resistance requirements; therefore, in case of application on existing buildings (as for the Isozaki tower), an enlargement of the section filled with high-strength materials could be foreseen for a suitable slab reinforcement, also providing for the opening of a channel in the rear part (2) that allows the carrying out routine inspection and maintenance operations of the device, and its repair and/or replacement in case of damage. The same concept also applies in case of new buildings. From a strictly technological point of view, the connection system is composed of a double system of hollow box-shaped metal tubes inserted one into the other, each with its own specific function to perform. The outer steel shell (3), ending in two protruding sections (4), is placed to protect the internal slider (5) and encloses the entire system, hiding the mechanical action from view; the sliding function, on the other hand, is reserved for the inner metal tube (6), being directly hinged to the slider, on one side, and welded to the horizontal transom (7) of the steel MF frame, on the other side. In

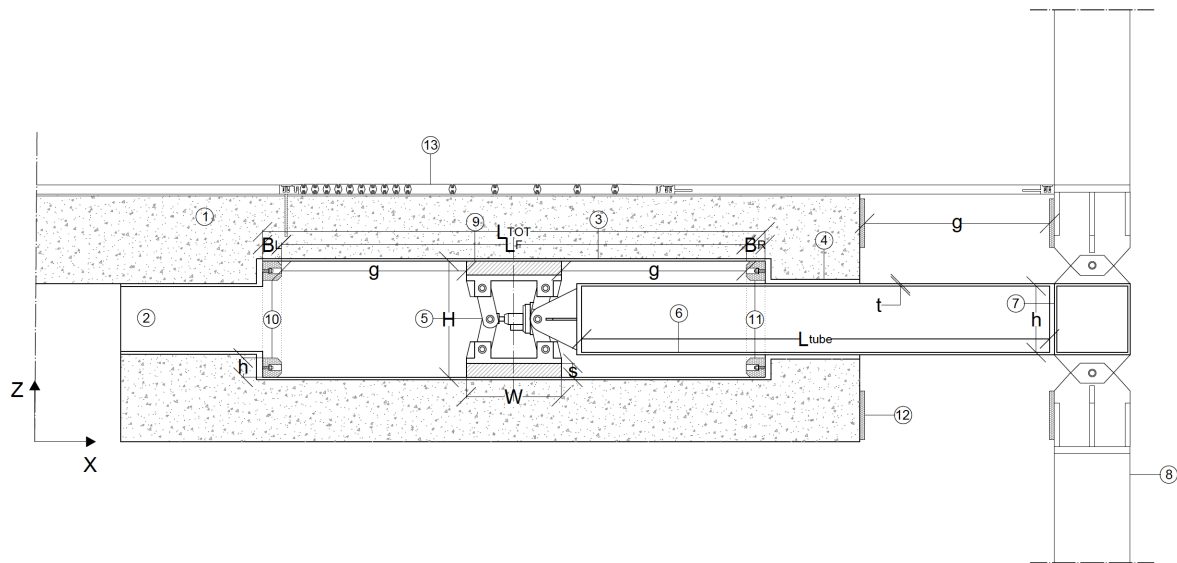


Figure 4.11: Layout proposal for the connection system consisting of a dissipative sliding device and two-sided rubber bumpers incorporated into the MF design

turn, the horizontal box-like profile of the façade frame is hinged at the top and bottom to the vertical elements (8), extending throughout the entire width of the building's façade at a fixed distance determined by the size of glass panels. The latter also affects the number of connectors to be placed floor by floor along the vertical development of the building. Being a design choice linked to various reasons (for example, additional weight due to the number and sizing of connectors, construction costs, installation difficulties, and so on), the devices could be incorporated in correspondence with each vertical mullion of the façade frame or every two or more glass panels, on alternating floors, and so on, clearly taking into account the effects that a different design layout can have on the system's dynamic performance in terms of the vibration damping efficiency. As will be seen in Chapters 6 and 7, in this study the connectors fit into the structural system of the case study buildings at a distance d from each other, where d is the fixed dimension of the MF panels and, being B the width of the building plan, the number of connectors depends on the relation $N_c = B/d$.

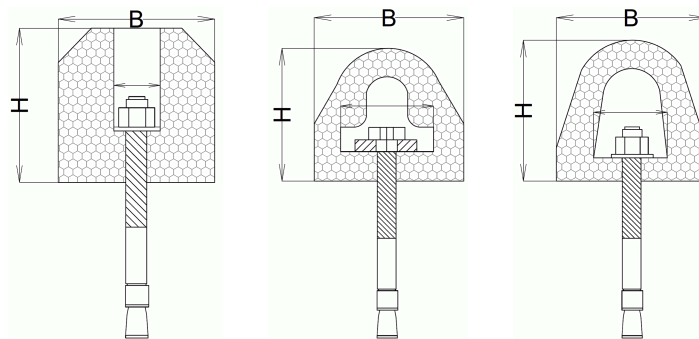


Figure 4.12: Examples of rubber bumper shapes with foldable bulb design for shock- and impact-absorption

Inside the metal shell, the slider is in contact at the top and bottom with a double layer of

sliding material (9) of height, s , and width, W , which creates the suitable surface for ensuring the axial translation of the device. This can slide freely along the entire length of the outer shell with the exception of two small lateral spaces occupied by the right bumper damper, B_R (10), and the left bumper damper, B_L (11), respectively. The two pairs of bumpers with height h are welded to the outer shell, aligned with the sliding surface of the device and their construction is such that the material element is bonded to a metal plate which incorporates a number of fixing holes allowing for simple installation. These can be realized with any custom size (40/50/60 mm and more) and any shape (rectangular, cylindrical, conical) with different materials, such as Natural Rubber (NR) [212], polystyrene [213], synthetic rubbers including Nitrile Butadiene Rubber (NBR), Ethylene Propylene Diene Monomer (EPDM), Styrene-Butadiene Rubber (SBR) [214]-[215] and polymers [216], as shown in Figure 4.12. The wide use of rubber (or elastomeric materials) for a shock-absorbing function is due to its combination of elastic properties, such as elongation capacity up to 1000% and high intrinsic damping, and viscous properties, such as energy absorption and storage capacity, which make it a unique material in this field [217], allowing it to absorb a greater vibratory stress before breakage or transferring vibrations [218]. In this study, NR conical bumpers with $L_B = 40.0$ mm width are assumed. An additional double bumper layer (12) is inserted on the external side of the floor and on the cladding frame to mitigate the impact between the structural floor slab and the façade. Finally, an extensible-grid floor expansion joint (13) provides the upper closure to the gap that is created between the structural floor and the façade frame when the MF begins to open. Specifically, the rectangular section joining system, without side sub-flooring flaps and visible screws, is made by means of a visible rigid central roller support in non-slip aluminum and lateral reinforced rubber gasket with high-resistance to vertical loads. The axial movement of the joint is allowed by the lateral sliding of the support on a system of rollers that do not interfere with vertical obstacles (pillars and/or walls). The reachable width (in mm) with the structural joint varies according to the length of the connector obtained from the size calculations, as well as the movements to which it is subject.

When the slider is in the middle position (with the MF partially open/closed), a double empty space (*gap*, g) is created between it and the lateral bumpers, which defines the maximum relative displacement that the Movable Façade can reach in one direction and the other. As emerges from Figure 4.13, the total length of the connection system (L_{tot}), includes the thickness of the two bumpers (B_1) and the sliding length (L_F), knowing that the latter is given by the sum of the slider's width (B_0) and the double gap between the slider and bumpers

$$L_{tot} = \underbrace{B_0 + 2g}_{L_F} + 2B_1$$

where g is given from

$$g = \frac{L_{tot} - B_0}{2} - B_1 \quad (4.23)$$

meaning that an increase in the gap is related to the reduction of B_0 and/or B_1 .

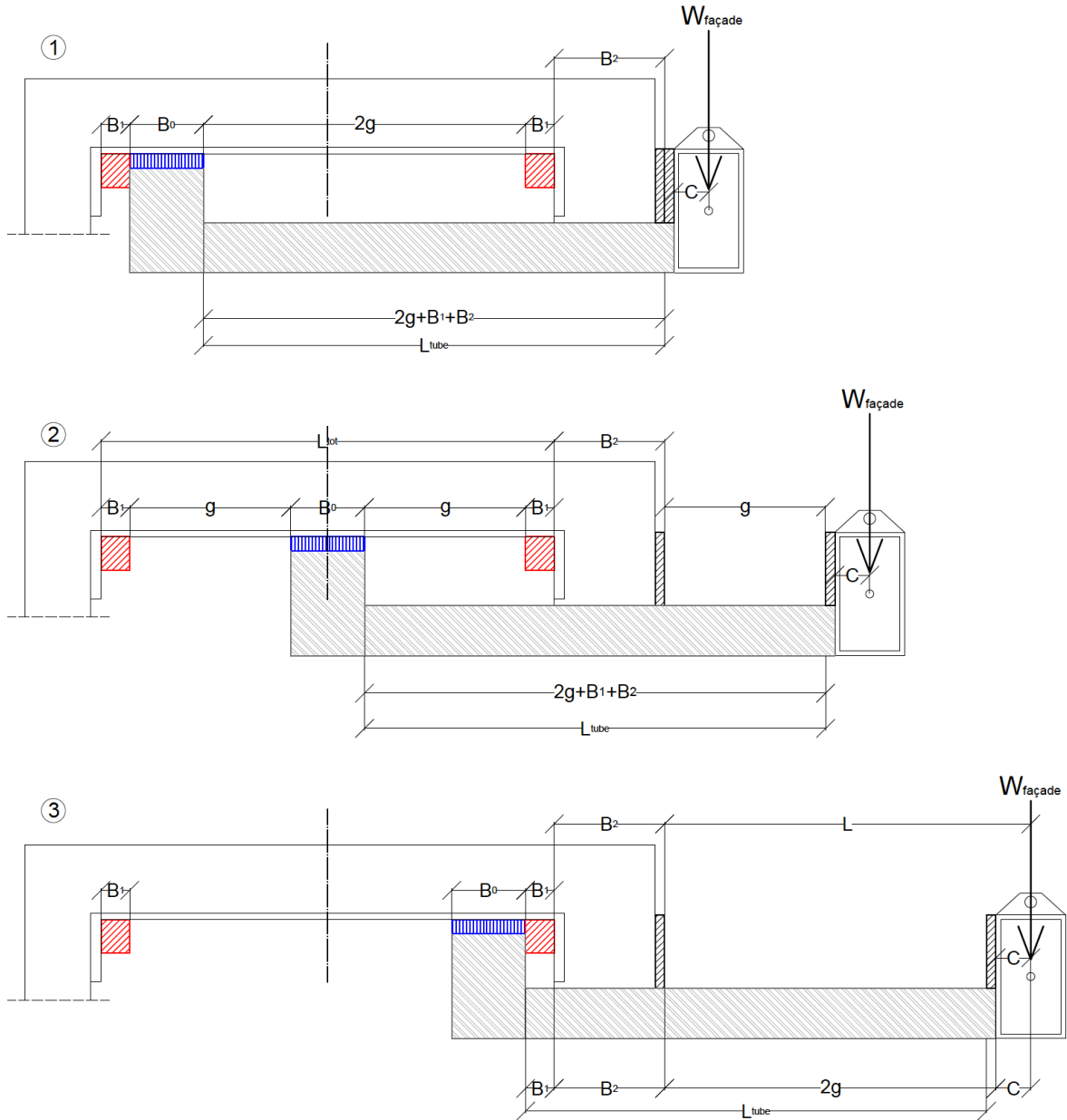


Figure 4.13: Pre-sizing sketches of the sliding connector in the three main design layouts: 1) closed façade, 2) partially open/closed façade and 3) open façade

By subtracting the thickness of the two bumpers, B_1 , from the total length, L_{tot} , the possible sliding length of the device, L_F , is obtained

$$L_F = L_{tot} - 2B_1 = 2g + B_0 \quad (4.24)$$

It should be noted that both the length of the connector and the height of the device are design variables conditioned by the façade weight, $W_{façade}$, which in turn determines the maximum allowable elongation, so they are set as a function of the size of the inner sliding

Table 4.3: Examples of inner connector sizing as a function of the initial gap imposed

g [m]	L [m]	L_F [m]	L_{tube} [m]	L_{tot} [m]
0.10	29.5	0.40	0.44	0.48
0.20	49.5	0.60	0.64	0.68
0.30	69.5	0.80	0.84	0.88
0.40	89.5	1.00	1.04	1.08
0.50	1.095	1.20	1.24	1.28
0.60	1.295	1.40	1.44	1.48
0.70	1.495	1.60	1.64	1.68

connector, L_{tube}

$$L_{tube} = 2g + B_1 + B_2 \quad (4.25)$$

As emerges from Figure 4.13, being directly welded to the frame, the sliding connector carries the weight of the entire glass and steel façade, which makes it require a proper design ensuring its construction feasibility and resistance to the vertical load weighing on it. The sizing of the internal connector is carried out resorting to the static diagram of a horizontal cantilever beam embedded on one side and with a free end on the other, on which the concentrated load due to the façade weight is applied. The span of the cantilever beam is equal to twice the gap multiplied by the center distance of the façade frame vertical profile, C

$$L = 2g + C \quad (4.26)$$

which gives

$$g = \frac{L - C}{2} \quad (4.27)$$

By way of example, by setting $B_0 = 20 \text{ cm}$, $B_1 = 4 \text{ cm}$, $B_2 = 22 \text{ cm}$, $C = 9.5 \text{ cm}$ and parameterizing the gap, g , related values of the cantilever beam span, L , the friction length, L_F , the inner connector length, L_{tube} , and the total length, L_{tot} , are listed in Table 4.3.

The sizing procedure and related steps for the application of the connection device on mid- and high-rise buildings are explained in detail in sections 6.5.1 and 7.5.1, respectively. From the preliminary sizing it emerged that for gaps greater than 75 cm , too large and demanding tubular profiles would be required for a feasible realization of the sliding façade connectors; furthermore, it might be appropriate to foresee profiles with a maximum length defined in proportion to the height and importance of the investigated case study. Based on this, it has been assumed that a maximum gap, g , equal to 0.50 m (which corresponds to a cantilever span of 1.095 m and a length of the inner tube of 1.24 m) for the 77.5 m tall generic building (Chapter 6), and equal to 0.70 m (related to a cantilever span of 1.495 m and a length of the inner tube of 1.64 m) for the 220 m tall Isozaki tower (Chapter 7), can lead to reasonable

façade displacements from a constructive point of view.

4.5 Mechanical characterization of the constitutive behavior

The constitutive behavior of the connection device can be well-explained by constructing stress-strain fields related through a set of constitutive laws. In this context, the connection system born from the integration of a friction slider and rubber bumpers could be suitably modeled from a composition of simple rheological elements connected in series, defining the mathematical framework useful for describing the mechanical characterization of its materials. Clearly, the required modeling complexity varies between the two mechanisms characterizing the connector; hence, their models depend on a different number of parameters managing their constitutive behavior. In order to obtain reliable numerical simulations, the key variables entering the governing equations of the adopted constitutive models, are adequately quantified and the calibration of models is carried out.

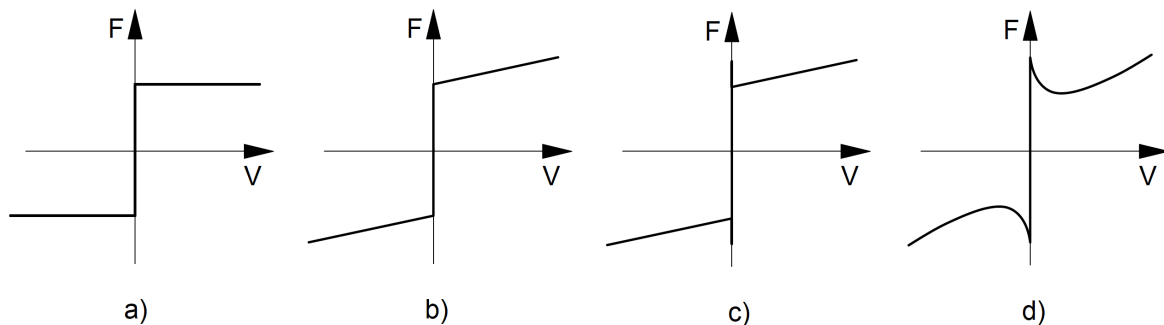


Figure 4.14: Force-velocity diagram of friction models: a) Coulomb friction, b) viscous friction combined with Coulomb friction, c) viscous friction combined with Coulomb and static friction and d) Stribeck friction

First, the constitutive modeling of the slider requires knowledge of the friction principle. As is known, friction is the force exerted between surfaces in contact moving relative to each other and, generally, it depends on their relative sliding velocity. When used for purposes such as energy dissipation and vibration control, friction can ameliorate the performances of vibrating structures [219]-[220], hence, its use is common in many engineering systems, including civil buildings [221]-[222]. Various simple and complex, steady-state and dynamic models, depicted in Figure 4.14, have been developed for modeling this phenomenon [223] in an attempt to understand the dependence of the frictional force on the sliding velocity between surfaces in contact (the so-called *Stribeck effect*¹³) [224]-[225] or, more generally, how friction can affect the dynamic behavior of vibrating systems [226]. A commonly used model of friction is the Coulomb (*sliding*) friction (Fig. 4.14 a), often referred to as *dry* friction, whose assumptions are fundamentally based on an empirical construct. Despite being a simple model not always providing a reliable representation of the friction behavior, such model is often useful to describe friction in mechanical contacts as its simple expression

¹³The Stribeck curve is a more advanced model of friction as a function of velocity which includes both Coulomb and viscous friction models, although it is valid only in steady-state form.

is able to take into account the main effects of *sticking* and *slipping* that are required in many numerical simulation applications.

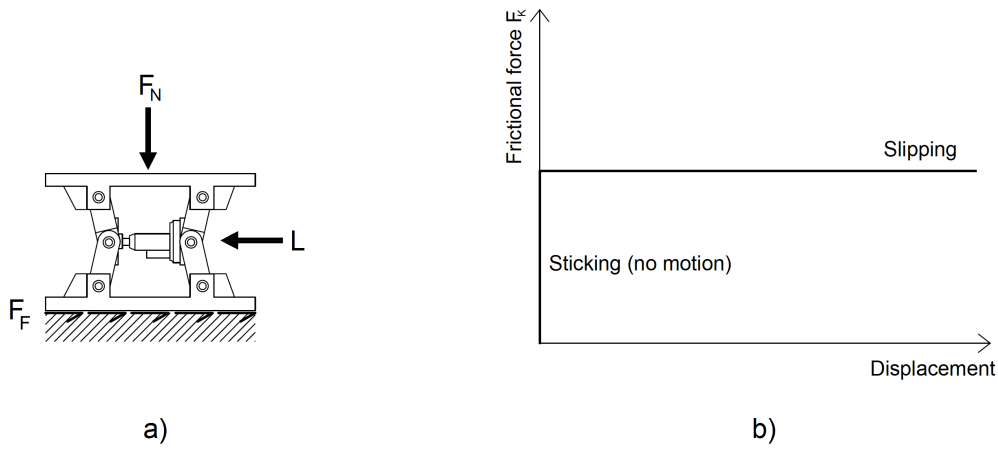


Figure 4.15: Frictional behavior of the slider (a) and pure Coulomb friction curve (b)

However, due to the nonlinearity of friction-related phenomena and problems, the determination of closed-form solutions for studying the systems' dynamic response is still uncertain. The first study on the forced dynamic response of Coulomb damped systems has its origins in Den Hartog's research, who determined an exact solution for the steady-state time response of SDOF systems in continuous *non-stick* regimes, also providing a formulation for the boundary between continuous and *stick-slip* motion [227]. Den Hartog's solution was subsequently extended by other authors who took into account different static and kinetic friction coefficients [228] or who used its approach to derive a closed-form solution for the response of a harmonically base-excited 2DOF system with Coulomb contact [229]. Recently, analytical expressions have also been proposed for the stationary response of harmonically excited MDOF systems with a single Coulomb friction contact [230].

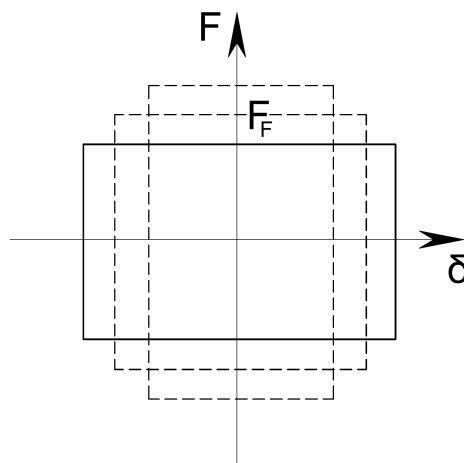


Figure 4.16: Force-displacement diagrams of Coulomb friction device for different friction threshold

As a first approximation, the modeling of the slider could be based on Coulomb's Law of friction, according to which the dynamic friction force is independent of the relative velocity

between the sliding surfaces. The frictional behavior adopted is depicted in Figure 4.15: as can be seen, the Coulomb friction is zero at zero displacement and has a fixed value at all displacements other than zero. This is in line with Coulomb's assumption that the friction force is equal and opposite to the resultant of the applied forces and no tangential motion occurs if the resultant of tangential forces is smaller than friction (*sticking*). When tangential motion occurs (*slipping*), the friction force always acts in a direction opposite to that of the relative velocity of surfaces, being proportional to the normal force according to the relation

$$F_F = \mu_F F_N \quad (4.28)$$

where F_F is the frictional force exerted by each surface on the other, μ_F is the friction coefficient for surfaces in relative motion (which is an empirical property of the contacting materials) and F_N is the normal force exerted by each surface on the other, directed perpendicular to the sliding surface.

The normal force, F_N , can be adjusted through an appropriate torque of the bolts that control the pressure on the friction surfaces, eventually with an active or semi-active control [231]. The friction device exhibits a typical rigid-perfectly plastic behaviour whose force-displacement cycle is a rectangular hysteretic loop with no work hardening, only depending on the friction threshold, F_F : higher or lower values of F_F modify the hysteretic area of the cycle (Fig. 4.16). It should be noted that previous authors have used this modeling approach, achieving suitable results [232].

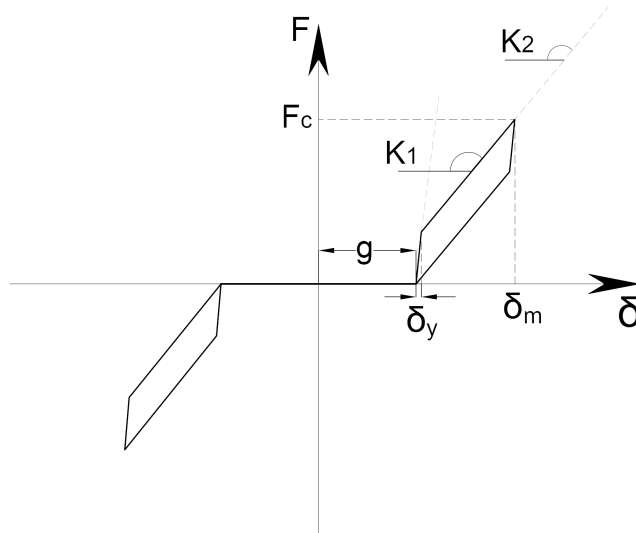


Figure 4.17: Bilinear truss contact model in series with a gap for impact simulation (S. Muthukumar, 2003)

Similarly, an effective constitutive model can be defined which describes the nonlinear behavior of rubber bumpers, in accordance with the contact models reviewed in section 4.2.2. To suitably simulate the response of rubber bumpers under impact loading, a Hertzdamp nonlinear model with hysteretic damping should be selected among the various models avail-

able in literature, as it allows to take into account the dissipation of the impact energy in a rational way. Since this model is difficult to implement in common numerical modeling software, the inelastic truss contact model proposed by S. Muthukumar & R. DesRoches, introduced in section 4.2.3, is used in this context, as shown in Figure 4.17.

As stated before, the model parameters are: the initial stiffness, K_{t_1} , the strain hardening stiffness, K_{t_2} , the yield deformation, δ_y , and the initial gap, g . To determine these parameters, we first need to develop an expression for the energy dissipated during impact, ΔE . According to this, the dissipation of energy is taken into account by following a different unloading path in the force-displacement curve of the inelastic truss contact model, forming a hysteresis loop

$$\Delta E = \frac{k_h \delta_m^{n+1} (1 - e^2)}{n + 1} \quad (4.29)$$

where k_h is the impact stiffness parameter from the Hertz contact model (section 4.2.2), δ_m is the expected maximum penetration, n is the Hertz coefficient taken as $3/2$ and e is the coefficient of restitution, whose typical values vary depending on whether the model used accounts for energy losses or not; for instance, both the Hertz and the linear spring model use $e = 1.0$ (no energy loss), while the Hertzdamp and Kelvin model use $e = 0.6$ (some energy loss).

The initial and secondary stiffnesses, K_1, K_2 , of the inelastic model can be defined assuming a secant stiffness, K_{eff} , based on

$$K_{eff} = k_h \sqrt{\delta_m} \quad (4.30)$$

which gives

$$K_1 = K_{eff} + \frac{\Delta E}{a \delta_m^2}; \quad K_2 = K_{eff} - \frac{\Delta E}{(1 - a) \delta_m^2} \quad (4.31)$$

where a is the yield parameter that allows the yield displacement, δ_y , to be expressed as a function of the expected maximum penetration, δ_m , according to the following expression

$$a = \frac{\delta_y}{\delta_m} \quad (4.32)$$

In order for the work hardening stiffness, K_{t_2} , to be greater than zero, the yield parameter, a , must satisfy the following relationship

$$a < 1 - \frac{2}{5}(1 - e^2) \quad (4.33)$$

The nonlinear impact model adopted in this context uses a coefficient of restitution, e , which takes into account a certain amount of energy dissipated during the impact, therefore, in accordance with the Hertzdamp model on which it is based, it is fixed $e = 0.6$ (meaning some energy loss). By selecting a COR equal to 0.6, it follows that a should be less than 0.744 according to Eq. 4.33. An appropriate choice of the yield parameter, a , is guided by the constitutive relations that constrain the different variables of the nonlinear contact model. Specifically, the yield parameter can be related to the initial stiffness, K_{t_1} , and secondary

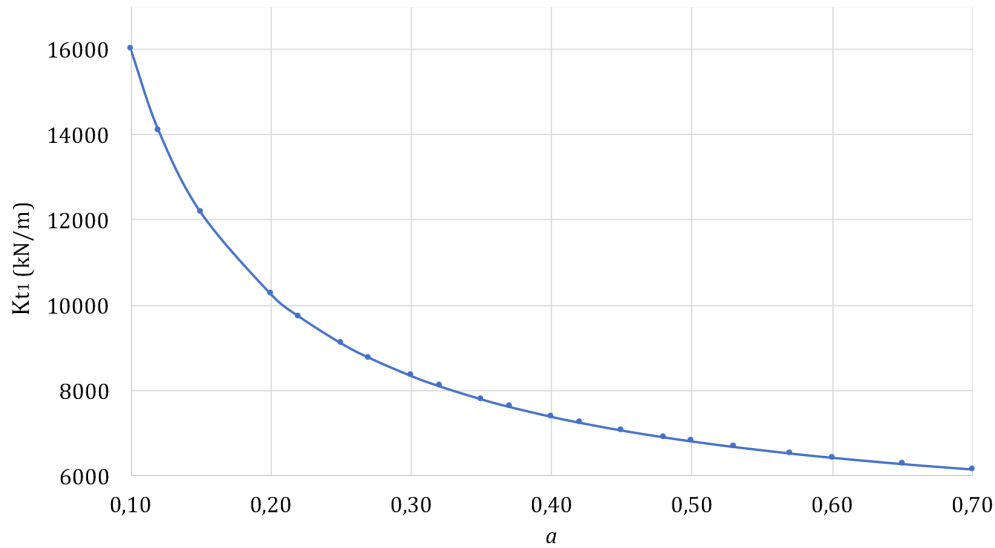


Figure 4.18: Initial stiffness, K_{t_1} , expressed as a function of the yield parameter, a

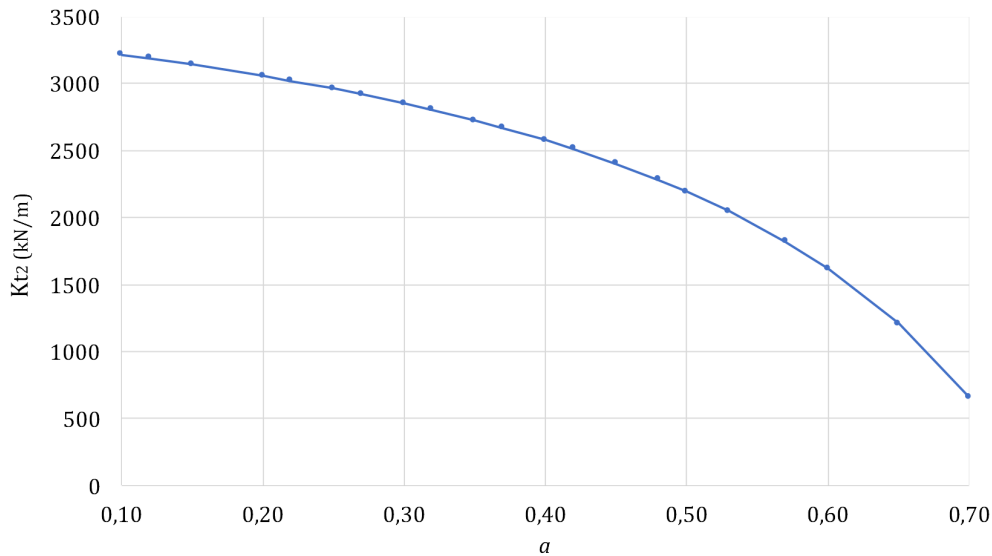


Figure 4.19: Secondary stiffness, K_{t_2} , expressed as a function of the yield parameter, a

stiffness, K_{t_2} , of the bumper through an exponential law with opposite curvature shown in Figures 4.18 and 4.19, respectively. The plots show the drop of the stiffnesses with the increase of the yield displacement, δ_y .

Alternatively, with the definition of the strain hardening ratio, γ

$$\gamma = \frac{K_{t_2}}{K_{t_1}} \quad (4.34)$$

it is also possible to express the yield parameter, a , as a function of the dimensionless ratio between the two stiffnesses, γ . As can be seen from Figure 4.20, the plot follows a concave parabolic trend, reaching a peak value $\gamma = 0.35$ for $a = 0.4$, while at the two extremes it goes from $\gamma = 0.2$ for $a = 0.1$ to $\gamma = 0.10$ for $a = 0.7$. In this study, $a = 0.1$ is taken (in line with the value assumed by Muthukumar) as higher impact stiffness of the bumpers is desired.

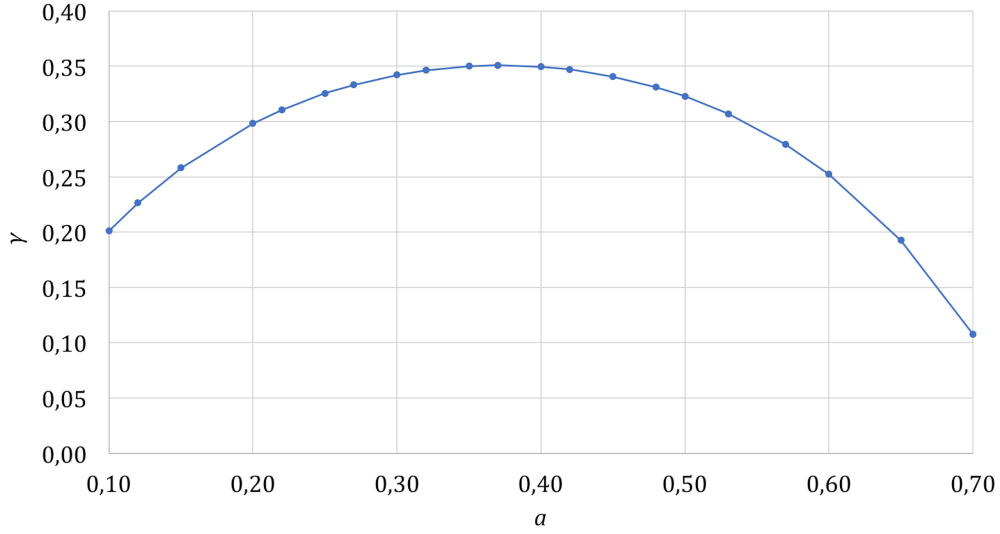


Figure 4.20: Strain hardening ratio, γ , expressed as a function of the yield parameter, a

As for the maximum penetration, δ_m , this is defined as a function of the bumper thickness, t_B , and the maximum strain ratio, $\delta_m/t_B = 0.8$

$$\delta_m = 0.04 \cdot 0.8 = 0.032 \quad \text{m} \quad (4.35)$$

which gives a yield displacement, according to Eq. 4.16

$$\delta_y = 0.1 \cdot 0.032 = 0.003 \quad \text{m} \quad (4.36)$$

Finally, using Eq. 4.4, the impact stiffness parameter, k_h , is estimated in line with the formulations reported in [Polycarpou, P. & Komodromos, P. (2013)]. Consequently, considering the dimensions of the rubber bumpers used ($40 \times 40 \times 10 \text{ m}$), the contact area A is 0.016 m^2 and the material's stiffness K_r is found to be equal to 55835 kN/m^2 . With the strain-rate multiplier equal to $\alpha = 2.25$ and the Hertz coefficient equal to $n = 1.5$, the impact stiffness for the dynamic response is immediately computed

$$k_h = 2.25 \frac{0.016 \cdot 55835}{0.04^{1.5}} = 2.25 \cdot 11167 = 25126 \quad \text{kN/m} \quad (4.37)$$

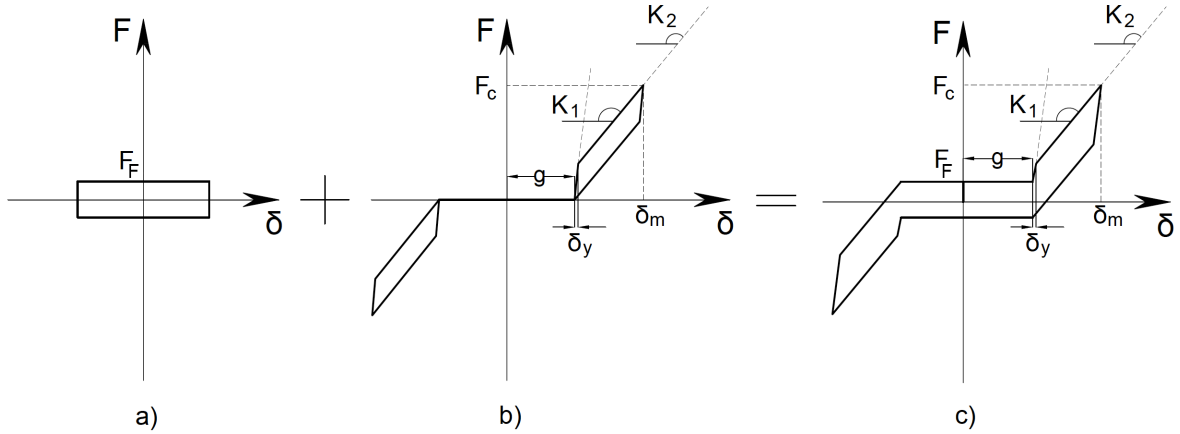
from which ΔE , K_{eff} , K_{t_1} and K_{t_2} can be directly derived resorting to Eqs. 4.29, 4.30 and 4.31, respectively.

All the constant parameters adopted for the formulation of the impact model are listed in Table 4.4. With reference to k_h , it should be noted that the impact stiffness just determined constitutes the reference value on the basis of which parametric investigations will be carried out in the following Chapters.

To summarize, the parameters of the bumper model are not independent of each other, rather, they are linked by constitutive relations designed to ensure that each force-displacement cycle dissipates an amount of energy consistent with the energy dissipated during the impact, ΔE . Based on this, the shape of each hysteretic loop cannot vary arbitrarily and the im-

Table 4.4: Impact parameters for the rubber bumper model adopted

e	a	δ_m	δ_y	n	k_h	ΔE	K_{eff}	K_{t1}	γ
[–]	[–]	[m]	[m]	[–]	[kN/m]	[kN]	[kN/m]	[kN/m]	[–]
0.6	0.1	0.032	0.003	1.5	25126	1.178	4494	16001	0.20

**Figure 4.21:** Force-displacement cycle of the friction device with bumpers (c) obtained from a perfect rigid-plastic model (a) and a bilinear contact model in series with a gap (b) combined in parallel

perfect model turns out to be well constrained. Hence, the only independent parameters of the bumper are the impact stiffness, k_h , which affects both the stiffness sections of the bumper, K_1 and K_2 , resulting in a more inflexible or soft impact, and the initial gap, g , which determines how soon the impact between the slider and the bumper occurs. The constitutive model of the dissipative connector consisting of a friction slider integrated with two-sided rubber bumpers is obtained by combining in series the bilinear truss contact model of the bumpers to the rigid-perfectly plastic cycle of the slider, as depicted in Figure 4.21.

4.6 Dynamic characterization of the basic operating modes

The different constitutive behaviors of the two mechanisms making up the façade connection system implies a different response when subject to dynamic excitation. Depending on the amplitude of the oscillations, the connection device can operate in different ways; to provide the reader with a better and clearer understanding of the system's dynamic behavior, the investigation of sample trajectories for both the friction slider and rubber bumpers is proposed and three basic operating modes are identified, which can be summarized as follows:

- *sliding* mode: this stage occurs when the oscillations take place without impacts with the bumpers and the motion is determined by the friction device alone;
- *sliding-bumping* mode: this stage occurs when the oscillation involves both a sliding part and two impacts with the bumpers on the two sides, resulting in a bilateral (positive and negative) impact;

- *colliding* mode: this stage occurs when the oscillation involves both a sliding part and one impact with the bumper on the two sides, resulting in a unilateral (positive or negative) impact.

Numerical modeling and related steps of simulation of the connection device are carried out using Python code [233].

4.6.1 *Sliding* mode

As anticipated, the *sliding* mode occurs in the absence of contact between the slider and bumpers, hence, the dynamic response cycle of the connection device depends exclusively on a frictional behavior. In Python domain, the Coulomb friction model adopted is simulated with a hysteretic uniaxial multilinear material object, whose envelope is defined by a list of force-deformation points. The key variable of this model is represented by the friction threshold, F_F , whose variation determines the elongation or flattening of the hysteretic cycle.

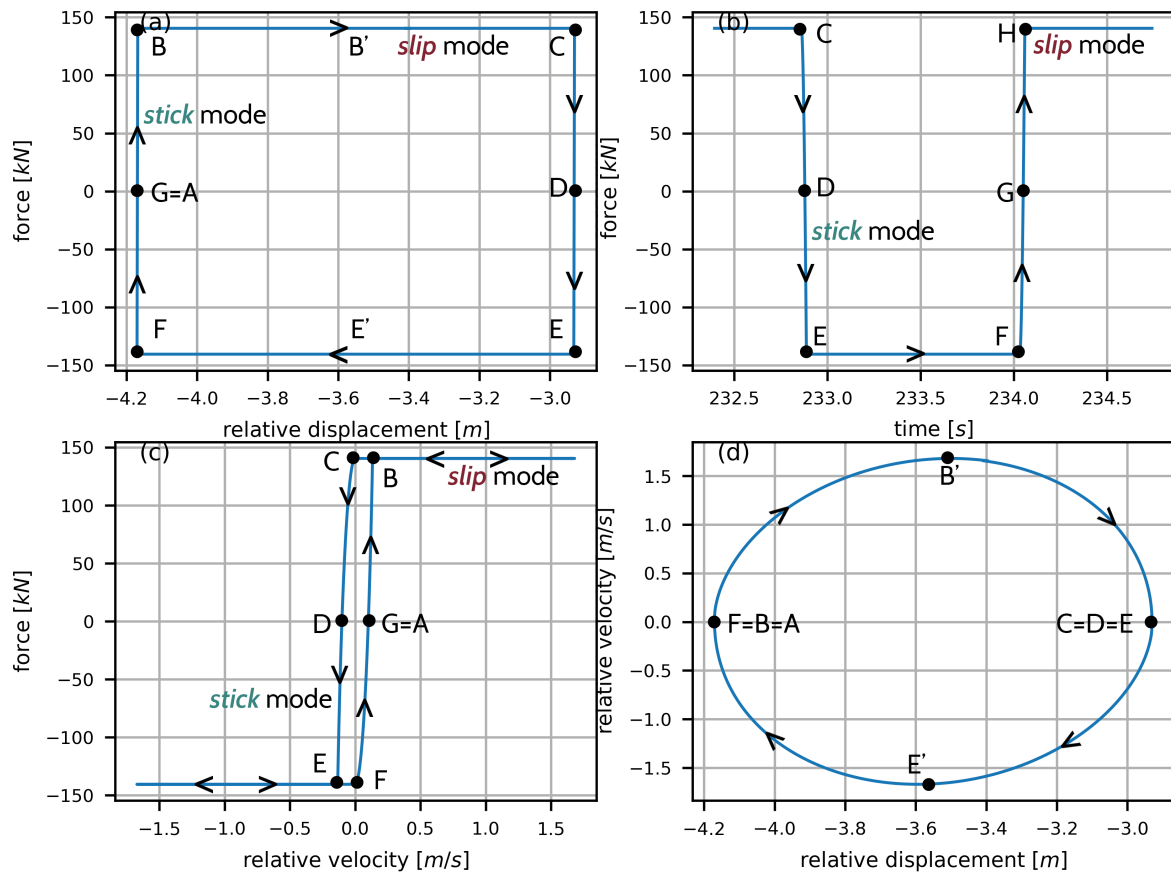


Figure 4.22: Sample dynamic trajectory related to the *sliding* mode

The blue line in Figure 4.22 summarizes the frictional behavior of the slider in a time interval of about 5 seconds. As can be seen, the cycle path is defined by the alternation of two characteristic states of motion (i.e., *sticking* and *slipping*), depending on F_F , which marks the transition between locking and unlocking phase. According to the standard formulation

expressed in Eq. 4.28, if the shear stresses are below the friction threshold (A-B section), there is zero relative motion of the surfaces and the slider is locked into the *stick* mode: the friction force increases with zero displacement and velocity and the diagram follows a vertical path with ideally infinite stiffness

$$K_F = \infty \quad \text{in the } \textit{stick} \text{ mode}$$

On the contrary, the contacting surfaces will *slip* when the shear stress across their interface overcomes the limiting frictional shear stress (B-C section): both the displacement and velocity increase at constant force, following a horizontal path with ideally zero stiffness

$$K_F = 0 \quad \text{in the } \textit{slip} \text{ mode}$$

From point B', the slider begins to slow down until it stops again in C. At this point, the force drops and goes to zero with null displacement and velocity (C-D section); returning to be lower than the friction force, it determines a second locking phase into the *sticking* mode. The dynamic cycle described under tension load, depicted in the upper part of diagrams, is repeated in case of a compressive load in the lower part of the plots.

4.6.2 *Sliding-bumping* mode

The second basic operating mode investigated, namely, the *sliding-bumping* mode, involves a bilateral contact with the two rubber bumpers that complete the design of the sliding connector. As stated in section 4.4, the bilinear truss contact model in series with a gap formulated by Muthukumar & Des Roches is taken to simulate the bumpers' dynamic response during a contact. The implementation of this numerical model in Python platform is obtained by selecting an impact material object from the OpenSeesPy library; as the impact object is implemented as a compression-only gap material, the yield deformation, δ_y , and the initial gap, g , are to be input as negative values.

The *sliding-bumping* mode is described in the sample dynamic trajectory of Figure 4.23. By observing first the force-displacement diagram, it can be noted that Region I (in the central part of the cycle) is characterized by a simple frictional behavior: the pure *sliding* mode happens at zero force with increasing displacement and velocity (A-B section). The impact with the right bumper, B_R , occurs at point B and this leads to entering region II, starting the *sliding-bumping* mode, which can be divided into two sub-phases. In the so-called *approaching* phase (i.e. the contact between the slider and the bumper), the MF reaches its maximum relative displacement, yielding a strong and sudden peak of force at decreasing velocity. This state is subdivided into two sections: B-C section, related to the bumper initial stiffness, K_1 , and C-D section, related to the bumper secondary stiffness, K_2 , in which the force and displacement keep on rising until reaching the maximum value. After that, the device stops into D-E section (*sticking* phase): here, the force decreases while both displacement and velocity remain constant. During the *restitution* phase (i.e. the separation of the slider from the bumper), the reduction of the contact force determines the area of

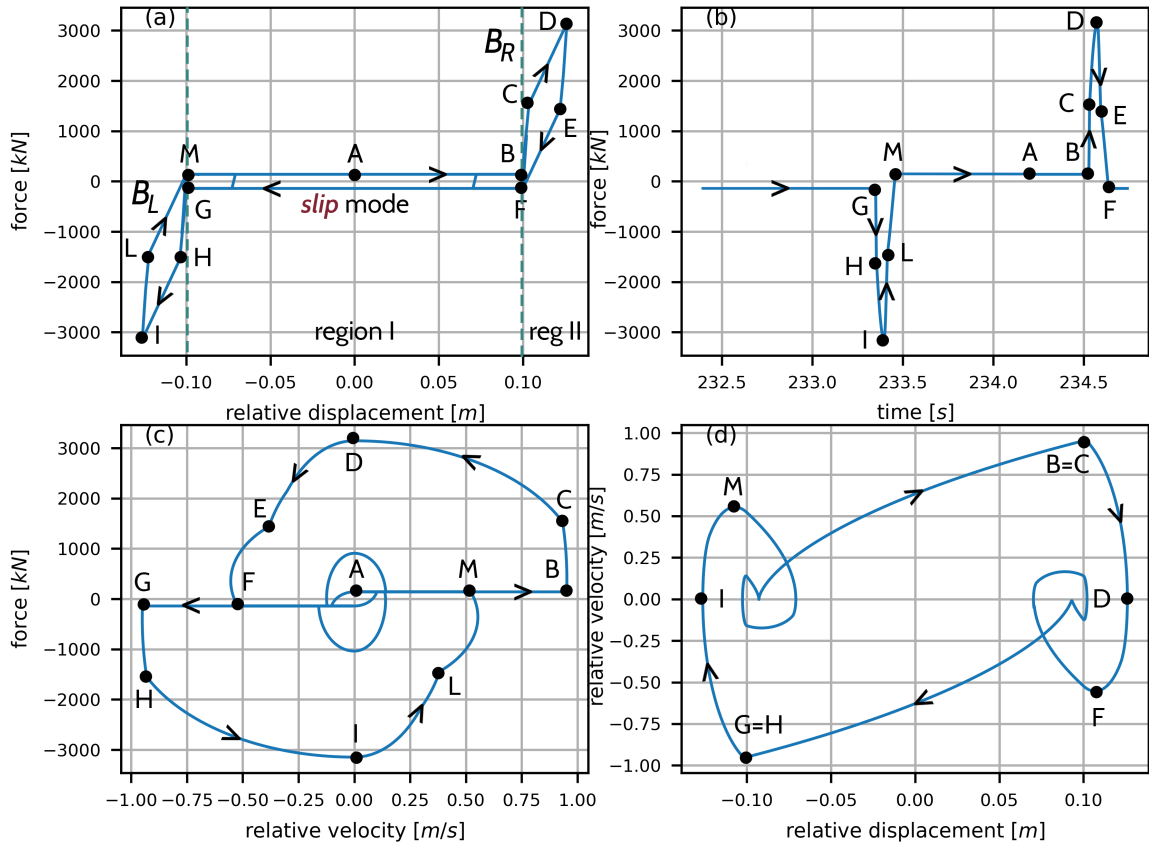


Figure 4.23: Sample dynamic trajectory related to the *sliding-bumping* mode

hysteretic loop, hence, the amount of dissipated energy during the contact, ΔE . The force-displacement cycle under tensile load ends with a quick drop to zero of contact force (E-F section); then, the same trajectory is repeated in the lower part of the diagram under a compressive load. The logic of the bumper's path just described is also reflected in the time-history of the contact force (Fig. 4.23 b), in the force-velocity diagram (Fig. 4.23 c) and in the phase portrait, that is, relative velocity-displacement diagram (Fig. 4.23 d).

4.6.3 Colliding mode

The *colliding* mode refers to the unilateral contact occurring with one of the two rubber bumpers, with the connector kept attached to the façade or to the structure, depending on which direction it is taken, rather than sliding in one direction and the other.

Although from a purely theoretical point of view, the basic operating modes of the connection device can be well-explained through the sample dynamic trajectories described by the first two extreme cases (namely, the *sliding* and the *sliding-bumping* modes), however, the *colliding* one represents another interesting behavior to investigate. As a matter of fact, this type of mode approaches the system's response when subject to a unidirectional dynamic excitation instead of a multidirectional load as in the *sliding-bumping* case, thus, leading to a one-sided impact and an attachment between the slider and the bumper (or the structure and the façade) that lasts over time. Depending on whether the force applied on the connector is

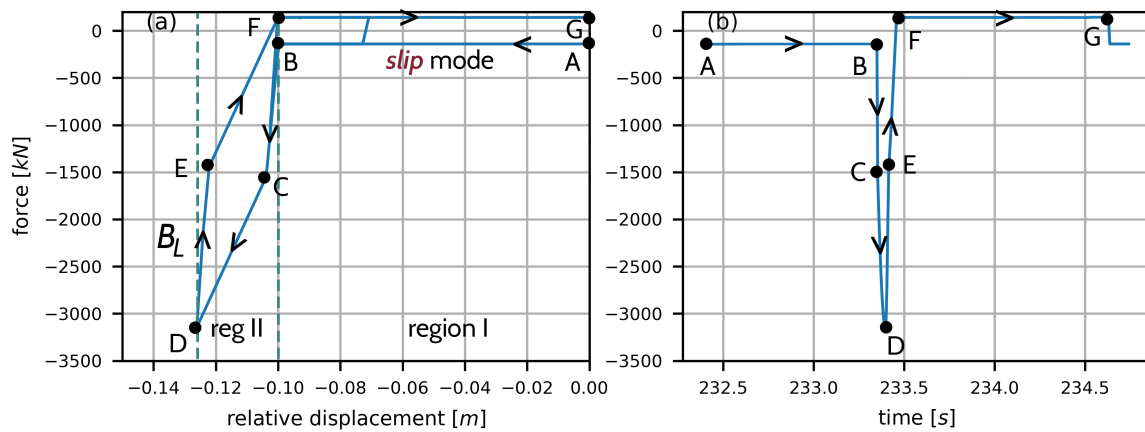


Figure 4.24: Sample dynamic trajectory related to negative *colliding* mode

negative (therefore, directed towards the structure) or positive (therefore, directed towards the façade), the dynamic cycle of the bumper related to the *colliding* mode will be directed towards left, with the contact force pointing downwards, as portrayed in Figure 4.24 or it will be facing right, with the contact force pointing upwards, as in Figure 4.25. As it was easy to guess, in both cases this corresponds to "halving" the dynamic trajectory associated with the bilateral contact of the *sliding-bumping* mode described in section 4.6.2.

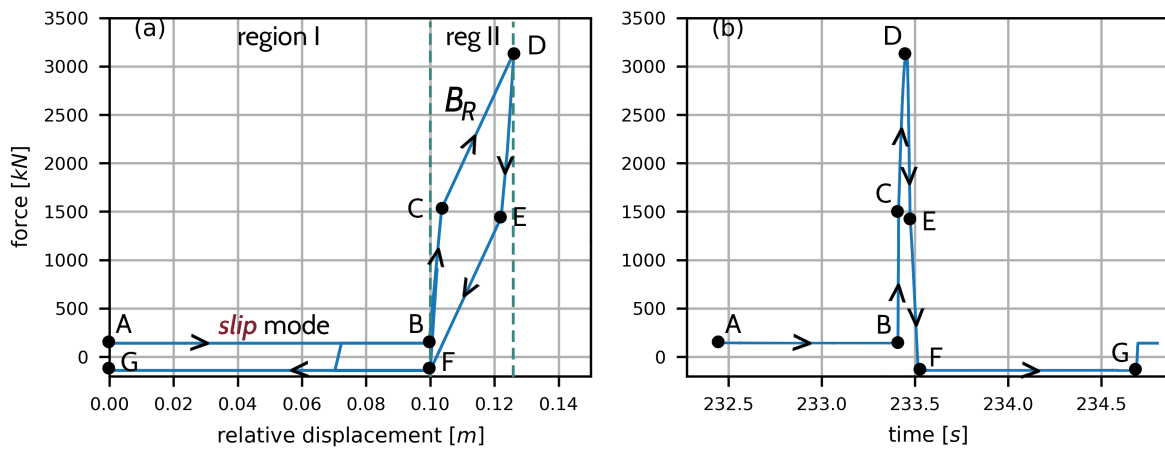


Figure 4.25: Sample dynamic trajectory related to positive *colliding* mode

The response scenario related to a negative *colliding* mode (Fig. 4.24) is characterized by the alternation of two main states (or regions), which can be directly read from the force-displacement diagram (Fig. 4.24 a) and the force time-history (Fig. 4.24 b). Region I begins with the well-known frictional *slip* mode, which occurs at constant force and negative displacement, directed towards the left side of the plot (A-B section). The transition towards region II occurs from point B when, due to the effect of the applied force exceeding the friction threshold of the slider, a unilateral contact between the slider and the left bumper, B_L , happens, leading to a drastic increase in the negative impact force (point C) during the so-called *approaching* phase (section B-C), until reaching the maximum value at point D.

separation phase (D-E section) is linked to a reduction of the contact force which gradually comes back to zero (E-F section) up to the initial *slip* mode (F-G section). The dynamic scenario associated with a negative colliding mode, investigated in a time interval of 5 seconds, also applies in the case of positive unilateral contact, as portrayed in Figure 4.25. As can be seen, the sample dynamic trajectory is consistent with that observed in the previous case, clearly showing an opposite trend extending to the positive side of the diagrams. The same response scenarios encountered throughout the investigated basic operating modes also apply in case of positive *colliding* cycle (that is, a first region related to a pure *slipping* mode of the slider and a second region related to the contact with the bumper, sections characterized by constant force with increasing relative displacement and velocity and sections characterized by increasing force with fixed relative displacement and velocity, and so on).

4.7 Closing remarks

This Chapter deals with the conception, design and modeling, from both a mechanical and dynamic point of view, of a dissipative connection system for MF capable of performing the dual function of structural control and resolution of Moon's problem about the excessive façade relative displacements. Aiming at this, a device consisting of a friction slider, which draws inspiration from the VFCC developed and tested by Laflamme and coworkers starting from 2016, integrated with a system of rubber bumpers, taken from the field of seismic pounding where they are typically used for the purpose of impact-absorption, is proposed. To provide the reader with a clearer theoretical background to which the two mechanisms of the connection system refer, a literature review of the most common and widespread contact models used by engineering community in the field of impact dynamics is offered, followed by the description of the reference friction model accounted for in this context for the development of the slider. Among the various impact models currently available, in the present study reference is made to a bilinear truss contact model in series with a gap developed by Muthukumar (2003) and Muthukumar & Des Roches (2006), which is extensively described in its mathematical formulations and constitutive laws. Similarly, it is proceeded with the introduction of the variable friction cladding connection (VFCC) device conceived and prototyped by a group of researchers from Iowa State University, taken as a reference friction model for the slider project. Once provided the theoretical bases, a general description of the connection system, from a construction point of view and sizing of its main components, is first dealt with. The mechanical characterization of the constitutive behavior and related steps of mathematical formulations, rheological models and constitutive laws takes place both for the friction slider and rubber bumpers. Finally, the Chapter closes with a detailed explanation of the system's dynamic behavior which, depending on whether or not a positive or negative, unilateral or bilateral contact occurs, can be divided into three basic operating modes: that is, *sliding*, *sliding-bumping* and *colliding* mode, each analyzed through specific sample dynamic trajectories.

Chapter 5

Preliminary evaluation of MF under harmonic load

5.1 Introduction

In the present Chapter, the vibration damping efficiency of the proposed MF connection system is evaluated by means of parametric simulations performed on a 2DOF model of a typical mid-rise building equipped with a monolithic MF under harmonic excitation acting on the façade. The influence of the friction threshold, the bumper impact stiffness and the initial gap, which are considered as main parameters, on the system's response is studied in depth. By selecting different combinations of frictional and impact features, devices with different responses can be obtained. A 25-storey, 77.5 m tall building equipped with a monolithic MF system integrated by dissipative sliders and bumpers is taken as a reference case study, whose performances are preliminary assessed resorting to an equivalent harmonically excited 2DOF model. Despite being a simplified load, the assumption of a sinusoidal signal could help a better and clearer understanding of the excitation frequency ranges on which the MF incorporated with the proposed connection devices can ameliorate or worsen the system's behavior. For carrying out the numerical analyzes, a careful discretization procedure is performed which allows the transition from the complete structural model to an equivalent SDOF system, also applying the same concept to the MF modeling as well. A parametric study aiming at investigate the influence of the key variables which characterize the behavior of the connection device on the overall system's response is conducted. By introducing suitable numerical indicators, the vibration and acceleration damping efficiencies of both the MF-equipped building and the façade are evaluated with respect to specific reference cases. In order to better understand the behavioral differences of the two mechanisms making up the connection system (namely, the friction slider and the rubber bumpers), the parametric investigation is conducted in two separate phases, focusing on the effectiveness of the slider in reducing structural displacements and accelerations compared to the *uncontrolled* case (that is, in the absence of MF) and on the effectiveness of bumpers in containing the façade relative displacement with respect to a design limit threshold. For each phase inves-

tigated, the dynamics of the system is well-explained by means of FRC, force-displacement and force-velocity loops, phase portraits, displacement and velocity time-histories, highlighting scenarios and phenomena occurring in the system's response related to the nonlinear behavior of the connection device (such as primary resonance, superharmonic resonances and hysteretic cycles).

5.2 Equivalent 2DOF modeling

Three-dimensional FEM of buildings naturally appear as systems of infinite degrees-of-freedom in which the motion is identified at each time, t , by a function of coordinate z , $v(z, t)$. Generally, the vibration analysis of MDOF systems is difficult and the numerical calculations are burdensome and time-consuming. In most cases, the estimate of all the higher modes of a structure is not necessary as the forced response of the fundamental frequency is often larger and thus more interesting. In this preliminary stage, it is convenient to use a SDOF lumped-mass model which suitably approximate the dynamic behavior of the multi-storey building.

A Rayleigh-like discretization process is introduced to approach the lowest natural frequency, allowing the dynamic behavior of the structural building to be reproduced with sufficient accuracy. The application of the method consists in matching a certain deformation curve to the fundamental vibrating mode [234], ensuring that the assumed deflection corresponds to the natural vibration curve. If this happens, the exact frequency is reached, thus, the approximation of the building with a SDOF model of generalised mass, \tilde{m} , and stiffness, \tilde{k} , can be made. The execution of modal analysis led to consider the structure, relative to its 1^o flexural mode along the y -axis, as a Euler-Bernoulli uniform cross-section cantilever beam constrained at the base, with distributed mass, $m(z)$, and inertia, $I(z)$, along the z -axis.

In applying Rayleigh procedure, the displacement profile of the structure described with the two-variable function, $u(x, t)$, is approximated by the so-called *shape function*, $\psi(x)$

$$u(x, t) = \psi(x)z(t) \quad (5.1)$$

where z is the top displacement.

In fact

$$\psi(H) = 1 \quad (5.2)$$

hence

$$u(H, t) = z(t) \quad (5.3)$$

This means fixing a shape for the beam deformation and assuming that during motion only the deflection amplitude varies accordingly to the generalized displacement coordinate, $z(t)$, which assumes the meaning of the degree-of-freedom of the system [235]-[236]. Having

to represent the deformation of a beam, the function $\psi(z)$ must be differentiable up to the second derivative (that is, the curvature) and continuous together with the first derivative. To respect the joint constraint at the base, it must be

$$\psi = \frac{\partial\psi}{\partial x} = 0 \quad \text{for} \quad x = 0 \quad (5.4)$$

The admissible functions that satisfy both conditions are

$$\psi(x) = \frac{x^2}{H^2} \quad \text{and} \quad \psi(x) = 1 - \cos \frac{\pi^2}{2H} \quad (5.5)$$

By assuming the deflection to be represented by a parabolic function of the first type, the first and second derivative become

$$\psi'(x) = \frac{2x}{H^2} \quad \text{and} \quad \psi''(x) = \frac{2}{H^2} \quad (5.6)$$

Considering the inertia forces, $I(x, t)$, acting on the structure

$$I(x, t) = -m(x)\ddot{u}(x, t) = -m(x)\psi\ddot{z}(t) \quad (5.7)$$

and applying the Principle of Virtual Displacements¹⁴ [237], the *generalized mass coefficient* (or generalized mass), \tilde{m} , and the *generalised stiffness coefficient* (or generalized stiffness), \tilde{k} , to be assigned to the SDOF model can be obtained. Following the same logic, the generalized force, $\tilde{f}(t)$, is calculated as well.

Given a profile of virtual displacements, $\tilde{v}(x)$

$$\begin{aligned} \mathcal{L}_{ext} &= \int_0^H I(x, t)\tilde{v}(x)dx + \int_0^H f(x, t)\tilde{v}(x)dx = \int_0^H [-m(x)\ddot{u}(x, t) + f(x, t)]\tilde{v}(x)dx = \\ &= \int_0^H [-m(x)\psi(x)\ddot{z}(t) + f(x, t)]\tilde{v}(x)dx \quad (5.8) \end{aligned}$$

$$\mathcal{L}_{int} = \int_0^H M(x, t)\tilde{\xi}(x)dx = \int_0^H EIu''(x, t)\tilde{v}''(x)dx = \int_0^H EI\psi''(x)z(t)\tilde{v}''(x)dx \quad (5.9)$$

and assuming

$$\tilde{v}(x) = \psi(x)\tilde{z} \quad (5.10)$$

it is

$$\tilde{v}''(x) = \psi''(x)\tilde{z} \quad (5.11)$$

hence

¹⁴The principle of virtual work states that the virtual work of the forces applied to a system in equilibrium is zero.

$$\begin{aligned}\mathfrak{L}_{ext} &= \int_0^H [-m(x)\psi(x)\ddot{z}(t) + f(x,t)]\psi(x)\tilde{z}dx = \\ &= \int_0^H [-m(x)\ddot{z}(t)[\psi(x)]^2 + f(x,t)\psi(x)]\tilde{z}dx\end{aligned}\quad (5.12)$$

$$\mathfrak{L}_{int} = \int_0^H EI\psi''(x)z(t)\psi''(x)\tilde{z}dx = \int_0^H EIz(t)[\psi''(x)]^2\tilde{z}dx\quad (5.13)$$

In accordance with the dynamic equilibrium, $\mathfrak{L}_{ext} = \mathfrak{L}_{int}$

$$\int_0^H [-m(x)\ddot{z}(t)[\psi(x)]^2 + f(x,t)\psi(x)]\tilde{z}dx = \int_0^H EIz(t)[\psi''(x)]^2\tilde{z}dx\quad (5.14)$$

which gives

$$\int_0^H [(m(x)[\psi(x)]^2\ddot{z}(t) + EI[\psi''(x)]^2z(t) - f(x,t)\psi(x))dx]\tilde{z} = 0\quad (5.15)$$

thus

$$\tilde{m}\ddot{z}(t) + \tilde{k}z(t) = \tilde{f}(t)\quad (5.16)$$

and, finally, the equivalent mass, stiffness and force to be applied on the SDOF model are obtained

$$\tilde{m} = \int_0^H m(x)[\psi(x)]^2dx\quad (5.17)$$

$$\tilde{k} = \int_0^H EI[\psi''(x)]^2dx\quad (5.18)$$

$$\tilde{f}(t) = \int_0^H f(x,t)\psi(x)dx\quad (5.19)$$

5.2.1 Movable Façade modeling

At this first stage of the Movable Façade modeling, the virtual displacements $u_1(x), u_2(x)$ can be considered, which lead to

$$\mathfrak{L}_{ext} = \int_0^H I_1\tilde{u}_1dx + \int_0^H I_s\tilde{u}_2dx + \int_0^H f\tilde{u}_2dx\quad (5.20)$$

$$\mathfrak{L}_{int} = \int_0^H M\tilde{\xi}_1dx + \sum_i N_i\tilde{\delta}_i\quad (5.21)$$

where I_1, I_2 are the inertia forces on the structure and on the façade, f is the distributed force acting on the façade, M is the bending moment on the structure, $\tilde{\chi}_1$ is the virtual curvature

of the structure, $\tilde{\delta}_i$ are the virtual relative displacements at the connection locations and N_i are the internal axial forces acting on the connection. At first approximation, the bending of the façade is neglected.

Assuming that the virtual displacements satisfy the kinematic constraints for the structure, it must be

$$\tilde{u}_1(0) = 0; \quad \tilde{u}'_1(0) = 0 \quad (5.22)$$

and the internal constraints

$$\tilde{\chi}_1(x) = \tilde{u}'_1(x); \quad \tilde{\delta}_i = \tilde{u}_2(x_i) - \tilde{u}_1(x_i) \quad (5.23)$$

Based on this assumptions, various choices of shape functions for the façade virtual displacements that meet the conditions imposed can be done.

Vertical façade

Firstly, shape functions for displacements, assuming a uniform displacement of the façade (always vertical façade) and virtual displacements consistent with them, are taken.

$$\begin{cases} u_1(x) = \psi(x)z_1 \\ u_2(x) = z_2 \end{cases} \quad (5.24)$$

$$\begin{cases} \tilde{u}_1(x) = \psi(x)\tilde{z}_1 \\ \tilde{u}_2(x) = \tilde{z}_2 \end{cases} \quad (5.25)$$

It follows that

$$\tilde{\chi}_1(x) = \psi''(x)\tilde{z}_1; \quad \tilde{\delta}_i = \tilde{z}_2 - \psi(x_i)\tilde{z}_1 \quad (5.26)$$

with the external and internal virtual works being like

$$\mathfrak{L}_{ext} = \left[\int_0^H I_1 \psi dx \right] \tilde{z}_1 + \left[\int_0^H (I_2 + f) dx \right] \tilde{z}_2 \quad (5.27)$$

$$\mathfrak{L}_{int} = \left[\int_0^H M \psi'' dx - \left(\sum_i N_i \psi_i \right) \right] \tilde{z}_1 + \left[\sum_i N_i \right] \tilde{z}_2 \quad (5.28)$$

where $\psi_i := \psi(x_i)$.

By introducing the following relations

$$I_1 = -m_1 \ddot{u}_1 = -m_1 \psi \ddot{z}_1 \quad (5.29)$$

$$I_2 = -m_2 \ddot{u}_2 = -m_2 \psi \ddot{z}_2 \quad (5.30)$$

$$M = EIu_1'' = EI\psi''z_1 \quad (5.31)$$

and substituting them into Eqs. 5.27 and 5.28, respectively, it becomes

$$\mathfrak{L}_{ext} = \left[-\left(\int_0^H m_1 \psi^2 dx \right) \ddot{z}_1 \right] \tilde{z}_1 + \left[-\left(\int_0^H m_2 dx \right) \ddot{z}_2 + \left(\int_0^H f dx \right) \right] \tilde{z}_2 \quad (5.32)$$

$$\mathfrak{L}_{int} = \left[\left(\int_0^H EI(\psi'')^2 dx \right) z_1 - \left(\sum_i N_i \psi_i \right) \right] \tilde{z}_1 + \left[\sum_i N_i \right] \tilde{z}_2 \quad (5.33)$$

With the further definition of the following notations

$$\tilde{M}_1 := \int_0^H m_1 \psi^2 dx \quad (5.34)$$

$$\tilde{K}_1 := \int_0^H EI(\psi'')^2 dx \quad (5.35)$$

$$M_2 := \int_0^H m_2 dx \quad (5.36)$$

$$F := \int_0^H f dx \quad (5.37)$$

$$N := \sum_i N_i \quad (5.38)$$

we get

$$\mathfrak{L}_{ext} = [-\tilde{M}_1 \ddot{z}_1] \tilde{z}_1 + [-M_2 \ddot{z}_2 + F] \tilde{z}_2 \quad (5.39)$$

$$\mathfrak{L}_{int} = [\tilde{K}_1 z_1 - \left(\sum_i N_i \psi_i \right)] \tilde{z}_1 + N \tilde{z}_2 \quad (5.40)$$

and, since it must be $\mathfrak{L}_{ext} = \mathfrak{L}_{int}$, then yields

$$\left[-\tilde{M}_1 \ddot{z}_1 - \tilde{K}_1 z_1 + \left(\sum_i N_i \psi_i \right) \right] \tilde{z}_1 + \left[-M_2 \ddot{z}_2 + F - N \right] \tilde{z}_2 = 0 \quad (5.41)$$

Hence, the equation of motion for a 2DOF system with the assumed vertical façade is derived

$$\begin{cases} \tilde{M}_1 \ddot{z}_1 + \tilde{K}_1 z_1 - \left(\sum_i N_i \psi_i \right) = 0 \\ M_2 \ddot{z}_2 + N = F \end{cases} \quad (5.42)$$

However, it should be noted that this not corresponds to a standard 2DOF system since the structure receives a force $(\sum_i N_i \psi_i)$ different from the one acting on the façade.

In particular, being

$$\psi(x) = \frac{x^2}{H^2} \quad (5.43)$$

where $H = 77.5 \text{ m}$ is the total building height and $h_i = 77.5/25 = 3.10 \text{ m}$ is the inter-storey height, one has

$$\frac{\sum_{j=1}^{25} N \left(\frac{3.10j}{77.5} \right)^2}{\sum_{i=1}^{25} N} = 0.3536 \lim_{X \rightarrow \infty} \frac{\sum_{i=1}^X N \left(\frac{bi}{bX} \right)^2}{\sum_{i=1}^X N} = \frac{1}{3} \quad (5.44)$$

$$\sum_{i=1}^{25} N \left(\frac{3.1i}{77.5} \right)^2 - \sum_{i=1}^{25} N = -16.16N \quad (5.45)$$

$$\sum_{i=1}^X N \left(\frac{bi}{bX} \right)^2 - \sum_{i=1}^X N = \frac{N}{2} + \frac{N}{6} \frac{1}{X} - \frac{2}{3}NX \quad (5.46)$$

Uniform relative displacement

A new proposal of assumption for the shape functions of MF virtual displacements is now explained, which is given by

$$\begin{cases} u_1(x) = \psi(x)z_1 \\ u_2(x) = u_1(x) + z_2 \end{cases} \quad (5.47)$$

$$\begin{cases} \tilde{u}_1(x) = \psi(x)\tilde{z}_1 \\ \tilde{u}_2(x) = \tilde{u}_1(x) + \tilde{z}_2 \end{cases} \quad (5.48)$$

Based on this, it follows that

$$\tilde{\chi}_1(x) = \psi''(x)\tilde{z}_1; \quad \tilde{\delta}_i = \tilde{z}_2 \quad (5.49)$$

with the external and internal virtual works being like

$$\begin{aligned} \mathfrak{L}_{ext} &= \left[\int_0^H I_1 \psi \tilde{z}_1 dx \right] + \left[\int_0^H (I_2 + f)(\psi \tilde{z}_1 + \tilde{z}_2) dx \right] = \\ &= \left[\int_0^H I_1 \psi dx + \int_0^H \psi (I_2 + f) dx \right] \tilde{z}_1 + \left[\int_0^H (I_2 + f) dx \right] \tilde{z}_2 \end{aligned} \quad (5.50)$$

$$\mathfrak{L}_{int} = \left[\int_0^H M \psi'' dx \right] \tilde{z}_1 + \left[\left(\sum_i N_i \right) \right] \tilde{z}_2 \quad (5.51)$$

By introducing the following relations

$$I_1 = -m_1 \ddot{u}_1 = -m_1 \psi \ddot{z}_1 \quad (5.52)$$

$$I_2 = -m_2\ddot{u}_2 = -m_2(\ddot{u}_1 + \ddot{z}_2) = -m_2\psi\ddot{z}_1 - m_2\ddot{z}_2 \quad (5.53)$$

$$M = EIu_1'' = EI\psi''z_1 \quad (5.54)$$

and substituting them into Eqs. 5.50 and 5.51, respectively, it becomes

$$\begin{aligned} \mathfrak{L}_{ext} = & \left[-\left(\int_0^H m_1\psi^2 dx\right)\ddot{z}_1 - \left(\int_0^H m_2\psi^2 dx\right)\ddot{z}_1 - \left(\int_0^H m_2\psi dx\right)\ddot{z}_2 + \left(\int_0^H f\psi dx\right) \right]\ddot{z}_1 + \\ & + \left[-\left(\int_0^H m_2\psi dx\right)\ddot{z}_1 - \left(\int_0^H m_2 dx\right)\ddot{z}_2 + \left(\int_0^H f dx\right) \right]\ddot{z}_2 \quad (5.55) \end{aligned}$$

$$\mathfrak{L}_{int} = \left[\left(\int_0^H EI(\psi'')^2 dx\right)z_1 \right]\ddot{z}_1 + \left[\left(\sum_i N_i\right) \right]\ddot{z}_2 \quad (5.56)$$

With the further definition of the following notations

$$\tilde{M}_1 := \int_0^H m_1\psi^2 dx \quad (5.57)$$

$$\tilde{K}_1 := \int_0^H EI(\psi'')^2 dx \quad (5.58)$$

$$M_2 := \int_0^H m_2 dx \quad (5.59)$$

$$F := \int_0^H f dx \quad (5.60)$$

$$\tilde{F} := \int_0^H f\psi dx \quad (5.61)$$

$$\tilde{M}_2 := \int_0^H m_2\psi^2 dx \quad (5.62)$$

$$\tilde{m}_2 := \int_0^H m_2\psi dx \quad (5.63)$$

$$N := \sum_i N_i \quad (5.64)$$

and, since it must be $\mathfrak{L}_{ext} = \mathfrak{L}_{int}$, then yields

$$\mathfrak{L}_{ext} = [-(\tilde{M}_1 + \tilde{M}_2)\ddot{z}_1 - \tilde{m}_2\ddot{z}_2 + \tilde{F}]\ddot{z}_1 + [-\tilde{m}_2\ddot{z}_1 - M_2\ddot{z}_2 + F]\ddot{z}_2 \quad (5.65)$$

$$\mathfrak{L}_{int} = [\tilde{K}_1 z_1] \tilde{z}_1 + N \tilde{z}_2 \quad (5.66)$$

Finally, the equation of motion for the 2DOF system with the assumed uniform relative displacement is obtained

$$\begin{cases} (\tilde{M}_1 + \tilde{M}_2) \ddot{z}_1 - \tilde{m}_2 \ddot{z}_2 + \tilde{K}_1 z_1 = \tilde{F} \\ M_2 \ddot{z}_2 + \tilde{m}_2 \ddot{z}_1 + N = F \end{cases} \quad (5.67)$$

Façade displacement proportional to structure displacement

Now assume the following shape functions for virtual displacements

$$\begin{cases} u_1(x) = \psi(x) z_1 \\ u_2(x) = \psi(x) z_2 \end{cases} \quad (5.68)$$

$$\begin{cases} \tilde{u}_1(x) = \psi(x) \tilde{z}_1 \\ \tilde{u}_2(x) = \psi(x) \tilde{z}_2 \end{cases} \quad (5.69)$$

it follows that

$$\tilde{\chi}_1(x) = \psi''(x) \tilde{z}_1; \quad \tilde{\delta}_i = \psi(x_i) \tilde{z}_2 - \psi(x_i) \tilde{z}_1 \quad (5.70)$$

with the external and internal virtual works being like

$$\mathfrak{L}_{ext} = \left[\int_0^H I_1 \psi dx \right] \tilde{z}_1 + \left[\int_0^H I_2 \psi dx + \int_0^H f \psi dx \right] \tilde{z}_2 \quad (5.71)$$

$$\mathfrak{L}_{int} = \left[\int_0^H M \psi'' dx - \left(\sum_i N_i \psi_i \right) \right] \tilde{z}_1 + \left[\sum_i N_i \psi_i \right] \tilde{z}_2 \quad (5.72)$$

Using Eqs. 5.29 and substituting them into Eqs. 5.71 and 5.72, respectively, it becomes

$$\mathfrak{L}_{ext} = \left[- \left(\int_0^H m_1 \psi^2 dx \right) \ddot{z}_1 \right] \tilde{z}_1 + \left[- \left(\int_0^H m_2 \psi^2 dx \right) \ddot{z}_2 + \left(\int_0^H f \psi dx \right) \right] \tilde{z}_2 \quad (5.73)$$

$$\mathfrak{L}_{int} = \left[\left(\int_0^H EI (\psi'')^2 dx \right) z_1 - \left(\sum_i N_i \psi_i \right) \right] \tilde{z}_1 + \left[\sum_i N_i \psi_i \right] \tilde{z}_2 \quad (5.74)$$

The following definitions can be introduced

$$\tilde{M}_1 := \int_0^H m_1 \psi^2 dx \quad (5.75)$$

$$\tilde{K}_1 := \int_0^H EI (\psi'')^2 dx \quad (5.76)$$

$$\tilde{M}_2 := \int_0^H m_2 \psi^2 dx \quad (5.77)$$

$$\tilde{F} := \int_0^H f \psi dx \quad (5.78)$$

$$\tilde{N} := \sum_i N_i \psi_i \quad (5.79)$$

and substituted into Eqs. 5.73 and 5.74, in order to get

$$\mathcal{L}_{ext} = [-\tilde{M}_1 \ddot{z}_1] \tilde{z}_1 + [-M_2 \ddot{z}_2 + \tilde{F}] \tilde{z}_2 \quad (5.80)$$

$$\mathcal{L}_{int} = [\tilde{K}_1 z_1 - \tilde{N}] \tilde{z}_1 + \tilde{N} \tilde{z}_2 \quad (5.81)$$

Equivalence of Eqs. 5.80 and 5.81 gives

$$\left[-\tilde{M}_1 \ddot{z}_1 - \tilde{K}_1 z_1 + \tilde{N} \right] \tilde{z}_1 + \left[-M_2 \ddot{z}_2 + \tilde{F} - \tilde{N} \right] \tilde{z}_2 = 0 \quad (5.82)$$

from which the equation of motion for the assumption of a façade displacement proportional to the structure displacement is derived

$$\begin{cases} \tilde{M}_1 \ddot{z}_1 + \tilde{K}_1 z_1 - \tilde{N} = 0 \\ \tilde{M}_2 \ddot{z}_2 + \tilde{N} = \tilde{F} \end{cases} \quad (5.83)$$

In this case, being $\psi(x) = \frac{x^2}{H^2}$ and $x_i = h_i$ where h is the inter-storey height, it becomes

$$\psi_i = \frac{h_i^2}{H} \quad (5.84)$$

where $H = N_s h$ (with $N_s = 25$ standing for the number of sliders).

Taken from Eq. 5.75

$$\tilde{N} := N \sum_{i=1}^{N_s} \left(\frac{h_i}{N_s h} \right)^2 = \left(\frac{(N_s + 1)(2N_s + 1)}{6N_s} \right) N = \left(\frac{(25 + 1)(2(25) + 1)}{6(25)} \right) N = 8.84N \quad (5.85)$$

Since the proposed connections are axial and do not allow the façades to rotate, the latter should bend like the structure. As stated before, by neglecting the MF bending stiffness, we should assume that the relative displacement between the structure and the façade keeps constant.

When the structure moves according to

$$u_1(x, t) = \psi(x) z_1(t); \quad \text{with} \quad \psi(x) = \left(\frac{x}{H} \right)^2 \quad (5.86)$$

we assume the façade to move with uniform relative displacement given from

$$u_2(x, t) = u_1(x, t) + z_2(t) \quad (5.87)$$

Being the inertia of the building, I_1 , and the façade, I_2 , equal to

$$I_1(x, t) = -m_1(x)\ddot{u}_1(x, t) = -m_1(x)\psi(x)\ddot{z}_1(t) \quad (5.88)$$

$$I_2(x, t) = -m_2(x)\ddot{u}_2(x, t) = -m_2(x)\psi(x)\ddot{z}_1(t) - m_2(x)\ddot{z}_2(t) \quad (5.89)$$

and the virtual displacements on the structure, $\tilde{v}_1(x)$, and on the façade, $\tilde{v}_2(x)$, equal to

$$\tilde{v}_1(x) = \psi(x)\tilde{z}_1; \quad \tilde{v}_2(x) = \psi(x)\tilde{z}_1 + \tilde{z}_2 \quad (5.90)$$

the external virtual work becomes

$$\begin{aligned} \mathcal{L}_{ext} &= \int_0^H I_1 \tilde{v}_1 dx + \int_0^H I_2 \tilde{v}_2 dx + \int_0^H f \tilde{v}_2 dx = \\ &= \int_0^H [-m_1 \psi \ddot{z}_1] [\psi \tilde{z}_1] dx + \int_0^H [-m_2 \psi \ddot{z}_1 - m_2 \ddot{z}_2] [\psi \tilde{z}_1 + \tilde{z}_2] dx + \int_0^H f [\psi \tilde{z}_1 + \tilde{z}_2] dx = \\ &= \int_0^H [-(m_1 + m_2) \psi^2 \ddot{z}_1 - m_2 \psi \ddot{z}_2 + f \psi \tilde{z}_1] [\tilde{z}_1] dx + \int_0^H [(-m_2 \psi \ddot{z}_1 - m_2 \ddot{z}_2 + f) \tilde{z}_2] dx \end{aligned} \quad (5.91)$$

while the internal virtual work is given by the bending of the structure and the relative displacement between the façade and the structure working against the internal forces acting on the connections, as follows

$$\begin{aligned} \mathcal{L}_{int} &= \int_0^H M(x, t) \tilde{\chi}(x) dx + \sum_{i=1}^{N_{conn}} N(x_i, t) (\tilde{v}_2 - \tilde{v}_1)(x_i) dx = \\ &= \int_0^H EI \psi''(x) z(t) \psi''(x) \tilde{z}_1 dx + \sum_{i=1}^{N_{conn}} N(x_i, t) \tilde{z}_2 dx \end{aligned} \quad (5.92)$$

It should be noted that although the approximation made for the equivalent modeling of façade, and the related assumption on virtual displacements, is not entirely correct, it can still be taken into consideration for a first preliminary analysis.

5.3 Description of the case study

The case study selected for the numerical simulation carried out in Python software is a mid-rise 25-storey building made of a Reinforced Concrete (RC) frame and an internal core made of RC walls. With a 40×25 m rectangular plan, symmetrical with respect to the two main axes, the building rises up to a total height of 77.5 m, having an inter-storey height of

3.10 *m*. From three-dimensional FE modeling of the building performed in SAP 2000, the total mass of the building without cladding ($m = 21571$ tons) is estimated based on a linear static analysis executed under dead load, whereas the mass of a standard façade is estimated in 515 *t*. The first vibrating mode associated to oscillations parallel to the *y*-direction has a period of 2.344 *s* with a fundamental frequency of 0.426 *Hz*, both derived from SAP modal analysis.

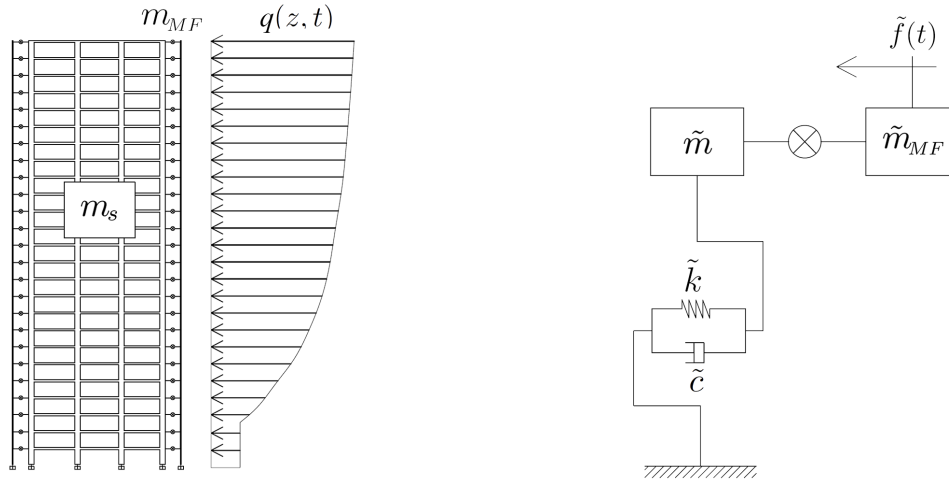


Figure 5.1: Structural frame of the 25-storey mid-rise building subjected to wind pressures (on the left) and 2DOF modeling of the building equipped with a monolithic MF system subjected to harmonic load (on the right)

Resorting to the discretization procedure carefully described in section 5.2, for both the modeling of the building and the monolithic façade, the transition from the complete structural model to an equivalent simplified 2DOF system takes place. Applying Eqs. 5.17 and 5.18, the generalized mass, \tilde{m} , and stiffness, \tilde{k} , to be assigned to the SDOF model of the mid-rise building under examination can be computed, respectively.

Assuming a SDOF system with uniformly distributed mass yields

$$\tilde{m} = m \int_0^H \left(\frac{x}{H} \right)^2 dx = \frac{mH}{5} \quad (5.93)$$

given that $(m \cdot H) = 21725$ tons, the generalized mass is

$$\tilde{m} = \frac{21725}{5} = 4345 \quad \text{tons} \quad (5.94)$$

Since we want the elastic response of the structure to have a period of $T = 2.344$ *s*, the correlated circular frequency is

$$\omega = \frac{2\pi}{T} = \frac{2\pi}{2.344} = 2.6851 \quad \text{rad/s} \quad (5.95)$$

Given that, the generalized stiffness can be derived from the well-known standard notation

Table 5.1: Parameters of the equivalent 2DOF model

f	ω	\tilde{m}	\tilde{k}	ξ	\tilde{c}	\tilde{m}_{MF}
[Hz]	[rad/s]	[tons]	[kN/m]	[–]	[kN · s/m]	[tons]
0.426	2.6851	4345	31327	0.01	233.33	130.35

(Eq. 3.3)

$$\tilde{k} = \omega^2 \tilde{m} = \left(\frac{2\pi}{2.344} \right)^2 4345 = 31327 \text{ kN/m} \quad (5.96)$$

And assuming a 1% critical damping ratio, the same procedure can be applied to derive the *generalized viscous damping coefficient* as well

$$\tilde{c} = 2\xi\tilde{m}\omega = 2 \cdot 0.01 \cdot 4345 \cdot 2.6851 = 233.33 \text{ kNs/m} \quad (5.97)$$

For the purposes of the following basic performance analyses, the building has been assumed to be equipped with MF realized by four rigid blocks capable to move independently in the direction orthogonal to the adjacent building surface. The mass of the bounding frames for the façade has been estimated by a preliminary stiffness-based design that lead to a total mass of about 865 *t*. The oscillating mass along the *y*-direction has been finally assumed to be equal to the 61.5% of the total, corresponding to the mass of the cladding of the two sides parallel to *x*-direction, finally yielding a mass ratio of 2.4%. Based on literature data taken from K.S. Moon and T.S. Fu & R. Zhang, mass ratios ranging from 1% to 10% can be taken. Indeed, considering that façade systems are heavy and their weight can vary considerably from one building to another depending on the cladding type (a DSF, for instance, is heavier than a traditional CW due to the double layer glazed skins), some authors use 1 – 2% mass ratios to avoid introducing a large amount of additional weight to the structure, others can go up to 10%. However, as envelopes are an already existing integral part of buildings, additional weights to the structure are not to be considered.

By lumping the 25 structural mass elements in the single generalised mass, \tilde{m} , and the 25 mass elements of the façade into a secondary lumped-mass, \tilde{m}_{MF} , the mechanical system schematized in Figure 5.1 is obtained. The parameters of the equivalent 2DOF numerical model are summarized in Table 5.1.

5.3.1 Sinusoidal modeling

A simple harmonic load directly applied to the secondary mass is used to excite the equivalent 2DOF system, simulating the wind pressure acting on the façade. Assuming a sinusoid with amplitude equal to the peak wind pressure, $q_p(z)$ (in kPa), with variable frequency, we get a force per unit length, $p(z)$ (in kN/m), given by

$$p(z) = q_p(z)B \quad (5.98)$$

where $q_p(z)$ is computed according to CNR-DT 207/2008 guidelines and $B = 40.0 \text{ m}$ is the dimension of the façade orthogonal to the wind direction.

Assuming to place the building under examination in the city of Milan (Lombardy, Italy), site-specific coefficients related to Zone 2, exposure category IV and roughness class B apply for estimate of $q_p(z)$, whose values are listed below

v_r	k_r	z_{min}	z_0	c_t
[m/s]	[-]	[m]	[m]	[-]
18.75	0.22	8	0.3	1

It is worth specifying that, in order not to excessively lengthen the discussion, this context is limited to reporting the values of the coefficients taken directly from the CNR, while an exhaustive and detailed description of all the steps for the calculation and simulation of wind load, with related explanation of all the coefficients used, is provided in Chapters 6 and 7 dealing with mid- and high-rise buildings subject to turbulent wind activity, respectively.

In accordance with [CNR Eq.3.9], by decomposing the force per unit length, $p(z)$, into its two contributions, $p_0 + p_1(z)$, it is possible to separate the constant term below z_{min} , (p_0), from the height-dependent term above z_{min} , ($p_1(z)$)

$$p(z) = \underbrace{p_0}_{\text{constant wind pressure}} + \underbrace{p_1(z)}_{\text{height-dependent wind pressure}}$$

which gives

$$p_0 = \underbrace{\left(\frac{1}{2} \rho v_r^2 k_r^2 \ln\left(\frac{z_{min}}{z_0}\right) c_t(z) \left[\ln\left(\frac{z_{min}}{z_0}\right) c_t(z_{min}) + 7 \right] \right)}_{q_{p_0}} B; \quad \text{for } z \leq z_{min}$$

$$p_1(z) = \underbrace{\left(\frac{1}{2} \rho v_r^2 k_r^2 \ln\left(\frac{z}{z_0}\right) c_t(z) \left[\ln\left(\frac{z}{z_0}\right) c_t(z) + 7 \right] \right)}_{q_{p_1(z)}} B; \quad \text{for } z > z_{min}$$

where $\rho = 1.225 \text{ kg/m}^3$ is the air density and the coefficients v_r , k_r , z_{min} , z_0 and c_t assume the relative value taken from the table.

Based on this, the forces per unit length are defined as

$$p_0 = \underbrace{\left(\frac{1}{2} (1.25) (18.75)^2 (0.22)^2 \ln\left(\frac{8}{0.3}\right) \ln\left(\frac{8}{0.3}\right) + 7 \right)}_{q_{p_0}} (40) = 14.363 \text{ kN/m}$$

$$p_1(z) = \underbrace{\left(\frac{1}{2} (1.25) (18.75)^2 (0.22)^2 \ln\left(\frac{z}{0.3}\right) \left[\ln\left(\frac{z}{0.3}\right) + 7 \right] \right)}_{q_{p_1(z)}} (40); \quad \text{for } z > z_{min}$$

Similarly, the resultant force, F , can be decomposed into the two terms, $F_0 + F_1(z)$, depending on whether it is computed below or above the minimum height, $z_{min} = 8 \text{ m}$.

A check of the resultant force gets

$$F_0 = z_{min}p_0 = 8(14.363) = 114.904 \quad \text{kN} \quad (5.99)$$

$$F_1(z) = zp_1(z) = \int_8^{77.5} 0.425 \ln(3.33z)[\ln(3.33z) + 7]dz = 1692.2 \quad \text{kN} \quad (5.100)$$

Therefore

$$F = \underbrace{114.904}_{F_0} + \underbrace{1692.2}_{F_1(z)} = 1807.1 \quad \text{kN}$$

with the mean wind pressure being

$$q = \frac{F}{A} = \frac{1807.1}{(77.5 \cdot 40)} = 0.5829 \quad \text{kPa} \quad (5.101)$$

In particular, from

$$f(x, t) = p(z) = q_p(z)B \quad (5.102)$$

it is possible to derive the generalized force, \tilde{f} , acting on the equivalent 2DOF model according to Eq. 5.19

$$\begin{aligned} \tilde{f} &= \int_0^8 p_0 \left(\frac{x}{77.5} \right)^2 dx + \int_8^{77.5} p_1(x) \left(\frac{x}{77.5} \right)^2 dx = \\ &= \int_0^8 (14.363) \left(\frac{x}{77.5} \right)^2 dx + \int_8^{77.5} (0.425) \ln(3.33z)(\ln(3.33z) + 7) \left(\frac{x}{77.5} \right)^2 dx = \\ &= 0.408 + 702.02 = 702.43 \quad \text{kN} \quad (5.103) \end{aligned}$$

It is worth noting that the equivalent sinusoidal force, \tilde{f} , corresponds to

$$\tilde{f} = \frac{702.43}{1807.1} \approx 40\% \quad F \quad (5.104)$$

5.4 Efficiency measures

The dynamical response of buildings equipped with MF can be investigated by numerical simulations of the action of an harmonic load on the façade comparing various design solutions. Whereas it is obvious that harmonic excitation is not a realistic model for actual loads acting on buildings, a proper understanding of the influence of the forcing frequency on the response of the structure is a basic information on the top of which the study of more complex dynamical excitation can be based. To this end, suitable frequency-dependent measures of the performance level are needed. The main performances goal that a MF system has to

achieve is to let the structure undergo displacements lower than those it would show with a standard fixed façade with accelerations consistent with serviceability criteria based on comfort level. However, as discussed above, good vibration damping performances of MF tend to be accompanied by large relative displacements of the façades that might exceed functionally acceptable values. Therefore, a further performance goal measuring the extent to which this problem is solved is considered, together the main ones, by requesting that the maximum relative displacement between the façade and the structure does not exceed the maximum value admissible on the basis of constructive and technological grounds. To implement the above concepts, for a given forcing amplitude, the performance of the MF at frequency ρ can be measured by three efficiency parameters, which aim to ascertain the improvement of the MF-equipped structure displacement (η) and acceleration (κ), and the façade relative displacement (ζ), compared to well-defined starting conditions.

The *structural displacement efficiency*, η , is evaluated with respect to the absolute displacement of the *uncontrolled* structure, \bar{u} , which corresponds to the case in the absence of Movable Façade (or with a conventional fixed façade)

$$\eta(\rho) := \frac{\bar{u} - u_{MF}}{\bar{u}} \quad (5.105)$$

where \bar{u} denotes the maximum displacement produced by the given excitation, \tilde{f} , on the *uncontrolled* SDOF structure and u_{MF} stands for the maximum displacement of the monolithic MF-equipped structure, both normalized with respect to the primary mass static displacement, f/k , with k and f given by Eqs. 5.18 and 5.103, respectively.

The response of *uncontrolled* SDOF structure under generalized force, \tilde{f} , is derived from

$$\bar{u}(\rho) = \frac{f/k}{(1 - \rho^2)^2 + (2\xi\rho)^2} \quad (5.106)$$

The *structural acceleration efficiency*, κ , is ascertained with respect to the acceleration limit value, \bar{a} (expressed in g), provided by the current standards for compliance with the building habitability requirements

$$\kappa(\rho) := \frac{\bar{a} - a_{MF}}{\bar{a}} \quad (5.107)$$

where a_{MF} and \bar{a} denote the maximum acceleration of the structure and the acceleration level associated with a chosen serviceability criterion, respectively.

The acceleration limit, \bar{a} , for ensuring a suitable well-being of the occupants during wind event is defined according to Eq. 2.22. Given the fundamental frequency of the building equal to $f = 0.426 \text{ Hz}$ and fixed an average return period, $T_R = 1 \text{ yr}$, as recommended for the assesment of human comfort, in the observation time interval considered ($T = 3600 \text{ s}$) it is obtained

$$\bar{a} = \sqrt{2 \ln(0.426 \cdot 3600)} \left(0.68 + \frac{\ln 1}{5}\right) e^{-3.65 - 0.41 \ln 0.426} = 0.05 \text{ g} \quad (5.108)$$

Finally, the *facade displacement efficiency*, ζ , is determined on the maximum allowable relative displacement of the MF system, \bar{v}

$$\zeta(\rho) := \frac{\bar{v} - v_B}{\bar{v}} \quad (5.109)$$

where v_B denotes the maximum façade-structure relative displacement and \bar{v} the maximum displacement admissible for constructive reasons. The preliminary design of a few case studies reported in section 4.4 seems to indicate that a value $\bar{v} = 0.75 \text{ m}$ could be used for the following analyses, although it is obvious that a more detailed design of the connection could lead to slightly modify it.

Displacement efficiency η and *Acceleration efficiency* κ can be positive or negative depending on whether MF reduces or amplifies the corresponding response with respect to the case of building with fixed cladding. Similarly, *Facade efficiency* ζ will be positive or negative depending on whether the relative displacement of the façade is lower or bigger than the admissible value. For a given excitation amplitude, the three efficiency parameters defined in Eqs. 5.105, 5.107 and 5.109 clearly depend on the forcing frequency and therefore provide only a local information.

It is then useful to define corresponding global efficiency measures as follows

$$E_\eta := \int_0^\infty \eta^+(\rho) d\rho; \quad E_\kappa := \int_0^\infty \kappa^+(\rho) d\rho; \quad E_\zeta := \int_0^\infty \zeta^+(\rho) d\rho \quad (5.110)$$

The performances of the proposed connection are now evaluated on the basis of numerical simulations of the response under harmonic excitation at fixed amplitude and various frequencies, making reference to the case study of a building equipped with MF, as described in the section 5.3.

A preliminary analysis of the response of the building with MF connected to the structure by simple friction sliders without bumpers is carried out in order to have a reference situation to evaluate bumper efficiency and to appreciate the problem of façade displacements.

5.5 Performance of the friction device without bumpers

In the first part of the study, the attention is paid to the structural vibration and acceleration damping efficiency of the friction slider, temporarily excluding the bumpers from the MF connection system, which will be taken into account in the following section. Hence, with reference to a pure *sliding* mode, the dynamic performance of the friction slider is assessed by means of a parametric investigation which evaluates the influence of the friction threshold on the equivalent 2DOF system's response. As noted before, the system is subject to a harmonic load of amplitude P and frequency Ω , applied to the secondary mass, whereas a Coulomb contact characterised by a friction force of amplitude F occurs between the two masses of the system.

The main parameter which influences the response of the simple Coulomb friction sliders

with equal static and dynamic friction coefficients is the force threshold which, for convenience in a parametric analysis, can be expressed as a multiple of the excitation amplitude by means of a dimensionless coefficient, α , defined as the friction ratio

$$F = \alpha P; \quad \text{with} \quad 0.1 \leq \alpha \leq 1.0 \quad (5.111)$$

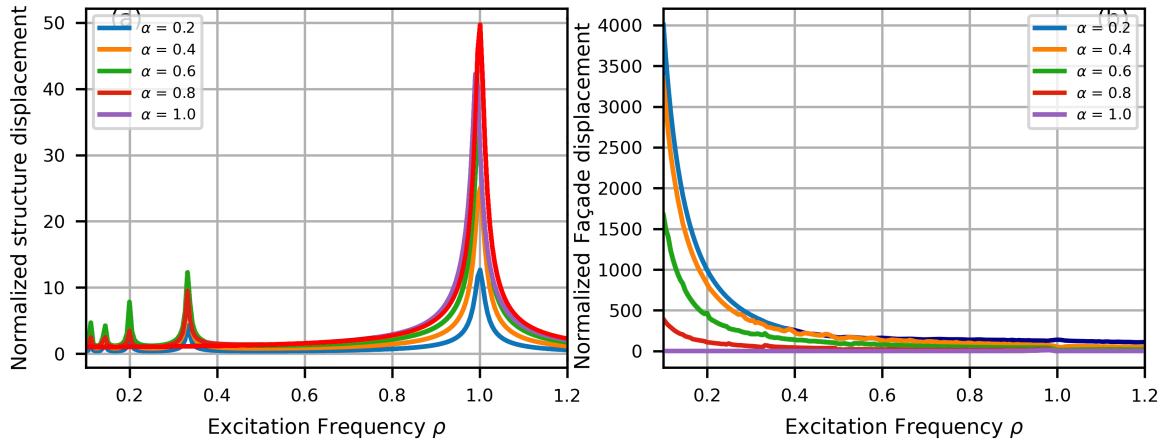


Figure 5.2: Frequency-response curves for the maximum displacements of the main structure (a) and façade (b) with $\alpha \in [0.2, 1.0]$. Displacements are normalized with respect to the static displacement P/k_s . It should be noted that the purple curve in (a) related to $\alpha = 1.0$ tends to the response of the structure with fixed façade (red curve)

Figure 5.2 a shows the FRC in terms of maximum displacement of the MF-equipped structure superimposed on the maximum displacement of the *uncontrolled* SDOF structure (red curve), while Figure 5.2 b illustrates the maximum relative displacement of the façade both normalized with respect to static displacement f/k for various values of the friction threshold ranging from $\alpha = 0.2$ to $\alpha = 1.0$. As can be seen, the lower the friction threshold, the more the structure response improves at the expense of very large relative displacements of the façade especially in the low frequency range, where they can reach orders of magnitude of several thousands times the static displacement. On the contrary, choosing high friction values lead to a more contained façade displacement which, however, corresponds to a structural response approaching the fixed façade case: this is consistent with the fact that due to a high friction threshold, the façade tends to stick to the structure, nullifying its relative displacement and reducing the system to a SDOF oscillator.

An interesting phenomenon can be observed in the force-displacement diagrams of Figure 5.3. The general trend shown by the slider at low excitation frequency ($\rho = 0.5$) and at resonant frequency ($\rho = 1.0$) is to move away from the origin as the friction threshold decreases, moving towards the left part of the plot and oscillating around non-zero mean values.

It turns out that, except for the case of $\alpha = 1.0$, the structure exhibits various resonances: the main one at $\rho = 1.0$ and four secondary ones that correspond to odd-superharmonic (or ultraharmonic) resonances, coupled with complex non-linear phenomena like asymmetry of vibrations and loss of contact [238]. Generally, in linear systems the number of resonance

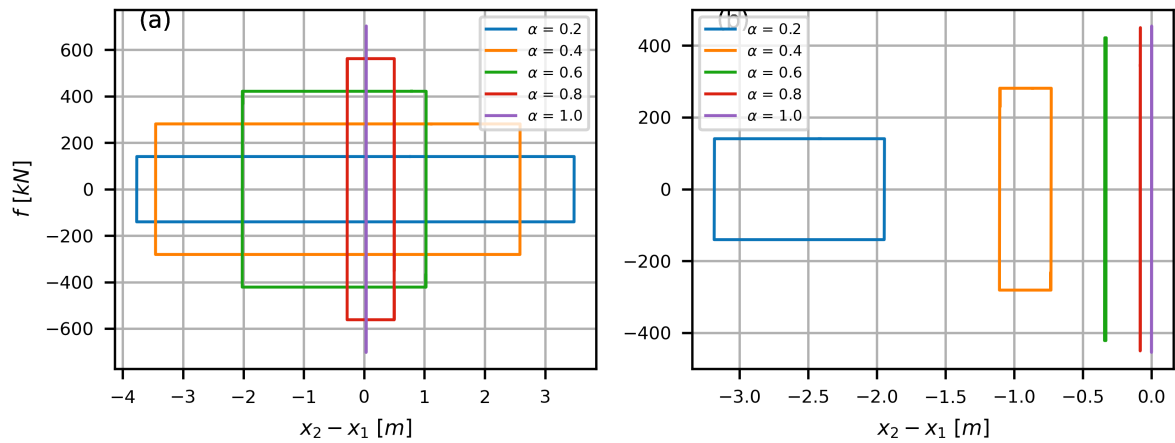


Figure 5.3: Force-displacement diagrams of the friction slider for $\alpha \in [0.2, 1.0]$ recorded at low excitation frequency $\rho = 0.5$ (a) and at resonant frequency $\rho = 1.0$ (b)

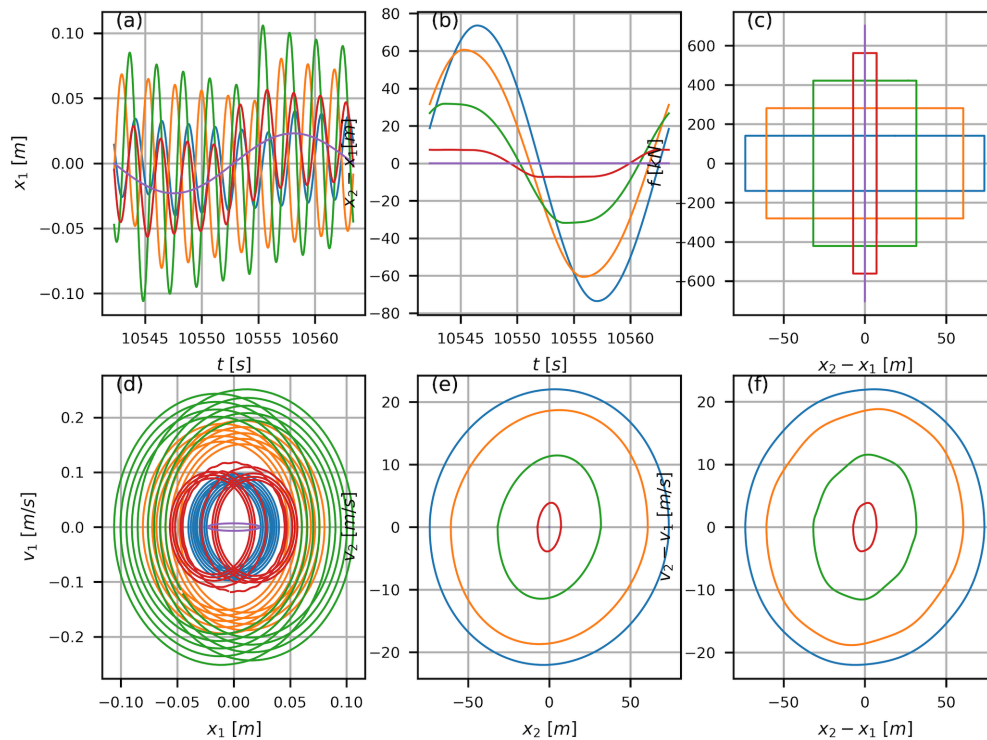


Figure 5.4: Absolute displacement of the primary mass (a), relative displacement of the secondary mass (b), relative force-displacement loop of the slider (c), absolute phase portrait of the primary mass (d), absolute phase portrait of the secondary mass (e) and relative phase portrait of the secondary mass (f) for $\alpha \in [0.2, 1.0]$ in correspondence of the superharmonic resonance at $\rho = 0.11$ (1/9)

peaks is not larger than the number of DOFs; as a result, for a SDOF linear system no more than one resonance peak is found and the analysis of dynamical systems may be focused only on the primary resonance. On the contrary, vibrations of harmonically excited non-linear systems are multiharmonic (that is, they contain a number of harmonics); hence, many kinds of resonances may be found [239]-[240]-[241] and this implies the occurrence of many peaks in a resonance graph [242]-[243]-[244]. According to [245], these resonances can take place

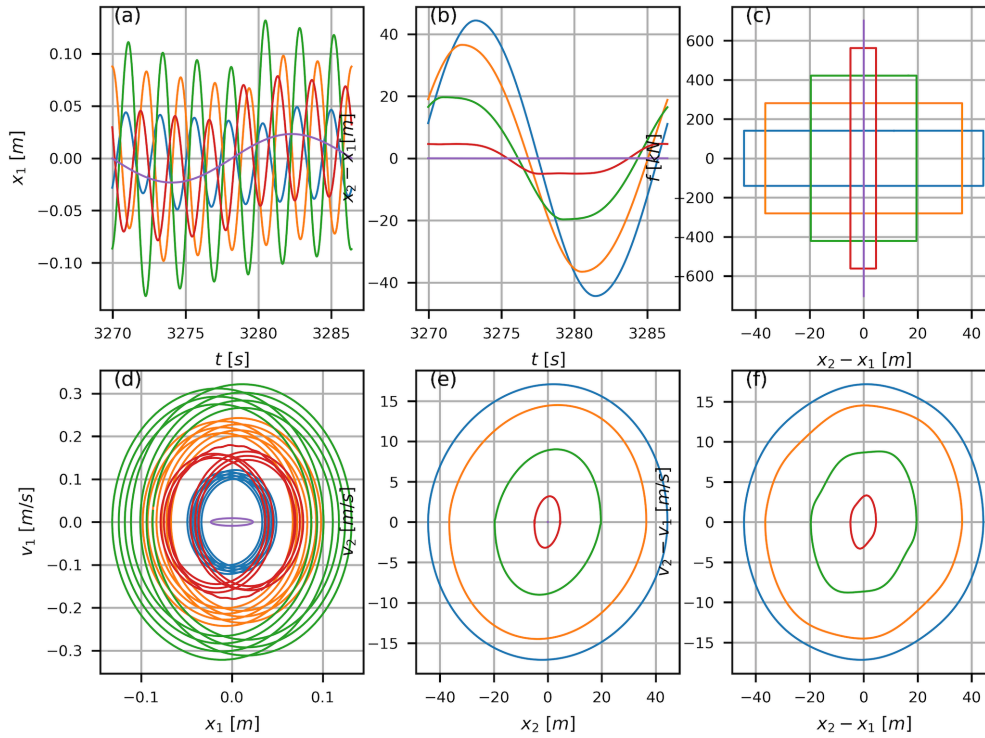


Figure 5.5: Absolute displacement of the primary mass (a), relative displacement of the secondary mass (b), relative force-displacement loop of the slider (c), absolute phase portrait of the primary mass (d), absolute phase portrait of the secondary mass (e) and relative phase portrait of the secondary mass (f) for $\alpha \in [0.2, 1.0]$ in correspondence of the superharmonic resonance at $\rho = 0.14$ ($1/7$)

when the forcing frequency, Ω , is in the following relation to the natural frequency, ω

$$\Omega = \frac{n}{m}\omega \quad (5.112)$$

where m and n are positive integers.

Depending on their values, the following kinds of resonances may take place in the system's response:

- primary (main) resonance, if $n = 1$ and $m = 1$;
- *super*-harmonic (*ultra*-harmonic) resonance, if $n = 1$ and $m > 1$;
- *sub*-harmonic resonance, if $n > 1$ and $m = 1$;
- *supersub*-harmonic resonance, if $m \neq 1$, $n \neq 1$ and $\frac{n}{m} \neq 1$

Based on this, in the resonance plot of Figure 5.2 a, a number of peaks is observed which are related to the superharmonic (or ultraharmonic) resonances ($n = 1$ and $m > 1$) taking place at excitation frequencies being below the natural frequency: specifically, they occur at $1/3$, $1/5$, $1/7$ and $1/9$, respectively, of the natural frequency, ω . This means that when the frequency of the 3th harmonic of vibrations approaches the natural frequency, ω , then, the amplitude of the 3th harmonic is amplifying and $1/3$ superharmonic resonance is a result

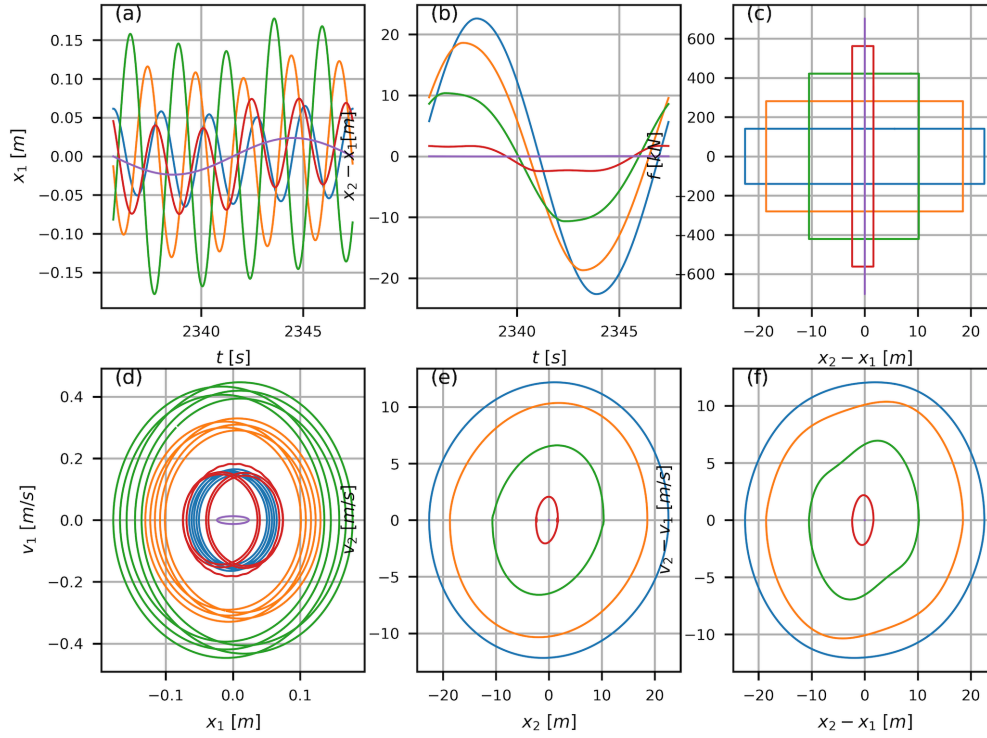


Figure 5.6: Absolute displacement of the primary mass (a), relative displacement of the secondary mass (b), relative force-displacement loop of the slider (c), absolute phase portrait of the primary mass (d), absolute phase portrait of the secondary mass (e) and relative phase portrait of the secondary mass (f) for $\alpha \in [0.2, 1.0]$ in correspondence of the superharmonic resonance at $\rho = 0.20$ ($1/5$)

of the amplification of the 3th harmonic, and so on. In this case, the frequency of the 3th superharmonic resonance, $\Omega_{s,3}$, follows the relation

$$\Omega_{s,3} = \frac{1}{3}\omega = 0.895 \text{ rad/s}; \quad \text{with } \rho = 0.33 \quad (5.113)$$

The same logic also applies for the subsequent superharmonic resonances, which will follow the relations

$$\Omega_{s,5} = \frac{1}{5}\omega = 0.537 \text{ rad/s}; \quad \text{with } \rho = 0.2 \quad (5.114)$$

$$\Omega_{s,7} = \frac{1}{7}\omega = 0.383 \text{ rad/s}; \quad \text{with } \rho = 0.14 \quad (5.115)$$

$$\Omega_{s,9} = \frac{1}{9}\omega = 0.298 \text{ rad/s}; \quad \text{with } \rho = 0.11 \quad (5.116)$$

The nature of the superharmonic resonances is the amplification of higher harmonics, the frequency of which is near the natural frequency ω . Clearly, superharmonic resonances are much more complex than primary resonance; for this reason, more than two curves may appear in the resonance diagrams. The behavior of the 2DOF system in correspondence with the superharmonic and primary resonances is deepened in Figures 5.4-5.8 where phase portraits (that is, relative velocity versus relative displacement cycles) and time histories clearly show

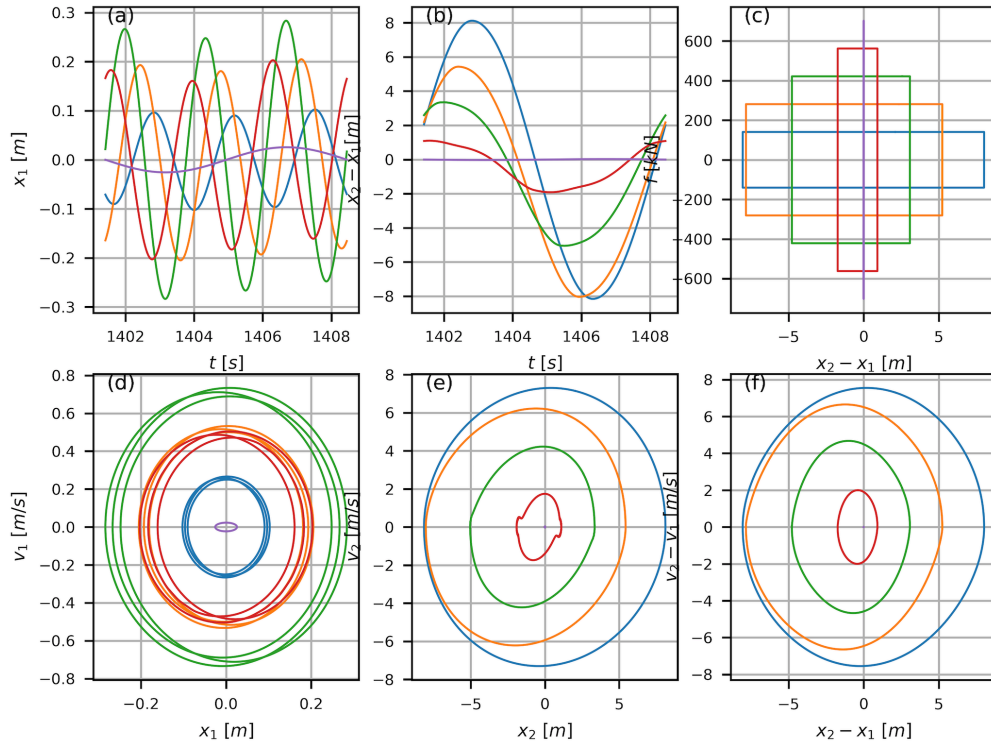


Figure 5.7: Absolute displacement of the primary mass (a), relative displacement of the secondary mass (b), relative force-displacement loop of the slider (c), absolute phase portrait of the primary mass (d), absolute phase portrait of the secondary mass (e) and relative phase portrait of the secondary mass (f) for $\alpha \in [0.2, 1.0]$ in correspondence of the superharmonic resonance at $\rho = 0.33$ ($1/3$)

the complexity of superharmonic resonances and their sophisticated kinematics. A summary diagram of the super-harmonics phenomenon is represented in the concluding phase portraits of Figure 5.9, where multiple superimposed curves appear at excitation frequencies $\rho = 0.14$ ($1/7$), $\rho = 0.20$ ($1/5$) and $\rho = 0.33$ ($1/3$).

As highlighted from the FRC, the dynamic response of the slider can considerably differ depending on the excitation frequency to which the 2DOF model is exposed. In order to provide a complete picture of the system's response subject to harmonic excitation, it may be useful to explore the time-domain as the forcing frequency varies, while setting a well-defined friction ratio, α . Figures 5.10, 5.11 and 5.12 show the time histories of absolute velocity (in m/s) of the primary mass, v_1 (a) and of the secondary mass, v_2 (b), together with the relative velocity (in m/s) between them, $v_2 - v_1$ (c) within the forcing frequency range, $\rho \in [0.2, 1.2]$, for $\alpha = 0.2, 0.5$ and 0.8 , respectively.

In line with the results discussed so far, the absolute velocity peak of the structure is recorded in correspondence of the primary resonance ($\rho = 0.98$), while the maximum façade relative velocity occurs at low frequency ($\rho = 0.2$).

In general, the more the façade is free to move with low friction values, the more the structural efficiency increases, leading to a marked improvement in the behavior of the MF-equipped building compared to the *uncontrolled* case (that is, with conventional fixed façade).

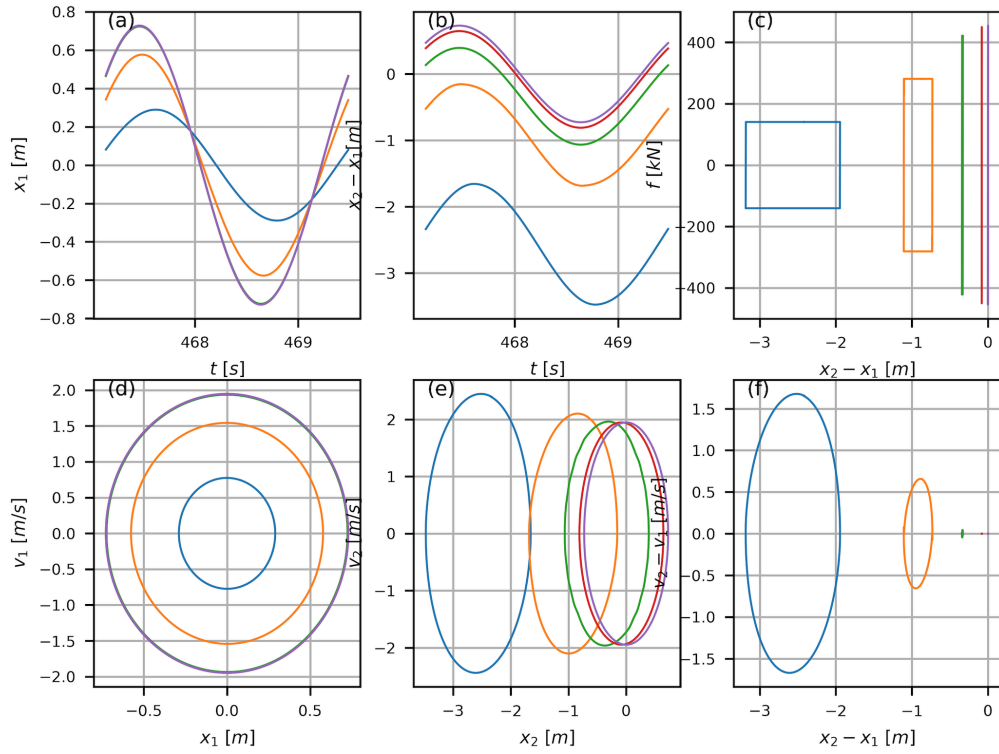


Figure 5.8: Absolute displacement of the primary mass (a), relative displacement of the secondary mass (b), relative force-displacement loop of the slider (c), absolute phase portrait of the primary mass (d), absolute phase portrait of the secondary mass (e) and relative phase portrait of the secondary mass (f) for $\alpha \in [0.2, 1.0]$ in correspondence of the primary resonance at $\rho = 1.0$ (1/1)

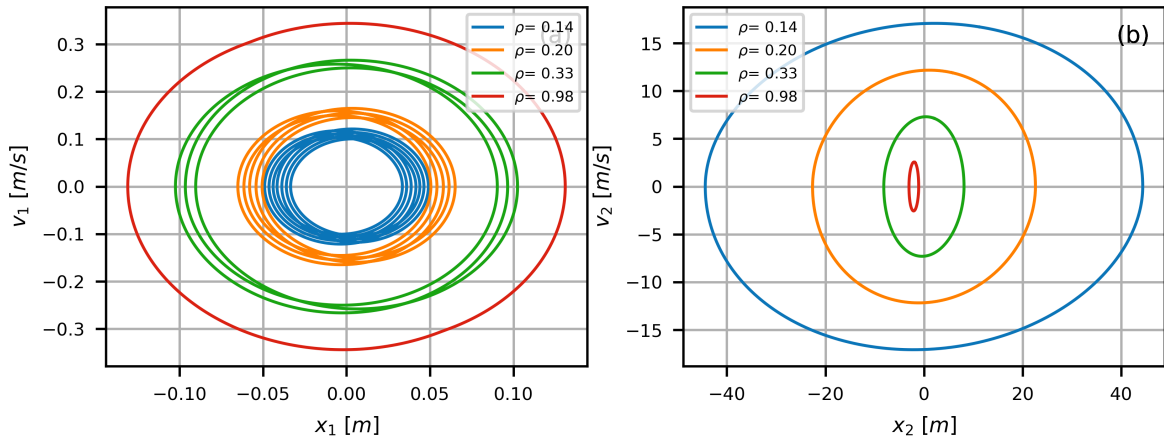


Figure 5.9: Phase portraits (absolute velocity-displacement diagrams) of the main structure (a) and façade (b) for $\alpha = 0.2$ in correspondence with the superharmonic resonances recorded at $\rho = 0.14$ (1/7), $\rho = 0.20$ (1/5) and $\rho = 0.33$ (1/3)

Unfortunately, this comes at the expense of excessive façade relative displacements. This opposite trend between the structure and the MF response is clearly highlighted in Figure 5.13, where the efficiency curves for the main structure (a-b) and façade (c) are portrayed, built on the numerical indices defined in Eqs. 5.105, 5.107 and 5.109, respectively. For clarity, only positive efficiency regions are plotted in Figure 5.13 a-b, that is, the areas where the

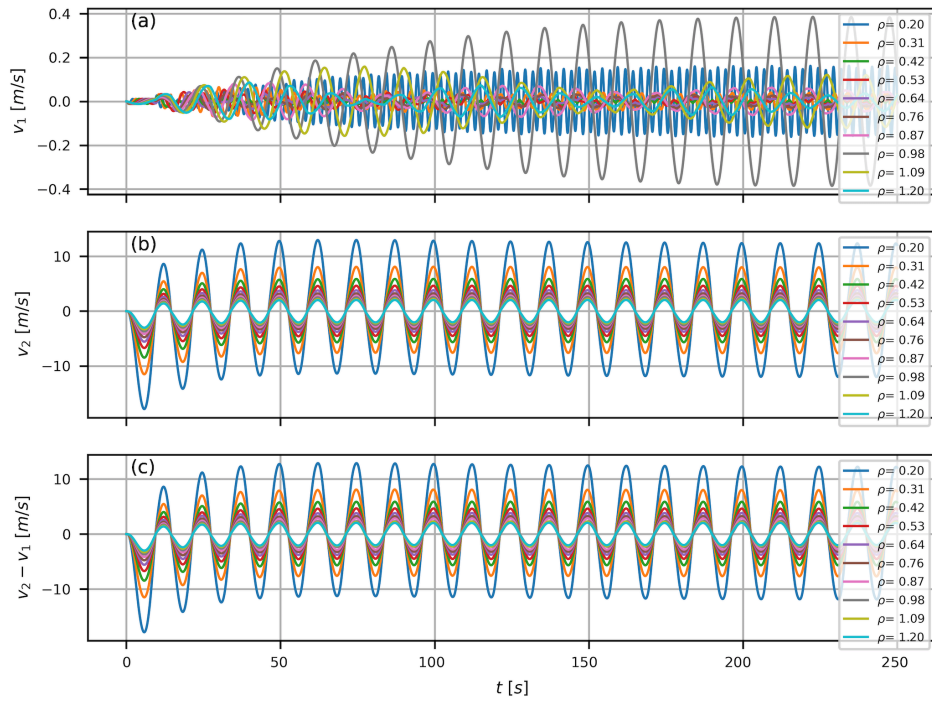


Figure 5.10: Time histories of (a) absolute velocity of the primary mass, v_1 (b) absolute velocity of the secondary mass, v_2 , and (c) relative velocity between the primary and secondary mass, $v_2 - v_1$, for $\alpha = 0.2$ in $\rho \in [0.2, 1.2]$

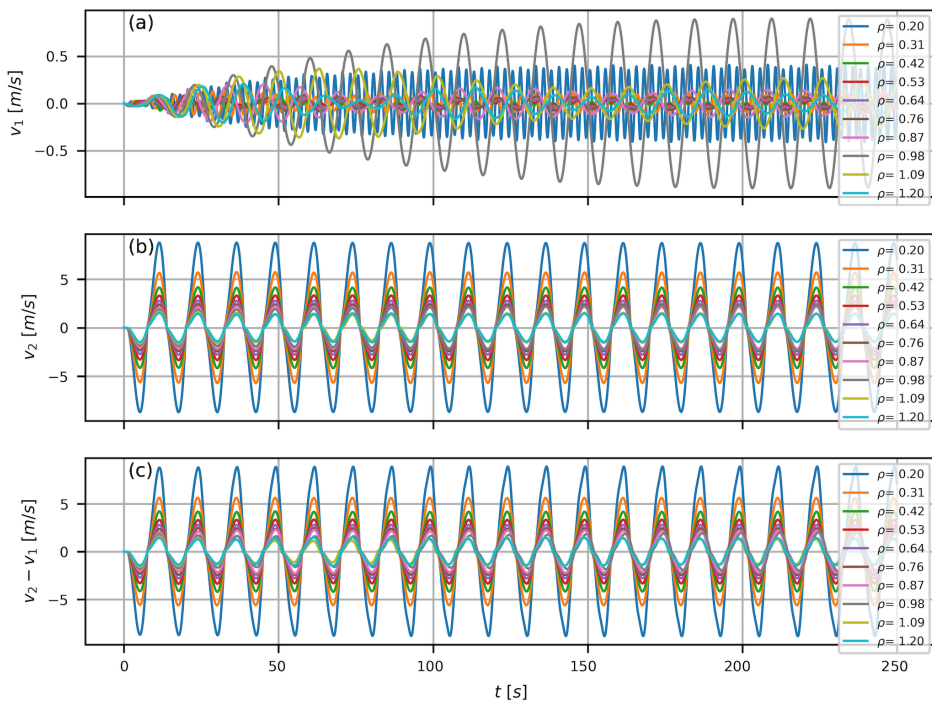


Figure 5.11: Time histories of (a) absolute velocity of the primary mass, v_1 (b) absolute velocity of the secondary mass, v_2 , and (c) relative velocity between the primary and secondary mass, $v_2 - v_1$, for $\alpha = 0.5$ in $\rho \in [0.2, 1.2]$

friction slider effectively reduces the structural response compared to the reference cases.

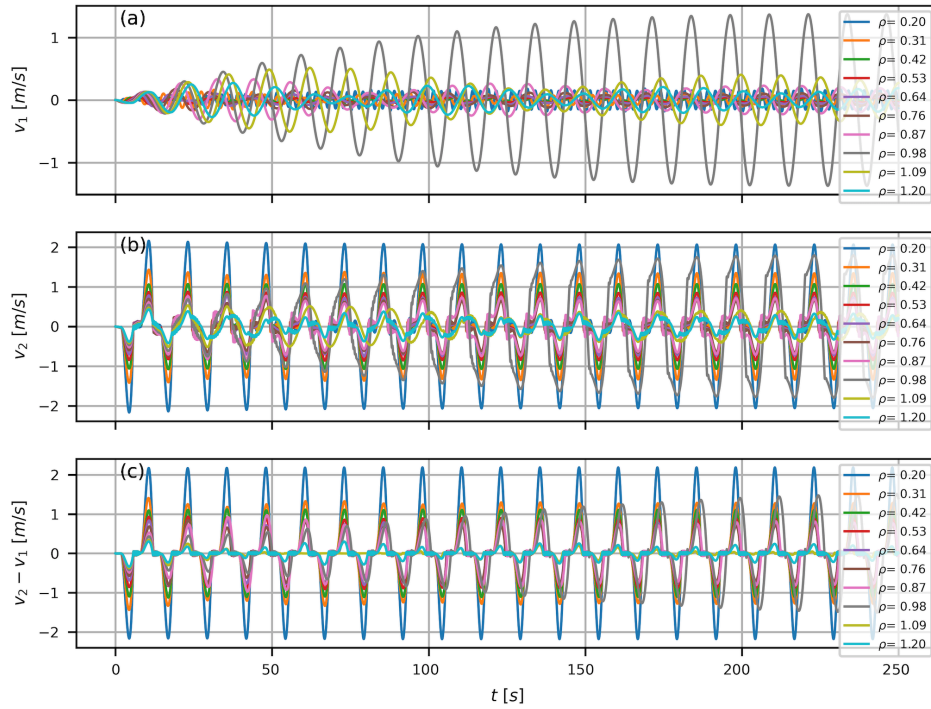


Figure 5.12: Time histories of (a) absolute velocity of the primary mass, v_1 (b) absolute velocity of the secondary mass, v_2 , and (c) relative velocity between the primary and secondary mass, $v_2 - v_1$, for $\alpha = 0.8$ in $\rho \in [0.2, 1.2]$

As can be seen from Figure 5.13 a, the structure efficiency strongly depends on the friction ratio: the more this is reduced, the more η increases and vice versa. With the blue curve corresponding to a low friction ratio ($\alpha = 0.2$), an almost 80% efficiency is achieved in the high-frequency range and about 60% at low excitation frequencies. However, the latter occurs at the price of an extremely negative façade efficiency ($\zeta = -12000\%$), meaning that the MF relative displacement far exceeds the imposed threshold of 0.75 m in the low frequency range (Fig. 5.13 c). On the other hand, a high friction ratio ($\alpha = 1.0$) implies a net worsening of the structural displacement with MF, significantly reducing the efficiency η over the entire frequency range. Choosing high value of α as friction threshold lead to push the smart façade system response close to the conventional façade response. In this case, the monolithic MF sticks to the structure, nullifying the relative displacement between the two masses and reducing the system to a SDOF oscillator. This is consistent with the marked increase in the façade efficiency ζ associated with $\alpha = 0.8$ (dark red curve), although still referring to negative values. As for the structural acceleration response, from Figure 5.13 b it is quite important to see that with any friction threshold, the MF system is able to ensure compliance with the occupational comfort requirement. Indeed, the efficiency curves obtained are always highly positive, settling on values between 70% and 90% until undergoing a drop at resonance, where the empty gap in the curves denotes the occurrence of limited ranges with negative efficiency values.

Finally, to provide the reader with an idea of the amount of energy dissipated by the slider during each hysteretic cycle of its force-displacement curve, the Jacobsen's area method is

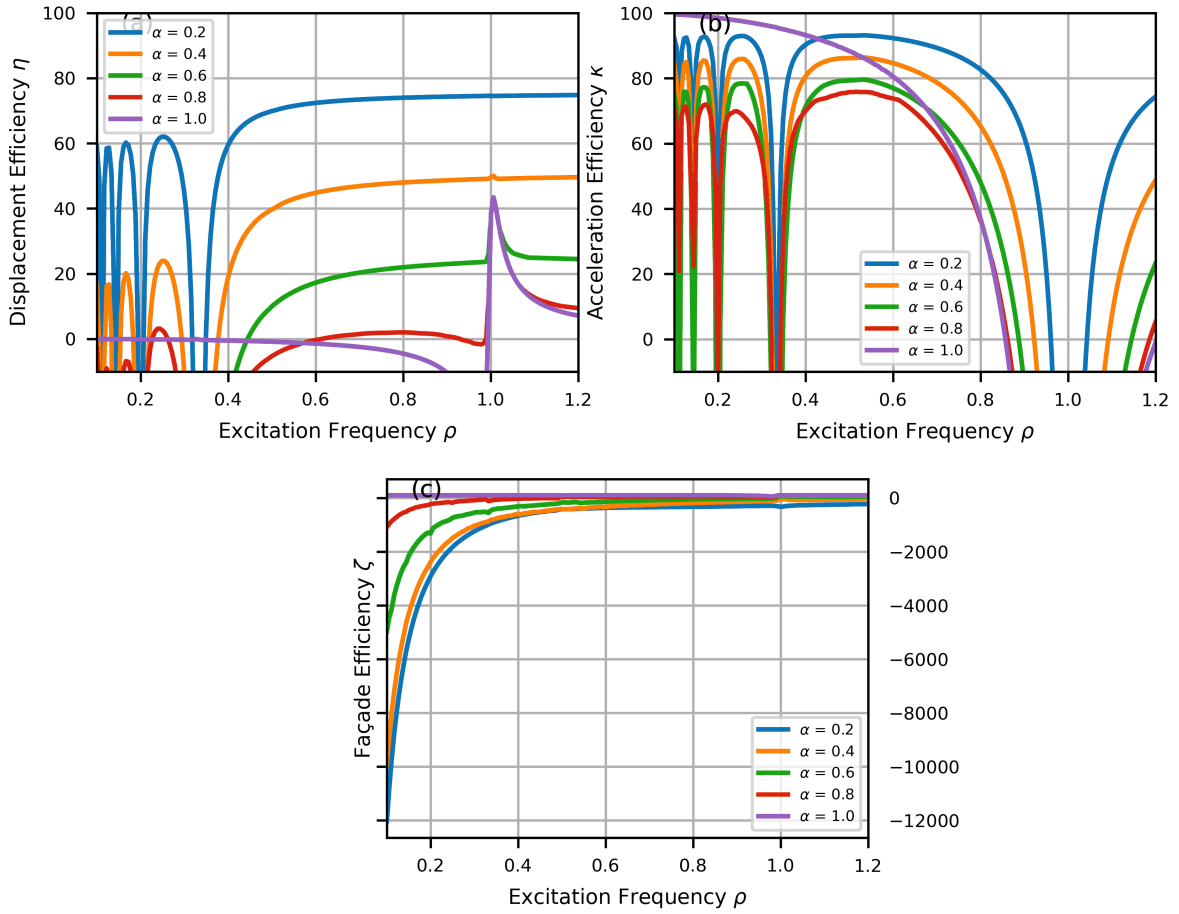


Figure 5.13: Displacement efficiency η (a), acceleration efficiency κ (b) and façade efficiency ζ (c) for $\alpha \in [0.2, 1.0]$

used to estimate the equivalent viscous damping (EVD) ratio, ξ_{eq} , for each friction threshold parameter imposed. According to an energy equivalence approach described in section 2.3.4, the EVD ratio is computed using Eq. 2.19. The values obtained are reported in Table 5.2.

Based on this preliminary results, the choice to assume a low friction ratio, α , for the purposes of structural vibration and acceleration control appears to be correct, even if that involves an unacceptable relative displacement response of the monolithic MF. This issue will be addressed in the next section, with the addition of the bumpers to the friction slider.

Table 5.2: Equivalent viscous damping (EVD) ratios for variable friction ratios, α

	α									
	0.1	0.2	0.3	0.4	0.5	0.6	0.7	0.8	0.9	1.0
ξ_{eq} [%]	68.60	68.61	68.61	68.65	68.82	68.23	68.59	68.22	69.04	69.51

5.6 Performance of the friction device with bumpers

The results of the parametric analysis carried out for variable friction threshold of the slider reveal a potentially promising structural control offered by MF integrated with low friction connection devices. Under the same circumstances, however, Moon's problem is encountered as the low friction threshold of the slider leads to negligible benefits in terms of the façade efficiency and its large relative displacements could compromise the application of the entire system. Fixed a low friction ratio, $\alpha = 0.2$, for a more than satisfactory structural response, the possibility of breaking down the cladding motion by adding the bumpers to the connection system is studied in this section, switching to the *sliding-bumping* mode. The vibration damping performance of the dissipative slider with bumpers is evaluated by means of a parametric investigation carried out by varying the two key variables affecting the bumper's dynamic behavior, namely, the initial gap, g , and the impact stiffness, k_h .

5.6.1 Influence of the initial gap

Within the *sliding-bumping* mode, the first parameter whose influence on the harmonically excited 2DOF system's response want to be explored is the width (in m) of the initial gap, g , between the slider and the bumper, evaluating whether a widening or narrowing of this intermediate space can be beneficial or disadvantageous on the system's dynamic performance. Having set a low friction ratio, $\alpha = 0.2$, to achieve a suitable structural control, and an impact stiffness parameter, $k_h = 300 \text{ MN}/m$, taken from Eq. 4.37, in an attempt to stop the façade motion avoiding further sliding, the parameterization of the initial gap is carried out in the qualitative range

$$0.10 \leq g \leq 0.75 \quad \text{m} \quad (5.117)$$

where $g = 0.10 \text{ m}$ represents the minimum distance to be guaranteed according to the thickness of the bumpers and $g = \bar{v} = 0.75 \text{ m}$ is the design limit value for the façade displacement set by the sizing of the connector executed in Chapter 4.

Figure 5.14 a shows the normalized absolute displacement curves of the primary mass with MF superimposed on the absolute displacement curve of the uncontrolled SDOF structure (red curve), while Figure 5.14 b shows the normalized relative displacement curves of the façade for $g \in [0.1, 0.7] \text{ m}$. Compared to the case of the slider alone portrayed in Figure 5.2, it is clear that the addition of bumpers involves a clear improvement in the secondary mass response in terms of lowering of its relative displacement: the more the gap narrows, the easier it is to contain the façade relative displacement over the entire frequency range. In contrast, the primary mass response appears to be almost insensitive to the gap variation; rather, an increase in the absolute displacement with respect to the *uncontrolled* condition is highlighted, above all, near the primary resonance and in correspondence with the superharmonic resonances, where the response peaks related to the three different gap values overhang the red curve representative of the structure in the absence of the façade.

Figure 5.15 shows the efficiency curves for the structure absolute displacement, η , and

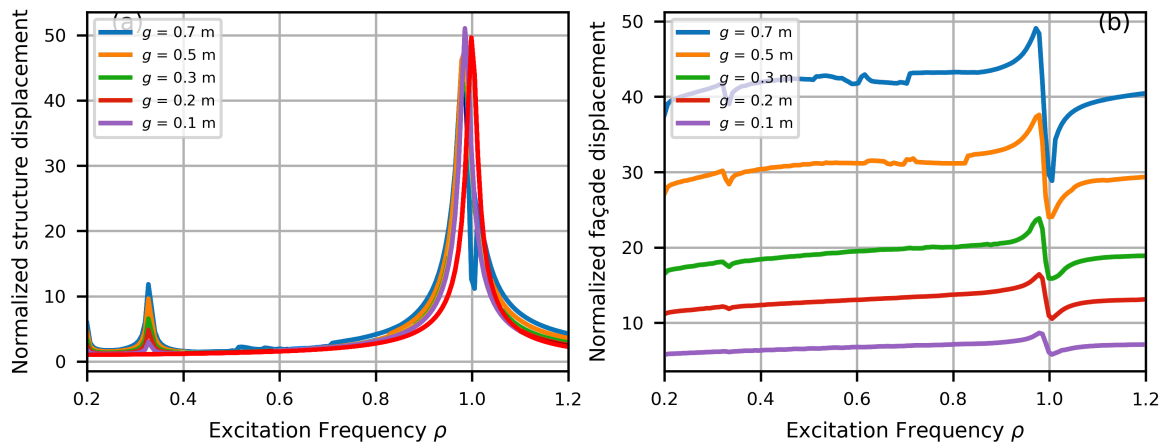


Figure 5.14: Frequency-response curves for the maximum displacements of the main structure (a) and façade (b) with $g \in [0.1, 0.7]$ m, $\alpha = 0.2$ and $k_h = 300$ MN/m. Displacements are normalized with respect to the static displacement P/k_s . The red curve represents the maximum displacement of the structure without MF

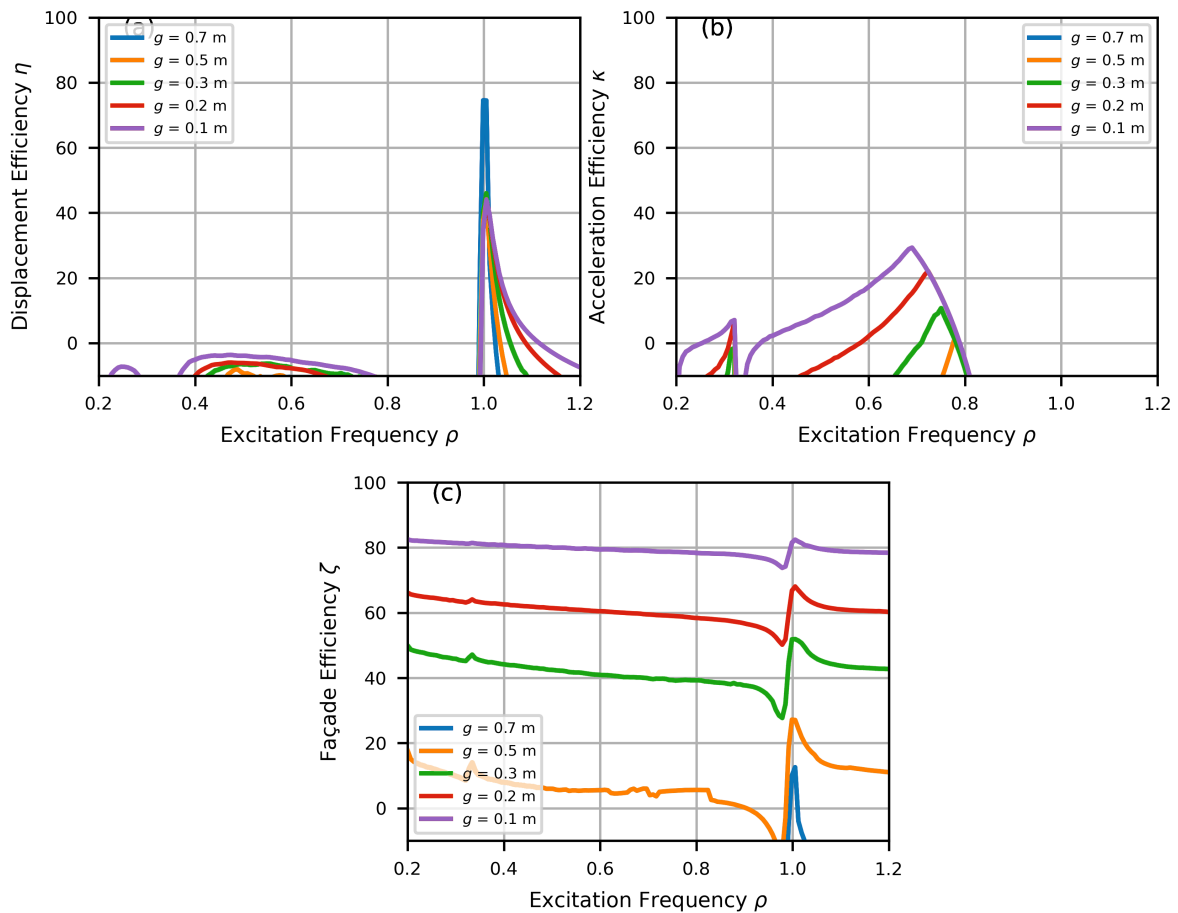


Figure 5.15: Displacement efficiency η (a), acceleration efficiency κ (b) and façade efficiency ζ (c) with $g \in [0.1, 0.7]$ m, $\alpha = 0.2$ and $k_h = 300$ MN/m

acceleration, κ , and façade relative displacement, ζ , obtained with the addition of bumpers for $g \in [0.1, 0.7]$ m. By comparing them with the efficiency curves obtained in the absence of

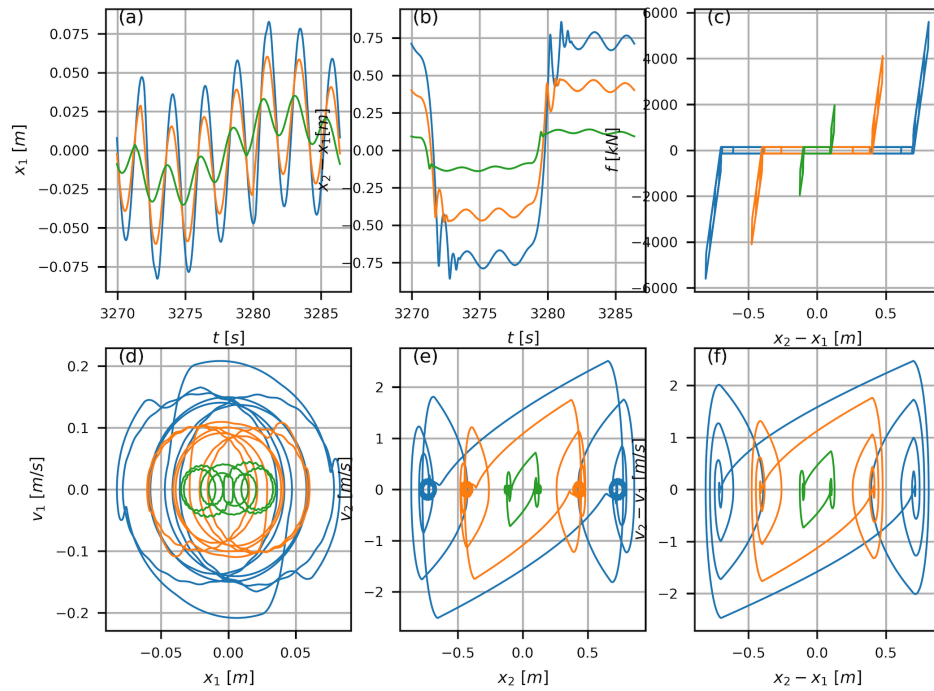


Figure 5.16: Absolute displacement of the primary mass (a), relative displacement of the secondary mass (b), relative force-displacement loop of the slider (c), absolute phase portrait of the primary mass (d), absolute phase portrait of the secondary mass (e) and relative phase portrait of the secondary mass (f) for $g \in [0.1, 0.7] m$ in correspondence of the superharmonic resonance at $\rho = 0.14$ ($1/7$)

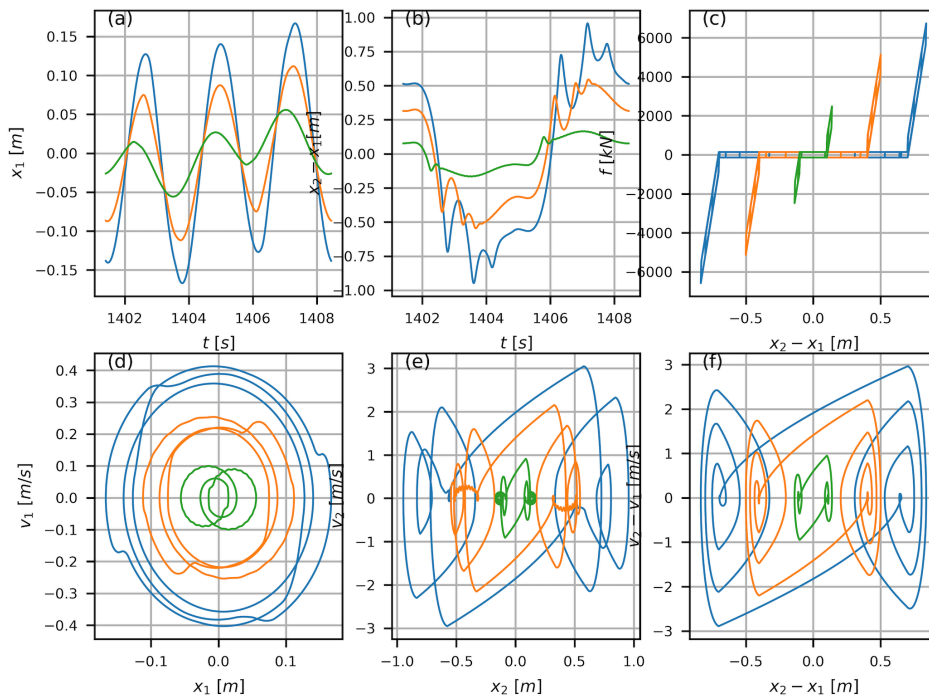


Figure 5.17: Absolute displacement of the primary mass (a), relative displacement of the secondary mass (b), relative force-displacement loop of the slider (c), absolute phase portrait of the primary mass (d), absolute phase portrait of the secondary mass (e) and relative phase portrait of the secondary mass (f) for $g \in [0.1, 0.7] m$ in correspondence of the superharmonic resonance at $\rho = 0.33$ ($1/3$)

bumpers, shown in Figure 5.13, it is immediate to see the transition from extremely negative efficiency values (Fig. 5.13 c) towards a highly positive façade efficiency (Fig. 5.15 c), whose trend is to double as g tightens; hence, starting from $\zeta = 20\%$ for $g = 0.70 m$, it goes beyond $\zeta = 80\%$ if related to $g = 0.10 m$.

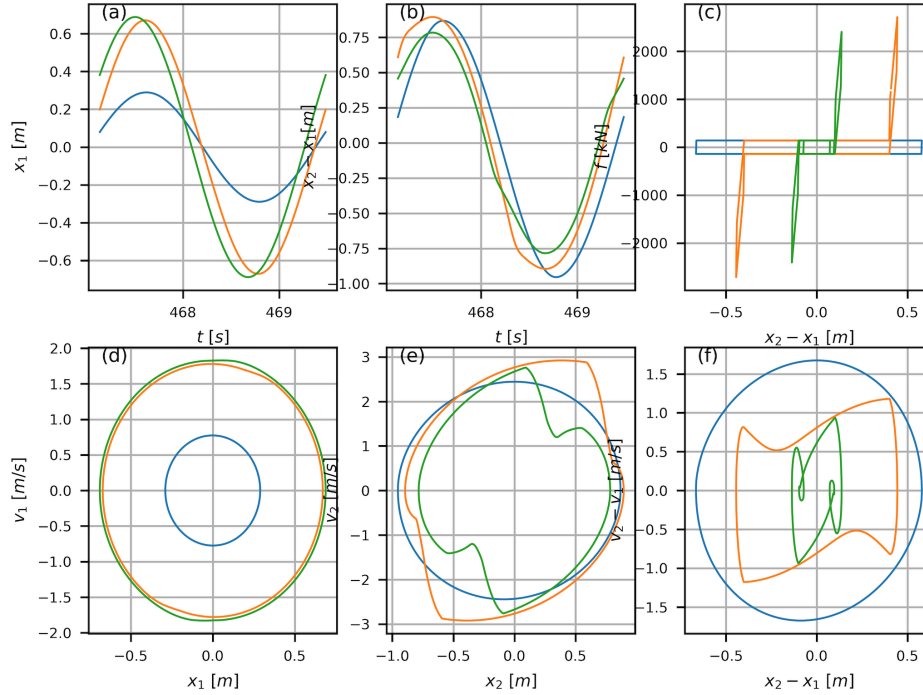


Figure 5.18: Absolute displacement of the primary mass (a), relative displacement of the secondary mass (b), relative force-displacement loop of the slider (c), absolute phase portrait of the primary mass (d), absolute phase portrait of the secondary mass (e) and relative phase portrait of the secondary mass (f) for $g \in [0.1, 0.7] m$ in correspondence of the primary resonance at $\rho = 1.0$

In general, for any tested value of the initial gap, g , an almost always positive efficiency, ζ , is achieved thus proving the success of the bumpers in containing the façade relative displacement within the limit value of $0.75 m$, defined in the design phase of the connectors. Nevertheless, the largely positive result achieved in the MF response is offset by a drop in the structural displacement efficiency, η , to which a shrinking of the positive efficiency region is also added, with the only exception represented by an isolated spike greater than 40% recorded in correspondence with the primary resonance at $\rho = 1.0$ (Fig. 5.15 a). A similar trend is also reflected in the structural acceleration efficiency curve, κ , shown in Figure 5.15 b, with the best results in terms of compliance with occupants' comfort related to a narrow gap ($\kappa = 30\%$ for $g = 0.10 m$).

The effect of a resizing of the gap width on the system's response is well highlighted in the hysteretic response diagrams portrayed in Figures 5.16-5.19, recorded at superharmonic resonances ($\rho = 0.14, 0.33$), at primary resonance ($\rho = 1.0$) and at high excitation frequency ($\rho = 1.2$), respectively, for $g \in [0.1, 0.7] m$. Time histories, force-displacement cycles and phase portraits clearly show the strong influence of a narrowing or widening of the gap on the reduction of the monolithic MF response, highlighting how the bumpers thus conceived

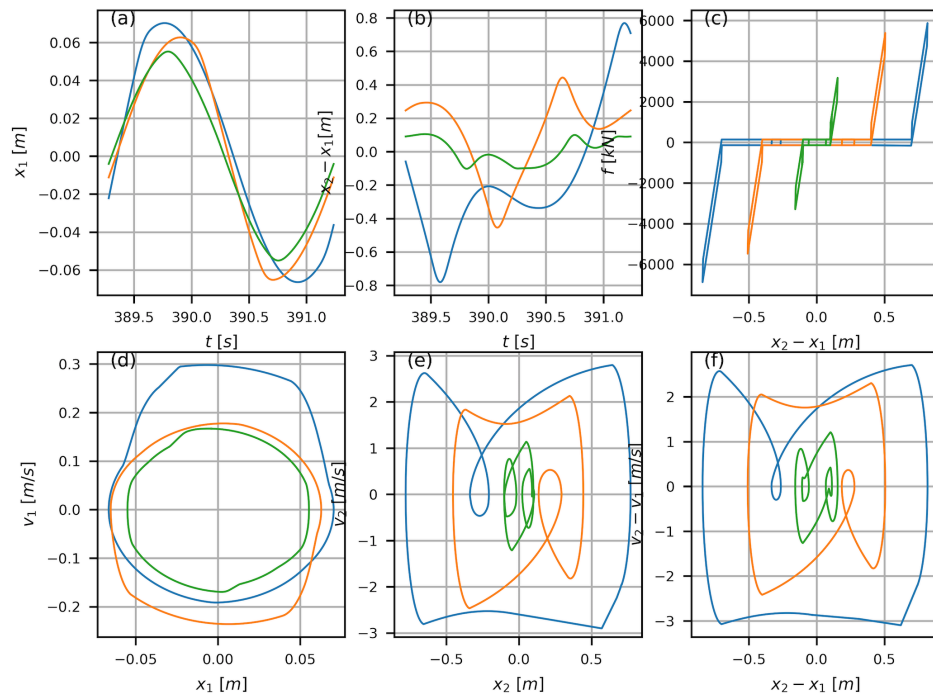


Figure 5.19: Absolute displacement of the primary mass (a), relative displacement of the secondary mass (b), relative force-displacement loop of the slider (c), absolute phase portrait of the primary mass (d), absolute phase portrait of the secondary mass (e) and relative phase portrait of the secondary mass (f) for $g \in [0.1, 0.7] m$ in correspondence of high-frequency excitation at $\rho = 1.2$

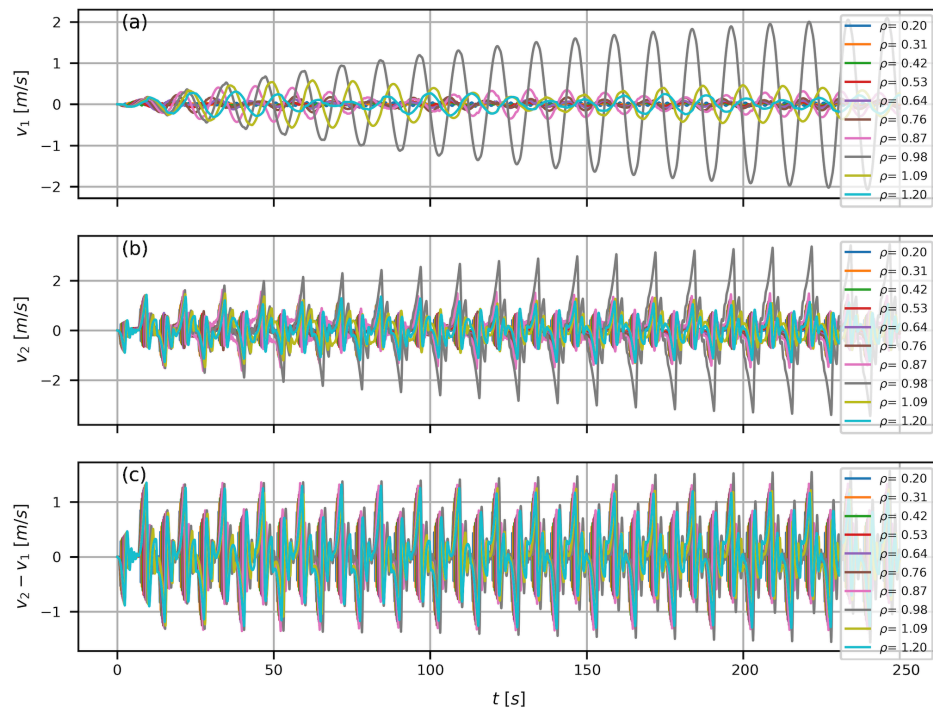


Figure 5.20: Time histories of (a) absolute velocity of the primary mass, v_1 (b) absolute velocity of the secondary mass, v_2 , and (c) relative velocity between the primary and secondary mass, $v_2 - v_1$, for $g = 0.1 m$ in $\rho \in [0.2, 1.2]$

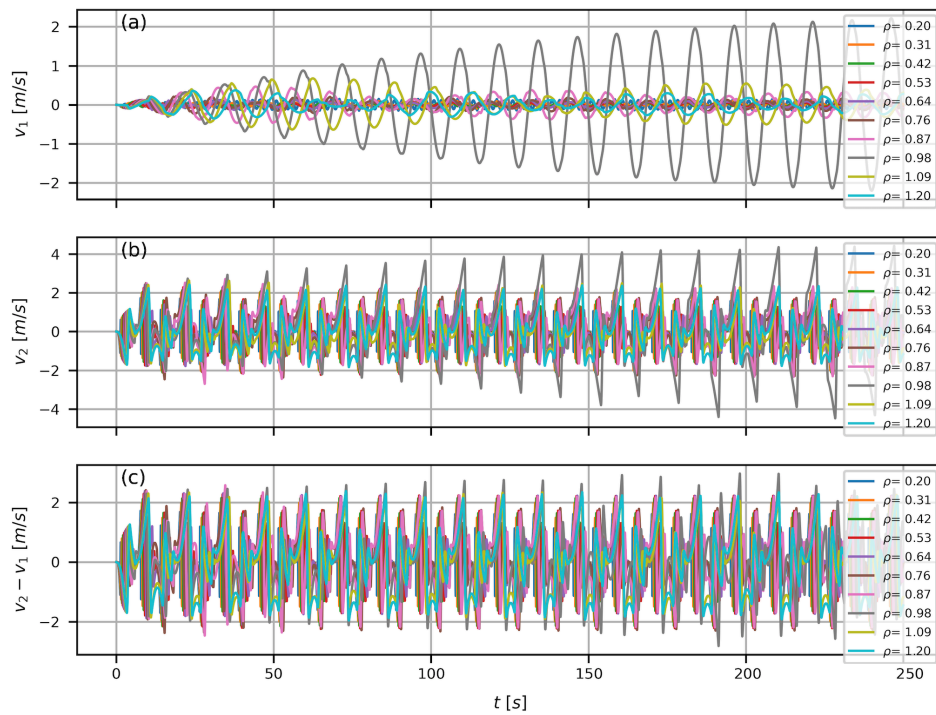


Figure 5.21: Time histories of (a) absolute velocity of the primary mass, v_1 (b) absolute velocity of the secondary mass, v_2 , and (c) relative velocity between the primary and secondary mass, $v_2 - v_1$, for $g = 0.4 m$ in $\rho \in [0.2, 1.2]$

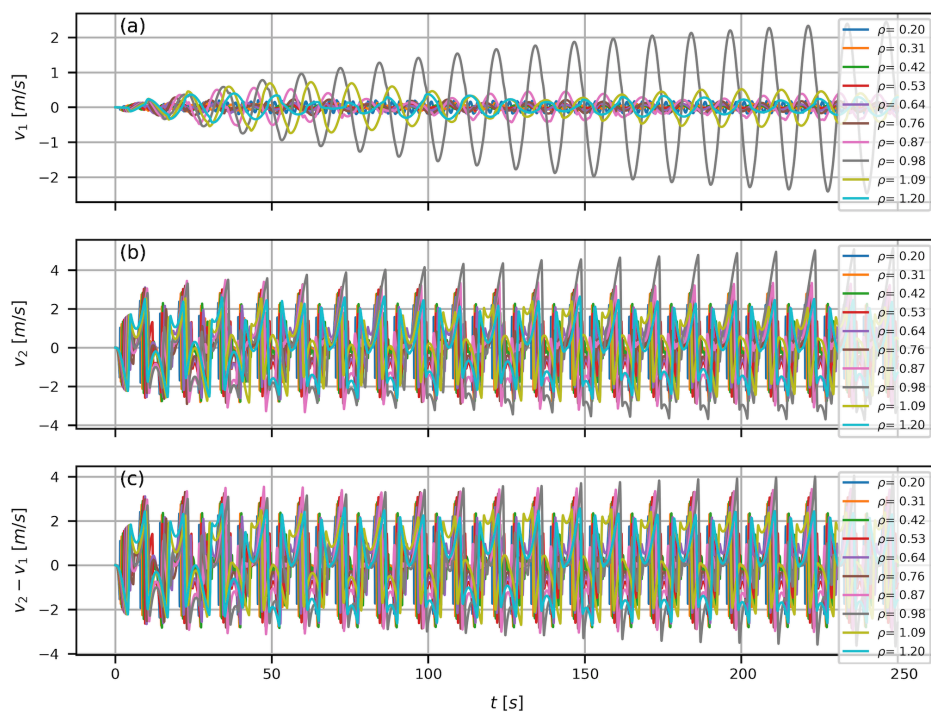


Figure 5.22: Time histories of (a) absolute velocity of the primary mass, v_1 (b) absolute velocity of the secondary mass, v_2 , and (c) relative velocity between the primary and secondary mass, $v_2 - v_1$, for $g = 0.7 m$ in $\rho \in [0.2, 1.2]$

Table 5.3: Equivalent viscous damping (EVD) ratios for variable initial gaps, g

	g [m]									
	0.10	0.17	0.23	0.30	0.37	0.43	0.50	0.57	0.63	0.70
ξ_{eq} [%]	11.27	11.41	11.44	11.42	11.36	11.27	11.19	11.12	10.98	10.96

and modeled are able to stop the façade motion when the imposed gap is reached, allowing a progressively less depth of the maximum penetration into the rubber layer during the contact between the slider and the bumper as the gap decreases.

The transition in the time domain makes it possible to analyze the complex and sophisticated nonlinear response of the bumper for a fixed value of the gap, as the forcing frequency ratio, ρ , varies. Figures 5.20, 5.21 and 5.22 show the time histories of absolute velocity of the structure (a) and façade (b) and the relative velocity between the two masses (c) for $g = 0.10, 0.40$ and 0.70 m, respectively, within the range $\rho \in [0.2, 1.2]$. As can be seen, the repeated contacts between the friction slider and the rubber bumper determine the succession of higher velocity peaks in the response of the secondary mass investigated in a time interval of 250 s, which tend to grow progressively as they approach the primary resonance ($\rho = 1.0$) and then decrease at high frequencies ($\rho = 1.2$).

As performed in the previous section, the evaluation of the equivalent viscous damping is also made with respect to variable initial gaps, assuming a 5% elastic damping ratio according to literature. The EVD ratios obtained are listed in Table 5.3.

Findings reached in this section allow to argue that a constructively acceptable relative displacement of the façade is constrained by the design of a connection device characterized by a narrow initial gap between the slider and the bumper. In this way, the issue of façade excessive motion would seem to be solved, at the price of a reduction of positive structural efficiency related to the bumpers' nonlinear behavior.

5.6.2 Influence of the impact stiffness

The last section of the investigation focuses on the parameterization of the impact stiffness of the bumper, expressed by the parameter k_h (in MN/m). Based on results of the previous sections, a low friction ratio, $\alpha = 0.2$, which ensures the reduction of the structural response compared to the *uncontrolled* case, \bar{u} , and a narrow initial gap, $g = 0.10$ m, for a well containment of façade relative displacements within the pre-set threshold, $\bar{v} = 0.75$ m, are fixed. The qualitative range for evaluating the influence of the impact stiffness on the system's response is based on the value of k_h computed in Eq. 4.37, hence

$$100 \leq k_h \leq 500 \text{ MN/m} \quad (5.118)$$

The structure and façade normalized displacement curves for $k_h \in [100, 500]$ MN/m are portrayed in Figure 5.23. As shown in Figure 5.23 a, the impact stiffness seems to have any noticeable effect on the dynamic response of the primary building mass, as any variation

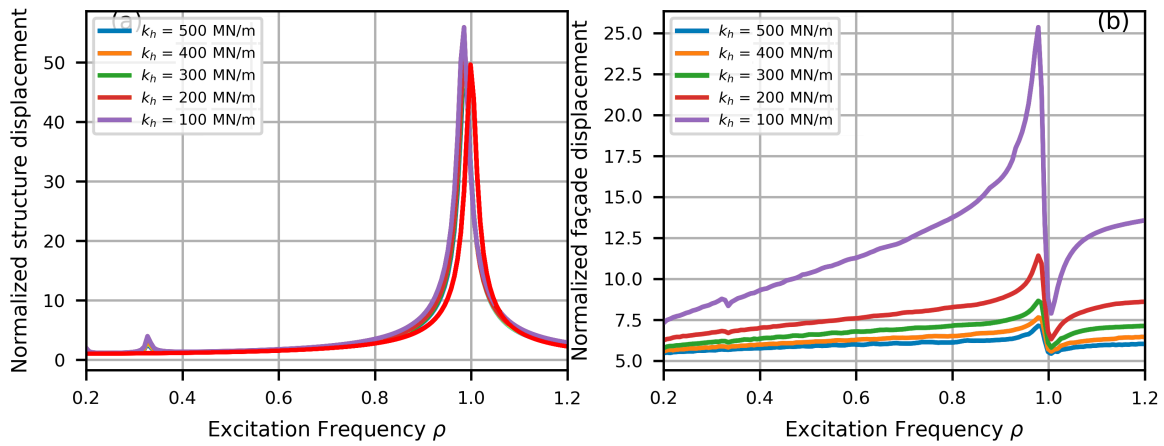


Figure 5.23: Frequency-response curves for the maximum displacements of the main structure (a) and façade (b) with $k_h \in [100, 500]$ MN/m, $\alpha = 0.2$ and $g = 0.10$ m. Displacements are normalized with respect to the static displacement f/k . The red curve represents the maximum displacement of the structure without MF

towards higher or lower values leaves the structural response curve unchanged on the previously selected friction threshold and initial gap imposed. Rather, the absolute displacement curve of the MF-equipped primary building mass is almost indistinguishable from that of the same mass in the absence of MF (red curve) proving that, under this combination of design parameters, the expected purpose of reducing the building response cannot be achieved. As in the previous case, an opposite trend results from the response of the secondary mass with the variation of the bumpers' impact stiffness (Fig. 5.23 b).

As it was easy to guess, the higher k_h , the more the relative displacement of façade is mitigated: by impacting against a more rigid bumper layer (blue curve corresponding to $k_h = 500$ MN/m), the relative sliding of the friction device is immediately locked without the possibility of a further penetration during the contact and this results in an immediate stop of the façade movement. On the contrary, a more deformable impact layer represented by a lower k_h value (green curve corresponding to $k_h = 100$ MN/m) involves a greater penetration of the slider into the rubber bumper in the contact between them, with the façade undergoing larger displacements compared to the structure, not being locked instantly.

The dynamic response of the 2DOF system for variable impact stiffnesses shown in the FRC of Figure 5.23, is reflected in Figure 5.24 which shows the efficiency curves for both structural displacement (a) and acceleration (b) and for the façade relative displacement (c) with variable impact stiffnesses. As for the structural efficiency, η , this proves to be almost insensitive to any variation of k_h , as no beneficial or disadvantageous effect is obtained by increasing or reducing the impact stiffness and the efficiency curve keeps constant with respect to the initial gap imposed, offering a graph faithful to that shown in Figure 5.15 a. The acceleration efficiency, κ , differs substantially from the displacement curve, showing that the impact stiffness of the bumpers greatly affects the acceleration response of the primary mass. In particular, stiffer bumper layers (blue curve) are responsible for greater accelerations, hence, reduced efficiency; on the contrary, more flexible bumpers (purple curve) produce

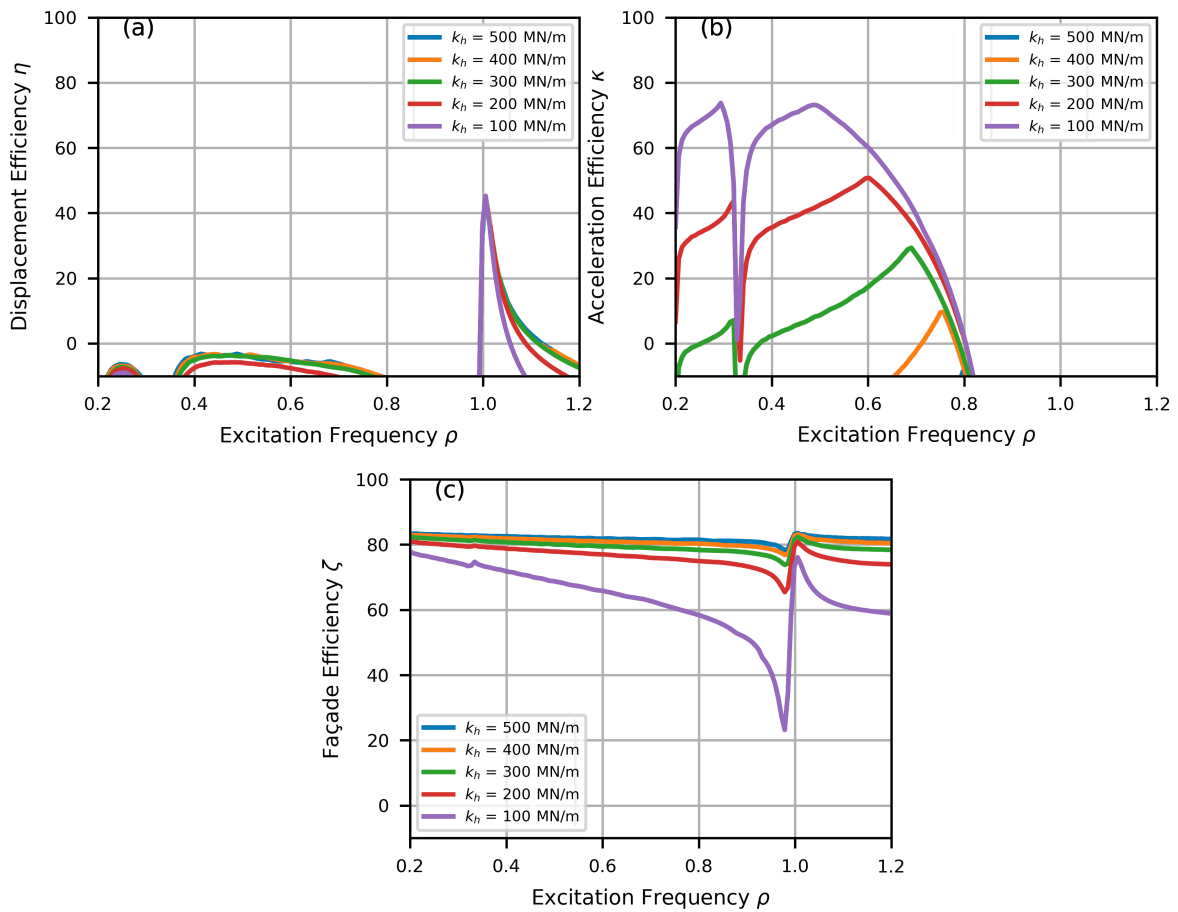


Figure 5.24: Displacement efficiency η (a), acceleration efficiency κ (b) and façade efficiency ζ (c) for $k_h \in [100, 500]$ MN/m

lower accelerations, hence, greater efficiencies (almost 80%).

Despite a substantial indifference of the structure to the variation of k_h , on the contrary, the possibility of reaching a positive façade vibration efficiency, ζ , over the entire frequency range is closely related to this parameter, which can be assumed as a key variable for the purpose of reducing the MF relative displacements. Clearly, the façade efficiency is higher as the impact stiffness increases and this is consistent with the fact that the slider collides with a stiffer layer which prevents further sliding, instantly locking the façade movement (blue curve corresponding to $k_h = 500$ MN/m). This results in an always positive efficiency, moving from a maximum of 84% in correspondence with the primary resonance at $\rho = 1.0$ to a minimum of 78% at $\rho = 0.97$. Conversely, a more flexible and deformable impact layer would be able to stop the sliding of the device in a longer time, allowing the façade to undergo larger displacements (purple curve corresponding to $k_h = 100$ MN/m), with a consequent slight reduction in the efficiency which switches to 75% at resonance and to 27% at $\rho = 0.97$.

As stated earlier, the addition of high-stiffness dissipative rubber bumpers to the friction slider entails greater complexity in the dynamic response of the connection device, essentially related to the strongly nonlinear behavior of bumpers. Despite this, it is precisely this mechanism that allows the excessive and impractical relative displacements of MF to be

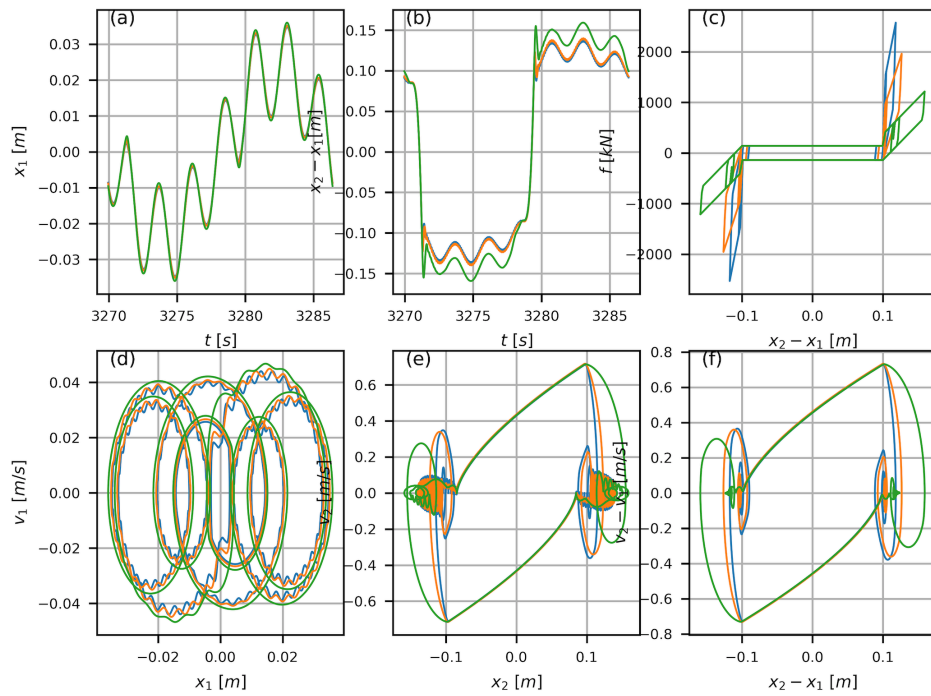


Figure 5.25: Absolute displacement of the primary mass (a), relative displacement of the secondary mass (b), relative force-displacement loop of the slider (c), absolute phase portrait of the primary mass (d), absolute phase portrait of the secondary mass (e) and relative phase portrait of the secondary mass (f) for $k_h \in [100, 500]$ MN/m at $\rho = 0.14$ (1/7)

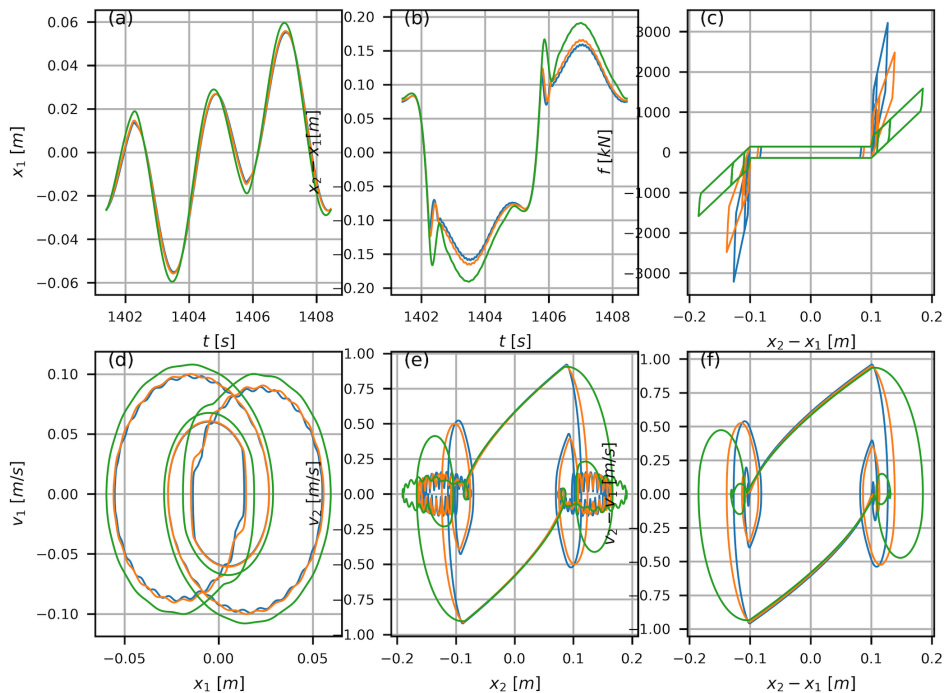


Figure 5.26: Absolute displacement of the primary mass (a), relative displacement of the secondary mass (b), relative force-displacement loop of the slider (c), absolute phase portrait of the primary mass (d), absolute phase portrait of the secondary mass (e) and relative phase portrait of the secondary mass (f) for $k_h \in [100, 500]$ MN/m at $\rho = 0.33$ (1/3)

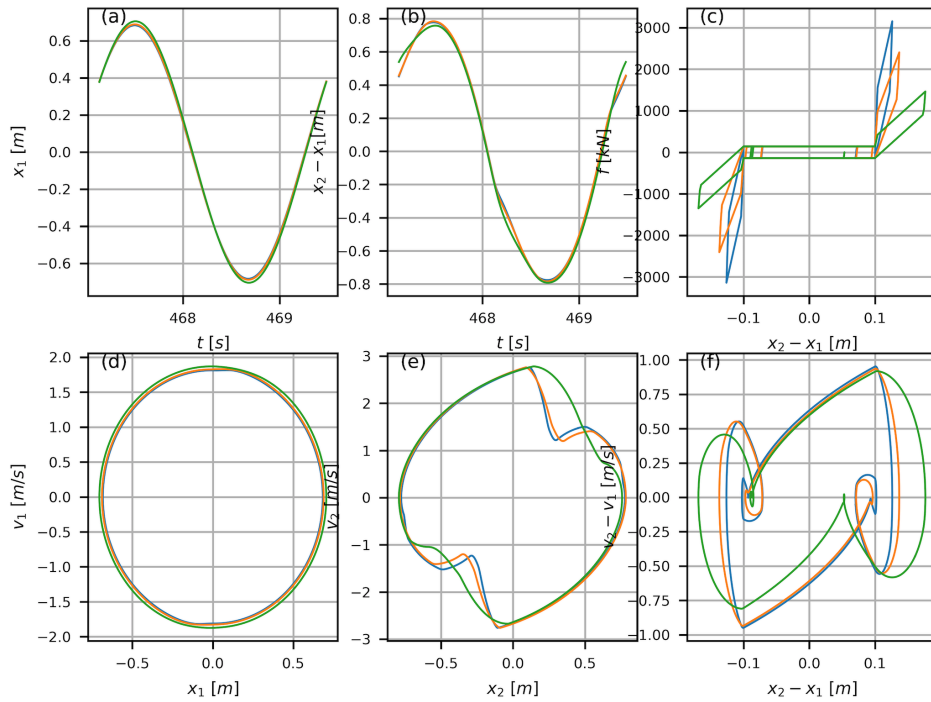


Figure 5.27: Absolute displacement of the primary mass (a), relative displacement of the secondary mass (b), relative force-displacement loop of the slider (c), absolute phase portrait of the primary mass (d), absolute phase portrait of the secondary mass (e) and relative phase portrait of the secondary mass (f) for $k_h \in [100, 500]$ MN/m at $\rho = 1.0$

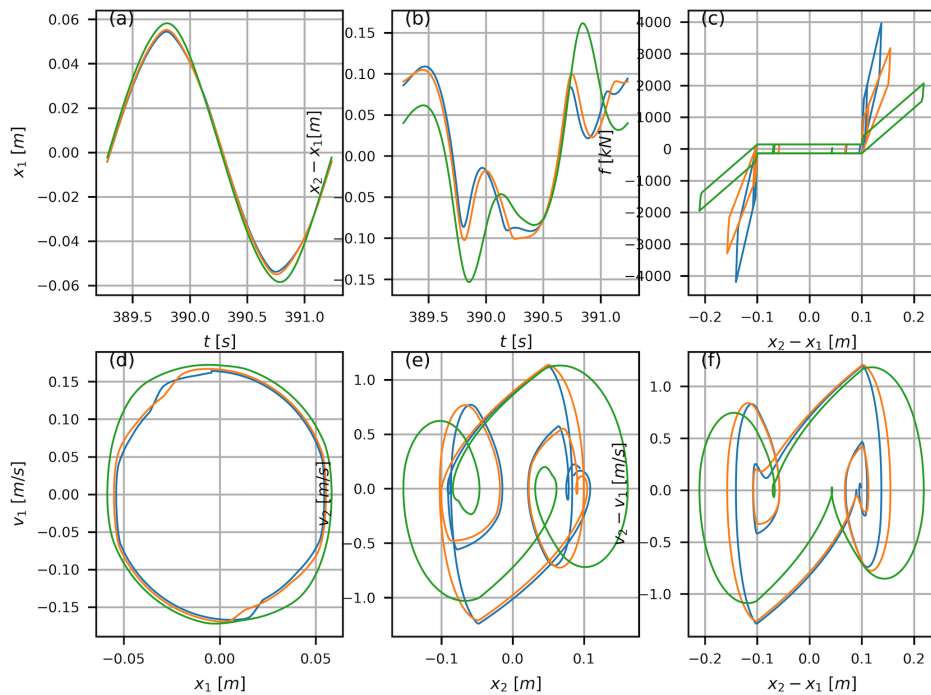


Figure 5.28: Absolute displacement of the primary mass (a), relative displacement of the secondary mass (b), relative force-displacement loop of the slider (c), absolute phase portrait of the primary mass (d), absolute phase portrait of the secondary mass (e) and relative phase portrait of the secondary mass (f) for $k_h \in [100, 500]$ MN/m at $\rho = 1.2$

Table 5.4: Equivalent viscous damping (EVD) ratios for variable impact stiffnesses, k_h

	k_h [MN/m]								
	100	150	200	250	300	350	400	450	500
ξ_{eq} [%]	11.29	10.85	10.78	10.32	10.18	10.22	10.45	10.81	10.65

stopped, with a more or less incident measure depending on the stiffness which realizes the shock-absorption layer. This aspect clearly emerges from the sophisticated hysteretic force-displacement diagrams and phase portraits depicted in Figures 5.25-5.28 for $k_h \in [100, 500]$ MN/m. The plots are generated at the superharmonic resonances, $\rho = 0.14$ and $\rho = 0.33$, at the primary resonance, $\rho = 1.0$ and at high frequency, $\rho = 1.2$, respectively. Furthermore, the EVD ratios associated with each force-displacement loop derived from the parameterization of the impact stiffness, k_h , are summarized in Table 5.4.

5.7 Results and discussion

The vibration damping performances of a monolithic Movable Façade connected to a generic mid-rise building by means of a friction slider with dissipative bumpers were evaluated through parametric nonlinear dynamic analyses in the previous sections. For each of the connector design parameters (i.e. the friction threshold of the slider, α , the initial gap, g , and the impact stiffness of the bumper, k_h) the reduction efficiency of both structural displacement and acceleration, and the façade relative displacement at a given forcing frequency, ρ , were explored with the introduction of suitably normalized frequency-dependent local indices (η , κ and ζ).

The introduction of the global indicators, E_η , E_κ and E_ζ , defined in Eq. 5.110, is useful to get the integrated value of the three efficiencies η , κ and ζ using the composite Simpson's rule and to quantify the overall areas of positive efficiency calculated over the entire frequency range, ρ . This allows to evaluate the results of the analyses in an overall way and not on a single frequency.

Figure 5.29 shows the three positive efficiency areas for variable friction threshold α . The displacement efficiency of both the structure (E_η) and façade (E_ζ) are superimposed on the same plot in Figure 5.29 a for a clearer and more immediate reading of their opposite behavior. As a matter of fact, while E_η and E_κ provide the best results for low α values (80% when $\alpha = 0.1$), which progressively decrease as the friction force increases, the façade efficiency E_ζ (orange curve) shows an opposite trend to that of the structure (blue curve), being negative for low friction thresholds (up to $\alpha = 0.5$) and reaching maximum efficiency levels for $\alpha = 1.0$. This result is consistent with the fact that for high friction force the MF sticks to the structure reducing the system to a SDOF oscillator.

Figure 5.30 shows the effect of the gap variation on the structural and façade response. Compared to the previous case, there is a clear reduction in both displacement and acceleration efficiency, with E_η and E_κ that fall almost close to zero and do not undergo variations

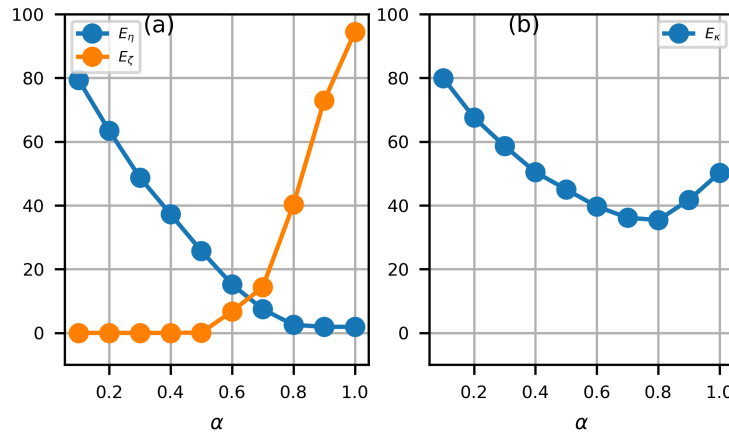


Figure 5.29: Positive efficiency areas for variable friction threshold, α : (a) superposition of the structure efficiency E_η (blue curve) and the façade efficiency E_ζ (orange curve) and (b) acceleration efficiency E_κ

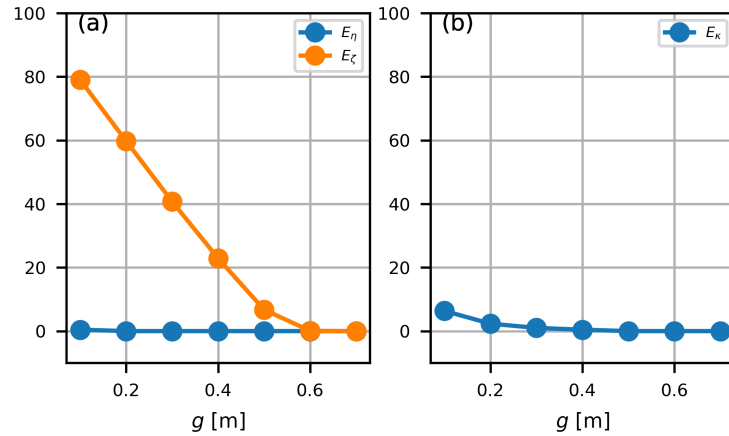


Figure 5.30: Positive efficiency areas for variable initial gap, g : (a) superposition of the structure efficiency E_η (blue curve) and the façade efficiency E_ζ (orange curve) and (b) acceleration efficiency E_κ

as the initial gap extends. The only exception to this negative trend is represented by the acceleration efficiency which rises to almost 10% for $g = 0.10$ m. As for the façade efficiency E_ζ (orange curve), the best result is obtained with narrow initial gaps which immediately limit the sliding of the friction device, locking relative displacements greater than those allowed by the fixed gap width. Observing the curves, it can be seen that with a minimum gap, such as $g = 0.10$ m, an efficiency of 80% is achievable; on the contrary, E_ζ drops to zero with a larger gap, such as $g = 0.70$ m.

Focusing on the stiffness effect in Figure 5.31, the displacement efficiency E_η does not undergo appreciable variations when the bumper layer stiffens: as shown by the blue curve in Figure 5.31 a, it tends to grow slightly for high values of k_h , keeping however on efficiency values of the order of 1%. On the other hand, the impact stiffness of the bumper seems to have an effect above all on the acceleration efficiency E_κ , which tends to increase as k_h decreases and vice versa, as shown in Figure 5.31 b. As it could be guessed, a more stiff

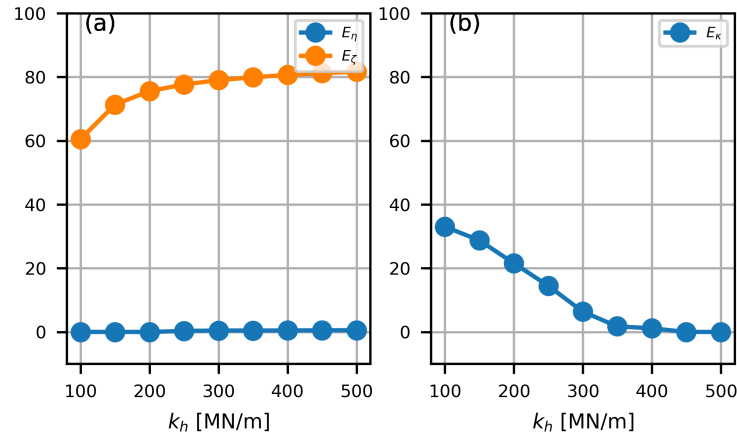


Figure 5.31: Positive efficiency areas for variable impact stiffness, k_h : (a) superposition of the structure efficiency E_η (blue curve) and the façade efficiency E_ζ (orange curve) and (b) acceleration efficiency E_κ

shock-absorber layer involves a greater acceleration peak in the structural response with consequent reduction of the efficiency ($E_\kappa = 0$ for $k_h = 500$ MN/m), vice versa, a more deformable bumper impacts less violently with the primary mass, bringing the efficiency to 33% for $k_h = 100$ MN/m. As expected, an opposite trend is obtained on the façade efficiency E_ζ (orange curve) which reaches high values especially for $k_h = 500$ MN/m (about 82.5%).

To summarize, the dynamic response of the 2DOF system significantly depends on the combination of the friction threshold, the initial gap and the impact stiffness of the bumper assumed for the numerical investigation. Choosing one combination rather than another could result in a completely different behavior of the system, hence a suitable design of the connection device should be made that takes into account both the structural and the Movable Façade dynamic response.

5.8 Closing remarks

Vibration damping performances of a monolithic MF incorporated with friction sliders and a system of dissipative rubber bumpers into a typical 25-storey, 77.5 m tall structural building are explored in the present Chapter. With the aim of helping to solve the still open issue of unacceptable façade relative displacements (Moon’s problem), while ensuring a suitable structural vibration control, a preliminary investigation is performed on an equivalent harmonically excited 2DOF system representing the monolithic MF-equipped multi-storey building. In order to explore the influence of the key variables characterizing the behavior of the connection device on the overall system’s response, a parametric study is conducted, which is developed into two separate parts depending on whether only the friction slider works (in the so-called *sliding* mode) or even the impact bumpers are active (determining the transition to the *sliding-bumping* mode). With the introduction of suitable numerical indexes normalized with respect to well-defined reference conditions, a better assessment of the structural displacement (η) and acceleration (κ) efficiency provided by the slider and

the façade displacement efficiency (ζ) provided by the bumpers is ensured. The first part of the analysis evaluates the effect of the friction threshold, expressed by means of the friction ratio (α), on the dynamic performances of the slider alone, showing that low friction values allow for a strong improvement in the structural control at the expense of a worsening in the MF response, which undergoes wide relative displacements mainly located at low excitation frequencies. The occurrence of Moon's problem justifies the transition to the second part of the study, which is focused on the evaluation of the bumpers' effectiveness in limiting the façade motion with respect to a design threshold displacement. Here, the parameterization involves two main variables: the size of the initial gap between the masses (g) and the impact stiffness of the bumper (k_h). In general, the addition of dissipative rubber bumpers has proved to be successful in containing the façade excessive movement within a pre-established maximum opening allowed by the technological cladding layout ($\bar{v} = 0.75 m$). Specifically, narrow gaps allow to further reduce the façade response compared to larger openings and it is also important to see how the façade displacement efficiency could be enhanced with an increase in the impact stiffness of the bumpers. However, the balance between the vibration damping efficiency of the façade and the structure is quite delicate and strongly depends on the excitation frequency under investigation. This can result in a loss of structural efficiency over some frequency range or in a marked improvement of the overall behavior of the primary mass over another frequency range. Based on this, the need to re-evaluate the performances of Movable Façades integrated with dissipative sliders and bumpers under the more realistic scenario of buildings subject to wind actions is pointed out, as the combination of several frequencies may give different results with respect to a single-harmonic excitation. An in-depth study of this issue will be addressed in the next Chapters.

Chapter 6

Generic building with MF under wind load

6.1 Introduction

Modern structures are increasingly designed as lean and flexible constructions, characterized by low natural frequencies (between 0.1 and 0.5 Hz) and low intrinsic damping levels (of the order of 1 – 5% [246]). As is known, the vibration frequency and period of a typical building mainly depend on two fundamental characteristics: the floor masses, including both dead and live loads, and the translating stiffness of the structural system adopted, which is affected by the section and layout of the load-bearing components, such as beams, pillars and walls, and the building height. The higher the building, the more the hazard that the upper floors will experience large wind-induced oscillations and accelerations becomes real. As stated in section 2.3, wind is a rather slow signal inducing low-frequency vibrations (usually, in the range 0.01 – 0.1 Hz [247]) which tend to excite above all high-rise constructions, risking to end up in the resonance condition that could greatly amplify their dynamic response, making them susceptible to excessive top deflections and accelerations.

Movable Façades, like the well-known TMD, refer to a possible solution to the problem of wind-induced vibrations. The dynamic performances of both MF and TMD have been firstly investigated in Chapter 3 through a parametric study performed in a linear context. Despite the high potential offered by the façade system which emerged from the analysis, the noticeable façade relative displacement evidenced a serious design limitation which could not allow the application of this approach in the field of dynamic motion control. However, the proposal of a suitable friction connection device (*slider*) incorporated with shock-absorber layers (*bumpers*) interposed in the gap between the building and the smart façade system, put forward in Chapter 4, has allowed for the deepening of MF for the vibration reduction of civil buildings. A nonlinear analysis carried out in Chapter 5 on the 2DOF model of a monolithic MF-equipped generic building subject to harmonic excitation revealed the success of the connection system in containing the large relative displacement of the secondary mass, although this occurred at the expense of nonlinear dynamics phenomena which affected the

structural response, leading to a partial loss of the vibration damping efficiency for some frequencies of the excitation. To overcome the limits imposed by the use of a lumped-mass model and the adoption of a simplified load, a more realistic scenario is needed, which provides a reliable system for the installation of Movable Façades incorporated with dissipative connections into the buildings.

In the present Chapter, the dynamic performances of a monolithic MF integrated with dissipative sliders and bumpers are assessed with reference to a wind-excited mid-rise building, as this type of structure can also be wind-sensitive and controlling the top acceleration and displacement response may be needed to ensure human comfort and avoid structural damage. By means of an equivalent MDOF modeling of the structure, the effectiveness of the connection device in both controlling the structural response and suppressing the façade relative displacement during wind activities is evaluated even along the building height, which cannot be accounted for in the previous simplified 2DOF modeling.

6.2 Generality on the case study

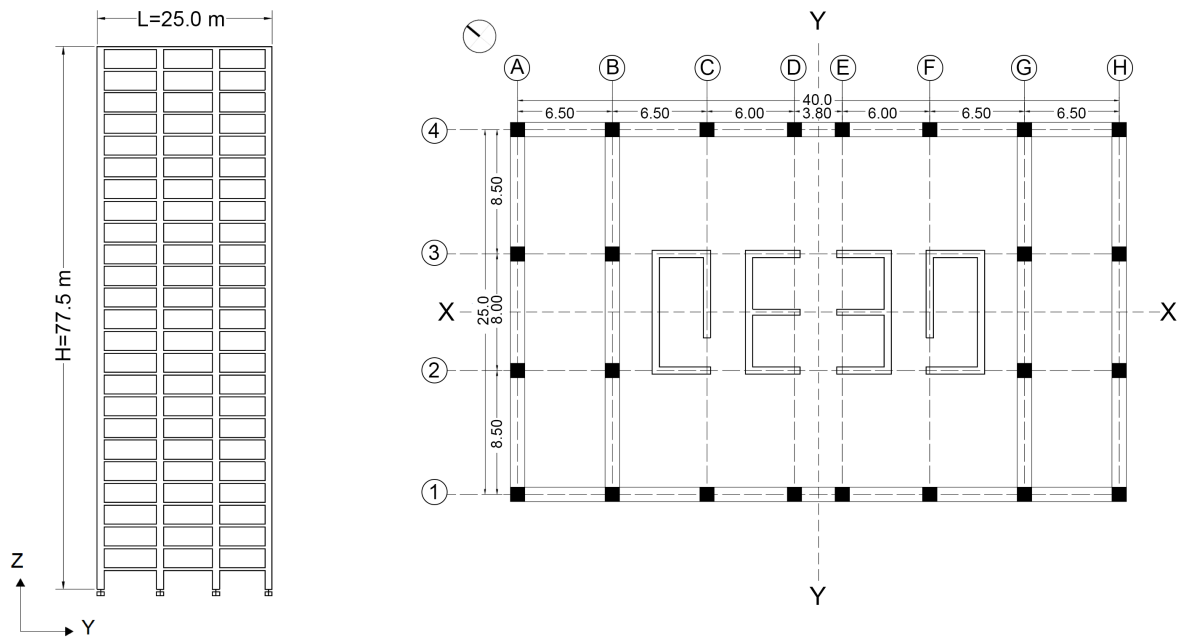


Figure 6.1: Diagram of the mid-rise building frame in the YZ plane with a typical floor plan

A 25-storey 77.5 m tall building, taken from [248], is depicted in Figure 6.1. Starting from a 40×25 m rectangular plan, in a symmetrical position with respect to the barycentric axes, the building rises up to a total height of almost 80 m, with an inter-storey height of 3.10 m. The mixed-type load-bearing structure consists of a reinforced concrete frame composed of 60×80 cm beams and 100×100 cm pillars and four baricentric cores with 50×60 cm perimeter walls. All the structural elements use the class C 40/50 RC and the A615gr60 reinforcement bar steel, whose mechanical properties are listed in Tables 6.1 and 6.2, respectively. The main dimensional elements of the building are summarized in Table 6.3. In the following tables, W_s

Table 6.1: Mechanical properties of C 40/50 reinforced concrete

W_s [kN/m ³]	M_s [tons/m ³]	E [GPa]	U [-]	A [W/mK]	G [GPa]	f_{ck} [MPa]
24.99	2.55	32	0.2	$1.0E - 05$	13	40

Table 6.2: Mechanical properties of A615-60 grade steel reinforcing bars

W_s [kN/m ³]	M_s [tons/m ³]	E [GPa]	U [-]	A_t [W/mK]	F_y [MPa]	F_{ye} [MPa]
76.97	7.849	210	0.3	$1.170E - 05$	413	455

stands for the weight per unit volume (in kN/m^3), M_s stands for the mass per unit volume (in $tons/m^3$), E and G represent the modulus of elasticity and the shear modulus (in GPa), respectively, U is the Poisson's coefficient, A_t gives the coefficient of thermal expansion (in W/mK), f_{ck} is the characteristic concrete cylinder strength (in MPa) and F_y, F_{ye} are the minimum and the expected yield stress (in MPa), respectively.

From the three-dimensional FEM of the building made up in SAP 2000, useful mechanical and material properties are obtained, from which a proper computation of the structural model depends. A modal analysis is executed to derive the dynamic properties of the building, including the vibrating modes and deformed shapes portrayed in Figure 6.2 and the natural periods and frequencies summarized in Table 6.4. Finally, a linear static analysis makes it possible to obtain the vertical reaction forces transferred at the base of the structure from dead load, allowing to estimate the total building mass, which is reported in Table 6.5. It is worth specifying that this mass value does not include the façade contribution, being intended exclusively as the mass of the structural building components. This is effectively verified by adding the contributions of the main elements making up the load-bearing structural system, including cores ($M_C = 7860$ tons), beams ($M_B = 9431$ tons) and pillars ($M_P = 4278$ tons), from which a total mass value ($M = 21569$ tons) in line with the result of the linear static analysis is gathered.

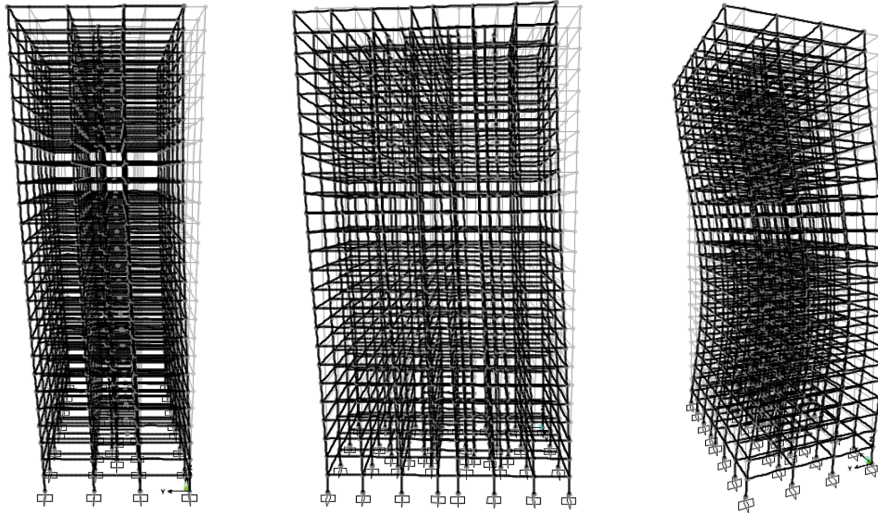
Assuming a conventional fixed cladding with 10 mm wired glass panels with a theoretical weight of $25 kg/m^2$ and $150 \times 50 \times 4$ mm extruded aluminum tubular profiles weighing about $4.14 kg/m^2$, an overall mass of approximately 335 tons is estimated, which agrees to a mass ratio $\mu = 1.55\%$, as results from Table 6.6. Clearly, for a one-sided cladding this value drops to 167.5 tons with $\mu = 0.78\%$. It is specified that the cladding mass, M_c , is added to the

Table 6.3: General characteristics of the mid-rise building

height H [m]	width B [m]	length L [m]	inter-storey height h [m]	$n.$ floor N [-]
77.5	40	25	3.10	25

Table 6.4: Modal periods and frequencies

	Frequency f [Hz]	Period T [s]	CircFreq ω [rad/s]	Eigenvalue ω^2 [rad ² /s ²]
mode 1 (y-axis)	0.426	2.344	2.679	7.180
mode 2 (x -axis)	0.709	1.409	4.459	19.88
mode 3 (torsional)	1.326	0.754	8.333	51.61

**Figure 6.2:** First three vibrating modes of the 25-storey building FEM implemented in SAP 2000: on the left, 1° flexural mode around y -axis, in the center, 2° flexural mode around x -axis; on the right, 3° torsional mode

structural mass, M_s , in order to simulate the conventional case of building with fixed façade (that is, in the absence of MF system) and, then, it is excluded from the mass computation and modeling of the MF-equipped building. In this case, in fact, the structural mass is accounted for separately with respect to the mass of the unilateral MF system, which will be calculated in section 6.5.

The dynamic behavior of the structure is studied in the two-dimensional plane, specifically, along the local y -axis, where the less lateral stiffness of the building can bring to a major wind-induced response. The choice to focus the study on the evaluation of the *along-wind* response implies the application of longitudinal forces parallel to the short side of the building plan and perpendicular to the long side. To ensure a limited time-consuming analysis, a unilateral MF system is expected to be incorporated along the wind-excited y -axis of the simulation

Table 6.5: Estimate of structural mass of the mid-rise building

OutputCase	CaseType	GlobalFZ	a_g	M	m
[-]	[-]	[kN]	[m/s ²]	[tons]	[tons/m]
Dead	Linear static	211613.644	9.81	21571.151	278.33

Table 6.6: Estimate of conventional façade mass of the mid-rise building

W_g [kg/m ²]	A_g [m ²]	$M_{g,tot}$ [tons]	W_a [kg/m]	section [mm]	$M_{f,tot}$ [tons]	M_c [tons]	M_s [tons]	μ [%]
25	6200	310	4.14	150 × 50 × 4	25	335	21571	1.55

domain. As a result, in the dynamic façade-structure interaction, the relative motion in the *along-wind* direction is the only movement allowed, while both the rotation and translation along the x -axis are prevented.

6.3 Equivalent MDOF modeling

The complex and time-consuming three-dimensional FEM of the multi-storey building requires the transition to a simplified and equivalent numerical model capable of suitably simulating the behavior of the real structure from a dynamic point of view. At this level of analysis, a simple SDOF lumped-mass system is not reliable enough to approximate it, thus a more refined MDOF distributed-mass model is used for the purpose. With reference to a typical shear-type deflection observed from the first vibrating mode around the local y -axis, the mid-rise building structure is schematized as a distributed-mass cantilever beam constrained at the base with a free end at the top. A circular section beam with constant elastic stiffness along the height, H , is taken, as portrayed in Figure 6.3.

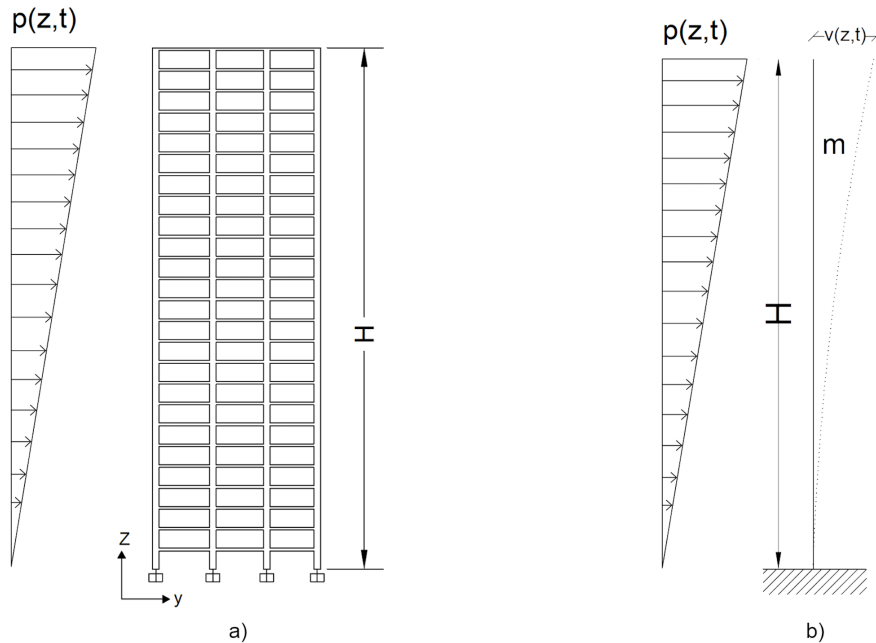


Figure 6.3: Transition from the 25-storey structural frame (a) to an equivalent cantilever beam model (b) subject to a linear distribution of wind pressures, $p(z,t)$

The equivalent parameters of the MDOF beam model are derived from the mechanical and dynamic properties of the building. It should be noted that the resulting parameters of

the equivalent numerical model have no physical meaning, therefore they may substantially differ from real ones. The matching of the equivalent MDOF model to the complete model of the building is successful if the natural frequency (f_1) and period (T_1) related to the 1st vibrating mode are met. From the cantilever beam diagram used to describe the static behavior of the multi-storey structure, the following parameters have been calibrated to be assigned to the MDOF beam model in Python environment:

- elastic modulus of the material used, E [GPa]
- tangential modulus of elasticity, G [GPa]
- cross-sectional area of the element, A [m^2]
- moment of inertia with respect to local z -axis, J_z [m^4]
- shear-area with respect to local y -axis, A^* [m^2]

Firstly, the equivalent modeling process requires the computation of the following mechanical properties for the cores:

- Area, A [m^2]
- Volume, V [m^3]
- Moments of inertia with respect to the two main axes, J_x and J_y [m^4]
- Mass, M [tons]
- Stiffness, K [kN/m]

The behavior of the four baricentric cores is suitably simulated with a flexural cantilever beam (sketched in Fig. 2.31 a) of length, L , equal to the total height of the building, H . For a typical flexural deflection, the bending stiffness, K , can be obtained by applying the well-known formula

$$K = \frac{3EJ}{l^3} \quad (6.1)$$

where E is the concrete elastic modulus, l [m] is the total beam length and J_i is the moment of inertia with respect to the i -th axis.

Being interested in evaluating the response of the building along the main y -axis, the inertia of the four cores with respect to the barycentric x -axis, J_x , is taken (Fig. 6.4), which is computed according to the Transport Theorem, $J_x = J_{x^*} + Y_G^2 \cdot A$

$$J_{x,1} = 2 \left[\left(\frac{1}{12} 3(0.5)^3 \right) 2 + \left(\frac{1}{12} 0.5(8.5)^3 \right) 2 \right] = 102 \quad m^4 \quad (6.2)$$

$$J_{x,2} = 2 \left[\left(\frac{1}{12} 3.25(0.5)^3 \right) 3 + \left(\frac{1}{12} 0.5(8.5)^3 \right) \right] = 51.38 \quad m^4 \quad (6.3)$$

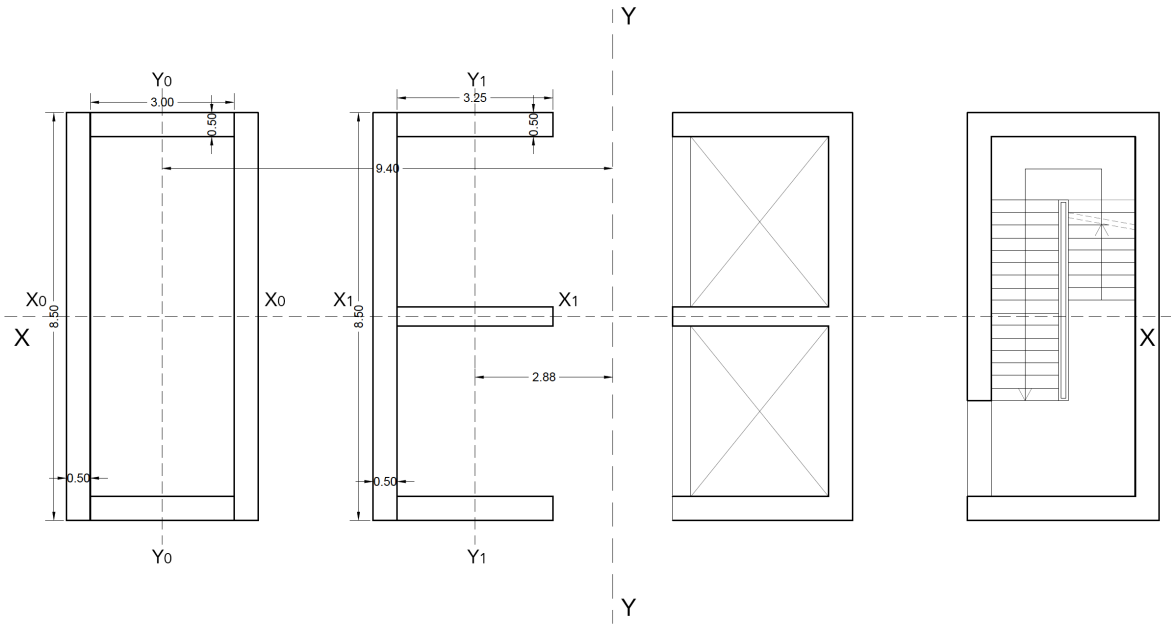


Figure 6.4: Computation of the core's inertia with respect to the barycentric x -axis, J_x

Table 6.7: Mechanical properties of the cores

A [m^2]	V [m^3]	M [tons]	J_x [m^4]	J_y [m^4]	K_x [kN/m]	K_y [kN/m]
40.60	136.71	$7.86E + 03$	153.86	$2.33E + 03$	$3.17E + 04$	$4.81E + 05$

$$J_x = J_{x,1} + J_{x,2} = 153.86 \quad m^4 \quad (6.4)$$

For completeness, the computation of the inertia with respect to the barycentric y -axis is also reported

$$J_{y,1} = 2 \left[\left(\frac{1}{12} 3(0.5)^3 \right) 2 + \left(\frac{1}{12} 0.5(8.5)^3 \right) 2 + (9.4)^2 11.5 \right] = 2134.76 \quad m^4 \quad (6.5)$$

$$J_{y,2} = 2 \left[\left(\frac{1}{12} 3.25(0.5)^3 \right) 3 + \left(\frac{1}{12} 0.5(8.5)^3 \right) + (2.88)^2 8.80 \right] = 197.36 \quad m^4 \quad (6.6)$$

$$J_y = J_{y,1} + J_{y,2} = 2332.12 \quad m^4 \quad (6.7)$$

The mechanical properties of the four concrete cores are listed in Table 6.7. As expected, the inertia with respect to the y -axis, J_y , is much greater than that related to the x -axis, J_x .

As for the 24 reinforced concrete columns, a typical shear-type deflection (sketched in Fig. 2.31 b) is assumed to simulate their dynamic behavior, therefore the standard formula

Table 6.8: Mechanical properties of the columns

A [m^2]	V [m^3]	M [$tons$]	J_x [m^4]	J_y [m^4]	K_x [kN/m]	K_y [kN/m]
24.0	74.4	$4.27E + 03$	2630	5419.4	$2.17E + 06$	$4.47E + 06$

may be used to evaluate the stiffness of the pillars

$$K = \frac{12EJ}{l^3} \quad (6.8)$$

The computations of the inertia with respect to the two main axes, x and y , J_x and J_y , performed in accordance with the aforementioned Transport Theorem, are given below

$$J_x = 16 \left[\frac{1}{12}(1)^4 + (12.5)^2 \right] + 6 \left[\frac{1}{12}(1)^4 + (4)^2 \right] = 2630 \quad m^4 \quad (6.9)$$

$$J_y = 4 \left[\frac{1}{12} + (1.9)^2 \right] + 4 \left[\frac{1}{12} + (7.9)^2 \right] + 8 \left[\frac{1}{12} + (14.4)^2 \right] + 8 \left[\frac{1}{12} + (20.9)^2 \right] = 5419.4 \quad m^4 \quad (6.10)$$

The main mechanical properties of the columns are summarized in Table 6.8. Based on this, it is possible to derive the parameters of the equivalent beam model. Given the elastic modulus, E , of C 40/50 reinforced concrete, the tangential modulus of elasticity, G , is derived knowing that the latter is equal to 40% of E

$$G = \frac{E}{2(1 + \nu)} \quad (6.11)$$

where ν is the Poisson's ratio.

Assuming a circular section beam element, the diameter, D_{EQ} , is determined adding the inertia of the core and pillars with respect to the barycentric x -axis, J_x

$$J_x = \frac{\pi D^4}{64} \Rightarrow D^{EQ} = \sqrt[4]{\frac{64J_x}{\pi}} = 15.431 \quad m \quad (6.12)$$

From the flexural stiffness, K , the concrete elastic modulus, E , and the inertia, J_x , it is possible to define the length, L_{EQ} , of the equivalent beam element, matching the stiffness related to the fundamental mode of the building

$$K = \frac{3EJ_x}{L^3} \Rightarrow L^{EQ} = \sqrt[3]{\frac{3EJ_x}{K}} = 77.49 \quad m \quad (6.13)$$

The cross-sectional area of the cylinder, A_{EQ} , is computed from the equivalent diameter, D_{EQ} , according to

$$A^{EQ} = \pi \cdot r^2 = 187.037 \quad m^2 \quad (6.14)$$

A shear-area, A^* , expressed as a percentage of the cross-sectional area, A^{EQ} , is assumed,

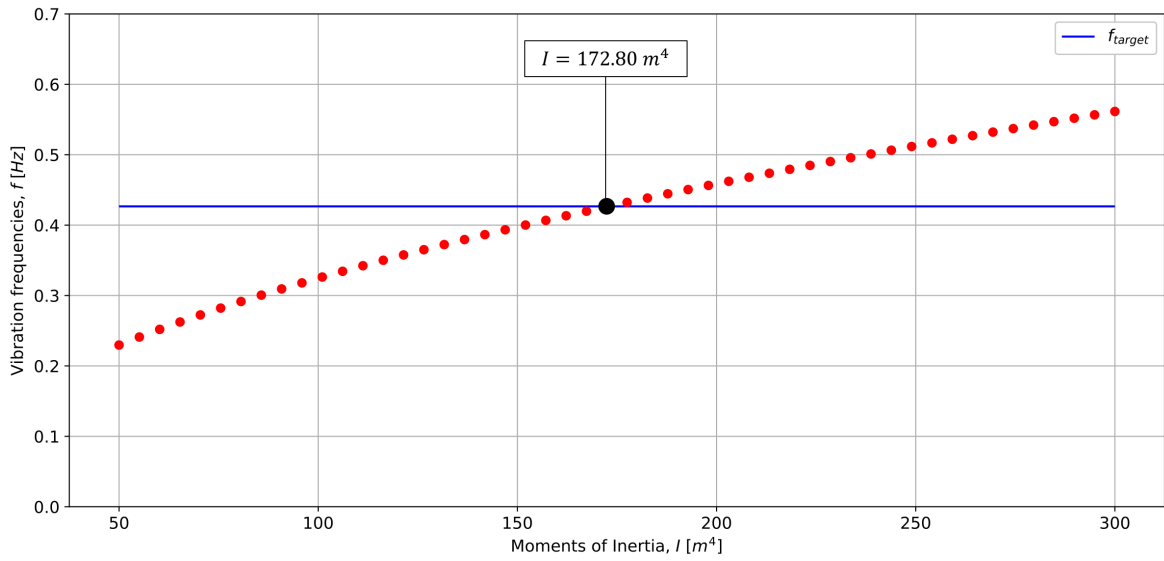


Figure 6.5: Calibration of the equivalent inertia, J_z , as a function of the vibration frequency, f_{target}

Table 6.9: Modal period and frequencies of the equivalent beam model

Mode	T	f	ω	ω^2
[-]	[s]	[Hz]	[rad/s]	[rad ² /s ²]
1	2.343	0.426	2.681	7.188

whose value is equal to $A^* = 0.8 \cdot A = 149.63 \text{ m}^2$. As regard the beam equivalent inertia, J^{EQ} , this is defined as function of the building fundamental frequency, $f = 0.426 \text{ Hz}$, as shown in Figure 6.5. Table 6.9 lists the natural period and frequencies related to the first vibrating mode of the equivalent MDOF model obtained from a modal analysis executed in Python; as expected, they satisfy the required frequency of the real building (f_{target}), against which they have been calibrated.

A discrete MDOF beam model consisting of 3-DOFs per node, which studies the behavior of the simple multi-storey building in the two-dimensional plane, has been implemented in OpenSeesPy, as depicted in Figure 6.6. The shear deformations are also accounted for by schematizing the structure as an ensemble of 26 nodes (each representing an entire 40 m wide floor) distributed along the vertical z -axis of the simulation domain, connected to each other by means of 25 elastic Timoshenko beam frame elements, extending over a total height of 77.5 m. The floor structural masses, $m_{s,i} = M/N_i = 862.84$ tons, are assigned to the 25 upper nodes, while the base node is massless and constrained. The equivalent geometric

Table 6.10: Mechanical parameters of the equivalent beam model

E	G	A	J_z	A^*
[GPa]	[GPa]	[m ²]	[m ⁴]	[m ²]
32	13	187.04	172.80	149.63

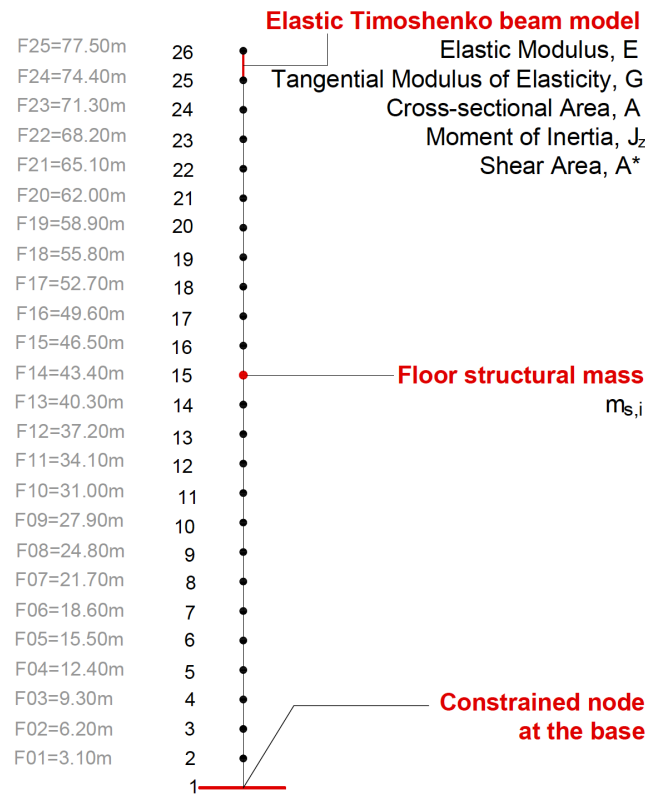


Figure 6.6: Equivalent MDOF model of the mid-rise building with highlighting of the main elements assigned

and material properties listed in Table 6.10 are attributed to each Timoshenko beam element object along direction 1. Finally, assuming for the first vibrating mode a critical damping ratio equal to $\xi = 0.01$, this is assigned to the beam members in the form of Rayleigh damping according to Eq. 5.97.

6.4 Wind load simulation

The multi-storey building is exposed to a longitudinal wind load evaluated with respect to both its static component (that is, the time-independent mean wind velocity variable with height, $v_m(z)$) and resonant component (that is, the turbulent wind velocity variable with time and height, $v_t(z, t)$), as explained in section 2.3. The fluctuating forces, $F_i(t)$, acting on each i -th node of the MDOF model are computed taking into account all the inter-storey heights of the building, starting from $z = 3.10 \text{ m}$, up to $z = H = 77.5 \text{ m}$. In order to ensure that the computation of the lateral forces is in line with the Italian building code, the directions contained in the CNR-DT 207/2008 *Instructions for the evaluation of wind actions and effects on the buildings* are followed. It is also specified that the CNR guidelines are consistent with the technical-scientific state of the art on the subject, acknowledging the main technical recommendations provided by national (*Technical Standards for Construction* (NTC), Ministerial Decree 14 January 2008) and international (*Eurocode 1: Actions on structures - General actions. Part 1-4: Wind actions*, CEN, EN 1991-1-4, 2005) standards

concerning the actions and effects of wind on buildings.

The generation of time-dependent turbulent wind histories, $v_t(t)$, needed for the wind velocity computation, $v(t)$, according to Eq. 2.9, implies the use of the Monte Carlo methodology, being the spectral representation approach the most widely used for its reliability and robustness. Specifically, the following scheme is followed:

- a. definition of the site characteristics where it is assumed to place the building;
- b. evaluation of the building shape, size and orientation;
- c. estimate of the mean wind velocity in the longitudinal direction variable with height, $v_m(z)$ (in m/s^{15}), according to a *constant mean approach*;
- d. numerical simulation of stationary Gaussian random processes through the Monte Carlo method;
- e. generation of a family of wind field space-time realizations within NOWS;
- c. estimate of the turbulent wind velocity in the longitudinal direction variable with time and height, $v_t(z, t)$ (in m/s);
- f. computation of longitudinal (or *along-wind*) pressures, $q(z, t)$ (in kPa);
- g. computation of longitudinal (or *along-wind*) forces, $F(z, t)$ (in kN).

According to the reference standard, the first step to be performed is the definition of the specific site and altitude features to which the computation of the basic wind velocity, v_b , is related based on [CNR Eq.3.1]

$$v_b = v_{b,0}c_a \quad (6.15)$$

where $v_{b,0}$ is the fundamental value of the basic wind velocity defined as the characteristic 10 minutes mean wind velocity at 10 m above ground level in open country terrain category II and c_a is the altitude coefficient given from [CNR Eq.3.2 a,b]

$$c_a = 1; \quad \text{for } a_s \leq a_0 \quad (6.16)$$

$$c_a = 1 + k_a \left(\frac{a_s}{a_0} - 1 \right); \quad \text{for } a_s > a_0 \quad (6.17)$$

being a_0 and k_a site-specific parameters and a_s the site altitude above sea level.

Assuming to place the structure in the city of Milan (Lombardy, Italy), one has $a_s = 120 < 1000$ m hence $c_a = 1$.

From [CNR Table 3.I] the following properties apply

Zone	Description	$v_{b,0}$ [m/s]	a_0 [m]	k_a
1	Lombardy	25	1000	0.40

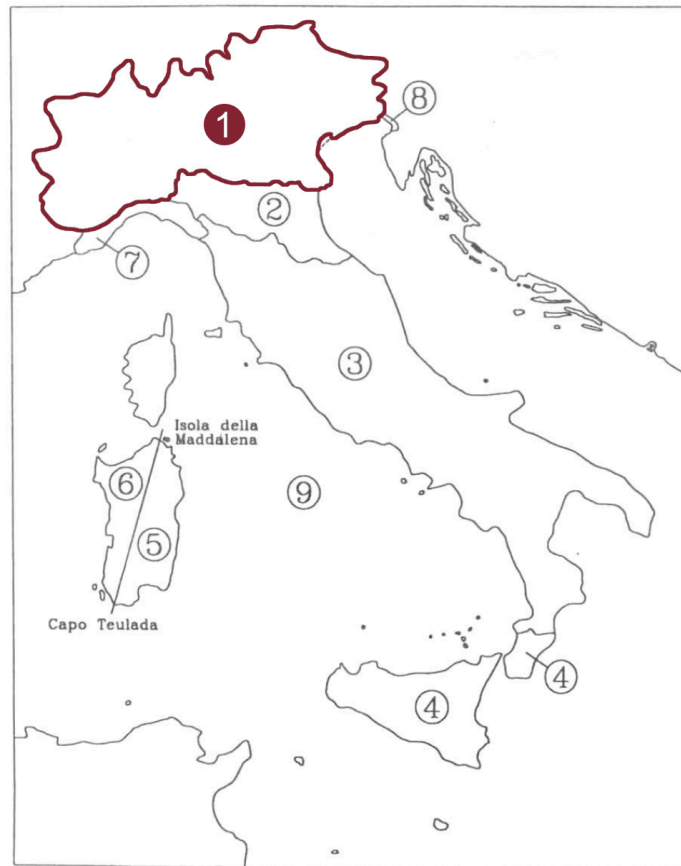


Figure 6.7: Different reference speed values for the Italian zones [CNR Figure 3.1]

As noted in section 2.3.5, short return periods ranging from 1 to 10 *yr* are typically used to assess the occupancy comfort levels related to wind-induced vibrations and accelerations [249]-[250]. According to this, a wind average return period, $T_R = 1 \text{ yr}$, is chosen which allow to evaluate the design reference velocity, v_r [CNR Eq.3.3]

$$v_r = v_b c_r \quad (6.18)$$

where v_b is the basic wind velocity defined as a function of wind direction and time of year at 10 *m* above ground of terrain category II and c_r is the return coefficient given from [CNR Eq.3.4a]

$$c_r = 0.75; \quad \text{for } T_R = 1 \text{ yr} \quad (6.19)$$

v_b [m/s]	c_r [-]	v_r [m/s]
25.00	0.75	18.75

The exposure category is determined from the ground local roughness of the site where the construction is assumed to be located. In this context, a class B (suburban area) is taken from [CNR Table 3.III], for which the following properties apply [CNR Table 3.II]

¹⁵To convert *m/s* into *km/h* multiply by 3.6.

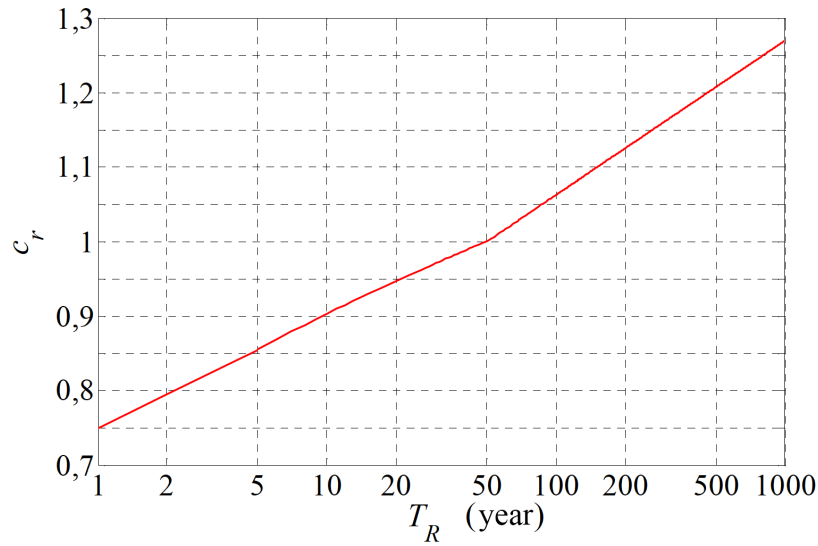


Figure 6.8: Diagram of the return coefficient c_r as a function of the return period T_R [CNR Figure 3.2]

Exposure category	k_r	z_0 [m]	z_{min} [m]
IV	0.22	0.30	8

where k_r is the terrain factor, z_0 is the roughness length, z_{min} is the minimum height and the terrain category IV is defined as the area in which at least 15% of the surface is covered with buildings and their average height exceeds 15 m.

The topographic and orographic features of the building place are approximated by setting the topographic coefficient, $c_t(z)$, equal to 1.

The mean wind velocity v_m at height z above the terrain depends on the ground roughness and orography and on the basic wind velocity, v_b , and should be determined according to [CNR Eq.3.5]

$$v_m(z) = v_r c_m(z) \quad (6.20)$$

where $c_m(z)$ is the mean wind profile coefficient which accounts for the variability of the mean wind velocity at the site of the structure due to the height above ground level and the ground roughness of the terrain upwind of the structure in the wind direction considered.

It is given by the relations [CNR Eq.3.6 a,b]

$$c_m(z) = 0.22 \cdot \ln\left(\frac{8}{0.3}\right) \cdot 8 = 0.720; \quad \text{for } z \leq 8 \quad (6.21)$$

$$c_m(z) = 0.22 \cdot \ln\left(\frac{z}{0.3}\right) \cdot 1; \quad \text{for } z > 8 \quad (6.22)$$

which becomes at the top

$$c_m(77.5) = 0.22 \cdot \ln\left(\frac{77.5}{0.3}\right) = 1.222 \quad (6.23)$$

Substituting Eqs. 6.21 and 6.22 into Eq. 6.20, the mean wind velocity at height z is given from

$$v_m(z) = 18.75 \cdot 0.722 = 13.54 \text{ m/s}; \quad \text{for } z \leq 8 \quad (6.24)$$

$$v_m(z) = 18.75 \cdot 0.22 \cdot \ln\left(\frac{z}{0.3}\right) \cdot 1; \quad \text{for } z > 8 \quad (6.25)$$

yielding a mean wind speed at the top equal to

$$v_m(77.5) = 18.75 \cdot 0.22 \cdot \ln\left(\frac{77.5}{0.3}\right) = 22.911 \text{ m/s} \quad (6.26)$$

In line with [CNR Figure 3.4] and [CNR Figure 4.2.2], the resulting profiles of $c_m(z)$ and $v_m(z)$, for exposure category IV and $T_R = 1$ yr, are portrayed in Figure 6.9.

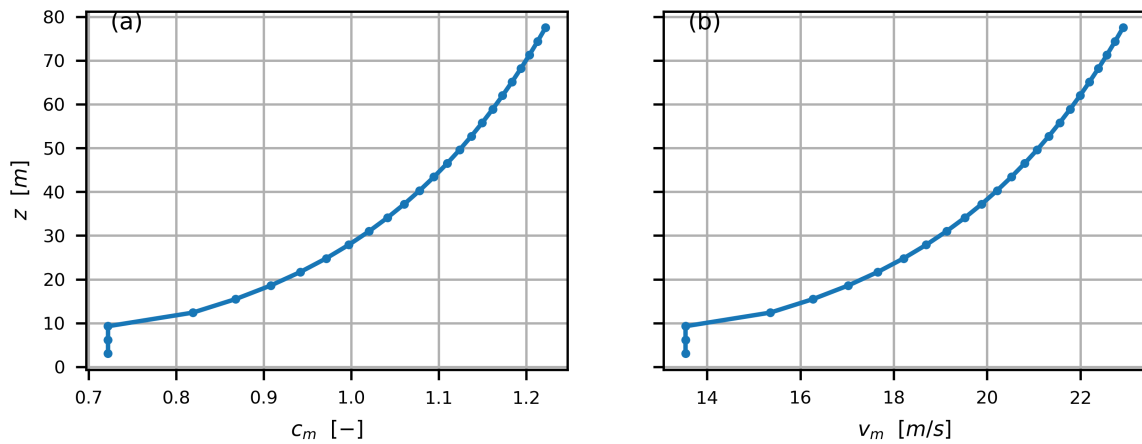


Figure 6.9: Profiles of $c_m(z)$ associated with IV exposure category (a) and $v_m(z)$ associated with $T_R = 1$ yr (b)

From Beaufort scale (Table 6.11), the corresponding degree to the static design wind velocity, defined according to Eq. 6.18, is identified, which is useful for extrapolating the 3-sec wind gust speed, $v_g(z)$, from the values listed in Table 6.12. In this context, a *severe wind* designation corresponding to the 7 wind scale is accounted for in the numerical investigations. The mean wind speeds and gust speeds applied along the heights z of the mid-rise building are listed in Table 6.13.

As stated in Chapter 2 (section 2.3.1), the wind velocity is obtained by adding up the contribution of the quasi-static mean component, $v_m(z)$, and the time-dependent fluctuating component, $v_t(z, t)$, according to Eq. 2.9 [251]. The fluctuating component of the *along-wind* velocity is generated within the NatHaz internet simulation portal (<http://windsim.ce.nd.edu/>) by means of the realization of Gaussian multivariate wind fields [252]. The digital simulation technique, based on the spectral representation of the wind field, involves obtaining a discrete frequency function with Cholesky decomposition and a FFT. By applying the FFT algorithm, the discretization procedure in both time-, space- and frequency-domain, required for the representation of the wind field as a stationary random process, are uniquely

Table 6.11: Beaufort Scale

Beaufort scale	designation	v_r [m/s]	v_r [km/h]
0	calm	0 ÷ 0,2	1
1	light air	0,3 ÷ 1,5	1 ÷ 5
2	light breeze	0,6 ÷ 3,3	6 ÷ 11
3	gentle breeze	3,4 ÷ 5,4	12 ÷ 19
4	moderate breeze	5,5 ÷ 7,9	20 ÷ 28
5	fresh breeze	8,0 ÷ 10,7	29 ÷ 38
6	strong breeze	10,8 ÷ 13,8	39 ÷ 49
7	severe wind	13,9 ÷ 17,1	50 ÷ 61
8	gale	17,2 ÷ 20,7	62 ÷ 74
9	severe gale	20,8 ÷ 24,4	75 ÷ 88
10	storm	24,5 ÷ 28,4	89 ÷ 102
11	violent storm	28,5 ÷ 32,6	103 ÷ 117
12	hurricane	> 32,7	> 118

Table 6.12: 3-sec wind gust speed as a function of the mean wind speed based on Beaufort scale and building height

Grade	3	4	5	6	7	8	9	10
v_r [m/s]	5,4	7,9	10,7	13,8	17,1	20,7	24,4	28,4
z [m]	$v_g(z)$				[m/s]			
10	8	11	15	19	24	29	34	40
20	8	12	16	21	26	31	37	43
30	9	12	17	22	27	32	38	45
40	9	13	17	22	28	33	39	46
50	9	13	18	23	28	34	40	47
60	9	13	18	23	29	35	41	48
70	9	14	18	24	29	36	42	49
80	9	14	19	24	30	36	42	49
90	10	14	19	24	30	36	43	50
100	10	14	19	25	31	37	44	51
110	10	14	19	25	31	37	44	51
120	10	14	19	25	31	38	44	52
130	10	15	20	25	31	38	45	52
140	10	15	20	26	32	38	45	53
150	10	15	20	26	32	38	45	53
160	10	15	20	26	32	39	46	53
170	10	15	20	26	32	39	46	54
180	10	15	20	26	33	39	46	54
190	10	15	20	26	33	40	47	54
200	10	15	21	27	33	40	47	55

Table 6.13: Mean wind speeds, $v_m(z)$, and gust speeds, $v_g(z)$, applied on heights z of the multi-storey building

floor	z	$c_m(z)$	$v_m(z)$	$v_g(z)$	floor	z	$c_m(z)$	$v_m(z)$	$v_g(z)$
[–]	[m]	[–]	[m/s]	[m/s]	[–]	[m]	[–]	[m/s]	[m/s]
25	77.50	1.222	22.91	29	12	37.20	1.060	18.49	28
24	74.40	1.213	22.28	29	11	34.10	1.041	18.12	27
23	71.30	1.204	21.77	29	10	31.00	1.020	17.73	22
22	68.20	1.194	21.55	29	9	27.90	0.997	17.31	27
21	65.10	1.184	21.32	29	8	24.80	0.971	16.86	27
20	62.00	1.173	21.08	29	7	21.70	0.942	16.37	26
19	58.90	1.162	20.85	29	6	18.60	0.908	15.83	26
18	55.80	1.150	20.59	29	5	15.50	0.868	15.24	26
17	52.70	1.137	20.33	29	4	12.40	0.819	14.56	25
16	49.60	1.124	20.05	28	3	9.30	0.755	13.97	24
15	46.50	1.110	19.77	28	2	6.20	0.720	13.54	22
14	43.40	1.094	19.47	28	1	3.10	0.720	13.54	20
13	40.30	1.078	18.83	28	0	0.00	0.720	13.54	20

linked by the choice of the following parameters:

- N_t , number of time instants in which the process is simulated;
- Δ_t , sampling step

from which the duration of the sampled signal, $T_p = N_t \Delta_t$, is obtained. The upper frequency limit of the harmonics reproduced in the simulation (that is, the *cut-off* frequency) is given by $f_c = 1/(2\Delta_t)$, while $\Delta_f = 1/T_p$ is the minimum distance between the frequencies of two distinct harmonics. In the following table the key variables adopted for the construction of turbulent wind velocity time histories are reported.

Duration, N	Cut-off frequency, f_c	Exposure category	Wind peak gust speed, $U_{3-s,10}$
[s]	[Hz]	[–]	[m/s]
5000	0.426	B	29

To summarize, the wind hazard incorporated in this study is simulated within the NatHaz portal referring to urban and suburban areas with numerous closely spaced obstructions (B-category) and assuming a 3-sec wind gust velocity at the top $v_g(z)$ of 29 m/s to be inserted within the Nows interface (Fig. 6.10). Then, the wind gust is added to the *along-wind* fluctuating force time-series assuming to have the same frequency, f_c , as that of the structure, f_1 , to simulate the worst case scenario [253]. It should be noted that the number of heights to be entered in the box z [m, ft] is equal to the number of vertical locations (i.e., the building floors) on which the wind velocities and forces are to be applied.

NatHaz
NOWS

NatHaz On-line Wind Simulator (NOWS) : Input Interface

User Inputs : Please select options and fill out input values. [On-line Unit Converter](#)

■ Please select the unit of input values (default : Metric)
If user would like to see English unit output, please select checkbox (default : Metric)

Metric(SI) unit [m, m/s] English unit [ft, mph] Output : English unit

■ Vertical (z), Horizontal (x) or 2-dimensional (x,z) locations for wind speed simulation
(Acceptable formats : Delimited by comma(,) or MATLAB-compatible, e.g., 4,8,12 or 4:4:12)

z [m, ft] :

x [m, ft] : z [m, ft] :

x [m, ft] : z [m, ft] :

■ Total number of frequency (N), cut-off frequency (fc).
Note that $\Delta t = 1/(2f_c)$; $T = 2 \cdot N \cdot \Delta t$ [in Ergodic SRM, $T = 2 \cdot N \cdot \Delta t$ (total number of locations)]

N (max = 18000) : f_c [Hz] (max = 5) :

■ Exposure category (A,B,C,D based on ASCE 7-98) and 3-sec gust wind speed ($U_{3-s,10}$)

A B C D $U_{3-s,10}$ [m/s, mph]

■ Wind simulation schemes

Discrete frequency function with Cholesky decomposition and FFT (max 200 locations)

Schur decomposition by AR model and polynomial approximation (max 100 locations)

Ergodic spectral representation with Cholesky decomposition and FFT (max 50 locations)

Conventional spectral representation method (max 200 locations)

Figure 6.10: NatHaz wind simulator user interface

Figure 6.11 shows the time histories of turbulent wind speeds (in m/s) applied on the 2nd ($z = 6.20 m$), 12th ($z = 37.20 m$) and 24th ($z = 74.40 m$) floor of the mid-rise building, respectively.

The wind speed components are used to derive the longitudinal kinetic pressure (in kPa) according to [CNR Eq.3.9]

$$q(z, t) = \frac{1}{2} \rho (v_m(z) + v_t(z, t))^2 c_e(z) = \frac{1}{2} \rho (2v_m v_t + v_m^2 + v_t^2) c_e(z) \quad (6.27)$$

where $\rho = 1.25 \text{ kg/m}^3$ is the air density and c_e is the exposure factor given from [CNR Eqs.3.10 a,b]

$$c_e(z) = (0.22)^2 \ln\left(\frac{8}{0.3}\right) \left[\ln\left(\frac{8}{0.3}\right) + 7 \right]; \quad \text{for } z \leq 8 \quad (6.28)$$

$$c_e(z) = (0.22)^2 \ln\left(\frac{z}{0.3}\right) \left[\ln\left(\frac{z}{0.3}\right) + 7 \right]; \quad \text{for } z > 8 \quad (6.29)$$

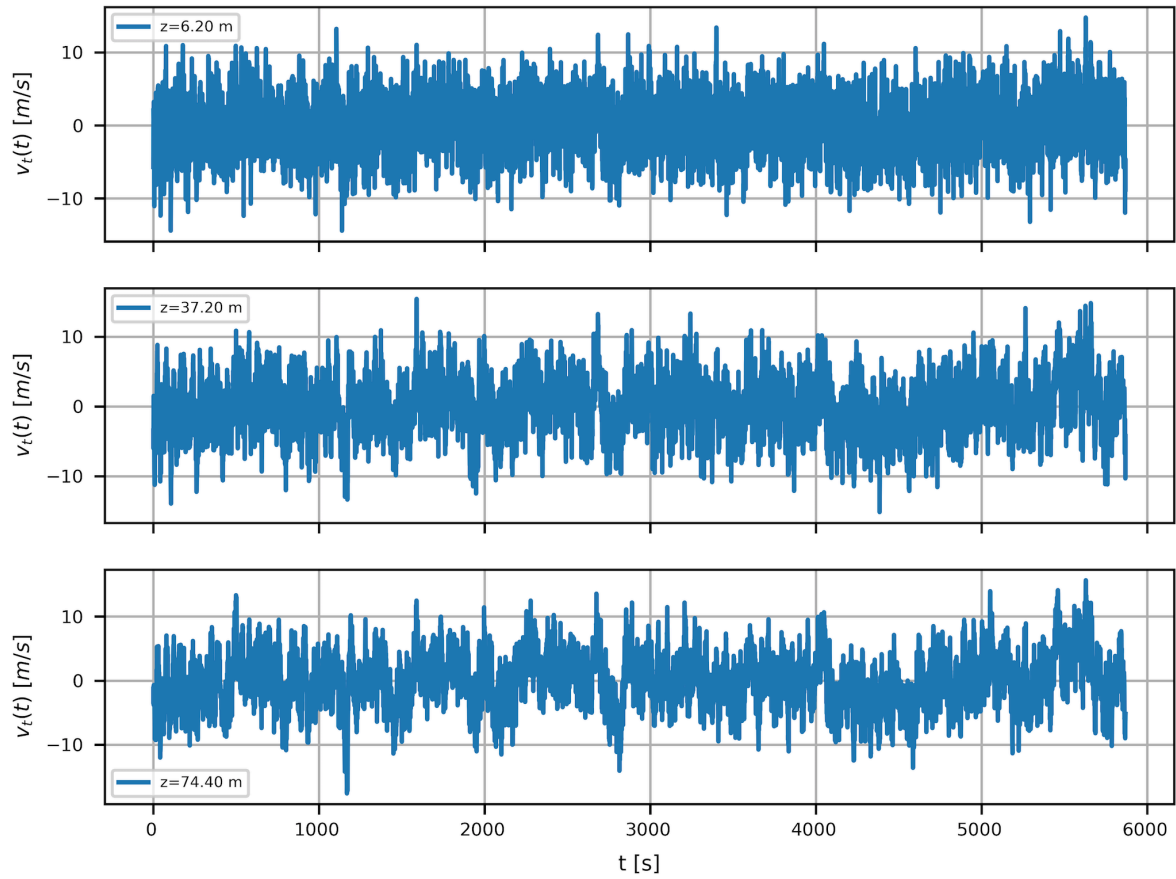


Figure 6.11: Turbulent wind velocities, $v_t(t)$, applied on the 2nd ($z = 6.20$ m), 12th ($z = 37.20$ m) and 24th ($z = 74.40$ m) floor of the mid-rise building

which gives at the top ($z = 77.5$ m)

$$c_e(77.5) = (0.22)^2 \ln\left(\frac{77.5}{0.3}\right) \left[\ln\left(\frac{77.5}{0.3}\right) + 7 \right] = 3.374 \quad (6.30)$$

According to Gong et al. (2019), $v_t(z, t)^2$ can be neglected for tall buildings or approximated into a steady component using its mean square, $\overline{v_t(z, t)^2}$

$$v_t(z, t)^2 \approx \overline{v_t(z, t)^2} = \overline{v_t(z, t)} + \sigma_{v_t}(z)^2 \quad (6.31)$$

where $\sigma_{v_t}(z)$ is the standard deviation of the longitudinal wind turbulence given from [CNR Eq.2.7]

$$\sigma_{v_t}(z) = I_v(z) v_m(z) \quad (6.32)$$

The turbulence intensity $I_v(z)$ at height z is defined as the standard deviation of the turbulence divided by the mean wind velocity [CNR Eq.3.7 a,b]

$$I_v(z) = \frac{\sigma_{v_t}(z)}{v_m(z)} = \frac{1}{\ln\left(\frac{8}{0.3}\right)}(8) = 0.304; \quad \text{for } z \leq 8 \quad (6.33)$$

$$I_v(z) = \frac{1}{\ln\left(\frac{z}{0.3}\right)}; \quad \text{for } z > 8 \quad (6.34)$$

providing at the top

$$I_v(77.5) = \frac{1}{\ln\left(\frac{77.5}{0.3}\right)} \cdot 1 = 0.180 \quad (6.35)$$

Hence, substituting Eqs. 6.33 and 6.34 into Eq. 6.32

$$\sigma_{v_t}(z) = \frac{1}{\ln\left(\frac{8}{0.3}\right)} \cdot 13.54 = 4.125 \text{ m/s}; \quad \text{for } z \leq 8 \quad (6.36)$$

$$\sigma_{v_t}(z) = \frac{1}{\ln\left(\frac{z}{0.3}\right)} (18.75) \cdot 0.22 \cdot \ln\left(\frac{z}{0.3}\right); \quad \text{for } z > 8 \quad (6.37)$$

By neglecting the mean square value of the wind fluctuation, $\overline{v_t(z,t)} = 0$, one has

$$v_t(z,t)^2 \approx \sigma_{v_t}(z)^2 \quad (6.38)$$

Substituting Eqs. 6.32 and 6.31 into Eq. 6.27 and simplifying, the peak kinetic pressure should take the form [CNR Eq.F.7]

$$q_p(z) = \frac{1}{2} \rho v_m^2(z) [1 + 7I_v(z)] \quad (6.39)$$

which gives at the top

$$q_p(77.5) = \frac{1}{2} 1.25 (22.91)^2 [1 + 7(0.180)] = 0.742 \text{ kPa} \quad (6.40)$$

Equivalently, the peak kinetic pressure can be estimated according to [CNR Eq.3.9] which derives from Eq. 6.39

$$q_p(z) = \frac{1}{2} \rho v_r^2 c_e(z) \quad (6.41)$$

Based on this, the peak wind pressure related to a return period $T_R = 1$ yr at the top is

$$q_p(77.5) = \frac{1}{2} 1.25 (18.75)^2 3.374 = 0.742 \text{ kPa} \quad (6.42)$$

Figure 6.12 portrays the trend of the exposure coefficient $c_e(z)$ and the wind peak pressure $q_p(z)$ along the height z of the building, in accordance with the [CNR Figs. 4.2.5-4.2.6]. The time histories of longitudinal wind pressures applied on the 2nd ($z = 6.20$ m), 12th ($z = 37.20$ m) and 24th ($z = 74.40$ m) floor of the mid-rise building, respectively, are shown in Figure 6.13.

The computation of wind pressures is useful for estimating the *along-wind* forces, $F(z,t)$, acting on the structure, which may be determined directly by using [CNR Eq.3.13 a]

$$F(z,t) = q(z,t) \bar{A} C_D \quad (6.43)$$

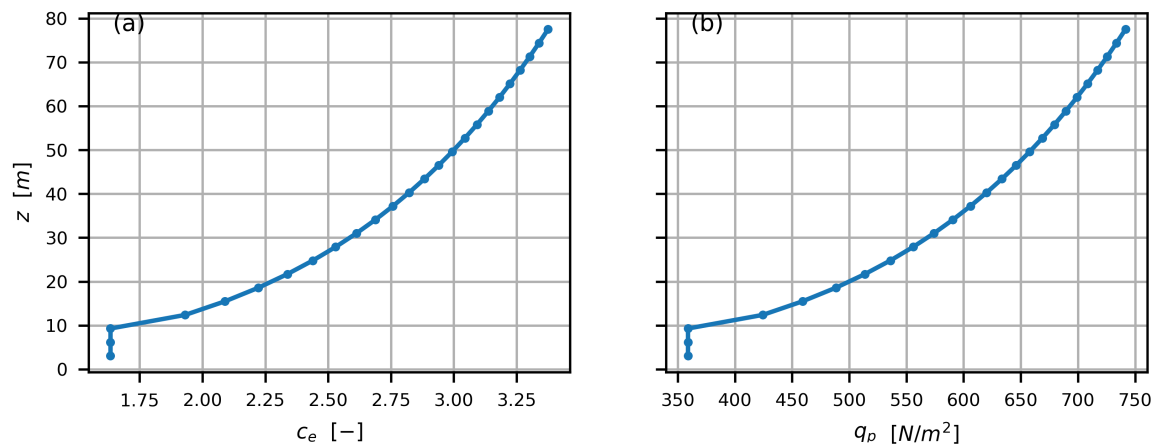


Figure 6.12: Profiles of $c_e(z)$ associated with IV exposure category (a) and $q_p(z)$ associated with $T_R = 1$ yr (b)

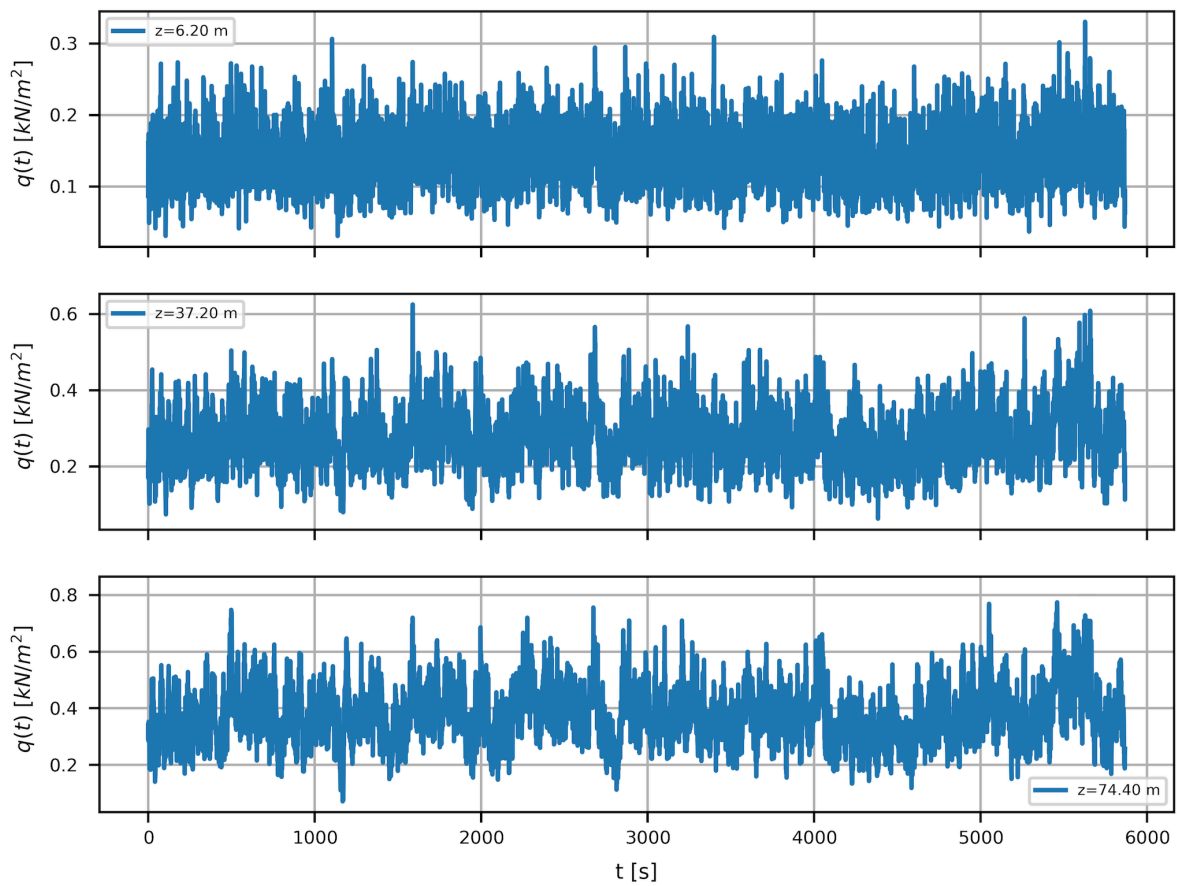


Figure 6.13: Wind pressures, $q(t)$, applied on the 2nd ($z = 6.20$ m), 12th ($z = 37.20$ m) and 24th ($z = 74.40$ m) floor of the mid-rise building

where \bar{A} is the wind-exposed façade area computed as $A = h \cdot L$, being h the inter-storey height and L the width of the building plan and C_D is the drag coefficient in the longitudinal

Table 6.14: Maximum longitudinal wind pressures (in kPa) and forces (in kN) per floor

floor	z	c_e	$\max(q(t))$	$\max(F(t))$	floor	z	c_e	$\max(q(t))$	$\max(F(t))$
[–]	[m]	[–]	[kPa]	[kN]	[–]	[m]	[–]	[kPa]	[kN]
25	77.50	3.37	0.742	108	12	37.20	2.75	0.606	177
24	74.40	3.33	0.734	214	11	34.10	2.68	0.591	172
23	71.30	3.30	0.726	212	10	31.00	2.61	0.574	168
22	68.20	3.26	0.717	209	9	27.90	2.53	0.556	162
21	65.10	3.22	0.708	207	8	24.80	2.43	0.536	156
20	62.00	3.18	0.699	204	7	21.70	2.33	0.514	150
19	58.90	3.13	0.690	201	6	18.60	2.22	0.488	142
18	55.80	3.09	0.679	198	5	15.50	2.09	0.459	134
17	52.70	3.04	0.669	195	4	12.40	1.93	0.424	124
16	49.60	2.99	0.658	192	3	9.30	1.73	0.381	111
15	46.50	2.94	0.646	189	2	6.20	1.63	0.358	94
14	43.40	2.88	0.633	185	1	3.10	1.63	0.358	67
13	40.30	2.82	0.620	181	0	0.00	1.63	0.358	0

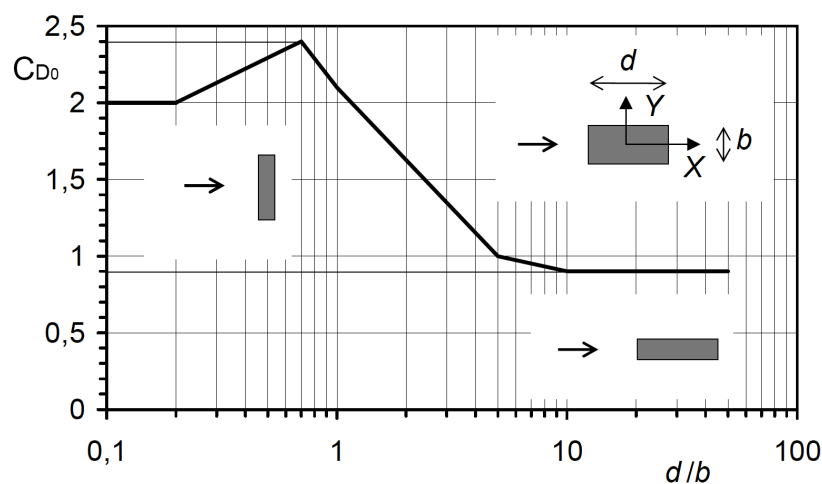
wind direction given by [CNR Eq.G.21]

$$C_D = 0.73 \ln(d/b) + 2.51; \quad \text{for } 0.2 < d/b < 0.7 \quad (6.44)$$

where $d/b = 25/40 = 0.625$ is the rectangular section's elongation ratio, which gives

$$C_D = 0.73 \cdot \ln(0.625) + 2.51 = 2.361 \quad (6.45)$$

for rectangular shapes with sharp edges, as shown in Figure 6.14.

**Figure 6.14:** Drag coefficients for rectangular sections [CNR Figure G.49]

The *along-wind* fluctuating forces (in kN) applied on the 2nd ($z = 6.20$ m), 12th ($z = 37.20$ m) and 24th ($z = 74.40$ m) floor of the mid-rise building, respectively, are plotted

in Figure 6.15. Given the duration of the sampled signal equal to $N = 5000$ s with an incremental time-step equal to $dt = t[1] - t[0] = 0.02$ s, time histories with a duration of about $t = 6000$ s are obtained. Table 6.14 lists the maximum *along-wind* pressures, $q(t)$ (in kPa), and forces, $F(t)$ (in kN), related to a 22.9 m/s mean wind speed at the top. As can be noted, the listed values related to the top floor are half those of the lower level due to a halved wind-exposed top flooring area.

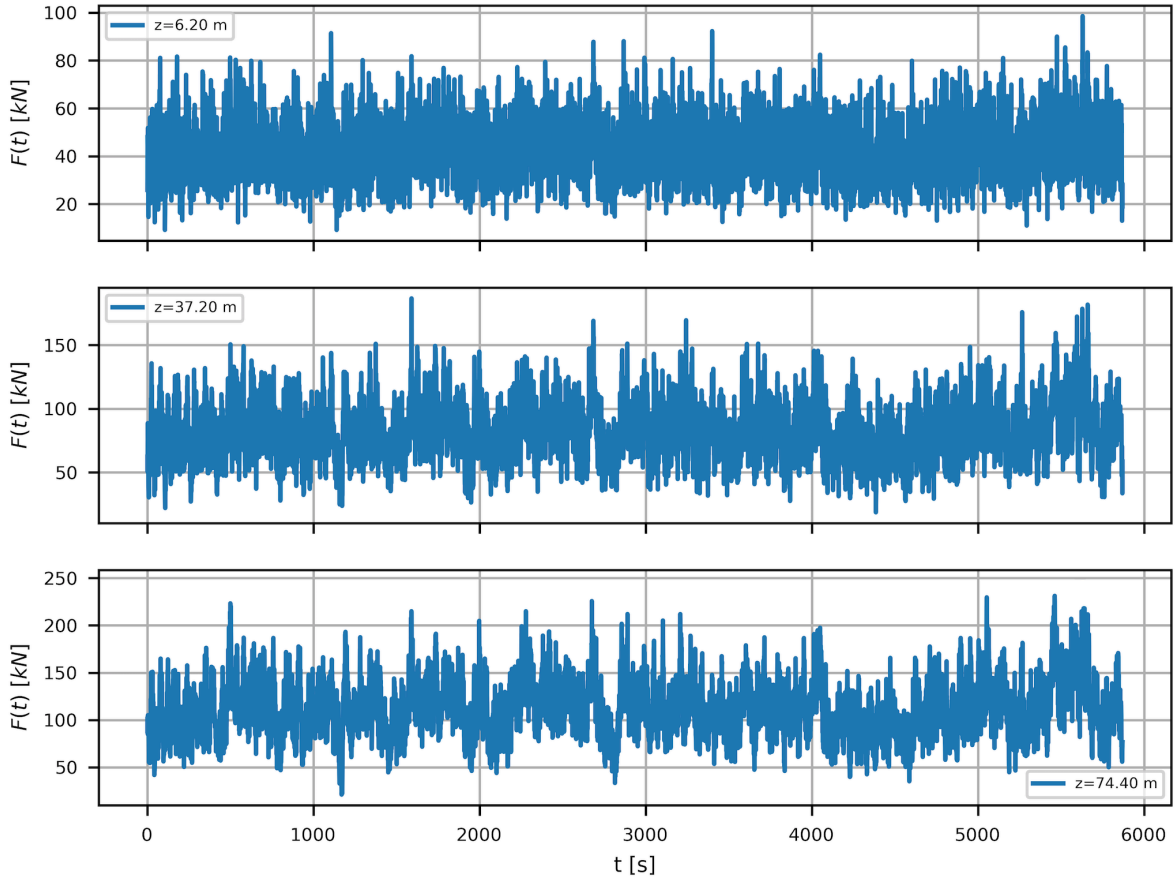


Figure 6.15: Fluctuating wind forces, $F(t)$, applied on the 2nd ($z = 6.20$ m), 12th ($z = 37.20$ m) and 24th ($z = 74.40$ m) floor of the mid-rise building

According to [CNR section E.1], it is possible to obtain the power spectrum of the turbulence, $S_v(z, \Omega)$, which allows to determine the frequency of the wind load on various heights z of the multi-storey building

$$S_v(z, \Omega) = \frac{(6.868) \frac{L_v(z)}{v_m(z)}}{\left[1 + 10.302 \left(\frac{\Omega L_v(z)}{v_m(z)}\right)\right]^{5/3}} \sigma_v^2(z) \quad (6.46)$$

where $L_v(z)$ is the integral scale of turbulence, which can be computed as

$$L_v(z) = \bar{L} \left(\frac{8}{z}\right)^\kappa = 42.109 \text{ m}; \quad \text{for } z \leq 8 \quad (6.47)$$

$$L_v(z) = \bar{L} \left(\frac{z}{\bar{z}} \right)^\kappa; \quad \text{for } z > 8 \quad (6.48)$$

where $\bar{z} = 200 \text{ m}$ is a reference height, $\bar{L} = 300 \text{ m}$ is a reference length and $\kappa = 0.61$ is a coefficient linked to the site exposure category provided by [CNR Table 3.IV].

Based on this, the integral scale of turbulence at the top is

$$L_v(77.5) = 300 \left(\frac{77.5}{200} \right)^{0.61} = 168.25 \text{ m} \quad (6.49)$$

In line with the expected trend of the turbulence intensity (I_v) and length scale (L_v) related to IV exposure category taken from [CNR Figs. 3.5-3.6], the turbulence profiles for the specific building under examination associated with a mean wind velocity $v_m = 22.91 \text{ m/s}$ at height $H = 77.5 \text{ m}$ are depicted in Figure 6.16. The values used to built the vertical profiles of both $I_v(z)$ and $L_v(z)$ for all heights z of the structure are listed in Table 6.15.

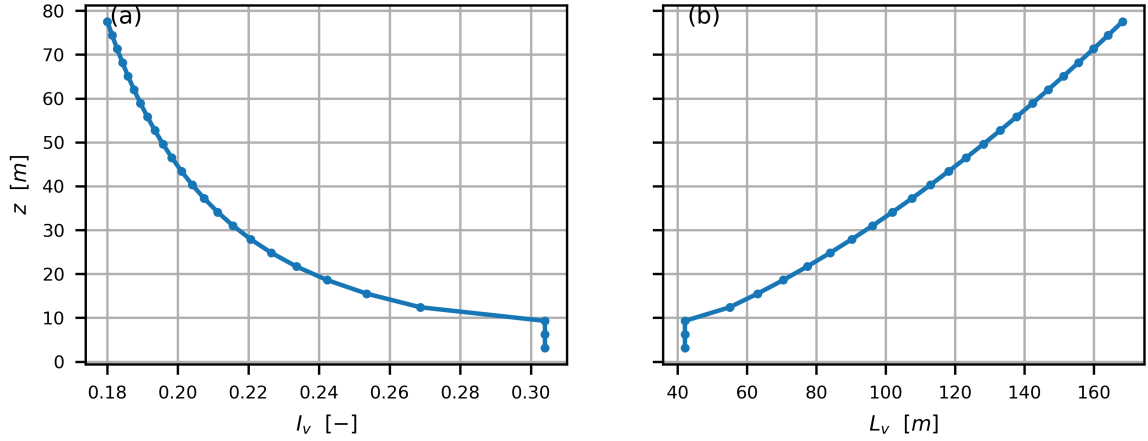


Figure 6.16: Profiles of turbulence intensity I_v (a) and length scale L_v (b) for the 77.5 m high generic building used to generate the wind inflow in the longitudinal direction

Finally, by denoting

$$y := \frac{\Omega S_v(z, \Omega)}{\sigma_v(z^2)} \quad \text{and} \quad x := \Omega \frac{L_v(z)}{v_m(z)} \quad (6.50)$$

Eq. 6.46 can be simplified as follows

$$y = \frac{(6.868)x}{[1 + (10.302)x]^{5/3}} \quad (6.51)$$

Based on the wind properties imposed, the period and frequencies of the excitation at $z \leq 8$ result

$$f = \frac{13.544}{42.109} 0.145 = 0.05 \text{ Hz}; \quad T = \frac{1}{f} = 21.44 \text{ s}; \quad \Omega = 2\pi f = 0.293 \text{ rad/s} \quad (6.52)$$

and, being the circular frequency of the mid-rise structure equal to $\omega = 2.679 \text{ rad/s}$

Table 6.15: Turbulence intensities, $I_v(z)$, and length scales, $L_v(z)$, for heights z of the mid-rise building

floor	z	I_v	L_v	floor	z	I_v	L_v
[–]	[m]	[–]	[m]	[–]	[m]	[–]	[m]
25	77.50	0.180	168.255	12	37.20	0.207	107.529
24	74.40	0.181	164.117	11	34.10	0.211	101.970
23	71.30	0.183	159.911	10	31.00	0.216	96.211
22	68.20	0.184	155.633	9	27.90	0.221	90.222
21	65.10	0.186	151.279	8	24.80	0.227	83.967
20	62.00	0.188	146.843	7	21.70	0.234	77.399
19	58.90	0.189	142.319	6	18.60	0.242	70.452
18	55.80	0.191	137.702	5	15.50	0.253	63.037
17	52.70	0.193	132.983	4	12.40	0.269	55.015
16	49.60	0.196	128.155	3	9.30	0.291	46.160
15	46.50	0.198	123.208	2	6.20	0.304	42.109
14	43.40	0.201	118.130	1	3.10	0.304	42.109
13	40.30	0.204	112.909	0	0.00	0.304	42.109

(taken from Table 6.4), the frequency ratio ρ is estimated

$$\rho = \frac{0.293}{2.679} = 0.10 \quad (6.53)$$

proving that low vibration frequencies are the most excited by dynamic wind action and this is substantially validated even at $z = 77.5 \text{ m}$

$$f = \frac{22.911}{168.25} 0.145 = 0.02 \text{ Hz}; \quad T = \frac{1}{f} = 50.64 \text{ s}; \quad \Omega = 2\pi f = 0.124 \text{ rad/s} \quad (6.54)$$

with

$$\rho = \frac{0.124}{2.679} = 0.05 \quad (6.55)$$

For completeness, the structural factor, c_{dD} , useful for determining the peak value of the longitudinal acceleration, is computed by applying the detailed method described in [CNR Appendix L, section L.2]. The structural factor should take into account the effect on wind actions from the non-simultaneous occurrence of peak wind pressures on the surface together with the effect of the vibrations of the structure due to turbulence. A detailed procedure for calculating the structural factor requires a sequence of operations suggested by [CNR Table L.I], aimed at evaluating:

- the background factor, B^2 , which allows for the lack of full correlation of the pressure on the structure surface;
- the aerodynamic admittance functions, R_h and R_b ;

Table 6.16: Parameters for evaluating the structural factor, c_{dD}

B^2	S_D	η_h	η_b	R_h	R_b	R_D^2	ν_D [Hz]	g_D	G_D	c_{dD}
0.555	0.069	6.680	2.155	0.138	0.358	0.269	0.243	3.340	2.201	0.922

- the resonance response factor, R_D^2 , which allows for turbulence in resonance with the considered vibration mode of the structure;
- the expected up-crossing frequency, $\nu_D \geq 0.08$ Hz;
- the peak factor, $g_D \geq 3$, which is defined as the ratio of the maximum value of the fluctuating part of the response to its standard deviation;
- the gust factor, G_D ;
- the structural factor, c_{dD} .

Once the geometric ($b = 25$ m, $h = 77.5$ m) and dynamic ($f_1 = 0.426$ Hz, $\xi_1 = 0.01$) parameters of the structure are assigned, the mean wind velocity, the intensity and the integral scale of turbulence at the reference height, $z_e = 0.6h = 46.5$ m, are evaluated

$$v_m(z_e) = 19.77 \text{ m/s}; \quad I_v(z_e) = 0.198; \quad L_v(z_e) = 123.208 \text{ m} \quad (6.56)$$

The background factor B^2 is provided by the relation [CNR Eq.L.4, Fig.L.4]

$$B^2 = \frac{1}{1 + 0.9 \left(\frac{25 \cdot 77.5}{123.208} \right)^{0.63}} = 0.555 \quad (6.57)$$

The resonant response factor R_D^2 is provided by the relations [CNR Eq.L.5-L.9]

$$\eta_h = 4 \frac{0.426 \cdot 77.5}{19.77} = 6.680; \quad \eta_b = 4 \frac{0.426 \cdot 25}{19.77} = 2.155 \quad (6.58)$$

$$R_h = \frac{1}{6.680} - \frac{1}{2 \cdot 6.680^2} (1 - e^{-2 \cdot 6.680}) = 0.138; \quad R_b = \frac{1}{2.155} - \frac{1}{2 \cdot 2.155^2} (1 - e^{-2 \cdot 2.155}) = 0.358 \quad (6.59)$$

$$S_D = \frac{6.868 \cdot 0.426 \cdot (123.208/19.77)}{[1 + 10.302 \cdot 0.426 \cdot (123.208/19.77)]^{5/3}} = 0.069 \quad (6.60)$$

$$R_D^2 = \frac{\pi}{4 \cdot 0.01} 0.069 \cdot 0.138 \cdot 0.358 = 0.269 \quad (6.61)$$

The expected up-crossing frequency ν_D is given by the relation [CNR Eq.L.11]

$$\nu_D = 0.426 \sqrt{\frac{0.269}{0.555 + 0.269}} = 0.243 \text{ Hz} \quad (6.62)$$

The peak factor in the longitudinal direction g_D is given by the relation [CNR Figure L.7 Eq.L.10]

$$g_D = \sqrt{2 \ln(0.243 \cdot 600)} + \frac{0.5772}{\sqrt{2 \ln(0.243 \cdot 600)}} = 3.340 \quad (6.63)$$

Finally, the structural factor c_{dD} is given by the relations [CNR Eq.L.2-L.3]

$$G_D = 1 + 2 \cdot 3.340 \cdot 0.198 \sqrt{0.555 + 0.269} = 2.201 \quad (6.64)$$

$$c_{dD} = \frac{2.201}{1 + 7 \cdot 0.198} = 0.922 \quad (6.65)$$

All the values obtained from previous calculations are listed in Table 6.16. Starting from the detailed method just described, it is possible to deduce a precautionary value of the coefficient for buildings similar to a parallelepiped with uniform mass and stiffness distribution. Resorting to the diagram of [CNR Figure L.9] for RC buildings, one has

$$c_{dD} = 1.04 > 0.922 \quad (6.66)$$

It should be noted that the simplified method obviously leads to a higher estimate of the value provided by the detailed method.

6.5 Design of monolithic MF

As anticipated in section 2.4.4, the MF is conceived as a cladding system capable of undergoing relative displacements with respect to the primary building structure due to flexible connectors which take advantage of the façade motion, allowing it to be used as a wind-induced vibration control system. On the simple mid-rise building described in section 6.2, a monolithic façade system is assumed to be applied, which is composed of a single uninterrupted vertical element spanning over the 25 building levels (according to the sketch of Fig. 3.1 a), not allowing any relative displacement between one floor and another, but just the relative motion of the overall façade with respect to the supporting building structure. By designing the cladding framework with high-strength metal profiles, it is ensured that the new façade system is able to carry the greater forces resulting from motion, compared to the conventional fixed aluminum façade, and transfer them to the load-bearing skeleton of the building through suitable connection devices. It is assumed to make the MF frame with S450 steel box-shaped $300 \times 150 \times 5$ mm mullions and $100 \times 300 \times 5$ mm transoms, sized to withstand both vertical (glass panels and frame self-weight) and horizontal loads (in this case, the longitudinal wind forces) and support oscillations without breaking. The main geometric and mechanical properties of both vertical and horizontal steel elements are shown in Tables 6.17 and 6.18, respectively.

Based on the metal profiles chosen for the façade project, the available mass ratio associated with the renewed glass and steel façade is estimated, being the mass value of the

Table 6.17: Geometric and mechanical properties of steel mullions

Material	$H \times B$	s	W_s	A	W_x	W_y	$M_{rd,x}$	$M_{rd,y}$
[-]	[mm]	[mm]	[kg/m]	[m ²]	[m ³]	[m ³]	[kNm]	[kNm]
S450	300	5	34.54	0.0044	$3.54E - 04$	$2.41E - 04$	138.79	94.49

Table 6.18: Geometric and mechanical properties of steel transoms

Material	$H \times B$	s	W_s	A	W_x	W_y	$M_{rd,x}$	$M_{rd,y}$
[-]	[mm]	[mm]	[kg/m]	[m ²]	[m ³]	[m ³]	[kNm]	[kNm]
S450	100	5	30.62	0.0039	$2.81E - 04$	$1.48E - 04$	110.17	58.03

monolithic MF useful to correctly size the connection system devices. By making the FEM of the MF system in SAP 2000 and subjecting it to a linear static analysis under dead load, the façade mass is established at 590 *tons*, linked to a mass ratio, μ , of 2.75%, as it is clear from Table 6.19. However, as a unilateral monolithic façade is being accounted for in the present study, just applied along the wind-excited side of the building, a halved mass ratio, $\mu = 1.4\%$, must be imposed, obtaining a one-sided façade mass of 295 *tons*. As it is easy to guess, the transition from aluminum to steel for the MF project on the mid-rise building involves an increase in the mass ratio of 44%.

6.5.1 Connector sizing and layout

According to the diagram depicted and explained in section 4.4, the link between the monolithic MF and the multi-storey structure is realized by means of a connection system consisting of friction devices with rubber bumpers incorporated in the floor slab on each level of the building. Figure 6.17 portrays a technical detail of the connector applied on the monolithic MF-equipped structure. Based on the assumptions made in Chapter 4, the insertion of a sliding device (2), taken from the VFCC model experimented by Laflamme et al. in 2020, within a system of double hollow rectangular metal profiles is expected. The movable inner tube (3) is directly welded to the slider, on one side, and to the façade frame (4), on the other; while in the outer fixed tube (1) the mechanical device is housed, at the ends of which 4 *cm* thick trapezoidal rubber bumpers (5) are welded to stop the sliding of the friction device and, consequently, the façade movement. Two other pairs of rubber pads (6) are added to absorb impacts outside the flooring slab; finally, an aluminum structural expansion joint (7) is placed at the pavement level to close the gap between the structure and the open cladding.

Table 6.19: Estimate of the mass ratio with steel and glass Movable Façade

FZ	a	W_{frame}	M_{frame}	A	W_{glass}	M_{glass}	M_{MF}	M	μ
[kN]	[m/s ²]	[kg]	[tons]	[m ²]	[kg/m ²]	[tons]	[tons]	[tons]	[%]
2189.6	9.81	223203	246	7800	40	344	590	21571	2.75

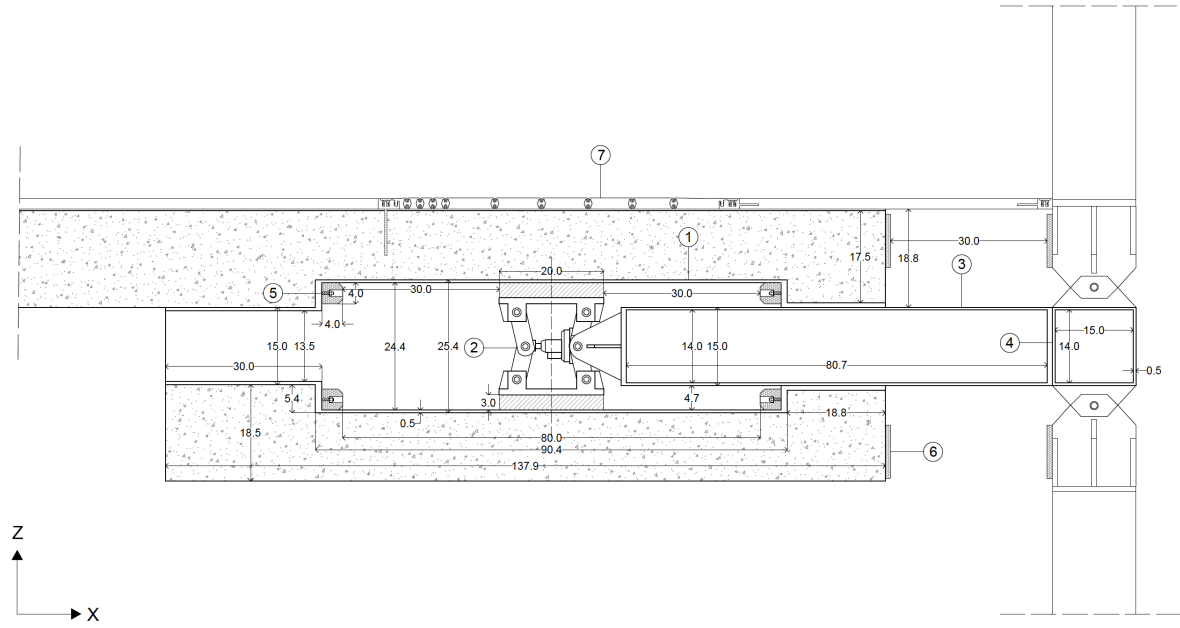


Figure 6.17: Cross-sectional detail of the connection device integrated into the monolithic MF portrayed in its partially open/closed layout

Table 6.20: Sizing of the façade connectors

M_{MF} [tons]	W_{MF} [kN]	N_d [-]	L [kN]	s [m]	g [m]	M_{max} [kNm]	f_{yd} [MPa]	W_x [cm ³]
				1.08	0.50	117.2		346.7
295	2894	27	108.5	0.68	0.30	73.8	338.1	218.3
				0.28	0.10	30.4		89.9

An appropriate sizing of the inner tube which, by favoring the sliding of the friction device, allows both the dissipation of the wind-induced vibration energy and the limitation of MF relative displacements within the pre-fixed gap, is basic to allow the applicability of the system. With reference to the open façade configuration, the connector approaches the static behavior of a cantilever beam fixed to the floor slab at one end. The span length, defined by the gap between the floor and the façade frame midpoint, is left as design parameter. At the free end of the cantilever beam, a concentrated load, L , due to the weight of the one-sided façade, W_{MF} , is applied, which is divided between the number of devices, N_d , placed on each floor. In this context, $N_d = B/d = 27$ is assumed, being $B = 40$ m the width of the building plan and $d = 1.5$ m a standard distance between the glass panels. The maximum bending moment, M_{max} , induced by the loading guides towards a suitable choice of metal profiles to be assigned to the connectors.

The high resistance performance of the connection device is ensured by selecting S355 steel profiles characterized by a yield stress, $f_{yd} = 338.10$ MPa, with a safety coefficient, $\gamma = 1.05$. Three gap values are set, $g = 0.50; 0.30; 0.10$ m, and the related dimensioning of connectors is carried out, as reported in Table 6.20. Based on this, hollow box-shaped

Table 6.21: Geometric and mechanical properties of the connection devices for various sizing calculations performed

g [m]	L_{tot} [m]	$b \times a$ [mm]	s [mm]	W [kg/m]	J_x [cm ²]	J_y [cm ⁴]	W_x [cm ³]	W_y [cm ³]
0.50	1.28	300 × 150	5	34.54	5296	1806	353.08	240.82
0.30	0.88	150 × 300	5	34.54	5296	1806	353.08	240.82
0.10	0.48	180 × 80	4	15.83	834.93	233.01	92.77	58.25

metal profiles are taken from OPPO tables as long as they satisfy the specific resistance modules, W_x , obtained from dimensional computations. The main geometric and mechanical properties of the selected profiles are summarized in Table 6.21.

6.5.2 Modeling of the MF connection system

The monolithic MF is numerically modeled by simply generating the nodes corresponding to each of the 25 floors of the structure and defining their coordinates, $y[i]$, along the z -axis, then, linking them vertically to each other by means of two-dimensional elastic beam-column elements. Each i -th node is placed at a distance, d , from the i -th node identifying the main structural floor. With the exception of the lower one ($z = 0.00$ m), which is fixed to the ground by a homogeneous SP constraint that prevents both rotation and translation along the y -axis, the upper ones are free to move in the local x -direction. Furthermore, each i -th façade node is attributed the corresponding floor mass aliquot, m_{MF} , given by

$$m_{MF} = \frac{\mu}{2} m_s = 0.01375 \cdot 862.84 = 11.86 \quad \text{tons} \quad (6.67)$$

The beam objects joining each i -th façade node with the i -th+1 node immediately above along the z -axis, are implemented within the simulation domain to suitably represent the steel frame elements, which are assigned the following geometric and material properties:

- cross-sectional area of profiles, A [m²]
- steel elastic modulus, E [GPa]
- moment of inertia of profiles, J [m⁴]

Clearly, being a two-dimensional problem, each elastic beam object is representative of an entire façade floor; therefore, the Young's modulus of steel, E , is attributed to each element as it is, whereas the cross-sectional area and the moment of inertia are derived from those of the tubular metal section multiplied by the number of vertical profiles per floor, N . Assuming for the glass panels a standard size equal to $b = 1.5$ m, $N = B/b = 27$ is obtained. The main properties of the façade elements are listed in Table 6.22, where it should be noted that the inertia about the local axis, J , has to be intended as the inertia of the section with respect to which the steel profiles are oriented.

Table 6.22: Mechanical parameters of the façade beam-column elements

N	A	E	J
$[-]$	$[m^2]$	$[GPa]$	$[m^4]$
27	0.117	210	$1.4E - 03$

Wind forces, $F(t)$, computed in section 6.4, are applied on the 25 upper nodes of the elastic beam objects, inducing shear stresses, V_{2-2} , and bending moments, M_{3-3} , in the vertical façade elements. The wind-induced reactions developed in the elastic frame members are printed using the *ops.eleDynamicalForce* command and the maximum stress values per node are shown in Table 6.23. It is specified that the listed values of the shear forces, V_{2-2} expressed in kN , and bending moments, M_{3-3} expressed in kNm , refer to the entire floor of the monolithic MF-equipped building, proving that the steel box-shaped profiles designed with a resisting bending moment relative to $x-x$ axes, $M_{Rd,x}$, obtained from Table 6.17, are capable of withstanding the maximum stresses induced by the applied load.

The relative motion of the façade with respect to the building structure is allowed by interposing the mechanical connection system made of friction devices with bumpers, described in section 6.5.1, between the 25 floors of the movable cladding and the building structural system. It is assumed to place the dissipative brackets on each height, z ; specifically, they could be installed on each side of the cladding glass panels, at the intersection between transoms and mullions within the steel frame.

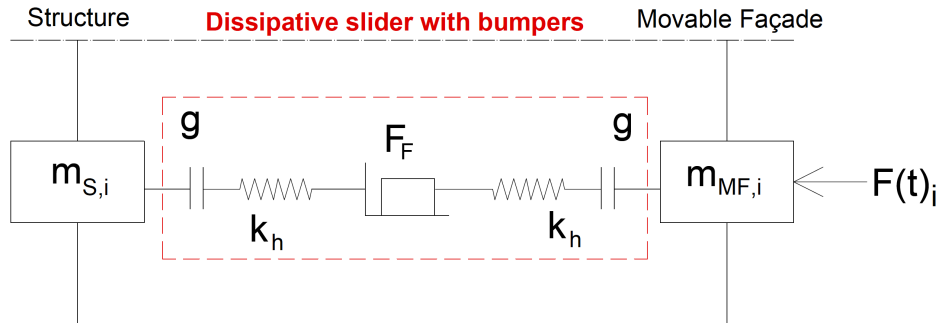


Figure 6.18: Representative diagram of the dissipative slider with bumpers that makes the connection at the i -th floor between the structural mass, $m_{s,i}$, and the façade mass, $m_{MF,i}$ subjected to wind force, $F(t)_i$

As anticipated in Chapter 4, the frictional behavior of the connection device is simulated with a uniaxial multilinear material object defined by an envelope of force-deformation points. The maximum friction force generated by the sliding of the device along the flat surface of the outer steel tube, is expressed by Eq. 4.28, being F_F the sliding friction force (in kN), μ_F the friction coefficient and F_N the component normal to the surface of the resultant forces acting on the slider. By neglecting the difference between static and dynamic (sliding) friction, a constant friction coefficient equal to $\mu_F = 0.47$ for steel surfaces is taken [254], yielding a

Table 6.23: Wind-induced reactions in the beam-column elements

floor	height [m]	MF beam element [-]	axial force	shear force	bending moment
			P [kN]	V_{2-2} [kN]	M_{3-3} [kNm]
25	77.50	50	0.0	47.879	74.214
24	74.40	49	0.0	55.964	86.745
23	71.30	48	0.0	55.952	86.725
22	68.20	47	0.0	35.945	55.715
21	65.10	46	0.0	12.352	19.146
20	62.00	45	0.0	13.794	21.380
19	58.90	44	0.0	34.109	52.869
18	55.80	43	0.0	63.416	98.295
17	52.70	42	0.0	88.481	137.145
16	49.60	41	0.0	103.092	159.792
15	46.50	40	0.0	113.802	176.393
14	43.40	39	0.0	128.300	198.865
13	40.30	38	0.0	142.938	221.554
12	37.20	37	0.0	150.150	232.732
11	34.10	36	0.0	152.264	236.010
10	31.00	35	0.0	164.942	255.661
9	27.90	34	0.0	163.239	253.075
8	24.80	33	0.0	164.239	254.571
7	21.70	32	0.0	167.239	259.221
6	18.60	31	0.0	156.793	243.029
5	15.50	30	0.0	138.896	215.289
4	12.40	29	0.0	122.827	190.382
3	9.30	28	0.0	104.947	162.668
2	6.20	27	0.0	94.258	146.101
1	3.10	26	0.0	69.735	108.089
0	0.00	25	0.0	69.025	214.197

normal force

$$F_N = \frac{F_F}{\mu_F A} \tag{6.68}$$

where $A = 0.3$ (in m^2) is the contact area between the device and the steel tube, given by the product of the slider width and the maximum sliding length. It is clear that the obtained F_N value stands for the overall normal force ($F_N \cdot N_{slider}$) acting on each connection link between the nodes of the model. The two pairs of trapezoidal rubber bumpers, inserted at the ends of the connection system sliding length, are simulated with impact material objects applied in both directions of the façade axial movement with specific impact stiffness, k_h , and initial gap, g . In this way, it is possible to implement the impact occurring between the slider and the rubber pad when the façade reaches the maximum opening allowed by its design constraint, preventing excessive relative (and absolute) displacements. Figure 6.18 shows an enlarged diagram of the connection system between two representative nodes of the i -th floor of the monolithic MF-equipped building.

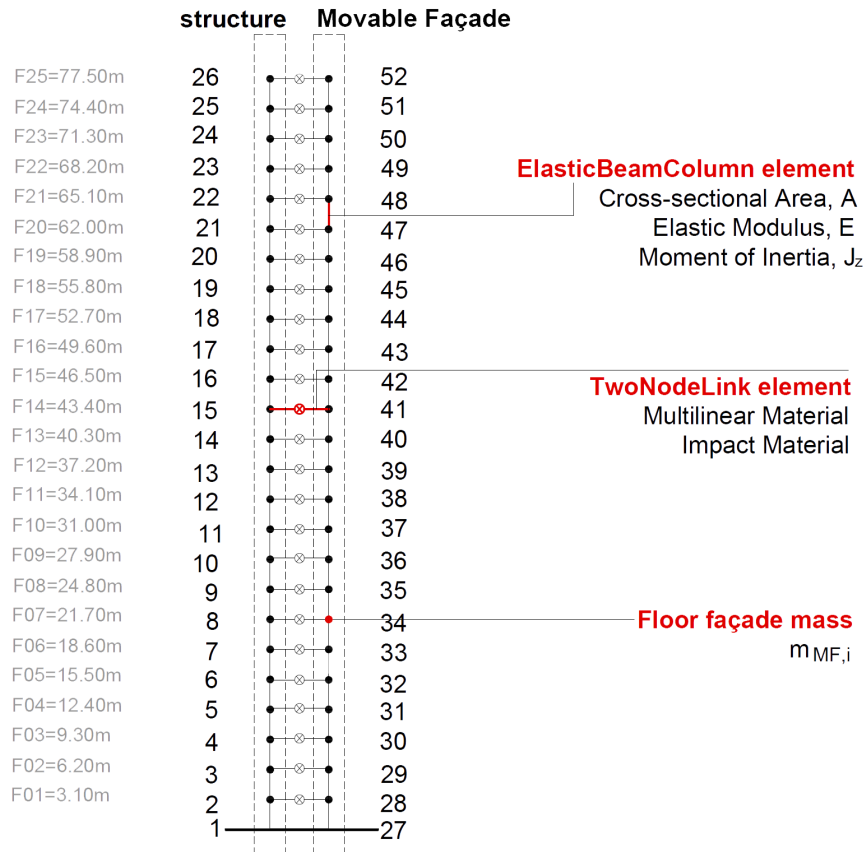


Figure 6.19: Equivalent MDOF model of the monolithic MF-equipped mid-rise building with highlighting of the main elements assigned

The implementation of the connection device model in the MDOF simulation domain takes place by means of two-node link element objects. Each link, defined by two nodes per floor along direction 1, is assigned both the multilinear and the impact material parameters,

as explained in section 4.5. The numerical model of the MF-equipped building built in OpenSeesPy is schematically depicted in Figure 6.19 and is composed of 56 nodes and 232 total elements.

6.6 Evaluation of MF dynamic performances

The simulations carried out in the OpenSeesPy platform are composed by the aggregation of component class objects which must be defined in order to clarify the type of analysis that is performed on the model. The component classes consist of *ConstraintHandler*, *DOF-Numberer*, *Integrator*, *SolutionAlgorithm*, *SolverSystemOfEquation* and *ConvergenceTest*. The selected constraint handler determines how the constraint equations are enforced in the analysis and how to handle the boundary conditions by using a Transformation method. A RCM numberer is chosen to provide the mapping between the degrees-of-freedom at the nodes and the equation numbers, which uses the reverse Cuthill-McKee scheme to order the matrix equations. As for the integrator which determines the predictive step for time $t + dt$ and specifies tangent matrix and residual vector at any iteration, an implicit Hilber-Hughes-Taylor (HHT) method that allows for energy dissipation and second order accuracy, which is not possible with a Newmark integrator, is used. By taking $\alpha = 0.67$, the method is unconditionally stable with the default values of β and γ

$$\beta = \frac{(2 - \alpha)^2}{4}; \quad \gamma = \frac{3}{2} - \alpha \quad (6.69)$$

For determining the sequence of steps taken to solve the nonlinear algebraic equation at the current time step, a Newton-Raphson solution algorithm is applied as it is the most widely used and robust method for this purpose, and within it, a BandGeneral solver system specifies how to store and solve the system of equations in the analysis. Finally, a NormUnbalance test, which uses the norm of the left hand side solution vector of the matrix equation to determine when convergence has been achieved, has been taken.

According to the fixed analysis classes, a time-step increment equal to $dt = 0.02$ s is selected, from which a transient analysis with one analysis step to perform and a total number of integration points equal to 250000 is carried out. Results of the analysis are presented based on the absolute displacement (in m) and acceleration (in g) of the structure and the relative displacement (in m) of the façade. By means of vertical floor profiles and top floor time-histories of the monolithic MF-equipped building superimposed on those of the *uncontrolled* building (i.e., with conventional fixed façade), a direct comparative study of the wind-induced response with and without MF is ensured. The dynamic behavior experienced by the connection device during the analysis cycles is displayed through hysteretic force-displacement loops. To better appreciate the beneficial effect of a monolithic MF incorporated with dissipative sliders, two numerical efficiency indexes are introduced, which quantify the level of reduction of the maximum absolute displacement, η , and acceleration, κ (both expressed in

%)

$$\eta := \frac{\bar{u} - u_{MF}}{\bar{u}}; \quad \kappa := \frac{\bar{a} - a_{MF}}{\bar{a}} \quad (6.70)$$

where u_{MF} and \bar{u} are the maximum lateral top displacement of the building with and without MF, respectively, a_{MF} is the top absolute acceleration of the MF-equipped building and $\bar{a} = a_p$ is the acceleration limit value for the well-being of building users according to the notations of section 2.3.5.

6.6.1 Building response with fixed façade

The dynamic response of the *uncontrolled* building, that is, designed with a conventional fixed cladding, is estimated by making the Timoshenko beam elements to undergo a transient analysis based on the fluctuating wind forces, $F(t)$, computed in accordance with Eq. 6.43. These are inserted in the simulation domain of the equivalent MDOF numerical model in the form of *Path* time-series directly applied on the 25 upper nodes of the beam element. Response profiles portrayed in Figure 6.20 show that under a 3-second wind gust speed, $v_g = 29 \text{ m/s}$ at the top, as defined in section 6.4, the 25-storey building in the absence of the façade system experiences a top lateral displacement of approximately 0.20 m (Fig. 6.20 a) with an amplitude of 0.31 m , a mean value of 0.042 m and a RMS of 0.054 m ; the inter-storey drift ratio is estimated to be 0.06% .

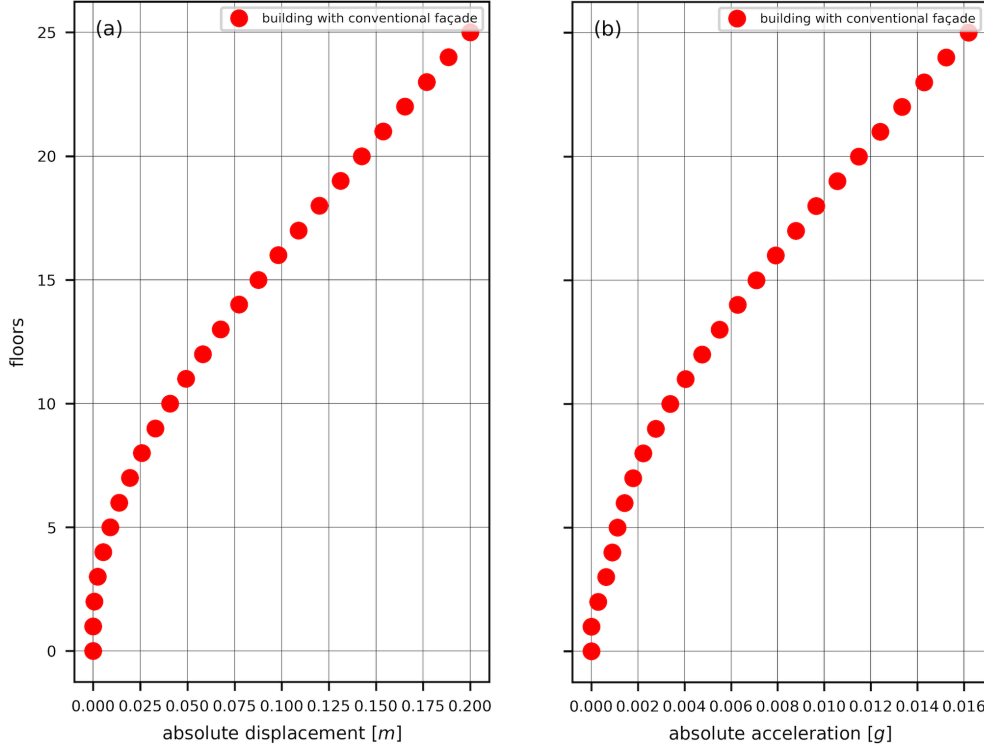


Figure 6.20: Maximum absolute displacement (a) and acceleration (b) of the multi-storey building with conventional fixed façade under wind load

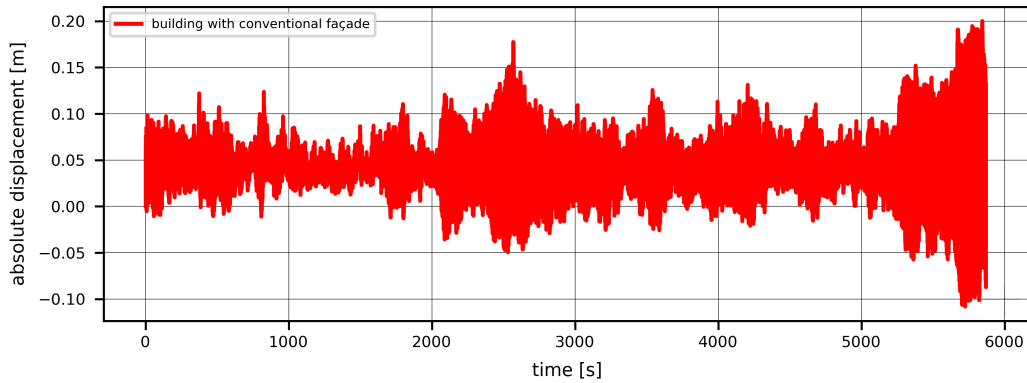


Figure 6.21: Top floor absolute displacement of the multi-storey building with conventional fixed façade under wind load

Table 6.24: Displacement values of multi-storey building top floor with conventional fixed façade

maximum [m]	amplitude [m]	RMS [m]	mean value [m]	inter-storey drift ratio [%]	minimum [m]
0.200	0.308	0.054	0.042	0.06	-0.156

As regards the response of the structure in terms of absolute acceleration, under the same applied load, the top floor reaches a peak of almost $0.017 g$ as emerges from Figure 6.20 b, even if this will be thorough in section 6.6.2, related to the assessment of serviceability performance and compliance with human comfort.

Figure 6.21 displays the top absolute displacement of the building with conventional fixed façade, which is characterized by the succession of narrower amplitude ranges and widely enlarged response areas, mainly located from 5500 s up to the end of the signal. The main response quantities, expressed in terms of maximum, minimum and RMS of the top floor absolute displacement, are listed for clarity in Table 6.24.

6.6.2 Building response with monolithic MF

In the following section, the reduction level of the building dynamic response is assessed with the incorporation of a monolithic MF system integrated with dissipative connection devices into the multi-storey structural building. As can be guessed, the addition of a Movable Façade to the exterior of construction involves the change of application of the fluctuating wind forces, $F(t)$, from the structure to façade, thus from the 25 nodes of Timoshenko beam elements to the 25 nodes of the elastic beam-column elements.

To evaluate the dynamic behavior of the connection system when set in motion by wind action, few output commands such as the elemental deformation and resisting force are added to the simulation domain to enable the construction of force-displacement diagrams which could help a better and clearer understanding of the connection device's response. For the specific assessment purpose, it is decided to reckon a well-defined design case, which will be used as a reference for the parametric investigations that will follow. The key variables defining the

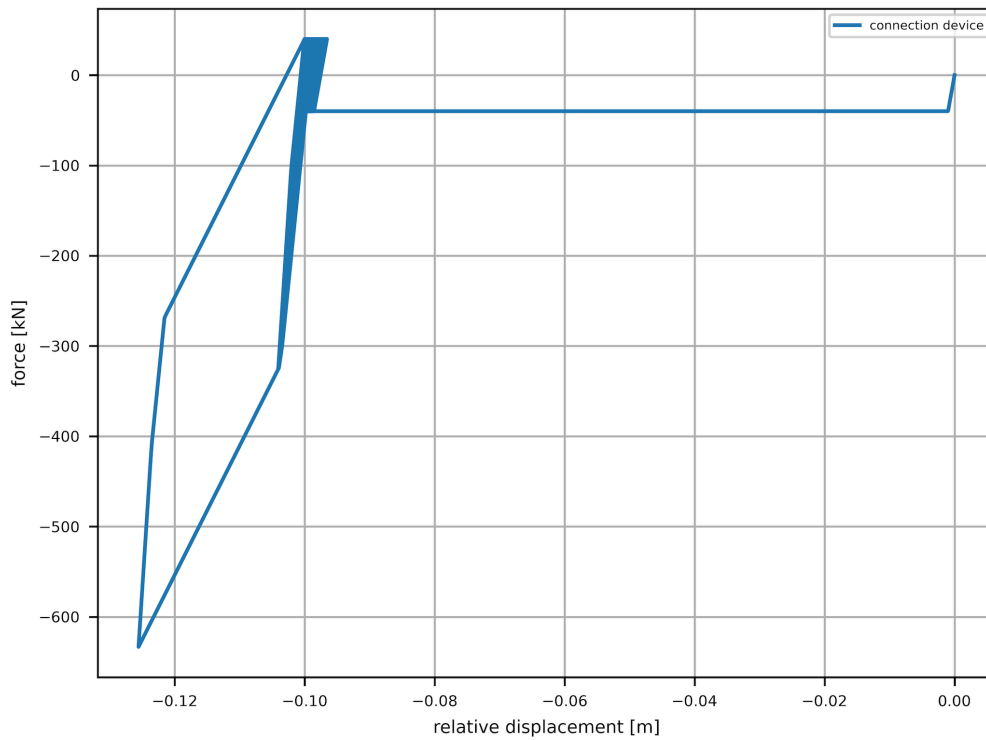


Figure 6.22: Force-displacement diagram of the connection device

Table 6.25: Properties of the connection device

F_F	F_N	L_{tot}	L_F	g	δ_m	δ_y	k_h	K_1	K_2
[kN]	[kN]	[m]	[m]	[m]	[m]	[m]	[MN/m]	[MN/m]	[MN/m]
40	141	0.48	0.40	0.10	0.032	0.003	100	14	18

dynamic performances of the device, namely, the friction threshold of the slider, the impact stiffness of the bumper and the initial gap between the structure and the monolithic MF, are assumed with the constant values taken from Table 6.25.

By looking at Figure 6.22, it can be shown that the sliding of the device makes the wind-excited façade to undergo an initial excursion, until the required gap of 0.10 m is reached and the movement stops, proving the effectiveness of the bumper in embedding its motion. Entering the *colliding* mode, the slider begins to dissipate energy and oscillate around the bumper on non-zero average values, leading to a maximum penetration inside the rubber bumper layer of about 2.5 cm and reaching a maximum contact force equal to $F_c = -600$ kN. When this happens, a high vibration reduction efficiency computed with respect to the maximum absolute displacement, $\eta = 54.4\%$, is recorded on the structural response.

The behavioral improvement of the building with monolithic MF is portrayed in Figure 6.23, showing the vertical trend of the structure absolute displacement (Fig. 6.23 a) and the façade relative displacement (Fig. 6.23 b). It is clear that the connection device has proved to be effective in both controlling the wind-induced vibrations and preventing the excessive façade motion, which is limited to 0.126 m (as for the relative displacement) and to 0.190

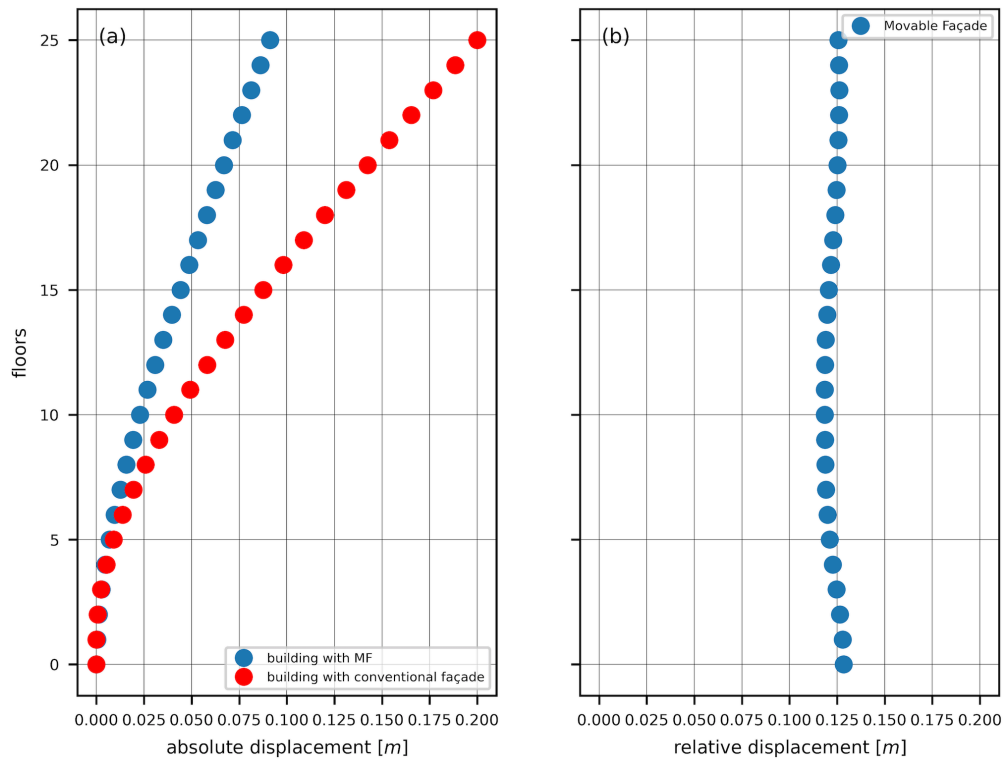


Figure 6.23: Absolute displacement of MF-equipped building superimposed on that with conventional façade (a) and relative displacement of monolithic MF (b)

Table 6.26: Top floor displacement efficiency of the MF-equipped building

Efficiency η [%]	Structure displacement [m]	MF rel. displacement [m]	MF abs. displacement [m]
54.4	0.091	0.126	0.190

m (as for the absolute displacement), thus contained within the practical and reasonable construction limit set during the connector design phase.

Basically, what emerges from the first investigation limited to a reference case study designed with well-defined values of the key variables of the connection device, is the promising potential of the monolithic MF system integrated with dissipative connection devices in keeping the façade relative displacements under control, while considerably improving the structural response in terms of absolute displacement compared to the case with conventional fixed cladding. This is substantially validated by numerical values reported in Table 6.26.

Compliance with performance criteria

The servicability limit state¹⁶ (SLS) is the design to ensure a structure is comfortable and useable. This includes vibrations and deflections (as well as cracking and durability), which may render the structure unsuitable for its intended use, causing occupant discomfort under routine conditions. In order to satisfy SLS criterion, the structure must remain functional for its intended use subject to routine loading. The need to control annoying wind-induced vibrations that can affect the well-being of the occupants or the building safety and stability makes it essential to check compliance with the existing wind performance criteria, both in terms of motion perception and deformation of structural and/or nonstructural components of the building. This means comparing the threshold values for the wind-induced acceleration and inter-storey drift ratio, provided by the current building codes, with the peak of absolute acceleration and the maximum inter-storey drift ratio caused by the applied wind load on the mid-rise building. As defined in section 2.3.5, the drift index, Δ_p , is uniquely considered to be the most suitable parameter to identify the level of safety damage associated with the wind-induced building motion, as well as the peak acceleration, a_p , is believed to be the best indicator for assessing the level of human comfort. Taking the reference threshold values for Δ_p and a_p from Eqs. 2.23 and 2.24, respectively, a comparative study with the response of the monolithic MF-equipped mid-rise building is carried out. Since the elastic response of the building towards a SLS is being evaluated, the habitability check is carried out considering a wind return period $T_R = 1$ yr; in particular, assuming a main office use for the multi-storey building, the habitability check gives

$$a_p = \frac{0.006}{0.426^{0.56}} = 0.00967 \approx 0.01 \text{ g}$$

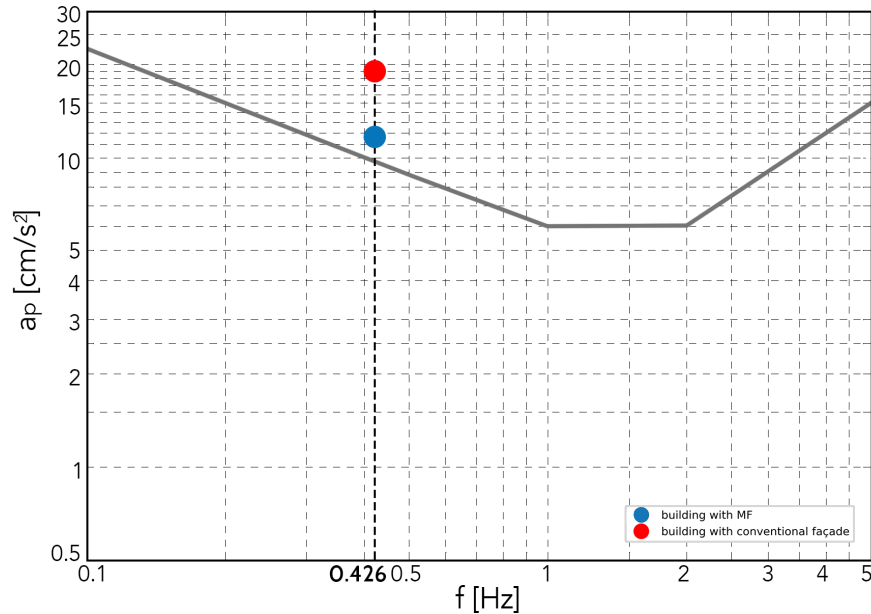
Results of the comparison are provided in Table 6.27. As can be seen, the maximum inter-storey drift ratio of both conventional building and MF-equipped building integrated with dissipative sliders is kept within the threshold value of structural safety imposed by the standards for the specific wind return period accounted for. Even if the drift limit of the building with MF ($\Delta = 0.12\%$) is double that of the building with standard façade ($\Delta = 0.06\%$), in both cases the operational limit state with no damage is guaranteed ($\Delta_p < 0.2\%$).

As for the motion perception criterion depicted in Figure 6.24, in both cases with conventional fixed façade (red dot) and monolithic MF (blue dot) the human comfort limit, a_p (gray curve), is not respected. As a matter of fact, the peak structural acceleration on the top floor (0.019 g for the fixed façade and 0.0115 g for the monolithic Movable Façade) is higher than the limit imposed by the regulations (0.01 g), meaning that the efficiency κ is negative, $\kappa = -15\%$. It should be noted, however, that the peak with MF is lower than the

¹⁶Limit state design (LSD) refers to a structural engineering design method. A degree of loading or other actions imposed on a structure can result in a 'limit state', where the structure's condition no longer fulfils its design criteria, such as; fitness for use, structural integrity, durability, and so on. Limit states are conditions of potential failure. All actions likely to occur during a structures design life are considered during the LSD method, to ensure that the structure remains fit for use with appropriate levels of reliability. LSD involves estimating the subjected loads on a structure, choosing the sizes of members to check, and selecting the appropriate design criteria. LSD requires two principal criteria to be satisfied: the ultimate limit state (ULS) and the serviceability limit state (SLS).

Table 6.27: Compliance with wind performance criteria of the MF-equipped mid-rise building

		building with conventional fixed façade	MF-equipped building
a_p [g]	0.01	0.019	0.0115
Δ_p [%]	0.20	0.06	0.12

**Figure 6.24:** Habitability check of the mid-rise building top floor with conventional façade (red dot) and with monolithic MF (blue dot) based on CNR-DT 207/2008 guidelines

peak in the absence of MF. With a proper change in the design parameters of the connector, it is possible to further improve the acceleration response of the structure with MF ensuring compliance with the comfort threshold, as will be seen in the following sections.

6.6.3 Parametric investigation

The outcomes of the reference test confirm the proper functioning of the monolithic MF incorporated within a generic multi-storey building in controlling the wind-induced structural vibrations due to the dissipative sliding devices and, above all, in suppressing the excessive façade relative displacement due to the brake-motion mechanism imposed by the bumpers. Besides the possibility of being used in place of the common anti-vibration methods such as the conventional TMD, the friction devices with bumpers would seem effective in solving the open issue of the unacceptable façade displacements that would not allow the application of MF for structural purposes, without compromising the structural vibration and acceleration damping efficiency. Clearly, the performance of the system could improve or worsen as the main parameters of the connection device are made to vary. Whether the façade dynamic behavior depends on the management of the device design properties is determined by performing a parametric investigation on the key variables influencing the output of the system, namely, the friction threshold of the slider, the width of the gap between the building and the

façade system and the impact stiffness of the bumpers. The results of the study are reported in the following subsections.

Influence of the friction threshold

The friction threshold of the slider, F_F , determines the force limit beyond which the device begins to slide, passing from the *locked* (or *stick* mode) to the *unlocked* (or *slip* mode), thus allowing the relative movement of the façade connector. The evaluation of the system dynamic performances with the parameterization of the friction threshold is made defining the tested values in relation to the maximum wind force applied to the building top floor (taken from Table 6.14). Hence, the following qualitative range is considered

$$40 \leq F_F \leq 120 \text{ kN}$$

while the other device parameters related to the bumpers' impact stiffness and the initial gap are selected from the constant values listed in Table 6.28.

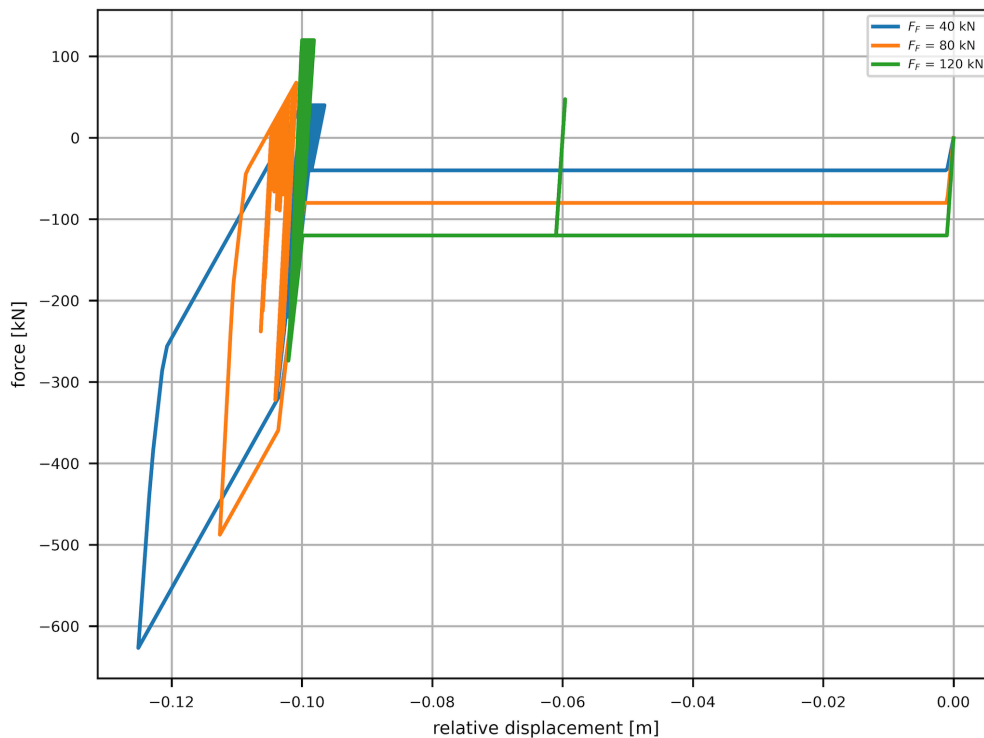


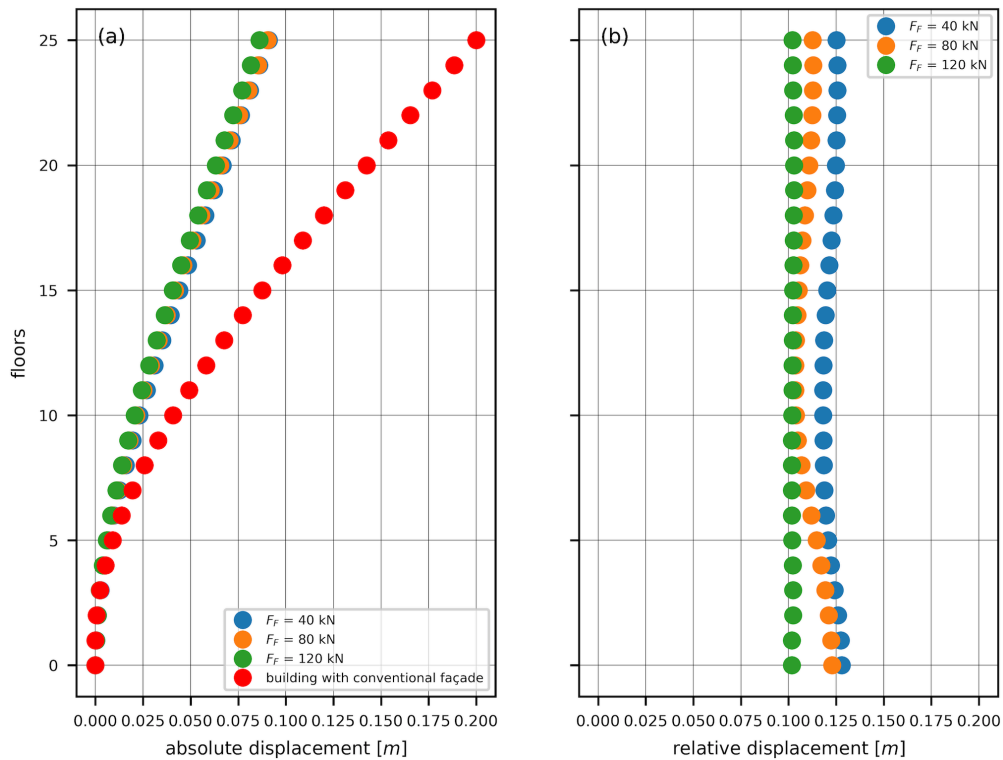
Figure 6.25: Force-displacement diagrams of the connection device for variable friction threshold, F_F

Figure 6.25 is meant to present an overview of the dynamic response of the connection device designed with different friction threshold values, resorting to parameterized force-displacement hysteresis diagrams. As it is clear, the growth of F_F reduces the peak of contact force experienced in the unilateral impact between the slider and the bumper, limiting the maximum penetration of the friction device to progressively lower values. Indeed, a maximum penetration of just 2.6 cm corresponds to $F_F = 40 \text{ kN}$, which passes to 1.4 cm for $F_F = 80$

Table 6.28: Fixed properties of the connection device for the parametric investigation on the friction threshold

L_{tot}	L_F	g	δ_m	δ_y	k_h	K_1	K_2
[m]	[m]	[m]	[m]	[m]	[MN/m]	[MN/m]	[MN/m]
0.48	0.40	0.10	0.032	0.003	100	14	18

kN and, finally, reaches 0.2 cm for $F_F = 120\text{ kN}$. This means that once the gap is closed, set to a reasonable limit value based on the connector dimensioning data, the façade undergoes further small slips before it stops completely and the order of magnitude of these depends on the friction threshold of the slider. At the same time, compliance with the constraint on the amount of energy dissipated during impact for each cycle, results in an extension of the hysteresis area for increasing F_F values, in line with Eq. 4.29.

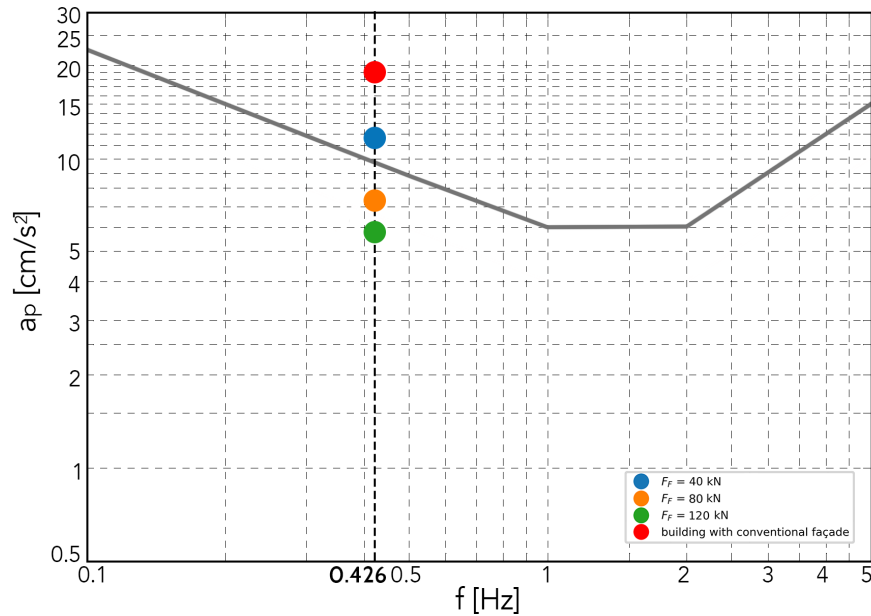
**Figure 6.26:** Absolute displacement of MF-equipped building superimposed on the structure response with conventional façade (a) and relative displacement of monolithic MF (b) for variable friction threshold, F_F

Less pronounced is the effect that a changeable friction threshold has on the structural response which does not show significant alterations for lower or higher F_F values, all producing a substantial reduction of the absolute displacement in an almost constant measure, as emerges from Figure 6.26 a. In fact, starting from a top lateral displacement of 0.20 m at the 25th floor, the maximum displacement with MF is limited to 0.09 m .

Even on the façade response the parameterization of the friction threshold does not produce significant variations, ensuring the limitation of relative displacements within the pre-set

Table 6.29: Top floor displacement efficiency for variable friction threshold, F_F

F_F [kN]	η [%]	Structure displacement [m]	MF rel. displacement [m]	MF abs. displacement [m]
40	54.4	0.091	0.126	0.190
80	55.2	0.089	0.114	0.189
120	56.9	0.086	0.102	0.185

**Figure 6.27:** Habitability check of the mid-rise building top floor with conventional façade (red dot) and with monolithic MF (blue dot) for variable friction threshold, F_F , based on CNR-DT 207/2008 guidelines. Gray curve defines the acceleration limit value, a_p , for different fundamental frequencies

gap of 0.10 m in all the tested cases, but above all at high friction force ($F_F = 120$ kN). In this case, the façade response profile is perfectly vertical while in the other two cases, especially at $F_F = 80$ kN, the relative motion tends to decrease along the height of the building, with the lower floors experiencing the greatest displacements; then, it increases again at the top, giving a wave pattern to the response profile (Fig. 6.26 b). The graphic results are checked with the numerical values listed in Table 6.29.

Finally, Figure 6.27 shows compliance with human comfort requirement for variable friction threshold of the sliding connection device. With the exception of the red dot related to the case with fixed façade, each colored dot corresponds to the peak acceleration of the MF-equipped building top floor obtained with a specific F_F value. As can be seen, the accel-

Table 6.30: Top floor acceleration efficiency for variable friction threshold, F_F

κ [%]	building with conventional fixed façade		
	F_F [kN]		
	-	40	80
	-	120	
	-90	-15	26
		42	

Table 6.31: Fixed properties of the connection device for the parametric investigation on the initial gap

F_F	F_N	δ_m	δ_y	k_h	K_1	K_2
[kN]	[kN]	[m]	[m]	[MN/m]	[MN/m]	[MN/m]
40	141	0.032	0.003	100	14	18

ation decreases as the friction threshold increases with a consequent increase in the efficiency κ (26% for $F_F = 80$ kN and 42% for $F_F = 120$ kN) and keeping the acceleration peak within the comfort limit (gray curve). On the contrary, it worsens as the friction threshold decreases with the consequent exceeding of the gray limit curve, a_p , for $F_F = 40$ kN ($\kappa = -15\%$). Table 6.30 lists the efficiency values.

Influence of the initial gap

The width of at-rest gap, g , defines the useful space to allow the axial translation of the façade, hence, the maximum relative distance that can be reached in relation to the design and technological constraints set. To find out whether any shortening or extension of this space can affect the dynamic performances of the MF system, a parametric analysis with regard to different initial gap sizes between the structure and the monolithic MF (or between the slider and the bumper) has been conducted. Three different gap variables are chosen to cover the most probable and achievable values in real-world applications, even with respect to the construction limits imposed by the connector design explained in section 4.4

$$0.10 \leq g \leq 0.50 \quad \text{m}$$

Numerical investigations are performed on the basis of the friction and the impact stiffness properties of the connection device set in Table 6.31.

In Figure 6.28, relative force-displacement diagrams of the connector are portrayed for different g values. As expected, the connection system can only benefit from a narrowing of the gap between the structure and the façade, resulting in a reduction of the monolithic MF movement. Choosing 0.10 m as initial gap lead to push the façade system response close to a relative displacement of 0.125 m, hence, with a maximum penetration of about 2.5 cm, against the 0.54 m associated with the widest gap tested ($g = 0.50$ m, which corresponds to a maximum penetration of 4 cm). While keeping unchanged the control over the structural displacement profile, as shown in Figure 6.29 a, it is quite important to see how sensitive is the system in terms of reducing the façade response, with regard to its relative displacement, with a narrowing of the gap, as emerges from Figure 6.29 b. Indeed, by looking at the efficiencies listed in Table 6.32, an almost negligible difference occurs between the η values as the gap varies, whereas much more relevant is the influence exerted on the MF response.

As regard the acceleration response of the tower with MF, Figure 6.30 shows compliance with human comfort requirement for variable initial gap, g , according to the parameters defined in Table 6.31. With the exception of the red dot related to the case with fixed

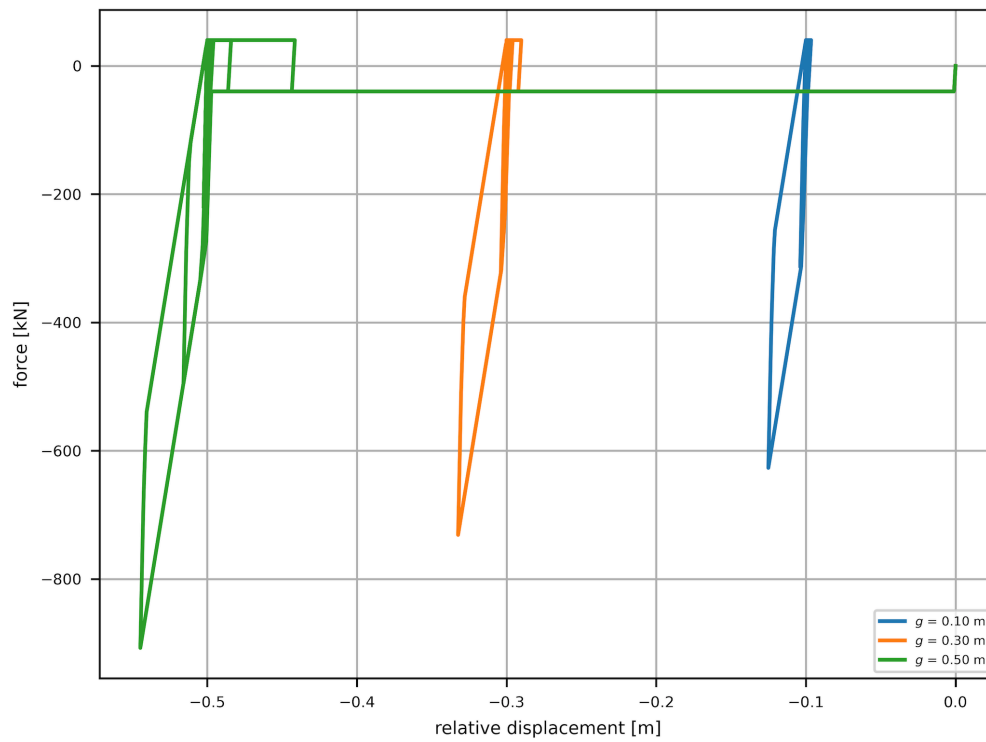


Figure 6.28: Force-displacement diagrams of the connection device for variable initial gap, g

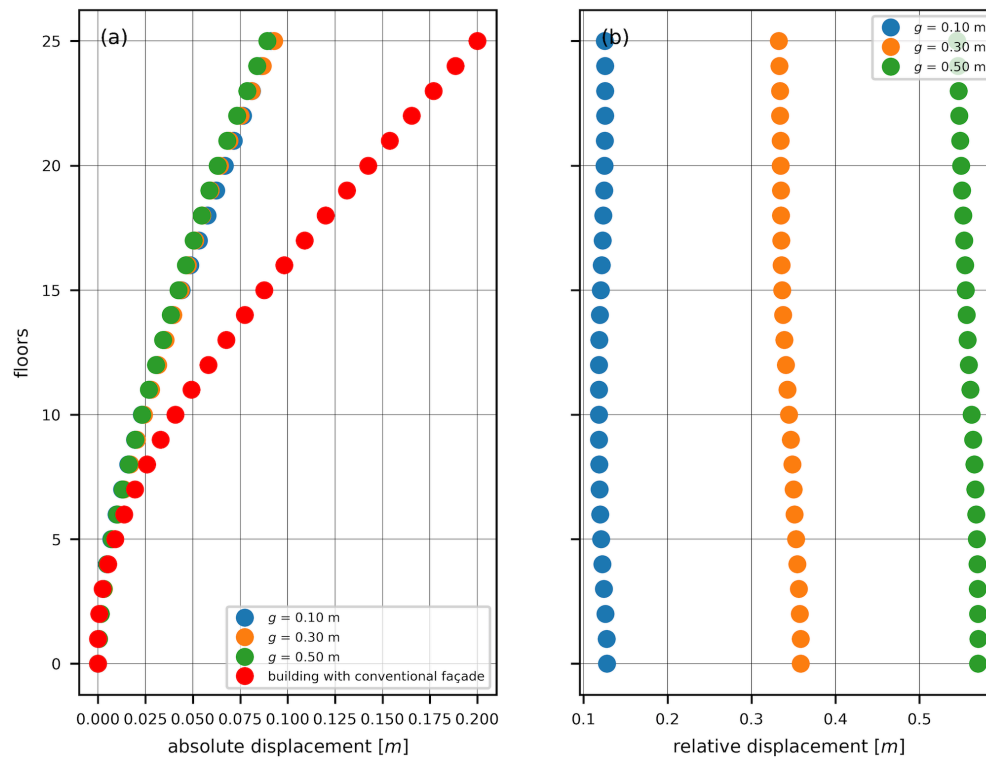
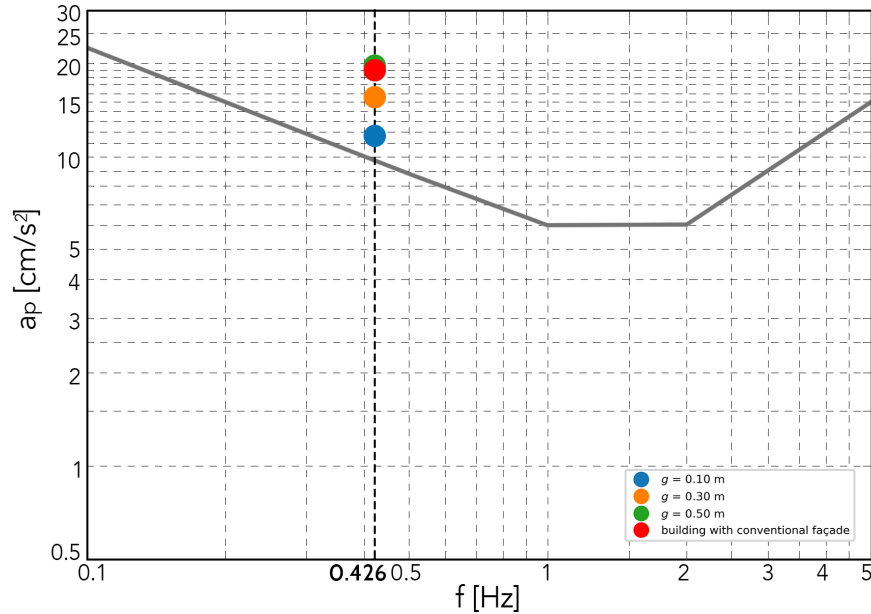


Figure 6.29: Absolute displacement of MF-equipped building superimposed on the structure response with conventional façade (a) and relative displacement of monolithic MF (b) for variable initial gap, g

Table 6.32: Top floor displacement efficiency for variable initial gap, g

g [m]	η [%]	Structure displacement [m]	MF rel. displacement [m]	MF abs. displacement [m]
0.10	54.4	0.091	0.126	0.190
0.30	54.9	0.090	0.332	0.374
0.50	55.4	0.089	0.545	0.587

**Figure 6.30:** Habitability check of the mid-rise building top floor with conventional façade (red dot) and with monolithic MF (blue dot) for variable initial gap, g , based on CNR-DT 207/2008 guidelines. Gray curve defines the acceleration limit value, a_p , for different fundamental frequencies

façade, each colored dot corresponds to the absolute acceleration of the MF-equipped mid-rise building top floor obtained with a specific initial gap. As can be seen, with the widening of the gap, the acceleration peak on the top floor increases and this implies the exceeding of the comfort threshold with extremely negative efficiency ($\kappa = -98\%$ for $g = 0.50$ m); vice versa, the narrowing of this space allows to limit the acceleration peak, even if maintaining a negative efficiency ($\kappa = -15\%$ for $g = 0.10$ m) based on the imposed friction threshold and impact stiffness of the bumper. The efficiency values κ for the three initial gaps, g , investigated are listed in Table 6.33.

According to this, a fair compromise for ensuring both a satisfactory structural control and resolution of Moon's issue can be represented by designing a monolithic MF incorporated

Table 6.33: Top floor acceleration efficiency for variable initial gap, g

	building with conventional fixed façade	g [m]		
	-	0.10	0.30	0.50
κ [%]	-90	-15	-53	-98.2

with dissipative connectors, as depicted in Figure 6.17, of limited sliding length and narrow gap between the friction device and the sideward bumpers.

Influence of the impact stiffness

In line with the outcomes presented so far, the reduction trend is now matched with increasing the impact stiffness of the connector and evaluating the influence of this key variable on the dynamic performances of monolithic MF. The range of investigation of the impact stiffness parameter, k_h , is estimated starting from the value derived from Eq. 4.37 and making an attempt to progressively increase it in a conscious way, obtaining

$$25 \leq k_h \leq 100 \text{ MN/m}$$

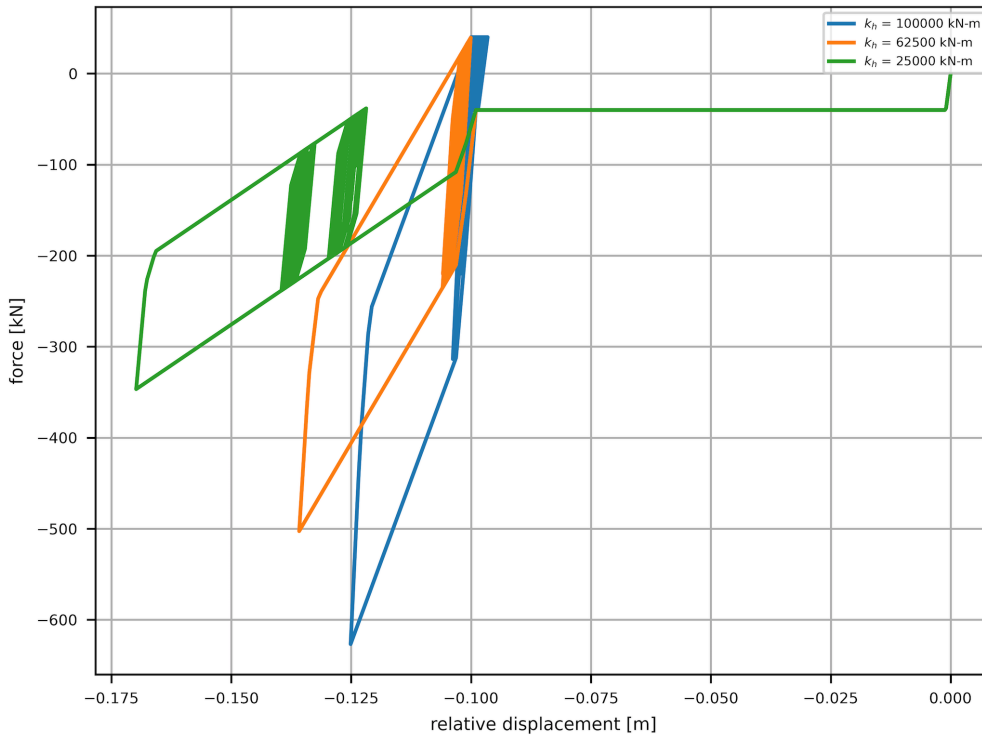


Figure 6.31: Force-displacement diagrams of the connection device for variable impact stiffness parameter, k_h

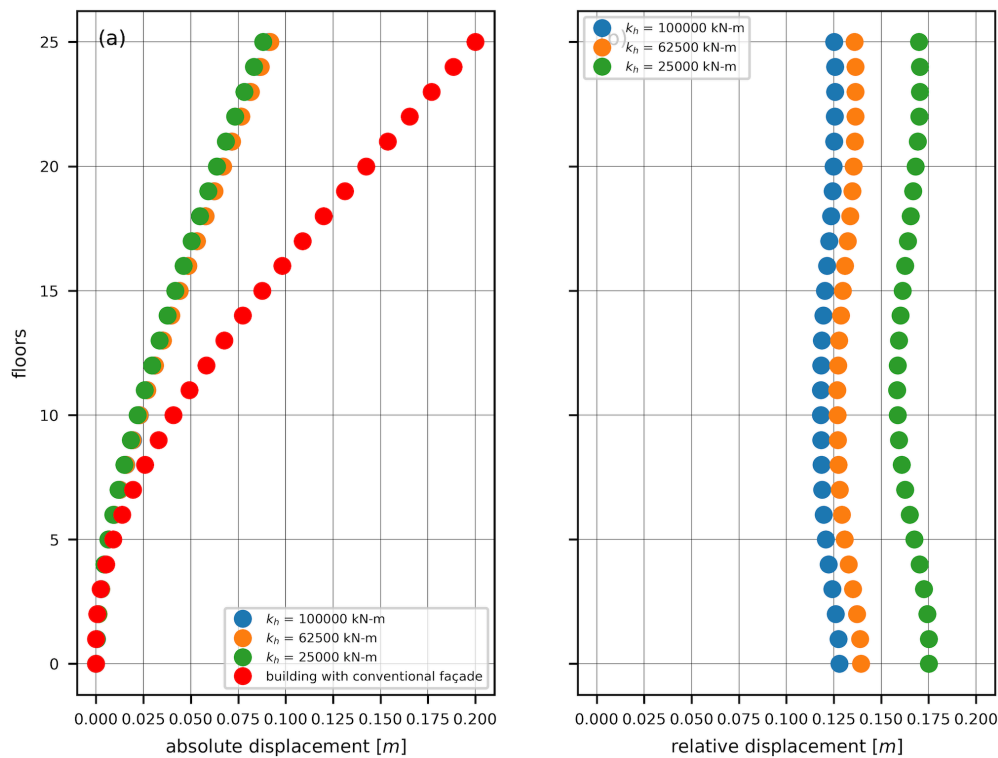
All the other mechanical and geometric properties that fully characterize the connection system assume the constant values listed in Table 6.34. The following figures and tables are intended to present an overview of the dynamical behavior provided by the connection device if designed with different impact stiffness values.

Figure 6.32 illustrates the relative force-displacement diagram for the three impact stiffness values tested, showing how a possible stiffening of the bumper layer (blue diagram) implies a tighter control on the relative displacement of the monolithic MF, which stops at 0.125 m away from the building, hence, with a maximum penetration of 2.5 cm with respect to the allowable limit of 0.10 m . On the contrary, if the bumper assumes a more deformable

Table 6.34: Fixed properties of the connection device for the parametric investigation on the impact stiffness

F_F	F_N	L_{tot}	L_F	g	δ_m	δ_y
[kN]	[kN]	[m]	[m]	[m]	[m]	[m]
40	141	0.48	0.40	0.10	0.032	0.003

configuration (green diagram), the obstruction of the façade relative motion would be less definite and this would allow a greater façade displacement with a wider penetration inside the bumper layer (about 7.0 cm), reaching approximately 0.17 m away from its starting position.

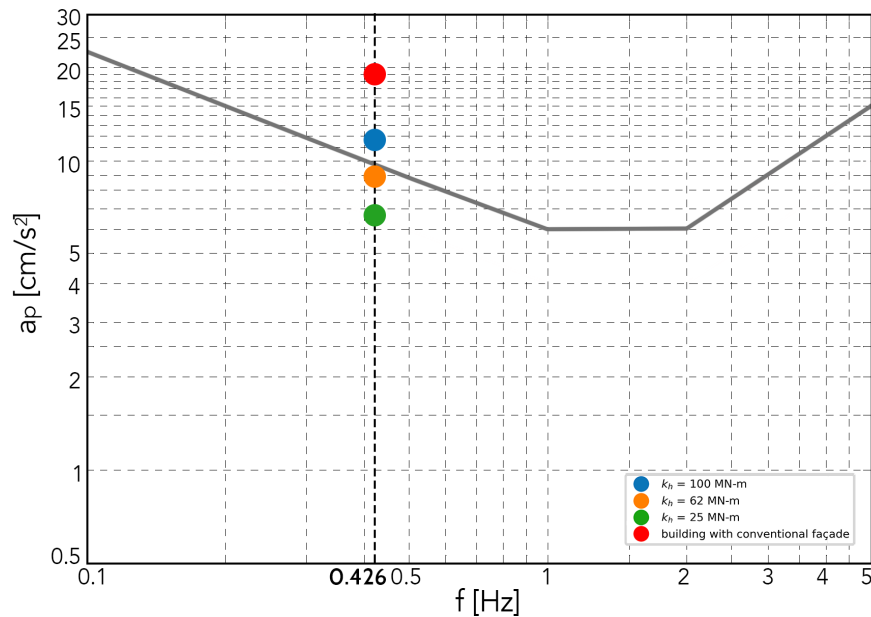
**Figure 6.32:** Absolute displacement of MF-equipped building superimposed on the structure response with conventional façade (a) and relative displacement of monolithic MF (b) for variable impact stiffness, k_h

While stiffening or softening the bumper layers leads to negligible benefits on the structural absolute displacement (Fig. 6.32 a), it is certainly more impactful on the façade relative displacement response (Fig. 6.32 b). As a matter of fact, the more rigid the bumper, the more the relative displacement of monolithic MF is contained by the high stiffness, reaching a maximum of 0.125 m at the top and 0.127 m at the bottom, while the more the bumper is deformable, the more the façade moves towards major displacements especially on the lower floors (about 0.175 cm). The results of the parametric study both on the MF-equipped structure and the monolithic façade are summarized in Table 6.35.

As regard the acceleration trend, it is clear that increasing the stiffness leads to a dis-

Table 6.35: Top floor displacement efficiency for variable impact stiffness, k_h

k_h [MN/m]	η [%]	Structure displacement [m]	MF rel. displacement [m]	MF abs. displacement [m]
25	55.9	0.088	0.170	0.223
50	55.1	0.090	0.141	0.210
100	54.4	0.091	0.126	0.190

**Figure 6.33:** Habitability check of the mid-rise building top floor with conventional façade (red dot) and with monolithic MF (blue dot) for variable impact stiffness, k_h , based on CNR-DT 207/2008 guidelines. Gray curve defines the acceleration limit value, a_p , for different fundamental frequencies

tinctly opposite effect compared to displacement response. As a matter of fact, the absolute acceleration of the building with monolithic MF grows in a directly proportional way to the impact stiffness of bumpers, due to the strong contact occurring between building and façade when the relative gap between them closes. Since this parameter directly affects the structural acceleration peak on the top floor, consequently, the efficiency κ , which will assume positive values when the stiffness is reduced and vice versa.

To better understand this aspect, Figure 6.33 shows the habitability check of Isozaki tower top floor for variable impact stiffness of the bumper. As expected, the reduction of k_h is beneficial in keeping the acceleration peak within the comfort threshold (green point,

Table 6.36: Top floor acceleration efficiency for variable impact stiffness, k_h

	building with conventional fixed façade		
	k_h [MN/m]		
	-	100	62.5
κ [%]	-90	-15	10.5

corresponding to $k_h = 25 \text{ MN/m}$), reaching an efficiency $\kappa = 32\%$; on the contrary, increasing the stiffness of the slider-bumper contact causes a structural acceleration greater than the admissible value (blue point) making the efficiency negative ($\kappa = -15\%$ for $k_h = 100 \text{ MN/m}$). Values are listed in Table 6.36.

6.7 Closing remarks

A 25-storey, 77 m tall multi-storey building, directly simulated into SAP 2000, is selected as a generic case study for the assessment of dynamic performances of a monolithic Movable Façade integrated with dissipative slider and bumpers subject to longitudinal wind load. The available FEM of the mid-rise building is useful for deriving the main mechanical (mass and stiffness), dynamic (frequencies, periods and deformed shapes) and material properties of the adopted structural system, based on which the equivalent MDOF numerical modeling and related steps are carried out using a Python code. Both the *along-wind* velocities and pressures are computed according to the Italian guidelines taken from CNR-DT 207/2008 instructions and the related *along-wind* fluctuating forces are obtained resorting to a digital simulation technique implemented in the *NatHaz Online Wind Simulator* (NOWS). With the introduction of suitable numerical indicators for the assessment of both structural displacement (η) and acceleration (κ) reduction efficiency, a comparative study between the wind-induced response of the building with conventional fixed façade (i.e., *uncontrolled* building) and with a monolithic MF is carried out. Through the analysis of a reference case, implemented with well-defined values of the connection device design parameters, followed by a detailed parametric investigation, the influence of the key variables that manage a proper design and modeling of the connection device on the MF dynamic performances is in-depth. The outcomes of the study conducted for variable friction threshold of the slider (F_F), impact stiffness of the bumper (k_h) and initial gap between the building and the façade system (g), validate the success of the MF connection device if applied on wind-excited mid-rise buildings, both in reducing the top lateral displacements and accelerations, compared to the case in the absence of monolithic MF system, hence with conventional fixed façade, and in containing the MF relative motion within acceptable constructive limits, avoiding the recurrence of Moon's problem on this type of structures. Specifically, it can be asserted that the absolute displacement reduction efficiency of the structure, η , is almost independent of the variation of the control parameters of the connection device, both with respect to the friction slider and to the dissipative bumper dampers' system. In this case, in fact, the dynamic performances of MF remain mostly constant on encouraging efficiency values, ranging between 54% and 56%, hence, proving the strong capability of the monolithic MF integrated with dissipative sliders in reducing structural vibrations compared to the *uncontrolled* case. Based on this result, the design variables of the connector can be appropriately combined in order to achieve suitable results also in terms of acceleration reduction efficiency, κ . Throughout the parametric investigations, the greatest reduction of the structural absolute acceleration is recorded in correspondence with higher friction threshold of the slider, $F_F = 120 \text{ kN}$ ($\kappa = 11\%$), lower

impact stiffness of the bumper, $k_h = 25 \text{ MN/m}$ ($\kappa = 40\%$), and narrower initial gap between the slider and the bumper (or between the façade and the structure). According to this assumption, a positive achievement also occurs on the façade response, in terms of limitation of its relative displacements and accelerations, thus showing that with a proper combination of the key variables, balanced and promising dynamic performances may be ensured both for the civil building and monolithic MF, also allowing for a remarkable compliance with wind performance criteria, both in terms of user's comfort (a_p) and the level of structural damage (Δ_p).

Chapter 7

Isozaki tower with MF under wind load

7.1 Introduction

To better appreciate whether the efficiency of the connectors may depend on the façade layout or the building dynamic properties, a new study is proposed in the present Chapter, which inquires the vibration damping performances of the sliders incorporated into the load-bearing structural system of a high-rise building¹⁷ equipped with a multiblock Movable Façade. Milan's Isozaki tower, a 51-storey, 220 m tall building (three times the height of the generic building of Chapter 6) has been selected for this purpose. The motivation behind the choice of this test case building is linked to the presence of four tubular steel buttresses placed on the two main glazed façades facing north-west (NW) and south-east (SE), respectively, required to withstand wind loads due to the high flexibility of the tower. The two pairs of struts are constrained at the structure base to fluid viscous dashpots which allow to dampen the wind-induced vibrations, transforming them into viscous friction, thus reducing the motion on the upper floors; however, this happens at the price of an unpleasant architectural impact. Ideally trying to replace the current devices with a Movable Façade incorporated with dissipative sliders, equally effective against dynamic wind load but less invasive from an aesthetic point of view, would be the goal of this research phase.

A shear deformable beam model that considers the effects of shear deformation and rotatory inertia is implemented to suitably simulate the behavior of the tower due to the presence of two imposing belt-trusses, responsible for angular deformations which distance the structural response from the Euler-Bernoulli beam theory. Despite its regular shape in plan and elevation, the different number of floors as well as the different distribution of mass and stiffness along the height compared to the building of Chapter 6, make the Allianz tower more flexible and with a higher vibration period (consequently, with a lower fundamental frequency) than the 25-storey building. Given the high vertical development of the

¹⁷According to *The Structural Design of Tall and Special Buildings*, the basic definition of a tall building -in the context of a journal audience- is a structure that is equal to or greater than 50 meters (165 feet) in height, or 14 stories or greater.

tower and taking advantage from the current cladding layout, a multiblock MF is preferred over the monolithic version, already checked on the mid-rise test case building. This means separating the surface of the curved glass envelope into eight independent movable parts between which the relative motion in the *along-wind* direction is allowed by means of the sliding connectors. It is worth noting that the choice of a multiblock solution is also linked to constructive feasibility issues on this type of structures. Following the procedure already described for the 77.5 m high building, an equivalent MDOF numerical modeling is performed over the MF-equipped Isozaki tower experiencing fluctuating wind forces digitally simulated at a well-defined frequency and gust wind speed. A comparative parametric study exploring the influence of the key variables that characterize the constitutive behavior of the connection device is conducted between the dynamic response of the tower with its conventional fixed façade and the dynamic response of the tower incorporated with the proposed connection devices. For each parametric investigation performed, the results obtained are expressed by means of vertical floor profiles of absolute and relative displacement and absolute acceleration, time-histories of lateral top displacement and hysteretic force-displacement diagrams of the friction device with bumpers which well-explain the nonlinear behavior of the connectors. Finally, compliance with wind performance criteria for high-rise buildings is checked.

7.2 Generality on Isozaki tower

According to the Council of Tall Buildings and Urban Habitat (CTBUH), Italy is 27th in the world ranking for the number of tall buildings on its territory, counting only on 4 towers over 150 m high, 2 over 200 m and none over 300 m. In the Italian race for skyscrapers, the American CTBUH claims the Isozaki Tower at the provisional 2nd place (at the 34th place in Europe) preceded by the Unicredit Tower by Pelli Clarke Pelli Architects (217.7 m high) and the still under construction Torre Regione Piemonte by Fuksas, which will rise to a total height of 209 m.

Isozaki tower, also known as Allianz tower, is a fifty-one-storey 209-metre-tall (202.2 meters from ground level) skyscraper located in Milan (Lombardy, Italy), in the renewed CityLife district (Fig. 7.1). First completed of the triptych planned in the new district under construction on the vacated site of the former trade fair of the city, the skyscraper bears the joint signature of the elderly Japanese master Arata Isozaki¹⁸ (Fig. 7.2) and the young Italian designer Andrea Maffei; it serves as the headquarters of the Allianz Group and the Italian parent company Allianz SpA; therefore, its use is primarily offices with a few areas reserved for services [255].

In the new headquarters of the German insurance company, each vertical segment consists of six levels having an inter-storey height of 3.90 meters (2.80 meters excluding flooring slabs, false ceilings and floating floors), for a total of forty-six floors for offices, three technicians

¹⁸Arata Isozaki is a Japanese architect, urban designer, and theorist from Ōita (Japan). He was awarded the RIBA Gold Medal in 1986 and the Pritzker Architecture Prize in 2019. Renowned for having designed one of the three new buildings in the center of Milan (the Isozaki Tower, from which it takes its name), since 2005 he has opened together with Andrea Maffei the Arata Isozaki & Andrea Maffei Associati S.r.l. studio to develop new projects in Italy.



Figure 7.1: Isozaki tower located in the CityLife district of Milan, Italy

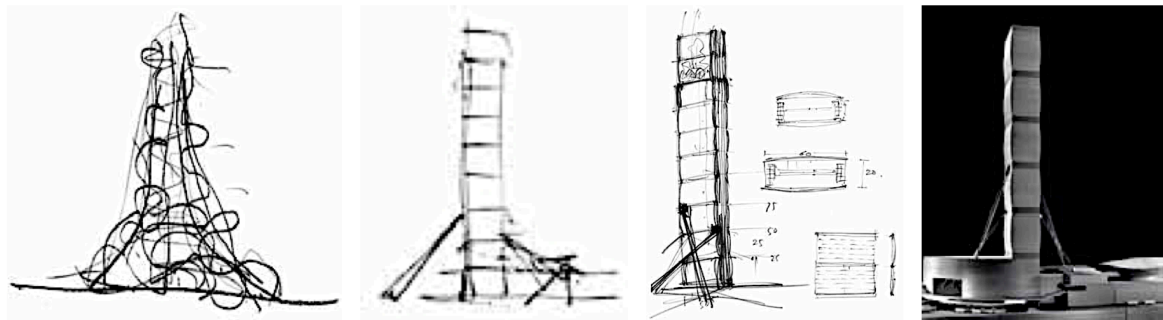


Figure 7.2: Arata Isozaki study sketches for the CityLife tower in Milan (2003). Source: Biagi, M. *Non è solo bella: la torre Allianz a Milano di IsozakiMaffei. Casabella 855*

and a triple-height hall that connects the subway 5 line with the elevated portion of CityLife central square. Internally, the organization of the spaces is perfectly rationalized: the concrete cores are distributed over the heads, freeing up an intermediate rectangular area of $24 \times 36 \text{ m}$ for the offices; 1.50 m is the step that regulates the cadence of the fixtures, the distribution of the fan coils (every 3 meters) and the span of the Steel Reinforced Concrete (SRC) pillars aligned behind the façade floors (every 6 meters). A computerized destination control system manages, through badges, the flows of employees and visitors through the two groups of side elevators: a low-rise, serving the first twenty-four floors, and the second high-rise, with exclusive access to the subsequent twenty-five floors. Three of the seven elevators are glazed and panoramic on each side and animate the narrow fronts of the tower with their movement.

At the foot, the *endless* tower insists on an underground parking plate and on a podium which, as anticipated, draws directly from the exit of the new underground line, hosting the canteen and two conference rooms, the largest with three hundred places. The design of all these elements -square, podium and entrance hall- is governed by the adoption of a special Penrose pattern, based on the aperiodic permutation of a pair of rhombuses, each with four



Figure 7.3: Worksite pictures of Isozaki tower under construction (2012-2015)

Table 7.1: General characteristics of Isozaki tower

height	length	width	inter-floor (1° - 4° levels)	inter-floor (5° - 51° levels)	$n.$ floors
H	B	L	h_1	h_2	N
[m]	[m]	[m]	[m]	[m]	[—]
202.20	60	24	5.00	3.90	51

sides of unit length in a golden ratio, which allows to manage and coordinate the layout/sizing of the spaces and the laying motif of flooring and cladding. When completed in 2015 (Fig. 7.3), the Isozaki tower was the Italian building with the highest number of floors, comprising 51 above-ground storeys and 3 levels of basement which accommodate 350 parking spaces. The inter-storey height of the first 3 above-ground levels is 5.00 m, the next 48 floors are 3.90 m high. The main dimensional properties of the tower are summarized in Table 7.1.

Its extended height, together with a rectangular plan approximately 60 m long by 24 m wide shown in Figure 7.4, makes the tower similar to a particularly slender rectangular cantilever beam, with the main longitudinal y -axis oriented in the south-west/north-east direction. The high slenderness ($\lambda = H/d \approx 8.40$, where H is the height and d is the width of the building [256]) and the low intrinsic damping (1%), combined with a high fundamental period of the structure and the low seismicity of Milan area, led to evaluate the wind as the most significant horizontal action in the design phase [257], prompting the designers to

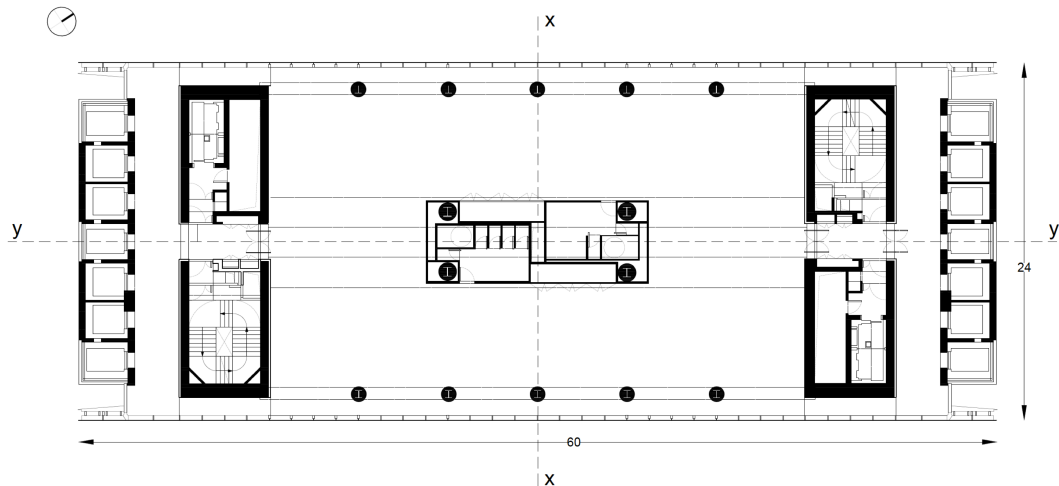


Figure 7.4: Typical floor plan

carry out wind tunnel tests conducted both in Canada and in Italy, at Milan's Polytechnic. Throughout these tests, it emerged that the overall verifiable top lateral displacement (on the 50th floor) would have been equal to 100 *cm*. This led the design team to introduce an additional energy dissipation system to avoid wind resonance phenomena and to reduce displacements and accelerations on the upper floors, improving both structural safety and human comfort.



Figure 7.5: Detail of the strut connected at the top to the curved glazed façade and constrained at the base to a pair of viscous dampers

The energy dissipation system was created by means of fluid viscous dampers (Fig. 7.5) placed at the base of four massive tubular steel buttresses, approximately 60 *m* long on the main front and 40 *m* on the rear, that further stiffen the already solid steel and concrete building [258]. Given their heavy weight, these exposed structures have been emptied and tripartite, while leaving them joined by large lightened steel handkerchiefs, so as to avoid

Table 7.2: Structural materials used during construction

Concrete	B450C rebar steel	S355 metal carpentry steel
$[m^3]$	$[tons]$	$[tons]$
87.780	13.817	2.230

the uncomfortable sail effect that would have had repercussions on the tower. Experimental studies were carried out at the Wind Tunnel of Milan Polytechnic (GVPM) based on a 1 : 100 scale model of Isozaki tower. The design wind in the north-west (NW) direction indicated in the documents drawn up by the University of Genoa in 2006 was reproduced and a 38 m/s maximum wind velocity was highlighted (with $T_R = 100$ years); hence, higher than the 33 m/s adirectional wind speed provided by the Italian legislation [259]. By modeling the viscous dampers in the FEM of the tower, it emerged that the overall verifiable displacement on the top floor (the 50th) would have been equal to 100 cm ; the four struts allowed to reduce the oscillations at the top by about 80 cm , reaching the current 20 cm .

The building, whose construction costs are around 150 million euros, boasts the LEED¹⁹ Gold level environmental certification.

7.2.1 Study of the structural system

The tower has been carefully designed to ensure adequate balance, stiffness and strength, especially to withstand wind actions. From a structural point of view, the building rests on a 5300 m^3 reinforced concrete foundation slab based in turn on sixty-two 31 m deep piles. On the foundation system, the load-bearing supporting structure is set up, which is composed of four decentralized cores in reinforced concrete of class C 40/50 with a C section, symmetrical with respect to the centerline, which extend from the foundation slab to the top for a total length of 218 m . The standard plan is presented as a large 24×36 m open space, free from intermediate pillars, with the only exception of two pairs of five circular columns arranged along the two long sides of the plan, containing the vertical metal carpentry in elevation. The walls of the concrete cores have variable thicknesses from 0.4 m to 1.2 m .

The tower is equipped with a total of 14 lifts, arranged symmetrically along the short sides, capable of reaching a top speed of 7 m/s ($= 25.2$ km/h). Four belt-trusses, two located at the 25th level and two at the 51st level, respectively, were cast by Unical S.p.A. on the longer side of the building to stiffen the slender structure and allow it to withstand horizontal actions. The two massive belt-trusses at the top are $36.10 \times 5.19 \times 0.90$ m wall beams, made of 240 m^3 high-strength synthetic fiber-reinforced (FRHSC) concrete (resistance class C 60/75 chosen in order to overcome the problems of handling complex structures). As for the two intermediate

¹⁹LEED (Leadership in Energy and Environmental Design) is the most widely used green building rating system in the world, which provides a framework for healthy, highly efficient, and cost-saving green buildings. LEED certification is a globally recognized symbol of sustainability achievement and leadership. It is available for all building types and all building phases including new construction, interior fit outs, operations and maintenance and core and shell. The number of points a project earns determines the level of LEED certification it receives. There are four levels of certification: certified (40-49 points), silver (50-59 points), gold (60-79 points) and platinum (80+ points).

Table 7.3: Materials and sections of the structural system

Structural element	Section [cm]	Material	
		RC	Steel
cores	40 ÷ 120	C40/50	B450C
perimeter columns	ϕ 65 ÷ 120	C40/50; C50/60; C70/85	B450C/S355
central columns	ϕ 85 ÷ 170	C40/50; C50/60; C70/85	B450C/S355
slabs	20 ÷ 50	C40/50	B450C
belt trusses (25° level)	3610 × 580	-	S355
belt trusses (51° level)	3610 × 519 × 900	C60/75	-
struts (north-west)	6300	-	S355
struts (south-east)	4200	-	S355

belt-trusses, these are 36.10×5.80 m reticular beams in metallic carpentry, weighing about 180 tons, deployed on site on a 5-day journey through an exceptional transport system 49 m long. Once they reached the area, they were placed at +101.50 m above sea level due to a Strand Jack lifting system.

The main quantities of structural materials used for the construction of Isozaki tower are derived from [260] and are listed in Table 7.2. The section and material properties of the main structural elements making up the supporting skeleton are summarized in Table 7.3. From the FEM of the tower taken from [261], deformed shapes and natural frequencies (in Hz) associated with the first three vibrating modes have been obtained. As can be seen from Figure 7.6, the 1st mode around the baricentric y -axis represents a typical shear deflection which is well-described by a Timoshenko beam model; the 2nd mode around the baricentric x -axis shows a flexural deformation, which is a typical behavior of the Euler-Bernoulli cantilever beam; finally, the 3rd mode depicts a torsional deformation. For the first 10 vibrating modes, a damping ratio ξ of 1% has been assumed (with the possibility of reaching 4% only with additional dampers).

For the purposes of numerical modeling and simulation, the second vibrating mode along the x -axis is taken into account, being the lateral stiffness of the building weaker in this direction, hence, more susceptible to wind activity: this means matching the fundamental frequency related to the 2nd vibrating mode, $f = 0.153$ Hz, in order to develop the equivalent MDOF numerical model, which will be addressed in detail in section 7.3. It is also assumed to

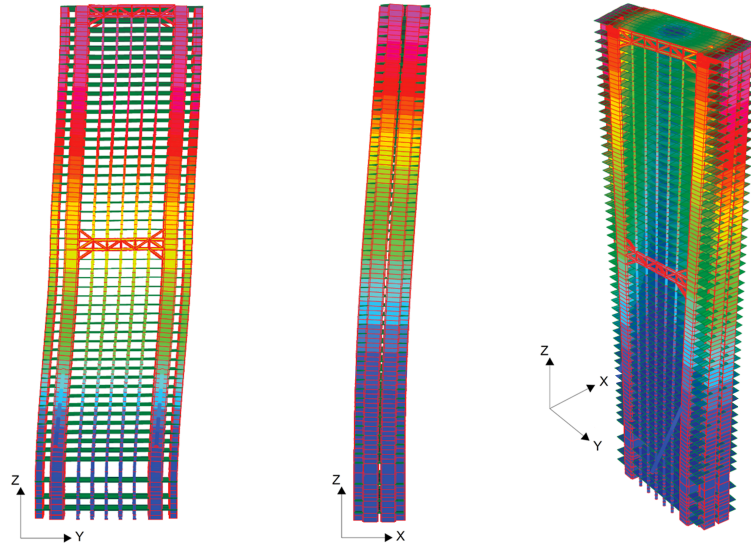


Figure 7.6: First three vibrating modes of Isozaki tower FEM implemented in Straus7: on the left, 1st flexural mode around y -axis, in the center, 2nd flexural mode around x -axis; on the right, 3rd torsional mode. Source: Crespi, P., and Longarini, N. (2010). *Analisi al vento dei nuovi alti edifici di Milano*

Table 7.4: Modal periods and frequencies

	T	ω	f	ω^2
	[s]	[rad/s]	[Hz]	[rad ² /s ²]
mode 1 (y -axis)	7.0922	0.8859	0.141	0.7848
mode 2 (x -axis)	6.5359	0.9613	0.153	0.9240
mode 3 (torsional)	3.8610	1.6273	0.259	2.6481

incorporate the MF system along the same longitudinal wind direction. Dynamic properties associated with the first three vibrating modes are listed in Table 7.4. According to the structural data collected so far, the floor masses of the tower are estimated and compared with the values known from [262], including both the structural material self-weights, the non-structural permanent loads and the accidental loads for the different use categories present, as defined in Chapter 3 of the 2018 *Technical Standards for Construction* (NTC). By adding both dead and accidental loads, a total building mass, M , is derived, within which the mass of a conventional fixed façade is also included.

Table 7.5: Mechanical properties

dead loads	live loads	mass	mass per unit length	mass per unit volume
L_d	L_l	M	m	ρ
[tons]	[tons]	[tons]	[tons/m]	[tons/m ³]
48954	30032	$7.89E + 04$	390	0.27

7.2.2 Study of the glazed envelope



Figure 7.7: Worksite picture of on-site installation of the glazed modules. Source: <https://www.focchi.it/it/>

Approximately 26000 m^2 of CW façades, made up of 4500 triple-curved glazed cellular elements, whose geometric deformation is produced according to the cold bending method, encase the tower. Based on $1.50 \times 3.90 \text{ m}$ standard size each, they were assembled in the workshop and only later placed on site (Fig. 7.7). In general, the envelope of the tower is characterized by 10 different cladding types; the side ones are partly glazed, making visible the structure of the panoramic elevators that lead to the upper floors of the building, while the main façade which encompasses the north-west and south-east sides of the building shows a curved double-glazed skin layout, with a curvature radius of 86 m , as illustrated in Figure 7.8. This is marked by 8 modules, each consisting of a six-storey cluster that is formally expressed in a façade that describes an arc of a circle ending in two cantilevered panels supported by steel beams, as shown in Figure 7.9. Every four overlapping modules is the technical floor.

The high transparency of the façades required the adoption of high-performance glass in terms of solar control to comply with the thermal performance defined by the plant designers. To this end, high-performance coating glasses have been adopted and, on the south-east facing facade, a 35% light gray screen printing on the intermediate glass to further reduce the solar gain inside the office floors was added too. The entrance lobby is a double-height space of exceptional transparency, as shown in Figure 7.10, due to the adoption of a frameless façade system supported by 8 m -high structural glass mullions with glass blades on the outside,

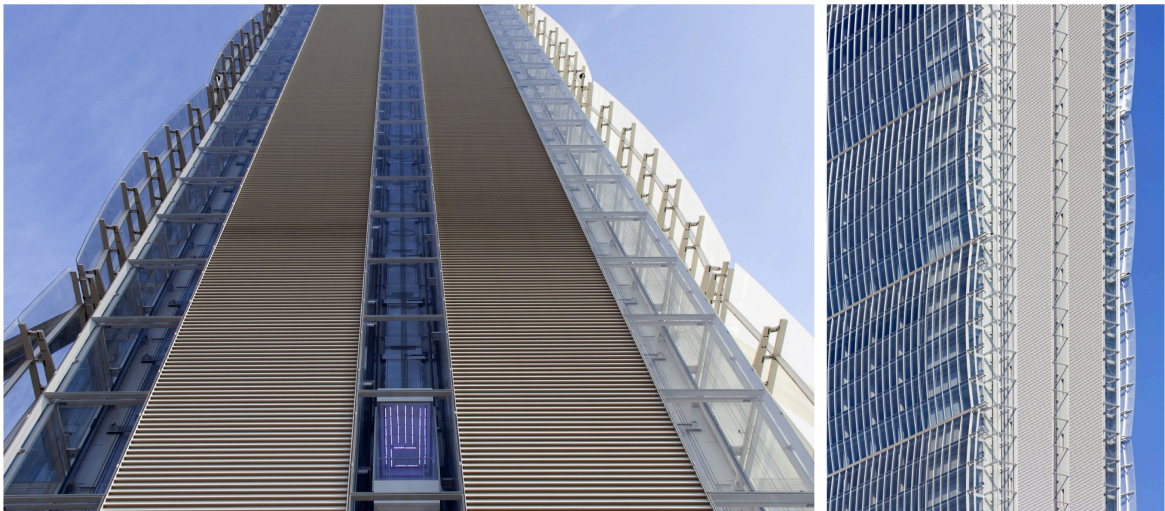


Figure 7.8: Perspective from below of the south-west corner with the alternately opaque and transparent façades of the elevators and the overhang of the curved glass panels (on the left) and lateral view of the rhomboidal volumes of the glazed façade (on the right). Source: <https://www.focchi.it/it/>



Figure 7.9: Detail of the curved glass cantilevered at the extremity of the façade. Source: <https://www.focchi.it/it/>

running from the ground level to the first floor. The glass panels are supported by a unitary thermal break system with a grid of extruded aluminum frame consisting of $150 \times 300 \times 5$ mm vertical mullions and $100 \times 300 \times 5$ mm horizontal transoms [263]. The mullions are curved like panels, while the transoms are 8° rotated with respect to façade [264].

By dividing the surface of each façade floor into 40 cells, a total of 1920 glass panels are



Figure 7.10: Interior views of the double-height lobby illuminated by the surrounding glass façades at the level of the entrance from the raised plaza

Table 7.6: General characteristics of Isozaki tower façade

A_{tot} [m^2]	N_s [-]	H_s [m]	$N_{floors/s}$ [-]	$B \times H$ panels [mm]	$N_{panels/s}$ [-]	N_{panels} [-]	A_{glass} [m^2]
23472	16	25	6	1500×3900	240	1920	11232

obtained. These are fixed to the aluminum frame, which is fixed in turn to the concrete wall behind it, with structural silicone and precise mechanical retainers. Figure 7.11 shows the cross-sectional detail of the curved glazed façade of Isozaki tower and its typical connection to structural flooring slabs. The main dimensional elements of the triple-glass slightly curved enclosure are summarized in Table 7.6, where the subscript 's' stands for 'shell'.

The cladding weight is estimated from the computation of the total glass panel surface ($2A_{glass} = 22500 m^2$), knowing that the weight per unit surface of the material used is $40 kg/m^2$; hence, a total mass of about 991 tons is derived. The aluminum frame self-weight of the current envelope is estimated from a $25 \times 60 m$ isolated cluster FEM simulated into SAP 2000, as shown in Figure 7.12. Materials and sections are assigned to the curved shell made with 252 frame elements and 287 joints constrained on each level by hinges. Tables 7.7 and 7.8 list the geometric and mechanical properties of materials and sections used for both vertical and horizontal frame components, respectively, which are depicted in Figure 7.13.

From a linear static analysis executed in SAP 2000 on the cluster model, the global reaction forces, FZ (in kN), induced by dead load at its base are derived and converted into loads (in kg). The weight obtained is multiplied by the number of shells (that is, 16), reaching the overall mass of the aluminum frame (in tons) to which the mass of the glazed surface is also added. Finally, the current mass ratio, μ , between the structure, M_s , and the

Table 7.7: Material properties and section of mullions

Frame	Section	Material	H	B	s	W_s
[-]	[-]	[-]	[mm]	[mm]	[mm]	[ton/m^3]
Mullion	Tube	Al 6061-T6	300	150	5	2.71

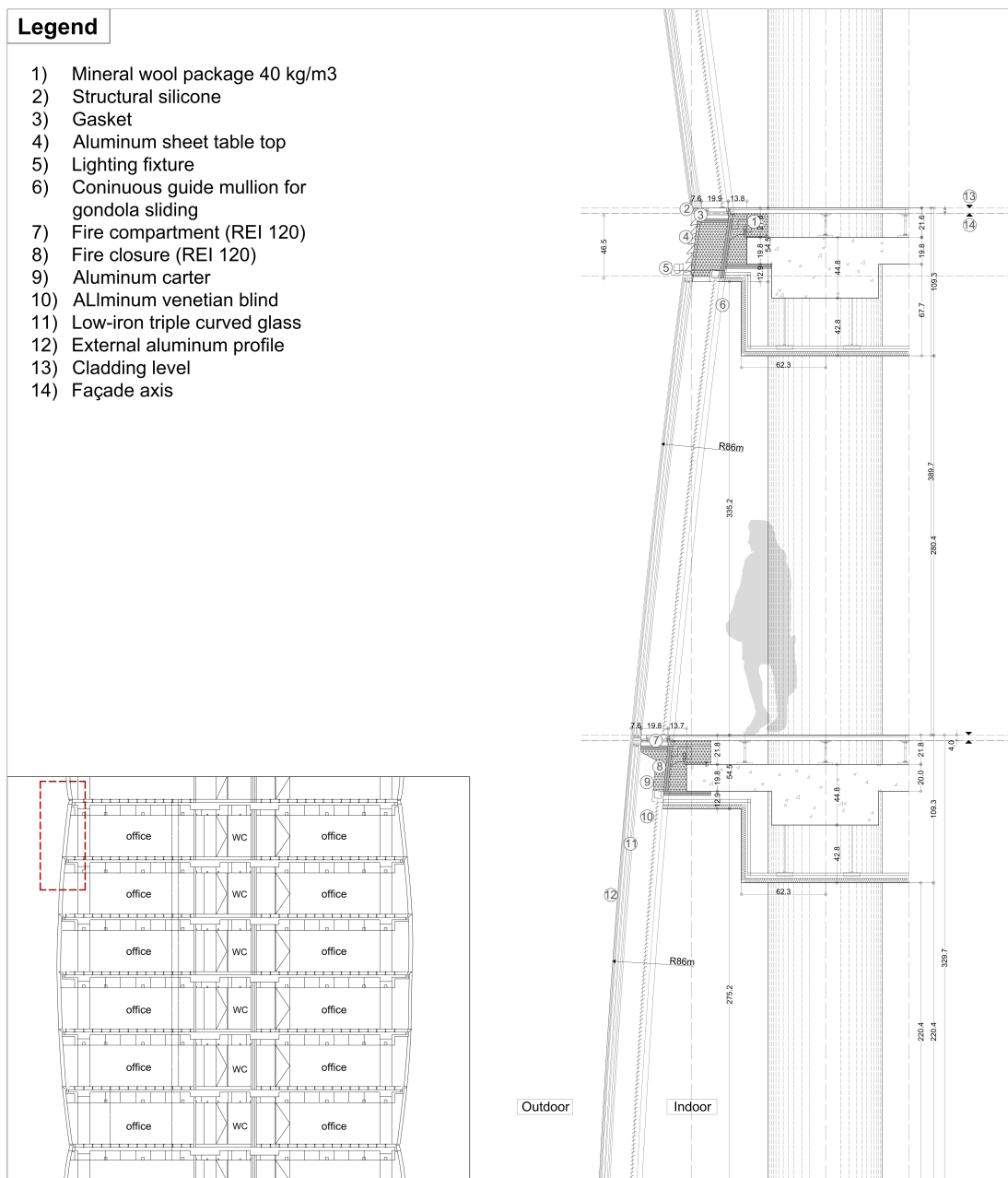


Figure 7.11: Cross-sectional detail of the curved glazed façade with assignment of the main components

aluminum glazed envelope, M_f , is estimated

$$\mu = \frac{M_f}{M_s} = \frac{1247}{78986} 100 = 1.56\% \quad (7.1)$$

All values are summarized in Table 7.9.

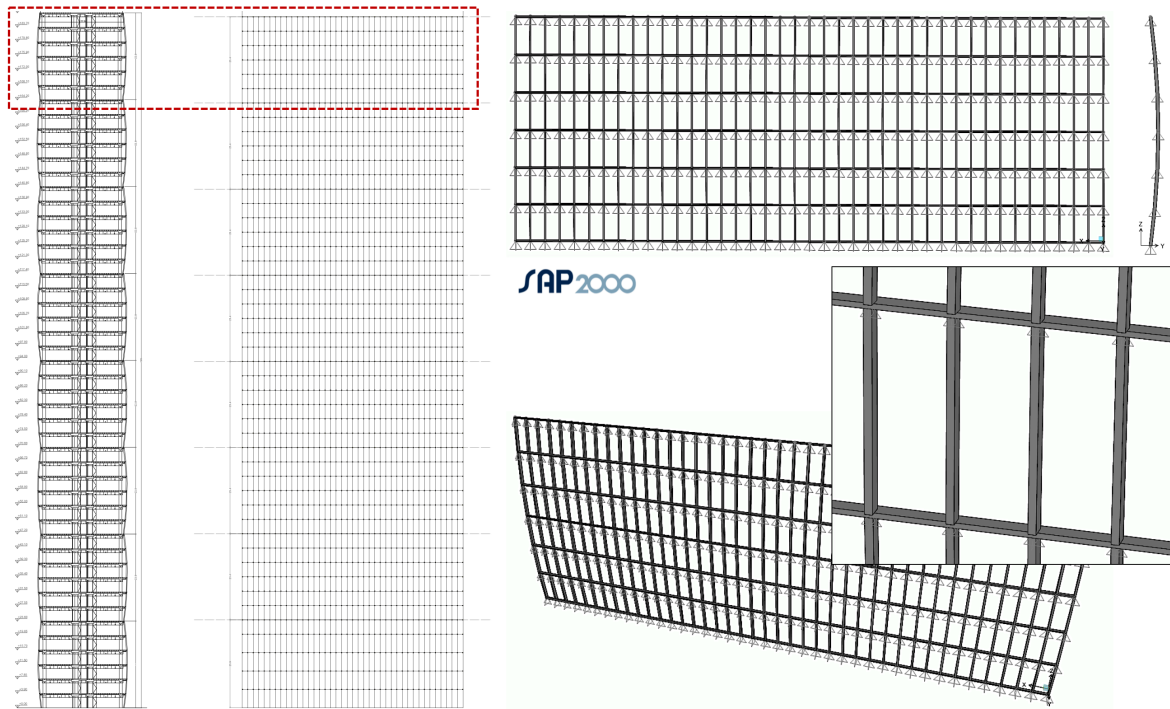


Figure 7.12: Main elevation and cross-section of Isozaki tower (on the left) and three-dimensional views of the top shell FEM made in SAP 2000 (on the right)

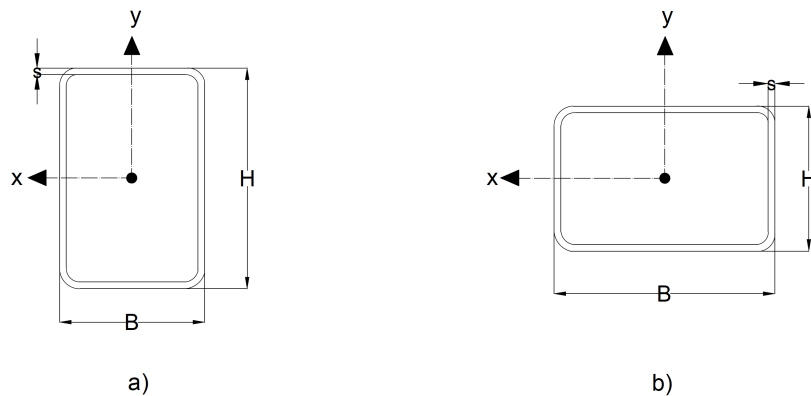


Figure 7.13: Characteristic section and dimensions of a) mullions and b) transoms

7.3 Equivalent MDOF modeling

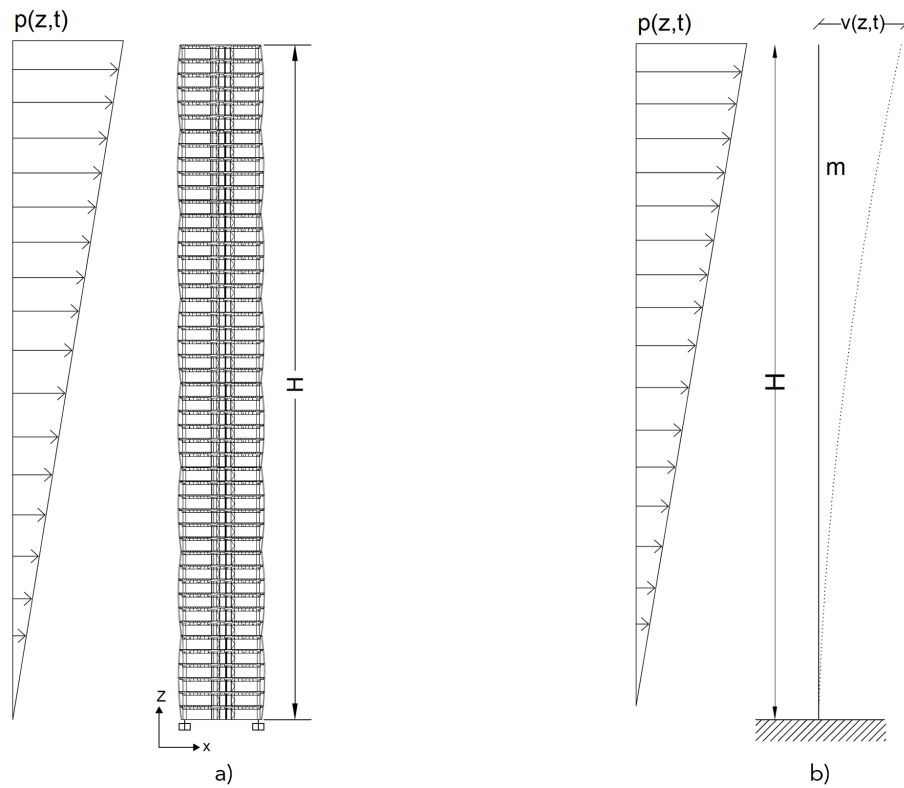
The high structural complexity and the large number of degrees-of-freedom of the complete FEM of the tower could considerably burden the numerical processing, resulting in enormously expensive and time-consuming analyses, thus, making it necessary to develop a suitable equivalent lower-order mechanical model able to approximate the behavior of the real structural building from a dynamic point of view. For the purposes of equivalent MDOF modeling, the 220 m high structure can be schematized resorting to the static diagram of a cantilever beam constrained at the base and free at the top. The transition from the complete structural model of Isozaki tower to the equivalent beam model with constant mass and elastic stiffness along the height, H , is shown in Figure 7.14. Following the procedure and

Table 7.8: Material properties and section of transoms

Frame	Section	Material	H	B	s	W_s
[-]	[-]	[-]	[mm]	[mm]	[mm]	[ton/m ³]
Transom	Tube	Al 6061-T6	100	300	5	2.71

Table 7.9: Estimate of conventional façade mass of Isozaki tower

FZ	a	W_s	N_s	$W_{tot,s}$	M_{frame}	M_{glass}	M_f	μ
[kN]	[m/s ²]	[kg]	[-]	[kg]	[tons]	[tons]	[tons]	[%]
157	9.81	15902	16	254432	256	991	1247	1.56

**Figure 7.14:** Transition from the 51-storey structural frame (a) to an equivalent cantilever beam model (b)

related steps described in section 6.3, the moment of inertia of the four concrete cores with respect to the barycentric y -axis, J_y (Fig. 7.15), is evaluated according to the well-known Transport Theorem (or Huygens Theorem)

$$J_y = 4 \left[\frac{1}{12} (4.8) 1.2^3 + 2 \left(\frac{1}{12} (0.8) 8.32^3 \right) + (4.84^2) 16.75 \right] = 702.30 \quad m^4 \quad (7.2)$$

A circular section beam element is used, whose equivalent diameter, D_{EQ} , is obtained

from the core inertia

$$J_y = \frac{\pi D^4}{64} \Rightarrow D^{EQ} = \sqrt[4]{\frac{64 J_y}{\pi}} = 10.94 \quad m \quad (7.3)$$

Assuming for the cores a typical Euler beam-like flexural deflection to which the well-known bending stiffness, K , applies, it is possible to define the length, L_{EQ} , of the equivalent beam element

$$K = \frac{3EJ_y}{L^3} \Rightarrow L^{EQ} = \sqrt[3]{\frac{3EJ_y}{K}} = 103.85 \quad m \quad (7.4)$$

where E is the elastic modulus of the material used and J_y is the inertia of the cores with respect to the y -axis.

The cross-sectional area of the cylinder, A_{EQ} , is computed from the equivalent length, L_{EQ} , and diameter, D_{EQ}

$$A^{EQ} = \pi r^2 = 93.94 \quad m^2 \quad (7.5)$$

from which a shear area, $A^* = 0.8A = 75.152 \quad m^2$, can be taken.

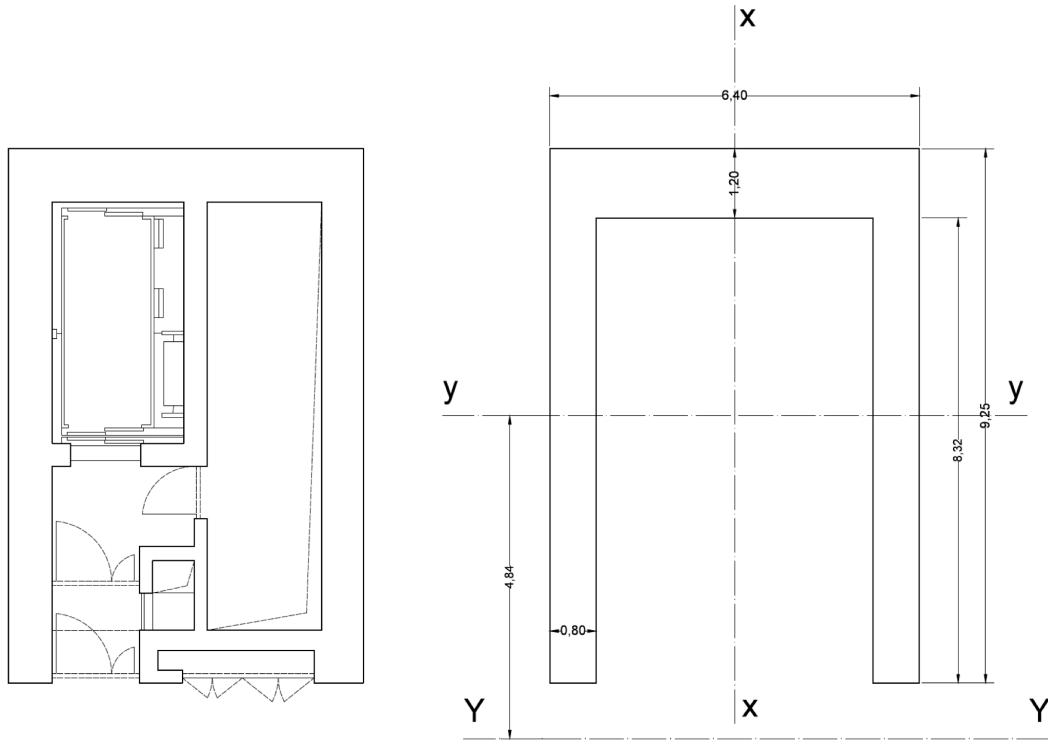


Figure 7.15: Computation of the core's inertia with respect to the barycentric y -axis, J_y

Finally, the equivalent inertia, J_{EQ} , is calibrated on the natural frequency of the structure related to its 2nd flexural mode around the x -axis, $f = 0.153 \quad Hz$, as shown in Figure 7.16. A modal analysis executed in Python environment gives the dynamic properties of the equivalent MDOF beam model related to its first vibrating mode, which are listed in Table 7.10. As expected, the values obtained for the equivalent numerical model are consistent with those of

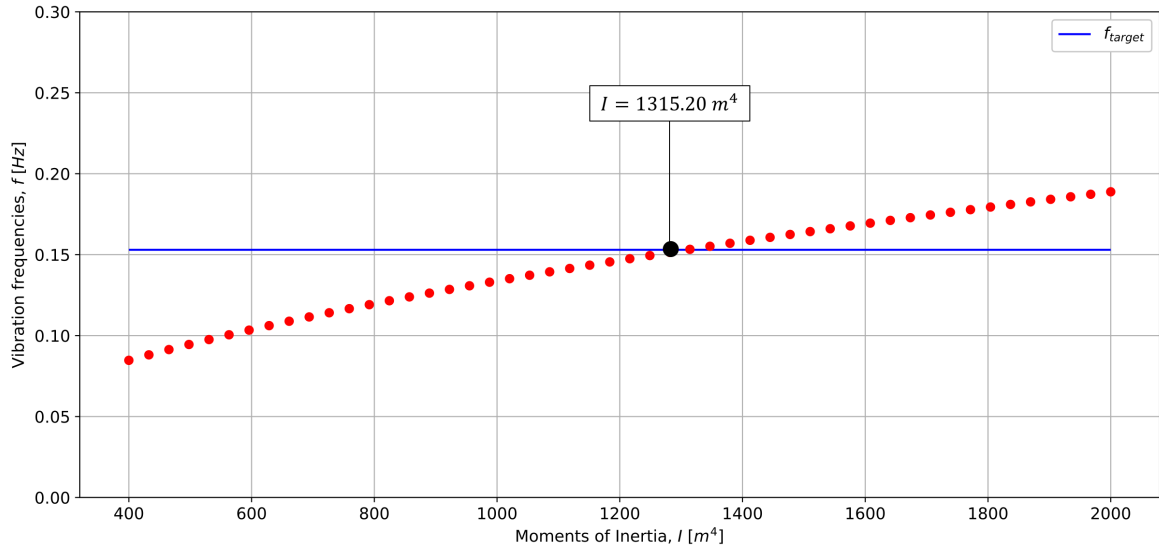
Table 7.10: Modal period and frequencies of the equivalent beam model

Mode	T	f	ω	ω^2
[-]	[s]	[Hz]	[rad/s]	[rad ² /s ²]
1	6.535	0.153	0.961	0.9243

Table 7.11: Mechanical parameters of the equivalent beam model

E	G	A	J_z	A^*
[GPa]	[GPa]	[m ²]	[m ⁴]	[m ²]
35.2	12.5	93.94	1315.20	75.15

the second flexural mode of the complete FEM of Isozaki tower, with respect to which they have been matched. Dynamic parameters of the equivalent MDOF model are summarized in Table 7.11.

**Figure 7.16:** Calibration of the equivalent inertia, J_z , as a function of the vibration frequency, f_{target}

The MDOF numerical model of Isozaki tower consisting of 52 nodes and 51 elements distributed along the z -axis is implemented in the two-dimensional plane of Python platform. The tower is modeled as an equivalent continuous structure with constant stiffness, K , distributed along the height, H , given by the combination of two cantilever beams accounting for both flexural and shear deformations. 51 elastic Timoshenko beam element objects connecting all the 52 nodes along the vertical global coordinate system are attributed the mechanical equivalent parameters listed in Table 7.11 along direction 1. It should be noted that the approximation of Isozaki tower with a frame member that includes the effects of shear deformation and rotary inertia on the slender beam vibrations is consistent with the presence of the two imposing belt-trusses placed at mid-height and at the top of the tower, respectively, which generates angular distortions, moving the tower away from Euler-Bernoulli's unde-

formable shear-beam model. Each node of the model is representative of an entire $L = 60.0$ m wide floor. By constraining the node at the base of the vertical cantilever beam, related structural floor masses, $m_{s,i} = M/N_i = 1547.05$ tons, are assigned to each of the 51 upper nodes. For the first vibrating mode, a 1% Rayleigh damping, is assumed. The equivalent MDOF beam model with the definition of its parameters is sketched in Figure 7.17.

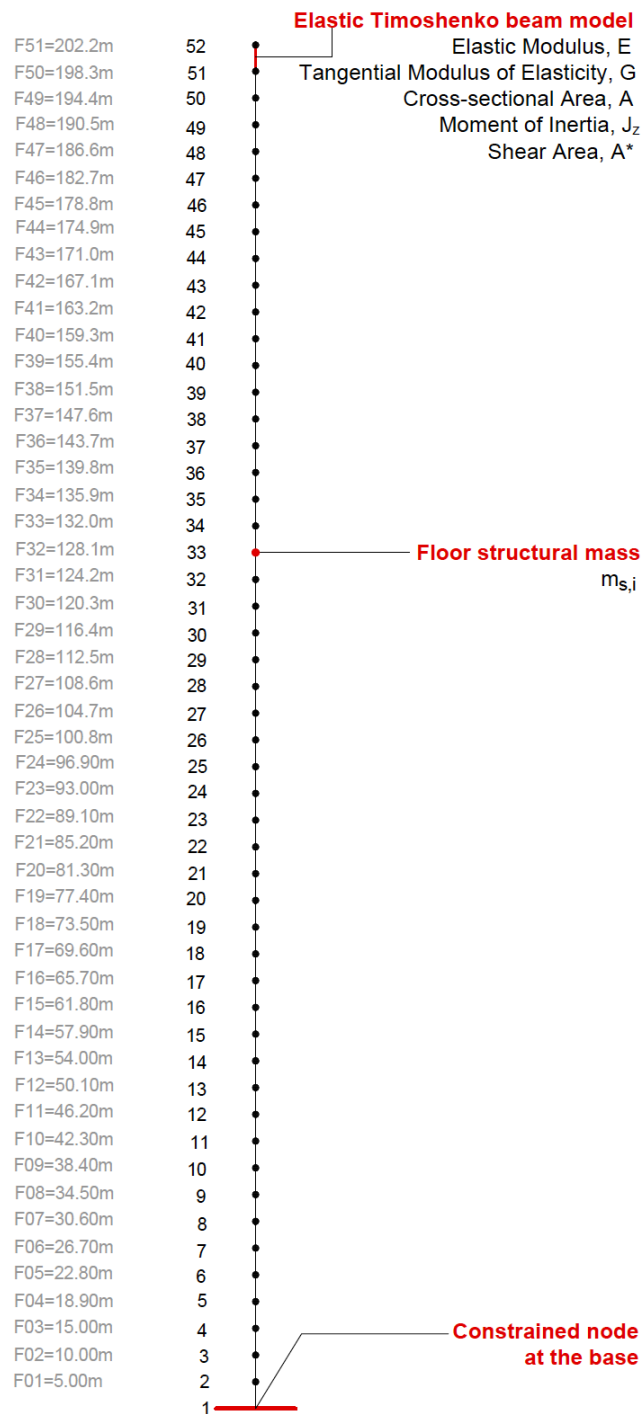


Figure 7.17: Equivalent MDOF model of Isozaki tower with highlighting of the main elements assigned

7.4 Wind load simulation

Although the main wind direction was found to be South-West (hence, normal to the short side of the building), in this context a North-West (NW) longitudinal design wind in the building reference system has been considered, acting directly on Isozaki tower façade (hence, normal to the long side of the building), as shown in Figure 7.18. According to the directions reported in CNR-DT 207/2008 and following the procedure applied in Chapter 6, useful instructions for a reliable estimate of the wind load limited to its longitudinal component are provided in this section, in line with the new geometric characteristics of the 220 m high-rise building. As stated in section 7.2, the skyscraper is located in the CityLife district of Milan (northern Italy), approximately 500 m above sea level.

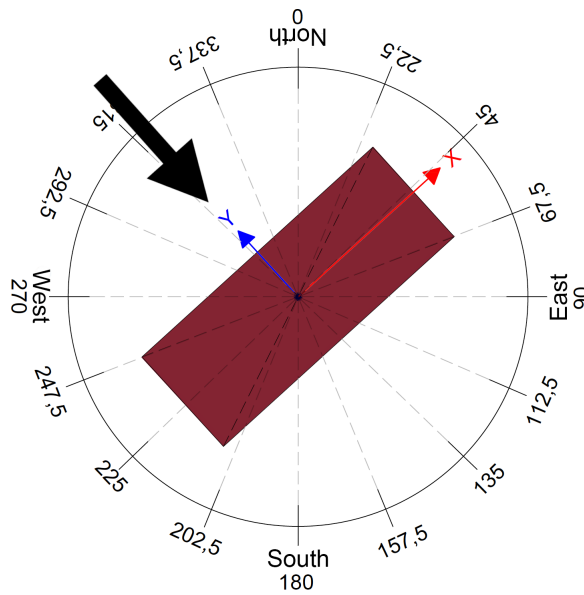


Figure 7.18: Design wind direction in the building reference system

By applying the prescriptions provided in section 6.4, the construction is located in Zone 2 (Fig. 6.7) to which a basic reference wind velocity, v_b , given by Eq. 6.15 is associated, where the basic reference velocity at sea level is $v_{b,0} = 25 \text{ m/s}$ [CNR Table 3.I] and the altitude coefficient is $c_a = 1$ (from Eq. 6.16, being $k_a = 0.40$, $a_s = 120 \text{ m}$ and $a_0 = 1000 \text{ m}$). Hence

$$v_b = v_{b,0} = 25 \text{ m/s} \quad (7.6)$$

In line with requirements of the Italian standard code, the design reference velocity, v_r , is expressed by means of Eq. 6.18. The analysis concerning the high-rise building serviceability performance requires the wind velocity to be evaluated in accordance with a design return period, $T_R = 1 \text{ yr}$; in this case $c_r = 0.75$ applies (from Eq. 6.19 and Fig. 6.8), giving

$$v_r = v_b \cdot c_r = 18.75 \text{ m/s} \quad (7.7)$$

By applying the criterion provided in section 6.4, it is assumed that the tower is located in the roughness class B [CNR Table 3.III] and it is also admitted that it rises more than 30

km away from the coast. With reference to [CNR Figure 3.3], it should be placed in exposure category IV, consequently, the ground factor, k_r , the roughness length, z_0 , and the minimum height, z_{min} , are [CNR Table 3.II]

$$k_r = 0.22; \quad z_0 = 0.30 \text{ m}; \quad z_{min} = 8 \text{ m} \quad (7.8)$$

In accordance with [CNR section 3.2.4. point (2)], since the tower is located in a flat area, a topography coefficient $c_t = 1$ is considered. Following the prescriptions provided in Chapter 6, the vertical profile of the mean wind velocity, v_m , related to $T_R = 1$ yr, is given by Eq. 6.20, where $v_r = 18.75 \text{ m/s}$ and c_m is the mean wind profile coefficient provided by Eqs. 6.21 and 6.22, respectively.

Based on this, it takes the form

$$c_m(z) = 0.22 \ln\left(\frac{8}{0.3}\right)8 = 0.722; \quad \text{for } z \leq 8 \quad (7.9)$$

$$c_m(z) = 0.22 \ln\left(\frac{z}{0.3}\right)1; \quad \text{for } z > 8 \quad (7.10)$$

and at the top of the high-rise structure, it becomes

$$c_m(202.20) = 0.22 \ln\left(\frac{202.20}{0.3}\right) = 1.432 \quad (7.11)$$

The profile of the mean wind velocity associated with the design return period, $T_R = 1$ yr, can be deduced by multiplying the design reference wind velocity, v_r , by the factor $c_r = 0.75$. Hence

$$v_m(z) = (18.75)0.722 = 13.54 \text{ m/s}; \quad \text{for } z \leq 8 \quad (7.12)$$

$$v_m(z) = (18.75)0.22 \ln\left(\frac{z}{0.3}\right)1; \quad \text{for } z > 8 \quad (7.13)$$

giving a mean wind speed at the top

$$v_m(202.20) = (18.75)0.22 \ln\left(\frac{202.20}{0.3}\right) = 26.867 \text{ m/s} \quad (7.14)$$

The resulting trend of $c_m(z)$ and $v_m(z)$ for exposure category IV and $T_R = 1$ yr is portrayed in Figure 7.19, consistently with the [CNR Figs. 4.2.1-4.2.2].

Faithfully reproducing the procedure applied for the generic building, the turbulence intensity, $I_v(z)$, can be estimated which is given by Eqs. 6.33 and 6.34. It assumes the form

$$I_v(z) = \frac{1}{\ln\left(\frac{8}{0.3}\right)}1(8) = 0.304; \quad \text{for } z \leq 8 \quad (7.15)$$

$$I_v(z) = \frac{1}{\ln\left(\frac{z}{0.3}\right)}1; \quad \text{for } z > 8 \quad (7.16)$$

where z is the height above ground expressed in m . According to this, the turbulence intensity

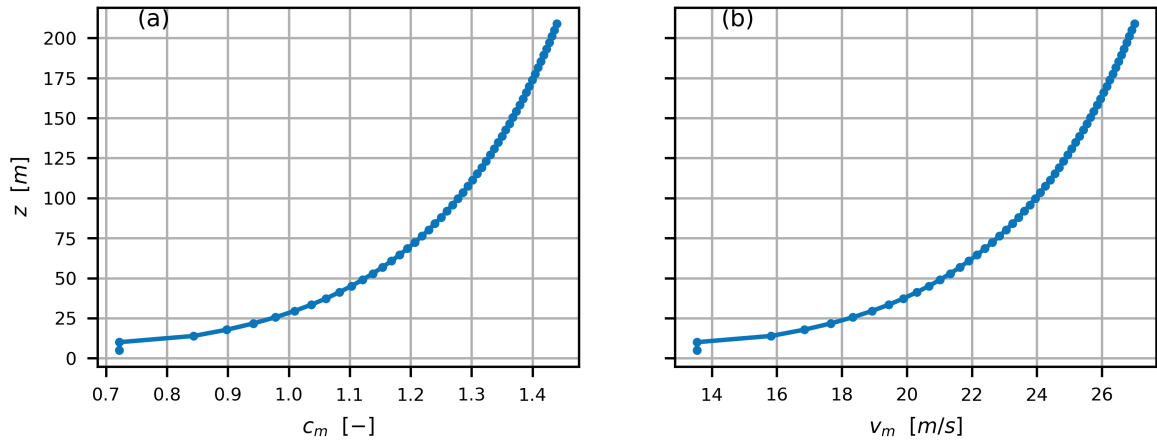


Figure 7.19: Profiles of $c_m(z)$ associated with IV exposure category (a) and $v_m(z)$ associated with $T_R = 1$ yr (b)

at the top is

$$I_v(202.20) = \frac{1}{\ln\left(\frac{202.20}{0.3}\right)} = 0.153 \quad (7.17)$$

Similarly, the integral scale of turbulence, $L_v(z)$, is given by Eqs. 6.47 and 6.48, which yield

$$L_v(z) = \bar{L} \left(\frac{8}{z}\right)^{0.61} = 42.109 \text{ m}; \quad \text{for } z \leq 8 \quad (7.18)$$

$$L_v(z) = \bar{L} \left(\frac{z}{8}\right)^{0.61}; \quad \text{for } z > 8 \quad (7.19)$$

Based on this, the integral scale of turbulence at the top is

$$L_v(202.20) = 200 \left(\frac{202.20}{300}\right)^{0.61} = 302.008 \text{ m} \quad (7.20)$$

In line with the expected trend of the turbulence intensity (I_v) and length scale (L_v) related to IV exposure category taken from [CNR Figs. 3.5-3.6], the turbulence profiles for the specific building under examination associated with a mean wind velocity, $v_m = 26.86$ m/s, at height $H = 202.20$ m are depicted in Figure 7.20. The values used to build the vertical profiles of both $I_v(z)$ and $L_v(z)$ for all heights z of Isozaki tower are listed in Table 7.12.

A wind intensity corresponding to the 7th degree of Beaufort scale, associated with a *severe wind* designation, is taken relating to a design reference velocity, $v_r = 18.75$ m/s. The imposed scale value is linked to well-defined gust velocities, $v_g(z)$, taken from Table 6.12. For clarity, Table 7.13 lists the mean wind speed, $v_m(z)$ and gust speed, $v_g(z)$, calculated for the various heights z of the building, starting from $z = 0$ m ($v_g = 24$ m/s) up to $z = 202.20$ m ($v_g = 33$ m/s).

Following the Monte Carlo method and using the NOWS platform, stationary Gaussian

Table 7.12: Turbulence intensities, $I_v(z)$, and length scales, $L_v(z)$, for heights z of Isozaki tower

floor	z	I_v	L_v	floor	z	I_v	L_v
[–]	[m]	[–]	[m]	[–]	[m]	[–]	[m]
51	202.20	0.153	302.009	25	100.80	0.172	197.517
50	198.30	0.154	298.442	24	96.90	0.173	192.819
49	194.40	0.154	294.848	23	93.00	0.174	188.047
48	190.50	0.155	291.225	22	89.10	0.176	183.197
47	186.60	0.155	287.574	21	85.20	0.177	178.263
46	182.70	0.156	283.892	20	81.30	0.179	173.240
45	178.80	0.156	280.180	19	77.40	0.180	168.122
44	174.90	0.157	276.436	18	73.50	0.182	162.903
43	171.00	0.158	272.659	17	69.60	0.184	157.574
42	167.10	0.158	268.849	16	65.70	0.186	152.128
41	163.20	0.159	265.004	15	61.80	0.188	146.553
40	159.30	0.159	261.123	14	57.90	0.190	140.840
39	155.40	0.160	257.204	13	54.00	0.193	134.975
38	151.50	0.161	253.247	12	50.10	0.195	128.942
37	147.60	0.161	249.250	11	46.20	0.199	122.723
36	143.70	0.162	245.212	10	42.30	0.202	116.295
35	139.80	0.163	241.131	9	38.40	0.206	109.631
34	135.90	0.164	237.005	8	34.50	0.211	102.698
33	132.00	0.164	232.832	7	30.60	0.216	95.452
33	128.10	0.165	228.611	6	26.70	0.223	87.834
31	124.20	0.166	224.340	5	22.80	0.231	79.769
30	120.30	0.167	220.016	4	18.90	0.241	71.143
29	116.40	0.168	215.637	3	15.00	0.256	61.789
28	112.50	0.169	211.201	2	10.00	0.285	48.250
27	108.60	0.170	206.704	1	5.00	0.304	42.109
26	104.70	0.171	202.144	0	0.00	0.304	42.109

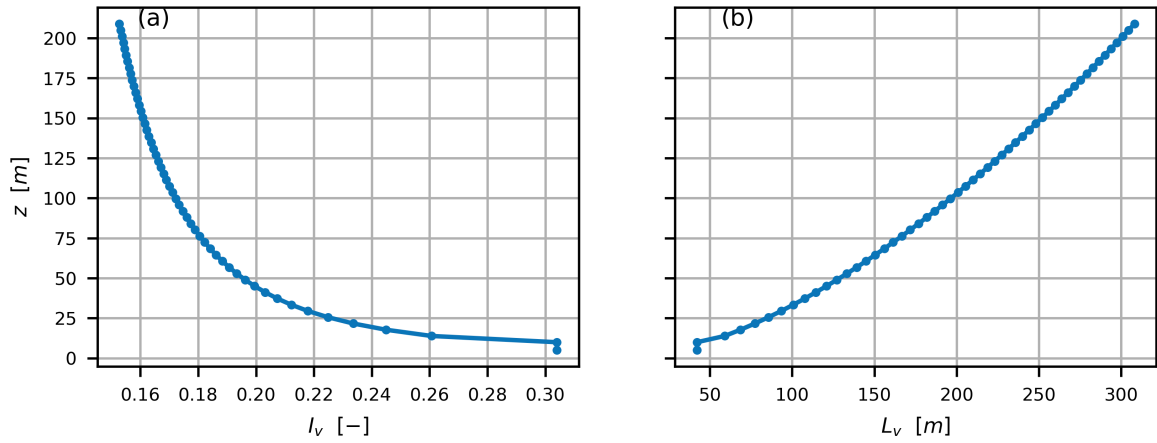


Figure 7.20: Profiles of turbulence intensity I_v (a) and length scale L_v (b) for the 202.20 m high Isozaki tower used to generate the wind inflow in the longitudinal direction

random processes are simulated and time histories of turbulent wind velocities, $v_t(z, t)$, are generated starting from a number of sampling points, $N = 5000$ s, a cut-off frequency, f_c , set on Isozaki fundamental frequency in the *along-wind* direction, $f = 0.153$ Hz, an exposure category B, and a 3-s gust wind speed, $u_{3-s,10}$, equal to 33 m/s at the top. Data to be entered in the NatHaz simulation portal user interface for processing the random signal are listed in the following Table.

Duration, N [s]	Cut-off frequency, f_c [Hz]	Exposure category [-]	Wind peak gust speed, $u_{3-s,10}$ [m/s]
5000	0.153	B	33

Fixed N with a $dt = t[1] - t[0] = 3.268$ s, an overall duration of the sampled signal equal to $t = 16000$ s is obtained. Figure 7.21 shows the time histories of turbulent wind velocities applied on the 5th ($z = 22.80$ m), 25th ($z = 100.80$ m) and 50th ($z = 198.30$ m) floor of Isozaki tower, respectively.

Given the mean wind velocity, v_m , and the turbulence intensity, I_v , for each height, z , it directly follows the estimate of peak kinetic pressure (in kPa) in the longitudinal direction, $q_p(z, t)$, carried out with reference to Eq. 6.39.

$$q_p(z) = \frac{1}{2} 1.25 (13.54)^2 [1 + 7(0.304)] = 0.359 \text{ kPa}; \quad \text{for } z \leq 8 \quad (7.21)$$

$$q_p(z) = \frac{1}{2} 1.25 v_m^2(z) [1 + 7I_v(z)]; \quad \text{for } z > 8 \quad (7.22)$$

with a peak value at the top ($z = 202.20$ m) equal to

$$q_p(202.20) = \frac{1}{2} 1.25 (26.86)^2 [1 + 7(0.153)] = 0.935 \text{ kPa} \quad (7.23)$$

Table 7.13: Mean wind speeds, $v_m(z)$, and gust speeds, $v_g(z)$, applied on heights z of Isozaki tower

floor	z	c_m	$v_m(z)$	$v_g(z)$	floor	z	c_m	$v_m(z)$	$v_g(z)$
[–]	[m]	[–]	[m/s]	[m/s]	[–]	[m]	[–]	[m/s]	[m/s]
51	202.20	1.433	26.86	33	25	100.80	1.280	23.99	31
50	198.30	1.429	26.78	33	24	96.90	1.271	23.83	30
49	194.40	1.424	26.70	33	23	93.00	1.262	23.63	30
48	190.50	1.420	26.62	33	22	89.10	1.253	23.48	30
47	186.60	1.415	26.53	33	21	85.20	1.243	23.30	30
46	182.70	1.411	26.44	33	20	81.30	1.232	23.10	30
45	178.80	1.406	26.35	32	19	77.40	1.222	22.90	29
44	174.90	1.401	26.26	32	18	73.50	1.210	22.69	29
43	171.00	1.396	26.17	32	17	69.60	1.198	22.46	29
42	167.10	1.391	26.08	32	16	65.70	1.186	22.22	29
41	163.20	1.386	25.98	32	15	61.80	1.172	21.97	29
40	159.30	1.380	25.83	32	14	57.90	1.158	21.70	28
39	155.40	1.375	25.78	32	13	54.00	1.142	21.42	28
38	151.50	1.369	25.67	32	12	50.10	1.126	21.11	28
37	147.60	1.364	25.56	32	11	46.20	1.108	20.77	28
36	143.70	1.358	25.45	32	10	42.30	1.089	20.41	28
35	139.80	1.352	25.34	31	9	38.40	1.067	20.01	27
34	135.90	1.345	25.22	31	8	34.50	1.044	19.57	27
33	132.00	1.339	25.10	31	7	30.60	1.017	19.07	27
33	128.10	1.332	24.98	31	6	26.70	0.988	18.51	26
31	124.20	1.326	24.85	31	5	22.80	0.953	17.86	26
30	120.30	1.319	24.72	31	4	18.90	0.911	17.09	24
29	116.40	1.311	24.58	31	3	15.00	0.861	16.13	24
28	112.50	1.204	24.44	31	2	10.00	0.771	14.46	24
27	108.60	1.296	24.30	31	1	5.00	0.722	13.54	24
26	104.70	1.288	24.15	31	0	0.00	0.722	13.54	24

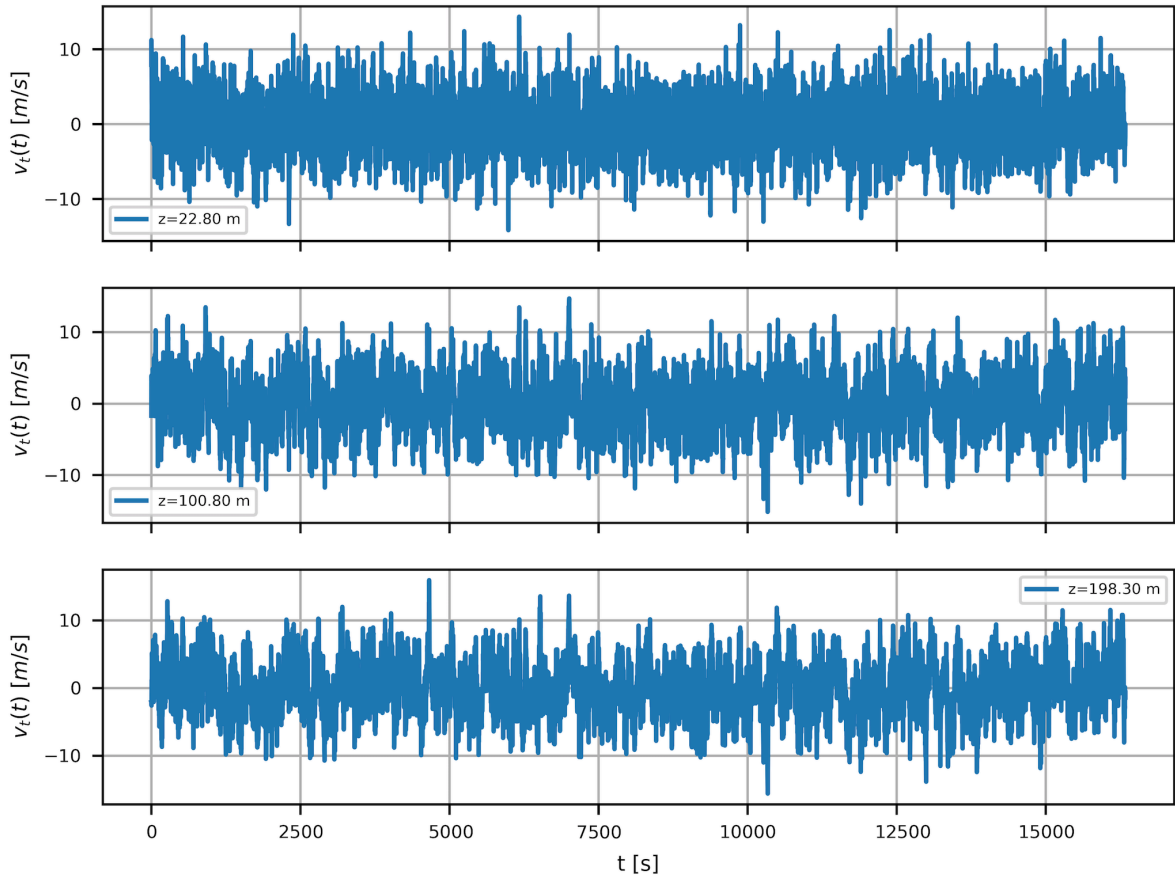


Figure 7.21: Turbulent wind velocities, $v_t(t)$, applied on the 5th ($z = 22.80$ m), 25th ($z = 100.80$ m) and 50th ($z = 198.30$ m) floor of Isozaki tower

Alternatively, given the exposure coefficient, $c_e(z)$, defined by Eqs. 6.28 and 6.29

$$c_e(z) = (0.22)^2 \ln\left(\frac{8}{0.3}\right) \left[\ln\left(\frac{8}{0.3}\right) + 7 \right] = 1.634; \quad \text{for } z \leq 8 \quad (7.24)$$

$$c_e(z) = (0.22)^2 \ln\left(\frac{z}{0.3}\right) \left[\ln\left(\frac{z}{0.3}\right) + 7 \right]; \quad \text{for } z > 8 \quad (7.25)$$

which provides at the top

$$c_e(202.20) = (0.22)^2 \ln\left(\frac{202.20}{0.3}\right) \left[\ln\left(\frac{202.20}{0.3}\right) + 7 \right] = 4.259 \quad (7.26)$$

the peak kinetic pressure related to a return period, $T_R = 1$ yr, can be deduced from Eq. 6.41

$$q_p(z) = \frac{1}{2} 1.25 (18.75)^2 1.634 = 0.359 \text{ kPa}; \quad \text{for } z \leq 8 \quad (7.27)$$

$$q_p(z) = \frac{1}{2} 1.25 (18.75)^2 c_e(z); \quad \text{for } z > 8 \quad (7.28)$$

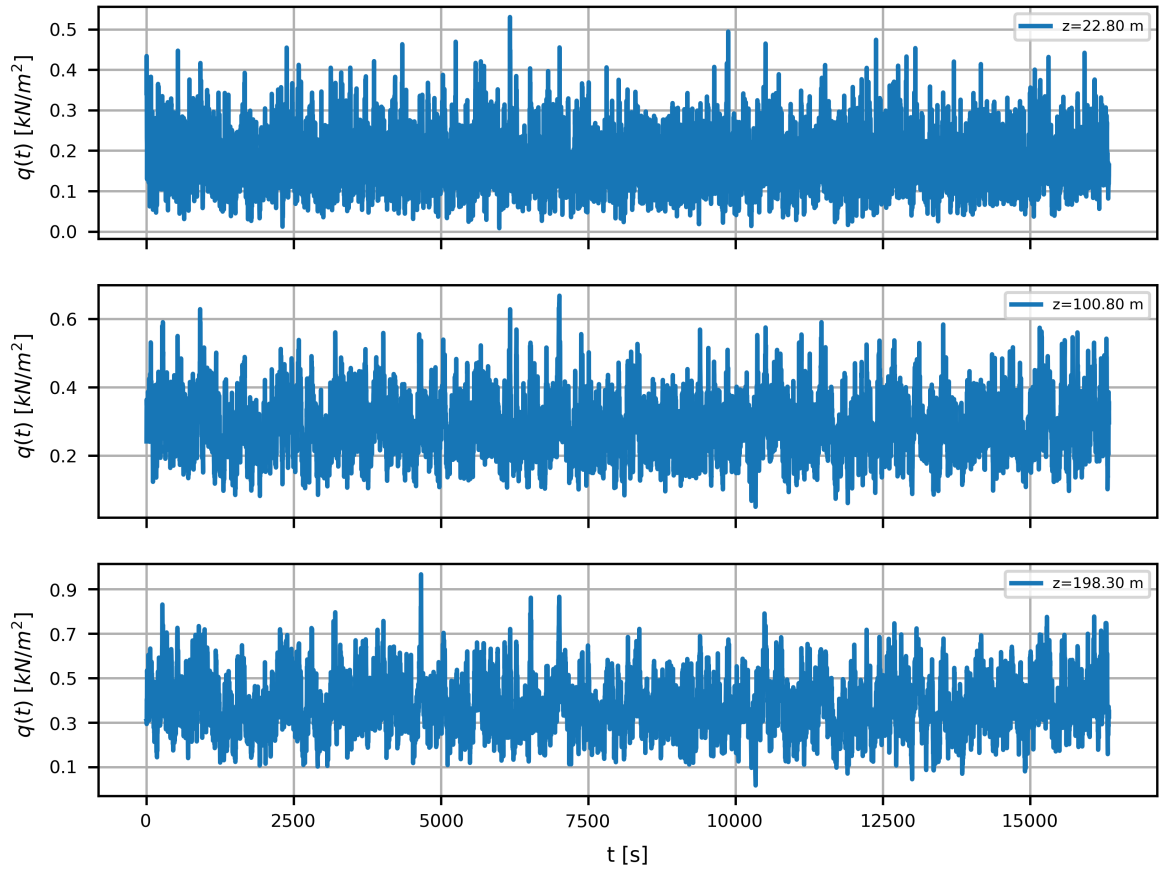


Figure 7.22: Wind pressures, $q(t)$, applied on the 5th ($z = 22.80\text{ m}$), 25th ($z = 100.80\text{ m}$) and 50th ($z = 198.30\text{ m}$) floor of Isozaki tower

with a peak value at the top equal to

$$q_p(202.20) = \frac{1}{2} 1.25 (18.75)^2 4.259 = 0.935 \text{ kPa} \quad (7.29)$$

It is immediate to see that in both cases the resulting values of $q_p(z)$ coincide. The peak kinetic pressure profile associated with the design return period $T_R = 1\text{ yr}$ can be deduced by multiplying the above profile by the factor $c_r^2 = 0.75^2 = 0.562$. Figure 7.23 portrays the trend of the exposure coefficient c_e and the wind peak pressure q_p along the height z of the tower, in accordance with the [CNR Figs. 4.2.5-4.2.6].

The time histories of *along-wind* pressures applied on the 5th ($z = 22.80\text{ m}$), 25th ($z = 100.80\text{ m}$) and 50th ($z = 198.30\text{ m}$) floor of Isozaki tower, respectively, are shown in Figure 7.22. Finally, the fluctuating wind forces in the *along-wind* direction, $F(z, t)$, can be computed from Eq. 6.43, being the elongation ratio for rectangular sections with sharp edges equal to $d/b = 0.4$; hence, the drag coefficient, C_D , taken from Eq. 6.44, is

$$C_D = 0.73 \ln(0.4) + 2.51 = 1.841 \quad (7.30)$$

Table 7.14 lists the peak values of longitudinal wind pressures (in kPa) and forces (in kN) related to a 26.86 m/s mean wind speed at the top.

Table 7.14: Maximum longitudinal wind pressures (in kPa) and forces (in kN) per floor

floor	z	c_e	$\max(q(t))$	$\max(F(t))$	floor	z	c_e	$\max(q(t))$	$\max(F(t))$
[–]	[m]	[–]	[kPa]	[kN]	[–]	[m]	[–]	[kPa]	[kN]
51	202.2	4.26	0.93	201	25	100.8	3.60	0.79	341
50	198.3	4.24	0.93	401	24	96.9	3.57	0.78	338
49	194.4	4.22	0.92	399	23	93.0	3.53	0.77	334
48	190.5	4.20	0.92	397	22	89.1	3.49	0.76	331
47	186.6	4.18	0.91	395	21	85.2	3.45	0.76	327
46	182.7	4.16	0.91	393	20	81.3	3.41	0.75	323
45	178.8	4.14	0.91	392	19	77.4	3.37	0.74	319
44	174.9	4.12	0.90	390	18	73.5	3.32	0.73	315
43	171.0	4.09	0.90	387	17	69.6	3.28	0.72	310
42	167.1	4.07	0.89	385	16	65.7	3.23	0.71	305
41	163.2	4.05	0.89	383	15	61.8	3.17	0.69	300
40	159.3	4.03	0.88	381	14	57.9	3.12	0.68	295
39	155.4	4.00	0.88	379	13	54.0	3.06	0.67	290
38	151.5	3.98	0.87	377	12	50.1	3.00	0.66	284
37	147.6	3.96	0.87	374	11	46.2	2.93	0.64	277
36	143.7	3.93	0.86	372	10	42.3	2.86	0.62	270
35	139.8	3.90	0.85	369	9	38.4	2.78	0.61	263
34	135.9	3.88	0.85	367	8	34.5	2.69	0.59	255
33	132.0	3.85	0.84	364	7	30.6	2.60	0.57	246
33	128.1	3.82	0.84	362	6	26.7	2.49	0.54	224
31	124.2	3.79	0.83	359	5	22.8	2.37	0.52	208
30	120.3	3.77	0.82	356	4	18.9	2.23	0.49	195
29	116.4	3.73	0.82	353	3	15.0	2.06	0.45	168
28	112.5	3.70	0.81	351	2	10.0	1.78	0.39	126
27	108.6	3.67	0.80	347	1	5.0	1.63	0.35	85
26	104.7	3.64	0.80	344	0	0.0	1.63	0.35	0

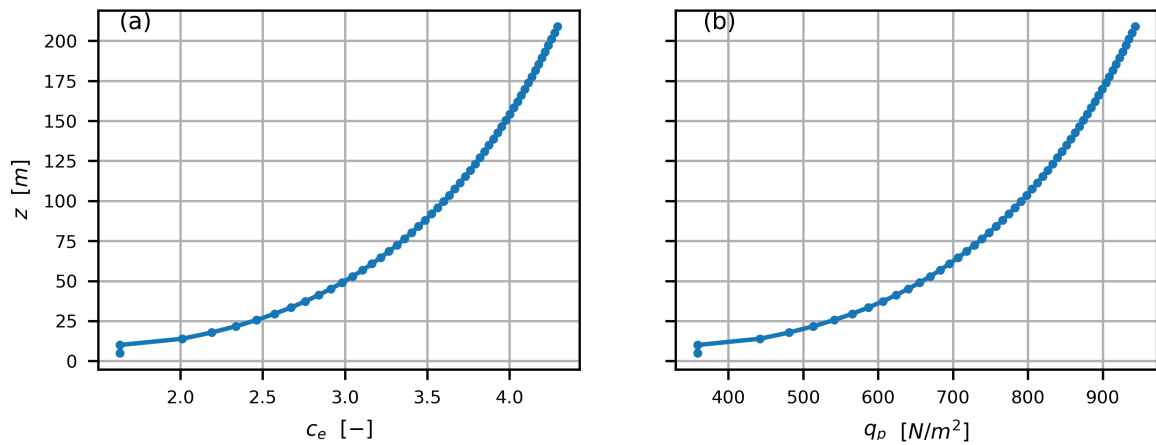


Figure 7.23: Profiles of c_e associated with IV exposure category (a) and $q_p(z)$ associated with $T_R = 1$ yr (b)

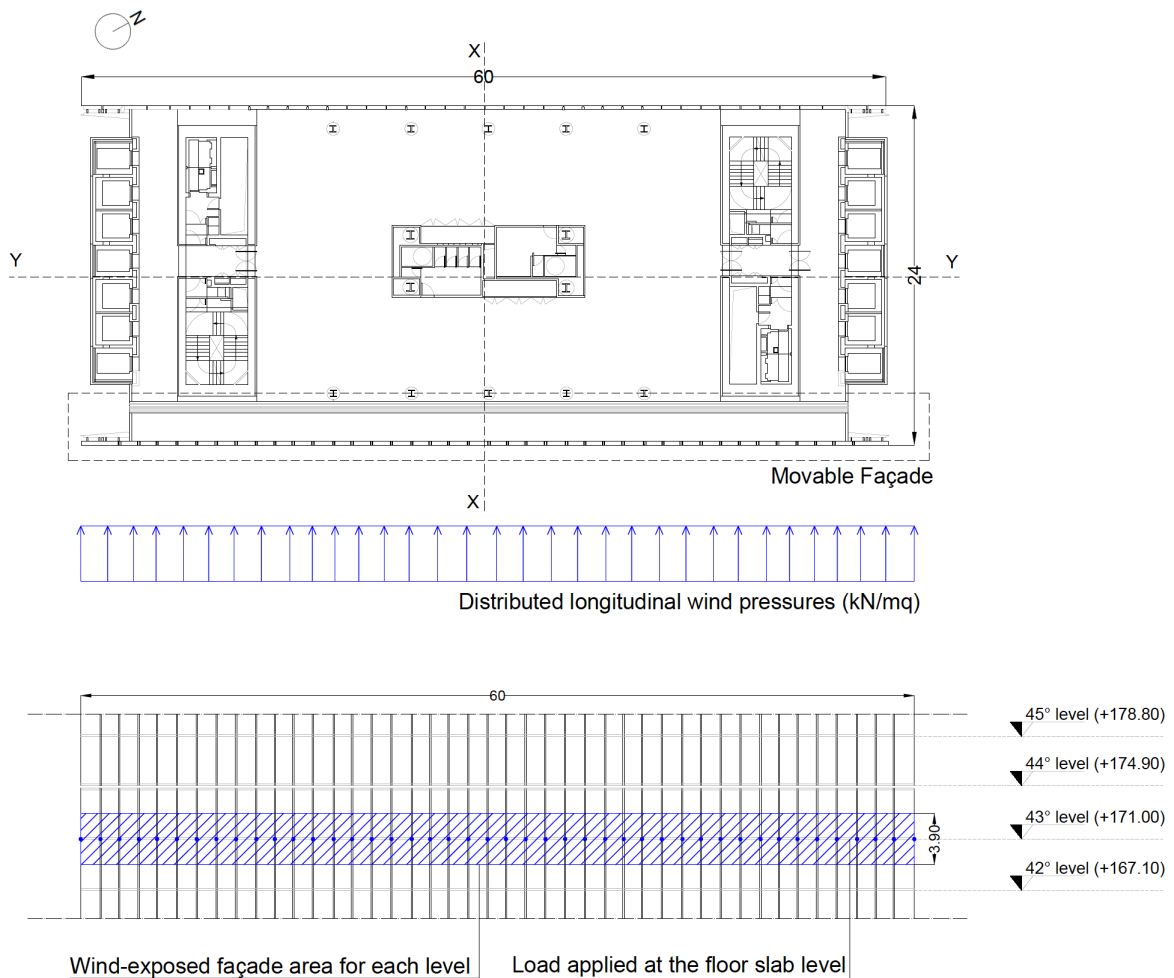


Figure 7.24: Diagram of longitudinal wind pressures, $q(t)$, applied on each inter-storey height, h , of Isozaki tower

As emerges from Figure 7.24, the assignment of wind load on Isozaki tower façade is carried out in the longitudinal direction, along the $x-x$ axis, where the MF system in also

applied. The wind-exposed façade area is divided into 51 bands, whose height coincides with the inter-storey height ($h = 3.90 \text{ m}$) and each band is centered on the position of the related floor slab. Multiplying the width of the building plan, $B = 60 \text{ m}$, by the height, h , each band receives an equal amount of wind load with the only exception of the top floor whose reference height is halved. This results into a uniform distribution of longitudinal wind pressures along each floor of the tower. Although this method is more time-consuming, the resultant wind forces, $F(z, t)$, are closer to real values.

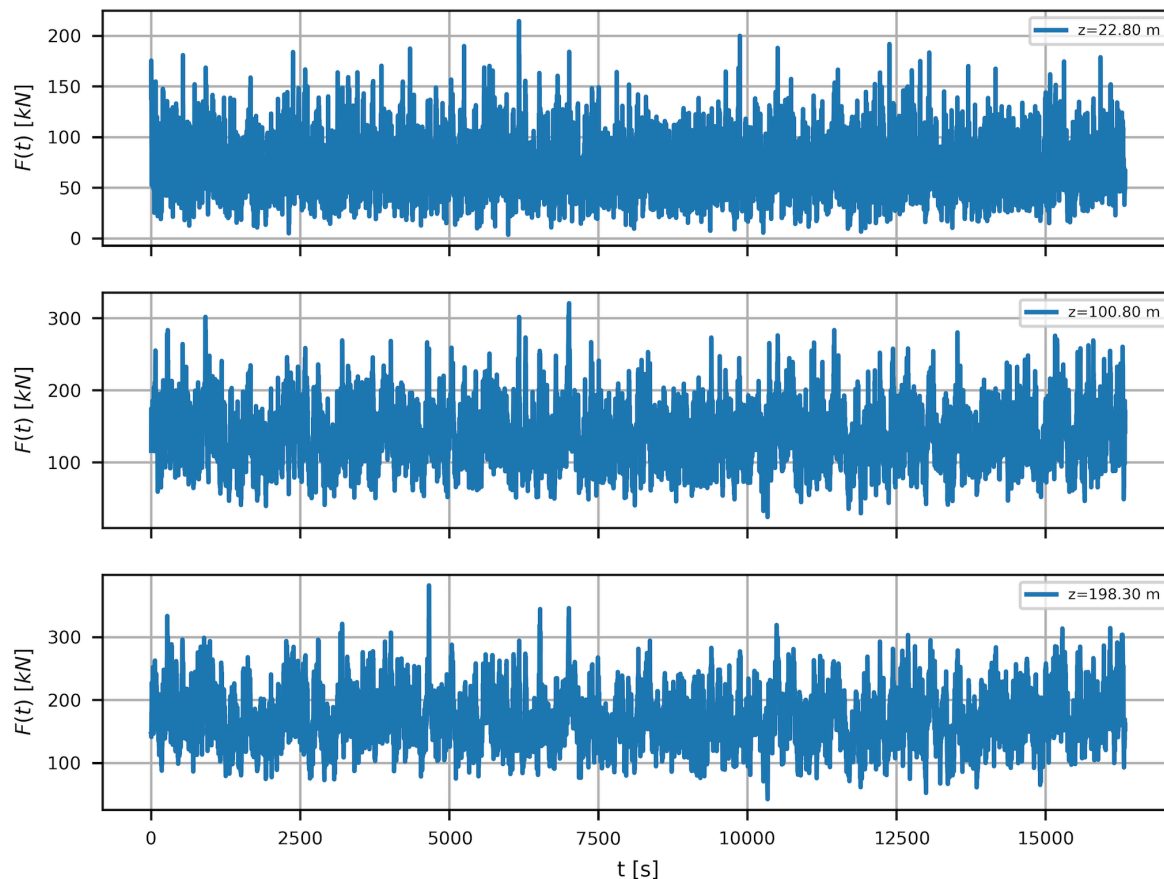


Figure 7.25: Fluctuating wind forces, $F(t)$, applied on the 5th ($z = 22.80 \text{ m}$), 25th ($z = 100.80 \text{ m}$) and 50th ($z = 198.30 \text{ m}$) floor of Isozaki tower

By implementing the fluctuating wind forces, $F(t)$, within Python simulation domain, these are applied to each i -th node of the equivalent MDOF model in the form of *path time series*; the associated LoadPattern type added to the simulation environment is a *plain pattern* with a constant factor. Finally, a load command in the axial direction is used to construct a NodalLoad object and add it to the enclosing LoadPattern. Time histories of fluctuating wind forces, $F(t)$ applied on the 5th ($z = 22.80 \text{ m}$), 25th ($z = 100.80 \text{ m}$) and 50th ($z = 198.30 \text{ m}$) floor of Isozaki tower, respectively, are shown in Figure 7.25.

For completeness, using the turbulence power spectrum, $S(z, \Omega)$, defined in Eq. 6.46, the same procedure executed for the mid-rise building case study, aimed at identifying the estimated frequency ratio between the tower and the wind load thus defined, can also be suggested for the high-rise structure. Clearly at $z \leq 8$, the same excitation frequency, f ,

Table 7.15: Parameters for evaluating the structural factor, c_{dD}

B^2	S_D	η_h	η_b	R_h	R_b	R_D^2	ν_D [Hz]	g_D	G_D	c_{dD}
0.519	0.100	5.364	0.585	0.169	0.702	0.930	0.123	3.129	2.235	1.041

period, T , and circular frequency, ω , defined by Eq. 6.52 occur, which give a frequency ratio

$$\rho = \frac{0.293}{0.961} = 0.304 \quad (7.31)$$

where $\omega = 0.961$ rad/sec is the circular frequency of Isozaki tower related to the x -axis.

Whereas, at the top ($z = 202.20$ m) one has

$$f = \frac{26.867}{302.008} \cdot 0.145 = 0.013 \text{ Hz}; \quad T = \frac{1}{f} = 78.12 \text{ s}; \quad \Omega = 2\pi f = 0.08 \text{ rad/s} \quad (7.32)$$

with

$$\rho = \frac{0.08}{0.961} = 0.083 \quad (7.33)$$

highlighting once again that the the wind action tends to excite above all the low vibration frequencies.

Finally, the detailed procedure described in section 6.4 for estimating the structural factor, c_{dD} , is also applied to the Isozaki tower. Firstly, the reference height $z_e = 0.6h = 132.0$ m is computed and the related mean wind velocity, turbulence intensity and integral scale are evaluated, whose values are

$$v_m(z_e) = 25.10 \text{ m/s}; \quad I_v(z_e) = 0.164; \quad L_v(z_e) = 232.832 \text{ m} \quad (7.34)$$

Hence, the geometric ($b = 24$ m, $h = 220$ m) and dynamic ($f_1 = 0.153$ Hz, $\xi_1 = 0.01$) characteristics of the structure are identified and the parameters for evaluating the structural factor are derived based on Eqs. 6.57-6.65, which are listed in Table 7.15.

7.4.1 Preliminary assessment of aeroelastic instability

For light, flexible or low damped structures, characterized by an aerodynamic shape susceptible to wind actions, displacements and velocities of the structure motion can be so large as to cause wind-structure (or aeroelastic) interaction phenomena which modify the incident wind, the aerodynamic actions and the building response. From the GVPM records, it emerges that the tower exhibits high across-wind stresses due to its shape (squat body without bevels) which favors the separation of the fluid vein in the areas adjacent to the edges, detaching vortices. This phenomenon triggers the *lift* force (that is, perpendicular to the wind) which, acting together with the *drag* force (that is, parallel to the wind), can induce vibrations on the structure; the latter, in turn, can trigger dangerous dynamic effects.

In this section, a preliminary assessment is carried out about the need to evaluate or not the effects of the main aeroelastic phenomena, such as vortex-shedding, synchronization (or *lock-in*), galloping and flutter. In accordance with the CNR instructions, analyses of this type require the wind velocity to be evaluated with respect to a design return period $T_R = 10T_{R,0} = 500$ yr, being $T_{R,0} = 50$ yr for ordinary buildings. In this case, $c_r = 1.207$ [CNR Eq.3.4, Figure 3.2], hence

$$v_r = 25.00 \cdot 1.207 = 30.175 \quad \text{m/s} \quad (7.35)$$

which gives a mean wind velocity at the top

$$v_m(202.20) = 30.175 \cdot 0.22 \cdot \ln\left(\frac{202.20}{0.3}\right) = 43.23 \quad \text{m/s} \quad (7.36)$$

Vortex-shedding occurs when vortices are shed alternatively from opposite sides of the structure; this gives rise to a fluctuating load perpendicular to the wind direction. Structural vibrations may occur if the frequency of vortex-shedding is the same as the fundamental frequency of the tower. This condition occurs when the characteristic 10 minutes mean wind velocity, v_m , at the cross-section where vortex-shedding occurs is equal to the critical wind velocity v_{crit} given from [CNR Eq.O.2]

$$v_{crit,i} = \frac{f_i \cdot b}{St} \quad (7.37)$$

where v_{crit} is the critical vortex-shedding velocity for the i -th mode in the most unfavorable position, f_i is the natural frequency of the considered flexural mode i of cross-wind vibration, b is the reference width of the cross-section at which resonant vortex-shedding occurs and St is the Strouhal number.

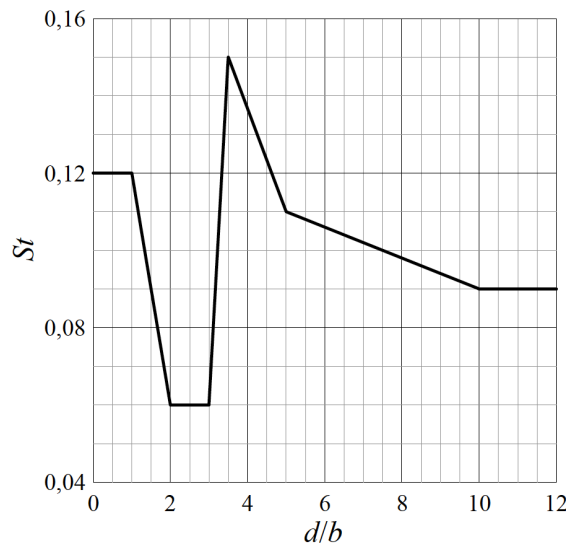


Figure 7.26: Values of the Strouhal number for rectangular cross-sections with sharp corners [CNR Figure O.5]

As shown in Figure 7.26, the Strouhal number for a cross-section ratio $d/b = 2.5$ is 0.06

[CNR Table O.I], therefore

$$v_{crit,i} = \frac{0.153 \cdot 24}{0.06} = 61.20 \quad \text{m/s} \quad (7.38)$$

The effect of vortex shedding should be investigated when the ratio of the largest (d) to the smallest (b) cross-wind dimension of the structure (both taken in the plane perpendicular to the wind) exceeds 6 or when [CNR Eq.O.3]

$$v_{crit,i} < v_{m,l} \quad (7.39)$$

where $v_{m,l}$ is the mean wind velocity evaluated at height z at which the critical speed occurs for $T_R = 500 \text{ yr}$.

Experience and theory show that the critical velocity causes the maximum transverse response of the building where the amplitude of the resonant mode of vibration is maximum. Knowing that the first vibrating mode is most excited when the critical vortex-shedding occurs at the top of the structure, a preliminary check is carried out at height $z = 202.20 \text{ m}$.

In this case

$$d/b = 60/24 = 2.5 \quad \text{and} \quad 61.20 > 43.23 \quad \text{m/s} \quad (7.40)$$

Hence, from the application of the standards, the structure would not seem to suffer from the vortex-shedding.

Galloping is a self-induced vibration of a flexible structure in cross-wind bending mode. Non circular cross-sections are prone to galloping, which starts at a special onset wind velocity v_{CG} given by [CNR Eq.P.2]

$$v_{CG} = \frac{2 \cdot Sc}{a_g} f_i \cdot b \quad (7.41)$$

where Sc is the Scruton number and a_g is the factor of galloping instability taken as 5.0 [CNR Table P.I].

The susceptibility of vibrations depends on the structural damping and the ratio of structural mass to fluid mass. This is expressed by the Scruton number, Sc_i , which is a function of the i -th vibrating mode [CNR Eq.O.4]

$$Sc_i = \frac{4\pi m_i \xi_{s,i}}{\rho b^2} \quad (7.42)$$

where m_i is the mass per unit length (kg/m) of the structure for the i -th mode, $\xi_{s,i}$ is the structural damping, ρ is the air density under vortex-shedding conditions (the recommended value is 1.25 kg/m^3) and b is the reference width of the cross-section at which resonant vortex-shedding occurs.

For Isozaki tower one has

$$Sc = \frac{4 \cdot 3.14 \cdot 353802 \cdot 0.01}{1.25 \cdot 24^2} = 61.75 \quad (7.43)$$

In general, if $Sc > 30$, the hazard of synchronization is very low and does not represent a particularly severe load condition. As a matter of fact, in order to avoid instability due to galloping, or to make its occurrence highly unlikely, it should be ensured that [CNR Eqs.P.4-P.5]

$$v_{CG,i} > v_{m,i} \quad \text{and} \quad \frac{v_{CG}}{v_{crit}} > 1.5 \quad (7.44)$$

In this case, being

$$v_{CG} = \frac{2 \cdot 61.75}{5} 0.153 \cdot 24 = 90.69 > 43.23 \quad \text{m/s} \quad (7.45)$$

the first condition is satisfied, even if

$$90.69/61.20 = 1.48 < 1.5 \quad (7.46)$$

meaning that interaction effects between vortex-shedding and galloping are likely to occur.

Divergence and flutter are instabilities that occur for flexible plate-like structures above a certain threshold or critical wind velocity. The instability is caused by the deflection of the structure modifying the aerodynamics to alter the loading. The Eurocode EN 1991-1-4:2004 [265] provides a means of assessing the susceptibility of the structure in terms of simple structural criteria. To be prone to either divergence or flutter, the structure should have an elongated cross-section with $b/d < 0.25$.

Being for Isozaki tower

$$b/d = 24/60 = 0.4 > 0.25 \quad (7.47)$$

the criterion is satisfied, hence, divergence and flutter are avoided.

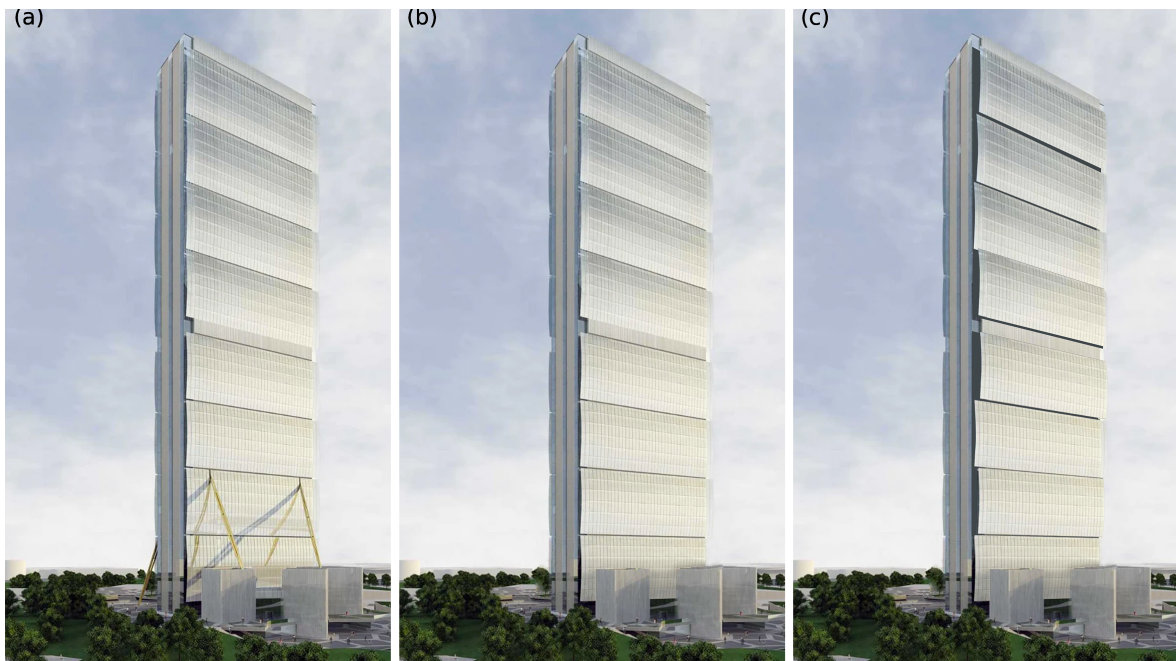
7.5 Design of multiblock MF

Unlike the monolithic MF system conceived for the 77.5 m 25-storey high building, for Isozaki tower the installation of a movable envelope divided into several detached parts capable of moving independently of each other is expected, in order to evaluate the effect deriving from the relative movement between one block and another on the overall system's behavior. As anticipated, this type of façade will be referred to as multiblock MF system (see the sketch of Fig. 3.1 b). Proceeding as in the mid-rise testing case, the analysis are carried out in the two-dimensional plane, thus, both the turbulent wind forces and the unilateral movable façade are applied perpendicularly to the longer side of the building, where the structural system has to deal with a lower lateral stiffness.

Table 7.16: Estimate of the mass ratio with steel and glass Movable Façade

FZ [kN]	a [m/s ²]	W_s [tons]	N_s [-]	M_f [tons]	A [m ²]	W_g [kg/m ²]	M_g [tons]	M_{MF} [tons]	M [tons]	μ [%]
451	9.81	46	16	814	22464	40	991	1804	78986	2.24

As for the mid-rise building, in order to carry the major stresses and forces generated by the axial movement, it is necessary to reinforce the elements constituting the structure of the cladding frame. Based on this, the MF design to be applied on the tower involves the strengthening of the framing, currently designed in aluminum, as described in section 7.2.2, with the same box-shaped steel tubes applied for the monolithic MF. Clearly, the replacement of aluminum with steel lead to an increased overall weight of the cladding structure, due to the greater vertical reaction forces, FZ , transmitted at the base from a heavier permanent load. The estimate of the MF mass and, consequently, of the available mass ratio, μ , is performed by modeling an appropriately sized façade shell in SAP 2000 and subjecting it to a linear static analysis under dead load. The resulting mass values from SAP analysis, related to the entire cladding system, are listed in Table 7.16. As can be seen, switching from an aluminum frame to a steel one, an increase in the mass ratio equal to 42% occurs.

**Figure 7.27:** 3D render of Isozaki tower (a) with struts, (b) without struts and (c) with a multiblock Movable Façade

However, the mass ratio of 2.24% referred to the whole façade must be halved ($\mu = 1.12\%$) in consideration of the fact that a one-sided steel and glass façade is accounted for to be incorporated on Isozaki tower structure in the longitudinal wind direction (specifically, along the x -axis of the building plan). This choice leads to assume a façade mass equal to $M_{MF} = 1804/2 = 902$ tons, which will be used for a proper sizing of the sliding connectors

Table 7.17: Geometric characteristics of the Movable Façade

$n.$ shells	length	width	$n.$ floors per shell	height
N_s	L	B	N_f/s	H
[–]	[m]	[m]	[–]	[m]
8	25.3	60.0	6	202.20

Table 7.18: Sizing of the façade connectors

M_{MF}	W_{MF}	N_s	N_d	W_s	L	s	g	M_{max}	f_{yd}	W_x
[tons]	[kN]	[–]	[–]	[kN]	[kN]	[m]	[m]	[kNm]	[MPa]	[cm ³]
						1.49	0.70	40.8		120.8
900	8829	8	40	1103.6	27.6	0.89	0.40	24.3	338.1	71.8
						0.29	0.10	7.7		22.8

in the next section.

The movable façade system conceived to be applied on Isozaki tower is subdivided into eight 60×25 moving shells, according to the building geometric characteristics, conceived to allow the relative movement between each group of floors. While for the mid-rise case study a straight frame has been designed, which observes the plan dimensions and the building floor number, for Isozaki tower the current curved layout and the eight shells into which the envelope is divided has been maintained (with the same panel size as the 25-storey building), while the struts are eliminated, hence, their contribution to the dynamic response of the tower is zero. Figure 7.27 shows a photorealistic render of Isozaki tower with and without struts, therefore with the installation of a multiblock MF capable of undergoing relative horizontal sliding under the action of wind. The main geometric and dimensional features of the movable façade are listed in Table 7.17.

7.5.1 Connector sizing and layout

The whole façade system is hinged at each level with the same mechanical connection system as the mid-rise building, being able to rotate and move in the axial direction while fixed in the vertical direction. The sliding brackets are assumed to be incorporated in the flooring slab between the Isozaki tower structural system and the movable block façade frame.

A possible design layout of the MF mechanical connection system is portrayed in Figure 7.28, highlighting the three typical configurations occurring when the MF is completely open (in the upper part), partially open/closed (in the middle) or completely closed (in the lower part). It is worth considering that all the layouts depicted can occur during a wind event due to positive or negative wind pressures acting upwind or downwind. As generically described in Chapter 4, the mechanical system is composed of double hollow box-like tubes: the outer tube (1) houses and protects the dissipative slider (inspired by Gong's VFCC as stated in section 4.3) (2), hiding the mechanical action from view; the inner tube (3) is the actual sliding element, which connects the device placed in the structural floor, to which it is hinged,

Table 7.19: Geometric and mechanical properties of the connection devices for various sizing calculations performed

g [m]	L_{tot} [m]	$b \times a$ [mm]	s [mm]	W [kg/m]	J_x [cm ²]	J_y [cm ⁴]	W_x [cm ³]	W_y [cm ³]
0.70	1.68	200 × 100	4	18.34	1240.29	420.77	124.03	84.15
0.40	1.08	150 × 60	5	15.70	544.17	124.17	72.56	41.39
0.10	0.48	100 × 40	4	8.29	125.68	28.21	25.14	14.11

with the steel transom of the façade frame (4), to which it is welded. The façade panels are considered to be hinged both at the base and at the top of the supporting structure, joined together along the horizontal development of each floor to avoid unwanted relative displacements between them. Four trapezoidal rubber bumpers (5), screwed and welded at the edges of the outer tube, should prevent the impact occurring between the slider and the metal profile of the connector when the wind-excited façade undergoes axial displacements from one side to the other. For the same reason, other four shock-absorbing layers (6) are placed between the floor and the façade frame. Finally, an aluminum structural expansion joint (7) is located at the floor level, closing the gap created when the cladding begins to open.

To allow the housing of the connection devices, a thickening of the floor section with an opening below are foreseen to guarantee the execution of inspection and maintenance operations of the sliders. The sizing of the connector is carried out resorting to the static diagram of a horizontal cantilever beam which better describes the behavior of the steel tube when the gap between the building and the MF is completely open. The beam is constrained to the structural floor at the fixed end and subject to a concentrated vertical load (that is, the weight of the unilateral movable façade) at the free end. From the previous section, a weight of about 8830 kN is obtained for the one-sided façade (W_{MF}) divided into $N_s = 8$ shells and, assuming a number of devices to be inserted in each floor equal to $N_d = 40$ (obtained from $B/d = 60/1.5$, where B is the width of the building plan and d is the distance between the façade panels), the vertical load, L , acting on each bracket is estimated, being equal to approximately 27.6 kN , whereas the axial load is neglected. The cantilever span, s , given by the distance between the floor slab and the midpoint of the façade frame, useful for the computation of the bending moment transmitted by the transversal load, is assumed as a design parameter, on which the size of the initial gap, g , directly depends according to Eq. 4.27.

Fixed the span length and obtaining the gap, the maximum bending moment, M_{max} , induced by the concentrated load is then evaluated, from which the minimum resistance modulus, W_x , that the selected S355 high-strength profile must ensure to withstand its own amount of load, is obtained. In the parametric analyses that will follow, three span length values will be taken, associated with three progressively decreasing gaps ($g = 0.70; 0.40; 0.10$ m). For each gap value investigated, the sizing of the connectors is performed based on Eq. 4.25, whose results are summarized in Table 7.18. OPPO-type rectangular steel boxed

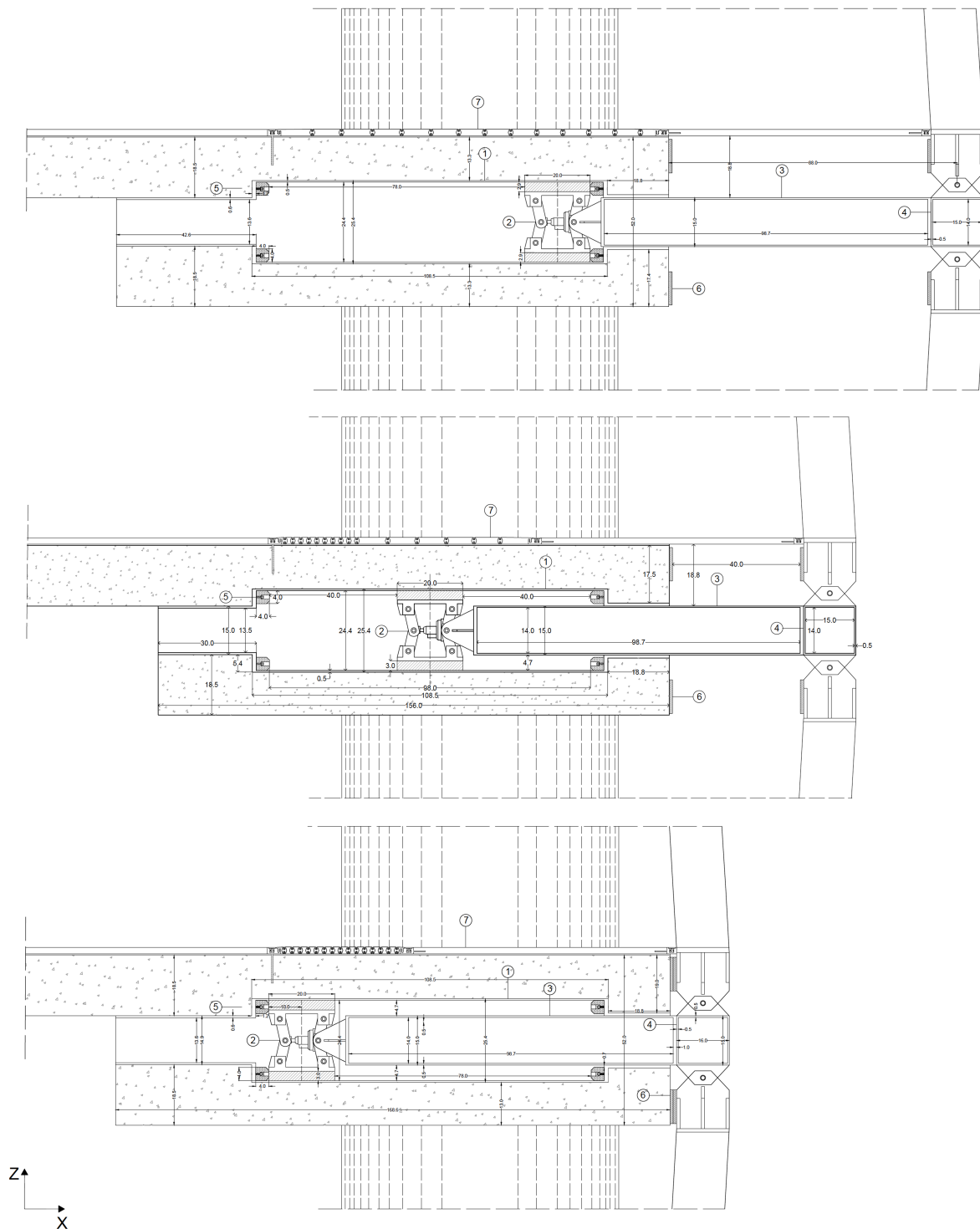


Figure 7.28: Cross-sectional detail of the connection device integrated into the multiblock MF portrayed in its open (upper part), partially open/closed (in the center) and closed (lower part) layout

tubes, with variable section and thickness according to the selected sizing case, are chosen to properly design the connectors. The main geometric and mechanical properties of the metal profiles are shown in Table 7.19. It is assumed that the connection between Isozaki tower

Table 7.20: Mechanical parameters of the façade beam-column elements

N	A	E	J
$[-]$	$[m^2]$	$[GPa]$	$[m^4]$
40	0.176	210	$2.1E - 03$

and the movable block façade will be made by arranging the devices thus designed for all the 51 building floors.

7.5.2 Modeling of the MF connection system

Numerical modeling and simulation of the movable façade composed of eight separate modules is performed in OpenSeesPy by means of two-dimensional *elastic beam-column* elements of length, H , linking the façade nodes along the z -axis and generating a second node per floor placed at distance d from each representative node of the structure. The ground node is massless and constrained in all directions, with the exception of the translation along the x -axis. Floor masses in x -direction, m_{MF} , are assigned equally to each upper node according to the following

$$m_{MF} = \frac{\mu}{2} m_s = 0.0112 \cdot 1547.05 = 17.68 \quad \text{tons} \quad (7.48)$$

or even

$$m_{MF} = \frac{M_{MF}}{N} = \frac{902}{51} = 17.68 \quad \text{tons} \quad (7.49)$$

where $\mu = 1.12\%$ is the halved mass ratio given from section 7.5 and m_s is the corresponding structural floor mass derived from section 7.3.

The eight shells into which the envelope is divided are generated by interrupting the beam element continuity at seven pairs of nodes, representative of the boundary floors between one module and another. For each pair of interrupted nodes, a third node is generated, which makes the connection between the node of the structure on the i -th floor and the first node of façade shell on the i -th+1 floor. Material properties and sections that make up the multiblock MF frame (A , E , J) are assigned to each beam element in the equivalent MDOF model, whose values are listed in Table 7.20.

By applying the fluctuating wind forces, $F_i(t)$, derived from section 7.4, to each i -th node of the MF model, the resultant stresses developed in the elastic beam elements of the cladding are printed by returning the *elemental dynamic force* in OpenSeesPy. The maximum frame stresses induced by wind load in the vertical steel profiles of the highest façade shell, including floors 44–51, are specified in Table 7.21. It should be noted that the listed values of the axial force, P , shear force, V_{2-2} , and bending moment, M_{3-3} , are to be intended as the overall values per floor; hence, with a resisting bending moment relative to y - y axes, $M_{Rd,y}$ [kNm], obtained from Table 6.17, the designed steel box sections are able to carry their own amount of bending moment induced by the applied wind load.

Table 7.21: Wind-induced reactions in the beam-column elements (levels 44-51)

floor	height	MF beam element	axial force	shear force	bending moment
			P	V_{2-2}	M_{3-3}
[-]	[m]	[-]	[kN]	[kN]	[kNm]
51	202.20	102	0.00	114.753	223.768
50	198.30	101	0.00	100.921	196.797
49	194.40	100	0.00	74.024	144.347
48	190.50	99	0.00	47.949	93.502
47	186.60	98	0.00	17.928	34.959
46	182.70	97	0.00	7.375	14.382
45	178.80	96	0.00	1.135	2.214

Based on the assumptions of section 7.5.1, in the two-dimensional simulation domain the connection between the 52 nodes of Isozaki tower and the 52 nodes of the multiblock MF is numerically modeled with two-node link element objects, defined by two nodes per floor, and assigning them the first translational direction of the *multilinear* and the *impact material* parameters related to the frictional and impacting behavior of the connection device, respectively, as described in section 4.5. To prevent the MF model from being unstable, multi-point constraints are created in direction 2 (that is, the translation along the y -axis) and 3 (that is, the rotation) between the eight pairs of MF nodes placed at the same z height, using an *equalDOF* command. In this way, the nodal degrees-of-freedom at node 105 (that is, the *slave* node) are constrained to be the same as those at the node 60 (that is, the *master* node), and so on. With 111 total nodes and 338 total elements, the equivalent MDOF model of Isozaki tower equipped with a multiblock MF and dissipative connectors is portrayed in Figure 7.29.

7.6 Evaluation of MF dynamic performances

The vibration and acceleration damping performances of MF-equipped Isozaki tower integrated with dissipative sliders are evaluated in this section. To perform the analysis in OpenSeesPy, for each component class defined in section 6.6 a specific type is selected and implemented in the numerical model. A transformation method is used to construct a single-point constraint handler; a RCM degree-of-freedom numbering object is selected as DOF-numberer and the transient integrator used for determining the predictive step for time $t + dt$ is a Hilber-Hughes-Taylor (HHT) integrator. By choosing the input parameters according to Eq. 6.69 (with $\alpha = 0.67$), the method is unconditionally stable. The LinearSOE and LinearSolver objects to store and solve the system of equations in the analysis are built with a BandGeneralSOE linear system of equation object. As for the convergence, this is achieved with a NormUnbalance test and, finally, a Newton-Raphson solution algorithm is created to solve the nonlinear algebraic equation at the current time step.

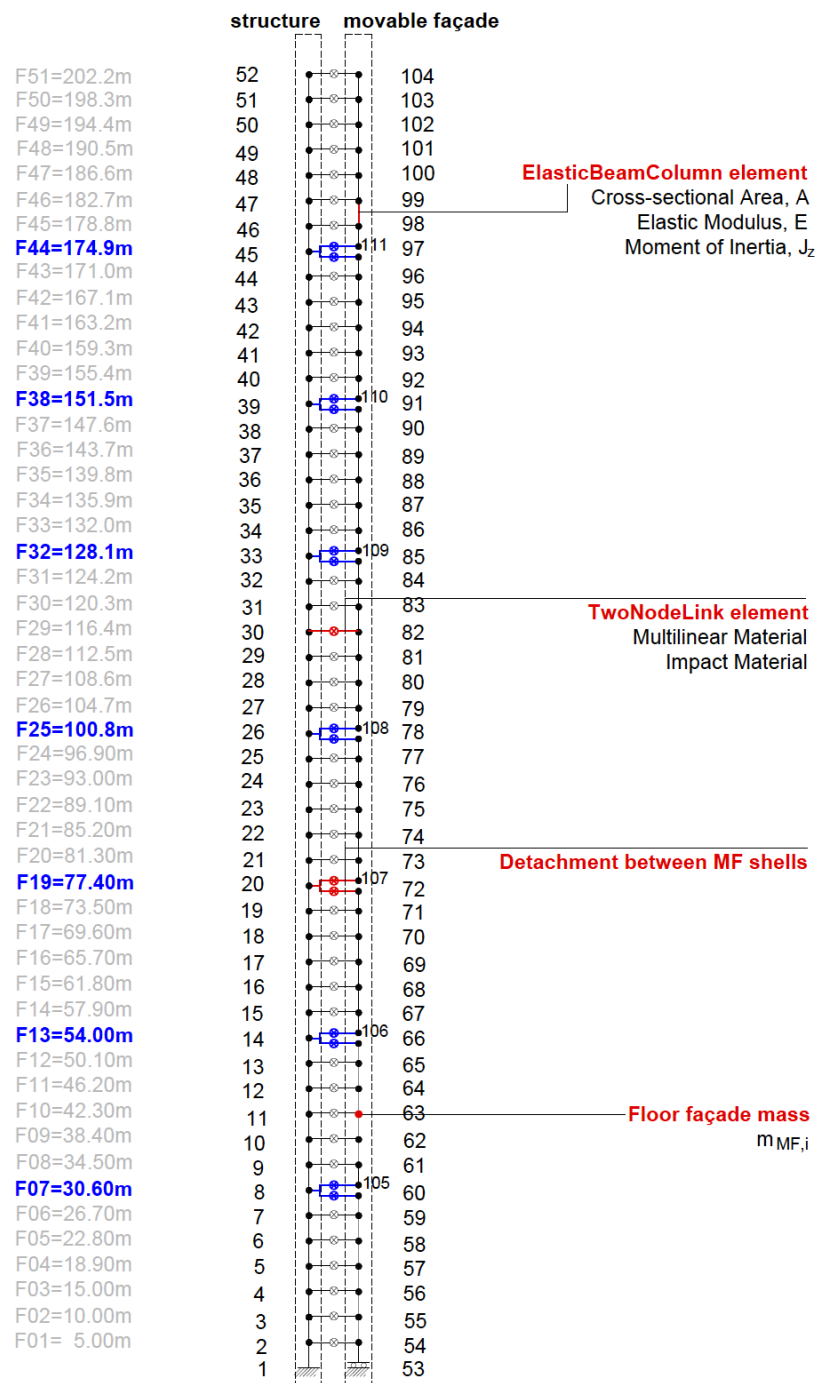


Figure 7.29: Equivalent MDOF model of the multiblock MF-equipped Isozaki tower with highlighting of the main elements assigned

Based on these component objects, a transient analysis with one analysis step to perform and a time-step increment equal to $dt = 0.02$ s is carried out, extending over a time interval of about 16000 s in accordance with the duration of the sampled signal. The total number of integration points thus obtained is equal to 450000, making the computation time extremely onerous. A turbulent wind load based on a 26.8 m/s mean wind velocity at the top, as defined in section 7.4, is implemented into the simulation platform by means of time-histories of

Table 7.22: Displacement values of Isozaki tower top floor with conventional fixed façade

maximum [m]	amplitude [m]	RMS [m]	mean value [m]	inter-storey drift ratio [%]	minimum [m]
0.838	1.231	0.274	0.176	0.08	-0.376

fluctuating forces, $F(z, t)$. Under such a dynamic excitation, the maximum absolute displacement (in m) and acceleration (in g) of Isozaki tower with and without MF (hence, with the current fixed façade) and the maximum relative displacement (in m) of multiblock MF are computed. A comparative investigation is performed by re-introducing the efficiency indices, η and κ , defined in Eq. 6.70, which quantify the level of reduction of structural displacement, with respect to the absence of MF, and structural acceleration with respect to the chosen serviceability criterion, respectively.

7.6.1 Building response with fixed façade

The equivalent MDOF model of Isozaki tower equipped with conventional fixed aluminum cladding is made to experience fluctuating wind forces, $F(z, t)$, computed in accordance to a $26.8 m/s$ mean wind velocity. These are firstly assigned to the 51 nodes of the elastic Timoshenko beam elements along the z -axis, simulating the wind load directly applied on the main structural building.

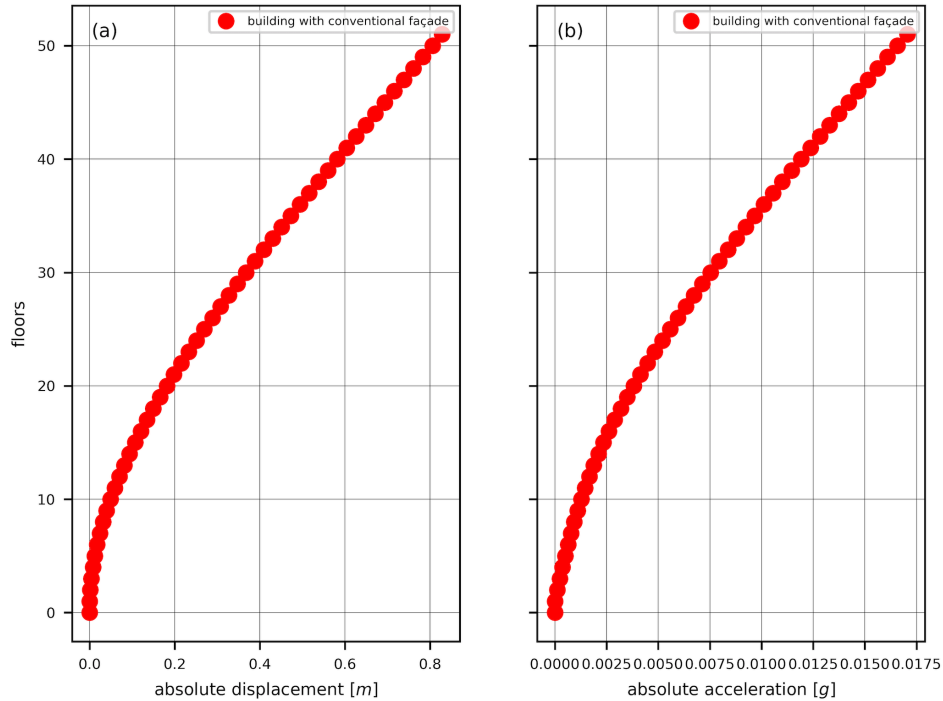


Figure 7.30: Maximum absolute displacement (a) and acceleration (b) of Isozaki tower with conventional fixed façade under wind load

As can be seen from vertical floor profiles of Figure 7.30, under a 3-second wind gust

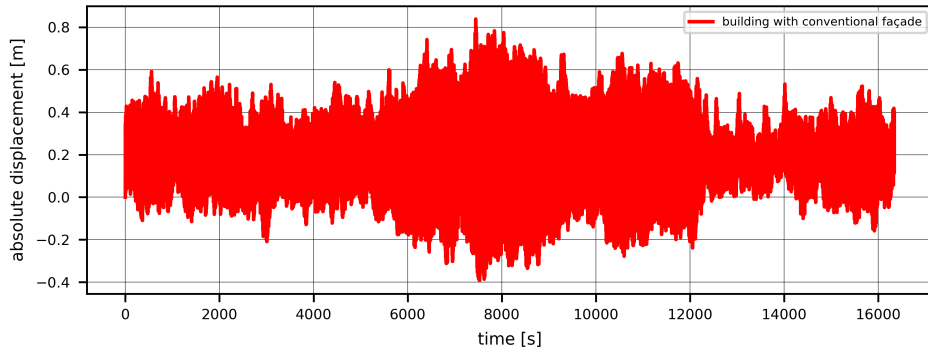


Figure 7.31: Top floor absolute displacement of Isozaki tower with conventional fixed façade under wind load

Table 7.23: Properties of the connection device

F_F	F_N	L_{tot}	L_F	g	δ_m	δ_y	k_h	K_1	K_2
[kN]	[kN]	[m]	[m]	[m]	[m]	[m]	[MN/m]	[MN/m]	[MN/m]
40	141	0.48	0.40	0.10	0.032	0.003	100	14	18

velocity, $u_{3-s,10}$, equal to 33 m/s at the top, the structure alone (that is, without the MF system) undergoes a top lateral displacement of 0.84 m (Fig. 7.30 a) with an amplitude of 1.231 m, a mean value of 0.176 m and a RMS of 0.274 m; the inter-storey drift ratio is estimated to be 0.08%. As regards the response of the structure in terms of absolute acceleration, a peak of 0.018 g is recorded on the top floor as emerges from Figure 7.30 b, even if this will be thorough in section 7.6.2, related to the assessment of serviceability performance and compliance with human comfort. Moreover, in the time-history related to the 51st level shown in Figure 7.31, a central area characterized by more pronounced absolute displacement peaks can be distinguished, roughly between 6000 and 12000 s, in which the amplitude of the response widely increases. All the response values referred to the top floor absolute displacement of the structure with the current fixed façade are summarized in Table 7.22.

7.6.2 Building response with multiblock MF

With the incorporation of a multiblock MF integrated with dissipative sliders and bumpers into the structural model of Isozaki tower, a comparative study of the wind-induced response with and without MF (that is, with the current fixed façade) is performed. As expected, the addition of MF with the connection devices implies the transition of the fluctuating wind forces, $F(z, t)$, first applied on the 51 nodes of the structural model, towards the 51 nodes of the façade beam model. The dynamic performances of the high-rise building equipped with a multiblock façade are preliminary assessed with respect to a reference case implemented with fixed values of the key variables that characterize the connection system's behavior, which are listed in Table 7.23.

As shown in the force-displacement diagram of Figure 7.32, the dissipative slider inte-

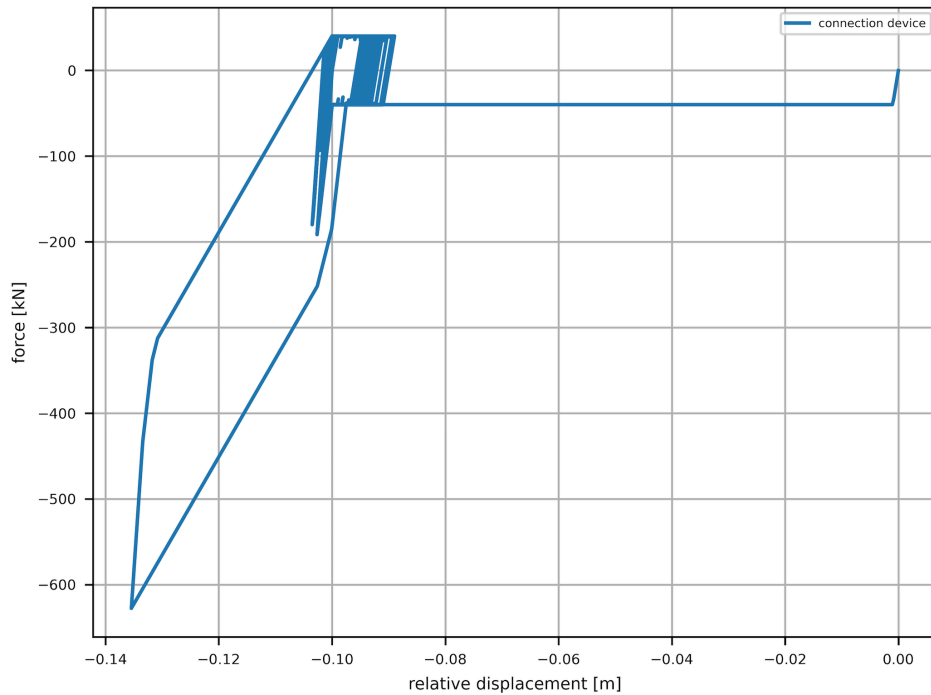


Figure 7.32: Force-displacement diagram of the connection device

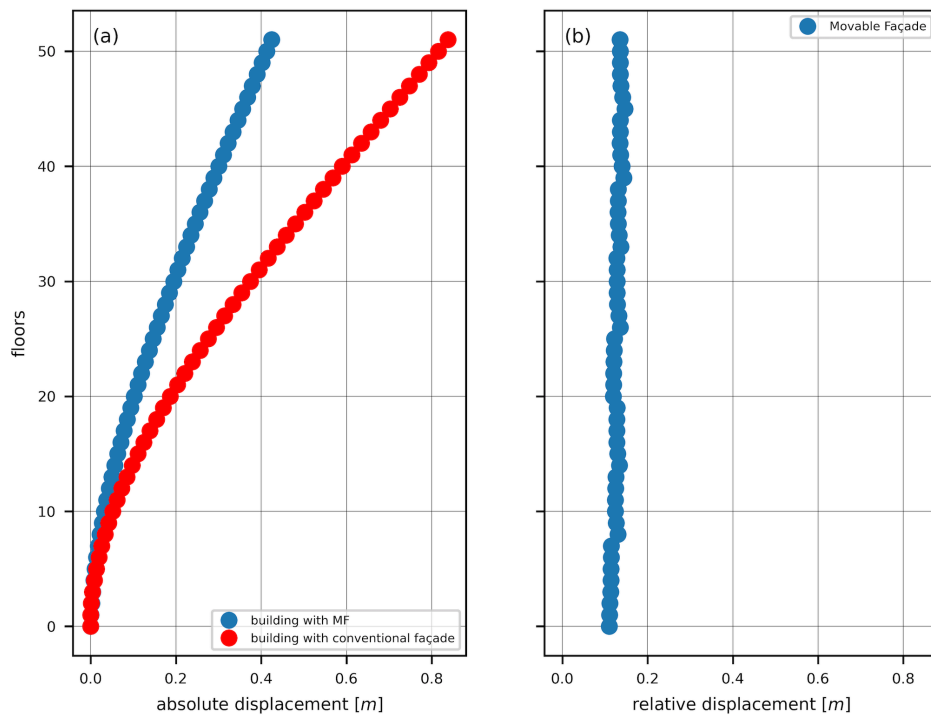


Figure 7.33: Absolute displacement of MF-equipped building superimposed on that with conventional façade (a) and relative displacement of multiblock MF (b)

grated with rubber bumpers proved to be effective in counteracting the façade relative displacement in the reference case analyzed: the wind load directed towards the MF activates the façade motion which experiences an initial excursion consistent with the width of the gap imposed ($g = 0.10 \text{ m}$). With about 3 cm of relative penetration within the bumper layer, the

slider moves towards the primary building structure (hence, towards the left side of the plot) entering the *colliding* mode defined in section 4.6.3, that occurs due to the unilateral contact between the friction slider and the rubber bumper. Close to the bumper, the slider keeps dissipating energy through progressively decreasing hysteretic loops around non-zero mean values. When this occurs, a very high efficiency ($\eta = 49.3\%$) is recorded on the structure response, with the façade undergoing a minimum relative displacement of about 13 cm.

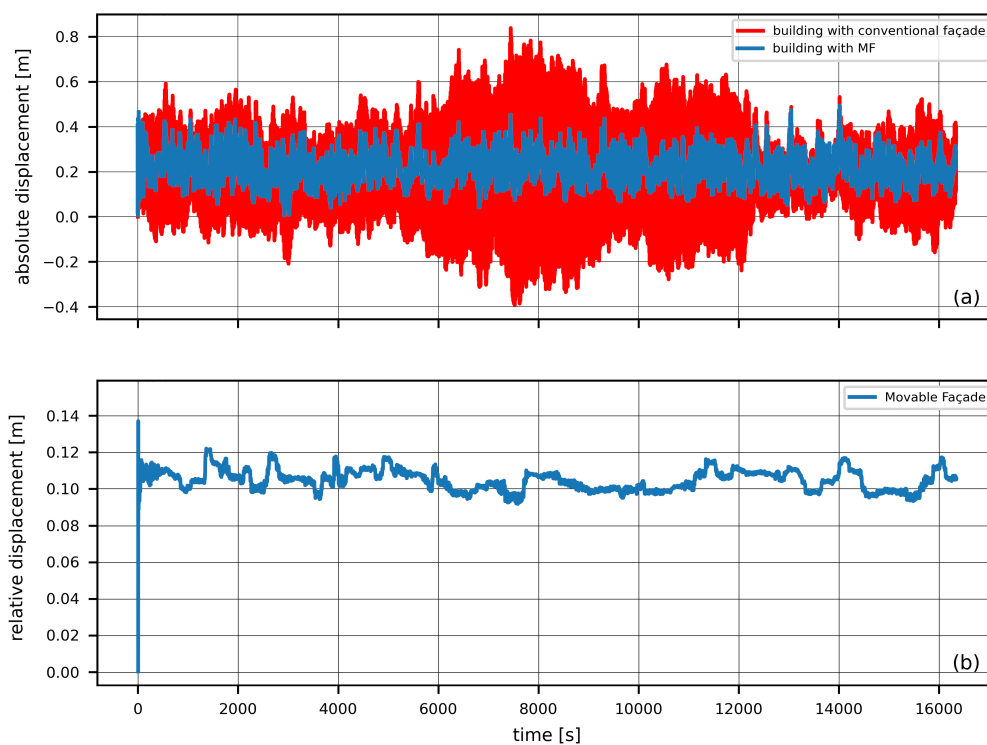


Figure 7.34: Top floor absolute displacement of the MF-equipped building (blue curve) superimposed on the structure response with conventional façade (red curve) under wind load (a) and relative displacement of the multiblock MF under wind load (b)

This effect is visible in Figure 7.33 which shows the vertical floor profiles of the MF-equipped Isozaki tower (blue curve) superimposed on that of the current structure (red curve), expressed in terms of absolute displacement (Fig. 7.33 a) and the multiblock MF expressed in terms of relative displacement (Fig. 7.33 b). As can be seen from the two plots, which refer to the maximum values of the response, a promising structural control obtainable with the MF connection system is highlighted under the imposed parameters, while safeguarding façade motion from Moon’s problem and keeping its relative displacement limited to a reasonable value.

The beneficial trend achievable with the incorporation of a multiblock MF and sliding connectors on the high-rise structural building is substantially validated by the time histories of top lateral displacement portrayed in Figure 7.34 recorded in a time interval of 16000 s. Figure 7.34 a compares the *controlled* absolute displacement of the building (blue curve) with the *uncontrolled* one (red curve) and, under the same reference parameters, Figure 7.34 b shows the top floor relative displacement of the multiblock façade.

Table 7.24: Top floor displacement efficiency of the MF-equipped building

Efficiency η [%]	Structure displacement [m]	MF rel. displacement [m]	MF abs. displacement [m]
49.3	0.424	0.135	0.515

The main outcome of this first study, taken as a reference case for subsequent parametric investigations, is that the proposed connection device proved to be able to perform the dual function of structural vibration damping and avoidance of excessive MF relative displacements. Specifically, the addition of dissipative bumpers characterized by narrow initial gap ($g = 0.10 \text{ m}$) and high impact stiffness ($k_h = 100 \text{ MN/m}$) to the frictional slider designed with low friction threshold ($F_F = 40 \text{ kN}$) allows to keep Moon's problem under control, while maintaining a high structural efficiency. In the next section, it will be investigated whether a possible design modification of the connector parameters can further improve the response of the system.

Compliance with performance criteria

In the structural design of tall buildings, the wind-related serviceability issues which may influence the occupants' well-being are often a limiting design criterion. High-rise buildings are required to not exceed two main serviceability limit states which define their functional performances and behavior under wind load, namely, deformation and motion perception. As these issues are particularly important to be checked on tall and slender steel and composite structures, this section focuses on ascertaining compliance with wind performance criteria, defined in accordance with the current building codes, with the addition of a multiblock MF and dissipative connection.

Based on the parameters assumed for the investigation of the reference case, it is possible to check if the admissible values related to human comfort, a_p , and structural safety, Δ_p , are exceeded or not, in order to ensure both protection of users' well-being and avoidance of damage to building components. According to the Italian CNR-DT 207/2008 guidelines, the peak value of the absolute acceleration computed with respect to a return period $T_R = 1 \text{ yr}$ is recommended for the assessment of human comfort levels and habitability of high-rise structures. With reference to the design limiting criteria defined in section 2.3.5, the acceleration limit value, a_p , derived from Eq. 2.23 can be assumed to carry out a preliminary check on the assessment of the user comfort level obtained with a multiblock MF incorporated with dissipative sliders in the high-rise building. Specifically, this should be estimated as a function of the fundamental frequency of the building in the longitudinal direction, f . As depicted in Figure 7.35, the habitability check (with and without Movable Façade) is carried out knowing that Isozaki tower is mainly intended for office use and its fundamental frequency in the longitudinal direction is $f = 0.153 \text{ Hz}$, giving

$$a_p = \frac{0.006}{0.153^{0.56}} = 0.0171 \text{ g}$$

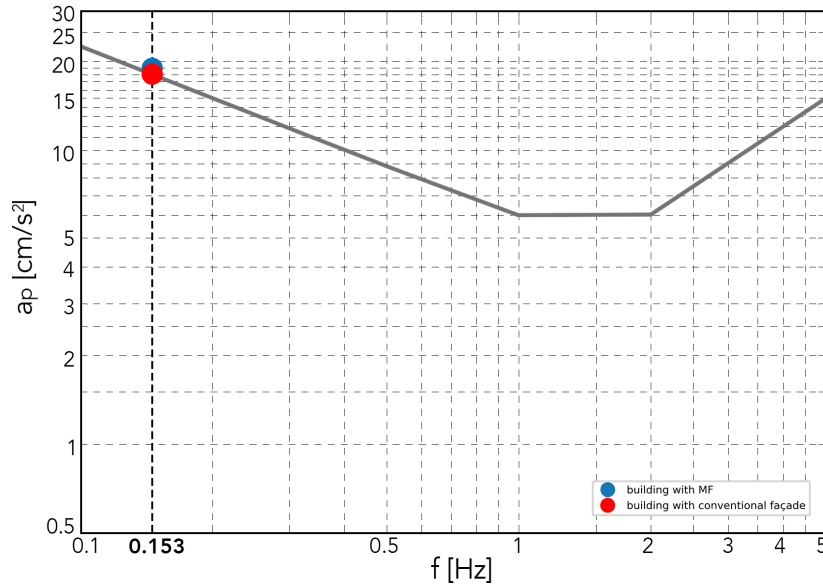


Figure 7.35: Habitability check of Isozaki tower top floor with the current façade (red dot) and with multiblock MF (blue dot) based on CNR-DT 207/2008 guidelines. The gray curve defines the acceleration limit value, a_p , for different fundamental frequencies of the buildings

Table 7.25: Compliance with wind performance criteria of MF-equipped Isozaki tower

		Isozaki tower with conventional façade	MF-equipped Isozaki tower
a_p [g]	0.017	0.018	0.019
Δ_p [%]	0.2	0.08	0.15

It should be noted that the gray curve in the diagram defines the acceleration limit value, a_p , for different fundamental frequencies, fixed $T_R = 1$ year. In accordance with Table 2.2, $a_p < 0.5\% g$ is not perceptible by building users. Similarly, taking the allowable inter-storey drift ratio, Δ_p , defined according to Eq. 2.24 yields

$$\Delta_p = \frac{1}{400} = 0.0025$$

Based on Table 2.3, $\Delta_p < 0.2\%$ corresponds to a fully operational performance level, hence with no damage.

The resulting values listed in Table 7.25 highlight that wind performance criteria related to the assessment of structural damage are satisfied with both a fixed façade and a multiblock MF designed with the parameters listed in Table 7.23. In both cases, $\Delta_p < 0.2\%$ even if the drift with MF exceeds that with traditional façade. Unlike the deformation serviceability issue, the motion perception criterion is not satisfied in either case as a_p is slightly higher than the standard limit (0.017) for both fixed (0.018) and Movable façade (0.019), resulting in a negative acceleration efficiency, $\kappa = -11\%$.

Table 7.26: Fixed properties of the MF connection device for the parametric investigation on the friction threshold

L_{tot}	L_F	g	δ_m	δ_y	k_h	K_1	K_2
[m]	[m]	[m]	[m]	[m]	[MN/m]	[MN/m]	[MN/m]
0.48	0.40	0.10	0.032	0.003	100	14	18

Table 7.27: Top floor displacement efficiency for variable friction threshold, F_F

F_F	η	Structure displacement	MF rel. displacement	MF abs. displacement
[kN]	[%]	[m]	[m]	[m]
40	49.3	0.424	0.135	0.515
120	49.5	0.423	0.126	0.502
200	49.8	0.420	0.109	0.459

7.6.3 Parametric investigation

The study of a reference case of MF-equipped Isozaki tower, implemented with well-defined values of the connection device main design parameters, allowed to validate the high potential of the multiblock MF system both in controlling structural vibrations, due to the frictional behavior of the slider, and in containing the excessive façade relative motion, due to the addition of a system of rubber bumpers. Solving Moon's problem appears to be possible, while preserving a high damping efficiency of the wind-induced structural response. To evaluate whether the dynamic performance of the multiblock MF is kept despite an alteration of the key variables, a parametric study executed for different friction threshold of the slider (F_F), impact stiffness of the bumper (k_h) and initial gap (g) between the structure and façade is addressed in the following subsections.

Influence of the friction threshold

The friction threshold of the slider is functional to determine the performance level of structural control offered by the dissipative façade system. The parameter F_F identifies the threshold value beyond which the slider overcomes the friction force and begins to slide due to the longitudinal wind force acting on it, dissipating energy and dampening the response of the building.

By making the friction threshold vary within the range

$$40 \leq F_F \leq 200 \quad \text{kN}$$

a first parametric study focusing on the effect of the friction threshold on the dynamic performances of MF system is performed, while fixing the gap width and the impact stiffness properties of rubber bumpers on the basis of the reference values listed in Table 7.26.

As shown in Figure 7.36, increasing the friction threshold means lowering the peak of contact force between the slider and the bumper, lengthening and narrowing the hysteresis

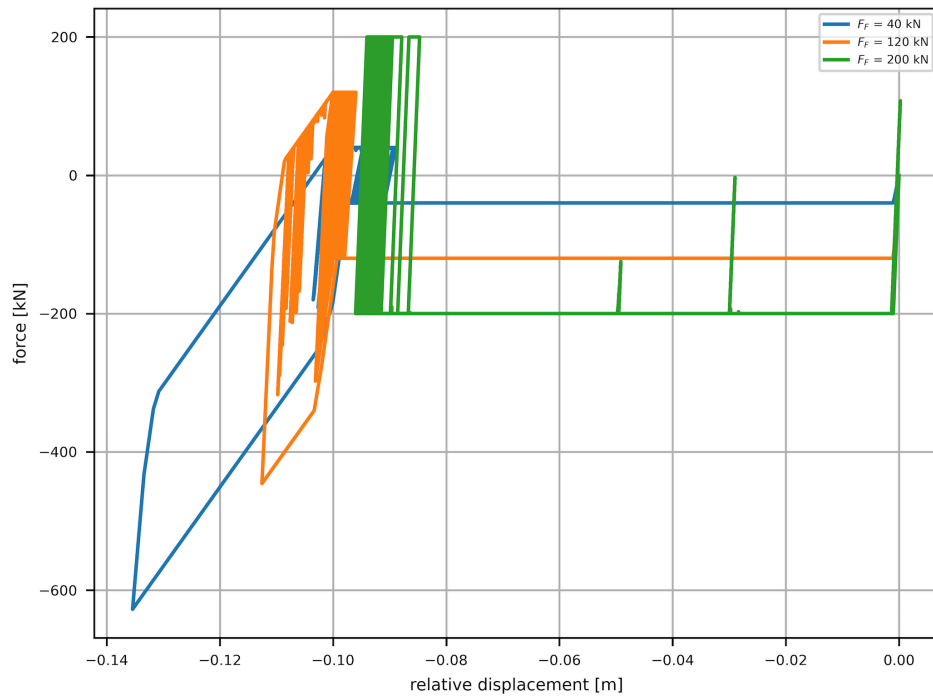


Figure 7.36: Force-displacement diagrams of the connection device for variable friction threshold, F_F

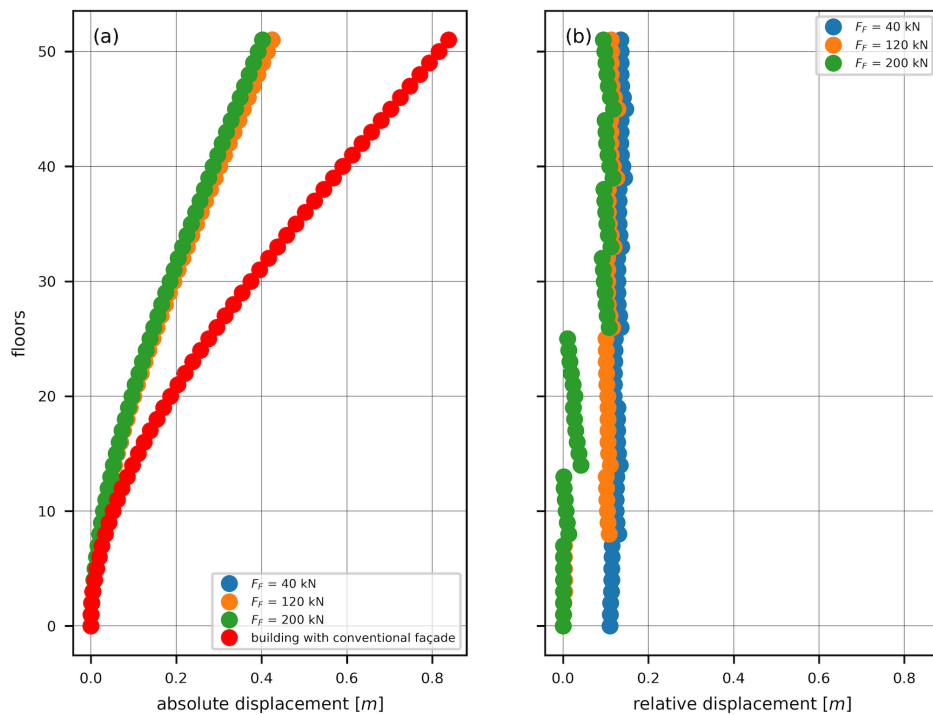


Figure 7.37: Absolute displacement of MF-equipped building superimposed on that with conventional façade (a) and relative displacement of multiblock MF (b) for variable friction threshold, F_F

area of the force-displacement cycle so that the amount of energy dissipated during impact remains unchanged. At the closing of the gap, $g = 0.10 \text{ m}$, a unilateral impact occurs

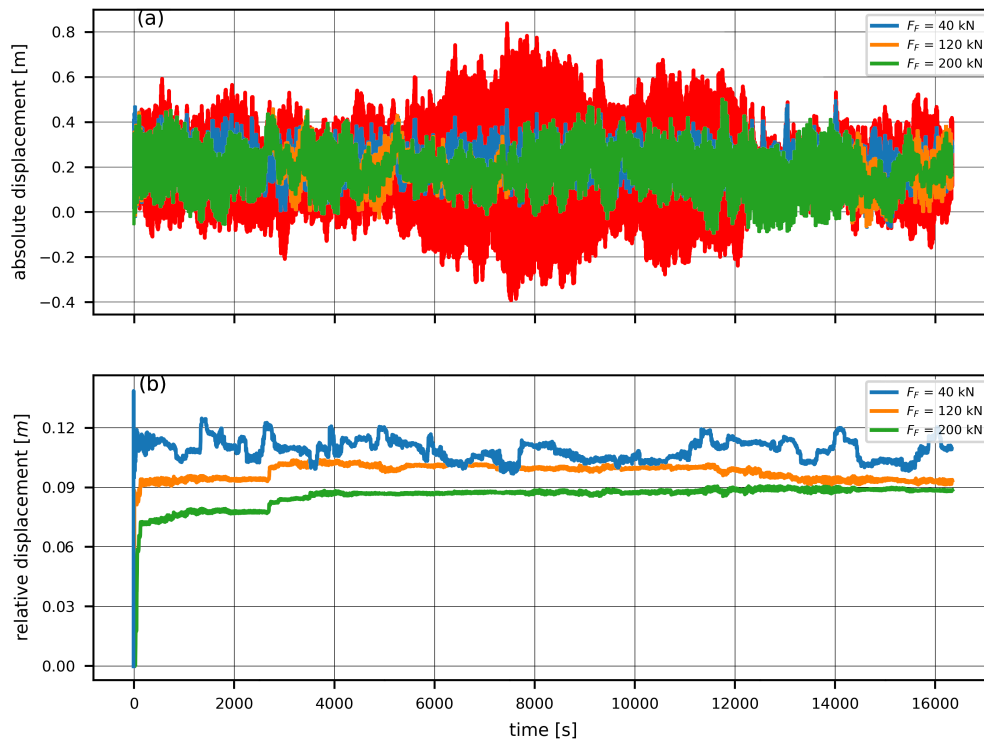


Figure 7.38: Top floor absolute displacement of MF-equipped building (a) and top floor relative displacement of multiblock MF (b) for variable friction threshold, F_F

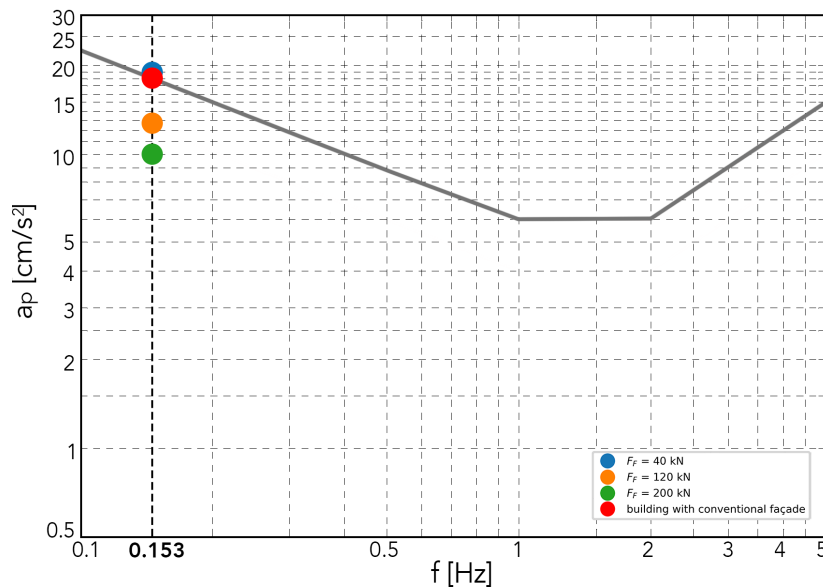


Figure 7.39: Habitability check of Isozaki tower top floor with conventional façade (red dot) and with multiblock MF for variable friction threshold, F_F , based on CNR-DT 207/2008 guidelines. Gray curve defines the acceleration limit value, a_p , for different fundamental frequencies

determining the beginning of the *colliding* mode, during which the slider keeps cycling around non-zero mean values progressively increasing with the rise of F_F .

By observing the profiles of absolute displacement of the MF-equipped tower (Fig. 7.37 a) and relative displacement of the façade (Fig. 7.37 b), it can be seen that for low friction

threshold ($F_F = 40 \text{ kN}$), the MF relative (and absolute) displacement tends to rise, reaching 0.13 m , while the more the friction increases ($F_F = 200 \text{ kN}$), the more the façade undergoes a well-contained top relative displacement (0.10 m), coming to stick to the structure profile and behaving as if it were a single system. In particular, the bonding to the structure begins from the first two façade shells on the lower floors and then progressively involves the upper shells as the friction threshold increases. At the same time, the structural displacement remains mostly unchanged, with only a slight increase of the efficiency for $F_F = 200 \text{ kN}$, which always settles on very high positive values ($\eta = 49.3\%$). The different trend between the structure and façade response as the friction threshold increases is confirmed by the time histories of Figure 7.38, which shows the top floor absolute displacement of the tower with MF (Fig. 7.38 a) and the top floor relative displacement of façade (Fig. 7.38 b) in a time interval of 16000 s. All the efficiencies η and displacement values of both structure and façade as the friction threshold F_F varies are shown in Table 7.27.

In accordance with the CNR-DT 207/2008 guidelines, Figure 7.39 shows compliance with human comfort requirement of Isozaki tower top floor with fixed façade and with MF for variable friction threshold, F_F . The gray line defines the acceleration limit value a_p for different fundamental frequencies, fixed $T_R = 1 \text{ year}$. With the exception of the red dot related to the case with fixed façade, each colored dot corresponds to the peak acceleration of the MF-equipped Isozaki tower top floor obtained with a specific F_F value. As can be seen, the acceleration efficiency κ improves as the friction threshold increases ($\kappa = 41.1\%$ for $F_F = 200 \text{ kN}$) keeping the acceleration peak within the comfort limit (gray curve), while worsens as the friction threshold decreases ($\kappa = -11\%$ for $F_F = 40 \text{ kN}$) with the consequent exceeding of the limit curve, a_p .

Influence of the initial gap

The initial gap between the primary building structure and the unilateral MF system defines the useful space for ensuring the façade axial displacement induced by the applied horizontal load. The possibility for the MF to undergo relative motion with respect to the building is strictly linked to the size of this space, whose width (in m) is the subject of the second parametric investigation. Whether the lengthening or shortening of the gap, g , between the structure and façade (or between the slider and bumpers) can affect the efficiency of the multiblock MF, is evaluated referring to the range of values suitably sized in section 7.5.1, which correspond to specific geometric and mechanical properties of the connectors

$$0.10 \leq g \leq 0.70 \text{ m}$$

Table 7.28 lists the fixed values of the friction slider and the bumper stiffness properties.

From the force-displacement diagrams portrayed in Figure 7.40 for variable gap widths, the beneficial effect of a limited sliding of the device, associated with a narrower initial space, is immediately noticed. It is also quite important to see that, for $g = 0.10 \text{ m}$ (blue diagram), the maximum contact force stops at about 500 kN , which corresponds to a maximum penetration of 3 cm ; for $g = 0.40 \text{ m}$ (orange diagram), the contact force reaches almost 1200 kN ,

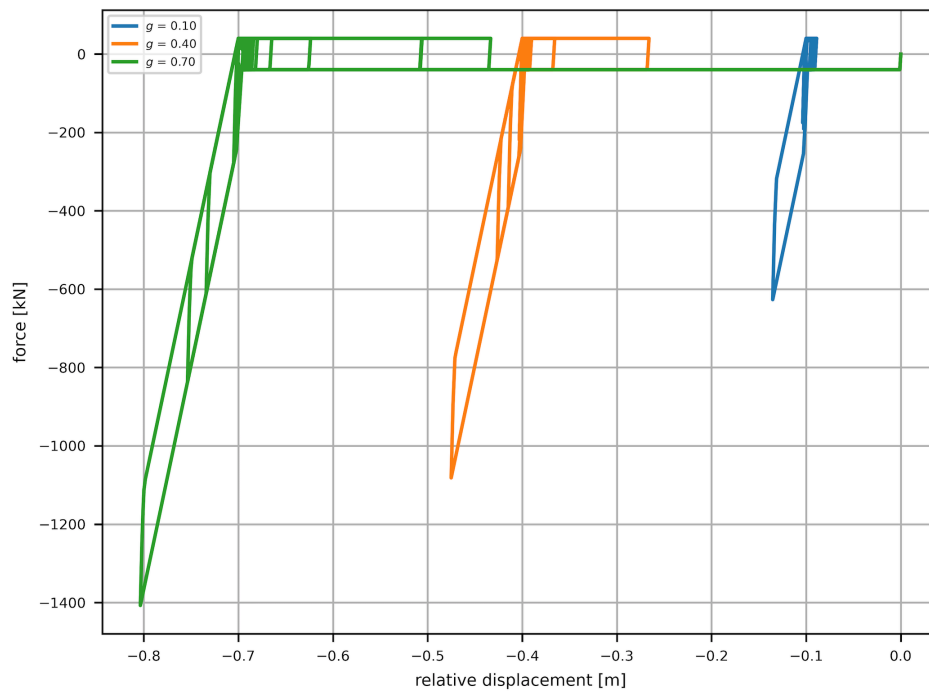


Figure 7.40: Force-displacement diagrams of the connection device for variable initial gap, g

Table 7.28: Fixed properties of the connection device for the parametric investigation on the initial gap

F_F [kN]	F_N [kN]	δ_m [m]	δ_y [m]	k_h [MN/m]	K_1 [MN/m]	K_2 [MN/m]
40	141	0.032	0.003	100	14	18

determining a maximum penetration inside the bumper layer of 7 cm; finally, for $g = 0.70$ m (green diagram) the contact force exceeds 1500 kN leading the slider to undergo a maximum penetration of almost 9 cm. It is worth mentioning that the blue diagram on the right side of the plot corresponds to the reference case.

Focusing the attention on the MF-equipped Isozaki tower response of Figure 7.41 a, it can be noted that any widening or narrowing of the initial gap has no tangible effect on the maximum absolute displacement of the building with MF, proving the successful of the proposed dissipative connection devices in reducing the wind-induced structural vibrations in all the cases investigated. The substantial insensitivity of the structure to the gap variation is validated by the top floor displacement time-history portrayed in Figure 7.42 a. As it can be seen, the dynamic performances remain almost unchanged for both large and narrow gaps, ranging between 0.42 m for $g = 0.10$ m (hence, with $\eta = 49.3\%$) and 0.44 m for $g = 0.70$ m (hence, with $\eta = 46.9\%$).

Nevertheless, as the size of the initial gap decreases, significant behavioral changes occur in the façade displacement, as shown in the vertical floor profiles of Figure 7.41 b and in the top floor time histories of Figure 7.42 b. As it was easy to guess, by lengthening the initial

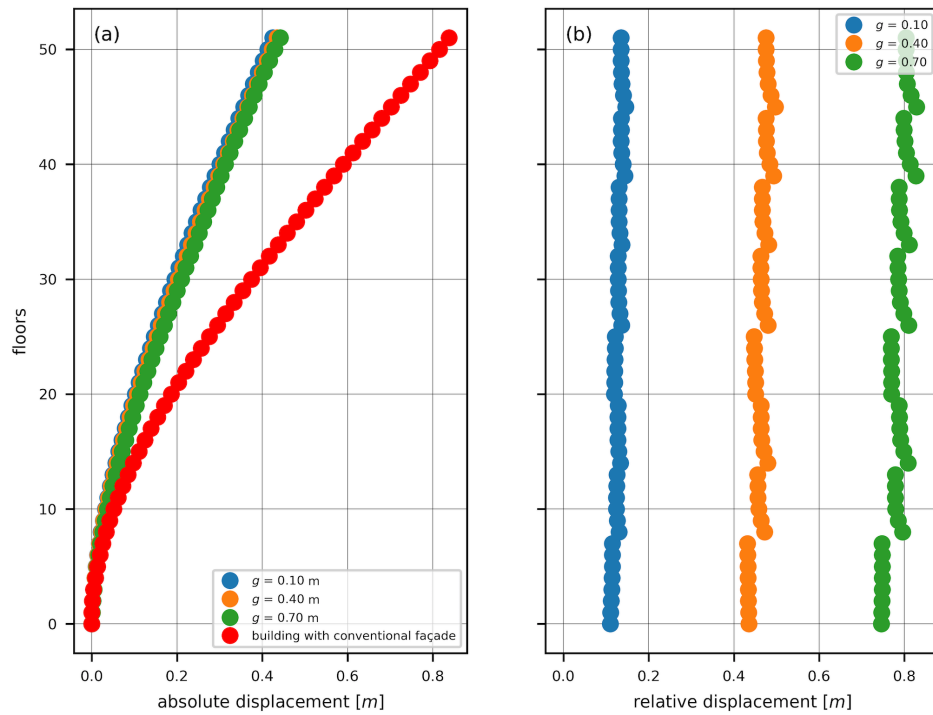


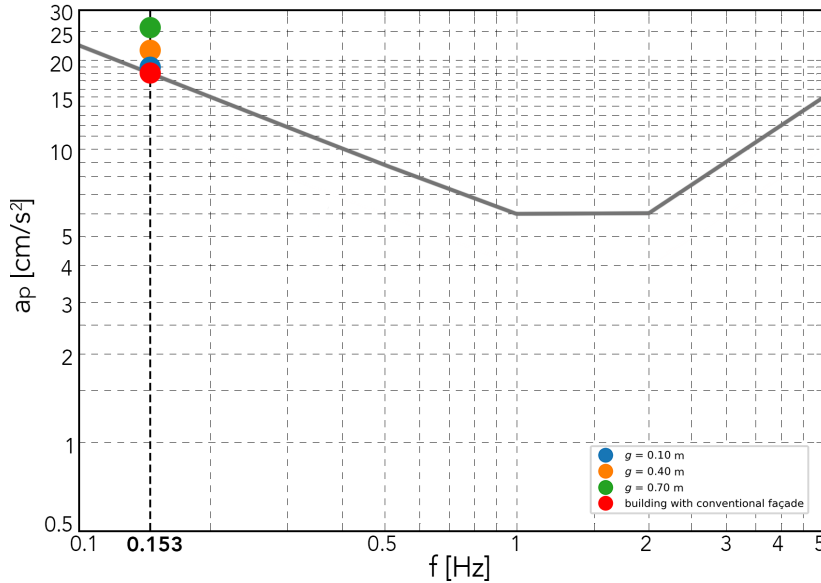
Figure 7.41: Absolute displacement of MF-equipped building superimposed on that with conventional façade (a) and relative displacement of multiblock MF (b) for variable initial gap, g



Figure 7.42: Top floor absolute displacement of MF-equipped building (a) and top floor relative displacement of multiblock MF (b) for variable initial gap, g

Table 7.29: Top floor displacement efficiency for variable initial gap, g

g [m]	η [%]	Structure displacement [m]	MF rel. displacement [m]	MF abs. displacement [m]
0.10	49.3	0.424	0.135	0.515
0.40	47.9	0.436	0.476	0.957
0.70	46.9	0.441	0.798	1.012

**Figure 7.43:** Habitability check of Isozaki tower top floor with conventional façade (red dot) and with multiblock MF for variable initial gap, g , based on CNR-DT 207/2008 guidelines. Gray curve defines the acceleration limit value, a_p , for different fundamental frequencies

gap, g , the movable blocks are allowed to perform greater movements with respect to the primary building structure and, consequently, the overall cladding displacement increases, reaching almost 0.80 m away from the tower ($g = 0.70\text{ m}$). Conversely, a narrower gap keeps the façade closer to the building, limiting its relative displacement to only 0.13 m ($g = 0.10\text{ m}$). Table 7.29 lists all the efficiency and displacement values for structure and façade with variable initial gap, g .

As regard the acceleration response of the tower with MF, Figure 7.43 shows compliance with human comfort requirement for variable initial gap, g , according to the parameters defined in Table 7.28. With the exception of the red dot related to the case with fixed façade, each colored dot corresponds to the peak of absolute acceleration of the MF-equipped Isozaki tower top floor obtained with a specific initial gap. As can be seen, with the widening of the gap, the acceleration peak on the top floor increases and this implies the exceeding of the comfort threshold with extremely negative efficiency ($\kappa = -52.9\%$ for $g = 0.70\text{ m}$); vice versa, the narrowing of this space allows to limit the acceleration peak even if maintaining a negative efficiency ($\kappa = -11\%$ for $g = 0.10\text{ m}$). Finally, $\kappa = -29.4\%$ for $g = 0.40\text{ m}$.

Table 7.30: Fixed properties of the connection device for the parametric investigation on the impact stiffness

F_F	F_N	L_{tot}	L_F	g	δ_m	δ_y
[kN]	[kN]	[m]	[m]	[m]	[m]	[m]
40	141	0.48	0.40	0.10	0.032	0.003

Influence of the impact stiffness

The parametric study conducted in the previous section highlighted that designing a connection device with low friction threshold to be overcome, in order to start sliding and dissipate energy, could be an advantageous solution for ensuring an adequate structural control on the high-rise building. Similarly, creating a façade system with a small gap between slider and bumpers allows to keep the MF relative displacement under control, reducing the sliding length of the device. However, the high impact stiffness tested so far for the dissipative bumpers' system has not proved to be advantageous for the purpose of reducing the structural acceleration at the top and maintaining the peak within the human comfort range defined by the standards. This is essentially due to the strong and sudden impact occurring between the structure and the façade which is related to the high stiffness of the shock-absorbing layer. By gradually reducing the stiffness of the bumpers, k_h , it is assessed whether this affects the structural acceleration in terms of compliance with the motion perception criterion.

The parametric study is carried out by setting the slider friction threshold and the bumper length properties according to the aforementioned reference values listed in Table 7.30, while varying the bumper stiffness within the range

$$25 \leq k_h \leq 100 \text{ MN/m}$$

where $k_h = 25 \text{ MN/m}$ is taken from Eq. 4.37.

In general, an increasing impact stiffness, k_h , determines a stronger contact force between the bumper and the friction slider, reaching almost $F_c = -700 \text{ kN}$ as shown in Figure 7.44, with the consequence of a much more marked and defined control on the wind-induced movement of the MF, whose relative displacement is kept within the limit of 0.13 m (blue diagram). Vice versa, a lower impact stiffness is synonymous of a more deformable and flexible bumper layer (green diagram), less capable of retaining the façade motion within a specific predetermined limit, allowing it to move further than 0.18 m away from its initial resting position due to a lower contact force ($F_c = -400 \text{ kN}$).

Despite the significant behavioral differences that occur in the force-displacement plots of the connection device for greater or lesser impact stiffnesses, however, the structural response does not undergo any appreciable change as k_h varies, as depicted in Figures 7.45 a and 7.46 a. For all the three cases investigated, an almost negligible effect emerges from the plots, proving that the absolute displacement of the tower with MF is totally insensitive to the bumper stiffness variation, stabilizing on a maximum value of 0.42 m with $\eta = 49.3\%$.

Clearly, the same cannot be said for the façade response since the impact stiffness of

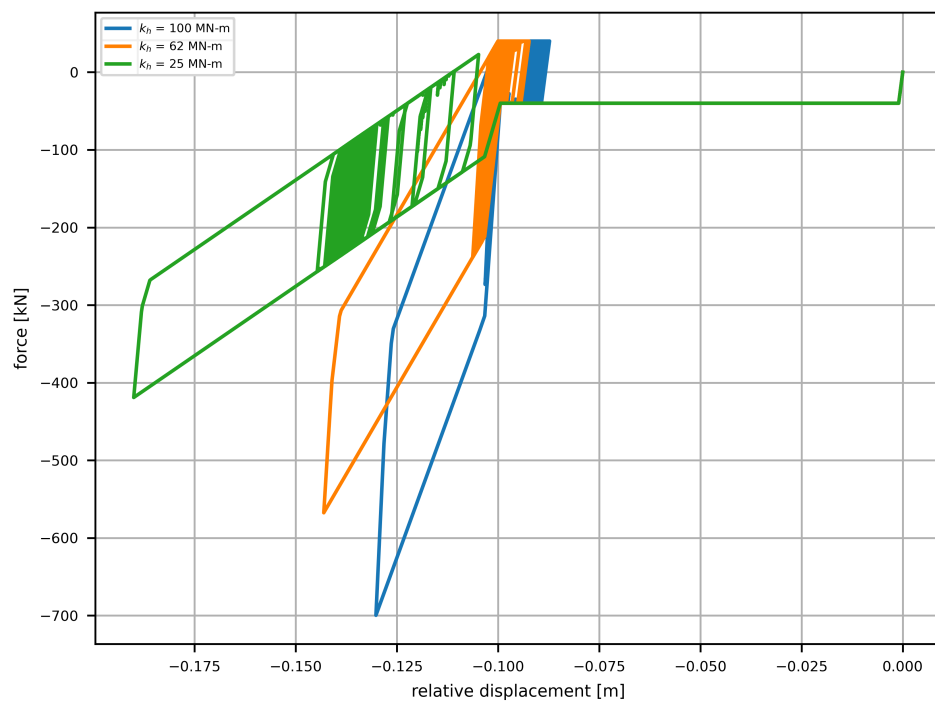


Figure 7.44: Force-displacement diagrams of the connection device for variable impact stiffness, k_h

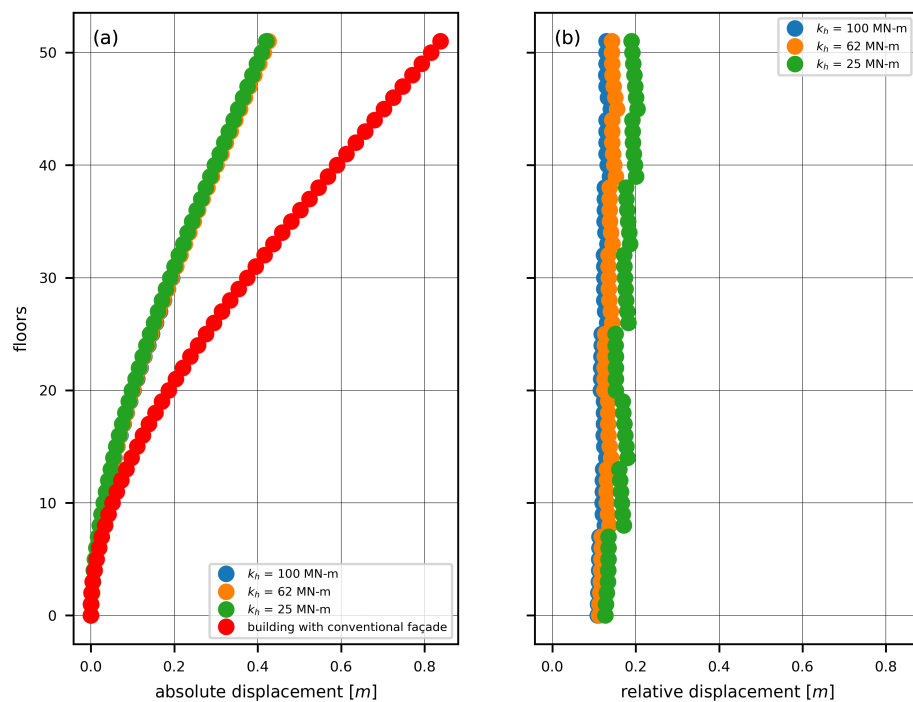


Figure 7.45: Absolute displacement of MF-equipped building superimposed on that with conventional façade (a) and relative displacement of multiblock MF (b) for variable impact stiffness, k_h

the bumper is a primary parameter for the purpose of restricting the MF relative displacements. Hence, its variation has a much more noticeable effect on the multiblock MF response. As expected, the higher the impact stiffness, the more effective the connection device is in

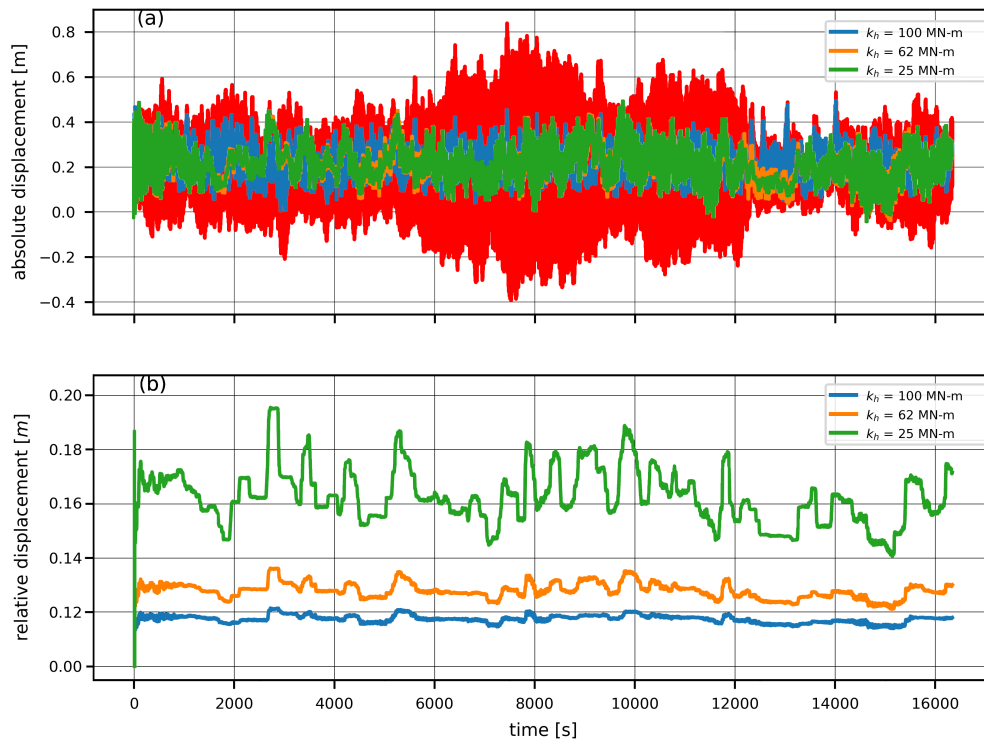


Figure 7.46: Top floor absolute displacement of MF-equipped building (a) and top floor relative displacement of multiblock MF (b) for variable impact stiffness, k_h

Table 7.31: Top floor displacement efficiency for variable impact stiffness, k_h

k_h [MN/m]	η [%]	Structure displacement [m]	MF rel. displacement [m]	MF abs. displacement [m]
25	49.1	0.426	0.190	0.590
62	49.2	0.425	0.151	0.545
100	49.3	0.424	0.135	0.515

containing and stopping the façade within a progressively decreasing relative displacement boundary, which goes from over 0.19 m for the lowest k_h tested, up to 0.13 m for the higher stiffness value tested (Figs. 7.45 b and 7.46 b). Efficiencies η and displacement responses of both the tower and MF for different impact stiffnesses, k_h are reported in Table 7.31.

Moreover, this parameter directly affects the structural acceleration peak on the top floor and, consequently, the efficiency κ , which will assume positive values when the stiffness is reduced and vice versa. To better understand this aspect, Figure 7.47 shows the habitability check for variable impact stiffness of the bumper. As expected, the reduction of k_h is beneficial in keeping the acceleration peak within the comfort threshold (green dot corresponding to $a_p = 0.012 g$ with $k_h = 25 MN/m$), reaching an efficiency $\kappa = 29.4\%$; on the contrary, increasing the stiffness of the slider-bumper contact causes a structural acceleration greater than the admissible value (blue dot corresponding to the reference $a_p = 0.019 g$ with $k_h = 100 MN/m$) making the efficiency negative ($\kappa = -11\%$).

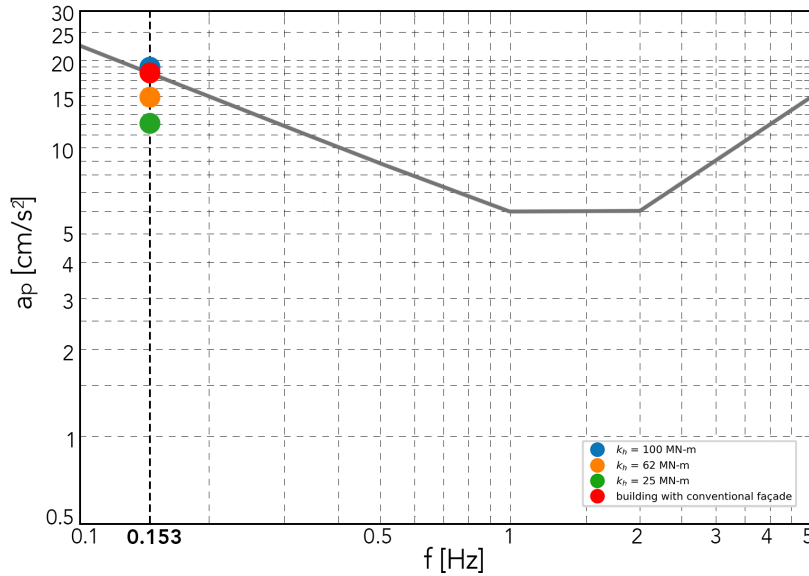


Figure 7.47: Habitability check of Isozaki tower top floor with conventional façade (red dot) and with multiblock MF for variable impact stiffness, k_h , based on CNR-DT 207/2008 guidelines. Gray curve defines the acceleration limit value, a_p , for different fundamental frequencies

7.7 Results and discussion

This section offers a critical analysis of the main findings achieved in order to provide a broad overview of displacement and acceleration results as a function of the connector design, highlighting how the MF connection system could impact on the response of both the structure and façade. Displacement results discussed so far can be summarized in the plots of Figures 7.48 and 7.49 which show the general trend of absolute displacement of the tower and the relative displacement of the façade, respectively, as the three main parameters of the connector vary. In Figure 7.48, the maximum absolute displacement of the MF-equipped Isozaki tower top floor (u_{str}) is expressed as a function of the friction threshold (Fig. 7.48 a), the initial gap (Fig. 7.48 b) and the impact stiffness of the bumper (Fig. 7.48 c), comparing it to the maximum absolute displacement in the absence of MF (red line). It is clear that the integration of a Movable Façade with dissipative connectors is successful in ensuring the reduction of structural vibrations by almost 50% with respect to the case of fixed façade, also keeping the high level of displacement efficiency η in all cases investigated. As a matter of fact, the response is kept constant around 0.42 m against over 0.80 m of the uncontrolled displacement.

Similarly, Figure 7.49 shows a summary of the façade behavior shown in the course of the parametric analyses, pointing out how the MF response is much more affected by the variation of the connector parameters with respect to the structure. Specifically, the MF relative displacement ($u_{façade}$) grows linearly with the size of the initial gap imposed (Fig. 7.49 c), exceeding the established threshold of 0.75 m for $g = 0.70$ m. On the contrary, the choice of a narrow gap $g = 0.10$ m allows to drastically reduce the façade motion, always keeping it in the proximity of the gap even when the friction threshold (Fig. 7.49 a) or the impact stiffness (Fig. 7.49 b) varies.

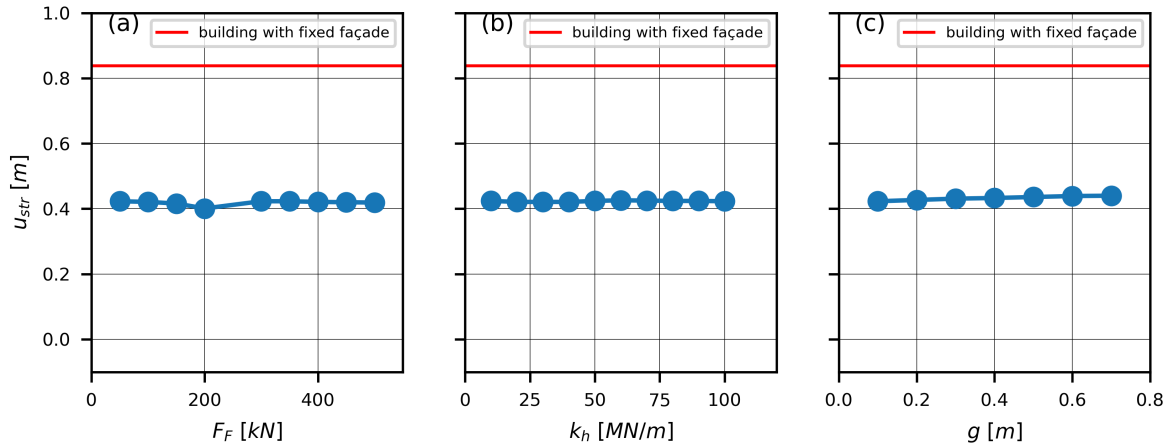


Figure 7.48: Maximum structural absolute displacements for variable a) friction threshold F_F , b) impact stiffness k_h and c) initial gap g . The red line represents the maximum displacement of the building with fixed façade ($= 0.838\text{ m}$)

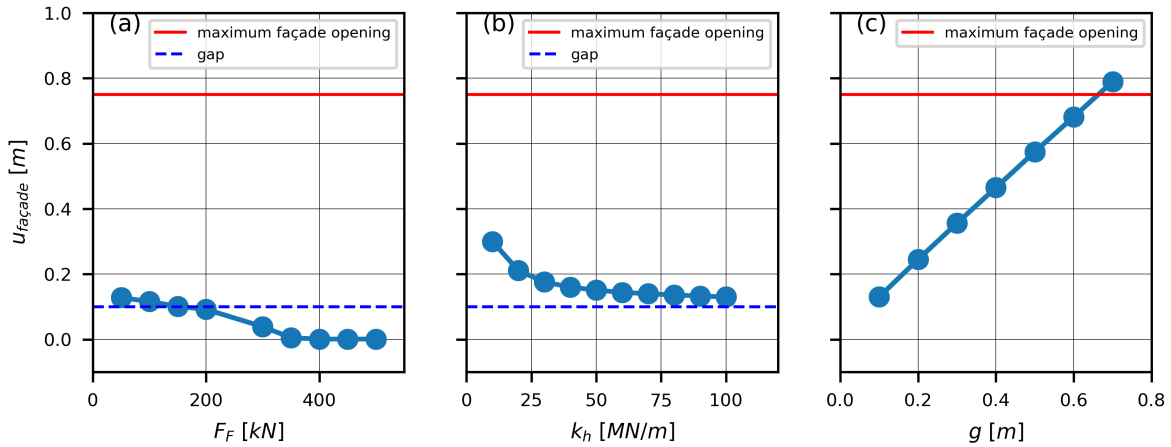


Figure 7.49: Maximum façade relative displacements for variable a) friction threshold F_F , b) impact stiffness k_h and c) initial gap g . The red line represents the allowable façade opening ($= 0.75\text{ m}$)

Finally, Figure 7.50 shows an overview of the acceleration response of Isozaki tower top floor with and without MF as the connector design parameters vary. The peak values of structural acceleration with fixed façade (blue dashed line) and with Movable Façade are compared with the standard acceleration limit value represented by the red line. In particular, Figure 7.50 a depicts the acceleration trend of the tower top floor for variable friction threshold, highlighting that high values of F_F offer an optimal response both with respect to the fixed façade and to building standards. In addition, Figure 7.50 b shows the same response quantity for different impact stiffnesses of the bumper ranging from 10 to 100 MN/m. Starting from a peak a_p slightly higher than the limit allowed by the standards for $k_h = 100$ MN/m, this tends to decrease due to lower impact stiffnesses, reaching a peak of 0.012 g for $k_h = 10$ MN/m. The positive results obtained are due to the reduced initial gap imposed. The extension of the gap, on the other hand, does not allow to reduce the structural acceleration peak, bringing it above the comfort limit value consistent with the motion perception

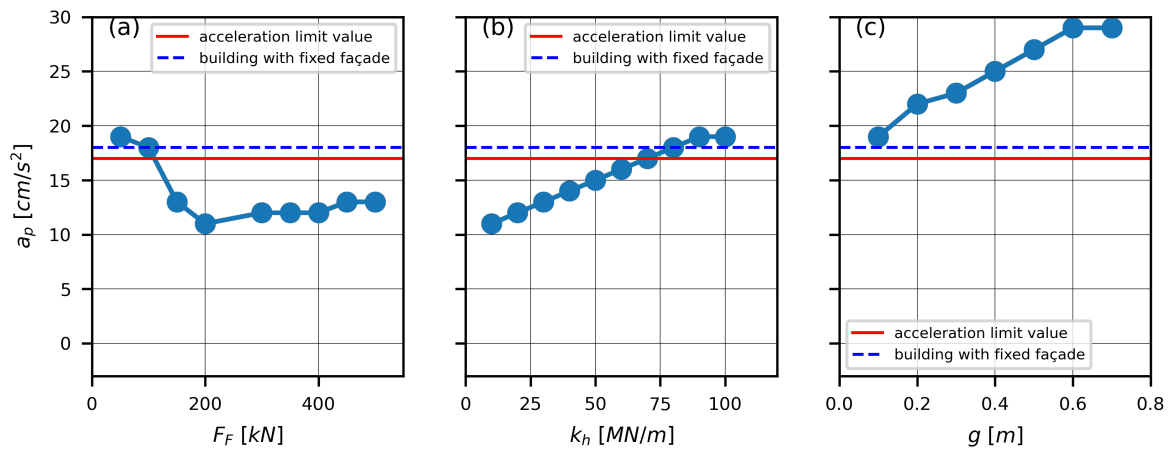


Figure 7.50: Maximum structural absolute accelerations for variable a) friction threshold F_F , b) impact stiffness k_h and c) initial gap g . The red line represents the standard acceleration limit value ($= 17 \text{ cm/s}^2$)

criterion, as is clear from Figure 7.50 c.

7.8 Closing remarks

The dynamic performances of a Movable Façade integrated with dissipative connections into the structural system of a high-rise building subject to turbulent wind load are explored in the present Chapter. Specifically, a multiblock MF system is assumed to be incorporated in the current 51-storey, 220 m tall Iozaki tower in Milan (Lombardy, Italy). Within Python environment, the building is numerically simulated as an equivalent MDOF Timoshenko beam model connected to elastic beam-column elements, representative of the façade vertical components, by means of two-node links which are assigned the frictional and impact material of the slider and bumpers, respectively. Transient analyzes are carried out according to a 3-second wind gust velocity consistent with the building site characteristics, with the MDOF numerical model experiencing fluctuating wind forces generated through the simulation of stationary random signals into the NOWS platform. With the introduction of suitable efficiency indexes (η, κ), a comparative study of the tower with and without MF (hence, with fixed façade), is performed. Preliminary investigations of a reference design case of the connection parameters prove the reliability of the system in being exploited on the tall structure equipped with a Movable Façade for a proper dynamic motion control. A high potential of the MF integrated with dissipative connectors is found both in limiting unreasonable façade relative displacements, due to the presence of the rubber bumper layers, and in ensuring a successful structural control (in terms of the top lateral displacement and acceleration), due to the dissipative frictional behavior of the slider. The possibility of solving Moon's problem of large cladding displacements even on tall constructions has led to performing more careful investigations in order to better appreciate the dynamical properties of the connection system when the key variables of the device are made to vary. The good performances of MF are preserved throughout further in-depth parametric analyses carried out for increasing

friction threshold of the slider (F_F), bumper's impact stiffness (k_h) and initial gap between the structure and façade (g). Qualitative ranges of investigations are selected to cover the most probable and achievable values. The analyses show that, after a proper calibration of the various design parameters, the MF could achieve the desired serviceability performance levels both in terms of accelerations and displacements, without impacting in a significant way the architecture of the building and ensuring a constructively admissible façade displacement. In conclusion, although real applications of Movable Façade are still to come, this work addressed some of the main conceptual issues to be solved. Of course, other problems remain to be solved, especially at the technological level, but the preliminary results obtained here seem to confirm that Moon's idea could become applicable.

Chapter 8

Conclusions

This Ph.D. dissertation has dealt with the problem of the large relative displacements of façade systems used for the purpose of wind-induced vibration damping in mid- and high-rise structural buildings. The dynamic motion control obtained by means of these advanced façade forms is based on a flexible or sliding connection mechanism conceived to reduce the amount of energy associated with dynamic wind loads transferred from the cladding panels to the building behind. As a result, as the façade moves substantially perpendicular to the building, the vibration of the primary structure is significantly reduced. In this context, the engineering envelopes used for structural purposes have been renamed as *Movable Façades* (MF). While potentially effective in ameliorating the dynamic behavior of tall buildings, the MF systems could be precluded from real-world applications due to the excessive motion they experience during wind activities which, if not contained within reasonable construction limits, would not allow their use as lateral motion control devices. The study on the structural dynamic motion control using *double skin façades* (DSF) conducted by K.S. Moon starting from 2005, then extended to further investigations by other researchers, provided the theoretical background to this Thesis. The author's conclusion that the excessive motion of DSF outer skins was a serious design limitation for the potential of the system as a structural motion control device in tall buildings regarding dynamic wind loads constituted the starting point of this research. The aim of the Thesis has been to deepen the study on the façade dynamic performances, extending the research to all the technological cladding layouts currently available today in addition to DSF, making a contribution to the possible resolution of Moon's problem about the uncontrolled relative displacements.

The topic was addressed through an exclusively numerical study conducted in three continuous steps of in-depth investigation and progressive development. SAP 2000 and Python code were used for the numerical analyses in all phases of the feasibility study. After introducing the concept underlying the functioning of the MF, which is familiar with the mechanism of the classic TMD, and defining the main construction types, including monolithic and multiblock MF, the preliminary phase involved a comparison between the vibration damping efficiency of monolithic MF and standard TMD performed in the context of linear dynamics. A parametric study exploring the effect of the main dimensionless parameters characteriz-

ing the response of both systems, specifically, the mass (μ), tuning (f), forcing frequency (ρ) and damping (ξ) ratios, was carried out considering equivalent 2DOF models subject to harmonic excitation applied directly on the primary mass, for the TMD-equipped building model, or on the secondary mass, for the MF-equipped building model, and focusing on the response in terms of the displacement amplitude. With the definition of a useful numerical index (η) for evaluating the relative efficiency of the systems and the introduction of three performance levels (undertuning, tuning and overtuning) related to smaller or larger values of f , the preliminary investigation ended up associating the best results with undertuned MF, which proved to be considerably more reliable than the corresponding TMD. Besides this, the good vibration damping performances of MF systems can only be pursued at the expense of unacceptable façade relative displacements, leading back to the well-known Moon's problem.

Based on the results obtained, the need to identify feasible solutions for limiting the large façade relative displacements, while preserving the dynamic performance of MF, hence allowing the system to be fully applicable in the field of structural vibration control, has emerged. To meet this double requirement, a suitable connection device, inspired by the VFCC device developed and tested by Laflamme and coworkers starting from 2016, was conceived and designed, setting its behavior on the joint action of two main mechanisms. A dissipative friction slider, based on a simple Coulomb's friction model, accounts for the dissipation of energy useful for structural control while a rubber bumper system, derived from the seismic pounding field, is necessary to restrain façade relative displacements exceeding a pre-defined design limit. The effectiveness of the friction slider incorporated with two pairs of bumper dampers was tested on the simple setting of 2DOF modeling under harmonic excitation, performing a parametric study in the frequency domain extended to the context of nonlinear dynamics. Two distinct phases characterized the assessment of the dynamic performance of the connection system, separately evaluating the structural vibration and acceleration control of the slider alone and the façade vibration control of rubber bumpers. With the introduction of specific numerical efficiency indicators, it was possible to evaluate any improvement or worsening of the behavior both for the primary mass absolute displacement (η) and acceleration (κ) and for the secondary mass relative displacement (ζ), normalizing the indices with respect to specific reference conditions, which were represented by the absence of monolithic MF for η , compliance with the habitability requirement for κ and a design threshold value for ζ . The efficiency of the slider was analyzed through a parametric investigation aimed at evaluating the influence of the friction threshold, expressed in terms of the dimensionless friction ratio (α) on the system performance, leading to the conclusion that an increase or decrease in the friction threshold strongly affects both the structure and façade response, with the two masses showing a clearly opposite trend. Low friction thresholds have been shown to have a highly positive effect in terms of increasing η as compared to the *uncontrolled* condition, but also at the expense of increasing the façade relative displacement. Conversely, high values of the friction ratio led to a drastic reduction of the efficiency with coupling of the monolithic MF to the structure. Moreover, the study of hysteretic force-displacement diagrams and

phase portraits of the friction slider, recorded at different forcing frequency ratios, enabled to highlight the occurrence of a number of secondary resonances, the so-called *superharmonic* (or *ultraharmonic*) resonances, coupled with complex nonlinear phenomena, like asymmetry of vibrations and loss of contact. After that, numerical parametric analyses, carried out by varying the bumpers' parameters (namely, the size of the initial gap and the impact stiffness), allowed to investigate the effect of the introduction of the two-sided obstacles on the secondary mass response, compared to the condition of the slider alone, and to notice possible issues associated with the occurrence of impact. The results of the analyses showed that, by properly selecting the design parameters of the bumpers (g and k_h), it is possible to guide the systems response in order to avoid, on the one hand, the occurrence of nonlinear dynamics phenomena that affect the primary mass response causing a reduction of the vibration and acceleration efficiency and, on the other hand, an excessive relative displacement of the monolithic MF, thus exploiting the occurrence of the impact to achieve the objective of solving Moon's problem, while safeguarding the structural control. Gradually narrow gaps had an advantageous action on the façade response but, on the contrary, worsened the efficiency performance on the primary mass. Similarly, an increase in the impact stiffness of the bumper, while being advantageous in terms of stopping the façade relative motion, was also linked to a slight worsening of the structural response in terms of both displacement and acceleration efficiency. The main outcome of this study was that bumpers may be very efficient in reducing the façade displacements while keeping dynamical efficiency; however, it also turned out that the balance between the vibration reduction efficiency and façade displacement control may be delicate, as quite different results can be obtained depending on the excitation frequency.

This result highlighted the need to extend the exploration of the performances of MF in the more realistic scenario of a building subject to wind action, where the combination of several frequencies can give different results than a single-harmonic excitation. Resorting to more refined equivalent MDOF models of both mid- and high-rise structural building excited by a well-defined cut-off frequency and gust velocity turbulent wind load, a new investigation was performed. With the processing of a stationary Gaussian random signal executed within the *NatHaz Online Wind Simulator* (NOWS), time histories in steady-state conditions of fluctuating *along-wind* forces were implemented in the simulation domain, based on which transient analyzes were performed. Two distinct but related studies, which involved a 25-storey, 77 m tall generic building and the 51-storey, 220 m tall Isozaki tower in Milan (Italy), have been conducted in parallel in order to better understand both the role played by the cladding layout and the dynamic properties of the tested building in affecting the vibration damping performances of the connection device. In this context, a monolithic façade with no interruptions was assumed for the lowest and stiffest building, while a MF divided into multiple detached parts was designed for the tallest and most flexible structure. For both investigations, the study of a reference case based on well-defined values of the control parameters of the connection device allowed to make meaningful preliminary considerations that

guided further in-depth parametric analyzes on the overall system response. First of all, the positive outcomes noticed under the single-harmonic forcing were confirmed by the analysis of the wind-excited MDOF models, proving the reliability of the connection design in being exploited, both on mid- and high-rise civil structures equipped with either a monolithic or a multiblock MF, for the specific purpose of dynamic motion control. The dynamic potential of the MF was preserved throughout the parametric investigations carried out for increasing values of the friction threshold, the bumper stiffness and the initial gap, whose impact on the system's response proved to be consistent with the results already discussed. The analyses show that, after a proper calibration of the various design parameters, the MF could achieve the desired serviceability performance levels both in terms of accelerations and displacements, without impacting in a significant way the architecture of buildings. In conclusion, although real applications of MF are still to come, this thesis addressed some of the main conceptual issues to be solved. Of course, several other problems remain to be solved, especially at the technological level, but the preliminary results obtained here seem to confirm that the idea initially advanced by Moon could become applicable.

Research limitations and further developments

The results reached in this Thesis could provide the basis for future developments and insights on the issue of Movable Façades and their potential application for vibration reduction of wind-excited structures. Overall, the research has showed that the wind-induced response of mid- and high-rise buildings can be substantially reduced by the incorporation of Movable Façades connected to the structural floor slab by means of frictional sliders and a system of rubber bumpers. However, the dissertation is not without still open issues and questions which require further investigations and details in order to be dissolved. This section recognizes and identifies some limitations that the research has faced in a succinct and structured way, pointing to ways of combating them:

- first of all, it is worth noting that the study has been limited to the *along-wind* motion of buildings, since a reliable *cross-wind* spectrum to simulate equivalent *cross-wind* forces could only be achieved by wind tunnel tests which was beyond the scope of the present work in terms of time and costs required;
- at this first stage, the research dealt with unilateral MF systems applied on the building side exposed to longitudinal wind forces, whose horizontal motion perpendicular to the structure was analyzed in the two-dimensional plan, as a possible three-dimensional modeling and investigation of the façade system applied to the entire building surface would have been extremely time-consuming and high computing power would be needed for this purpose;
- as for the façade technological design, two main types of layouts were investigated, namely, the monolithic and the multiblock MF, being the most representative among the feasible construction methods of this engineering façade system, even though other

cladding configurations could also be investigated, which consider a different subdivision of the cladding geometry and different constraint conditions between the façade panels;

- the study on the influence of the design and mechanical properties of the connection system was conducted based on an exclusively qualitative investigation of the device's control parameters in line with reasonable values drawn from real-world applications.

Based on the assumptions made, in a future development it could be thought of extending the investigation to two-sided MF-equipped buildings also subject to *cross-wind* pressures and it could be interesting to investigate the influence of other feasible design layouts of the façade panels (in terms of both shape configuration and cladding surface subdivision) on the overall system's response, although already satisfactory in the design forms studied. Furthermore, from a technological point of view, a specific study should be done to better understand the connection mechanism that binds the different construction types of MF to the structure by means of the proposed sliding devices. As in this context a qualitative parametric study that explores the influence of the device design parameters on the dynamic performances of the system was carried out, an optimization process extending the range of investigation of the key variables characterizing the behavior of the connection devices could be useful to ensure an optimal design of the MF system in the vibration control field. Finally, further research could be required which allows to explore the benefits linked to the use of smart materials, such as SMA or *metal foams*, to be incorporated into the impact-absorbing bumper layers, taking advantage from the proposed connection design and providing for the possibility of its use under multi-hazard scenarios.

References

- [1] SCHULTZ, J., AND KATZ, N. Origami-inspired façade design: parametric studies for architectural and structural efficiency. *Façade Tectonics Institute. 2018 World Congress* (2018), 1-9.
- [2] ELNIMEIRI, M., AND GUPTA, P. Sustainable structure of tall buildings. *The Structural Design of Tall and Special Buildings* **17:5** (2008), 881-894. doi:<https://doi.org/10.1002/tal.471>.
- [3] AELENEI, L., BRZEZICKI, M., KNAACK, U., LUIBLE, A., PERINO, M., AND WELLERSHOFF, F. Adaptive façade network-europe. *TU Delft Open* (2015).
- [4] LOONEN, R., TRCKA, M., CÓSTOLA, D., AND HENSEN, J.M. Climate adaptive building shells: state-of-the-art and future challenges. *Renewable and Sustainable Energy Reviews* **25** (2013), 483-493. doi:<http://dx.doi.org/10.1016/j.rser.2013.04.016>.
- [5] YEOMANS, D. The origins of the modern curtain wall. *ATP Bulletin* **32:1** (2001), 13-18. doi:<https://doi.org/10.2307/1504688>.
- [6] SCHITTICH, C. Building skins: concepts, layers, materials. *Edition Detail* (2001).
- [7] BOEKE, J., KNAACK, U., AND HEMMERLING, M. Superposition matrix for the assessment of performance-relevant adaptive façade functions. *Journal of Façade Design and Engineering* **7:2** (2019), 1-114. doi:<https://doi.org/10.7480/jfde.2019.2.2463>.
- [8] AKSAMIJA, A. Thermal, energy and daylight analysis of different types of double skin façades in various climates. *Journal of Façade Design & Engineering* **6:1** (2018), 1-39. doi:[10.7480/jfde.2018.1.1527](https://doi.org/10.7480/jfde.2018.1.1527).
- [9] KNAACK, U., KLEIN, T., BILOW, M., AND AUER, T. Façades. Principles of Construction. *Ria Stein* (2014). doi:<https://doi.org/10.1515/9783038211457.36>.
- [10] LOPEZ, M., RUBIO, R., MARTÍN, S., CROXFORD, B., AND JACKSON, R. Active materials for adaptive architectural envelopes based on plant adaptation principles. *Journal of Façade Design and Engineering* **3:1** (2015), 27-38. doi:[10.3233/FDE-150026](https://doi.org/10.3233/FDE-150026).
- [11] ASHBY, M.F., EVANS, T., FLECK, N.A., GIBSON, L.J., HUTCHINSON, J.W., AND WADLEY, H.G. Metal foams: a design guide. *Elsevier* (2000).

- [12] BANHART, J. Manufacture, characterisation and application of cellular metals and metal foams. *Progress in Materials Science* **46:6** (2001), 559-632. doi:[https://doi.org/10.1016/S0079-6425\(00\)00002-5](https://doi.org/10.1016/S0079-6425(00)00002-5).
- [13] FANZAGA, M., LIAO, Z., AND ZOBEC, M. The emergence of advanced façades in China. *Council of Tall Buildings and Urban Habitat* **3** (2012), 20-25.
- [14] BOSWELL, C.K. Exterior building enclosures. *Design Process and Composition for Innovative Façades* (2013).
- [15] OGDEN, R.G. Curtain wall connections to steel frames. *The Steel Construction Institute* (1992). doi:<http://hdl.handle.net/10068/667720>.
- [16] FLANSBJER, M., HONFI, D., WILLIAMS PORTAL, N., MUELLER, U., LARRAZA, I., EDGAR, J.O., AND WLASAK, L. Structural behaviour of RPC sandwich façade elements with GFRP connectors. *VII International Congress on Architectural Envelopes* (2015).
- [17] HERZOG, T., KRIPPNER, R., AND LANG, W. Façade construction manual. *Walter de Gruyter* (2012).
- [18] FLANSBJER, M., WILLIAMS PORTAL, N., AND VENNETTI, D. Verification of the structural performance of textile reinforced reactive powder concrete sandwich façade elements. *Applied Science* **9:12** (2019), 1-26. doi:<https://doi.org/10.3390/app9122456>.
- [19] MURRAY, S., AND MURRAY, S.C. Contemporary curtain wall architecture. *Princeton Architectural Press* (2009).
- [20] PATTERSON, M. Structural glass façades and enclosures. *John Wiley & Sons* (2011).
- [21] BOS, F., AND LOUTER, C. Structural glass in architecture. *Encyclopedia of Glass Science, Technology, History, and Culture* **2** (2021), 1071-1090. doi:<https://doi.org/10.1002/9781118801017.ch9.1>.
- [22] HINMAN, E. Blast safety of the building envelope. *Whole Building Design Guide* (2011).
- [23] YEOMANS, D. The origins of the modern curtain wall. *APT Bulletin-Fredericksburg VA* **32:1** (2001), 13-18. doi:<https://doi.org/10.2307/1504688>.
- [24] SABER, H.H., AND LACASSE, M.A. High performance roofing and walls technologies: task 5, parametric study of curtain wall systems for selection of components and optimization of thermal performance. *National Research Council of Canada* (2016). doi:<https://doi.org/10.4224/23002872>.

- [25] CHENG, X., HUANG, G., YANG, Q., AND ZHOU, X. Influence of architectural façades on wind pressures and aerodynamic forces of tall buildings. *Journal of Structural Engineering* 147,1 (2021), 1-14. doi:[https://doi.org/10.1061/\(ASCE\)ST.1943-541X.0002867](https://doi.org/10.1061/(ASCE)ST.1943-541X.0002867).
- [26] BANIOPOULOS, C.C., NIKOLAIDIS, T.N., AND MOUTSANIDIS, G. Optimal structural design of glass curtain-wall systems. *Proceedings of the Institution of Civil Engineers-Structures and Buildings* 169:6 (2016), 450-457. doi:<https://doi.org/10.1680/jstbu.13.00088>.
- [27] KASSEM, M., AND MITCHELL, D. Bridging the gap between selection decisions of façade systems at the early design phase: issues, challenges and solutions. *Journal of Façade Design and Engineering* 3 (2015), 165-183. doi:10.3233/FDE-150037.
- [28] BANIOPOULOS, C., NIKOLAIDIS, T., AND MOUTSANIDIS, G. Optimal structural design of glass curtain-wall systems. *Institution of Civil Engineers. Proceedings. Structures and Buildings* 169:6 (2016), 450-457. doi:<https://doi.org/10.1680/jstbu.13.00088>.
- [29] CHEN, K., AND LU, W. Design for manufacture and assembly oriented design approach to a curtain wall system: a case study of a commercial building in Wuhan, China. *Sustainability* 10:7 (2018), 1-16. doi:<https://doi.org/10.3390/su10072211>.
- [30] KAN, K., CHEONG, A., AND SESHADRI, K. Building envelope & lighting systems (2016).
- [31] POIRAZIS, H. Double skin façades for office buildings. *Report EBD* (2004), 1-192.
- [32] BOAKE, T.M., HARRISON, K., COLLINS, D., CHATHAM, A., AND LEE, R. Understanding the general principles of the double skin façade system. *Associate Professor & School of Architecture, University of Waterloo* 2 (2003), 1-18.
- [33] DUBOIS, M.C., AND BLOMSTERBERG, A. Energy saving potential and strategies for electric lighting in future north european, low energy office buildings: a literature review. *Energy and Buildings* 43:10 (2011), 2572-2582. doi:<https://doi.org/10.1016/j.enbuild.2011.07.001>.
- [34] SAROGLU, T., THEODOSIOU, T., GIVONI, B., AND MEIR, I.A. Studies on the optimum double-skin curtain wall design for high-rise buildings in the mediterranean climate. *Energy and Buildings* 208 (2020), 1-18. doi:<https://doi.org/10.1016/j.enbuild.2019.109641>.
- [35] PAPPAS, A., AND ZHAI, Z. Numerical investigation on thermal performance and correlations of double skin façade with buoyancy-driven airflow. *Energy and Buildings* 40:4 (2008), 466-475. doi:<https://doi.org/10.1016/j.enbuild.2007.04.002>.

- [36] HAMZA, N. Double versus single skin façades in hot arid areas. *Energy and Buildings* **40**:3 (2008), 240-248. doi:<https://doi.org/10.1016/j.enbuild.2007.02.025>.
- [37] DI GIOVANNI G. Double skin façades integrate con smart dampers per lo smorzamento delle vibrazioni indotte dal vento in edifici alti. *Master's thesis. Università degli Studi di Roma La Sapienza* (2018).
- [38] GHAFFARIANHOSEINI, A., GHAFFARIANHOSEINI, A., BERARDI, U., TOOKEY, J., LI, D.H.W., KARIMINIA, S. Exploring the advantages and challenges of double-skin façades (DSFs). *Renewable and Sustainable Energy Reviews* **60** (2016), 1052-1065. doi:<https://doi.org/10.1016/j.rser.2016.01.130>.
- [39] GUBINA, E. A technical review of double skin façades. *PhD thesis. Wien* (2021). doi:[10.34726/hss.2021.23576](https://doi.org/10.34726/hss.2021.23576).
- [40] OESTERLE, E. Double-skin façades: integrated planning (2001).
- [41] SHAMERI, M.A., ALGHOUL, M.A., SOPIAN, K., ZAIN, M.M., AND ELAYEB, O. Perspectives of double skin façade systems in buildings and energy saving. *Renewable and Sustainable Energy Reviews* **15**:3 (2011), 1468-1475. doi:<https://doi.org/10.1016/j.rser.2010.10.016>.
- [42] URBÁN, D., ROOZEN, N.B., ZAKO, P., RYCHTARIKOVA, M., TOMAOVI, P., AND GLORIEUX, C. Assessment of sound insulation of naturally ventilated double skin façades. *Building and Environment* **110** (2016), 148-160. doi:<https://doi.org/10.1016/j.buildenv.2016.10.004>.
- [43] PATRÍCIO, J., SANTOS, A., AND MATIAS, L. Double-skin façades: acoustic, visual and thermal comfort indoors. *Proceedings of Healthy Buildings* **2** (2006), 37-42.
- [44] CHAN, A.S., CHOW, T.T., FONG, K.F., AND LIN, Z. Investigation on energy performance of double skin façade in Hong Kong. *Energy and Buildings* **41** (2009), 1135-1142. doi:<https://doi.org/10.1016/j.enbuild.2009.05.012>.
- [45] ALIBABA, H.Z., AND OZDENIZ, M.B. Energy performance and thermal comfort of double-skin and single-skin façades in warm-climate offices. *Journal of Asian Architecture and Building Engineering* **15**:3 (2016), 635-642. doi:<https://doi.org/10.3130/jaabe.15.635>.
- [46] XU, C., XI, Q., AND MA, Q. Technical characteristics and energy performance of double skin façades: a review. *E3S Web of Conferences* **248** (2021), 1-4. doi:<https://doi.org/10.1051/e3sconf/202124801029>.
- [47] STREICHER, W., HEIMRATH, R., HENGESBERGER, H., MACH, T., AND WALDNER, R. State of the art of double skin façades in Europe: the results of WP1 of the BESTFAÇADE Project. *Proceedings of the AIVC 27th Conference* (2006), 20-22.

- [48] HØSEGGEN, R., WACHENFELDT, B.J., AND HANSEN, S.O. Building simulation as an assisting tool in decision making. Case study: with or without a double-skin façade? *Energy and Buildings* **40** (2008), 821827. doi:10.1016/j.enbuild.2007.05.015.
- [49] SAMIR, H., AND SHAHIN, M. Adaptive building envelopes of multistory buildings as an example of high performance building skins. *Alexandria Engineering Journal* **58** (2019), 345-352. doi:https://doi.org/10.1016/j.aej.2018.11.013.
- [50] ATTIA, S., FAVOINO, F., LOONEN, R., PETROVSKI, A., AND MONGE-BARRIO, A. Adaptive façades system assessment: an initial review. *Advanced Building Skins* (2015), 1265-1273. http://hdl.handle.net/2268/187576.
- [51] MA, Y., ZHANG, Q., ZHANG, D., SCARPA, F., LIU, B., HONG, J. The mechanics of shape memory alloy metal rubber. *Acta Materialia* **96** (2015), 89-100. doi:https://doi.org/10.1016/j.actamat.2015.05.031.
- [52] GARCÍA-MORENO, F. Commercial applications of metal foams: their properties and production. *Materials* **85:9,2** (2015). doi:https://doi.org/10.3390/ma9020085.
- [53] AMARANTE DOS SANTOS, F., BEDON, C., MICHELETTI, A. Explorative study on adaptive facades with superelastic antagonistic actuation. *Structural Control and Health Monitoring* **27:4** (2020), 1-24. doi:https://doi.org/10.1002/stc.2463.
- [54] AELENEI, L., AELENEI, D., ROMANO, R., MAZZUCHELLI, E.S., BRZEZICKI, M., AND RICO-MARTINEZ, J.M. Case studies - adaptive façade network. *TU Delft Open* (2018). doi:http://hdl.handle.net/10400.9/3130.
- [55] ROMANO, R. Smart skin envelope. integrazione architettonica di tecnologie dinamiche e innovative per il risparmio energetico. *PhD thesis. Università degli Studi di Firenze* (2011).
- [56] ALTOMONTE, S. Involucro architettonico come interfaccia dinamica. *Alinea Editrice* (2005).
- [57] LOUTER, C., AKILO, M., MIRI, B., NEESKENS, T., RIBEIRO SILVEIRA, R., TOPCU, O., VAN DER WEIJDE, I., ZHA, C., BILOW, M., TURRIN, M., KLEIN, T., AND O'CALLAGHAN, J. Adaptive and composite thin glass concepts for architectural applications. *Heron* **63(1/2)** (2018), 199-200. doi:http://heronjournal.nl/63-12/9.html.
- [58] RIBEIRO SILVEIRA, R. Flexible transparency: a study on thin glass adaptive façade panels. *Master's thesis. TU Delft Faculty of Architecture and the Built Environment* (2016). http://resolver.tudelft.nl/uuid:fd32f4fc-6dab-4468-83f2-53abcc12e715.
- [59] TOPCU, O. Kinetic thin glass façade: a study on the feasibility of a water-and airtight kinetic façade with a bending-active thin glass element. *Master's thesis. TU Delft*

- Faculty of Architecture and the Built Environment* (2017). <http://resolver.tudelft.nl/uuid:77099af6-9d82-4d24-95e9-919fac11d0e8>.
- [60] MIRI, B. Flexible transparency with smart materials: a study on adaptive thin glass façade developed with shape memory alloy. *Master's thesis. TU Delft Faculty of Architecture and the Built Environment* (2018).
- [61] CARASSALE, L., AND SOLARI, G. Monte Carlo simulation of wind velocity fields on complex structures. *Journal of Wind Engineering and Industrial Aerodynamics* **94** (2006), 323-339. doi:<https://doi.org/10.1016/j.jweia.2006.01.004>.
- [62] HUI, Y., LI, B., KAWAI, H., AND YANG, Q. Non-stationary and non-Gaussian characteristics of wind speeds. *Wind & Structures* **24**:1 (2017), 59-78. doi:[10.12989/was.2017.24.1.059](https://doi.org/10.12989/was.2017.24.1.059).
- [63] MOHAMMADI, A. Wind performance-based design for high-rise buildings. *PhD thesis. Florida International University* (2016). doi:[10.25148/etd.FIDC001201](https://doi.org/10.25148/etd.FIDC001201).
- [64] AZAD, A.K., AND ALAM, M.M. Determination of wind gust factor at windy areas of Bangladesh. *Proceedings of the 13th Asian Congress of Fluid Mechanics* (2010), 521-524.
- [65] SWAMI, B.P. Study of wind speeds in India and their effects on typical structures. PhD thesis. IIT Delhi (1987).
- [66] ALINEJAD, H., KANG, T.H., AND JEONG, S.Y. Performance-based wind design framework proposal for tall buildings. *Wind and Structures* **32**:4 (2021), 283-292. doi:<https://doi.org/10.12989/was.2021.32.4.283>.
- [67] RAJMANI, A., AND GUHA, P. Analysis of wind & earthquake load for different shapes of high-rise building. *International Journal of Civil Engineering & Technology* **6**:2 (2015), 38-45.
- [68] LAMB, S., KWOK, K.C., AND WALTON, D. Occupant comfort in wind-excited tall buildings: motion sickness, compensatory behaviours and complaint. *International Journal of Wind Engineering and Industrial Aerodynamics* **119** (2013), 1-12. doi:<https://doi.org/10.1016/j.jweia.2013.05.004>.
- [69] RAYCHAUDHURI, S. Introduction to Monte Carlo simulation. *2008 Winter Simulation Conference. IEEE* (2008), 91-100. doi:[10.1109/WSC.2008.4736059](https://doi.org/10.1109/WSC.2008.4736059).
- [70] KUMAR, B.D., AND SWAMI, B.L.P. Wind effects on tall building frames-influence of dynamic parameters. *Indian Journal of Science and Technology* **3**:5 (2010), 583-587.
- [71] EKMAN, V.W. On the influence of the earth's rotation on ocean-currents (1905).

- [72] VAN DER HOVEN, I. Power spectrum of horizontal wind speed in the frequency range from 0.0007 to 900 cycles per hour. *Journal of Atmospheric Sciences* **14**:2 (1957), 160-164. doi:[https://doi.org/10.1175/1520-0469\(1957\)014<0160:PSOHWS>2.0.CO;2](https://doi.org/10.1175/1520-0469(1957)014<0160:PSOHWS>2.0.CO;2).
- [73] SINHAMAHAPATRA, S., DUTTA, R., AND MANDAL, S. Along and across wind parameters acting on tall structures. *International Journal of Research in Engineering, Science and Management* **2**:7 (2019), 557-561.
- [74] SHINOZUKA, M., YUN, C.B., AND SEYA, H. Stochastic methods in wind engineering. *Journal of Wind Engineering and Industrial Aerodynamics* **36**:2 (1990), 829-843. doi:[https://doi.org/10.1016/0167-6105\(90\)90080-V](https://doi.org/10.1016/0167-6105(90)90080-V).
- [75] SHINOZUKA, M. Simulation of multivariate and multidimensional random processes. *The Journal of the Acoustical Society of America* **49**:1b (1971), 357-368. doi:<https://doi.org/10.1121/1.1912338>.
- [76] WITTIG, L.E., AND SINHA, A.K. Simulation of multicorrelated random processes using the FFT algorithm. *The Journal of the Acoustical Society of America* **58**:3 (1975), 630-634. doi:<https://doi.org/10.1121/1.380702>.
- [77] LI, Y., AND KAREEM, A. Simulation of multivariate random processes: hybrid DFT and digital filtering approach. *Journal of Engineering Mechanics* **119**:5 (1993), 1078-1098. doi:[https://doi.org/10.1061/\(ASCE\)0733-9399\(1993\)119:5\(1078\)](https://doi.org/10.1061/(ASCE)0733-9399(1993)119:5(1078)).
- [78] SHINOZUKA, M., AND DEODATIS, G. Simulation of stochastic processes by spectral representation. *Applied Mechanics Reviews* **44**:4 (1991), 191-204. doi:<https://doi.org/10.1115/1.3119501>.
- [79] CHAJES, M.J., ZHANG, L., AND KIRBY, J.T. Dynamic analysis of tall building using reduced-order continuum model. *Journal of Structural Engineering* **122**:11 (1996), 1284-1291. doi:[https://doi.org/10.1061/\(ASCE\)0733-9445\(1996\)122:11\(1284\)](https://doi.org/10.1061/(ASCE)0733-9445(1996)122:11(1284)).
- [80] MALEKINEJAD, M., AND RAHGOZAR, R. A simple analytic method for computing the natural frequencies and mode shapes of tall buildings. *Applied Mathematical Modelling* **36** (2012), 3419-3432. doi:<https://doi.org/10.1016/j.apm.2011.10.018>.
- [81] CHAJES, M.J., ROMSTAD, K.M., AND MCCALLEN, D.B. Analysis of multiple-bay frames using continuum model. *Journal of Structural Engineering* **119**:2 (1993), 522-546. doi:[https://doi.org/10.1061/\(ASCE\)0733-9445\(1993\)119:2\(522\)](https://doi.org/10.1061/(ASCE)0733-9445(1993)119:2(522)).
- [82] HUTCHINSON, J.R. Shear coefficients for Timoshenko beam theory. *Journal of Applied Mechanics* **68**:1 (2001), 87-92. doi:<https://doi.org/10.1115/1.1349417>.
- [83] PICCARDO, G., TUBINO, F., AND LUONGO, A. Equivalent Timoshenko linear beam model for the static and dynamic analysis of tower buildings. *Applied Mathematical Modelling* **71** (2019), 77-95. doi:<https://doi.org/10.1016/j.apm.2019.02.005>.

- [84] DYM, C.L., AND WILLIAMS, H.E. Estimating fundamental frequencies of tall buildings. *Journal of Structural Engineering* (2007), 1-15. doi:[https://doi.org/10.1061/\(ASCE\)0733-9445\(2007\)133:10\(1479\)](https://doi.org/10.1061/(ASCE)0733-9445(2007)133:10(1479)).
- [85] PICCARDO, G., TUBINO, F., AND LUONGO, A. Equivalent non linear beam model for the 3-D analysis of shear-type buildings: application to aeroelastic instability. *International Journal of Non-Linear Mechanics* **80** (2016), 52-65. doi:<https://doi.org/10.1016/j.ijnonlinmec.2015.07.013>.
- [86] CLUNI, F., GIOFFRÈ, M., AND GUSELLA, V. Dynamic response of tall buildings to wind loads by reduced order equivalent shear-beam models. *Journal of Wind Engineering and Industrial Aerodynamics*, **123** (2013), 339-348. doi:<https://doi.org/10.1016/j.jweia.2013.09.012>.
- [87] RAINIERI, C., FABBROCINO, G., COSENZA, E. Smorzamento strutturale: modelli teorici e valutazioni sperimentali. In: *XIII Convegno ANIDIS "L'ingegneria sismica in Italia"*. IMREADY (2009).
- [88] LAGOMARSINO, S. Forecast models for damping and vibration periods of buildings. *Journal of Wind Engineering and Industrial Aerodynamics* **48:2,3** (1993), 221-239. doi:[https://doi.org/10.1016/0167-6105\(93\)90138-E](https://doi.org/10.1016/0167-6105(93)90138-E).
- [89] HEITZ, T., GIRY, C., RICHARD, B., AND RAGUENEAU, F. How are the equivalent damping ratios modified by nonlinear engineering demand parameters? *6th ECCOMAS Thematic Conference on Computational Methods in Structural Dynamics and Earthquake Engineering COMPDYN* (2017), 15-17. doi:<https://hal.archives-ouvertes.fr/hal-01634677>.
- [90] DWAIRI, H., AND KOWALSKY, M. Investigation of Jacobsen's equivalent viscous damping approach as applied to displacement-based seismic design. *13th World Conference on Earthquake Engineering* **228** (2004), 1-15.
- [91] RODRIGUES, H., AND VARUM, H. A comparative analysis of energy dissipation and equivalent viscous damping of rc columns subjected to uniaxial and biaxial loading. *Engineering Structures* **35** (2012), 149-164. doi:<https://doi.org/10.1016/j.engstruct.2011.11.014>.
- [92] GRIFFIS, L.G. Serviceability limit states under wind load. *Engineering Journal* **30:1** (1993), 1-16.
- [93] KWOK, K.C., HITCHCOCK, P.A., AND BURTON, M.D. Perception of vibration and occupant comfort in wind-excited tall buildings. *Journal of Wind Engineering and Industrial Aerodynamics* **97:7,8** (2009), 368-380. doi:<https://doi.org/10.1016/j.jweia.2009.05.006>.
- [94] TAMURA, Y. Wind and tall buildings. *Wind and Tall Buildings* (2009), 1000-1025. doi:[10.1400/116467](https://doi.org/10.1400/116467).

- [95] LI, Q.S., WU, J.R., LIANG, S.G., XIAO, Y.Q., AND WONG, C.K. Full-scale measurements and numerical evaluation of wind-induced vibration of a 63-story reinforced concrete tall building. *Engineering Structures* **26** (2004), 1779-1794. doi:<https://doi.org/10.1016/j.engstruct.2004.06.014>.
- [96] MELBOURNE, W.H., AND PALMER, T.R. Accelerations and comfort criteria for buildings undergoing complex motions. *Journal of Wind Engineering and Industrial Aerodynamics* **41**:1,3 (1992), 105-116. doi:[https://doi.org/10.1016/0167-6105\(92\)90398-T](https://doi.org/10.1016/0167-6105(92)90398-T).
- [97] XU, Y.L., AND CHEN, J. Characterizing nonstationary wind speed using empirical mode decomposition. *Journal of Structural Engineering* **130**:6 (2004), 912-920. doi:[https://doi.org/10.1061/\(ASCE\)0733-9445\(2004\)130:6\(912\)](https://doi.org/10.1061/(ASCE)0733-9445(2004)130:6(912)).
- [98] CNR-DT 207/2008. Istruzioni per la valutazione delle azioni e degli effetti del vento sulle costruzioni (2008).
- [99] PETRINI, F., AND CIAMPOLI, M. Performance-based wind design of tall buildings. *Structure and Infrastructure Engineering* **8**:10 (2012), 954-966. doi:<https://doi.org/10.1016/j.cnsns.2011.105818>.
- [100] GRIFFIS, L., PATEL, V., MUTHUKUMAR, S., AND BALDAVA, S. A framework for performance-based wind engineering. *Advances in Hurricane Engineering: Learning from our past* (2013), 1205-1216. doi:<https://doi.org/10.1061/9780784412626.105>.
- [101] GHOBARAH, A. On drift limits associated with different damage levels. *International Workshop on Performance-Based Seismic Design* **28** (2004), 1-12.
- [102] GHOBARAH, A. Performance-based design in earthquake engineering: state of development. *Engineering Structures* **23**:8 (2001), 878-884. doi:[https://doi.org/10.1016/S0141-0296\(01\)00036-0](https://doi.org/10.1016/S0141-0296(01)00036-0).
- [103] CHAN, C.M., AND WONG, K.M. Structural topology and element sizing design optimisation of tall steel frameworks using a hybrid OCGA method. *Structural and Multidisciplinary Optimization* **35**:5 (2008), 473-488. doi:<https://doi.org/10.1007/s00158-007-0151-1>.
- [104] ANAJAFI, H., AND MEDINA, R.A. Comparison of the seismic performance of a partial mass isolation technique with conventional TMD and base-isolation systems under broad-band and narrow-band excitations. *Engineering Structures* **158** (2018), 110-123. doi:<https://doi.org/10.1016/j.engstruct.2017.12.018>.
- [105] TRIBUTSCH, A., AND ADAM, C. Evaluation and analytical approximation of tuned mass damper performance in an earthquake environment. *Smart Structures and Systems* **10**:2 (2012), 155-179.

- [106] HALIS GUNEL, M., AND EMRE ILGIN, H. A proposal for the classification of structural systems of tall buildings. *Building and Environment* **42** (2007), 2667-2675. doi:<https://doi.org/10.1016/j.buildenv.2006.07.007>.
- [107] BASKARAN, A. Wind engineering studies on tall building transitions in research. *Building and Environment* **28** (1993), 1-19. doi:[https://doi.org/10.1016/0360-1323\(93\)90002-K](https://doi.org/10.1016/0360-1323(93)90002-K).
- [108] KAYVANI, K. Design of high-rise buildings: past, present and future. *23rd Australasian Conference on the Mechanics of Structures and Materials (ACMSM 23)* (2014), 15-20.
- [109] SAAED, T.E., NIKOLAKOPOULOS, G., AND JONASSON, J.E. A state-of-the-art review of structural control strategies (2014).
- [110] MOON, K.S. Dynamic interrelationship between the evolution of structural systems and façade design in tall buildings: from the home insurance building in Chicago to the present. *International Journal of High-Rise Buildings* **7:1** (2018), 1-16. doi:<https://doi.org/10.21022/IJHRB.2018.7.1.1>.
- [111] MOON, K.S. Integrated damping systems for tall buildings. *AEI* (2015), 134-140. doi:<https://doi.org/10.1061/9780784479070.012>.
- [112] DING, F., AND KAREEM, A. Tall buildings with dynamic façade under winds. *Engineering* (2020). doi:<https://doi.org/10.1016/j.eng.2020.07.020>.
- [113] ABDELRAZAQ, A., BURTON, M.B., AND KWOK, K.C.S. Wind-induced motion of tall buildings: designing for occupant comfort. *International Journal of High-Rise Buildings* **4:1** (2015), 1-8. doi:<https://doi.org/10.21022/IJHRB.2015.4.1.001>.
- [114] FARGHALY, A.A., AND SALEM AHMED, M. Optimum design of TMD system for tall buildings. *International Scholarly Research Notices* (2012). doi:[10.5402/2012/716469](https://doi.org/10.5402/2012/716469).
- [115] AIMAR, F. Edifici alti e grattacieli. Aspetti strutturali (2016).
- [116] JAFARI, M., AND ALIPOUR, A. Methodologies to mitigate wind-induced vibration of tall buildings: a state-of-the-art review. *Journal of Building Engineering, Elsevier* (2020), 1-60. doi:<https://doi.org/10.1016/j.jobbe.2020.101582>.
- [117] IRWIN, P.A. Wind engineering challenges of the new generation of super-tall buildings. *Journal of Wind Engineering and Industrial Aerodynamics* **97:7,8** (2009), 328-334. doi:<https://doi.org/10.1016/j.jweia.2009.05.001>.
- [118] ALI, M.M., AND MOON, K.S. Structural developments in tall buildings: current trends and future prospects. *Architectural Science Review* **50:3** (2007), 205-223. doi:<https://doi.org/10.3763/asre.2007.5027>.

- [119] IRWIN, P.A. Bluff body aerodynamics in wind engineering. *Journal of Wind Engineering and Industrial Aerodynamics* **96**:6,7 (2008), 701-712. doi:<https://doi.org/10.1016/j.jweia.2007.06.008>.
- [120] MOON, K.S. Sustainable structural engineering strategies for tall buildings. *The Structural Design of Tall and Special Buildings* **17**:5 (2008), 895-914. doi:<https://doi.org/10.1002/tal.475>.
- [121] ALI, M.M., AND MOON, K.S. Advances in structural systems for tall buildings: emerging developments for contemporary urban giants. *Buildings* **8**:104 (2018), 1-34. doi:<https://doi.org/10.3390/buildings8080104>.
- [122] TAMURA, Y., AND KAREEM, A. Advanced structural wind engineering. *Springer* (2014). doi:<https://doi.org/10.1007/978-4-431-54337-4>.
- [123] FANG, J.Q., LI, Q.S., JEARY, A.P., AND LIU, D.K. Damping of tall buildings: its evaluation and probabilistic characteristics. *The Structural Design of Tall Buildings* **8**:2 (1999), 145-153. doi:[https://doi.org/10.1002/\(SICI\)1099-1794\(199906\)8:2<145::AID-TAL127>3.0.CO;2-1](https://doi.org/10.1002/(SICI)1099-1794(199906)8:2<145::AID-TAL127>3.0.CO;2-1).
- [124] MAURER. Tuned mass and viscous dampers. Technical information and products. *Structural Protection Systems* (2011), 1-32.
- [125] ELIAS, S., AND MATSAGAR, V. Wind response control of tall buildings with a tuned mass damper. *Journal of Building Engineering* **15** (2018), 51-60. doi:<https://doi.org/10.1016/j.jobe.2017.11.005>.
- [126] MONDAL, J., NIMMALA, H., ABDULLA, S., AND TAFRESHI, R. Tuned liquid damper. technical information and products. *Proceedings of the 3rd International Conference on Mechanical Engineering and Mechatronics* **68** (2014), 1-7.
- [127] BIGDELI, Y., AND KIM, D. Damping effects of the passive control devices on structural vibration control: TMD, TLC and TLCD for varying total masses. *KSCE Journal of Civil Engineering* **20**:1 (2016), 301-308. doi:<https://doi.org/10.1007/s12205-015-0365-5>.
- [128] CAO, L., LAFLAMME, S., TAYLOR, D., AND RICLES, J. Simulations of a variable friction device for multihazard mitigation. *Journal of Structural Engineering* **142**:12 (2016), 1-35. doi:[https://doi.org/10.1061/\(ASCE\)ST.1943-541X.0001580](https://doi.org/10.1061/(ASCE)ST.1943-541X.0001580).
- [129] AMADIO, C., AND BEDON, C. Passive control systems for the blast enhancement of glazing curtain walls under explosive loads. *The Open Civil Engineering Journal* **11**:1 (2017), 396-419. doi:[10.2174/1874149501711010396](https://doi.org/10.2174/1874149501711010396).
- [130] AMADIO, C., AND BEDON, C. Glass façades under seismic events and explosions: a novel distributed-TMD design concept for building protection. *Glass*

- Structures & Engineering* **3:2** (2018), 257-274. doi:<https://doi.org/10.1007/s40940-018-0058-9>.
- [131] MA, G.W., AND YE, Z.Q. Energy absorption of double-layer foam cladding for blast alleviation. *International Journal of Impact Engineering* **34** (2007), 329-347. doi:<https://doi.org/10.1016/j.ijimpeng.2005.07.012>.
- [132] WU, C., AND SHEIKH, H. A finite element modelling to investigate the mitigation of blast effects on reinforced concrete panel using foam cladding. *International Journal of Impact Engineering* **55** (2013), 24-33. doi:<https://doi.org/10.1016/j.ijimpeng.2012.11.006>.
- [133] YANG, Y., FALLAH, A.S., SAUNDERS, M., AND LOUCA, L.A. On the dynamic response of sandwich panels with different core set-ups subject to global and local blast loads. *Engineering Structures* **33** (2011), 2781-2793. doi:<https://doi.org/10.1016/j.engstruct.2011.06.003>.
- [134] ALBERDI, R., PRZYWARA, J., AND KHANDELWAL, K. Performance evaluation of sandwich panel systems for blast mitigation. *Engineering Structures* **56** (2013), 2119-2130. doi:<https://doi.org/10.1016/j.engstruct.2013.08.021>.
- [135] THEOBALD, N.B., AND NURICK, G.N. Experimental and numerical analysis of tube-core claddings under blast loads. *International Journal of Impact Engineering* **37** (2010), 333-348. doi:<https://doi.org/10.1016/j.ijimpeng.2009.10.003>.
- [136] VAN PAEPEGEM, W., PALANIVELU, S., DEGRIECK, J., VANTOMME, J., REYEMEN, B., KAKOGIANNIS, D., VAN HEMELRIJCK, D., AND WASTIELS, J. Blast performance of a sacrificial cladding with composite tubes for protection of civil engineering structures. *Composites: Part B* **65** (2014), 131-146. doi:<https://doi.org/10.1016/j.compositesb.2014.02.004>.
- [137] WELLERSHOFF, F., FÖRCH, M., LORI, G., ZOBEC, M., CASUCCI, D., AND GROSSER, P. Façade brackets for blast enhancement. *Engineered Transparency 2018. Glass in Architecture and Structural Engineering* **2:5,6** (2018), 351-367. doi:<https://doi.org/10.1002/cepa.936>.
- [138] PINELLI, J.P., CRAIG, J.I., GOODNO, B.J., AND HSU, C.C. Passive control of building response using energy dissipating cladding connections. *Earthquake Spectra* **9:3** (1993), 529-546. doi:<https://doi.org/10.1193/1.1585728>.
- [139] LU, S. Performance-based design procedure for a novel semi-active cladding connection applied to blast mitigation. *PhD thesis. Iowa State University* (2017). <https://lib.dr.iastate.edu/etd/16171>.
- [140] GOODNO, B.J., PINELLI, J.P., AND CRAIG, J.I. An optimal design approach for passive damping of building structures using architectural cladding. *Eleventh World Conference on Earthquake Engineering* **1453** (1996).

- [141] AMADIO, C., AND BEDON, C. Viscoelastic spider connectors for the mitigation of cable-supported façades subjected to air blast loading. *Engineering Structures* **42** (2012), 190-200. doi:<https://doi.org/10.1016/j.engstruct.2012.04.023>.
- [142] AMADIO, C., AND BEDON, C. Numerical assessment of vibration control systems for multi-hazard design and mitigation of glass curtain walls. *Journal of Building Engineering* **15** (2018), 1-13. doi:<https://doi.org/10.1016/j.jobbe.2017.11.004>.
- [143] AMADIO, C., AND BEDON, C. ADAS dampers for the hazard protection of multi-storey buildings with glazing envelopes: a feasibility study. *Bollettino di Geofisica Teorica ed Applicata* **60:2** (2019), 197-220. doi:10.4430/bgta0253.
- [144] CHEN, W., AND HAO, H. Numerical study of blast-resistant sandwich panels with rotational friction dampers. *International Journal of Structural Stability and Dynamics* **13:5** (2013), 1-32. doi:<https://doi.org/10.1142/S0219455413500144>.
- [145] WANG, Y., LIEW, J.R., LEE, S.C., ZHAI, X., AND WANG, W. Crushing of a novel energy absorption connector with curved plate and aluminum foam as energy absorber. *Thin-Walled Structures* **111** (2017), 145-154. doi:<https://doi.org/10.1016/j.tws.2016.11.019>.
- [146] PINELLI, J.P., CRAIG, J.I., GOODNO, B.J., AND HSU, C.C. Passive control of building response using energy dissipating cladding connections. *Earthquake Spectra* **9:3** (1993), 529-546. doi:<https://doi.org/10.1193/1.1585728>.
- [147] BAIRD, A., PALERMO, A., AND PAMPANIN, S. Controlling seismic response using passive energy dissipating cladding connections. *New Zealand Society for Earthquake Engineering Conference* (2013).
- [148] DAL LAGO, B., BIONDINI, F., AND TONIOLO, G. Experimental investigation on steel W-shaped folded plate dissipative connectors for horizontal precast concrete cladding panels. *Journal of Earthquake Engineering* **22:5** (2018), 778-800. doi:10.1080/13632469.2016.1264333.
- [149] MOON, K.S. Dynamic interrelationship between technology and architecture in tall buildings. *PhD thesis. Massachusetts Institute of Technology* (2005).
- [150] AZAD, A. Application of smart façade system in reduction of structural response during wind loads. *PhD thesis. School of Civil and Environmental Engineering. University of Technology, Sydney* (2016).
- [151] ABTAHI, P. Energy dissipating façade systems designed to reduce structural response during earthquakes. *PhD thesis. Centre for Infrastructure Engineering. Western Sydney University* (2017).
- [152] MOON, K.S. Tall building motion control using double skin façades. *Journal of Architectural Engineering* **15:3** (2009), 84-90. doi:[https://doi.org/10.1061/\(ASCE\)1076-0431\(2009\)15:3\(84\)](https://doi.org/10.1061/(ASCE)1076-0431(2009)15:3(84)).

- [153] FU, T.S., AND ZHANG, R. Integrating double-skin façades and mass dampers for structural safety and energy efficiency. *Journal of Architectural Engineering* (2016), 1-12. doi:[https://doi.org/10.1061/\(ASCE\)AE.1943-5568.0000218](https://doi.org/10.1061/(ASCE)AE.1943-5568.0000218).
- [154] PIPITONE, G., BARONE, B., AND PALMERI, A. Optimal design of double-skin façades as vibration absorbers. *Structural Control and Health Monitoring* **25** (2018), 1-16. doi:<https://doi.org/10.1002/stc.2086>.
- [155] NGO, T., DING, C., LUMANTARNA, R., GHAZLAN, A., AND ZOBEC, M. Structural performance of double-skin façade systems subjected to blast pressures. *Journal of Structural Engineering* **141**:12 (2015), 1-9. doi:[https://doi.org/10.1061/\(ASCE\)ST.1943-541X.0001317](https://doi.org/10.1061/(ASCE)ST.1943-541X.0001317).
- [156] ZHANG, Y., SCHAUER, T., WERNICKE, L., VRONTOS, A., ENGELMANN, M., WULFF, W., AND BLEICHER, A. Design of moveable facade elements for energy harvesting and vibration control of super slender tall buildings under wind excitation. *Proceedings of the PowerSkin Conference* (2021), 327-338.
- [157] MICHELI, L., ALIPOUR, A., LAFLAMME, S., AND SARKAR, P. Performance-based design with life-cycle cost assessment for damping systems integrated in wind excited tall buildings. *Engineering Structures* **195** (2019), 438-451. doi:<https://doi.org/10.1016/j.engstruct.2019.04.009>.
- [158] GONG, Y., CAO, L., LAFLAMME, S., QUIEL, S., RICLES, J., AND TAYLOR, D. Characterization of a novel variable friction connection for semiactive cladding system. *Structural Control and Health Monitoring* (2018), 25-6. doi:<https://doi.org/10.1002/stc.2157>.
- [159] CAO, L., LU, S., LAFLAMME, S., QUIEL, S., RICLES, J., AND TAYLOR, D. Performance-based design procedure of a novel friction-based cladding connection for blast mitigation. *International Journal of Impact Engineering* **117** (2018), 48-62. doi:<https://doi.org/10.1016/j.ijimpeng.2018.03.003>.
- [160] CAO, L., LU, S., LAFLAMME, S., QUIEL, S., RICLES, J., AND TAYLOR, D. Motion-based design approach for a novel variable friction cladding connection used in wind hazard mitigation. *Engineering Structures* **181** (2019), 397-412. doi:<https://doi.org/10.1016/j.engstruct.2018.12.033>.
- [161] CAO, L., LU, S., LAFLAMME, S., QUIEL, S., RICLES, J., AND TAYLOR, D. Variable friction cladding connection for seismic mitigation. *Engineering Structures* **189** (2019), 243-259. doi:<https://doi.org/10.1016/j.engstruct.2019.03.066>.
- [162] XIANG, P., AND NISHITANI, A. Seismic vibration control of building structures with multiple tuned mass damper floors integrated. *Earthquake Engineering & Structural Dynamic* **43** (2014), 909-925. doi:<https://doi.org/10.1002/eqe.2379>.

- [163] ANAJAFI, H., AND MEDINA, R.A. Partial mass isolation system for seismic vibration control of buildings. *Structural Control and Health Monitoring* **25** (2018), 1-16. doi:<https://doi.org/10.1002/stc.2088>.
- [164] CONNOR, J.J. Introduction to structural motion control. *Prentice-Hall* (2003).
- [165] CHOPRA, A.K. Dynamics of structures. Theory and applications to earthquake engineering. *Prentice-Hall* (2017).
- [166] DI GIOVANNI, G., AND BERNARDINI, D. Vibration damping performances of buildings with moving façades under harmonic excitation. *Journal of Vibration Engineering & Technologies* (2020), 1-10. doi:<https://doi.org/10.1007/s42417-020-00247-w>.
- [167] DEN HARTOG, J.P. Mechanical vibrations. *Courier Corporation* (1985).
- [168] BERNARDINI, D., AND REGA, G. Evaluation of different SMA models performances in the nonlinear dynamics of pseudoelastic oscillators via a comprehensive modeling framework. *International Journal of Mechanical Sciences* **130** (2017), 458-475. doi:<https://doi.org/10.1016/j.ijmecsci.2017.06.023>.
- [169] HU, G., HASSANLI, S., KWOK, K.C., AND TSE, K.T. Wind-induced responses of a tall building with a double-skin façade system. *Journal of Wind Engineering and Industrial Aerodynamics* **168** (2017), 91-100. doi:<https://doi.org/10.1016/j.jweia.2017.05.008>.
- [170] BHASKARARAO, A.V., AND JANGID, R.S. Seismic analysis of structures connected with friction dampers. *Engineering Structure* **28** (2008), 690-703. doi:<https://doi.org/10.1016/j.engstruct.2005.09.020>.
- [171] AMADIO, C., AND BEDON, C. Multiple dissipative devices for blast-resisting cable-supported glazing façades. *Modeling and Simulation in Engineering* (2013), 1-13. doi:<http://dx.doi.org/10.1155/2013/964910>.
- [172] MOON, K.S. Integrated damping systems for tall buildings: tuned mass damper/double skin façade damping interaction system. *The Structural Design of Tall and Special Buildings* **25:5** (2016), 232-244. doi:<https://doi.org/10.1002/tal.1237>.
- [173] GONG, Y., CAO, L., AND LAFLAMME, S. Numerical verification of variable friction cladding connection for multihazard mitigation. *Journal of Vibration and Control* **4:1** (2020), 1-8. doi:<https://doi.org/10.1177/1077546320923933>.
- [174] BEDON, C., ZHANG, X., SANTOS, F., HONFI, D., KOZOWSKI, M., ARRIGONI, M., FIGULI, L., AND LANGE, D. Performance of structural glass façades under extreme loads-design methods, existing research, current issues and trends. *Construction and Building Materials* **163** (2018), 921-937. doi:<https://doi.org/10.1016/j.conbuildmat.2017.12.153>.

- [175] AMADIO, C., AND BEDON, C. Enhancement of the seismic performance of multi-storey buildings by means of dissipative glazing curtain walls. *Engineering Structures* **152** (2017), 320-334. doi:<https://doi.org/10.1016/j.engstruct.2017.09.028>.
- [176] PIPITONE, G., BARONE, G., AND PALMERI, A. Stochastic design of double-skin façades as seismic vibration absorbers. *Advances in Engineering Software* **142** (2020), 102749. doi:<https://doi.org/10.1016/j.advengsoft.2019.102749>.
- [177] MOON, K.S. Structural design of double skin façades as damping devices for tall buildings. *Procedia Engineering* **14** (2011), 1351-1358. doi:<https://doi.org/10.1016/j.proeng.2011.07.170>.
- [178] FU, T.S., AND ZHANG, R. Integrating double-skin façades and mass dampers for structural safety and energy efficiency. *Journal of Architectural Engineering* **22:4** (2016), 1-12. doi:[https://doi.org/10.1061/\(ASCE\)AE.1943-5568.0000218](https://doi.org/10.1061/(ASCE)AE.1943-5568.0000218).
- [179] PIPITONE, G., BARONE, G., AND PALMERI, A. Optimal design of double-skin façades as vibration absorbers. *Structural Control and Health Monitoring* **25:2** (2018), 1-16. doi:<https://doi.org/10.1002/stc.2086>.
- [180] GONG, Y., CAO, L., LAFLAMME, S., QUIEL, S., RICLES, J., AND TAYLOR, D. Performance evaluation of a variable friction cladding system for seismic hazard mitigation (2016), 1-8.
- [181] HAMEED, A., SALEEM, M., QAZI, A.U., SAEED S., AND BASHIR, M.A. Mitigation of seismic pounding between adjacent buildings. *Pakistan Journal of Science* **64:4** (2012), 326-333.
- [182] GAGNON, L., MORANDINI, M., AND GHIRINGHELLI, G.L. A review of friction damping modeling and testing. *Archive of Applied Mechanics* **90:1** (2020), 107-126. doi:<https://doi.org/10.1007/s00419-019-01600-6>.
- [183] BHASKARARAO, A.V., AND JANGID, R.S. Harmonic response of adjacent structures connected with a friction damper. *Journal of Sound and Vibration* **292:3,5** (2006), 710-725. doi:<https://doi.org/10.1016/j.jsv.2005.08.029>.
- [184] FERRARA, L., FELICETTI, R., TONIOLO, G., AND ZENTI, C. Friction dissipative devices for cladding panels in precast buildings. *European Journal of Environmental and Civil Engineering* **15:9** (2011), 1319-1338. doi:<https://doi.org/10.1080/19648189.2011.9714857>.
- [185] MANEETES, H., AND MEMARI, A.M. Introduction of an innovative cladding panel system for multi-story buildings. *Buildings* **4:3** (2014), 418-436. doi:<https://doi.org/10.3390/buildings4030418>.
- [186] ZHANG, D., SCARPA, F., MA, Y., HONG, J., AND MAHADIK, Y. Dynamic mechanical behavior of nickel-based superalloy metal rubber. *Materials & Design* **56:69,77** (2014), 1980-2015. doi:<https://doi.org/10.1016/j.matdes.2013.10.088>.

- [187] MA, Y., ZHANG, Q., ZHANG, D., SCARPA, F., LIU, B., AND HONG, J. The mechanics of shape memory alloy metal rubber. *Acta Materialia* **96** (2015), 89-100. <https://doi.org/10.1016/j.actamat.2015.05.031>.
- [188] YE, K., LI, L., AND ZHU, H. A note on the Hertz contact model with nonlinear damping for pounding simulation. *Earthquake Engineering & Structural Dynamics* **38**:9 (2009), 1135-1142. doi:<https://doi.org/10.1002/eqe.883>.
- [189] WARNOTTE, V., STOICA, D., MAJEWSKI, S., AND VOICULESCU, M. State of the art in the pounding mitigation techniques. *Intersectii/Intersections* **4**:3 (2007), 102-117.
- [190] POLYCARPOU, P., AND KOMODROMOS, P. Numerical investigation of the effectiveness of rubber shock-absorbers as a mitigation measure for earthquake-induced structural poundings. *Computational Methods in Earthquake Engineering* **30** (2013), 417-436. doi:[10.1007/978-94-007-6573-3_20](https://doi.org/10.1007/978-94-007-6573-3_20).
- [191] STEFANI, G., DE ANGELIS, M., AND ANDREAUS, U. Experimental and numerical investigation of base isolated sdof system impact against bumpers under harmonic base excitation. *Eccomas Procedia COMPDYN* (2019), 3333-3343.
- [192] KOMODROMOS, P. Simulation of the earthquake-induced pounding of seismically isolated buildings. *Computers and Structures* **86** (2008), 618-626. doi:<https://doi.org/10.1016/j.compstruc.2007.08.001>.
- [193] CHAU, K.T., WEI, X.X., GUO, X., AND SHEN, C.Y. Experimental and theoretical simulations of seismic poundings between two adjacent structures. *Earthquake Engineering & Structural Dynamics* **32** (2003), 1-18. doi:<https://doi.org/10.1002/eqe.231>.
- [194] CHAU, K.T., AND WEI, X.X. Pounding of structures modelled as non-linear impacts of two oscillators. *Earthquake Engineering & Structural Dynamics* **30** (2001), 633-651. doi:<https://doi.org/10.1002/eqe.27>.
- [195] MAVRONICOLA, E.A., POLYCARPOU, P.C., AND KOMODROMOS, P. Effect of planar impact modeling on the pounding response of base-isolated buildings. *Frontiers in Built Environment* **2**:11 (2016), 1-16. doi:<https://doi.org/10.3389/fbuil.2016.00011>.
- [196] KHATIWADA, S., CHOUW, N., AND BUTTERWORTH, J.W. A generic structural pounding model using numerically exact displacement proportional damping. *Engineering Structures* **62** (2014), 33-41. doi:<https://doi.org/10.1016/j.engstruct.2014.01.016>.
- [197] MUTHUKUMAR, S. A contact element approach with hysteresis damping for the analysis and design of pounding in bridges. *PhD thesis. Georgia Institute of Technology* (2003).

- [198] STEFANI, G., DE ANGELIS, M., AND ANDREAUS, U. Numerical study on the response scenarios in a vibro-impact single-degree-of-freedom oscillator with two unilateral dissipative and deformable constraints. *Communications in Nonlinear Science and Numerical Simulation* **99** (2021), 1-30.
- [199] ANAGNOSTOPOULOS, S.A. Equivalent viscous damping for modeling inelastic impacts in earthquake pounding problems. *Earthquake Engineering & Structural Dynamics* **33** (2004), 897-902. doi:<https://doi.org/10.1002/eqe.377>.
- [200] KENNETH, H., AND CROSSLEY, E. Coefficient of restitution interpreted as damping in vibroimpact. *Journal of Applied Mechanics* (1975), 440-445. doi:<https://doi.org/10.1115/1.3423596>.
- [201] JANKOWSKI, R. Nonlinear viscoelastic modelling of earthquake-induced structural pounding. *Earthquake Engineering & Structural Dynamics* **34**:6 (2005), 595-611. doi:<https://doi.org/10.1002/eqe.434>.
- [202] ANAGNOSTOPOULOS, S.A., AND SPILIOPOULOS, K.V. An investigation of earthquake induced pounding between adjacent buildings. *Earthquake Engineering & Structural Dynamics* **21**:4 (1992), 289-302. doi:<https://doi.org/10.1002/eqe.4290210402>.
- [203] ANAGNOSTOPOULOS, S.A. Pounding of buildings in series during earthquakes. *Journal of Structural Engineering and Structural Dynamics* **16** (1988), 44-456. doi:<https://doi.org/10.1002/eqe.4290160311>.
- [204] ANAGNOSTOPOULOS, S.A., AND SPILIOPOULOS, K.V. Analysis of building pounding due to earthquakes. *Structural Dynamics* **1** (1991), 479-484.
- [205] NADERPOUR, H., BARROS, R.C., KHATAMI, S.M., AND JANKOWSKI, R. Numerical study on pounding between two adjacent buildings under earthquake excitation. *Shock and Vibration* (2016), 1-9. doi:<https://doi.org/10.1155/2016/1504783>.
- [206] MUTHUKUMAR, S., AND DESROCHES, R. Evaluation of impact models for seismic pounding. *Proceedings of the 13th World Conference on Earthquake Engineering* 235 (2004), 1-11.
- [207] BANERJEE, A., CHANDA, A., AND DAS, R. Historical origin and recent development on normal directional impact models for rigid body contact simulation: a critical review. *Archives of Computational Methods in Engineering* **24**:2 (2017), 397-422. doi:<https://doi.org/10.1007/s11831-016-9164-5>.
- [208] KOMODROMOS, P., POLYCARPOU, P.C., PAPALOIZOU, L., AND PHOCAS, M.C. Response of seismically isolated buildings considering poundings. *Earthquake Engineering & Structural Dynamics* **36** (2007), 1605-1622. doi:<https://doi.org/10.1002/eqe.692>.

- [209] KAJITA, Y., KITAHARA, T., NISHIMOTO, Y., AND OTSUKA, H. Estimation of maximum impact force on natural rubber during collision of two steel bars. *1st European Conference on Earthquake Engineering and Seismology (1st ECEES)* (2006), 3-8.
- [210] GUO, A., CUI, L., AND HUI, L. Impact stiffness of the contact-element models for the pounding analysis of highway bridges: experimental evaluation. *Journal of Earthquake Engineering* **16:8** (2012), 1132-1160. doi:<https://doi.org/10.1080/13632469.2012.693243>.
- [211] MUTHUKUMAR, S., AND DESROCHES, R. A Hertz contact model with non-linear damping for pounding simulation. *Earthquake Engineering & Structural Dynamics* **35** (2006), 811828. doi:<https://doi.org/10.1002/eqe.557>.
- [212] POLYCARPOU, P., KOMODROMOS, P., AND POLYCARPOU, A. A nonlinear impact model for simulating the use of rubber shock absorbers for mitigating the effects of structural pounding during earthquakes. *Earthquake Engineering & Structural Dynamics* **42** (2013), 81-100. doi:<https://doi.org/10.1002/eqe.2194>.
- [213] REZAVANI, A., AND MOGHADAM, A.S. Using shaking table to study different methods of reducing effects of buildings pounding during earthquake. *13th World Conference on Earthquake Engineering* **698** (2004), 1-10.
- [214] ANDREAUS, U., AND DE ANGELIS, M. Influence of the characteristics of isolation and mitigation devices on the response of single-degree-of-freedom vibroimpact systems with two-sided bumpers and gaps via shaking table tests. *Structural Control and Health Monitoring* **27** (2020), 1-21. doi:<https://doi.org/10.1002/stc.2517>.
- [215] STEFANI, G. Experimental and numerical study of vibro-impact systems with two-sided constraints. *PhD thesis. Università degli Studi di Roma La Sapienza* (2021). <http://hdl.handle.net/11573/1549811>.
- [216] MIARI, M., CHOONG, K.K., AND JANKOWSKI, R. Seismic pounding between adjacent buildings: identification of parameters, soil interaction issues and mitigation measures. *Soil Dynamics and Earthquake Engineering* **121** (2019), 135-150. doi:<https://doi.org/10.1016/j.soildyn.2019.02.024>.
- [217] UCAR, H., AND BASDOGAN, I. Dynamic characterization and modeling of rubber shock absorbers: a comprehensive case study. *Journal of Low Frequency Noise, Vibration and Active Control* **37:3** (2018), 509-518. doi:<https://doi.org/10.1177/1461348417725954>.
- [218] MENTE, P., MOTAUNG, T.E., AND HLANGOTHI, S.P. Natural rubber and reclaimed rubber composites: a systematic review. *Polymer Sciences* **2:1,7** (2016), 1-19. doi:[10.4172/2471-9935.100015](https://doi.org/10.4172/2471-9935.100015).

- [219] IBRAHIM, R.A. Friction-induced vibration, chatter, squeal, and chaospart i: mechanics of contact and friction. *Applied Mechanics Reviews* **47:7** (1994), 209-226. doi:<https://doi.org/10.1115/1.3111079>.
- [220] IBRAHIM, R.A. Friction-induced vibration, chatter, squeal, and chaospart ii: dynamics and modeling. *Applied Mechanics Reviews* **47:7** (1994), 227-253. doi:<https://doi.org/10.1115/1.3111080>.
- [221] FERRI, A.A. Friction damping and isolation systems. *Journal of Vibration and Acoustics* **117:b** (1995), 196-206. doi:<https://doi.org/10.1115/1.2838663>.
- [222] BERMAN, A.D., DUCKER, W.A., AND ISRAELACHVILI, J.N. Experimental and theoretical investigations of stick-slip friction mechanisms. *Physics of Sliding Friction* **311** (1996), 51-67. doi:[10.1007/978-94-015-8705-1_3](https://doi.org/10.1007/978-94-015-8705-1_3).
- [223] KIKUWE, R., TAKESUE, N., SANO, A., MOCHIYAMA, H., AND FUJIMOTO, H. Fixed-step friction simulation: from classical coulomb model to modern continuous models. *IEEE/RSJ International Conference on Intelligent Robots and Systems* (2005), 1009-1016. doi:[10.1109/IR05.2005.1545579](https://doi.org/10.1109/IR05.2005.1545579).
- [224] JACOBSON, B. The Stribeck memorial lecture. *Tribology International* **36:11** (2003), 781-789. doi:[https://doi.org/10.1016/S0301-679X\(03\)00094-X](https://doi.org/10.1016/S0301-679X(03)00094-X).
- [225] WOYDT, M., AND WÄSCHE, R. The history of the Stribeck curve and ball bearing steels: The role of Adolf Martens. *Wear* **268:11-12** (2010), 1542-1546. doi:<https://doi.org/10.1016/j.wear.2010.02.015>.
- [226] KARNOPP, D. Computer simulation of stick-slip friction in mechanical dynamic systems. *Journal of Dynamic Systems, Measurement, and Control* **107:1** (1985). doi:[10.1115/1.3140698](https://doi.org/10.1115/1.3140698).
- [227] DEN HARTOG, J.P. LXXIII. Forced vibrations with combined viscous and coulomb damping. *The London, Edinburgh, and Dublin Philosophical Magazine and Journal of Science* **9:59** (1930), 801-817. doi:<https://doi.org/10.1080/14786443008565051>.
- [228] SHAW, S.W. On the dynamic response of a system with dry friction. *Journal of Sound and Vibration* **108:2** (1986), 305-325. doi:[https://doi.org/10.1016/S0022-460X\(86\)80058-X](https://doi.org/10.1016/S0022-460X(86)80058-X).
- [229] YEH, G.C.K. Forced vibrations of a twodegreeoffreedom system with combined Coulomb and viscous damping. *The Journal of the Acoustical Society of America* **39:14** (1966). doi:<https://doi.org/10.1121/1.1909863>.
- [230] MARINO, L., AND CICIRELLO, A. Dynamic response of multi-degree-of-freedom systems with a Coulomb friction contact under harmonic excitation. *Nonlinear Dynamics* **106** (2021), 16751709. doi:<https://doi.org/10.1007/s11071-021-06966-3>.

- [231] DOWNEY, A., SADOUGHI, M., CAO, L., LAFLAMME, S., AND HU, C. Passive variable friction damper for increased structural resilience to multi-hazard excitations. *International Design Engineering Technical Conferences and Computers and Information in Engineering Conference* (2018), 1-9. doi:<https://doi.org/10.1115/DETC2018-85207>.
- [232] DIMOVA, S., MESKOURIS, K., AND KRÄTZIG, W.B. Numerical technique for dynamic analysis of structures with friction devices. *Earthquake Engineering & Structural Dynamics* **24**:6 (1995), 881-898. doi:<https://doi.org/10.1002/eqe.4290240607>.
- [233] PELLACINI, F. *Fondamenti di programmazione in Python* (2016).
- [234] THOMPSON, W.T. *Theory of vibration with applications* (second edition). *George Allen & Unwin LTD* (1981). doi:<https://doi.org/10.1201/9780203718841>.
- [235] GAVARINI, C. *Dinamica delle strutture*. *Editoriale ESA* (1978).
- [236] CRAIG JR, R.R., AND KURDILA, A.J. *Fundamentals of structural dynamics*. *John Wiley & Sons* (2006).
- [237] PAZ, M., AND KIM, Y.H. *Structural dynamics. Theory and Computations* (2019).
- [238] YANG, J.H., SANJUÁN, M.A., AND LIU, H.G. Vibrational subharmonic and superharmonic resonances. *Communications in Nonlinear Science and Numerical Simulation* **30**:1,3 (2016), 362-372. doi:<https://doi.org/10.1016/j.cnsns.2015.07.002>.
- [239] DENKOWSKI, Z., MIGÓRSKI, S., AND PAPAGEORGIOU, N.S. *An introduction to nonlinear analysis: theory*. *Springer Science & Business Media* (2013).
- [240] KLIGERMAN, Y. Multiple solutions in dynamic contact problems with friction. *International Joint Tribology Conference* **37068** (2003), 5-12. doi:<https://doi.org/10.1115/2003-TRIB-0257>.
- [241] FYRILLAS, M.M., AND SZERI, A.J. Control of ultra-and subharmonic resonances. *Journal of Nonlinear Science* **8**:2 (1998), 131-159. doi:<https://doi.org/10.1007/s003329900046>.
- [242] THOMPSON, J.M.T., AND STEWART, H.B. *Nonlinear dynamics and chaos*. *John Wiley & Sons* (2002).
- [243] TOLSTOI, D.M. Significance of the normal degree of freedom and natural normal vibrations in contact friction. *Wear* **10**:3 (1967), 199-213. doi:[https://doi.org/10.1016/0043-1648\(67\)90004-X](https://doi.org/10.1016/0043-1648(67)90004-X).
- [244] NAYFEH, A.H. The response of single degree of freedom systems with quadratic and cubic non-linearities to a subharmonic excitation. *Journal of Sound and Vibration* **89**:4 (1983), 457-470. doi:[https://doi.org/10.1016/0022-460X\(83\)90347-4](https://doi.org/10.1016/0022-460X(83)90347-4).

- [245] KOSTEK, R. Analysis of the primary and superharmonic contact resonances part 1. *Journal of Theoretical and Applied Mechanics* **51**:2 (2013), 475-486.
- [246] LI, Q.S., YANG, K., WONG, C.K., AND JEARY, A.P. The effect of amplitude-dependent damping on wind-induced vibrations of a super tall building. *Journal of Wind Engineering and Industrial Aerodynamics* **91**:9 (2003), 1175-1198. doi:[https://doi.org/10.1016/S0167-6105\(03\)00080-1](https://doi.org/10.1016/S0167-6105(03)00080-1).
- [247] BURTON, M.D. Effects of low frequency wind-induced building motion on occupant comfort. PhD thesis. Hong Kong University of Science and Technology (2006). doi:10.14711/thesis-b924350.
- [248] FABRIZI, A. Impiego di sistemi innovativi di protezione sismica per edifici alti esistenti. Master's thesis. Università degli Studi di Roma La Sapienza (2019).
- [249] GRIFFIS, L.G. Serviceability limit states under wind load. *Engineering Journal* (1993), 1-16.
- [250] BASHOR, R., KIJEWski-CORREA, T., AND KAREEM, A. On the wind-induced response of tall buildings: the effect of uncertainties in dynamic properties and human comfort thresholds. *Proceedings of Americas Conference on Wind Engineering*, **31** (2005).
- [251] MALHOTRA, A., ROY, T., AND MATSAGAR, V. Effectiveness of friction dampers in seismic and wind response control of connected adjacent steel buildings. *Shock & Vibration* (2020), 1-21. doi:<https://doi.org/10.1155/2020/8304359>.
- [252] KWON, D., AND KAREEM, A. NatHaz on-line wind simulator (NOWS): simulation of Gaussian multivariate wind fields. *NatHaz Modeling Laboratory Report* (2006). <http://windsim.ce.nd.edu/>.
- [253] MICHELI, L., ALIPOUR, A., LAFLAMME, S., AND SARKAR, P. Performance-based design with life-cycle cost assessment for damping systems integrated in wind excited tall buildings. *Engineering Structures* **195** (2019), 438-451. doi:<https://doi.org/10.1016/j.engstruct.2019.04.009>.
- [254] BALTAY, P., AND GJELSVIK, A. Coefficient of friction for steel on concrete at high normal stress. *Journal of Materials in Civil Engineering* **2**:1 (1990), 46-49. doi:[https://doi.org/10.1061/\(ASCE\)0899-1561\(1990\)2:1\(46\)](https://doi.org/10.1061/(ASCE)0899-1561(1990)2:1(46)).
- [255] ALLIEVI, L., FERRERO, S., MUSSI, A., PERSIO, R., AND PETRELLA, F. Structural and geotechnical design of a piled raft for a tall building founded on granular soil. *Proceedings of the 18th International Conference on Soil Mechanics and Geotechnical Engineering* (2013), 2659-2661.
- [256] LONGARINI, N., AND CRESPI, P.G. Analisi al vento della torre Isozaki-Maffei in Citylife a Milano modellazione attraverso Midas Gen.

- [257] TRABUCCO, D. Torre Isozaki di Citylife a Milano: tutto sulle strutture. *Council of Tall Buildings and Urban Habitat*.
- [258] CASTELLANO, M.G., BORELLA, R., PIGOUNI, A.E., AND INFANTI, S. Wind and earthquake damping system for the Isozaki/Allianz Tower in Milan, Italy. *ce/papers*, 1:2,3 (2017), 1447-1456. doi:<https://doi.org/10.1002/cepa.187>.
- [259] LONGARINI, N. Alti edifici: problematiche strutturali. In: *Evoluzione nel mondo delle costruzioni* (2010), 365-385. <http://hdl.handle.net/11311/981880>.
- [260] FINZI, B., AND ROSSINI, L. Le strutture metalliche di una grande opera civile: la torre Isozaki.
- [261] CRESPI, P., AND LONGARINI, N. Analisi al vento dei nuovi alti edifici di Milano. *Atti dell'XI Convegno Nazionale di Ingegneria del Vento, IN-VENTO-2010* (2010), 1-17.
- [262] PIZZOLATO, F. Studio del comfort negli edifici alti soggetti all'azione del vento. *Master's thesis. Università degli Studi di Padova* (2015).
- [263] BIAGI, M. Non è solo bella: la torre Allianz a Milano di IsozakiMaffei. *Casabella* **855**, 4-17.
- [264] SCAVINO, G. Curtain wall design: the seismic behaviour of glazing façades. Master's thesis. Politecnico di Milano (2014). <http://hdl.handle.net/10589/94309>.
- [265] EUROPEAN COMMITTEE FOR STANDARDIZATION. Eurocode 1: Actions on structures - general actions. part 1-4: Wind actions. *CEN, EN 1991-1-4* (2005).